

AD-A081 883

COLORADO UNIV AT BOULDER DEPT OF ASTRO-GEOPHYSICS

F/0 20/9

PLASMA WAVE TURBULENCE AND PARTICLE HEATING CAUSED BY ELECTRON --ETC(U)

NOV 79 M V GOLDMAN

F49620-76-C-0005

UNCLASSIFIED

CU-1036

AFOSR-TR-80-0167

NL

1-6

AD-A081 883

AD-A081 883

AD-A081 883

AD-A081 883

AD-A081 883

AD-A081 883

AD-A081 883

AD-A081 883

AD-A081 883

AD-A081 883

AD-A081 883

AD-A081 883

AD-A081 883

AD-A081 883

AD-A081 883

AD-A081 883

AD-A081 883

AD-A081 883

AD-A081 883

AD-A081 883

AD-A081 883

AD-A081 883

AD-A081 883

AD-A081 883

AD-A081 883

AD-A081 883

AD-A081 883

AD-A081 883

AD-A081 883

AD-A081 883

AD-A081 883

AD-A081 883

AD-A081 883

AD-A081 883

AD-A081 883

AD-A081 883

AD-A081 883

AD-A081 883

AD-A081 883

AD-A081 883

AD-A081 883

AD-A081 883

AD-A081 883

AD-A081 883

AD-A081 883

UNCLASSIFIED

SECURITY CLASSIFICATION OF THIS PAGE (When Data Entered)

REPORT DOCUMENTATION PAGE		READ INSTRUCTIONS BEFORE COMPLETING FORM
1. REPORT NUMBER AFOSR-TR- 80-0167	2. GOVT ACCESSION NO.	3. RECIPIENT'S CATALOG NUMBER
4. TITLE (and Subtitle) PLASMA WAVE TURBULENCE AND PARTICLE HEATING CAUSED BY ELECTRON BEAMS, RADIATION AND PINCHES		5. TYPE OF REPORT & PERIOD COVERED Final
		6. PERFORMING ORG. REPORT NUMBER
7. AUTHOR(s) Martin V Goldman		8. CONTRACT OR GRANT NUMBER(s) F49620-76-C-0005^{law}
9. PERFORMING ORGANIZATION NAME AND ADDRESS Department of Astro-Geophysics University of Colorado Boulder, CO 80309		10. PROGRAM ELEMENT, PROJECT, TASK AREA & WORK UNIT NUMBERS 61102F 2301/A7
11. CONTROLLING OFFICE NAME AND ADDRESS AFOSR/NP Bolling AFB, Bldg. #410 Wash DC 20332		12. REPORT DATE Nov 1979
		13. NUMBER OF PAGES 526
14. MONITORING AGENCY NAME & ADDRESS (if different from Controlling Office)		15. SECURITY CLASS. (of this report) unclassified
		15a. DECLASSIFICATION/DOWNGRADING SCHEDULE
16. DISTRIBUTION STATEMENT (of this Report) Approved for public release; distribution unlimited.		
17. DISTRIBUTION STATEMENT (of the abstract entered in Block 20, if different from Report)		
18. SUPPLEMENTARY NOTES		
19. KEY WORDS (Continue on reverse side if necessary and identify by block number)		
20. ABSTRACT (Continue on reverse side if necessary and identify by block number) For electron beams, a theory of the dynamics of driven Langmuir wave turbulence was developed. In low density beams, Langmuir wave evolution was found to be governed by nonlinear index of refraction effects, and associated self-focusing, rather than by wave reaction back on the beam. In laser-plasma interactions, the nonlinear theoretical work was verified experimentally in collaboration with Dr. N. Peacock of Culham Laboratories. In an experiment on nonlinear interactions of a carbon dioxide laser with a dense plasma focus device, almost		

UNCLASSIFIED

SECURITY CLASSIFICATION OF THIS PAGE (When Data Entered)

100 percent anomalous absorption of the radiation was observed, along with intense Langmuir turbulence. The results were published in Physical Review Letters. A classical theory of the Raman-induced Kerr effect was developed. A computer code was developed to help determine plasma temperatures, radiation, impurity distributions, and overall plasma evolution in Z-pinch plasmas.

UNCLASSIFIED

(12)

AIR FORCE OFFICE OF SCIENTIFIC RESEARCH

(9) FINAL REPORT. 1 Aug 76-1 Oct 79,

August 1, 1976 to October 1, 1979

(6)

Plasma Wave Turbulence and Particle Heating
Caused by Electron Beams, Radiation and Pinches.

(10)

Martin V. Goldman Principal Investigator

Contract (15) F49620-76-C-0005

CU #1036

(11)

November 1979

1533122

(12) 528

(14) 1-1036

(16) 2341 (17) A7

(18) AFSCR (19) TR-80-0167

DTIC
ELECTE
MAR 17 1980
S D C

AIR FORCE OFFICE OF SCIENTIFIC RESEARCH (AFSC)
NOTICE OF TECHNICAL INFORMATION
This report is the property of the AFSC and is
applicable to the AFSC and is
Distribution is unlimited.
A. D. ENOCH
Technical Information Officer

088425

43

TABLE OF CONTENTS

	PAGE
I. INTRODUCTION	1
II. ACCOMPLISHMENTS AND COLLABORATIONS	4
A. Publications and Ph.D. Theses	4
B. Miscellaneous Topics Currently Under Preparation for Publication	12
C. Invited and Contributed Talks	15
D. Conferences Organized	19
REFERENCES	20
APPENDICES	22

CU 1036
November 1979

Accession For	
NTIS GRA&I	<input checked="checked" type="checkbox"/>
DDC TAB	<input type="checkbox"/>
Unannounced	<input type="checkbox"/>
Justification	
By _____	
Distribution/ _____	
Availability Codes	
Dist	Available for special
A	

LIST OF APPENDICES

- A. "Radiation from a Strongly Turbulent Plasma: Application to Electron Beam Excited Solar Emissions," M. V. Goldman, G. F. Reiter, and D. R. Nicholson, Phys. Fluids 23, 1980; preprint.
- B. "Dimensionality and Dissipation in Langmuir Collapse," M. V. Goldman, K. Rypdal, and B. Hafizi, accepted for publication in Physics of Fluids; preprint.
- C. "Parametric Instabilities in Weakly Magnetized Plasma," J. C. Weatherall, M. V. Goldman, and D. R. Nicholson, submitted to Astrophysical Journal; preprint.
- D. "A Statistical Theory of Langmuir Turbulence," D. F. DuBois, H. A. Rose, and M. V. Goldman, Journal de Physique, Colloque #7, Suppl. #7, Tome 40, pg. 601 (1979); preprint.
- E. "Two Examples of the Decay Instability in an Inhomogeneous Plasma," T. H. Rudolph, Ph.D. Thesis, University of Colorado, 1979; draft.
- F. "Effects of Impurity Radiation on Reversed-Field Pinch Evolution," and "The Numerical Solution of the Multi-Fluid, Quasi-Equilibrium MHD Equations in One Dimension," E. J. Caramana, Ph.D. Thesis, University of Colorado, 1979.
- G. "Comparison of Raman Induced Kerr Effect (RIKE) with Incoherent Scatter (INSC) in a Plasma," M. V. Goldman, Memorandum to R. Hellwarth and N. Peacock, October 1978.
- H. "Plasmon-Plasmon Interactions," D. F. DuBois and M. V. Goldman, Phys. Rev. Lett. 40, 1978; reprint.
- I. "Nonlinear Langmuir Waves During Type III Solar Radio Bursts," D. R. Nicholson, M. V. Goldman, P. Hoyng, and J. C. Weatherall, Astrophys. J. 223, 605 (1978); reprint.
- J. "Virial Theory of Direct Langmuir Collapse," M. V. Goldman and D. R. Nicholson, Phys. Rev. Lett. 41, 406 (1978); reprint.
- K. "Cascade and Collapse of Langmuir Waves in Two Dimensions," D. R. Nicholson and M. V. Goldman, Phys. Fluids 21, 1766 (1978); reprint.
- L. "Absorption of CO₂ Laser Light by a Dense, High Temperature Plasma," N. J. Peacock, N. J. Forrest, P. D. Morgan, M. V. Goldman, T. Rudolph, and A. A. Offenberger, Journal de Physique, Colloque C6, Tome 38, 43 (1977); reprint.

I. Introduction

This report describes work performed under AFOSR Contract #F49620-76-C-0005 during the period August 1, 1976 to October 1, 1979. The subject of research has been the theory of "Plasma Wave Turbulence and Particle Heating Caused by Electron Beams, Radiation, and Pinches." The period covered is the first three years of a comprehensive research program concerned with the nonlinear behavior of plasmas subjected to intensely energetic sources.

One of the significant developments in plasma physics over the past decade has been the theoretical and experimental progress made in our understanding of nonlinear plasma wave evolution in response to external sources: A wide variety of radiation sources such as lasers,^{1,2} microwaves,^{3,4} and radar,^{5,6} and of electron beam sources such as solar electron streams^{7,8} and laboratory beams⁹ can excite plasma wave instabilities in target plasmas. The waves saturate into a turbulent spectrum¹⁰ and may heat the plasma, accelerate plasma particles, and/or emit their own radiation. Such processes have been linked to inertial¹¹ and magnetic¹² controlled thermonuclear fusion schemes, radar communications in the earth's ionosphere, and type III solar radio bursts^{7,8}. The phenomena also bear heavily on certain fundamental questions of plasma turbulence, such as wave collapse in phase space, electric-field envelope-soliton evolution,^{13,14} and the nature of so-called "strong turbulence."¹³

Over the past three years we have achieved major advances in the three subject areas of our contract research: electron beams, radiation, and plasma pinch devices.

In connection with electron beams, we have developed a theory of the dynamics of driven Langmuir wave turbulence. Such turbulence controls beam stability, plasma radiation, particle heating and transport phenomena, for a class of high velocity, electron beams. In low density beams, Langmuir wave evolution was found to be governed by nonlinear index of refraction effects, and associated self-focusing, rather than by wave reaction back on the beam (quasilinear effects). We have verified such behavior numerically, developed an analytical theory, and found approximate estimates and bounds for the radiation from such electron beams. Our results compare favorably with measurements of volume emissivity of electromagnetic radiation from Langmuir turbulence driven by electron beams of solar origin.^{15,16} (Also, see Appendices A, B, C, D, I, J, and K of this report.) Recently, megawatts of radiation around the plasma frequency were also measured from higher density relativistic beams in laboratory plasmas,¹⁷ lending an extra significance to this line of research.

In the area of laser-plasma interactions, we have demonstrated the experimental significance of our nonlinear theoretical research in a collaboration with Dr. N. Peacock, of Culham Laboratories. Peacock's experiment on nonlinear interactions of a CO₂ laser with a dense plasma focus device,

was undertaken at our suggestion. Almost 100% anomalous absorption of the radiation was observed, along with intense Langmuir turbulence. These results, and theoretical analysis of the intensity of Langmuir turbulence, are described in a joint Physical Review Letter,² subsequent publications,¹⁸ and a Ph.D. thesis by Mr. T. Rudolph (see Appendix E).

We have also made advances in the area of laser-plasma diagnostics. A classical theory of the Raman-induced Kerr effect (RIKE) has been developed (see Appendix G). It exhibits the advantage of the coherent RIKE diagnostic over incoherent scattering, as an optical diagnostic in a high density plasma.

The third area of research supported under this contract has to do with atomic physics and transport processes in high beta Z-pinchs. This research has now been completed in the form of a Ph.D. thesis by Mr. E. Caramana (see Appendix F). The computer code developed by Mr. Caramana will help determine plasma temperatures, radiation, impurity distributions, and overall plasma evolution in Z-pinch plasmas such as the reversed field Z-pinch and plasma focus devices.

II. Accomplishments and Collaborations

Our accomplishments under Air Force sponsorship can best be described within the categories of publications, presentations, collaborations, and other research. Below, we list items under these categories, with a brief description of the nature and significance of the research. The list is in reverse chronological order, beginning with the new results of the period 10/1/78-9/30/79 (items A.1 to A.6, B.1 to B.3 and C).

A. Publications and Ph.D. Theses

1. "Radiation From a Strongly Turbulent Plasma: Application to Electron Beam Excited Solar Emissions,"
Martin V. Goldman, George F. Reiter*, and Dwight R. Nicholson,
Phys. Fluids 23, 1980 [attached as Appendix A].

This work represents a new theory of electromagnetic emission induced in plasmas by high velocity, low density electron beams. The electron beam causes Langmuir waves to grow in the plasma. At a threshold wave energy density which can be a small fraction of the beam energy density, the Langmuir wave packets begin to self-focus and quickly collapse spatially, due to field-dependent index of refraction effects. Transverse nonlinear currents associated with the electrostatic Langmuir waves cause radiation to be emitted at the plasma frequency and its first harmonic. In this paper, we

*Consultant, supported by AFOSR.

have used self-similar solutions for the collapsing Langmuir fields to calculate the current strengths. A crude statistical theory of the volume density of collapsing packets then enables us to estimate the volume emissivity for radiation. These estimates are consistent with observations of second harmonic radiation from almost relativistic electron beams of solar origin. Intense fundamental radiation is also predicted. This work may impact on recent laboratory experiments¹⁷ performed at the University of California at Irvine, in which relativistic electron beams are observed to produce up to 10 megawatts of radiation power at frequencies around 100 Ghz. Such emission may be a powerful diagnostic relating to beam-plasma interactions.

2. "Dimensionality and Dissipation in Langmuir Collapse," M. V. Goldman, K. Rypdal, and B. Hafizi, accepted for publication in *Physics of Fluids* [attached as Appendix B].

This paper contains a myriad of new results concerning the collapse of Langmuir waves. The self-similar form assumed in our emissivity calculation is here studied numerically in accessible parameter regimes. In the regime of adiabatic ions and three-dimensional spherical symmetry about a wave packet with non-zero momentum, the collapse is seen to quickly approach self-similar form, even for initial energies only slightly above threshold. We also obtain the effects of Langmuir wave collision damping on the collapse threshold, and prove some interesting analytical results about

one-dimensional pulsating solitons. This paper contains results about the dynamical behavior of Langmuir wave evolution which could be extremely significant and relevant to strong Langmuir turbulence excited by electron or radiation beams.

3. "Parametric Instabilities in Weakly Magnetized Plasma," J. C. Weatherall*, M. V. Goldman, and D. R. Nicholson, submitted to Astrophysical Journal, 1979 [attached as Appendix C].

Our earlier work on beam excited Langmuir turbulence neglected guiding magnetic fields. This paper studies the effects of a weak magnetic field on the wave-wave interactions associated with Langmuir collapse. It is found that even a weak magnetic field tends to make the instability more one-dimensional, and can suppress the forward cone of modulational instabilities altogether. This work is significant for its influence on subsequent studies of magnetic collapse by our group and others. Weak magnetic fields may inhibit or distort Langmuir collapse and turbulence due to beams (currently under study).

4. "A Statistical Theory of Langmuir Turbulence," D. F. DuBois**, H. A. Rose, and M. V. Goldman, Journal de Physique, Colloque #7, Suppl. #7, Tome 40, pg. 601 (1979) [attached as Appendix D].

*Ph.D. student supported by AFOSR.

**Consultant supported by AFOSR.

This work is concerned with a statistical treatment of the (Zakharov) equations which govern nonlinear Langmuir wave dynamics such as soliton formation in one dimension (or collapse, in two or more dimensions). The method is a generalization of the well-known direct-interaction approximation (DIA) used in Navier-Stokes theory of neutral fluids. The problem is formulated in this paper in a manner which is amenable to further numerical computation. The physics of the self-focusing instability is identified for the first time in a statistical theory. This research area is important because a knowledge of the Langmuir wave correlation functions is essential to an understanding of their role in transport phenomena and particle heating. Also, the statistical approach offers the possibility of finding "averaged" general properties of the nonlinear phenomena occurring in strong Langmuir turbulence.

5. "Two Examples of the Decay Instability in an Inhomogeneous Plasma," T. H. Rudolph, Ph.D. thesis, University of Colorado, 1979 [attached as Appendix E].

This work represents a first draft of the Ph.D. thesis of Terence Harvey Rudolph, who has been supported by the present AFOSR contract since 1976. It consists of detailed numerical and analytical work concerning the Langmuir turbulence excited by intense radiation in plasmas with density gradients. Two examples are treated: radio waves in the ionosphere and CO_2 radiation incident on a dense plasma focus

device. In the former case electron cyclotron damping is taken into account, when the HF radio wave is near twice the electron cyclotron frequency. The theory is relevant to ionospheric modification experiments¹⁹ conducted in 1972-3. In the CO₂ laser case, an application is made to the scattering experiment of Peacock, et al.^{2,18}. We find qualitative agreement with Peacock's scattering measurements of turbulent electron density correlations near the plasma frequency. The thesis is concerned mainly with the convective nature of parametric instabilities. Langmuir wave packets grow only while they are in the intense radiation field and satisfy the momentum (index) matching conditions.

6. "Effects of Impurity Radiation on Reversed-Field Pinch Evolution," "The Numerical Solution of the Multi-Fluid, Quasi-Equilibrium MHD Equations in One Dimension," Ph.D. thesis of Edward J. Caramana, 1979 [attached as Appendix F].

This is the final version of the Ph.D. thesis of E. Caramana, who has been supported by the present AFOSR contract since 1976. The influence of impurity ion radiation on the evolution of a reversed-field pinch plasma is studied by means of a one-dimensional, MHD simulation code that includes both plasma transport and impurity effects. Radiation barriers are encountered, and limits are found in the acceptable level of low Z impurities that may be present if meaningful heating is to occur. A criterion for radiation

barrier burn-through is derived. Also, thermal instabilities in the reversed field pinch are explored. It is found that current perturbations remaining from this pinch formation phase can be greatly enhanced by the presence of impurity cooling.

7. "Plasmon-Plasmon Interactions," D. F. DuBois* and M. V. Goldman, Phys. Rev. Lett. 40, 1978 [attached as Appendix H].

This paper represents a spin-off of our research on the statistical theory of nonlinear Langmuir wave evolution. It is concerned with whether or not a "bound state" of two plasmons can occur, due to the nonlinear interaction corresponding to the ponderomotive force. Our conclusion was that such a state may be marginally achievable in a degenerate semiconductor plasma and might be observable. These results now appear to be relevant to strong plasma turbulence induced by beams.

8. "Nonlinear Langmuir Waves During Type III Solar Radio Bursts," Dwight R. Nicholson, Martin V. Goldman, Peter Hoyng, and James C. Weatherall,** Astrophys. J. 223, 605 (1978) [attached as Appendix I].

In this paper we first showed numerically how electron beams can directly produce Langmuir wave collapse and turbulence. The model Zakharov equations for a Langmuir electric field driven by the beam were solved in two dimensions (the

*Consultant supported by AFOSR.

**Student supported by AFOSR.

minimum number of dimensions needed for collapse to be present). The beams chosen for study were those of solar origin, at velocities about one-third the speed of light and beam density about 10^{-6} times the background plasma density. Such beams are known to produce electromagnetic emission near the plasma frequency and its first harmonic. Both linear instability and collapse thresholds were studied. Langmuir packets were first observed to grow linearly due to beam instability and then decouple from the beam and rapidly collapse when their energy density exceeds threshold. This behavior should contribute to beam stability, since this wave energy density for collapse is low compared to the beam energy density. This work led to an analytical theory presented in the next paper:

9. "Virial Theory of Direct Langmuir Collapse," M. V. Goldman and D. R. Nicholson, Phys. Rev. Lett. 41, 406 (1978) [attached as Appendix J].

In this Physical Review Letter, a general virial theorem was proven, without any assumption of special symmetries, and used to calculate the threshold and time for direct collapse of a two-dimensional Langmuir wave packet of the type driven by certain types of electron beams. The analysis is shown to apply to "bump-on-tail" beam instabilities, when the "bump" is broad, low, and at high velocity. The analytic theory was shown to be in very good agreement with our earlier numerical analysis.

10. "Cascade and Collapse of Langmuir Waves in Two Dimensions," Dwight R. Nicholson and Martin V. Goldman, Phys. Fluids 21, 1766 (1978) [attached as Appendix K].

This paper is mostly numerical, and applies to hotter plasmas, in which the Langmuir waves have a larger group velocity, and become more intense. The virial theorem of the previous Letter does not apply because the ions can no longer be treated as adiabatic. We observe various nonlinear wave phenomena, including one important scenario which has long been a subject of speculation in the Soviet literature and elsewhere, but has never been shown to occur: A slow cascade of energy to longer scale lengths (smaller wave numbers), followed by a fast spatial collapse to short scales. This work is again intrinsically two-dimensional.

11. "Absorption of CO₂ Laser Light by a Dense, High Temperature Plasma," N. J. Peacock, M. J. Forrest, P. D. Morgan, M. V. Goldman, T. Rudolph, and A. A. Offenberger, Journal de Physique, Colloque C6, Tome 38, 43 (1977) [attached as Appendix L].

The interaction between a pulsed CO₂ laser beam and the plasma produced in a focus device is investigated theoretically and experimentally. The beam is grossly affected by the plasma, and absorption during the compressed pinch phase, when the plasma frequency exceeds the CO₂ frequency, is much more complete than can be predicted by classical resistivity.

Enhanced density fluctuations at the Langmuir frequency were measured directly by forward scattering from a probe ruby laser beam, and found to be a factor of 30 above the thermal level. A WKB treatment of the electron-ion decay instability, including convection in the inhomogeneous plasma is reasonably consistent with the observations (also see Appendix E for a more complete version of the theory).

B. Miscellaneous Topics Currently Under Preparation for Publication

1. "Break-Up and Reconstitution of Langmuir Wave Packets in Two Dimensions," T. Tajima, J. N. LeBoef, J. M. Dawson, and M. V. Goldman.

This work represents a first attempt to study ponderomotive force nonlinearities of Langmuir wave packets in homogeneous two-dimensional particle-in-cell simulation. At our suggestion, the U.C.L.A. plasma numerical studies group studied the evolution of an initial coherent Langmuir wave packet of Gaussian shape. We found the unexpected phenomenon of periodic packet break-up and reconstitution, with a time period inversely proportional to the initial packet energy density. Thus far, a satisfactory quantitative theory of the recurrence has proven elusive, although a heuristic explanation is possible. The packet is below the threshold for direct collapse, so there is no contradiction with our previous results concerning collapse. This work is currently

being prepared for submission as a Physics of Fluids Research Note.

2. "Thermal Self-Focusing of Finite Width Microwave Beams in the Ionosphere," M. V. Goldman and R. Perkins.

This research is concerned with the effects of intense radiation on the ionosphere. It is particularly relevant to schemes to transmit to earth via microwaves, the energy collected by photo-voltaic cells on board geostationary satellites (this is the so-called solar-power-satellite or S.P.S., concept). It represents a collaboration begun with Prof. R. Perkins, of Princeton, in July 1979. We have studied thermal-self-focusing instabilities driven by the microwave beam. Such instabilities correspond to self-consistent density motions, and their effect on the index of refraction seen by the beam. They are driven by the Joule heating term in the electron temperature equations rather than by ponderomotive force (as in the Langmuir wave self-focusing instabilities). The Joule heating causes thermal conduction along magnetic field lines. The resulting density fluctuations are capable of producing striations in the original beam. We have taken into account the finite width of the beam (as an eigenvalue problem), and saturation in the steady state striation problem (via Joule heating nonlinearity). It was found that the thermal self-focusing instability can be induced in the F region of the ionosphere using present-day HF radar facilities, and should also be present for the SPS microwave beam. Experiments to test this theory are currently underway.

3. "Raman-Induced Kerr Effect--A New Laser Plasma Diagnostic," M. V. Goldman and R. Hellwarth [see attached memorandum, Appendix G].

The idea of the Raman-Induced Kerr effect is as follows: A plasma irradiated by a broadband laser is put between cross polarizers. No plasma wave "signal" is transmitted by this probe until a second, circularly polarized, narrowband laser is turned on, at which time a strong coherent signal is detected. This signal carries imprinted upon it the spectrum of plasma collective modes, and can yield valuable information concerning electron beam or laser excited wave turbulence.

We have developed a theory of this effect, based on the physics of ponderomotive force. It exhibits the potential advantage of the Raman-Induced Kerr effect (RIKE) over incoherent scattering, as an optical diagnostic in a high density plasma. The signal from RIKE is theoretically predicted to be stronger than that from incoherent scatter by a factor of about 10^6 , due to coherence effects. While Appendix G does not take plasma inhomogeneity effects into account, recent work we have performed shows the advantage of RIKE can still be as great as 10^6 . We are still hoping to explicitly incorporate magnetic field effects, before publishing the work in this memorandum.

This diagnostic is currently being employed by Dr. Peacock of Culham Laboratories to measure plasma wave turbulence in the plasma focus device.

There is considerable interest within the plasma physics community concerning our theoretical development of RIKE. After our presentation at the American Physical Society Meeting in Colorado Springs we were approached by numerous experimentalists seeking potential applications of RIKE to magnetic plasmas. Among them were Prof. H. C. Praddaude, of MIT National Magnet Lab, who is seeking a diagnostic for the toroidal device ALCATOR, and Dr. P. Forman, of Los Alamos Scientific Laboratory, who is seeking a diagnostic for a dense pinch device. In the case of ALCATOR, typical plasma densities are between 10^{14} and 10^{15} , temperatures between one and two keV, and magnetic fields between 50-100 kG. We are hoping to explore the suitability of laboratory plasmas such as these for the RIKE diagnostics.

C. Invited and Contributed Talks (Chronological Order)

1. "Absorption of CO_2 Laser Light by a Dense, High Temperature Plasma," N. J. Peacock, M. J. Forrest, M. V. Goldman, A. A. Offenberger; invited talk presented in Brechtsgaden, Germany, October 6, 1976; Sixth Conference on Plasma Physics and Controlled Nuclear Fusion Research, paper number IAEA-CN-35/G4-4.

2. " CO_2 -Excited Langmuir Turbulence in a Dense Plasma Focus," presented by M. Goldman as a contributed talk at the 18th Annual Meeting of the Division of Plasma Physics of the American Physical Society, San Francisco, 11-76 (#1-G-5).

3. "Langmuir Shock with Landau Damping," D. R. Nicholson and M. V. Goldman, 18th Annual Meeting of the Division of Plasma Physics of the American Physical Society, San Francisco, November 1976 (#8-B-7).
4. "Electron Plasma Wave Instabilities in Type III Solar Radio Bursts," M. V. Goldman and D. R. Nicholson, 149th Meeting of the American Astronomical Society, Honolulu, Hawaii, January 18, 1976 (#17.13.03).
5. "Nonlinear Theory of Type III Radio Bursts," D. R. Nicholson, P. Hoyng, and M. V. Goldman, Meeting on Solar and Interplanetary Physics, Tucson, Arizona, January 12, 1977.
6. "Two-Dimensional Nonlinear Evolution of Parametric Instabilities," D. R. Nicholson and M. V. Goldman, Anomalous Absorption Conference, Ann Arbor, Michigan, May 18, 1977.
7. "Electromagnetic Radiation from a Strongly Turbulent Plasma Due to Soliton Collapse," G. Reiter, M. V. Goldman, and D. R. Nicholson, American Physical Society Annual Meeting, Plasma Physics Division, Atlanta, Georgia, November 1977.
8. "Nonlinear Langmuir Waves During Type III Solar Radio Bursts," J. Weatherall, D. R. Nicholson, M. V. Goldman, and G. Reiter, American Physical Society Annual Meeting, Plasma Physics Division, Atlanta, Georgia, November 1977.
9. "Nonlinear Langmuir Waves in Two and Three Dimensions," M. V. Goldman and D. R. Nicholson, American Physical Society Annual Meeting, Plasma Physics Division, Atlanta, Georgia, November 1977.

10. "Beam-Induced Langmuir Wave Collapse," M. V. Goldman, Culham Laboratories, England, October 19, 1977.
11. "Direct Collapse of Langmuir Waves," M. V. Goldman, Imperial College, London, October 1977.
12. "Type III Solar Radio Bursts," M. V. Goldman, Imperial College, London, November 1977.
13. "Virial Theory of Direct Collapse," M. V. Goldman, Winter School on Turbulence, Observatoire de Nice, France, January 13, 1978.
14. "Beam Induced Langmuir Wave Collapse," M. V. Goldman, two talks given at U.C.L.A., March 1978.
15. "Nonlinear Langmuir Waves," D. R. Nicholson and M. V. Goldman, National Radio Science Meeting, Boulder, Colorado, January 1978.
16. "Type III Solar Radio Wave Emission by Strong Plasma Turbulence," invited talk given by M. Goldman at the NASA/JPL Workshop in Planetary and Astrophysical Magnetospheres, Snowmass, Colorado, August 1, 1978.
17. "Raman-Induced Kerr Effect--A New Laser-Plasma Diagnostic," M. V. Goldman and R. W. Hellwarth, American Physical Society Annual Meeting, Plasma Physics Division, Colorado Springs, November 1978; Bull. Am. Phys. Soc. 23, 893 (1978).
18. "Statistical Theories of the Zakharov Equations for Langmuir Turbulence," H. Rose, D. F. DuBois, M. Espedal, M. V. Goldman, and D. R. Nicholson, Ann. Phys. Soc. Meeting,

Colorado Springs, November 1978; Bull. Am. Phys. Soc. 23, 298 (1978).

19. "Numerical Study of Strong Langmuir Trubulence," D. F. Nicholson, M. V. Goldman, D. F. DuBois, and G. Reiter, Ann. Phys. Soc. Meeting, Colorado Springs, November 1978; Bull. Am. Phys. Soc. 23, 892 (1978).

20. "Modulational and Parametric Langmuir Wave Instabilities in a Weakly Magnetized Plasma," J. Weatherall, M. V. Goldman, and D. R. Nicholson, Ann. Phys. Soc. Meeting, Colorado Springs, November 1978; Bull. Am. Phys. Soc. 23, 787 (1978).

21. "Soliton Radiation During Type III Solar Bursts," G. Reiter, M. V. Goldman, and D. R. Nicholson, Ann. Phys. Soc. Meeting, Colorado Springs, November 1978; Bull. Am. Phys. Soc. 23, 783 (1978).

22. "Nonlinear Langmuir Waves During Type III Solar Radio Bursts," D. R. Nicholson, M. V. Goldman, T. Van Grunsven, P. Hoyng, G. Reiter, T. Rudolph, and J. Weatherall, International Symposium on Solar-Terrestrial Physics, Innsbruck, Austria, June 1978.

23. "Nonlinear Langmuir Waves," D. R. Nicholson and M. V. Goldman, National Radio Science Meeting, Boulder, Colorado, January 1978.

24. "A Statistical Theory of Langmuir Turbulence," D. F. DuBois, H. Rose, and M. V. Goldman, XIV Conference Internationale sue les Phenomenes d'Ionisation dans les Gaz, Grenoble, France, July 9-13, 1979.

25. "Nonlinear Evolution of Intense Langmuir Waves in a Homogeneous Plasma," M. V. Goldman, University of California at Los Angeles, February 1978.

26. "Collapse of Langmuir Wave Packets," M. V. Goldman, University of California at Los Angeles, March 1978.

27. "Nonlinear Plasma Waves and Electromagnetic Emission," M. V. Goldman, University of Southern California, May 1978.

28. "Raman-Induced Kerr Effect," M. V. Goldman, University of California at Irvine, January 1979.

29. "Nonlinear Plasma Waves and Electromagnetic Emission," M. V. Goldman, University of California at Irvine, January 1979.

30. "Plasmon-Wave Solitons in Solar Radio Emission," M. V. Goldman, University of Colorado, April 1979.

31. "Langmuir Turbulence Driven by Electron Beams," M. V. Goldman, Aspen Center for Physics, June 1979.

D. Conferences Organized

Professor Goldman was the organizer and chairman of an international workshop at the Aspen Center Physics held in June 1979, on the topic, "Fundamental Problems in Plasma Physics." The research sponsored by this contract was the subject of extensive discussion and collaboration at this workshop.

References

1. S. Jackel, B. Perry, and M. Lubin, Phys. Rev. Lett. 37, 95 (1976).
2. M. J. Forrest, P. D. Morgan, N. J. Peacock, K. Kuriki, M. V. Goldman, and T. Rudolph, Phys. Rev. Lett. 37, 1681 (1976).
3. R. P. H. Chang, M. Prokolab, and B. Grek, Phys. Rev. Lett. 28, 206 (1972).
4. R. Stenzel and A. Y. Wong, Phys. Rev. Lett. 28, 274 (1972).
5. F. W. Perkins and P. K. Kaw, J. Geophys. Res. 76, 282 (1971).
6. H. C. Carlson, W. E. Gordon, and R. L. Showen, J. Geophys. Res. 77, 1242 (1972).
7. K. Papadopoulos, G. L. Goldstein, and R. Smith, Astrophys. J. 190, 1242 (1972).
8. S. Bardwell and M. V. Goldman, Astrophys. J. 209, 912 (1976).
9. A. Y. Wong and B. H. Quon, Phys. Rev. Lett. 34, 1499 (1975).
10. D. F. DuBois and M. V. Goldman, Phys. Rev. Lett. 28, 218 (1972).
11. P. K. Kaw and J. M. Dawson, Phys. Fluids 12, 2585 (1969); D. W. Forslund, et al., Phys. Rev. Lett. 36, 35 (1975).
12. W. M. Hooke and S. Barnabei, Phys. Rev. Lett. 29, 1281 (1972).
13. V. E. Zakharov, Sov. Phys. JETP 35, 908 (1972).
14. G. J. Morales and Y. C. Lee, Phys. Fluids 19, 690 (1976).
15. D. A. Gurnett and R. R. Anderson, Science 194, 1159 (1976).
16. M. V. Goldman, G. F. Reiter, and D. R. Nicholson, Physics of Fluids, January 1980.

17. Experiments of G. Benford, University of California at Irvine, 1978-1979.
18. D. F. DuBois, H. A. Rose, and M. V. Goldman, Journal de Physique, Colloque #7, Suppl. #7, Tome 40, pg. 601 (1979).
19. P. A. Fialer, Radio Sci. 9, 923 (1974).

APPENDIX A

"Radiation from a Strongly Turbulent Plasma:
Application to Electron Beam-Excited Solar Emissions"

Physics of Fluids

January 1980

Martin V. Goldman, George F. Reiter, and Dwight R. Nicholson

CU 1036

November 1979

August 1979

Radiation from a strongly turbulent plasma:
Application to electron beam-excited solar emissions

Martin V. Goldman

Department of Astro-Geophysics, University of Colorado,
Boulder, Colorado 80309

George F. Reiter

Physics Department, Brookhaven National Laboratory,
Upton, New York 11973

Dwight R. Nicholson

Department of Physics and Astronomy, University of Iowa,
Iowa City, Iowa 52242

The emission of radiation at the plasma frequency and at twice the plasma frequency from beam-excited strong Langmuir turbulence, for the case of low-density high-velocity warm beams is considered. Under these conditions, Langmuir wave packets undergo (direct) collapse in a time short compared with one e folding of a beam mode. The wave packet energy density threshold for collapse depends only on the beam temperature and velocity, not on the beam density. Upper and lower limits on the volume emissivity for harmonic emission from these collapsing wave packets are found. Within most of this range, the emissivity is large enough to account for observations of second harmonic radiation during type III solar radio wave bursts. The radiation at the fundamental is many orders of magnitude larger than predicted by weak turbulence theory.

I. Introduction

In this paper we treat the emission of radiation from collapsing Langmuir wave packets excited by an electron beam of high velocity and low density. Emission rates at the plasma frequency, ω_p , and the first harmonic, $2\omega_p$, are calculated for a non-magnetic plasma with parameters appropriate to the solar wind plasma during so-called type III solar radio wave emission. The parameter space for Langmuir collapse and subsequent radiation is very rich, and many distinctly different phenomena can occur under different conditions. We believe the work of this paper deals with one of the simplest cases (possessing significant measured data), and probably has at least qualitative significance to other regimes of strong Langmuir turbulence.

The subject of type III solar radio-wave emission provides a unique arena for the interaction of modern nonlinear plasma physics with space physics. In this paper we shall show that conditions are commonly found in the solar wind, during type III bursts, when highly nonlinear evolution of electron plasma waves (Langmuir waves) can occur. This evolution can take the form of spatial "collapse"^{1,2} of Langmuir wave-packets of initially very low energy density. The collapse is essentially a nonlinear index-of-refraction effect, in which Langmuir waves are

confined by ponderomotive force, and intensify and steepen in an unstable manner which can only be stopped by eventual dissipation of energy into resonant electrons. A plasma in this condition is said to be "strongly turbulent."

The emission of electromagnetic waves from the collapsing Langmuir wave packets is estimated in this paper using various dynamical and statistical models. Most of these lead to favorable comparisons with recent observations by Gurnett and Anderson³ at $\frac{1}{2}$ AU. We believe that previous attempts⁴ at calculating this emission have been inconsistent (see Sec. VI).

One result of increasingly sophisticated and far-reaching experiments in space has been the establishment of a firmer foundation for the basic physics of type III bursts. There is now general agreement that an electron beam is launched during a flare event on the sun, and that as this beam propagates out in the solar wind along a magnetic field line, it excites Langmuir waves, which in turn produce radiation at the local plasma frequency and at its first harmonic. As the beam propagates from the sun to the earth and beyond, it encounters local plasma frequencies which progressively decrease by more than four orders of magnitude. The measured radiation shows this characteristic drop in frequency as a function of time. Spacecraft experiments on board satellites have detected the electron beam, Langmuir wave, and the emitted radiation, although the data on Langmuir waves have been rare, and difficult to obtain. A sketch of the events associated with a type III burst is depicted in Fig. 1. Measurements have been

made from the earth-orbiting satellites,^{5,6} IMP6, 8, and from the solar-orbiting satellites,³ HELIOS 1, 2.

Our concern in this paper is mainly with the emissivity measurements obtained by Gurnett and Anderson³ at twice the local plasma frequency near HELIOS 1 (near 0.5 AU). In the strongest burst observed by them (March 31, 1976, 18:10 U.T.), a radiation intensity of $10^{-17} \text{ W m}^{-2} \text{ Hz}$ was measured. This leads to a volume emissivity (assuming isotropic emission) of⁷

$$J(2\omega_p) = 1.6 \times 10^{-23} \text{ ergs cm}^{-3} \text{ s}^{-1} \text{ ster}^{-1} . \quad (1)$$

Langmuir waves were observed simultaneously, with an energy density (in units of the background particle energy density, $nk_B T$) of

$$W \equiv \frac{\langle |\mathcal{E}|^2 \rangle}{4\pi n k_B T} \approx 1.4 \times 10^{-5} . \quad (2)$$

These Langmuir waves generally occurred as "spikes" with characteristic dimensions of 25-100 km or larger. (Structures of smaller size, such as the collapsing Langmuir wave packets discussed in this paper, would be too small to have been detected by the HELIOS spacecraft.) The background plasma parameters associated with these measurements were $n_e = 42$ electrons per cm^3 , and $k_B T_e = 10 \text{ eV}$ ($T_e = 1.2 \times 10^5 \text{ }^\circ\text{K}$). We shall use these parameters in our calculations.

The plan of this paper will be as follows:

In Sec. II we shall treat the excitation of Langmuir waves by a typical electron beam associated with type III bursts and show how the beam determines the shape and spatial density of Langmuir wave packets up to the time at which their energy density begins to exceed the collapse threshold.

Section III is devoted to the subsequent collapse, and describes how a steady state is set up in which the beam acts as a source of energy density, and resonant wave-particle interaction (Landau damping) acts as a dissipative sink. Conditions for stabilizing the beam against quasilinear plateau formation are also discussed here. The similarity solutions for collapsing wave packets in the adiabatic and supersonic regimes are presented.

In Sec. IV (and in the Appendix) we discuss the general problem of emission of electromagnetic waves by the nonlinear currents associated with Langmuir waves. It is shown that harmonic emission cannot be of lower order than quadrupole. Emission cannot occur from the beam-driven Langmuir waves without some form of nonlinear saturating wave interactions because of kinematical constraints. We estimate the harmonic and fundamental emission that occurs in the later stages of collapse by using similarity solutions and constants of the motion to approximate the Fourier transform of the emitting currents.

Calculation of the volume emissivity requires that we know (on the average) how many collapsing wave packets are present per unit volume. Models for this "density of collapsing packets" are developed in Sec. V, based on energy conservation in the steady state power flow associated with Langmuir waves. The volume emissivity is calculated and compared with the measured value.

In Sec. VI we present detailed criticisms of other work on strong turbulence emissivity. In the Appendix we explain why the collapsing wave packets are mainly longitudinal.

II. Excitation of Langmuir Waves by the Beam

We shall assume a simple model of the electron beam and the background plasma. The beam will be assumed to be stationary, spatially homogeneous, and having a Gaussian distribution in velocity space centered around $v_b \approx c/2$, with an isotropic half-width, $\Delta v \approx v_b/3$:

$$f_b(v) = \frac{n_b \exp[-(v-v_b)^2/2\Delta v]}{(2\pi\Delta v^2)^{3/2}}, v_b \approx \frac{c}{2}, \quad \frac{\Delta v}{v_b} = \frac{1}{3}. \quad (3)$$

The beam density will be taken to be no greater than 10^{-6} times the background electron density, n_e :

$$n_b/n_e \lesssim 10^{-6}. \quad (4)$$

The background plasma is assumed to be a Maxwellian with density $n_e = 42$, and temperature 10 eV, as in the experiments at $\frac{1}{2}$ AU of Gurnett and Anderson.³ This implies that $n_b \leq 4.2 \times 10^{-5} \text{ cm}^{-3}$, and $v_e/v_b \approx 9 \times 10^{-3}$, where $v_e = (k_B T_e/m_e)^{1/2}$ is the electron thermal velocity associated with one degree of freedom.

We note that the assumption of a time-stationary beam is an approximation. Since the beam is injected with velocity dispersion at the site of a flare, the faster electrons will arrive downstream before the slower ones so that v_b (and possibly Δv) are functions of time. The effects of this on the excited Langmuir waves were studied by Magelssen and Smith,⁸ who took into account reabsorption of Langmuir waves by the beam, and determined that the beam could propagate over large distances. A relatively low level of Langmuir waves resulted ($W \approx 10^{-4}$). However, the time scale for such effects is long compared with a collapse time, and we have ignored such space-time variation of the beam.

In this paper we show that Langmuir energy densities on the order of $W \approx 10^{-4}$ are unstable against spatial collapse. These energy densities are a small fraction of the beam energy unless n_b/n_e is much smaller than 10^{-6} . This justifies the neglect of the change in the beam due to homogeneous quasi-linear beam relaxation. Since the process of spatial collapse takes energy out of resonance with the beam, we can also view collapse as a potential mechanism for stabilizing the beam against plateau formation.

The beam distribution of Eq. (3) causes the growth of a \underline{k} -space wave packet of Langmuir waves, centered around the wave vector \underline{k}_0 , which satisfies the Cerenkov condition,

$$\underline{k}_0 \approx \omega_p \hat{v}_b / v_b, \quad (5a)$$

or

$$\frac{k_0}{k_D} = \frac{v_e}{v_b} = 9 \times 10^{-3}. \quad (5b)$$

The resulting growth rate of resonant Langmuir waves is,

$$\frac{\gamma_B}{\omega_p} = \left(\frac{\pi}{8}\right)^{\frac{1}{2}} \frac{n_b}{n_0} \left(\frac{v_b}{\Delta v}\right)^2 \frac{k_0^2}{k_{||}^2 + k_{\perp}^2} Z \exp(-Z^2/2), \quad (6)$$

where

$$Z \equiv (v_b / \Delta v) (k_{||} - k_0) / k_{||}. \quad (7)$$

We note that the background magnetic field has been neglected in Eq. (6). This is completely justified, since the ratio of electron cyclotron frequency to plasma frequency is small (see Sec. VI).

The fastest growing Langmuir waves have $k_{||} = \theta(k_0)$, and $k_{\perp} = 0$. We will determine the \underline{k} -space shape of the Langmuir wave packet determined by Eq. (6). At a given time, t , the wave energy system will have been amplified by the factor $A(\underline{k}) \equiv \exp[2\gamma_B(\underline{k})t]$. We determine the half-widths by the condition $A(\underline{k}_0 + \Delta \underline{k}) = A(\underline{k}_0)/2$. The parallel and perpendicular half-widths are therefore obtained from the following equation

$$\gamma_B(\underline{k}_0 \pm \Delta \underline{k}) / \gamma_B(\underline{k}_0) = 1 - \ln 2 / \ln A(\underline{k}_0). \quad (8)$$

Choosing $A(k_o) = 2 \times 10^4$ (10 e foldings), yields,

$$\frac{\Delta k_{\perp}}{k_o} = \left(\frac{\ln 2}{\ln A} \right)^{\frac{1}{2}} \approx \frac{1}{4}, \quad (9a)$$

$$\frac{\Delta k_{\parallel}}{k_o} = \left(\frac{\ln 2}{\ln A} \right)^{\frac{1}{2}} \frac{\Delta v}{v_b} \approx \frac{1}{4} \frac{\Delta v}{v_b}. \quad (9b)$$

We note that the perpendicular half-width, $\Delta k_{\perp}/k_o$, is determined entirely from the factor $k_o^2/(k_{\parallel}^2 + k_{\perp}^2)$ in Eq. (6), while the parallel half-width, $\Delta k_{\parallel}/k_o$, is determined entirely from the factor $2 \exp(-Z^2/2)$. The shape of the k-space wave packet is therefore elongated in the perpendicular directions, producing a kind of pancake, as shown in the two-dimensional projection in Fig. 2.

This model assumes the amplification of spatially homogeneous noise, so that the convective nature of the beam instability is irrelevant. We also note, in this connection, that a typical excursion distance of a Langmuir wave packet in the perpendicular direction (during a collapse time) is 1 km, whereas the perpendicular spatial width of the electron beam has been measured⁵ to be at least 80 earth radii. This justifies the neglect of the finite spatial width of the beam in our treatment.

The phases of the Fourier modes in the beam-unstable Langmuir wave packet will be random, since we have assumed it is homogeneous white noise being amplified. This leads to a multitude of wave packets in real space, with mean spatial half-widths of $\Delta x_{\parallel} \approx (\Delta k_{\parallel})^{-1}$, and $\Delta x_{\perp} \approx (\Delta k_{\perp})^{-1}$, as depicted

in Fig. 2. For the parameters considered here, a typical real-space packet measures about 3 by 10 km. This would be too small a packet to be measured by current spacecraft techniques³ at 1/2 AU. We shall assume the mean distance between wave packets to be on the order of this mean size.

This will constitute our picture of Langmuir waves while they are subject to beam growth, but before they have reached the critical intensity for nonlinear wave-wave interactions. We should remark, in passing, that the beam contribution to the dispersion relation of the Langmuir waves is negligible because $n_b/n_e \lesssim 10^{-6}$ [inequality (4)].

III. Langmuir Wave Collapse

The electron beam creates the configuration of real-space Langmuir wave packets just described. The packets grow in time. When one of these packets is sufficiently intense, it can collapse "directly,"² in a time which is fast compared with one beam growth e folding time. This process has recently been discussed at length by two of the present authors.^{2,9}

A. Predictions of the Virial Theorem for Initially
Adiabatic Collapse

In brief, the threshold for collapse of a wave packet depends simply on its k-space widths (in the limit when its group velocity is less than sound speed, and assuming that its energy density is sufficiently less than the mass ratio). The critical energy density for an anisotropic wave packet is a slight generalization of the result in Ref. 2,

$$W_{th} = 24 \frac{(\Delta k_{||})^2 + (\Delta k_{\perp})^2}{k_D^2}, \quad (10)$$

provided that

$$W \ll 16 \, m/M, \quad (11a)$$

and,

$$\frac{k_o^2}{k_D^2} \ll \frac{2}{9} \frac{m}{M}, \quad (11b)$$

where W is the energy density defined in Eq. (1), m/M is the electron to ion mass ratio, Δk is the k-space half-width of the packet, and k_D is the wave number. The inequalities (11) are the

conditions for adiabatic ions. In the later stages of collapse the ion inertia becomes important, and the inequalities (11) are strongly violated. However, the threshold condition (10) is justifiably adiabatic. From Eqs. (5) and (9) we have

$$\begin{aligned}\Delta k_{\perp}/k_D &= 2.2 \times 10^{-3}, \\ \Delta k_{\parallel}/k_D &= 7.5 \times 10^{-4}.\end{aligned}\tag{12}$$

The larger of these dominates in Eq. (10), and

$$W_{th} \approx 10^{-4}.\tag{13}$$

The adiabatic condition (11a) is then seen to be well-satisfied, but (11b) is only marginally satisfied. Nevertheless, numerical calculations⁹ indicate the validity of this description under the present circumstances.

Next, we note that the energy W_{th} represents a small fraction of the energy density in the electron beam, when $n_b/n_e \approx 10^{-6}$. Under these circumstances

$$W_b \equiv \frac{n_b v_b^2}{n_e \Theta_e} \approx 10^{-2},\tag{14}$$

hence, the wave-wave interactions inherent in collapse occur before the wave-particle interactions governing homogeneous beam plateau formation. Since the wave energy of resonant modes never becomes comparable to the beam energy, the collapse process would seem to suppress quasilinear plateau formation!

We also note that W_{th} is independent of the beam density n_b , whereas W_{beam} decreases with n_b . Hence, for n_b/n_e significantly smaller than 10^{-6} , it is likely that collapse will be prohibited because not enough energy is available in the beam to elevate the waves to threshold energy. Measurements indicate that 10^{-6} is probably an upper limit for type III bursts.

These facts also help guarantee that the collapse time is shorter than a beam growth time. The collapse time predicted from virial theorem arguments² is

$$\omega_p t_v = 4 \left[\sqrt{3} \frac{\Delta k}{k_D} (W - W_{th})^{\frac{1}{2}} \right]^{-1}. \quad (15)$$

(Near threshold, this is of the same order as the collapse time associated with similarity solutions¹.) A typical value for t_v is about 0.1 sec, compared with about 1 sec for γ_B^{-1} . For n_b/b_e less than 10^{-6} the beam instability will be even slower.

A model for steady state must go farther, and follow the power injected by the beam to its ultimate dissipation in the plasma. Our qualitative picture of this process is exhibited in Fig. 3. Here, the "state" of a Langmuir wave packet is characterized by two parameters: its energy density W , and the square of a characteristic spatial half-width Δx (in units of the Debye length). These two parameters form a kind of two-dimensional phase space for Langmuir wave packets. Packets above the dashed line are subject to collapse, according to Eq. (10). Due to the beam instability, a wave packet executes a trajectory in the phase space, as illustrated in Fig. 3. Packets of a

size set by the beam parameters [Eq. (9)] grow until they exceed threshold. They then quickly collapse to smaller size and larger W . This collapse becomes supersonic when the adiabatic conditions (11) are violated. We assume that the collapse continues until Δx becomes on the order of about 5 Debye lengths, and that the collapse then ceases, with power flowing into electrons due to wave particle interaction. The power balance this implies will be treated explicitly in Sec. V. We note from Fig. 3 that the packet size decreases by two orders of magnitude, and its energy density increases from 10^{-4} at threshold, to order unity when Landau damping can occur.

In the adiabatic regime, above threshold, the Langmuir wave evolution should be accurately described² by the cubic nonlinear Schrödinger equation

$$i\partial_{\bar{t}}\bar{\mathcal{E}} + \frac{1}{2}\bar{v}^2\bar{\mathcal{E}} + |\bar{\mathcal{E}}|^2\bar{\mathcal{E}} = 0, \quad (16)$$

here, $\bar{t} = \omega_p t$, $\bar{r} = rk_D/\sqrt{3}$, and $\bar{\mathcal{E}}$ is the dimensionless envelope of the plasma oscillations. The total real Langmuir wave field, E_L , is given, in physical units in terms of the envelope $\bar{\mathcal{E}}$ as

$$E_L = \text{Re} \left[(32\pi n)^{\frac{1}{2}} (\theta_e + \theta_i)^{\frac{1}{2}} \bar{\mathcal{E}} \exp(-i\omega_p t) \right]. \quad (17)$$

In the early adiabatic stages of collapse, the evolution of a given initial wave packet can be described by virial theorem arguments.² In addition to the threshold, W_{th} [Eq. (10)], and the collapse time, t_v [Eq. (15)], these arguments predict the dependence of the square width, $\langle \delta r^2 \rangle$, of the packet, on time,

$$\langle \delta r^2 \rangle = \langle \delta r^2 \rangle_0 \times (1 - t^2/t_v^2) , \quad (18a)$$

and also the dependence of the energy density, if one assumes that the shape of the packet remains Gaussian

$$W(t) \propto \langle \delta r^2 \rangle^{-D/2} , \quad (18b)$$

where D is the number of spatial dimensions of Eq. (16).

B. Adiabatic Similarity Solution

In the later stages of adiabatic collapse, it is likely that the packet has distorted in shape and has begun to approach the shape of the similarity solution.¹ The similarity solution is of the form

$$\bar{\epsilon} = (\bar{t}_a - \bar{t})^{-1/2} \underline{R}(\underline{u}) , \quad (19a)$$

$$\underline{u} \equiv \underline{r}/(\bar{t}_a - \bar{t})^{1/2} . \quad (19b)$$

When (19) is inserted into (16), an ordinary differential equation for \underline{R} results

$$\frac{1}{2} (1 + \underline{u} \cdot \partial_{\underline{u}}) \underline{R} + \frac{1}{2} \partial_{\underline{u}}^2 \underline{R} + |\underline{R}|^2 \underline{R} = 0 . \quad (19c)$$

We can arbitrarily set $|\underline{R}|$ to be of order unity at its maximum. Then, we find that the collapse time of the adiabatic similarity solution is

$$\omega_p t_a = 8 W^{-1} , \quad (20a)$$

where we have assumed the spatial average $\langle |\bar{\epsilon}|^2 \rangle = |\bar{\epsilon}_{\max}|^2/2$.

Note, this differs from the virial theorem prediction, although when W is several times W_{th} , they are numerically close.

(In essence, the similarity solution does not "remember" initial scale lengths, such as Δk^{-1} .) From (19a) we also get a prediction from the similarity solution about how W varies with time

$$W_s(t) = \frac{W(0)}{(\bar{t}_a - \bar{t})} . \quad (20b)$$

This is in agreement with (18b) only in two dimensions. Also, the half-width of the collapsing self-similar solution can be much narrower than $\langle \delta r^2 \rangle$.

C. Supersonic Similarity Solution

As W increases, the collapse becomes supersonic, in the sense that the inequality (11a) is violated. At this time, the cubic nonlinear Schrödinger equation, (16), no longer provides a correct description, and we must employ the so-called Zakharov² equations, which allow for ion inertial effects, and electromagnetic dispersion.¹⁰ These equations may be written as

$$\left(i \partial_{\bar{t}} \tilde{\epsilon} + \tilde{\nabla} \cdot \tilde{\nabla} + \frac{c^2}{3v_e^2} \tilde{\nabla} \times \tilde{\nabla} \times - \frac{\tilde{n}}{2} \right) \tilde{\epsilon} = 0 , \quad (21a)$$

$$(\partial_{\bar{t}}^2 - \beta \tilde{\nabla}^2) \tilde{n} = \tilde{\nabla}^2 |\tilde{\epsilon}|^2 , \quad (21b)$$

where, \tilde{n} is the ion density fluctuation, and the dimensionless units are¹⁰

$$\tilde{t} = \frac{2}{3} \frac{m}{M} \omega_p t , \quad \tilde{\mathbf{r}} = \frac{2}{3} \left(\frac{m}{M} \right)^{\frac{1}{2}} \mathbf{r} k_D ,$$

$$\tilde{n} = \frac{3}{2} \frac{M}{m} \frac{\delta n}{n_0} , \quad \beta \equiv 1 + \frac{\gamma_i \theta_i}{\theta_e} , \quad (22)$$

where m/M is the electron-to-ion mass ratio, and γ_i is the usual ratio of ion specific heats. The real electric field of the Langmuir waves in physical units in terms of the dimensionless

envelope $\tilde{\mathcal{E}}$ is

$$\underline{E}_L = \text{Re} \left[\left(\frac{m}{M} \right)^{\frac{1}{2}} (32\pi n_0/3)^{\frac{1}{2}} \tilde{\mathcal{E}} \exp(-i\omega_p t) \right] . \quad (23)$$

in the extreme supersonic limit, only the $\partial_{\tilde{t}}^2$ term need be retained on the left side of Eq. (16). Equations (21) then have a well-known three-dimensional (supersonic) similarity solution,^{10,11} given by

$$\tilde{\mathcal{E}} = \frac{1}{\tilde{t}_s - \tilde{t}} \underline{R}(\underline{u}) , \quad \underline{u} = \frac{\tilde{r}}{(\tilde{t}_s - \tilde{t})^{2/3}} ,$$

$$\tilde{n} = \frac{1}{(\tilde{t}_s - \tilde{t})^{4/3}} \underline{\eta}(\underline{u}) , \quad (24)$$

where \tilde{t}_s is the supersonic collapse time, and $|\underline{R}|$ is again chosen to have a maximum equal to unity. This implies that the time for supersonic collapse is given (in real units), by

$$\omega_p t_s = \left(\frac{m}{3M} W_{so} \right)^{-\frac{1}{2}} , \quad (25a)$$

where W_{so} is the value of $\mathcal{E}_{\max}^2/8\pi n_0$ at the time supersonic collapse begins. If the supersonic stage follows an initially adiabatic collapse, as we are assuming here, we can roughly take $W_{so} \approx 16 m/M$ [from (11a)], so that

$$\omega_p t_s = \left(\frac{3}{16} \right)^{\frac{1}{2}} \frac{M}{m} . \quad (25b)$$

We shall use these similarity solutions later to calculate the emission from collapsing Langmuir waves. There is numerical

evidence that certain initial field configurations relax into similarity solutions,¹⁰⁻¹² but the analytical foundations for why this is so remain largely unknown. It is also useful to note that the dimensionless dispersion collapse time \tilde{t}_s is simply $(12)^{-1/2}$.

In summary, the role of Langmuir collapse is indicated in the energy flow diagram in Fig. 4. Most of the electron stream energy remains intact during its propagation from the sun. A small fraction of this energy [see Eqs. (10) and (14)] goes into Langmuir waves due to the bump-on-tail instability. Some of the resulting Langmuir wave packets collapse due to nonlinear wave interactions. During the collapse, a small fraction of the Langmuir energy is radiated away, mainly at $2\omega_p$. However, most of the Langmuir energy is eventually dissipated by coupling to electrons and ions in the late stages of collapse, which we do not treat explicitly in this paper.

It is important to note that a strong conversion of the Langmuir waves into (transversely-polarized) radiation is not expected, because the parameter $c^2/3v_e^2$ is much greater than one, and the early fields are entirely longitudinal. This matter is discussed in some detail in the Appendix. In the next section we treat the conversion into radiation by familiar techniques for given current distributions, and obtain expressions for the emission from a single collapsing Langmuir wave packet.

IV. Emissivity of Radiation from Langmuir Wave Packets

The transverse nonlinear currents, \underline{j}^{nl} , associated with (longitudinal) Langmuir waves can lead to emission of radiation at $2\omega_p$ and at ω_p . We assume a model of independent emissions associated with the current of each of an assembly of Langmuir wave packets. The emissivity of a given wave packet is then a simple function of the nonlinear current \underline{j}^{nl} . By standard techniques, we find

$$\frac{dP}{d\Omega} = \frac{c r^2}{4\pi} \frac{1}{T} \int_0^T dt \underline{E} \times \underline{B} = \frac{\hat{r}}{4\pi c^2 T} \int_{-\infty}^{+\infty} \frac{d\omega}{2\pi} \omega K |\underline{j}^{nl}(\underline{K}, \omega)|^2 \sin^2 \phi, \quad (26)$$

where \underline{r} is a position vector from the current distribution to an observation point in the radiation zone, the wave vector \underline{K} is defined as $\underline{K} = (\hat{r}/c) [\omega^2 - \omega_p^2(\underline{r})]^{1/2}$, and ϕ is the angle between $\underline{j}^{nl}(\underline{K}, \omega)$ and \hat{r} . Equation (26) takes into account the fact that the observation point is imbedded in the plasma with a local plasma frequency $\omega_p(\underline{r})$ which varies on the scale of an AU.

The geometry is illustrated in Fig. 5. Note, the factor $\sin^2 \phi$ guarantees that only the transverse component of the current contributes to the emission. The time average is over a time T which is long compared with the dominant frequency, ω_0 (T may be set equal to the collapse time).

We are interested in nonlinear currents centered about a dominant frequency, ω_0

$$\underline{j}^{nl}(\underline{r}, t) = \frac{1}{2} \underline{j}^{nl}(\underline{r}, t) \exp(-i\omega_0 t) + \text{c.c.} , \quad (27)$$

where the time-dependence of the envelope $\underline{j}^{nl}(\underline{r}, t)$ is slow on the scale of ω_0^{-1} . Making use of this slowness, Eq. (26) can be expressed in terms of the envelope current as

$$\frac{dP}{d\Omega} \approx \frac{K_0 \omega_0 \sin^2 \phi_0}{8\pi c^2} \frac{1}{T} \int_0^T dt |\underline{j}^{nl}(\underline{k}_0, t)|^2 , \quad (28a)$$

where

$$\underline{k}_0 \equiv \frac{\hat{r}}{c} [\omega_0^2 - \omega_p^2(\underline{r})]^{1/2} , \quad (28b)$$

is the principal wave vector of the emitted radiation, and $\omega_p(\underline{r})$ is the plasma frequency at the observation point. Also, ϕ_0 is the angle between \hat{r} and $\underline{j}^{nl}(\underline{k}_0, \omega = 0)$.

We now need to develop expressions for the appropriate nonlinear currents. These currents arise from the beating of first or second order electron density fluctuations with the velocity of electrons oscillating in the Langmuir field.

The current which gives rise to emission at the plasma frequency is third order in the Langmuir field

$$4\pi \partial_{t-\omega_p} \underline{j}^{nl}(\underline{r}, t) = \omega_p^2 \frac{\delta n_2}{n_0} \underline{E}_L , \quad (29)$$

where δn_2 is the density driven by the ponderomotive force in Eq. (21b), and hence second order¹³ in the Langmuir field, \underline{E}_L . The relationship between δn_2 and the dimensionless n is given in Eq. (22c). We note that, although \underline{E}_L is entirely longitudinal, the product $\delta n_2 \underline{E}_L$ has a transverse component, in general. Also note that in the adiabatic limit δn_2 reduces simply to $-|\vec{E}|^2$ [see Eq. (16)].

The current at $2\omega_p$ is second order in the Langmuir field, \underline{E}_L

$$4\pi\partial_t J_{2\omega_p}^{nl}(\underline{r}, t) = \omega_p^2 \frac{2\delta n_1}{n_0} \underline{E}_L. \quad (30a)$$

Here, δn_1 is the first order density of electrons oscillating at the plasma frequency. (The factor 2 arises because the emission frequency is $2\omega_p$.) An expression for δn_1 follows immediately from Poisson's equation for the Langmuir field, \underline{E}_L ,

$$n_1 = -\nabla \cdot \underline{E}_L / 4\pi e. \quad (30b)$$

A. Emission at $2\omega_p$

It is easy to prove that there can be no dipole emission at $2\omega_p$. The standard multipole expansion for $j^{nl}(\underline{k}, t)$ is generated by writing the spatial Fourier transform of the current in terms of the Kronecker delta, $\delta_{\ell m} = \nabla_m r_\ell$:

$$j_\ell^{nl}(\underline{k}, t) = \int d^3\underline{r} (\nabla_m r_\ell) j_m^{nl}(\underline{r}, t) \exp(-i\underline{k} \cdot \underline{r}) \quad (31)$$

In the dipole approximation, $\underline{k} \cdot \underline{r}$ is set equal to zero. After an integration by parts and application of the continuity equation, this yields $j^{nl}(\underline{k}, t) \sim -i\omega_0 \underline{d}$, where \underline{d} is the dipole moment of the nonlinear charge density distribution. Hence, whenever the spatial integral of $j^{nl}(\underline{r}, t)$ vanishes, there is no dipole emission. We can show ^{that} this is the case for harmonic emission by using Eqs. (30) for the nonlinear current $J_{2\omega_p}^{nl}$. If $\underline{E}_L = \text{Re}[\underline{\mathcal{E}} \exp(-i\omega_p t)]$, then $J_{2\omega_p}^{nl} = \text{Re}[j_2^{nl} \exp(-2i\omega_p t)]$, where the envelope,

$j_{2\omega_p}(\underline{r})$ is proportional to $(\underline{\nabla} \cdot \underline{\mathcal{E}}) \underline{\mathcal{E}}$, from Eq. (30). Since $\underline{\mathcal{E}}$ is predominantly curl-free (see the Appendix), there follows the vector identity,

$$j_{2\omega_p}^{nl}(\underline{r}, t)_\ell = \frac{-ie/m}{4\pi\omega_p} \nabla_i (\mathcal{E}_i \mathcal{E}_\ell - \delta_{i\ell} \underline{\mathcal{E}} \cdot \underline{\mathcal{E}}/2) . \quad (32)$$

Hence, $\int d^3\underline{r} j_{2\omega_p}^{nl}$ vanishes, by the divergence theorem, and there is no dipole emission at $2\omega_p$.

To find the emissivity for harmonic emission in terms of the field $\underline{\mathcal{E}}$ of a Langmuir wave packet, take the spatial Fourier transform of the current given in (32). Upon integrating by parts,

$$j_{2\omega_p}^{nl}(\underline{k}_0, t)_m = \frac{-eK_{0\ell}}{4\pi\omega_{pm}} \int d^3\underline{r} \exp(-i\underline{k}_0 \cdot \underline{r}) (\mathcal{E}_\ell \mathcal{E}_m - \delta_{\ell m} \underline{\mathcal{E}} \cdot \underline{\mathcal{E}}/2) . \quad (33)$$

For simplicity, let us assume the Langmuir field direction remains essentially parallel to \underline{k}_0 during collapse. The current does not depend very strongly on the field direction because one term goes as $\underline{\mathcal{E}} \cdot \underline{\mathcal{E}}$ in Eq. (33). We write,

$$\underline{\mathcal{E}}(\underline{r}, t) = \hat{k}_0 A \exp(i\theta/2) , \quad (34)$$

where the (real) scalar amplitude A , and phase, θ , depend on space and time. From Eq. (33), we find

$$j_{2\omega_p} = \frac{e(K_0/2 - \underline{K}_0 \cdot \hat{k}_0 \hat{k}_0)}{4\pi\omega_{pm}} \int d^3\underline{r} \exp[i(\underline{K}_0 \cdot \underline{r} - \theta)] A^2 , \quad (35)$$

The magnitude of the emission depends in detail upon the space-time evolution of $A(\underline{r}, t)$ and $\theta(\underline{r}, t)$. We shall assume that A^2 collapses, and that θ starts out as $2\underline{k}_0 \cdot \underline{r}$, and does not evolve pathologically.

We note parenthetically, however, some recent evidence¹² that the nonlinear behavior may consist of periodic break-up and reconstitution, rather than collapse, due to ponderomotive effects in the phase. Since no theoretical understanding yet exists concerning the competition of such behavior with collapse, it is not taken into account in the present paper. We assume here that collapse continues down to scale lengths of several Debye lengths.

In the very early phases of collapse there cannot be substantial emission because of the momentum mismatch, $\underline{k}_0 - 2\underline{k}_0$, in the phase factor in the integrand of Eq. (35). There is strong phase mixing, as we shall soon show. As A^2 collapses more and more, the phase-mixing becomes less important. By the time the collapse has become supersonic ($W > 16 m/M$), emission can occur.

The amount of emission depends sensitively on the shape of A^2 , as supersonic collapse proceeds to still smaller scales. There have been no calculations of the three-dimensional evolution of A^2 and θ predicted by Zakharov equations. Model equations studied by Budneva, et al.,¹¹ suggest that a small collapsing core breaks away from an initially Gaussian packet, leaving the (essentially) Gaussian corona behind. The core eventually tends toward the form of a similarity solution to the equations.

We shall estimate the current in two different ways. First, we shall assume that the entire Gaussian corona collapses. This will lead to an upper bound on the emissivity. Then we shall assume that only the (much smaller) core collapses, and tends towards a supersonic similarity solution. This will give less emission. The actual emissivity probably lies between the two limits.

In order to present a coherent discussion of the various spatial scales, we introduce the following definitions.

Define $L_{||, \perp}(t)$ as the half-widths of A^2

$$A^2(z=L_{||}, r=0) = A^2(z=0, r=L_{\perp}) \equiv A^2(0,0)/2, \quad (36a)$$

and $\ell_{||, \perp}$ as the scale-lengths of the phase:

$$\ell_{||, \perp} \equiv |\theta|/|\nabla_{||, \perp} \theta|. \quad (36b)$$

We now discuss the implications of the time-dependence of $L(t)$ and $\ell(t)$ for the size of the current, $j_{2\omega_p}$ in Eq. (35). We begin with the time $t = 0$ at which the beam-amplified Langmuir wave packets begin their collapse.

i) Onset of collapse ($t = 0$)

Initially, the packet moves at a phase velocity equal to the beam velocity, so the phase is

$$\theta = 2k_0 \cdot \underline{r}, \quad [\ell_{||} = (2k_0)^{-1}, \ell_{\perp} = 0] \quad (37a)$$

The half-widths $L_{||}$ and L_{\perp} correspond to the half-widths of the initial packet defined by Eqs. (9) and (12)

$$L_{||}(0) = (\Delta k_{||})^{-1}, \quad L_{\perp}(0) = (\Delta k_{\perp})^{-1}. \quad (37b)$$

If we assume that A^2 is Gaussian, the integral for $j_{2\omega_p}$ can be performed. It is proportional to

$$j_{2\omega_p} \propto \exp[-(K_0 - 2k_0)^2 L_{||}^2/4], \quad (37c)$$

which is vanishingly small. This result corresponds to the

well-known fact that beam-driven Langmuir wave packets cannot emit type III radiation at $2\omega_p$ in the absence of nonlinear (or other) interactions which broaden their k -space widths. This is because momentum conservation demands that the photon wave vector, \underline{K}_0 , be equal to the sum of two Langmuir wave vectors \underline{k}_{01} and \underline{k}_{02} , which lie within the packet. Since $K_0 = \sqrt{3}\omega_p/c$ (by 28b), and $k_0 = \omega_p/v_b$ (by 5a), we see that this is not possible for beams with speeds v_b of order $c/2$ or smaller. The situation is illustrated in Fig. 6.6. Essentially, the wave packet is too narrow in \underline{k} -space to contain Langmuir wave vectors \underline{k}_{01} and \underline{k}_{02} sufficiently smaller in magnitude than \underline{k}_0 to add up to \underline{K}_0 . The mathematical expression of this is that the exponent $-(K_0 - 2k_0)^2 L_{||}^2/4$, in Eq. (37c) is a large negative number initially.

However, as the packet collapses, $(K_0 - 2k_0)^2 L_{||}^2/4$, tends to zero. The reduction factor $\exp(-(K_0 - 2k_0)^2 L_{||}^2/4)$ is no longer effective the time $L_{||}$ has become small enough for the following condition to be satisfied:

$$L_{||}(t)k_0 \lesssim 1, \quad (38)$$

for no phase mixing (here, we have used the fact that K_0 is of order k_0 , and assumed that $\lambda_{||}$ does not get much smaller than $L_{||}$.) By this time, the packet has broadened^{2,9} sufficient in \underline{k} space, so that it contains pairs of wave vectors [such as \underline{k}_1 and \underline{k}_2 in Fig. 6(b)], which properly sum to \underline{K}_0 . Put in another way, the phase factor in the integrand of Eq. (35) is longer effective in phase-mixing the integral by the time inequality (38) is satisfied.

To proceed further, we need models of the time-dependence of $L_{||}$. The most optimistic of these assumes a collapsing Gaussian corona. This leads to an upper bound on the emissivity:

ii) Coronal collapse model

In the adiabatic stage we can use the scaling implied by the virial theorem [see Eqs. (18)]

$$L_{||,\perp} = (\Delta k_{||,\perp})^{-1} (1-t^2/t_V^2)^{1/2} . \quad (39)$$

We also assume that $\theta = 2k_0 \cdot \underline{r}$. This is acceptable in the adiabatic stage as long as $L_{||,\perp} k_0 > 1$, since plasmon momentum is conserved.² Another conserved quantity is the plasmon number,^{1,2}

$$N \equiv \int d^3r A^2 = \text{const.} \quad (40)$$

Equations (39) and (40), taken together with the assumption of a Gaussian shape, give us the time-dependence of the space-averaged energy density, $W(t)$ [see also Eq. (18b)]:

$$W(t) = \frac{W(0)}{(1-t^2/t_V^2)^{3/2}} . \quad (41)$$

For phase-mixing to disappear, Eq. (38) must be satisfied. Using the expression for $L_{||}$ in Eq. (39), this gives the time, t_0 , at which a collapsed corona begins to emit harmonic radiation:

$$(1-t_0^2/t_V^2)^{1/2} \sim \Delta k_{||}/k_0 = 1/12 . \quad (42)$$

However, at this time, according to Eq. (41), the energy density

$W(t_0)$ will have increased by three orders of magnitude, and the collapse will be well into the supersonic regime. If the entire corona collapses enough for phase mixing to be negligible, then the current in Eq. (35) becomes proportional to the plasmon number N in Eq. (40). Since N is an invariant of the Zakharov equations (21), it is conserved even in the supersonic stage of collapse. We can therefore find an upper bound on $j_{2\omega_p}$ by using N to evaluate the integral during the supersonic regime. N can be evaluated from the initial Gaussian conditions:

$$N = \epsilon_0^2 \pi^{3/2} (\Delta k_{\parallel})^{-1} (\Delta k_{\perp})^{-2} = 192 \pi^{5/2} \frac{n_0}{k_D^3} \frac{k_D}{\Delta k} \frac{W(t=0)}{W_{th}} \quad (43)$$

Using this as the value for the integral in Eq. (35), and inserting into the emissivity formula (28a) yields an upper bound for the emissivity during the supersonic stage of collapse

$$\left. \frac{dP}{d\Omega} \right|_{2\omega_p}^{\max} = 108 \sqrt{3} \pi \sin^2 \phi_0 \left(\frac{k_D}{\Delta k_{\parallel}} \right)^2 \left(\frac{W}{W_{th}} \right)^2 \left[\left(\frac{v_e}{c} \right)^5 \frac{n}{k_D^3} \omega_p \right] \quad (44a)$$

The angular factor is

$$\sin^2 \phi_0 = 1 - [(\hat{k}_0 \cdot \hat{K}_0)^2 - \frac{1}{2}]^2 \quad (44b)$$

This factor has its largest value (of unity) when the radiation comes out in a 45° cone about the beam direction, which is in agreement with the known¹⁴ coupling of radiation at $2\omega_p$ to two Langmuir waves in parametric instability theory.

We note, in passing, that the maximum total energy radiated, according to Eq. (44) is 10^{-3} times the total energy in the Langmuir packet. Hence, it is indeed valid to ignore the

effect of radiation losses on the collapse process (see Fig. 4).

iii) Core collapse; similarity solutions

A very different picture emerges if we assume that the collapsing packet quickly assumes the form of a similarity solution. In the adiabatic stage, the packet width of a similarity solution, $L_{||}$, can be considerably smaller than that of a Gaussian corona [Eq. (39)]. Budneva, et al.,¹¹ have studied the adiabatic collapse of a spherically symmetric scalar field obeying a cubic nonlinear Schrödinger equation [the scalar version of our Eq. (16)]. The corona of an initially Gaussian packet substantially above threshold was observed to remain essentially stationary, while a narrowly spiked core collapsed and approached the form of a similarity solution. A repetition of these calculations near threshold also seems to show self-similarity. Under such conditions we might expect much less emission.

The width of an adiabatic similarity solution is obtained, roughly, by setting $u = 1$ in Eq. (19b). Then, the half-widths, $L_{||}^{as}$ and L_{\perp}^{as} , of the adiabatic similarity solutions are:

$$L_{||}^{as} \approx L_{\perp}^{as} \approx (\Delta k_{\perp})^{-1} \left(\frac{W_{th}}{W} \right)^{\frac{1}{2}} (1-t/t_a)^{\frac{1}{2}}. \quad (45a)$$

Note, the half-widths are independent of Δk_{\perp} , since $W_{th} \approx 24(\Delta k_{\perp})^2/k_D^2$. In effect, the similarity shape is independent of the initial shape, and is narrower, particularly when $W \gg W_{th}$. However, in our case, W is only slightly greater than W_{th} , so the half-width $L_{||}^{as}$ appears to be proportional to $(\Delta k_{\perp})^{-1}$. This is much smaller than the parallel half-width

of the initial Gaussian packet, $L_{||}^0 = (\Delta k_{||})^{-1}$. The presumption is that a narrow spike is superposed over the broad Gaussian corona. Pereira and Sudan¹⁶ have shown that initially anisotropic two-dimensional packets tend to become more isotropic as collapse gets underway, so the scaling of $L_{||}^{a.s.} \approx L_{\perp}^{a.s.}$ is not surprising. We must note, however, that Eq. (45a) has no validity until collapse is well underway.

The scaling of the energy density of an adiabatic similarity solution with time is given from Eq. (19a):

$$W(t) = \frac{W(0)}{(1-t/t_a)} . \quad (45b)$$

Comparing (45a) with (45b), we see that, in three-dimensions, the half-width volume decreases at a faster rate than the energy density increases, hence,

$$\int_C d^3r A^2 \propto (1-t/t_a)^{1/2} , \quad (45c)$$

where C indicates integration over the core. The contribution of the core to the N invariant is therefore small. (Phase-mixing may still be expected at larger r, due to K_0 and the self-similar phases.) We now calculate the (smaller) emission from the similarity core.

From Eqs. (45a) and (38), we find the time, t_1 , at which the collapsed core can begin to contribute to the current, $j_{2\omega_p}$, without substantial phase-mixing:

$$(1-t_1^2/t_a^2)^{1/2} \approx \Delta k_{\perp}/k_0 \approx 1/4 . \quad (45d)$$

According to (45b), the energy will have increased by a factor of 16 at this time, and the collapse will shortly enter the supersonic stage. We shall assume all the emission occurs in the supersonic stage, since by then a supersonic core of similarity form may have had time to develop.

The half-widths $L_{||, \perp}^{ss}$ of a supersonic similarity solution are obtained from Eqs. (22-24) by setting $u = 1$:

$$L_{||}^{ss} \approx L_{\perp}^{ss} \approx (1-t/t_s)^{2/3} / \frac{2}{3} (12)^{1/3} (m/M)^{1/2} k_D, \quad (46a)$$

where $t = 0$ is now the onset time for the supersonic stage of collapse, and $W = 16 m/M$. (We note that $\int_C d^3r A^2$ is small but invariant in the supersonic stage.) At $t = 0$, the phase-mixing criterion (38), yields $k_o L_{||}^{ss} = 0.3$, so the current $j_{2\omega_p}$ can be evaluated with the phase factor in the integrand of Eq. (35) ignored. The result for the current may be written as,

$$j_{2\omega_p} = - \frac{9\omega_p^2}{ck_D^4} \left(\frac{3}{4\pi} n_0 \frac{M}{m} \right)^{1/2} \underline{I}_2, \quad (46b)$$

where

$$\underline{I}_2 = \hat{K}_{0l} \int d^3u (R_l R_m - \delta_{lm} \underline{R} \cdot \underline{R} / 2), \quad (46c)$$

and \underline{R} is the similarity field, defined in Eq. (24). As discussed beneath that equation, $|\underline{R}|$ has a maximum value equal to one. Its half-width is also of order unity, so we expect $|\underline{I}_2|$ to be of order unity as well. The emissivity that follows from this current is found [via Eq. (28a)] to be

$$\left. \frac{dP}{d\Omega} \right|_{2\omega_p}^{ss} = \frac{3^5 \sqrt{3}}{64\pi^2} \frac{M}{m} \left[\left(\frac{v_e}{c} \right)^5 \frac{n}{k_D^3} \omega_p \Theta \right], \quad (47)$$

where we have approximated $|\underline{I}_2|^2 = 1$. This estimate gives substantially less emission than that of the coronal collapse model, Eq. (44), because the core is so much smaller than the corona. For the parameters we have been considering, $|dP/d\Omega|_{2\omega_p}^{ss}$ is about 10^{-6} times smaller than $|dP/d\Omega|_{2\omega_p}^{\max}$.

There is a clear need, here, for numerical work to determine the time-dependent shape of a three-dimensional collapsing packet, under type III conditions. Unfortunately, the Zakharov equations should not be solved in fewer than three dimensions, because the N integral of a truncated similarity solution only goes to zero with time in three dimensions [cf., Eq.(45c)] One cannot use spherical or even cylindrical symmetry, because such symmetries require zero field at the origin,¹¹ due to the vector nature of the envelope. A full three-dimensional numerical solution of the vector Zakharov equations is prohibitively expensive at this time. However, some insight has been gained by further studies of model equations for a scalar envelope, such as that of Budneva, et al.¹¹ In particular, we have found narrow cores in packets close to threshold in recent¹⁵ numerical work using Budneva's model, which suggest that the emissivity may lie closer to the lower estimate of Eq. (47).

B. Emission at the Fundamental

The treatment of emission of radiation at frequencies close to the plasma frequency is somewhat more challenging. We must have approximate frequency matching between the Langmuir waves and the radiation: $\omega_p^2 + c^2 K_o^2 = \omega_p^2 + 3v_e^2 k_o^2$. This means that the wave number K_o of the fundamental is much smaller than the wave number k_o of the Langmuir waves. [$K_o = \sqrt{3}v_e k_o / c \ll k_o$, as long as $v_e/c \ll 1$ (see Appendix).] In order to conserve momentum, one requires either dynamical ions or strong spatial inhomogeneity. In the present calculation we ignore background plasma inhomogeneity, so we do not allow local or global density gradients to absorb the extra momentum. In the conventional discussions of fundamental emission it is usually assumed that ions or ion-acoustic waves take up the required momentum. The corresponding "weak" turbulence process involves the scattering of a Langmuir wave (plasmon) off ions and its transformation into a photon: $\ell \rightarrow i+t$. This may even occur as a stimulated process (instability).

We shall make the case here that fundamental emission can also occur in "strong" turbulence, i.e., from collapsing Langmuir wave packets. It is clear that emission cannot occur in the subsonic stage of collapse, because the ions are adiabatic, and momentum cannot be conserved. However, fundamental emission can occur in the supersonic stage when the ions are dynamic.

(An argument has been advanced that a collapsing wave packet cannot emit radiation at ω_p because the associated density cavity "traps" it. This argument is specious because the wavelength of such radiation is much longer than the characteristic size of the cavity. The emission occurs from this packet as a whole, in a manner analogous to the radiation by an antenna. This is stated mathematically in the Appendix.)

The current which governs the fundamental emission is given by Eq. (29). The Fourier transform of its envelope is

$$j_{\omega_p}(\underline{k}_0, t) = \frac{i\omega_p}{4\pi} \int d^3\underline{r} \exp(-i\underline{k}_0 \cdot \underline{r}) \frac{\delta n_2(\underline{r}, t)}{n_0} \underline{\mathcal{E}}_L(\underline{r}, t), \quad (48)$$

In the adiabatic stage of collapse, δn_2 is proportional to $-|\underline{\mathcal{E}}|^2$. The dominant phase in the integral is then in $\exp(-i\underline{k}_0 \cdot \underline{r})$ which arises from $\underline{\mathcal{E}}_L(\underline{r}, t)$. This causes the integral to phase mix to zero [see Eq. (35)], so that there is indeed no emission in the adiabatic stage.

In the supersonic stage, the prediction from the supersonic similarity solutions (21)-(25) is that

$$j_{\omega_p}(\underline{k}_0, t) = \frac{i\omega_p}{k_D^3} (12)^{1/6} \frac{3}{\sqrt{2}} \left(\frac{3n_0}{4\pi}\right)^{1/2} \frac{1}{(1-t/t_s)^{1/3}} \underline{I}_1, \quad (49a)$$

where,

$$\underline{I}_1 \approx \int d^3\underline{u} \eta(\underline{u}) \underline{R}(\underline{u}), \quad (49b)$$

and the dimensionless density and field supersonic similarity solutions η and \underline{R} are defined in Eq. (24). We have omitted the phase factor $\exp(i\underline{k}_0 \cdot \underline{r})$, which is always of order unity.

In the absence of phase mixing, we expect the magnitude of I_1 to be of order unity. The current is then inserted into the emissivity formula (28). The time-averaging interval T is chosen to be t_s , the collapse time. The result may be written as

$$\left. \frac{d\bar{P}}{d\Omega} \right|_{\omega_p}^{ss} = \frac{3^4 \sqrt{3} (12)^{1/3}}{64\pi^2} \frac{k_o}{k_D} |I_1|^2 \left[\left(\frac{v_e}{c} \right)^3 \frac{n\theta\omega_p}{k_D^3} \right]. \quad (50)$$

It is of interest to compare this with the similarity solution prediction of emission at the harmonic (Eq. 47):

$$\frac{\left. \frac{d\bar{P}}{d\Omega} \right|_{\omega_p}^{ss}}{\left. \frac{d\bar{P}}{d\Omega} \right|_{2\omega_p}^{ss}} \approx \frac{k_o}{k_D} \frac{c^2}{v_e^2} \frac{m}{M}. \quad (51a)$$

The large factor c^2/v_e^2 in Eq. (51a) arises because the harmonic emission is quadrupole, whereas the fundamental emission is dipole. The small factors k_o/k_D and m/M correspond, respectively, to the smallness of the wave number and the higher-order field dependence in the fundamental emission.

The ratio on the right side of Eq. (51a) is about 0.2 for our parameters, indicating almost as much fundamental as harmonic emission from a single collapsing packet in its supersonic phase, provided that the similarity form is justified. It is also of interest to compare this value with the value obtained from weak turbulence theory. The weak turbulence estimate¹⁷ depends upon the assumed distribution of $\langle |E_K|^2 \rangle$. Taking the ratio of the result predicted by (50) to the weak turbulence result gives,

$$\frac{d\bar{P}/d\Omega \Big|_{\omega_p}^{ss}}{d\bar{P}/d\Omega \Big|_{\omega_p}^{wt}} = \beta N \frac{m}{M} \frac{c}{v_e} , \quad (51b)$$

where β depends upon the assumed form of the distribution of wave energy, and can vary by three orders of magnitude with assumptions that Smith¹⁷ takes to be reasonable. We will take $\beta = 1$. Here, N is the number of particles in a Debye cube; $N \approx 10^{10}$ for the plasma we are considering. The numerical value of the ratio in (51b) is therefore $\sim 10^9$. The enormous enhancement over the weak turbulence result is readily understandable. The weak turbulence processes require a spontaneous fluctuation in the ion density on a scale of the Debye length. In order that the longitudinal fluctuations can scatter into transverse fluctuations, these have amplitude for occurring that decreases as $1/N$. The collapsing wave packet makes its own density fluctuation, and thus this factor is absent. To be more precise, the power radiated depends upon

$$\frac{dP}{d\Omega} \propto \int \left\langle \frac{\delta n(o)}{n_o} \underline{E}(o) \cdot \frac{\delta n(r)}{n_o} \underline{E}(r) \right\rangle d^3r .$$

The weak turbulence assumption is that the correlation function can be factored. Since $\langle \underline{E}(o) \cdot \underline{E}(r) \rangle$ will only be significant over distances the order of λ_D^3 , this is roughly

$$\frac{dP}{d\Omega} \propto W \int_{|r| < \lambda_D} \left\langle \frac{\delta n(o)}{n_o} \frac{\delta n(r)}{n_o} \right\rangle d^3r .$$

If

$$\delta\tilde{N} \equiv \int_{|r| < \lambda_D} d^3r \delta n(r) ,$$

then

$$\frac{dP}{d\Omega} \propto W \lambda_D^3 \left\langle \frac{\delta\tilde{N}}{N} \frac{\delta\tilde{N}}{N} \right\rangle ,$$

and by the central limit theorem $\langle \delta\tilde{N} \delta\tilde{N} \rangle \propto N$. Consequently, $dP/d\Omega \propto W \lambda_D^3 / N$. In the strong turbulence case, δn is driven by \underline{E} , is not statistically independent, and there is no factor of N in the expression for the power radiated, resulting in many orders of magnitude more emission.

In fact, fundamental emission is observed for bursts which are interpreted to originate near the sun, with intensities which are comparable to the harmonic intensities from the same burst.¹⁸ This is essentially inexplicable from the weak turbulence viewpoint, which fails by many orders of magnitude to predict sufficient radiation in the fundamental. The collapse mechanism discussed here needs to be modified to treat the situation near the sun, but the argument given here is quite general and suggests that strong turbulence effects can provide an explanation for the observed radiation.

At $\frac{1}{2}$ AU there has been no observation of fundamental radiation, which, in view of the relatively large amplitudes predicted by (51b) is apparently inconsistent with the similarity solution predication. This may be due to refraction by random inhomogeneities in the background plasma density which could have the effect that only radiation emitted at the location of

maximum density would be able to escape. Inasmuch as the pulse of radiation emitted by the soliton has a frequency spread of only about $10^{-4} \omega_p$, inhomogeneities of the order of only $\partial n/n_0 \approx 10^{-4}$ would have a profound effect.¹⁹ We note that a uniform gradient on a scale smaller than or comparable to the random inhomogeneities would eliminate the self trapping.

V. Density of Collapsing Packets and Volume Emissivity

Thus far, we have only found expressions for the emission from a single collapsing wave packet. We must now go further, and estimate the number density of collapsing packets (in the various stages of collapse), in order to calculate the volume emissivity and make comparisons with measurements.

Our model for steady state was described beneath Eq. (15), and is summarized in Fig. 3. Langmuir wave packets receive energy from the beam, collapse, and finally surrender their energy to particles via wave-particle interactions. The wave packets in real space fill the volume occupied by the beam. Their "discreteness" arises from the interference of beam-amplified random-phase Langmuir noise. We may define a wave packet roughly by finding the spatial mean value, $|\underline{\mathcal{E}}(\underline{r})|^2$ over some large volume, and letting the packets consist of the simply-connected volume in which $|\mathcal{E}(\underline{r})|^2 > \overline{|\underline{\mathcal{E}}(\underline{r})|^2}$. The packets will be distributed in terms of energy and in terms of spatial widths. At a given instant, some will be growing (due to the beam), some will be in various stages of collapse, and some will be dissipating their energy into electrons. In the ensemble or space average sense a steady state or quasi-steady state is assumed to exist.

The instantaneous rate of work performed by the beam on the waves is

$$P_{in} = \int \frac{d^3 k}{(2\pi)^3} \gamma_g(\underline{k}) |\underline{\mathcal{E}}_{\underline{k}}|^2 = \gamma_g \int_R \frac{d^3 \underline{k}}{(2\pi)^3} |\underline{\mathcal{E}}_{\underline{k}}|^2, \quad (52)$$

where $\gamma_g(\underline{k})$ is the growth rate of Langmuir waves in resonance with the beam [Eqs. (6) and (7)], γ_g is the peak growth rate, and R indicates integration over resonant modes only.

The modes in resonance with the beam are those lying in the phase space volume centered about \underline{k}_0 , within the bounds of the beam-determined widths, $\Delta k_{||}$ and Δk_{\perp} , as in Fig. 2 [see, also, Eqs. (9)]. In real space, those wave packets which are well into collapse will not have appreciable Fourier components in the resonance region. In order to estimate P_{in} we next need to consider how the packet and energy densities are related.

The packet densities are related to the total Fourier energy spectrum by

$$\int \frac{d^3 k}{(2\pi)^3} |\underline{\mathcal{E}}_{\underline{k}}|^2 = \int d^3 \underline{r} |\underline{\mathcal{E}}(\underline{r})|^2 \approx v \sum_U n_U U, \quad (53)$$

where

$$U = \int_P |\underline{\mathcal{E}}(\underline{r})|^2 d^3 \underline{r} \quad (54)$$

is the energy in one packet (denoted by the subscript P), and n_U is the density of packets with given energy, U . We expect most of the total energy to reside in packets which satisfy or almost satisfy the condition for collapse. These packets will all be clustered about a critical value, U_0 , with a density n_0 . We have, then, approximately,

$$\int \frac{d^3 k}{(2\pi)^3} |\underline{\mathcal{E}}_{\underline{k}}|^2 \approx v n_0 U_0. \quad (55)$$

The mean spacing of these packets is assumed to be on the order of their volume, which is determined by the beam. This "close-packing" assumption tells us that n_0 is on the order of the inverse volume of a packet, or,

$$n_0 \approx (\Delta k_{\parallel}) (\Delta k_{\perp})^2 / 8, \quad (56)$$

where Δk_{\parallel} and Δk_{\perp} are the half-widths given by Eqs. (9).

The average resonant mode energy depends on which of two distinct packet-evolution scenarios occurs:

In the first case, the number of packets which remain slightly below the collapse threshold during one collapse time is much greater than the number collapsing. This might be expected on the grounds that the collapse time is much less than γ_g^{-1} , so, at any given time, there are still a large number of wave packets below the critical W , contributing to the beam power input in Eq. (52).

A second possibility is that there is a quasi-periodic behavior in time with period on the order of γ_g^{-1} , in which there is cyclical resonant mode depletion. Resonant mode energy builds up during the growth phase, creating a majority of energy-contributing packets on the verge of collapse. They all collapse together quickly, causing a severe depletion of resonant mode energy for a time on the order of γ_g^{-1} . During this time, amplification of noise (and perhaps residual fragments of packets) occurs, and the process repeats. A long term time average gives a resonant mode energy equal to some small

fraction, F , of the total mode energy given in (55).

In either case, the average input power is [from Eq. (52) and (55)],

$$\bar{P}_{in} \approx \gamma_g F n_o V U_o , \quad (57)$$

where $F \approx 1$ according to the first scenario, and $F \ll 1$ in the second. It is not easy to decide between these scenarios on the basis of existing theory or numerical simulation,⁹ so we shall leave F undetermined, for the moment.

(The problem with numerical simulation is that the "box" size would have to be chosen large enough to contain a statistically significant distribution of wave packets. This seems to be prohibitively costly at present.)

The spatial density, n_c , of collapsing packets can be estimated by equating \bar{P}_{in} to the rate of energy flow, P_c , where,

$$P_c \approx \frac{1}{\tau_c} n_c V U_o . \quad (58)$$

Here τ_c is the appropriate collapse time. Equating (57) and (58),

$$n_c = \gamma_g \tau_c (F n_o) . \quad (59)$$

The density of adiabatic collapsing packets is then obtained by letting τ_c equal the adiabatic collapse time, t_a , given in Eq. (20a)

$$n_{ad} = \frac{\gamma_g}{\omega_p} \frac{g}{W} (F n_o) , \quad (60)$$

and the density of supersonic collapsing packets, by letting τ_c equal the supersonic collapse time, t_s , given in Eq. (25b)

$$n_{ss} = \frac{\gamma_g}{\omega_p} \frac{\sqrt{3}}{4} \frac{M}{m} (F n_o) . \quad (61)$$

We can use Eq. (61) to calculate the volume emissivity:

If we combine Eqs. (44), (61), and (56), we obtain an upper bound on the volume emissivity for emission at $2\omega_p$:

$$J_{2\omega_p} = n_{ss} \left. \frac{dP}{d\Omega} \right|_{2\omega_p}^{\max} = \frac{3^4 \pi}{8} F \frac{\gamma_g}{\omega_p} \frac{M}{m} \left(\frac{\Delta k_{\perp}}{k_D} \right)^2 \left(\frac{k_D}{\Delta k_{\parallel}} \right) \left(\frac{W}{W_{th}} \right)^2 \left(\frac{v_e}{c} \right)^5 n \omega_p^{\Theta}, \quad (62)$$

We evaluate this for the following parameters:

$$n_e = 40 \text{ cm}^{-3}, \quad \Theta_e = 10 \text{ eV},$$

$$n_b/n_e = 10^{-6}, \quad \Delta v_b/v_b = 1/3, \quad W = 2W_{th}$$

and Δk_{\parallel} and Δk_{\perp} as given by Eqs. (12). The maximum growth rate is taken (from Eq. 6) to be

$$\frac{\gamma_g}{\omega_p}^{\max} = \left(\frac{\pi}{8e} \right)^{1/2} \frac{n_b}{n_o} \left(\frac{v_b}{\Delta v_b} \right)^2 .$$

The resulting evaluation gives

$$J_{2\omega_p} = 2 \times 10^{-17} F \text{ ergs cm}^{-3} \text{ sec}^{-1} \text{ ster}^{-1} \quad (63)$$

This is to be compared with the measured value in Eq. (1), which gives 2×10^{-23} . The upper bound provided by the theory when F is larger than 10^{-6} is adequate to make collapsing-packet emission an attractive candidate to account for observed radiation at twice the plasma frequency.

Even if the collapse quickly approached similarity form, so that the core emissivity, (47) were more appropriate than the coronal emissivity, (44), the volume emissivity with F of order unity would still be consistent with the observed emission. However, as we discussed below Eq. (47), no one has demonstrated that three-dimensional Langmuir packets just above threshold will quickly converge to the form of similarity solutions. We note further that only the most pessimistic assumption of core emissivity and cyclical resonant mode depletion ($F \ll 1$) leads to a theoretical volume emissivity below the observed levels.

As an important side issue, it is worth pointing out once more that either of our statistical models ($F = 1$, or $F \ll 1$) is consistent with the absence of quasilinear beam plateau formation. This is because the wave energy density of beam-resonant modes can never greatly exceed the collapse threshold, which is well below the beam energy density [see Eq. (13) and (14), and the discussion which follows].

VI. Contrast with Previous Theoretical Work

We wish to point out here the main differences between the theory proposed here and an earlier attempt at treating emission from stable solitons, due to Papadopoulos and Freund.⁴

A central difference hinges on the role that the magnetic field plays in the evolution of the solitons. Papadopoulos and Freund assert that the effect of the magnetic field is to produce stable, that is, not collapsing, essentially one-dimensional solitons. This argument relies, in part, on their claim that the magnetic field plays an important role in the linear stage of beam-mode growth, and distorts the real-space wave packets into one-dimensional "pancakes." We assert that the magnetic field is irrelevant in shaping the beam-mode packets. The ratio of $\omega_{ce}/\omega_p \approx 10^{-2}$ at 0.45 AU, so one would a priori expect a rather small effect.

The argument that Papadopoulos and Freund rely on is stated more explicitly in a preprint of Smith, et al.,²⁰ where they claim that the angular spread in wave vector space of the growing modes excited by the two-stream instability is less than 1° for $\omega_c/\omega_p \approx 10^{-2}$. This conclusion is erroneous, and based on an incorrect application of a standard formula for the growth rate of the unstable modes in the presence of a magnetic field²⁴ (Akhiezer, et al.),

$$\gamma \propto \frac{K_{||}^2}{K_{||}^2 + K_{\perp}^2} g(K_{\perp}^2 R_B^2),$$

where $R_B = \Delta V_B / \omega_{ce}$ and

$$g(a) = e^{\frac{1}{2}} \sum_{\ell=-\infty}^{\infty} e^{-a} I_{\ell}(a) \exp[-(1+\ell/K_{||} R_B)^2/2],$$

where $I_{\ell}(a)$ is the Bessel function. Papadopoulos and Freund claim that the growth rate is only significant when $K_{||} R_B \ll 1$, basing their claim on the approximation of $g(a)$ by the term with $\ell = 0$. This approximation is totally unjustified for larger a , however, since $K_{||} R_B = (V/V_B)/(\omega_{ce}/\omega_p) \approx 10$, and approximately 20 terms need to be kept in the series. If one does this, one finds that $g(0) = 1$, $g(a) = 0.9989$, i.e., the dispersion relation is extremely insensitive to $K_{\perp} R_B$ for these values of $K_{||} R_B$. Furthermore, it should be noted that in the limit of vanishing field, $K_{||} R_B \rightarrow \infty$, all terms in the series must be summed. Papadopoulos and Freund's result is obtained by taking the strong field limit of the dispersion relation, and then applying it for weak fields.

Their argument that the solitons are stable is based on the assertion that they are essentially one dimensional. Since the assertion is false, there is no evidence which suggests that they are indeed stable. We note that Petviashvili²² has argued that there are indeed static localized solutions of the equations one obtains by including the magnetic field in the linear part of the equation of motion (A2). It is not clear whether such solutions really exist (since he relied on a

numerical solution of the equation to prove existence), or if they are stable. In any case, the linear and transverse dimensions of these entities will bear no relation to the dimensions of the packets formed by the modes that grow in the presence of the beam, and we think they will play no role in the problem.

A second major difference lies in the relationship between the linear growth rate of the unstable beam modes, γ_B , and the average level of energy in the plasma oscillations, W . The picture of Papadopoulos and Freund⁴ is that the energy is transferred out of the beam modes by the modulational instability, acting uniformly throughout the plasma. By an argument that they think reasonable, they then conclude that $\gamma_B \sim \gamma_{NL}$ is the condition for a steady state. γ_{NL} has the same dependence on the parameters of the problem as $1/\tau_c$, where τ_c is the collapse time of the solitons, and in this way they obtain $\gamma_B \propto W$, $W < m/M$, or $\gamma_B \propto (m/M)^{1/2} W^{1/2}$, $W > m/M$.

Our picture is that the transfer of energy is due to the direct collapse of wave packets, which occurs when the energy in the unstable modes has grown so that $W \geq (\Delta K)^2$. W is fixed by the velocity spread, not the intensity of the beam. The collapse does not occur throughout all space, and, in fact, the density of collapse, n_c , can be computed from an energy balance equation

$$\gamma_B W = \frac{1}{\tau_c} (W L_c^3) n_c ,$$

as long as $\gamma_B < 1/\tau_c$, $n_c < 1/L_c^3$. When $\gamma_B \geq 1/\tau_c$, the collapsing solitons are closely packed, and the physical situation is similar to the picture that Papadopoulos and Freund propose in that n_c would remain at $1/L_c^3$ as γ_B increased, and $\gamma_B \approx 1/\tau_c$. However, this regime is inappropriate for the type III parameters, in which the ratio of beam to background density n_b/n_e is never expected to exceed 10^{-6} , so that $\gamma_B \leq (1/10)(1/\tau_c)$. As shown by Goldman and Nicholson,² direct collapse is the dominant energy transfer mechanism in this regime, not the modulational instability.

VII. Conclusions

In conclusion, we believe the models we have developed in this paper for electromagnetic wave emission from collapsing Langmuir wave packets, give the best possible state-of-the-art estimates for such emission. Reasonable models give predictions which are well above the volume emissivity observed during type III bursts, Eq. (1). Further numerical work on the dynamical and statistical details of collapse would be highly desirable, but the need for working in three-dimensions may make the cost prohibitive [see discussion below Eq. (47)]. Further theoretical work is also necessary, particularly in the refinement of our statistical assumptions.

Acknowledgments

One of us (M.V.G.) would like to thank the Guggenheim Foundation for a Fellowship held during part of this research, and also to acknowledge helpful conversations with R. Hellwarth, V. Zakharov, F. Tappert, C. Kennel, D. Smith, and D. F. DuBois. This work was also supported by the National Science Foundation, Atmospheric Research Section under ATM 76-14275, and by the Air Force Office of Scientific Research (M.V.G. and G.F.R.) under contract F49620-76-C-0005. The work of one of us (D.N.) was also supported by the Solar Terrestrial Research Program, Division of Atmospheric Sciences, National Science Foundation, ATM 78-22487 and by U.S. Department of Energy Grant No. EY-76-5-02-2059. We thank the National Center for Atmospheric Research, supported by the National Science Foundation, for computer time used in this study.

APPENDIX DERIVATION OF EQUATIONS FOR TRANSVERSE AND LONGITUDINAL FIELDS

We want to show that if $c' \equiv c/v_T \gg 1$, then a consistent solution of the equations of motion for a plasma can be obtained in the form

$$\underline{\mathcal{E}} = \underline{\mathcal{E}}_0 + \underline{\mathcal{E}}_{\perp}/(c')^2,$$

where $\underline{\mathcal{E}}_0 = -\underline{\nabla}\phi$, and $|\underline{\mathcal{E}}_{\perp}| \sim |\underline{\mathcal{E}}_0|$. The field, $\underline{\mathcal{E}}$, is always predominantly longitudinal. The longitudinal part, $\underline{\mathcal{E}}_0$, satisfies a modified form of the Zakharov equations, and $\underline{\mathcal{E}}_{\perp}$ is the radiation field. We begin with Eqs. (21), with all tildas omitted from dimensionless quantities

$$i \frac{\partial \underline{\mathcal{E}}}{\partial t} - c'^2 \underline{\nabla} \times \underline{\nabla} \times \underline{\mathcal{E}} + \underline{\nabla}(\underline{\nabla} \cdot \underline{\mathcal{E}}) = \frac{\eta}{2} \underline{\mathcal{E}}, \quad (\text{A1})$$

$$(\partial_t^2 - \beta^2 \nabla^2) \eta = \nabla^2 |\underline{\mathcal{E}}|^2, \quad (\text{A2})$$

where $c' = c/\sqrt{3}v_T$, and will be assumed $\gg 1$. If we make the ansatz $\underline{\mathcal{E}} = \underline{\mathcal{E}}_0 + \underline{\mathcal{E}}_{\perp}/c'^2$, $\underline{\mathcal{E}}_0 = -\underline{\nabla}\phi$, we find, to lowest order in $1/c'^2$:

$$i \frac{\partial \underline{\mathcal{E}}_0}{\partial t} - \underline{\nabla} \times \underline{\nabla} \times \underline{\mathcal{E}}_{\perp} + \underline{\nabla}(\underline{\nabla} \cdot \underline{\mathcal{E}}_0) = \frac{\eta}{2} \underline{\mathcal{E}}_0, \quad (\text{A3})$$

$$i \frac{\partial (\underline{\nabla} \times \underline{\mathcal{E}}_{\perp})}{\partial t} - c'^2 \nabla^2 (\underline{\nabla} \times \underline{\mathcal{E}}_{\perp}) = c'^2 \underline{\nabla} \times \left(\frac{\eta}{2} \underline{\mathcal{E}}_0 \right), \quad (\text{A4})$$

$$\frac{\partial^2 \eta}{\partial t^2} - \beta \nabla^2 \eta = \nabla^2 |\underline{\mathcal{E}}_0|^2 . \quad (\text{A5})$$

We Fourier transform (A4) for the transverse field $\underline{\mathcal{E}}_\perp$, in time and invert the resulting Helmholtz equation:

$$\nabla \times \underline{\mathcal{E}}_{\perp, \omega} = \frac{1}{4\pi} \int \frac{\exp(iK|\mathbf{r}-\mathbf{r}'|)}{|\mathbf{r}-\mathbf{r}'|} \nabla \times \left(\frac{\eta}{2} \underline{\mathcal{E}}_0 \right)_\omega d^3 r' ,$$

$$K \equiv \omega / (c')^2 . \quad (\text{A6})$$

Integrating (A6) by parts and substituting in (A3) we have

$$\begin{aligned} K^2 \underline{\mathcal{E}}_{0, \omega} + \frac{1}{4\pi} \nabla \times \nabla \times \int \frac{\exp(iK|\mathbf{r}-\mathbf{r}'|)}{|\mathbf{r}-\mathbf{r}'|} \left[\frac{\eta}{2} \underline{\mathcal{E}}_0(\mathbf{r}') \right] d^3 r' + \nabla (\nabla \cdot \underline{\mathcal{E}}_{0, \omega}) \\ = \left(\frac{\eta}{2} \underline{\mathcal{E}}_0 \right)_\omega . \end{aligned} \quad (\text{A7})$$

Consider fundamental emission (near the plasma frequency ω_p).

If we set $K = 0$ in the integral on the left side of (A7)

it is just the transverse part of the current $(\eta \underline{\mathcal{E}}_0 / 2)$.

Since for any vector field, $\underline{A}(\mathbf{x}, t) = \underline{A}_L(\mathbf{x}, t) + \underline{A}_T(\mathbf{x}, t)$, where L and T designate the longitudinal and transverse parts of the vector, we find that $\underline{\mathcal{E}}_0$ satisfies the equation

$$i \frac{\partial \underline{\mathcal{E}}_0}{\partial t} + \nabla (\nabla \cdot \underline{\mathcal{E}}_0) = \left(\frac{\eta}{2} \underline{\mathcal{E}}_0 \right)_L , \quad (\text{A8})$$

the corrections due to finite values of K being of order $1/c'$.

Equations (A8) and the divergence of (A1) imply that

$$i \frac{\partial}{\partial t} \nabla \cdot \underline{\mathcal{E}}_\perp + \nabla^2 (\nabla \cdot \underline{\mathcal{E}}_\perp) = 0 , \quad (\text{A9})$$

and hence if $\nabla \cdot \underline{\mathcal{E}}_{\perp} = 0$, initially [or at least $\sigma(1/c')$] it will be zero for all time, and the solution of (A6) can be taken to be

$$\underline{\mathcal{E}}_{\perp, \omega} = - \frac{1}{4\pi} \int \frac{\exp(iK|\mathbf{r}-\mathbf{r}'|)}{|\mathbf{r}-\mathbf{r}'|} \left[\frac{n}{2} \underline{\mathcal{E}}_0(\mathbf{r}') \right]_{T, \omega} d^3r' . \quad (\text{A10})$$

The problem therefore breaks up into two parts: the solution of the equations of motion for the longitudinal field (A8) determined entirely by the longitudinal part of the current $(\delta n/n_0) \underline{\mathcal{E}}_0$, and the radiation produced by that field, determined by the transverse part of the current (A10). The emissivity formula (28a) which we have used can be derived from (A10).

The supersonic similarity solutions and plasmon number invariant arguments we have employed for the field $\underline{\mathcal{E}}$ are based on the field equation (A1). Since we have just demonstrated that the transverse part of $\underline{\mathcal{E}}$ is of order $(c')^{-2}$ times smaller than the longitudinal part, our solutions can also be regarded as satisfying (A8).

We note that if second harmonic terms are included in the current, these will have a negligible effect on the motion of $\underline{\mathcal{E}}_0$. The radiation due to these terms is calculated from (A10) with the appropriate current, and $K = (\sqrt{3/2})(1/c)$.

REFERENCES

1. V. E. Zakharov, Zh. Eksp. Teor. Fiz. 62, 1745 (1972) [Sov. Phys.-JETP 35, 908 (1972)].
2. M. V. Goldman and D. R. Nicholson, Phys. Rev. Lett. 41, 406 (1978).
3. D. A. Gurnett and R. R. Anderson, Science 194, 1159 (1976); J. Geophys. Res. 82, 632 (1977).
4. K. Papadopoulos and H. P. Freund, Geophys. Res. Lett. 5, 881 (1978).
5. D. A. Gurnett and L. A. Frank, Solar Phys. 45, 477 (1975).
6. R. J. Fitzenreiter, L. D. Evans, and R. P. Lin, Solar Phys. 46, 437 (1976).
7. D. F. Smith and D. R. Nicholson, in Wave Instabilities in Space Plasmas, Eds., P. J. Palmadesso and K. Papadopoulos (Reidel, Dordrecht, 1979).
8. G. R. Magelssen and D. F. Smith, Solar Phys. 55, 211 (1977).
9. D. R. Nicholson, M. V. Goldman, P. Hoyng, and J. C. Weatherall, Ap. J. 223, 605 (1978).
10. V. E. Zakharov, A. F. Mastryukov, and V. S. Synakh, Fiz. Plazmy 1, 614 (1975) [Sov. J. Plasma Phys. 1, 339 (1975)].
11. O. B. Budneva, V. E. Zakharov, and V. S. Synakh, Fiz. Plazmy 1, 606 (1975) [Sov. J. Plasma Phys. 1, 335 (1975)].
12. A. A. Galeev, R. Z. Sagdeev, Y. S. Sigov, V. P. Shapiro, and V. I. Sherdenko, Fiz. Plazmy 1, 10 (1975) [Sov. J. Plasma Phys. 1, 5 (1975)].

13. T. Tajima, J. LeBoef, J. Dawson, and M. V. Goldman (to be published).
14. M. V. Goldman, Ann. Phys. (N.Y.) 38, 117 (1966); see p. 154.
15. M. V. Goldman, K. Rypdal, and B. Hafizi (to be published).
16. N. Pereira, R. Sudan, and J. Denavit, Phys. Fluids 20, 936 (1977).
17. D. F. Smith, Adv. Astron. Astrophys. 7, 147 (1970).
18. D. F. Smith, Space Sci. Rev. 16, 91 (1974).
19. D. F. Smith and D. Sime (to be published).
20. R. A. Smith, M. L. Goldstein, and K. Papadopoulos (to be published).
21. A. I. Akhiezer, I. A. Akhiezer, R. V. Polovin, A. G. Sitenko, and K. N. Stepanov, Plasma Electrodynamics (Pergamon, New York, 1975).
22. V. I. Petviashvili, Fiz. Plazmy 1, 15 (1975) [Sov. J. Plasma Phys. 1, 28 (1975)].

FIGURE CAPTIONS

- Fig. 1 Type III solar radio burst, showing an electron stream emanating from a flare and propagating to the earth along a magnetic field line. The radio wave emission is produced by beam-unstable Langmuir waves, and has been detected in space (by the indicated satellites), and on earth.
- Fig. 2 Contours of constant Langmuir wave energy density in real and Fourier space, at an initial time, t_0 , and a later time, t_1 (after some real-space collapse has occurred). The initial Fourier-space wave packet consists of beam-unstable (resonant) modes, with random phases, centered about the wave vector $\underline{k}_0 = \hat{v}_b \omega_p / v_b$, forming a packet of size $\Delta k_{||}$ by Δk_{\perp} . In real space, this corresponds to packets of size 3 km by 10 km.
- Fig. 3 Trajectory of the state of a collapsing wave packet, shown in a "phase" space, in which a packet is labelled by its square width, $(\Delta x)^2 / \lambda_D^2$, and its mean energy, $W = \langle |\mathcal{E}|^2 \rangle_{\text{PACKET}} / 4\pi n_0$. Energy is injected into packets of a width set by the beam instability. The collapse is initially adiabatic, then supersonic, and finally ends in wave-particle energy transfer.

Fig. 4 Energy flow during a type III solar radio burst. Most of the energy remains in the beam. A smaller fraction goes into beam-unstable Langmuir waves, some of which collapses. A small fraction of the Langmuir energy goes into radiation. When a packet has collapsed to a size of several Debye lengths it surrenders its energy to electrons and ions.

Fig. 5 Emission from a single collapsing Langmuir wave-packet. Photons of frequency ω , and wave vector \underline{K}_0 are radiated into the solid angle $d\Omega$ about the observation point, \underline{r} . Note this observation point is imbedded in the plasma [with local plasma frequency, $\omega_p(\underline{r})$].

Fig. 6 Momentum conservation requirements for emission of harmonic radiation (at $2\omega_p$) by a wave packet. Initially, the packet is centered around \underline{k}_0 , and is too small to contain two plasmon wave vectors which sum to the photon wave vector, \underline{K}_0 . After some collapse, the packet has enlarged in \underline{k} space, and contains enough plasmon pairs of the proper momentum to conserve.

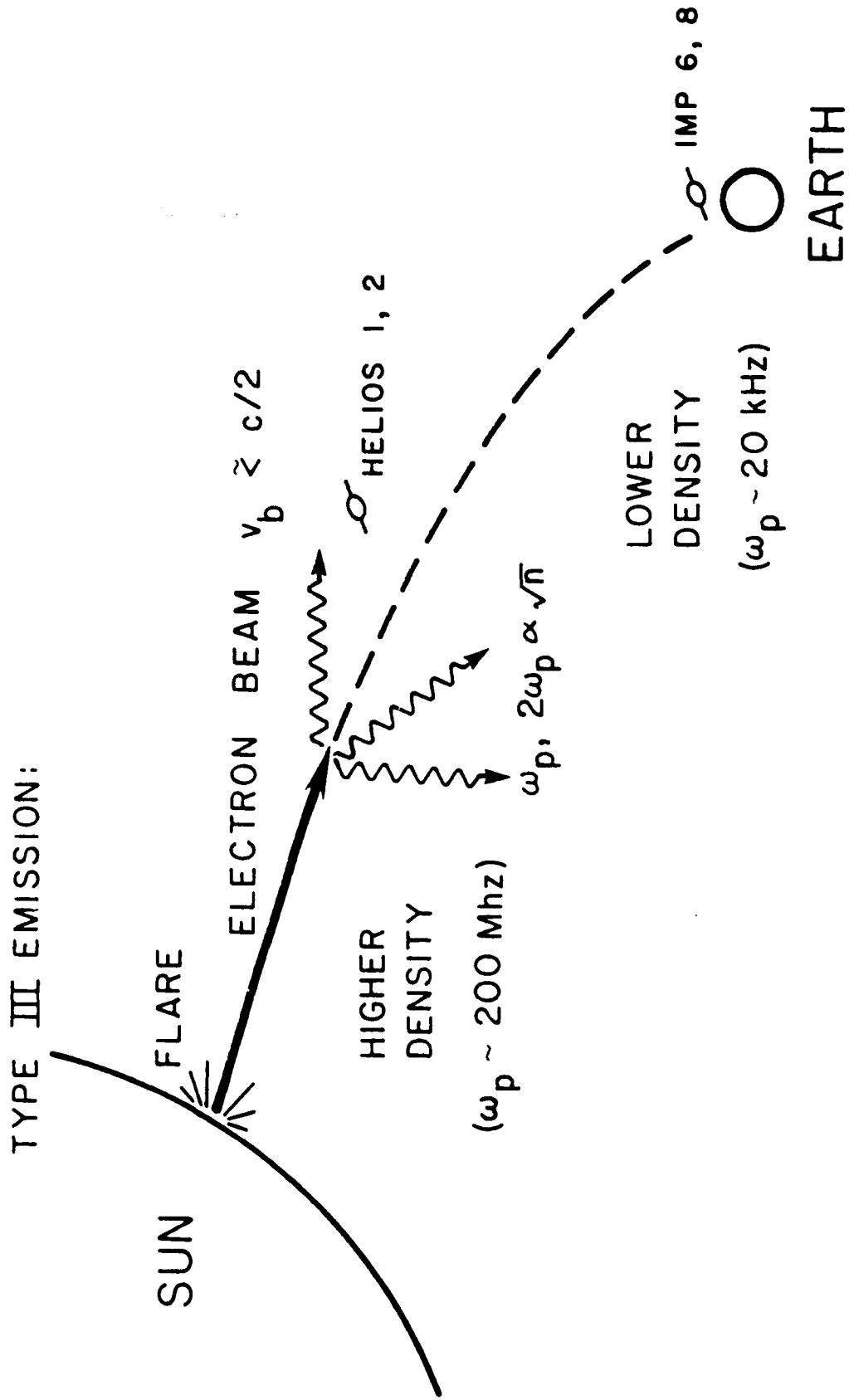
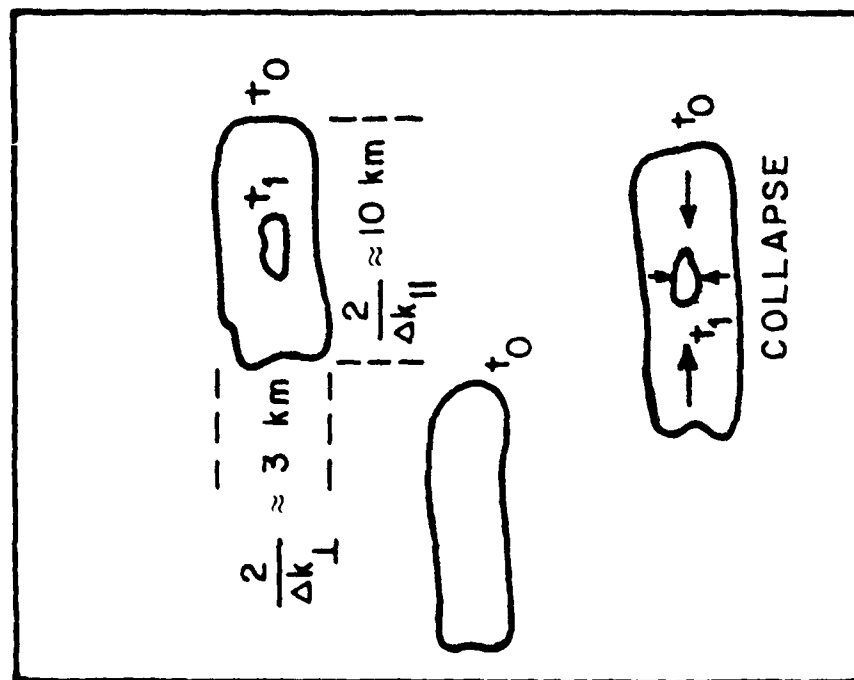
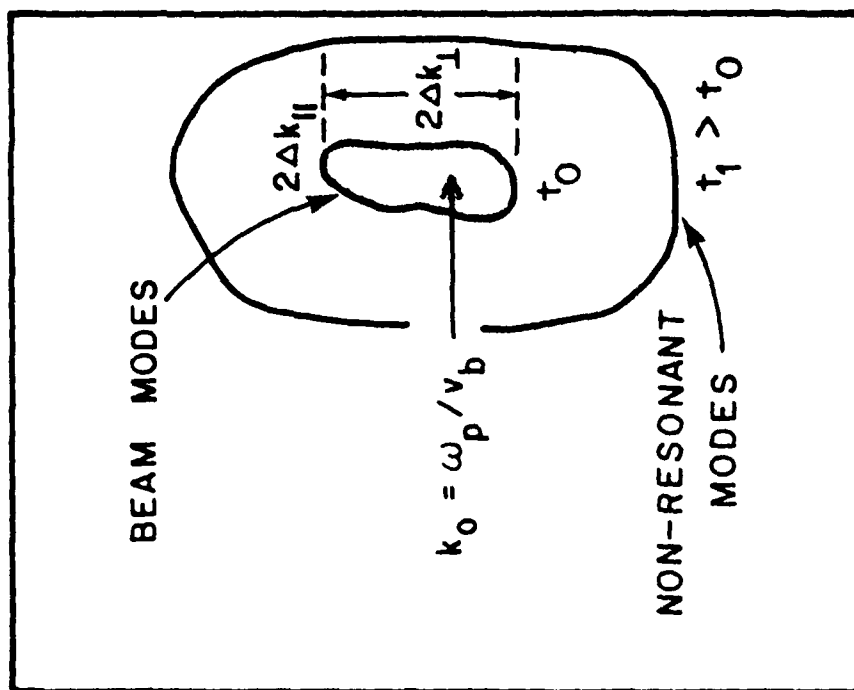


FIGURE 1



$$|\underline{\varepsilon}(\underline{r})|^2$$



$$|\underline{\varepsilon}(\underline{k})|^2$$

FIGURE 2

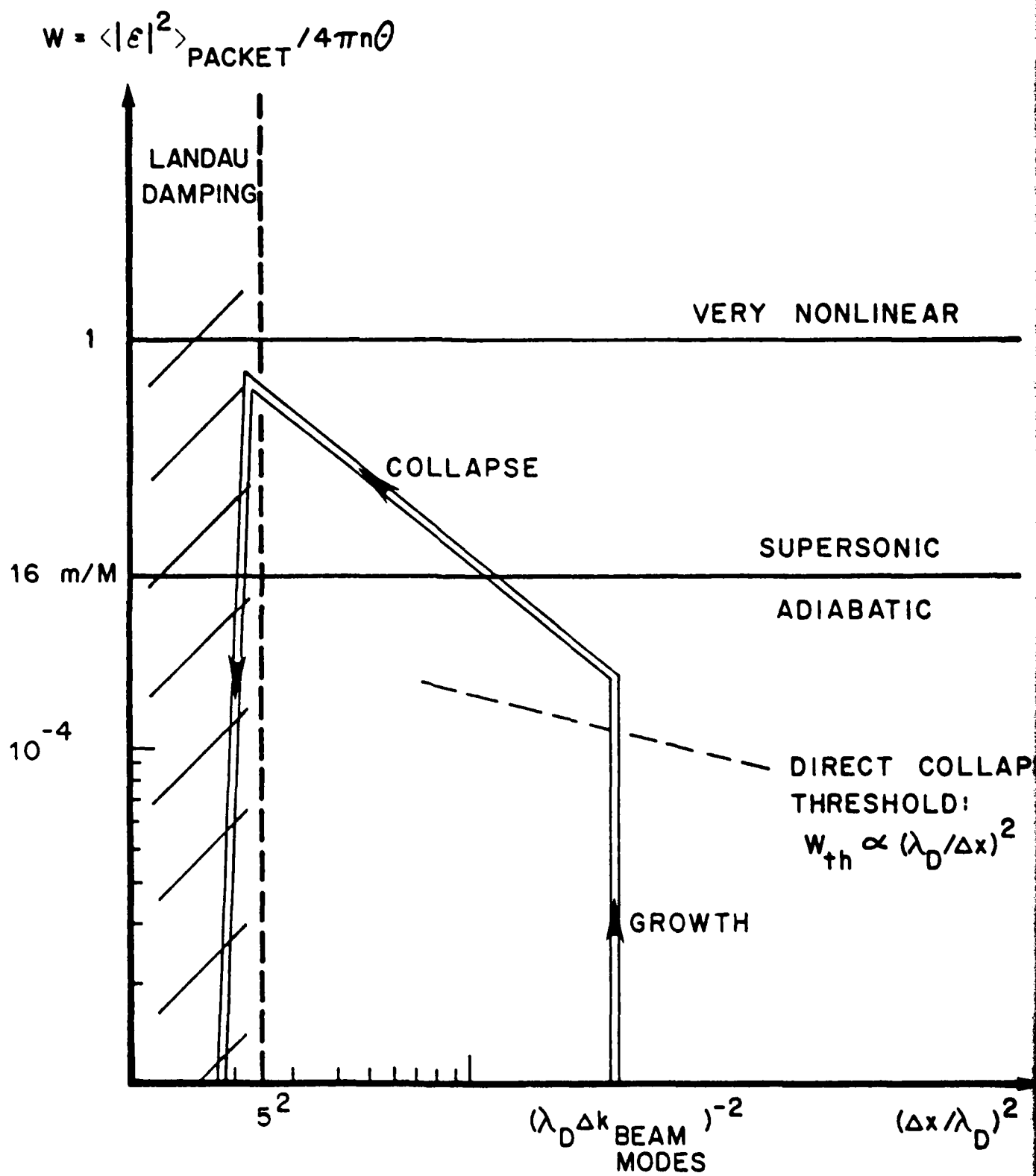


FIGURE 3

ENERGY FLOW

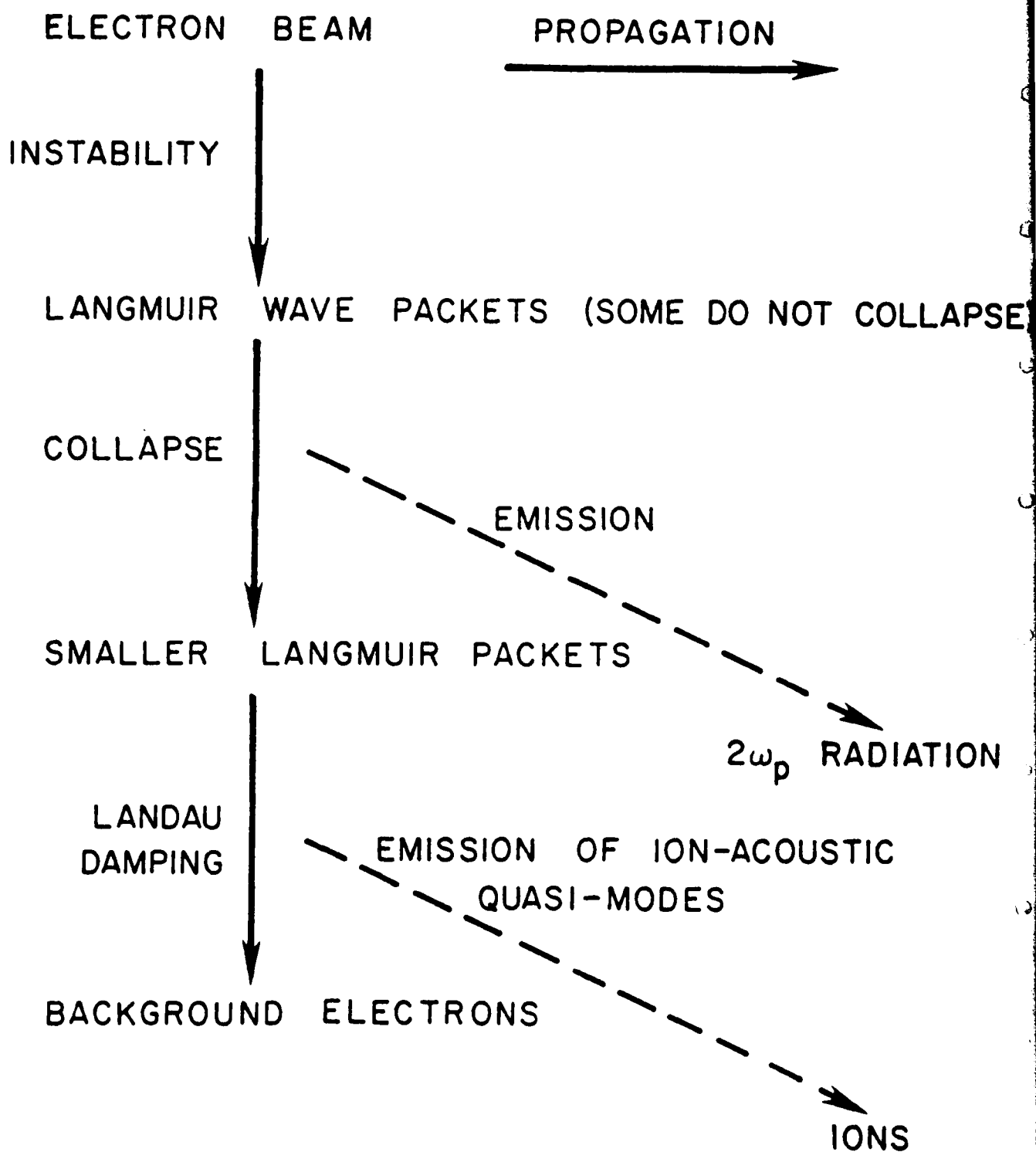


FIGURE 4

COLLAPSING LANGMUIR
WAVE - PACKET

$$\omega, \underline{k}_0 = \frac{\hat{r}}{c} [\omega^2 - \omega_p^2(r)]^{1/2}$$

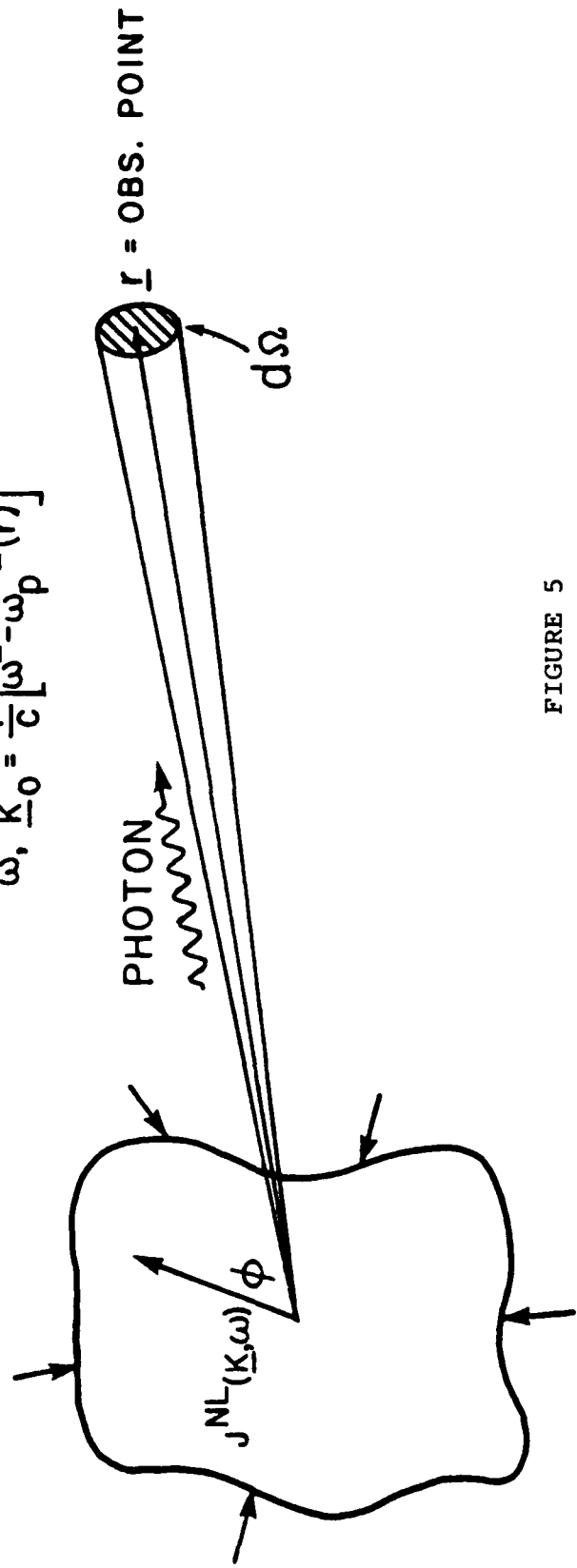
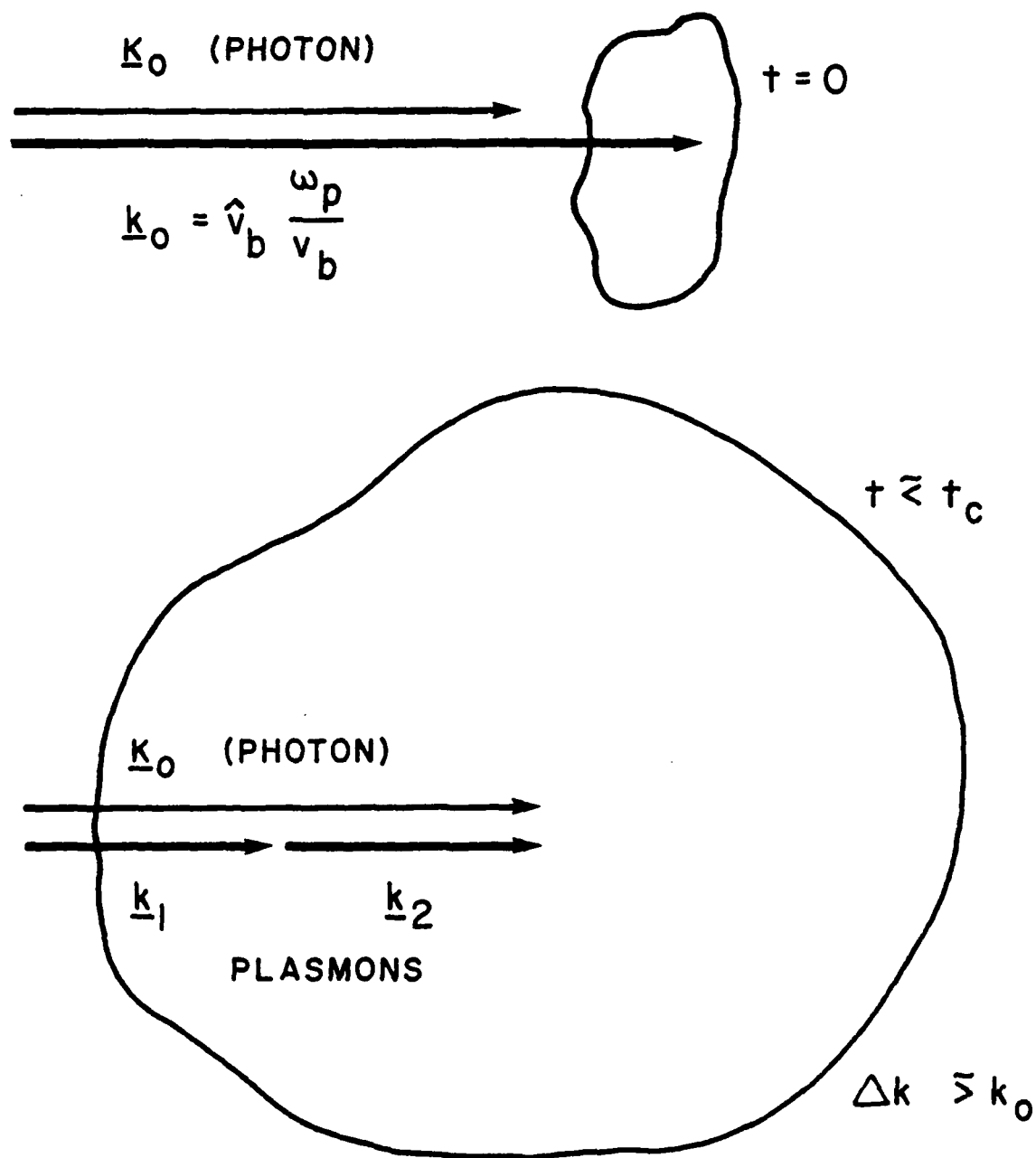


FIGURE 5

LANGMUIR PACKETS IN \underline{k} -SPACE



MOMENTUM MATCH: $\underline{k}_1 + \underline{k}_2 \approx \underline{k}_0$
FOR EMISSION

FIGURE 6

APPENDIX B

"Dimensionality and Dissipation in Langmuir Collapse"

Accepted by Physics of Fluids

September 1979

M. V. Goldman, K. Rypdal, and B. Hafizi

CU 1036

November 1979

Dimensionality and dissipation in Langmuir collapse

M. V. Goldman, K. Rypdal,* and B. Hafizi

Department of Astro-Geophysics, University of Colorado,
Boulder 80309

The nonlinear Schrödinger equation provides a model for Langmuir evolution at low energy density and wave number. We study this equation using virial theorem techniques and find stationary solitons and pulsating solitons (related to "breathers") in one dimension, and collapsing packets in two or more dimensions. Initial wave-packet collapse thresholds and times are found, with and without constant collisional damping. In three dimensions a narrow collapsing core is observed to break away from an initially Gaussian packet, and become asymptotically self-similar with time.

*Present address: Institute of Mathematical and Physical Sciences, University of Tromsø, Norway.

I. INTRODUCTION

It was Zakharov¹ who first pointed out the relevance of optical self-focusing phenomena to the nonlinear behavior of large amplitude Langmuir waves. Whether the waves are electromagnetic or electrostatic is of little consequence. The associated ponderomotive force pushes electrons out of a spatial region, and they drag along the ions. The lowered density creates a higher index of refraction in which rays undergo total internal refraction and can be trapped if the nonlinearity is strong enough. In one dimension, this nonlinearity can exactly balance linear dispersion (diffraction) of a wave packet, leading to the formation of an envelope soliton. In two or more dimensions, nonlinear refraction can permanently exceed dispersion. When this occurs, a stationary balance is impossible and the packet collapses spatially. The collapse threshold can occur at initial Langmuir energy densities which are still many orders of magnitude smaller than the background electron density, so simple nonlinear models are expected to provide a good description of the early stages of collapse.

In the so-called Zakharov equations,^{1,2} the (slow time) electron density in the Langmuir wave equation is allowed to be nonlinear. Quasineutrality is assumed, and the (ion or

electron) density obeys a second, ion-acoustic wave equation with a source term proportional to the ponderomotive force of the Langmuir waves. These coupled equations have been used extensively²⁻⁵ to describe Langmuir collapse. They provide the dynamical basis for what is often called "strong" Langmuir turbulence.

In the early stages of collapse, at low wave energy densities, the time-dependent (inertial) term in the ion density equations is negligible. The ions are then adiabatic, and the density is proportional to the negative of the ponderomotive force. Under these conditions, the envelope approximation to the Langmuir wave equation leads to a Schrödinger equation with cubic nonlinearity.

This paper is concerned with effects of spatial dimensionality and collisional damping on solutions to the nonlinear Schrödinger equation (NLSE) for a vector field envelope, \mathcal{E} . Goldman and Nicholson have recently shown⁶ that the NLSE provides a good model for the early nonlinear evolution of certain beam-excited Langmuir wave instabilities. When the beam growth-rate is slow compared to the nonlinear (collapse) time-scale, the role of the beam is essentially only to determine the shape of a "linear" Langmuir wave packet, which is then used as an initial value for the undriven NLSE. Under these conditions, virial theorem techniques¹ have been used to find the threshold and collapse

time of two-dimensional⁶ Langmuir packets. Two-dimensional theory and numerical analyses^{4,6} show that such direct adiabatic collapse is very likely to play an important role in the saturation of beam instabilities at very low beam densities. An important example is furnished by the solar-generated electron beams responsible for type III radio bursts.⁴

One of the purposes of the present paper is to show how the assumption of near-Gaussian spatial behavior of the Langmuir field leads to a closure approximation in the virial theory. With this approximation, we are able to estimate the threshold and find an upper bound for the collapse time of three-dimensional Langmuir packets. Additional numerical work, based not on the virial theorem but on the Schrödinger equation for a spherically symmetric scalar field, shows a self-similar collapsing core developing out of an initial three-dimensional wave packet close to threshold.

In one dimension, the virial theorem with closure approximation leads to very simple predictions of pulsating solitons which are consistent with the results of detailed numerical solutions⁷ based on inverse scattering theory. The pulsating solitons have amplitudes slightly higher than for the corresponding stationary (sechx) solitons. They are closely related to "breathers," which are strictly periodic bound states of two solitons. (The one-dimensional nonlinear

Schrödinger equation has been used extensively^{8,9} as a model for nonlinear behavior of deep water waves. The "recurrence" observed by Yuen and Ferguson⁸ in this connection may be closely related to pulsating solitons and "breathers.")

Other observations in the present paper have to do with the competition between modulational instabilities and collapse, and with comparisons between the virial theorem and similarity solutions. A number of these observations are based on similar phenomena in nonlinear optics,¹⁰ in which a laser beam undergoes total self-focusing at moderate intensities, and the higher intensities "break-up" into filaments.

We have derived a virial theorem for the NLSE with constant damping included. In two dimensions, this results in a dissipative threshold for direct collapse, enabling us to predict the role of collisional damping in Langmuir collapse.

The plan of this paper is as follows: In Section II we treat the NLSE using general virial theorem arguments. In Section III we explore the evolution of initial Gaussian wave packets in one, two, and three dimensions. Section IV is devoted to the effects of damping on collapse. Section V deals with self-similar behavior, in general, and, for the special case of three-dimensional spherically-symmetric collapse of a scalar field. In the Appendix we study the conditions of validity for the NLSE model of Langmuir collapse (i.e., the adiabatic ion and electrostatic field approximations).

AD-A081 883

COLORADO UNIV AT BOULDER DEPT OF ASTRO-GEOPHYSICS

F/8 20/9

PLASMA WAVE TURBULENCE AND PARTICLE HEATING CAUSED BY ELECTRON --ETC(U)

NOV 79 M V GOLDMAN

F49620-76-C-0005

CU-1036

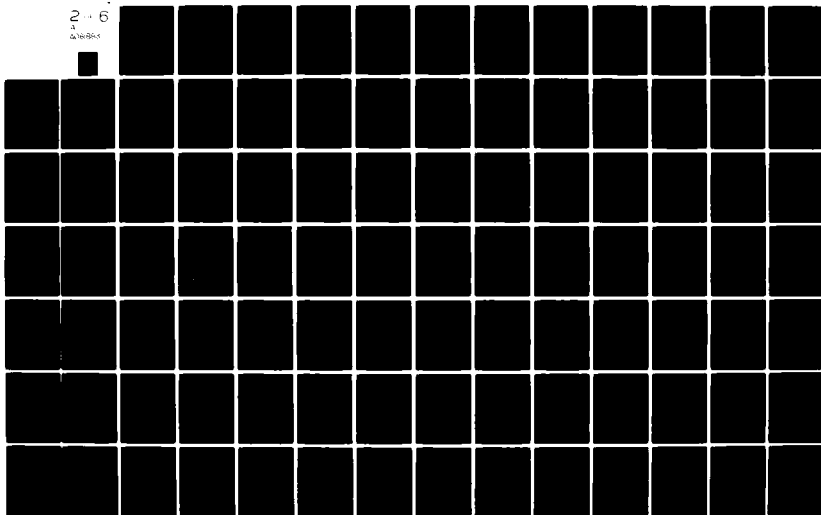
AFOSR-TR-80-0167

NL

UNCLASSIFIED

2 + 6

3 10/10/80



II. CONSERVATION LAWS AND VIRIAL THEOREMS

The most general way to derive conservation laws for field equations is to exploit the invariance properties of the corresponding Lagrangian. The Lagrangian density for Zakharov's equations (see Appendix) is given by Gibbons et al.¹¹ In the limit of electrostatic waves and adiabatic ions, their expression reduces to

$$L = \frac{i}{2} [E_m^* \dot{E}_m - E_m \dot{E}_m^*] - \frac{1}{2} (\nabla_m E_m) (\nabla_i E_i^*) + \frac{1}{2} (E_m E_m^*)^2. \quad (1)$$

From the Euler-Lagrange equations,

$$\frac{\partial}{\partial t} \frac{\delta L}{\delta \dot{E}_m^*} = \frac{\delta L}{\delta E_m^*}, \quad (2)$$

the nonlinear Schrödinger equation follows:

$$i \dot{E} + \frac{1}{2} \nabla^2 E + |E|^2 E = 0. \quad (3)$$

Here, we have used the variational derivative of the Lagrangian $L \equiv \int L d^D r$,

$$\frac{\delta L}{\delta E_n^*} \equiv \frac{\partial L}{\partial E_n^*} - \nabla_\ell \frac{\partial L}{\partial (\nabla_\ell E_n^*)}. \quad (4)$$

Note that we have treated E_n and E_n^* as independent generalized coordinates. Variation with respect to E_n gives the complex conjugate NLSE. The relation between the dimensionless units employed here, and physical units is given by: $t \rightarrow \omega_p t$, $r \rightarrow k_D r / \sqrt{3}$, and $|E|^2 \rightarrow |E|^2 / [32\pi n_0 (\theta_e + \theta_i)]$. The

electron plasma frequency is ω_p ; the Debye wave number, k_D ; the background plasma density, n_0 ; and the electron and ion temperatures in energy units are θ_e and θ_i . \underline{E} is the envelope of the electric field, $\underline{E}(\underline{r}, t) = \text{Re}(\underline{E}e^{-i\omega_p t})$.

The conservation laws for plasmon number, energy, and momentum follow generally from Noether's theorem¹² and the invariance of the Lagrangian under a gauge transformation $\underline{E} \rightarrow \underline{E}e^{i\phi}$, under translation in time, and under translation in space, respectively. Alternatively, they can be obtained directly. Continuity of plasmon number density, $|\underline{E}(\underline{r})|^2$, follows directly by multiplying NLSE with \underline{E}^* and subtracting the complex conjugate, giving the following continuity equation:

$$\frac{\partial |\underline{E}|^2}{\partial t} + \nabla \cdot \underline{S} = 0, \quad (5)$$

where \underline{S} is the plasmon current density

$$\underline{S}_\ell = \frac{1}{2i} (E_n^* \nabla_\ell E_n - E_n \nabla_\ell E_n^*) . \quad (6)$$

Energy and momentum conservation can be derived from the following (D+1)-dimensional energy-momentum tensor:

$$T_{\mu\nu} = \frac{-\partial L}{\partial(\partial E_\ell / \partial x_\mu)} \frac{\partial E_\ell}{\partial x_\nu} - \frac{\partial L}{\partial(\partial E_\ell^* / \partial x_\mu)} \frac{\partial E_\ell^*}{\partial x_\nu} + L \delta_{\mu\nu}, \quad (7)$$

where the indices μ and ν can assume values $0, 1, \dots, D$, and $x_0 \equiv t$, $(x_1, \dots, x_D) \equiv \underline{r}$.

From the Euler-Lagrange equations (2), and the fact that L does not depend explicitly on time and space (translational

invariance), we easily verify that

$$\nabla_{\mu} T_{\mu\nu} = 0, \quad \mu, \nu = 0, 1, \dots, D. \quad (8)$$

This is a set of $(D+1)$ continuity equations, one for energy,

$$\frac{\partial H}{\partial t} + \nabla \cdot \underline{Q} = 0, \quad (9)$$

where the energy (Hamiltonian) density H and the energy flux vector \underline{Q} are defined as

$$H \equiv -T_{00} = \frac{1}{2} [(\nabla_n E_n)(\nabla_{\ell} E_{\ell}^*) - (E_n E_n^*)^2], \quad (10)$$

$$Q_{\mu} = -T_{\mu 0} = -\text{Re}(\nabla_n E_n^* \dot{E}_{\mu}), \quad \mu = 1, \dots, D, \quad (11)$$

and one equation for each momentum component

$$\frac{\partial P_{\nu}}{\partial t} + \nabla_{\mu} T_{\mu\nu} = 0, \quad \mu, \nu = 1, \dots, D, \quad (12)$$

where the momentum density \underline{P} and the stress tensor $T_{\mu\nu}$ are defined as

$$P_{\nu} = T_{0\nu} = \frac{1}{2i} (E_{\ell}^* \nabla_{\nu} E_{\ell} - E_{\ell} \nabla_{\nu} E_{\ell}^*), \quad \nu = 1, \dots, D \quad (13)$$

$$T_{\mu\nu} = \text{Re}(\nabla_{\ell} E_{\ell}^* \nabla_{\nu} E_{\mu}) + L \delta_{\mu\nu}, \quad \mu, \nu = 1, \dots, D. \quad (14a)$$

Note that the momentum density P_{ν} is here identical to the current density, S_{ν} , in Eq. (6). The time derivatives in L can be eliminated by means of the NLSE (3), and by applying the relation $\nabla \nabla \cdot \underline{E} \approx \nabla^2 \underline{E}$ (valid for electrostatic fields; see Appendix), we find

$$L \approx -\frac{1}{2} \left[|\underline{E}|^4 + \underline{\nabla} \cdot \text{Re}(\underline{E}^* \underline{\nabla} \cdot \underline{E}) \right], \quad (15)$$

which inserted in Eq. (14) gives $T_{\mu\nu}$ in the simple form of Goldman and Nicholson:⁶

$$T_{ij} = \text{Re}[(\underline{\nabla} \cdot \underline{E}) \underline{\nabla}_i \underline{E}_j^*] - \frac{1}{2} \delta_{ij} [|\underline{E}|^4 + \underline{\nabla} \cdot (\text{Re} \underline{E}^* \underline{\nabla} \cdot \underline{E})]. \quad (14b)$$

The three continuity equations above can be integrated to yield the following conserved quantities, assuming localized fields: $N = \int |\underline{E}|^2 d^D r$, $H = \int H d^D r$, and $P = \int P d^D r$. They can also be used to explore the particle-like behavior of a wave packet by defining the average of any quantity using the normalized plasmon number density $|\underline{E}|^2/N$ as a weighting function;

$$\langle f(\underline{r}) \rangle \equiv \int (|\underline{E}|^2/N) f(\underline{r}) d^D r.$$

If we multiply Eq. (5) by \underline{r} and integrate by parts, we find the Ehrenfest theorem for the velocity of the centroid coordinate of the wave packet:

$$\partial_t \langle \underline{r} \rangle = \underline{S}/N = \underline{P}/N = \text{const.} \quad (16)$$

Similarly, by Eqs. (5) and (12), and again using $\underline{S} = \underline{P}$, we can prove the following virial theorem for the time evolution of the mean square spatial deviation $\langle \delta r^2 \rangle \equiv \int (|\underline{E}|^2/N) |\underline{r} - \langle \underline{r} \rangle|^2 d^D r$;

$$\partial_t^2 \langle \delta r^2 \rangle = 2 \left[\frac{1}{N} \int T_{\ell\ell} d^D r - \left(\frac{\underline{S}}{N} \right)^2 \right]. \quad (17)$$

From Eq. (14) we find $T_{\ell\ell} = 2H + \frac{1}{2}(2-D)|E|^4 + (D/2)\nabla \cdot (\text{Re}\underline{E}^* \nabla \underline{E})$, which, inserted in Eq. (17), gives

$$\partial_t^2 \langle \delta r^2 \rangle = 2A + (2-D) \langle |E|^2 \rangle, \quad (18a)$$

where

$$A \equiv 2H/N - S^2/N^2, \quad (18b)$$

is a constant of motion. By integrating twice in time, we get

$$\langle \delta r^2 \rangle = At^2 + Bt + C + (2-D) \int_0^t dt' \int_0^{t'} dt'' \langle |E|^2 \rangle, \quad (19)$$

where $B \equiv \partial_t \langle \delta r^2 \rangle_{t=0}$ and $C \equiv \langle \delta r^2 \rangle_{t=0}$. This is the result of Goldman and Nicholson.¹¹ If the number of spatial dimensions $D \geq 2$ and the conserved quantity $A < 0$, it follows that $\langle \delta r^2 \rangle$ will collapse to zero in a finite time. This general result is based on the assumption of adiabatic ions and electrostatic fields, both of which are eventually violated when $\langle \delta r^2 \rangle$ becomes sufficiently small (see Appendix).

Thus, in the late stages of the collapse, the collapse may radiate ion-acoustic waves as well as electromagnetic waves. If these effects are not sufficient to stop the collapse, it will finally be stabilized by Landau-damping when $\langle \delta r^2 \rangle^{1/2}$ becomes of the same order of magnitude as the Debye length λ_D . The useful form of the virial theorem for the NLSE depends on the identity $\underline{S} = \underline{P}$. This identity is not satisfied by the more general Zakharov's equations. Hence, a useful virial theorem that can describe the late stages of a

collapse has not been derived. At the present time, the most fruitful approaches to these problems seem to be numerical integration of Zakharov's equations and particle simulations.

III. GAUSSIAN PACKETS

A. Threshold and collapse time

We treat an initial Langmuir wave packet of the form

$$\underline{E}(\underline{r}, t=0) = -\underline{\nabla}\phi_0 \exp(-\Delta k^2 r^2/D) \exp(i\mathbf{k}_0 \cdot \underline{r}) \quad , \quad (20a)$$

where we assume that the k-space width of the packet, Δk , is much less than the wave number k_0 :

$$\epsilon = \Delta k/k_0 \ll 1. \quad (20b)$$

(In the Appendix we shall see that $\epsilon \ll 1$ is the condition for neglecting electromagnetic effects.) We note several features of this initial wave packet: It is purely electrostatic, since it is the gradient of a potential. As long as $\Delta k \ll k_0$, the field \underline{E} points essentially in the \mathbf{k}_0 direction, and has a maximum value,

$$E_0 \equiv |\underline{E}_{\max}(t=0)| \approx k_0 \phi_0 \quad , \quad (20c)$$

where ϕ_0 is assumed to be real and constant. If we evaluate

the mean packet momentum density, \underline{S}/N , we find

$$\underline{S}/N = \underline{k}_0 [1 + O(\epsilon^2)] . \quad (21)$$

The factor D in the exponent of the Gaussian is equal to the number of spatial dimensions considered. Its presence guarantees us that Δk^2 is indeed the correct measure of the packet's k -space width: To justify this interpretation, we note that

$$N^{-1} \int |\underline{E}_k|^2 |\underline{k} - \underline{k}_0|^2 \frac{d^D k}{(2\pi)^D} \approx (\Delta k)^2 , \quad (22)$$

by using the inequality $\Delta k \ll k_0$, and Eq. (20a).

The physical quantities and invariants defined in Section II can be evaluated for the initial field of Eq. (20), and expressed entirely in terms of E_0 , Δk , k_0 , and D . For example, to zero order in ϵ ,

$$N \approx E_0^2 \left(\frac{D\pi}{2\Delta k^2} \right)^{D/2} , \quad (23)$$

$$\langle \delta r^2 \rangle_0 \approx \left(\frac{D}{2\Delta k} \right)^2 , \quad (24)$$

$$\langle |\underline{E}|^2 \rangle \approx E_0^2 / 2^{D/2} . \quad (25)$$

The invariant A , defined in Eq. (18b), is

$$A \equiv \frac{2H}{N} - \left| \frac{\underline{S}}{N} \right|^2 = \Delta k^2 - \frac{E_0^2}{2^{D/2}} . \quad (26)$$

The threshold for collapse for $D = 2$ (two dimensions) is $A < 0$. This is also an upper bound on the three-dimensional threshold:

$$E_0^2|_{\text{threshold}} = 2^{D/2} \Delta k^2 . \quad (27)$$

For our Gaussian initial packet, the integration constants B and C in Eq. (19) are easily evaluated. We find $B = 0$, and $C = (D/2)^3 / \Delta k^2$. From Eqs. (19) and (26) the time t_c follows:

$$t_c = |C/A|^{1/2} = D/2 \Delta k^2 (P-1)^{1/2} . \quad (28)$$

This is the virial theorem prediction of the collapse time for $D = 2$, and an upper bound on the collapse time for $D = 3$. The quantity P is defined as:

$$P \equiv E_0^2 / 2^{D/2} \Delta k^2 . \quad (29)$$

When $D = 2$, P is the ratio of field energy to threshold energy. We shall use P in our treatment for arbitrary D , although its interpretation as wave to threshold energy holds only for $D = 2$.

B. Gaussian approximation

In general, as a packet develops nonlinearly, it does not preserve its Gaussian shape. If P is much greater than one, the packet may be unstable against "breaking-up" into smaller packets (modulational instability¹³). One-dimensional "breathers" may have many spatial oscillations when $P \gg 1$.

In three dimensions, even very close to threshold, self-similar behavior² develops asymptotically, as the collapse proceeds. Using a scalar NLSE, Budneva, et al.² have shown that an initial three-dimensional Gaussian packet with $P \gg 1$ soon develops such a feature. We show in Section V that such a feature also develops when $P \gtrsim 1$ (near threshold). A quickly-collapsing core of similarity form rises at the center of the packet. This core becomes singular, and its width goes to zero for non-zero $\langle \delta r^2 \rangle$. However, the threshold for collapse and the early time behavior of $\langle \delta r^2 \rangle$ are well-described by the virial theorem methods we are about to describe.

Assuming the packet remains approximately Gaussian, a closure scheme for Eqs. (18) may be formulated with $D = 1$ or

$D = 3$. The problem is with the quantity $\langle |E|^2 \rangle$, which is not an invariant. We shall make the (Gaussian) approximation that

$$\langle |E|^2 \rangle = Q N \langle \delta r^2 \rangle^{-D/2}, \quad (30a)$$

where Q is assumed constant. We may evaluate Q at $t = 0$, using Eqs. (23)-(25). To zero order in ϵ , the result is

$$Q = (D/4\pi)^{D/2}. \quad (30b)$$

Inserting Eqs. (30) into the time-evolution Eq. (19) for $\langle \delta r^2 \rangle$ enables it to be integrated by potential theory methods. A first integral is

$$\dot{\xi}^2/2 + V(\xi) = E, \quad \xi \equiv \langle \delta r^2 \rangle. \quad (31a)$$

Here, E is an arbitrary integration variable, and the "potential" $V(\xi)$ is given by

$$V(\xi) = -2A\xi - 2NQ\xi^{(1-D/2)}. \quad (31b)$$

Equations (31) are convenient for studying effects of dimensionality on the evolution of solitary wave packets.

Calculations of characteristic times, such as pulsation and collapse times, are easier if we express the potential in terms of the normalized coordinate $\eta \equiv \xi/\xi_{t=0}$, where $\xi_{t=0} = (D/2\Delta k)^2$ is the initial mean square spatial width of the wave packet,

$$V = \frac{D^2}{2} [(P-1)\eta - P\eta^{1-D/2}]. \quad (32)$$

Note that the potential for the initial packet ($\eta = 1$) is $V(\xi_{t=0}) = -D^2/2$, hence independent of the initial parameters. We study the implications of the potential of Eq. (32) for various cases:

D = 1. For $A < 0$, ($P > 1$), the potential has the concave shape of Fig. 1. For a Gaussian packet the potential has a minimum at $\eta_0 \equiv \frac{1}{4}(1-P^{-1})^{-2}$ and a zero-point at $\eta_1 \equiv (1-P^{-1})^{-2}$. This allows bounded, oscillating solutions about the equilibrium point η_0 . For $P = 2$ we find that $\eta_0 = 1$, which is the initial coordinate, thus giving the stationary equilibrium solution corresponding to the well-known NLSE-soliton $E = \alpha \text{sech}(\alpha x) \exp(i\alpha^2 t/2)$. Since $\eta_1 > 1$ for all $P > 1$, and $\eta_1 \rightarrow 1$ as $P \rightarrow \infty$, it is clear that full collapse never occurs. For sufficiently large P the oscillations about η_0 will be so large that the minimum η will be below the limits of validity of the NLSE as given in the Appendix B.

Assuming $(P-1)$ is sufficiently small (see Appendix B), our theory gives pulsating solutions corresponding to the bound states near the bottom of the potential well in Fig. 1. $\langle \delta x^2 \rangle$ oscillates periodically, and, by the invariance of $\int dx |E|^2$, so does $|E|_{\max}^2$.

This behavior appears to be related to certain numerical solutions obtained by Satsuma and Yajima,⁷ who apply the inverse scattering method to solve for the time evolution of an initial wave packet of form

$$E(x,0) = \alpha \text{sech} x. \quad (33)$$

When $a = 1 + \epsilon$, and $\epsilon \ll 1$, they also observe oscillations in $|E|_{\max}^2$, but these oscillations slowly relax, presumably due to "continuum" radiation of Langmuir waves. We do not observe such damping of the oscillations, probably because "continuum" radiation is excluded by the assumption of localized fields in the spatially-Gaussian closure approximation.

The validity of our treatment of periodic pulsations of one single wave packet requires that the packet does not break up due to secondary instabilities in a time shorter than the period. The possibility of such a break-up is not accounted for in our Gaussian model. The period is obtained by integrating Eq. (31) using Eq. (32),

$$\tau = \frac{F(P)}{2 |E_0|}, \quad (34a)$$

where the function $F(P)$ is defined by the integral

$$F(P) \equiv \pm \frac{P}{\sqrt{2}} \int_{\eta_{\text{turn}}}^1 \frac{d\eta}{[P\eta^{\frac{1}{2}} - (P-1)\eta - 1]^{\frac{1}{2}}}. \quad (34b)$$

The positive sign is for $P > 2$, ($\eta_{\text{turn}} < 1$), the negative sign for $P < 2$ ($\eta_{\text{turn}} > 1$). $F(P)$ is plotted in Fig. 3. The period predicted by our Eqs. (34) are in good agreement with the numerical results exhibited in Figure 2 of Ref. 7. As $P \rightarrow 1^+$, the period goes to infinity.

The growth rate of secondary instabilities such as modulational instability and parametric decay¹³ is $\gamma_s \sim |E_0|^2$. If we let $f = \gamma_s t_s$ be the number of e-folding needed for the noise

to grow to nonlinear levels, we get

$$\frac{\tau}{t_s} = \frac{F(P)}{f}.$$

The value of f depends on the noise level from which the unstable waves are amplified, however, even very conservative estimates give $f \gtrsim 10$. This means that "breathing" and break-up times are of the same order of magnitude for $2 < P \lesssim 10^2$. Break-up instabilities are effective only if the packet size is larger than the shortest unstable wavelength; $\langle \delta r^2 \rangle^{1/2} = 1/(2\Delta k) > \lambda_s = \pi/|E_0|$ or, equivalently, $P \gtrsim 2\sqrt{2}\pi^2 \approx 28$. If this threshold is exceeded, the wave packet will break up into smaller packets on a time scale of the same order as the pulsation period. We do not expect our theory to apply under these conditions.

A different way to view one-dimensional "break-up" behavior when $P \gg 2$ is provided by the work of Satsuma and Yajima.⁷ They studied initial packets of the form given in Eq. (33) for $a = 1, 2, 3$, also (see their Figure 1). The case $a = 1$ corresponds to the usual single soliton, but $a = 2$ and 3 correspond to "breathers," which are exactly periodic pulsating bound states of two or three solitons. The case $a = 3$, in particular, shows markedly non-Gaussian behavior, as the packet splits into two and three narrower packets in the course of its periodic behavior. (Similar behavior was also observed by Yuen and Ferguson,⁸ in what they call "complex" recurrence.) If we set the area under our Gaussian packet equal to the area under their sech x packet, we obtain a relation between our P and their a :

$$P = \pi a^2 / \sqrt{2} . \quad (35)$$

From this we see that $a = 1$ corresponds to $P \approx 2$ in the single soliton result. The case $a = 2$ corresponds to $P \approx 9$, which is a somewhat lower bound for validity than found from consideration of modulational instabilities.

For $P < 1$ ($A > 0$), the potential in Fig. 1 is monotonically decreasing for all $\eta > 0$, so any localized wave packet will disperse spatially with time. Break-up, recurrence, or collapse will never occur.

$D = 2$. In this case, the term containing $\langle |\underline{E}|^2 \rangle$ vanishes, and no approximation is necessary in the virial theorem. The potential $V(\xi)$ is linear with slope $-2A$, giving collapse for $A < 0$, and spatial dispersion for $A > 0$. Threshold for collapse, and collapse time, are given by Eqs. (27) and (28), respectively.

$D = 3$. The potential for $A < 0$ grows monotonically from minus infinity at $\xi = 0$, approaching the straight line $-2A\xi$ as $\xi \rightarrow \infty$. Consequently, collapse occurs for all initial wave packets, and an upper bound for the collapse time is found by considering collapse along the linear potential $-2A\xi$. This gives the expression of Eq. (27). The convex shaped potential appearing for $A > 0$ has an unstable equilibrium for $\eta_0 \equiv [2(P^{-1}-1)]^{-2/3}$. Collapse for a Gaussian wave packet occurs when $\eta_0 > 1$, or

$$P > 2/3 . \quad (36)$$

The threshold condition $P > 1$ for $D = 2$ corresponds to the threshold condition $E_0^2 > 2\Delta k^2$, while Eq. (36) for $D = 3$ requires $E_0^2 > (2^{5/2}/3)\Delta k^2$. This means that the threshold is slightly lower in three dimensions.

The virial theorem prediction for the collapse time, valid for all $P > 2/3$, is easily obtained by integration of Eq. (31),

$$t_c = \frac{G(P)}{|E_0|^2} , \quad (37)$$

where $G(P)$ is defined by the integral

$$G(P) \equiv \frac{3P}{\sqrt{2}} \int_0^1 \frac{d\eta}{[P\eta^{-1/2} - (P-1)\eta - 1]^{1/2}} , \quad (38)$$

which is plotted in Fig. 3.

The collapse time predicted by (37) is an upper limit. We shall see in Sec. V that a self-similar "core" can collapse faster than $\langle \delta r^2 \rangle$.

The threshold condition for break-up, that the packet size is larger than the smallest unstable wavelength, now becomes $P > \sqrt{2}(\pi/3)^2 \approx 1.6$, while the ratio

$$\frac{t_c}{t_s} = \frac{G(P)}{f} , \quad (39)$$

is smaller than unity only for $0.7 < P \leq 10$. Hence for large P ($P > 10$), a wave packet should break up into smaller packets before it has had time to collapse. If the smaller packets have P in the range where $t_c/t_s < 1$ they will collapse. This

succession of break-up and collapse has been referred to as indirect collapse.⁶

Similar phenomena are well known in nonlinear optics.⁹ A nonlinear laser beam with $P \gg 1$ breaks up into intense filaments, whereas when P is closer to one, the beam self-focusses as a whole.

IV. EFFECT OF DAMPING ON TWO-DIMENSIONAL COLLAPSE

We next introduce a local damping term of the form $i\gamma \underline{E}$ on the left side of the NLSE, Eq. (3). The conservation laws, Eqs. (5), (9), and (12) are modified in the following manner:

$$(\partial_t + 2\gamma)N = 0 \quad \text{or} \quad N = N_0 \exp(-2\gamma t) . \quad (40)$$

Since there is no driver, the plasmon number decreases exponentially with time. The momentum behaves the same way:

$$(\partial_t + 2\gamma)\underline{P} = 0 \quad \text{or} \quad \underline{P} = \underline{S} = \underline{S}_0 \exp(-2\gamma t) . \quad (41)$$

However, the energy H has a more subtle evolution equation:

$$(\partial_t + 2\gamma)H = \gamma N \langle |\underline{E}|^2 \rangle . \quad (42)$$

An initially negative H may become positive if the effective source on the right side is large enough. Sufficiently large dissipation causes the nonlinear refraction term ($\propto |\underline{E}|^4$) in H to decrease faster than the dispersion term ($\propto |\nabla \cdot \underline{E}|^2$). Hence H and A eventually change from negative to positive, and collapse stops. The virial theorem takes the form (for $D = 2$)

$$(\partial_t + 2\gamma)^2 \langle \delta r^2 \rangle = 2A . \quad (43)$$

Assuming an approximately Gaussian wave packet, Eqs. (30) implies that $\langle |\underline{E}|^2 \rangle = (D^2/\pi^2)^{D/2} \langle \delta r^2 \rangle^{-D/2} N_0 \exp(-2\gamma t)$, which can be inserted in Eq. (42). We restrict ourselves to treat the case $D = 2$ for which Eq. (42) may be written in the form

$$\partial_t A = \frac{\gamma}{\pi} \frac{N_0}{\langle \delta r^2 \rangle} \exp(-2\gamma t) . \quad (44)$$

In Eq. (43) and Eq. (44) we make the following substitutions

$$\tau = t/t_c, \quad \nu = \gamma t_c , \quad (45)$$

$$x(\tau) = \frac{\exp(2\nu\tau)}{2t_c (P\nu)^{1/2}} \langle \delta r^2 \rangle , \quad y(\tau) = \frac{t_c A}{(P\nu)^{1/2}} , \quad (46)$$

where t_c is the collapse time of Eq. (28). The resulting equations are

$$\partial_\tau^2 x = y \exp(2\gamma\tau) , \quad \partial_\tau y = x^{-1} , \quad (47)$$

with initial conditions

$$\begin{aligned} x(0) &= 1/2\alpha^{1/2} \\ x'(0) &= v\alpha^{-1/2} \\ y(0) &= -\alpha^{-1/2} , \end{aligned} \quad (48a)$$

$$\alpha \equiv v/(1-P^{-1}) . \quad (48b)$$

This initial-value problem has been solved numerically for various values of P and α . For a given P , there exists a critical value $\alpha_c(P)$. For $\alpha < \alpha_c$, the packet collapses completely. For $\alpha \gtrsim \alpha_c$, the variable x defined in Eq. (46) decays to a minimum, x_{\min} , and then increases. The packet size, $\langle \delta r^2 \rangle$ asymptotically approaches a constant, due to the balance between linear dissipation and linear dispersion. This can be seen from Eqs. (47). As $x \rightarrow \infty$, y goes to a constant, and x approaches $\exp(2\gamma t)$. From the definition of x , this implies that $\langle \delta r^2 \rangle$ approaches a constant. From Eq. (43), we see that $\langle \delta r^2 \rangle \rightarrow A/2\gamma^2$. In the asymptotic limit, only linear dispersion contributes to H , so $A \rightarrow \langle \delta r^2 \rangle^{-1}$, and $\lim_{t \rightarrow \infty} \langle \delta r^2 \rangle \sim \gamma^{-1}$. This may be of little interest, however, because $|E|^2$ has damped to a small value by this time, and the packet is linear.

In Figure 4 we show some typical curves of $\langle \delta r^2 \rangle$ versus time, for various values of the damping. Each curve is shown as a dashed line after the plasmon number, N , has decreased by one order of magnitude.

In Fig. 5 the quantity $\beta \equiv x_{\min}/x(0)$ has been plotted versus α for various P -values. These plots show that collapse is stabilized for $\alpha > \alpha_c \approx 1/3$. Thus, we have non-collapsing solutions for $\gamma > \gamma_c$, where the critical damping rate γ_c is given by

$$\gamma_c \approx (1-P^{-1})/(3t_c). \quad (49)$$

If the collapse proceeds too far before stabilization occurs, the NLSE breaks down and results based on the virial theorem are not reliable. Initial wave packet conditions for which the NLSE remains valid throughout the nonlinear evolution are given in the Appendix.

V. SELF-SIMILAR BEHAVIOR

A. Scaling laws

By making the self-similar substitution^{1,2}

$$\underline{E} = (t_c - t)^{-\frac{1}{2}} \underline{R}(\underline{u}) , \quad \underline{u} \equiv (t_c - t)^{-\frac{1}{2}} \underline{x} , \quad (50)$$

in Eq. (3), we get rid of the time-dependence:

$$\frac{i}{2} (1 + \underline{u} \cdot \partial_{\underline{u}}) \underline{R} + \frac{1}{2} \partial_{\underline{u}}^2 \underline{R} + |\underline{R}|^2 \underline{R} = 0 . \quad (51)$$

At collapse threshold the nonlinear pressure term must balance the dispersion term, hence we get for the ratio of field energy to threshold energy

$$P \sim \left| \frac{|\underline{R}|^2 \underline{R}}{\frac{1}{2} \partial_{\underline{u}}^2 \underline{R}} \right| \sim (R_{\max} \Delta u)^2 . \quad (52)$$

Here Δu is the half-width of the function $\underline{R}(\underline{u})$. Assuming that the first term in Eq. (51) is of same order of magnitude as the nonlinear term (which is obviously true for $P \gg 1$), we find that $R_{\max} = \mathcal{O}(1)$. From Eq. (50), it then follows that

$$t_c = \mathcal{O}(|E_0|^{-2}) . \quad (53)$$

This always turns out to be a faster time than that predicted by virial theory. (An example will be given below.)

The self-similar solution in Eq. (50) has some peculiar properties which might tend to obscure its relation to arbitrary initial value problems. For example, its N -invariant is infinite in three dimensions (although not in two). To see this, we note first that Eq. (50) implies

$$N = (t_c - t)^{\frac{1}{2}} \int d^3u |R(u)|^2 . \quad (54)$$

However, in the limit of large u , the last two terms in Eq. (51) are negligible, and $R \propto u^{-1}$. Hence, the integral in (54) diverges. Indeed, this must be the case, in order for N to be time-independent. However, in any initial value problem of physical interest, N is always finite. What role can self-similar solutions play in arbitrary initial-value problems? This question is addressed next.

B. Numerical studies of three-dimensional collapse

We support our discussion with numerical solutions of a scalar NLSE in spherical symmetry:

$$i \frac{\partial \psi}{\partial t} + \frac{1}{2r^2} \frac{\partial}{\partial r} \left(r^2 \frac{\partial \psi}{\partial r} \right) + |\psi|^2 \psi = 0 , \quad (55)$$

with boundary conditions

$$\left(\frac{\partial \psi}{\partial r} \right)_{r=0} = \psi_{r \rightarrow \infty} = 0 .$$

This equation follows from the vectorial NLSE (3) under certain conditions. Assume that the electric field envelope E has a

rapidly oscillating spatial phase factor $\exp(i\mathbf{k}_0 \cdot \mathbf{r})$, where k_0 is much larger than the k -space width Δk of the spatial envelope. Under this assumption the electric field can be represented in terms of a scalar function $\phi(\mathbf{r}', t)$:

$$\mathbf{E}(\mathbf{r}', t) = \nabla[\phi(\mathbf{r}', t)/k_0] \approx i\phi(\mathbf{r}', t)\hat{\mathbf{k}}_0. \quad (56)$$

This immediately gives a scalar NLSE in ϕ , but it is not spherically symmetric because $\phi(\mathbf{r}', t)$ still contains the non-symmetric phase factor. This means that the wave-packet has a non-zero momentum, $\mathbf{p}' = N'\mathbf{k}_0$. However, the momentum can be removed by the following gauge-frame transformation

$$\phi(\mathbf{r}', t) = \psi(\mathbf{r}, t) \exp(i\mathbf{k}_0^2 t/2 + i\mathbf{k}_0 \cdot \mathbf{r}'), \quad (57)$$

$$\mathbf{r} = \mathbf{r}' - \mathbf{k}_0 t, \quad (58)$$

under which the NLSE and the constants of motion N and A [see Eq. (18b)] are invariant. The momentum transforms as

$$\mathbf{p} = \mathbf{p}' - N'\mathbf{k}_0 = 0,$$

so $\psi(\mathbf{r}, t)$ does not contain the phase factor $\exp(i\mathbf{k}_0 \cdot \mathbf{r})$, and it is possible to impose spherical symmetry to obtain Eq. (55)

Equation (55) was solved by Budneva et al. for an initial Gaussian shape corresponding to $P = 8.5$. (Threshold is $P = 2/3$.) We solve it for several P values, both below and above threshold, and the results can be summed up as follows: For

all $P > 2/3$ a collapsing "core" develops whose collapse time is less than one-half of the collapse time derived from the virial theorem under the Gaussian approximation.

However, the collapse threshold condition, $P = 2/3$, obtained from the virial theorem with the Gaussian closure approximation provides a surprisingly good criterion for "core" collapse. When $P < 2/3$ the corona disperses ($\langle \delta r^2 \rangle$ grows monotonically), in agreement with virial theorem predictions. Just below threshold, however, we have the situation of a collapsing core co-existing with a dispersing corona, indicating that core and corona can behave independently of each other.

In Fig. 6 we illustrate a solution to Eq. (55) (the factor $\frac{1}{2}$ in the dispersion term has been scaled away, by stretching r by a factor $\sqrt{2}$, in order to correspond to the equation of Budneva, et al.). Figure 6 shows the build-up of the core for $P = 4/3$ (two times threshold). The intensity is displayed at time $t = 1.2$. The dotted curve shows the corresponding shape if the packet has remained of Gaussian shape and collapsed in accordance with virial theorem arguments. The steepness of the core is of much less consequence when we recall that moments and invariants are weighted by r^2 when three-dimensional integrations are performed.

For example, at early times, the virial theorem prediction of width $\langle \delta r^2 \rangle$ is well satisfied. If we assume that

$$|1 - \langle \delta r^2 \rangle / \langle \delta r^2 \rangle_0| \ll 1,$$

then the virial result, Eq. (31), may be integrated analytically to yield,

$$\langle \delta r^2 \rangle \approx \langle \delta r^2 \rangle_0 (1 - at^2) ,$$

$$a \equiv \left(\frac{3}{2} P - 1 \right) \frac{E_0^4}{18 P^2} . \quad (59)$$

This curve is plotted in Fig. 7 for $P = 4/3$ ($E_0^2 = 2.39$). Superimposed on it are the results for $\langle \delta r^2 \rangle$ obtained by spatial integration of the numerical solutions to (55), at various times. By the time $t = 1.2$ (corresponding to Fig. 6), the non-Gaussian character of the core is causing the numerically determined $\langle \delta r^2 \rangle$ values to fall about 1% below the virial theorem predictions. This happens because Eq. (59) was obtained by assuming Q is constant, and equal to the value given in Eq. (30b). In the actual numerical solution, Q has increased by a factor of 2 by the time $t = 1.2$, and it is this non-Gaussianity which is causing the slight lowering of the $\langle \delta r^2 \rangle$ points.

The virial theorem prediction for the collapse time [Eq. (37)] gives $t \approx 3.2$. However, the collapse of the core is seen to occur at $t \approx 1.33$, by arguments we shall advance shortly. At this time $\langle \delta r^2 \rangle$ is non-zero and comes from a tail which remains even when the core has gone singular. This time is indicated on Fig. 7 as $t_c^{(s)}$. The significance of the virial theorem predictions of $\langle \delta r^2 \rangle$ beyond $t_c^{(s)}$ are not clear. The nature of the problem will be summarized later.

In Fig. 8 we verify that the field is self-similar at $r = 0$, and determine the collapse time by extrapolation. According to the scalar-field version of Eq. (50), if the field is self-similar at the origin, then $\psi(0,t) = R(0)(t_c - t)^{-\frac{1}{2}}$. Hence, in Fig. 8, we have plotted $|\psi(0,t)|^{-2}$ versus time and have found the expected straight line, with $|\psi(0,t_c)|^{-2} = 0$ at $t_c^{(s)} = 1.3265$.

Of more interest is the question of the spatial extent of the self-similarity. Consider the field at two times t_1 and t_2 , such that $t_1 < t_2 < t_c^{(s)}$. If the field is self-similar at t_1 , with respect to the later time t_2 , then it must have the form $\psi_{ss}(r,t_1)$ which is related to $\psi(r,t_2)$ by

$$\psi_{ss}(r,t_1) = \alpha_{21}\psi(r/\alpha_{21},t_2) ,$$

$$\alpha_{21} \equiv \left(\frac{t_c^{(s)} - t_2}{t_c^{(s)} - t_1} \right)^{\frac{1}{2}} . \quad (60)$$

In Fig. 9 we have plotted the quantities

$$|\psi|^2/|\psi_{ss}|^2 - 1 ,$$

for $t_2 = 1.3220$, and three different values of the earlier time t_1 . This represents the percent difference between $|\psi|^2$ and the self-similar solution, as a function of radius, for the three earlier times. At times later than 1.30, $|\psi|^2$ is self-similar to within 15% up to radii of about $r = 3.7$. At these times the half-width of the peak occurs at $r < 0.5$, so a relatively long self-similar tail is observed.

How much of a contribution to the "number invariant," N , is made by the self-similar part of the solution? To answer this question we have plotted, in Fig. 10, the volume integral of $|\psi|^2$ up to radius r , as a function of r ,

$$N_r(t) \equiv 4\pi \int_0^r dr r^2 |\psi(r,t)|^2, \quad (61)$$

at the initial time, and at two later times. Note, N_∞ is the plasmon number invariant, N , here equal to about 14. The arrows on the curves at $t = 1.2$ and at 1.31 indicate the radius at which $|\psi|^2$ deviates from self-similarity by $\pm 25\%$. We note that about half of N comes from the self-similar portion of the solution. The dots indicate the radius at which the half-maximum in $|\psi|^2$ occurs for each time. Most of the contribution of the self-similar portion of $|\psi|^2$ to N comes from the tail rather than the peak. As the collapse proceeds, the self-similar peak makes a vanishingly small contribution to N , while the self-similar tail makes an increasing contribution.

The important issue of what happens to the entire tail (and to $\langle \delta r^2 \rangle$), after the collapse of the central peak at time $t_c^{(s)}$, cannot be resolved within the context of the present theory. A proper resolution should take into account the inevitable break-down of the Schrödinger equation and the need for more physical processes. In the Langmuir wave application, this means the inclusion of a dynamic ion response and, possibly, energy transfer to electrons. The criteria for neglect of these physical effects are described in the Appendix.

Acknowledgments

One of us (M.V.G.), would like to thank the Guggenheim Foundation for a Fellowship held during part of this research, and also to acknowledge helpful conversations with G. Reiter, D. Nicholson, F. Tappert, and H. H. Chen. This work was supported by the National Science Foundation, Atmospheric Sciences Section, and by the Air Force Office of Scientific Research. The work of one of us (K.R.) was also supported by the Institute of Mathematical and Physical Sciences, University of Tromsø, Norway. We thank the National Center for Atmospheric Research, supported by the National Science Foundation, for computer time used in this study.

APPENDIX

Here we briefly review the plasma physics conditions which must be satisfied for the validity of the cubic Schrödinger equation (3) in the text. We begin with a more general set of equations, the "Zakharov equations," which have been used extensively¹⁴ to describe nonlinear Langmuir and electromagnetic wave evolution

$$i\mathbf{E} + \frac{1}{2}\nabla \nabla \cdot \mathbf{E} - \frac{C^2}{2} \nabla \times \nabla \times \mathbf{E} - \delta n \mathbf{E} = 0, \quad (\text{A } 1)$$

$$(C_s^{-2} \partial_t^2 - \nabla^2) \delta n = \nabla^2 |\mathbf{E}|^2. \quad (\text{A } 2)$$

The units here are the same as described after Eq. (3); in addition, δn is the low frequency electron (or ion) density response, in units of $2n_0$, where n_0 is the average background density. The parameters C and C_s are, respectively, the speed of light and the ion-acoustic sound speed, in units of $\sqrt{3} v_e$, where v_e is the electron thermal speed, $(\theta_e/m_e)^{1/2}$. There are five conditions for the validity of the Zakharov equations (A1) and (A2):

- i) $(k/k_D) |\mathbf{E}| \ll 1$ (dipole approximation);
- ii) $\omega_{\text{SLOW}} \ll \omega_p$ (slow-fast time separation);
- iii) neglect of wave-particle interactions ($k/k_D \ll 1$, $\theta_e \gg \theta_i$);
- iv) quasi-neutrality;

v) linear ion response to ponderomotive force ($\delta n \ll n_0$).

We shall be concerned here mainly with the conditions for two further approximations, which lead to the cubic Schrödinger equation. These are, respectively, the electrostatic approximation ($\nabla \times \underline{E} = 0$), and the adiabatic ion approximation

$$|C_s^{-2} \partial_t^2 \underline{E}| \ll |\nabla^2 \underline{E}| \text{ in Eq. (A2).}$$

We begin by assuming the electrostatic approximation, and then show that this approximation can be well satisfied in the adiabatic limit, provided that the packet also satisfies certain criteria in k-space.

With $\nabla \times \underline{E} = 0$, it follows that $\nabla \cdot \nabla \underline{E} = \nabla^2 \underline{E}$, in Eq. (A1). In the adiabatic limit, the first term on the left side of (A2) is neglected in comparison to the second term. For localized fields, (A2) then integrates to $\delta n = -|E|^2$, and (A1) becomes the cubic Schrödinger equation. An a posteriori examination of the terms on the left side of (A2) then gives us the necessary inequality for the adiabatic limit:

$$|C_s^{-2} \partial_t^2 |E|^2| \ll |\nabla^2 |E|^2| \quad . \quad (A3)$$

From Eqs. (5) and (12), and the identity of current and momentum densities for the Schrödinger equations, we find

$$\partial_t^2 |E|^2 = \nabla_i \nabla_j T_{ij} \quad . \quad (A4)$$

The stress tensor is given by Eq. (14b). It may be rewritten in a useful form by expressing the field in terms of an amplitude and phase:

$$\underline{E} = \underline{A} \exp(i\theta) , \quad \underline{A}, \theta \text{ real} . \quad (\text{A5})$$

Then,

$$T_{ij} = (\underline{\nabla} \cdot \underline{A}) (\underline{\nabla}_i A_j) + \underline{u} \cdot \underline{A} u_i A_j - \frac{\delta_{ij}}{2} [A^4 + \underline{\nabla} \cdot (\underline{A} \underline{\nabla} \cdot \underline{A})] , \quad (\text{A6})$$

where,

$$\underline{u} \equiv \underline{\nabla} \theta , \quad (\text{A7})$$

corresponds to the packet velocity [note, with the help of (A5), the current density, (6) may be rewritten as $\underline{S} = \underline{u} |\underline{E}|^2$]. In order to reduce the inequality (A3) still further, we consider a wave packet which is centered about wave vector \underline{k}_0 and has a k-space width Δk :

$$\underline{A} \sim \underline{A}_0 \exp(-r^2 \Delta k^2) , \quad \underline{u} = \underline{k}_0 . \quad (\text{A8})$$

From (A6) we see that the various terms in the stress tensor are then of the following orders:

$$\underline{T} = O[(\Delta k)^2 A^2] + O[k_0^2 A^2] + O[A^4] + O[(\Delta k)^2 A^2] . \quad (\text{A9})$$

Hence, (A3) and (A4) yield the following inequality for the adiabatic limit:

$$O[(\Delta k)^2] + O(k_0^2) + O(|\underline{A}|^2) \ll C_s^2 = r \frac{m}{M} , \quad (\text{A10})$$

where $\underline{r} = (1/3)(1 + \gamma_i \theta_i / \theta_e)$, and γ_i is the usual ratio of ion specific heats. The condition on the wave numbers means essentially that the packet velocities (or group velocity, in the limit $\Delta k \ll k_0$) must be much less than sound speed, so that the

ions can follow the packet spatial translation. The condition on the amplitude, $|A|$, means that the packet's collapse speed also must be much less than sound speed. Both conditions are theoretically met, for example, in the case of the type III solar radio emission.^{6,15}

It is also useful to examine the adiabaticity criterion (A3) for the case of self-similar solutions of form (40). Once again, if $(R)_{\max}$ and $(\partial_u R)_{\max}$ are considered to be of order unity, the adiabaticity condition (A3) becomes $|E|_{\max}^2 \ll c_s^2$, for non-translating similarity solutions.

Next, we show that the condition for electrostatic approximation in the adiabatic limit is merely

$$\Delta k \ll k_0, \quad \text{for electrostatic approx.} \quad (\text{A11})$$

Here we imagine an initially pure electrostatic packet (such as may arise from a beam instability, for example^{6,15}), centered around wave vector k_0 . As the packet collapses, its effective k-space width, Δk , increases. As long as Δk remains much less than k_0 , the term $c^2 \nabla \times \nabla \times \underline{E} / 2$ on the left of Eq. (A1) may be ignored.

The demonstration consists of two parts. First we require that the transverse part of \underline{E} be much smaller than the longitudinal part. This has been shown in references 2 and 15, where $|\underline{E}_T|/|\underline{E}_L|$ is shown to be of order c^{-2} . Given $|\underline{E}_L| \gg |\underline{E}_T|$, we may take the longitudinal and transverse parts of (B-1) and write them approximately as

$$i\dot{\underline{E}}_L + \frac{1}{2}\nabla^2 \underline{E}_L - (\delta n \underline{E}_L)_L = 0, \quad (A12)$$

$$i\dot{\underline{E}}_T + \frac{c^2}{2} \nabla^2 \underline{E}_T - (\delta n \underline{E}_L)_T = 0. \quad (A13)$$

Note that if we can demonstrate $|\delta n \underline{E}_L|_T \ll |\delta n \underline{E}_L|_L$, it will then follow that the third term in (A12) can be written approximately as $(\delta n \underline{E}_L)_L + (\delta n \underline{E}_L)_T = \delta n \underline{E}_L$, and the resulting equation is equivalent to (A1), in the electrostatic approximation. The condition $|\delta n \underline{E}_L|_T \ll |\delta n \underline{E}_L|_L$, with $\delta n \approx -|\underline{E}_L|^2$ (adiabatic approximation), may be written as,

$$\left| \int d^3 \underline{r}' \frac{\underline{\nabla}' \times \underline{\nabla}' \times (|\underline{E}_L|^2 \underline{E}_L)}{|\underline{r} - \underline{r}'|} \right| \ll \left| \int d^3 \underline{r}' \frac{\underline{\nabla}' \cdot \underline{\nabla}' \cdot |\underline{E}_L|^2 \underline{E}_L}{|\underline{r} - \underline{r}'|} \right| \quad (A14)$$

Next, take \underline{E}_L to be of the form $\underline{E}_L = \underline{A}_0 \exp(-r^2 \Delta k^2) \exp(i \underline{k}_0 \cdot \underline{r})$, as in (A5) and (A8). Then, since $\underline{\nabla}' \times \underline{E}_L(\underline{r}') = 0$, the left side is of order $\Delta k/k_0$ smaller than the right side, when $\Delta k \ll k_0$. This demonstrates that $\Delta k \ll k_0$ is indeed the condition for the electrostatic approximation, in the adiabatic limit. Together with the inequality (A10), this defines the conditions for converting the Zakharov equations (A1) and (A2) into the cubic Schrödinger Eq. (3). However, we note that these conditions are based on spatially Gaussian packets. If collapse has proceeded sufficiently into the self-similar regime, these estimates may have to be modified.

REFERENCES

1. V. E. Zakharov, Zh. Eksp. Teor. Fiz. 62, 1745 (1972) [Sov. Phys.-JETP 35, 908 (1972)].
2. V. E. Zakharov, A. F. Mastryukov, and V. S. Synakh, Fiz. Plazmy 1, 614 (1975) [Sov. J. Plasma Phys. 339 (1975)];
P. B. Budneva, V. E. Zakharov, and V. S. Synakh, Fiz. Plasma 1, 606 (1975) [Sov. J. Plasma Phys. 1, 335 (1975)].
3. A. A. Galeev, R. Z. Sagdeev, Y. S. Sigov, V. P. Shapiro, and V. I. Shevchenko, Fiz. Plazmy 1, 10 (1975) [Sov. J. Plasma Phys. 1, 5 (1975)].
4. D. R. Nicholson, M. V. Goldman, P. Hoyng, J. C. Weatherall, Astrophys. J. 223, 605 (1978).
5. N. Pereira, R. Sudan, and J. Denavit, Phys. Fluids 20, 936 (1977).
6. M. V. Goldman and D. R. Nicholson, Phys. Rev. Lett. 41 406 (1978).
7. J. Satsuma and N. Yajima, Supp. of Prog. of Theor. Phys. 55, 284 (1974).
8. H. C. Yuen and W. E. Ferguson, Phys. Fluids 21, 1275 (1978).
9. H. C. Yuen and B. M. Lake, Phys. Fluids 18, 958 (1975).
10. B. R. Suydam, IEEE J. Quantum Electron. 11, 225 (1975);
A. J. Campillo, S. L. Shapiro, and B. R. Suydam, Appl. Phys. Lett. 23, 628 (1973).
11. J. Gibbons, S. G. Thornhill, M. J. Wordrop, and D. Ter Harr, J. Plasma Phys. 17, 153 (1977).
12. I. M. Gelfand and S. F. Fomin, Calculations of Variations (Prentice-Hall, New Jersey, 1963).

13. S. Bardwell and M. V. Goldman, *Astrophys. J.* 209, 912 (1976).
14. E. A. Kuznetsov, *Sov. Phys.-JETP* 39, 1003 (1974).
15. M. V. Goldman, G. Reiter, and D. Nicholson, "Radiation from a strongly turbulent plasma: Application to electron beam-excited solar emissions," accepted by *Physics of Fluids* (1979).

FIGURE CAPTIONS

- Fig. 1 Pseudopotential $V(\eta)$ for $D = 1$. ($\eta \equiv \langle \delta r^2 \rangle / \langle \delta r^2 \rangle_0$.)
- Fig. 2 Pseudopotential $V(\eta)$ for $D = 3$. ($\eta \equiv \langle \delta r^2 \rangle / \langle \delta r^2 \rangle_0$.)
- Fig. 3 Functions $F(P)$ and $G(P)$ versus P .
- Fig. 4 $\langle \delta r^2 \rangle / \langle \delta r^2 \rangle_0$ versus time τ for $v = 0.15, 0.4$, and 5.0 . Curves are dotted for times when N has damped by more than one order of magnitude.
- Fig. 5 $\beta = x_{\min}/x(0)$ plotted versus α for $P = 1.5, 2, 3, 5$, and ∞ .
- Fig. 6 Initial Gaussian ($t=0$), and nearly collapsed solution with a core of similarity form ($t = 1.2$). Dotted curve is the solution at $t = 1.2$ in the Gaussian approximation.
- Fig. 7 Spherically symmetric numerical determination of $\langle \delta r^2 \rangle$ (x-marks) as a function of time, versus virial theorem prediction [solid curve--see Eq. (59)], for the case $P = 4/3$, $t_c^{(s)} = 1.3265$.
- Fig. 8 $|\psi(0,t)|^{-2}$ versus time, showing self-similar approach to singularity in $|\psi(0,t)|^2$ at $r = 0$, and $t_c^{(s)} = 1.3265$.

Fig. 9 $|\psi|^2/|\psi_{ss}|^2 - 1$ as a function of r at $t = 1.2, 1.3,$ and 1.31 . This exhibits the relative percentage difference between $|\psi|^2$, and $|\psi_{ss}|^2$. The latter is reconstituted from $|\psi(t = 1.3220)|^2$, under the assumption of self-similarity.

Fig. 10 $N_r = 4\pi \int_0^\infty dr r^2 |\psi|^2$ as a function of r for $t = 0, 1.2,$ and 1.31 . The radii at which $|\psi|^2$ is equal to its half-maximum are shown on each curve as a dot. The cut-off points for deviation from self-similarity by more than 25% are shown by arrows.

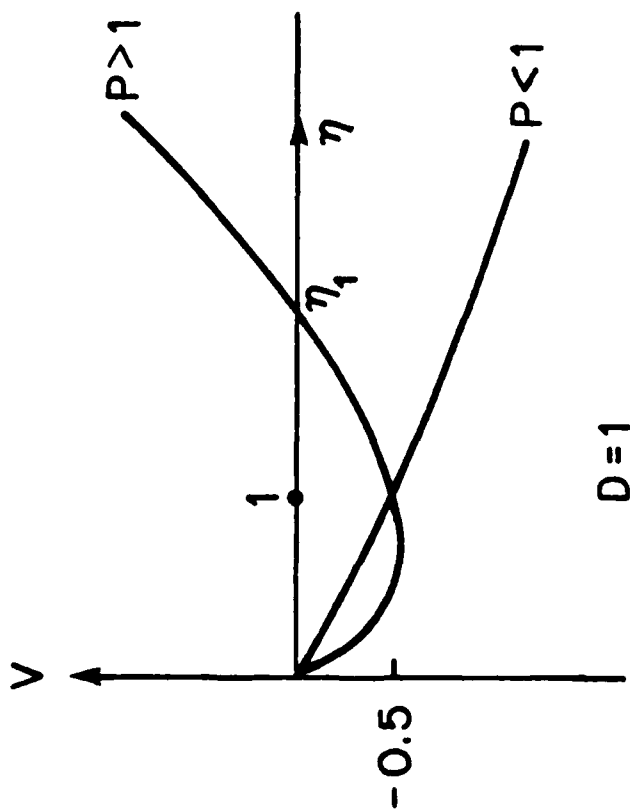


FIGURE 1

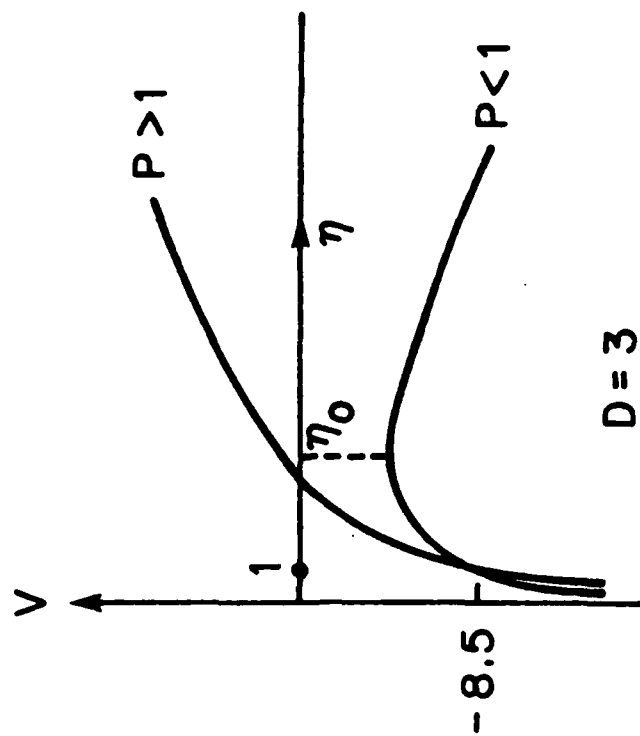


FIGURE 2

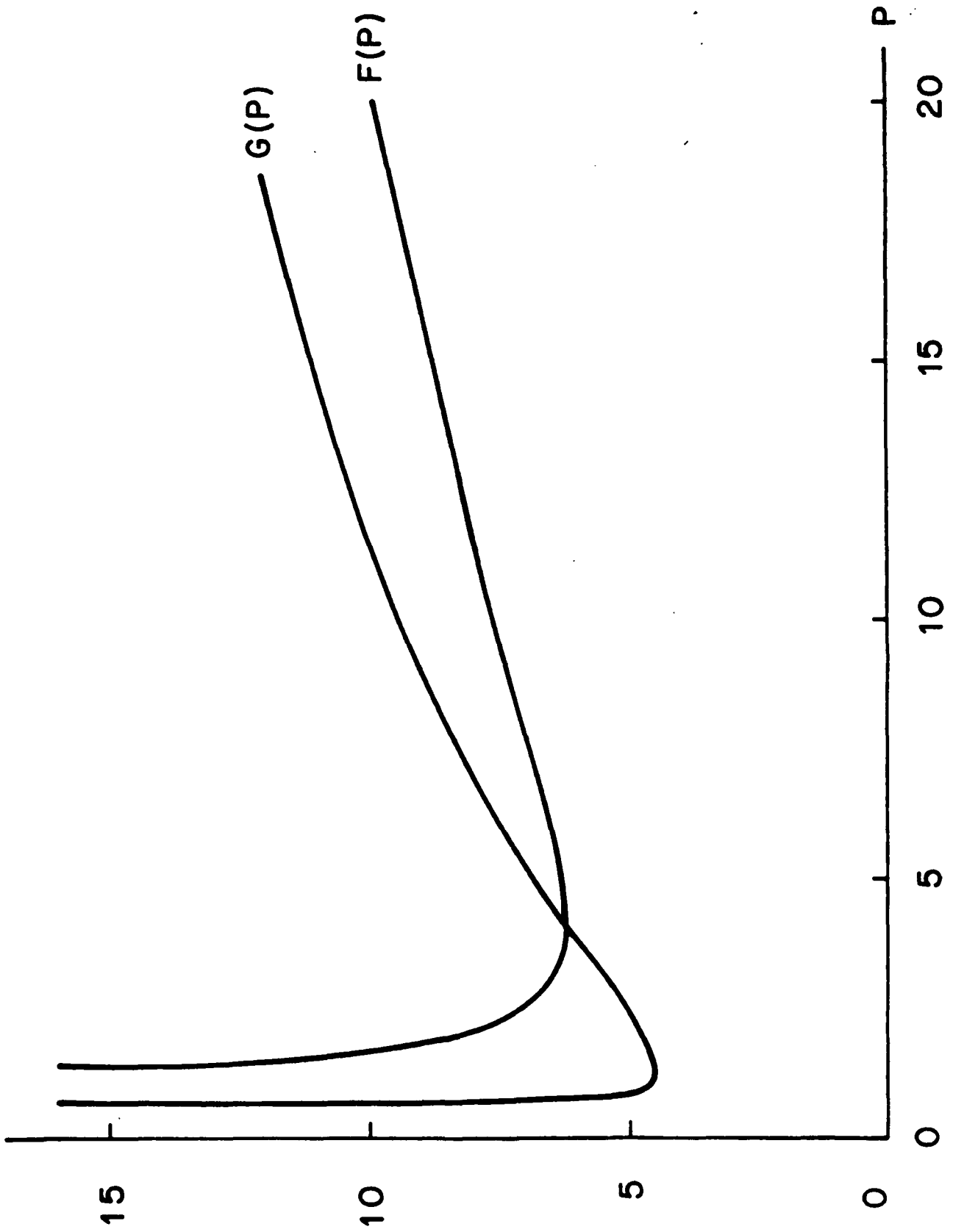


FIGURE 3

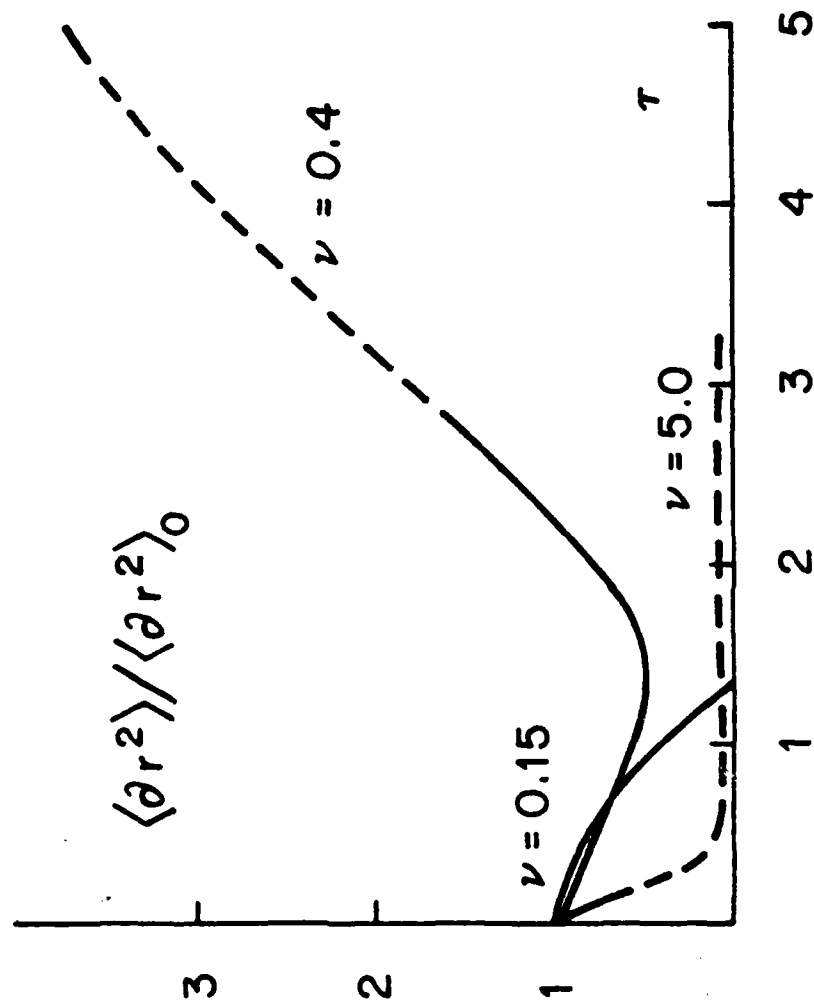


FIGURE 4

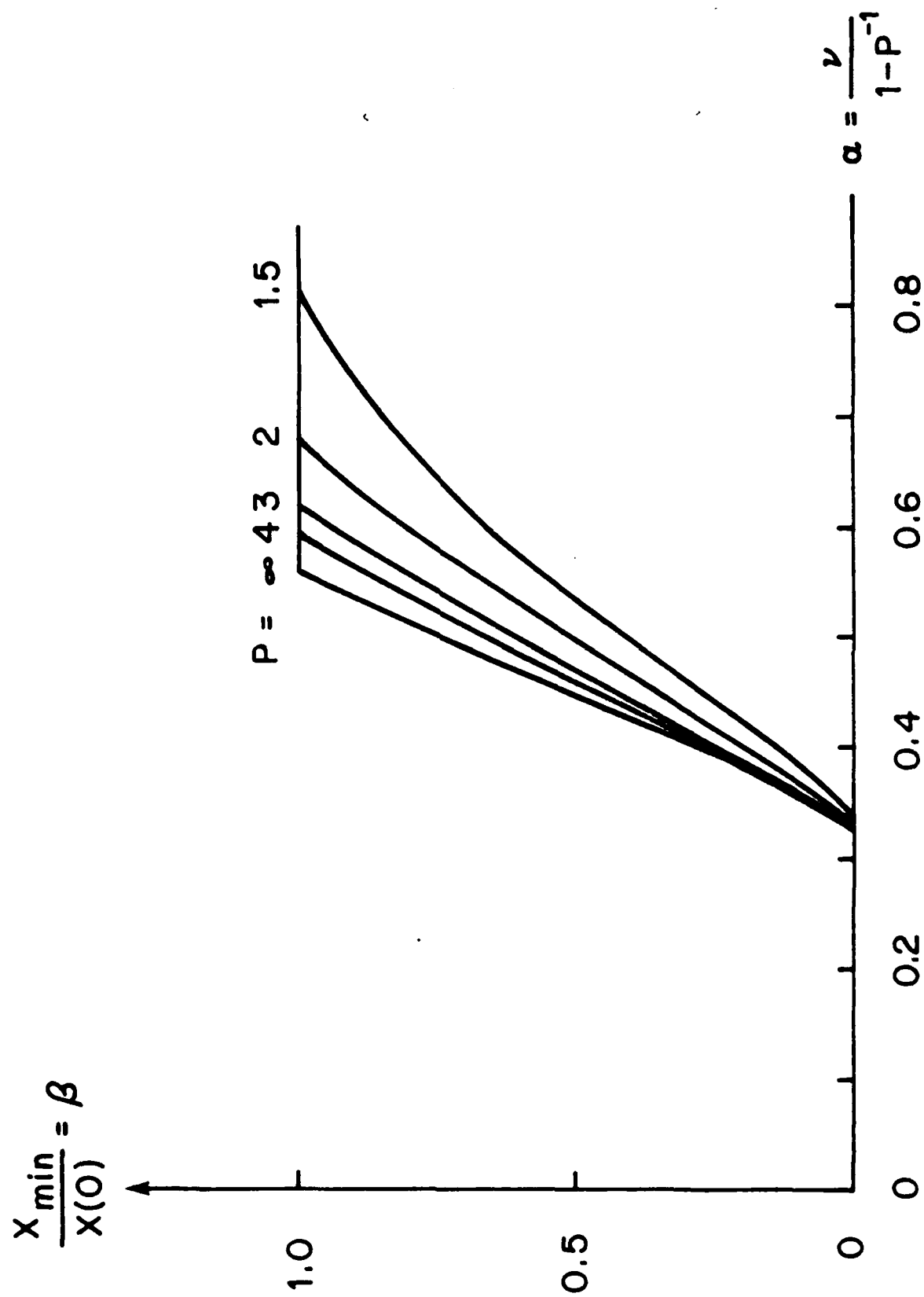


FIGURE 5

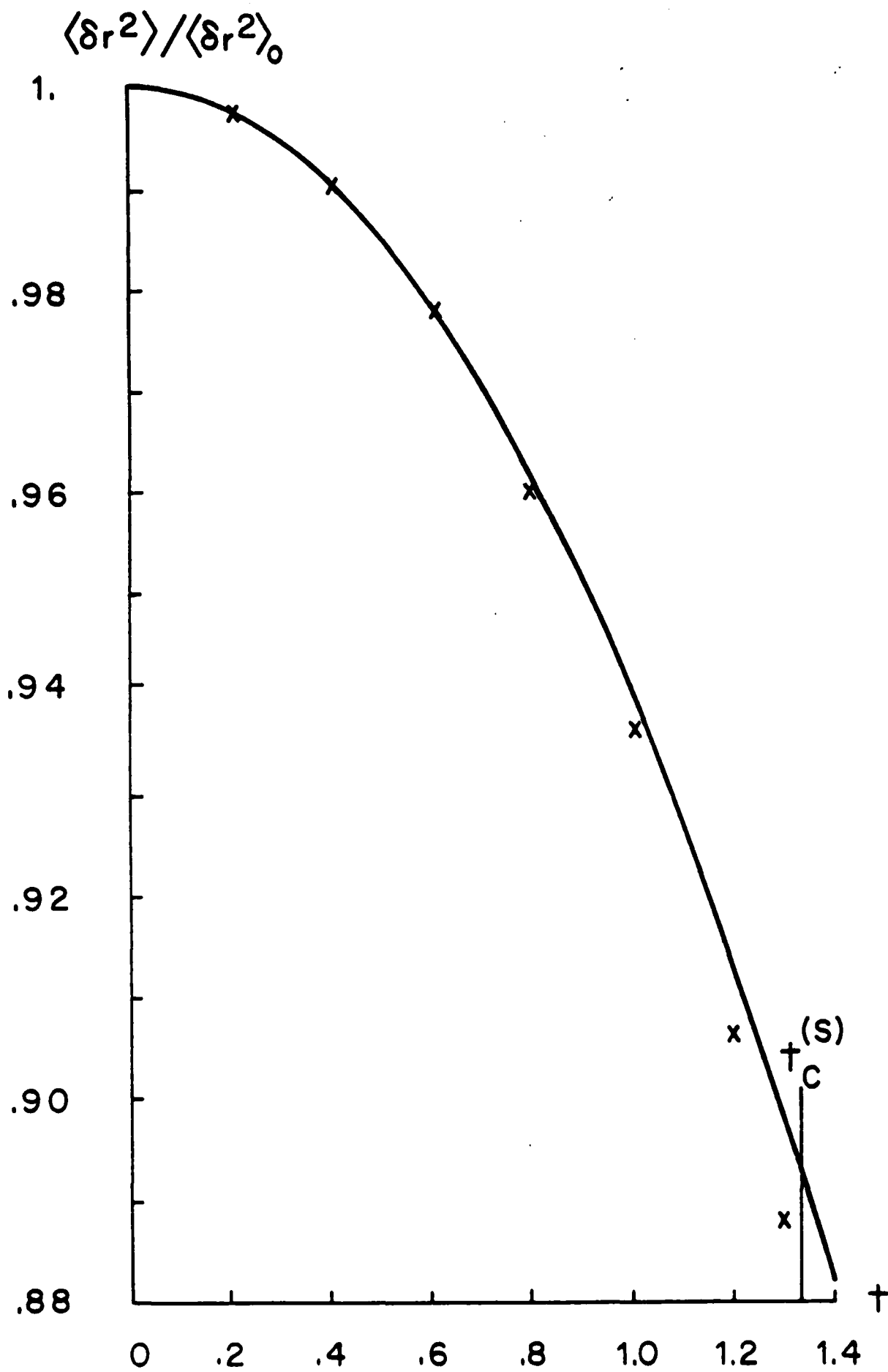


FIGURE 7

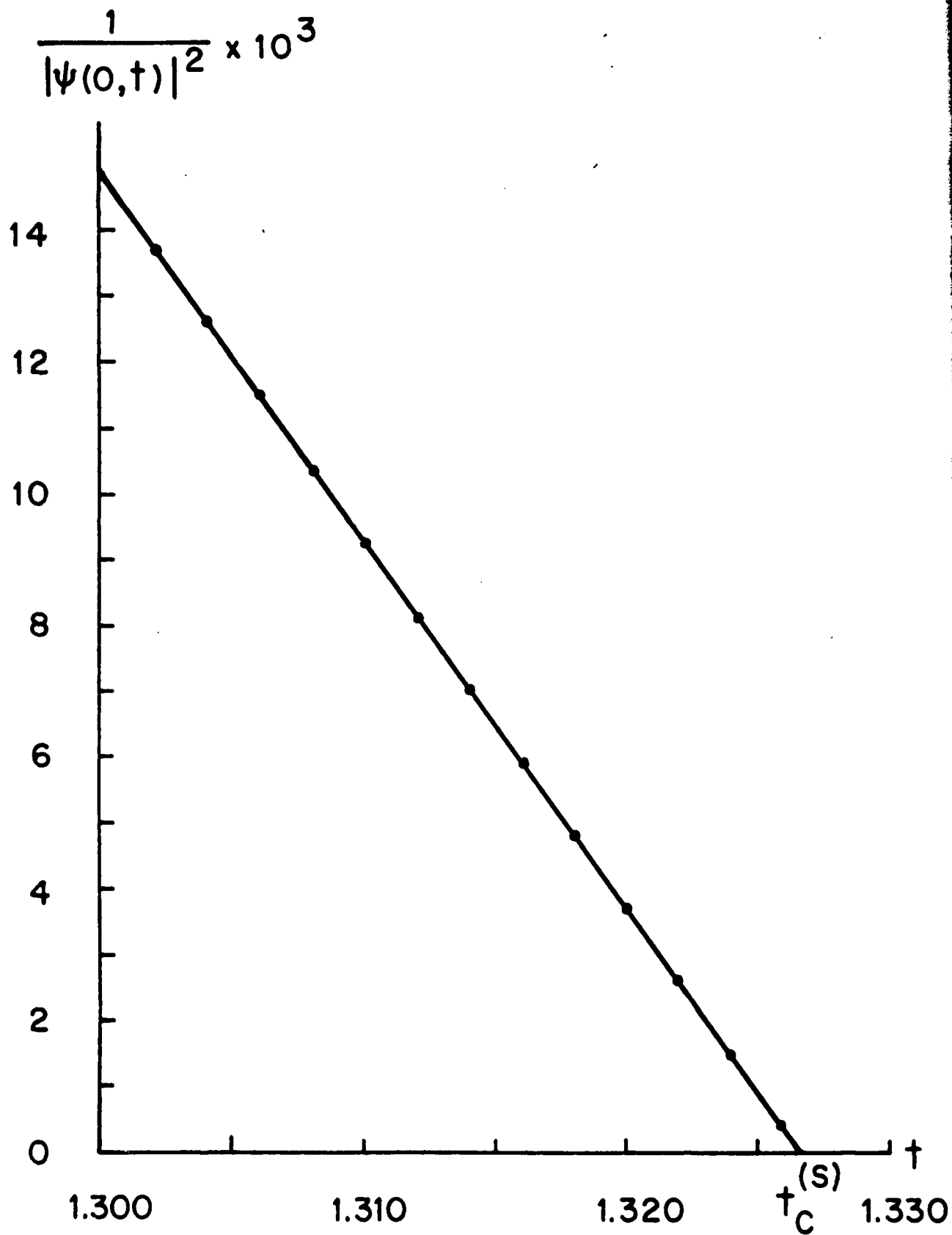


FIGURE 8

$|\psi|^2/|\psi_{ss}|^2 - 1$, AS A %

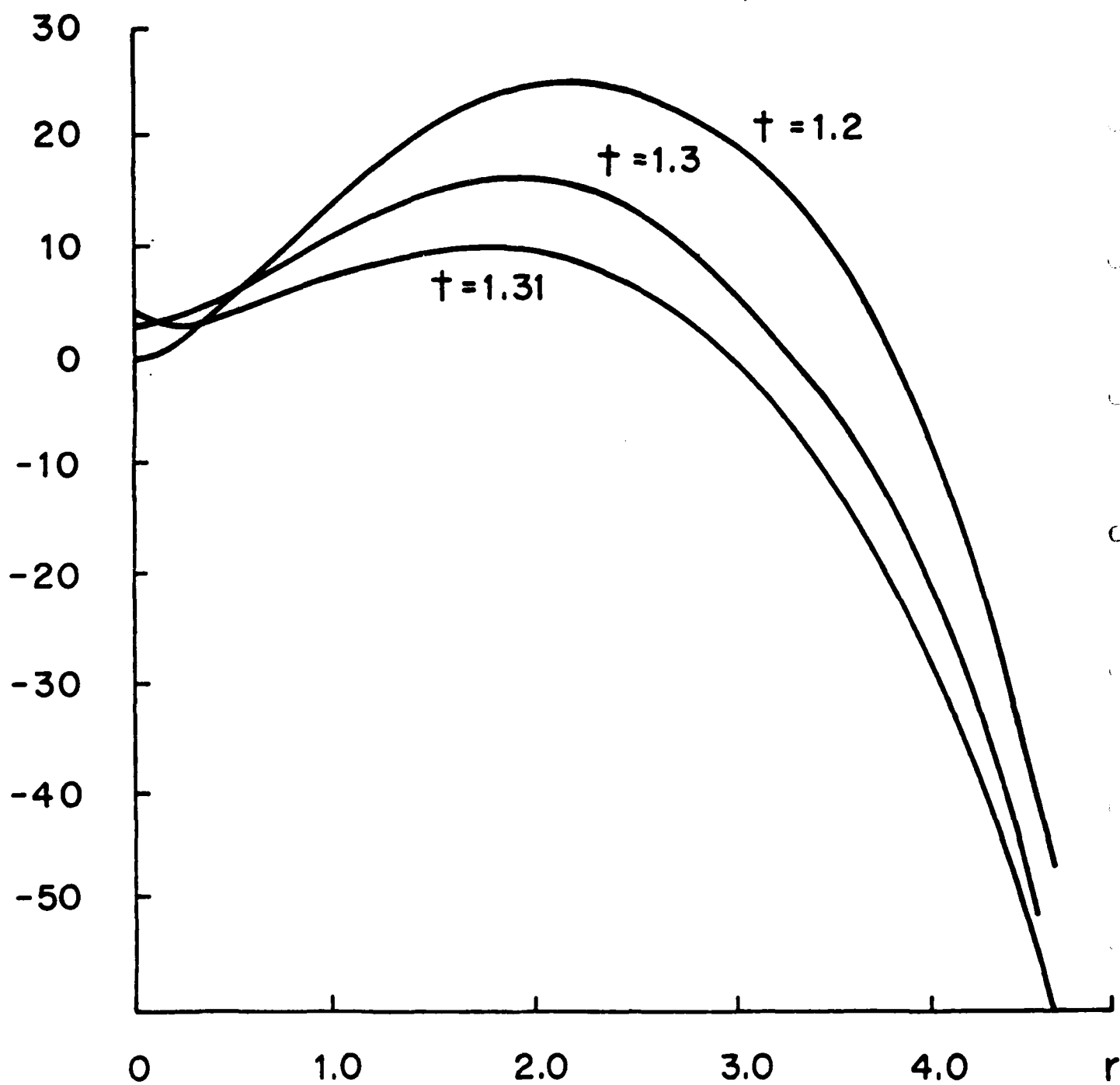


FIGURE 9

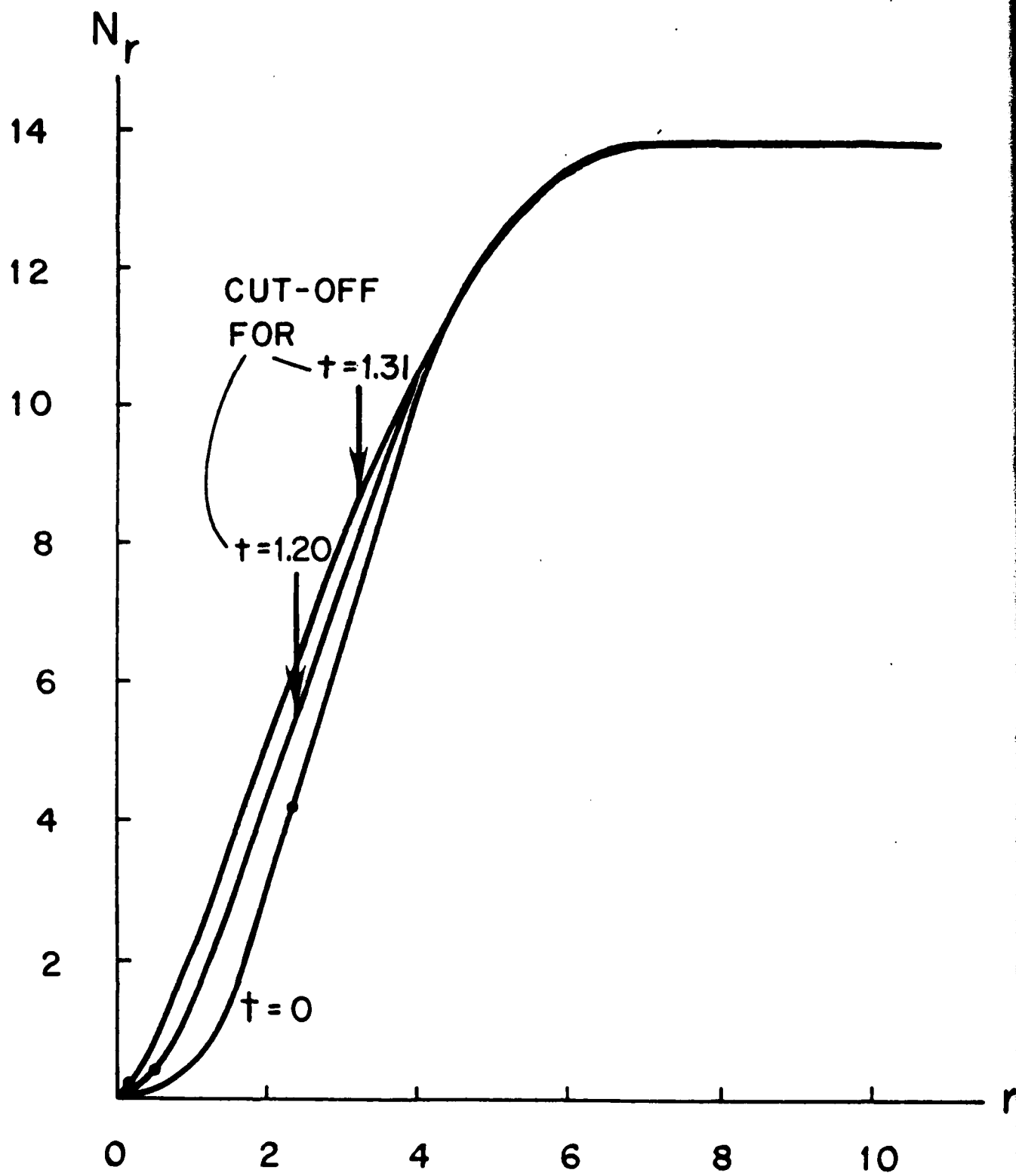


FIGURE 10

PARAMETRIC INSTABILITIES IN WEAKLY MAGNETIZED PLASMA

J. C. Weatherall and M. V. Goldman

Department of Astro-Geophysics, University of Colorado

and

D. R. Nicholson

Department of Physics and Astronomy, University of Iowa

Received 1979 November

ABSTRACT

Parametric instabilities in a weakly magnetized plasma are discussed. The results are applied to waves excited by electron streams which travel outward from the Sun along solar wind magnetic field lines, as in a Type III solar radio burst.

Subject headings: plasmas - Sun: radio radiation

I. INTRODUCTION

Intense waves in plasmas are known to cause parametric instabilities, resulting in the transfer of energy from the intense wave to other waves; for a review see Nishikawa et al. (1976). An important astrophysical phenomenon involving such intense waves is the Type III solar radio burst, involving a stream of electrons which travel outward from the Sun along solar wind magnetic field lines; for reviews, see Nicholson et al. (1978), D. F. Smith and Nicholson (1980), and Goldstein, Papadopoulos, and R. A. Smith (1980). There has been a great deal of work involving the application of parametric instability theory to Type III solar radio bursts; see Papadopoulos et al. (1974), Bardwell and Goldman (1976), R. A. Smith et al. (1976), Nicholson et al. (1978), Goldman and Nicholson (1978), Nicholson and Goldman (1978), and references therein.

There is a substantial body of literature concerning parametric instabilities in a magnetized plasma; see, e.g., Kaw (1976), Porkolab and Goldman (1976), Kaufman and Stenflo (1975), Sanuki and Schmidt (1977), and Dysthe and Pécseli (1978). Nevertheless, previous applications of parametric instability theory to Type III bursts have not treated magnetic field effects systematically. [See, however, a qualitative discussion in Nicholson et al. 1978. Also see a preprint by Freund and Papadopoulos (1979) for a treatment of some, but not all, magnetic field effects.] This paper

represents a step in the direction of a proper inclusion of the effects of magnetic field on wave evolution during Type III bursts. It is a direct generalization of the earlier work of Bardwell and Goldman (1976).

II. PARAMETRIC INSTABILITIES

An electron stream travelling through a background plasma gives rise to Langmuir waves (high frequency electron plasma waves with frequency near the local electron plasma frequency) through the well known beam-plasma instability. As a first approximation, the spectrum of stream-excited Langmuir waves can be represented by a single large amplitude monochromatic wave. As discussed in detail by Bardwell and Goldman (1976), this is in many respects not a very good approximation, but it allows analytic progress, the results of which may have important implications for the true situation.

Our theoretical model thus consists of an intense single monochromatic Langmuir wave (the "pump" wave) travelling along a uniform background magnetic field B_0 in an infinite, homogeneous plasma. The electric field of this intense wave is given by

$$\underline{E}(\underline{r}, t) = E \hat{x} \cos(k_0 x - \omega_0 t) , \quad (1)$$

where E is a real constant, and \hat{x} is the magnetic field direction. Even though E is an intense wave, we assume that it is still weak enough that it propagates as a linear wave and satisfies the linear Langmuir dispersion relation

$$\omega_o^2 = \omega_e^2 + 3k_o^2 v_e^2, \quad (2)$$

where ω_e is the electron plasma frequency, $\omega_e^2 = 4\pi n_o e^2 / m_e$; the average electron density is n_o ; the electronic charge has magnitude e ; the electron mass is m_e ; the thermal speed $v_e = T_e / m_e$; and the electron temperature T_e has units of energy so that Boltzmann's constant does not appear explicitly.

In accordance with standard parametric instability theory, we suppose that high frequency and low frequency fluctuations in the plasma are coupled together by the pump wave and grow exponentially. In general, the coupling involves the pump wave, a low frequency wave characterized by a complex frequency ω and wavenumber \underline{k} , and two high frequency waves characterized by the frequencies and wavenumbers $(\omega_o + \omega, \underline{k}_o + \underline{k})$ and $(\omega_o - \omega^*, \underline{k}_o - \underline{k})$. For simplicity, we assume throughout this paper that all waves are longitudinal, having electric fields parallel to their wavenumbers. The possibility of electromagnetic decay waves is briefly discussed in the last section. The low frequency wave is therefore characterized by an electric field E_L of the form

$$\underline{E}_L(\underline{r}, t) = \frac{1}{2} \underline{E}_L \hat{k} \exp(-i\omega t + i\mathbf{k} \cdot \underline{r}) + \frac{1}{2} \underline{E}_L^* \hat{k} \exp(i\omega^* t - i\mathbf{k} \cdot \underline{r}), \quad (3)$$

while the high frequency electric fields are

$$\begin{aligned} \underline{E}_+(\underline{r}, t) = & \frac{1}{2} \underline{E}_+ \hat{k}_+ \exp[-i(\omega_0 + \omega)t + i(\mathbf{k}_0 + \mathbf{k}) \cdot \underline{r}] \\ & + \frac{1}{2} \underline{E}_+^* \hat{k}_+ \exp[i(\omega_0 + \omega^*)t - i(\mathbf{k}_0 + \mathbf{k}) \cdot \underline{r}], \end{aligned} \quad (4)$$

and

$$\begin{aligned} \underline{E}_-(\underline{r}, t) = & \frac{1}{2} \underline{E}_- \hat{k}_- \exp[-i(\omega_0 - \omega^*)t + i(\mathbf{k}_0 - \mathbf{k}) \cdot \underline{r}] \\ & + \frac{1}{2} \underline{E}_-^* \hat{k}_- \exp[i(\omega_0 - \omega)t - i(\mathbf{k}_0 - \mathbf{k}) \cdot \underline{r}], \end{aligned} \quad (5)$$

where $\hat{k}_\pm \equiv \widehat{\mathbf{k}_0 \pm \mathbf{k}}$ are unit vectors in the $\mathbf{k}_0 \pm \mathbf{k}$ directions.

The relation among the four different wave vectors is shown in Figure 1. While Figure 1 is drawn in the k_x - k_y plane, all figures in this paper can be rotated around the k_x -axis to obtain a fully three-dimensional picture.

The high frequency and low frequency modes couple together to produce new normal modes described by the dispersion relation:

$$\frac{1}{\chi_e(\omega, \mathbf{k})} + \frac{1}{\chi_i(\omega, \mathbf{k})} = -k^2 \lambda_e^2 \frac{\omega_0}{4} \left[\frac{\mu_+^2}{\epsilon(\omega_0 + \omega, \mathbf{k}_0 + \mathbf{k})} + \frac{\mu_-^2}{\epsilon(\omega_0 - \omega, \mathbf{k}_0 - \mathbf{k})} \right], \quad (6)$$

where the angular factors are

$$\mu_{\pm} \equiv \hat{k}_0 \cdot \hat{k}_{\pm} , \quad (7)$$

the electron Debye length $\lambda_e \equiv v_e/\omega_e$, and the dimensionless energy density,

$$W_0 \equiv \frac{E^2}{4\pi n_0 T_e} . \quad (8)$$

Kaw (1976) uses an equation similar to (6) to study instabilities of electrostatic waves in a magnetized plasma, but with a dipole pump. [The reader may recall that in studying linear longitudinal waves, one writes Poisson's equation $\nabla \cdot \underline{E} = 4\pi\rho$ as $ik(1+\chi_e+\chi_i)E = 0$, where the electron susceptibility χ_e is proportional to that portion of the charge density ρ due to electron motion and the ion (in this paper, proton) susceptibility χ_i is proportional to that portion of the charge density ρ due to ion motion. The combination $\epsilon = 1+\chi_e+\chi_i$ is called the linear dielectric function, and the dispersion relation for the wave involved is contained in the expression $\epsilon = 0$.] In the next two sections we evaluate the dispersion relation (6) in the unmagnetized case.

III. UNMAGNETIZED CASE

We first solve the dispersion relation (6) neglecting the background magnetic field, with parameters roughly corresponding to a typical Type III solar radio burst at a position one-third of a solar radius above the Sun's

surface. These are (Bardwell and Goldman 1976): $n_o = 10^8$ cm^{-3} , $T_e = T_i = 140$ eV, $k_o \lambda_e = 0.05$, and $W_o = 10^{-4}$. In the unmagnetized limit, we take the dielectric function needed on the right side of (6) from fluid theory (Krall and Trivelpiece 1972)

$$\epsilon(\omega_o \pm \omega, \underline{k}_o \pm \underline{k}) = \pm 2 \frac{\omega}{\omega_e} - 3k^2 \lambda_e^2 \mp 6\underline{k} \cdot \underline{k}_o \lambda_e^2, \quad (9)$$

where throughout this paper $|\omega| \ll \omega_e, \omega_o$.

For the low frequency susceptibilities needed on the left of (6), we use the results of kinetic theory, as has previously been done by Bardwell (1976). This is somewhat more accurate than the fluid model employed by Bardwell and Goldman (1976) especially in the present case of equal electric and ion temperatures. The results of the fluid and kinetic approaches are in quite good qualitative agreement, and differ quantitatively only by factors of less than 2. The kinetic susceptibilities for species s are (Montgomery 1971)

$$\chi_s(\omega, \underline{k}) = \frac{1}{k^2 \lambda_e^2} [1 + \zeta_s Z(\zeta_s)] , \quad (10)$$

where

$$\zeta_s \equiv \frac{\omega}{2^{1/2} k v_s} , \quad (11)$$

with v_s the thermal speed of species s and Z the plasma dispersion function (Fried and Conti, 1961) which arises because the background electron and ion distribution functions have been taken to be Maxwellian.

The dielectric function (9) and the susceptibilities (10) are inserted in the dispersion relation (6) which is then solved numerically to yield the complex frequency $\omega(\underline{k})$. The imaginary part of this frequency is then plotted as a function not of \underline{k} , but rather as a function of the Langmuir wave vector, $\underline{k}^L \equiv \underline{k}_0 - \underline{k}$. Figure 2 shows the resulting contours of constant growth rate. This two-dimensional contour plot can be rotated about the $\hat{k}_x(\hat{B}_0)$ axis to yield a fully three-dimensional contour plot. Figure 2 is in agreement with the corresponding figure in Bardwell and Goldman (1976). As discussed in detail by Bardwell and Goldman (1976), there are three distinct regimes of instability; these are labelled PDI (parametric decay instability), SMI (stimulated modulational instability), and OTS (oscillating two-stream instability). The maximum growth rate ω_i in each of the three regimes is close to $\omega_i/\omega_e \approx 1.3 \cdot 10^{-5}$ in the present case. The properties of these three regimes in the unmagnetized case have been reviewed by Bardwell and Goldman (1976); in the next section we consider the modification of these three regimes in the weakly magnetized situation.

IV. WEAKLY MAGNETIZED CASE

In this section we consider the modification of the previous results in the presence of a weak magnetic field. In this paper "weak" means that the electron gyrofrequency

$\Omega_e \equiv eB_0/m_e c$ (c is the speed of light) is much less than the electron plasma frequency ω_e . For example, with the solar corona parameters of the previous section and a reasonable magnetic field strength of 2.5 gauss, we have $\Omega_e/\omega_e = 0.1$. Note that while the magnetic field is weak in the sense we have described, the magnetic field energy density for the present parameters exceeds the kinetic energy density of the background electrons (i.e., this is a low β plasma).

The magnetic field affects both the high frequency and the low frequency wave motions. For the high frequency longitudinal waves, the electrons feel a $\underline{v} \times \underline{B}$ force in addition to an electric field force, and the dielectric function becomes (Ginzburg, 1964)

$$\epsilon(\omega_0 \pm \omega, \underline{k}_0 \pm \underline{k}) = \pm 2 \frac{\omega}{\omega_e} - 3k^2 \lambda_e^2 \mp 6 \underline{k} \cdot \underline{k}_0 \lambda_e^2 + (\mu_{\pm}^2 - 1) \frac{\omega_e^2}{\omega^2}, \quad (12)$$

which must be used on the right side of the dispersion relation (6).

There are also magnetic field effects on the low frequency wave motions. For heuristic purposes, suppose we ignore the strong ion Landau damping of ion acoustic waves in an equal temperature plasma and use the dispersion relation $\omega = kc_s$ to estimate a typical ion-acoustic frequency. With the sound speed $c_s \approx (T_e/m_i)^{1/2}$ and a typical

low frequency wavenumber $k\lambda_e \sim 0.02$, we have $\omega/\omega_e \sim 4 \cdot 10^{-4}$. The ion gyrofrequency $\Omega_i \sim 5 \cdot 10^{-5} \omega_e$, and the ion (proton) plasma frequency is $\omega_{pi} \sim 0.02 \omega_e$. Thus, the frequency ordering of interest is $\Omega_i \ll |\omega| \ll \omega_{pi} < \Omega_e \ll \omega_e$.

For most of the wavenumbers k_L in Figure 2, the product of the ion gyroradius ρ_i , with the low-frequency wavenumber, $k = |\underline{k}_0 - \underline{k}_L|$, is substantially greater than unity. We find that the modification of the low frequency ion susceptibility due to a magnetic field is insignificant for most of the wavenumbers in this problem. The exception is the OTS. Along the dashed line labelled A in Figure 2, ω is purely imaginary, and at maximum growth rate $|\omega| = 1.0 \cdot 10^{-5} < \Omega_i$ and $k\rho_i \sim 1$. We shall find that the OTS branch is substantially suppressed, but we attribute this to the low frequency effects on the electrons, not to $k\rho_i \sim 1$. So, although they are included, the magnetic effects on the low frequency ion motion do not seem to be important.

As for the electrons, the fact that $|\omega| \ll \Omega_e$ (and typically $k_y \rho_e \ll 1$ where ρ_e is the electron gyroradius) means that the low frequency electron motion is indeed strongly magnetized. In other words, electrons are not free to follow low frequency motions across the field lines, but rather they begin an $\underline{E} \times \underline{B}_0$ drift when subjected to low frequency electric fields perpendicular to the field lines. Along the magnetic field lines the electrons are perfectly free to move, like beads on a wire. As discussed in

somewhat more detail by Nicholson et al. (1978), the net result of these parallel and perpendicular effects is that for angles ($\sim k_y/k_x$) which are greater than $(m_e/m_i)^{1/2}$ from perpendicular to \hat{B}_0 , there is no effect of the magnetic field on the low frequency wave motions (m_i is the proton mass). Only in the small range of angles $|k_y/k_x| < (m_e/m_i)^{1/2}$ are the electron motions inhibited greatly, and the low frequency wave properties modified. As we shall see, the instability growth rates in this small range of angles can be severely reduced because of the inhibition of electron motion across field lines.

Let us perform a simple analytic calculation to illustrate one case of a reduction in growth rate due to the magnetic field. We focus our attention on the dashed line labelled A in Figure 2. Along this line where $\underline{k} \cdot \underline{k}_0 = 0$, the instability is purely growing with $\omega = i\omega_i$. Now suppose we have a plasma with cold ions and a growth rate whose magnitude is small. The unmagnetized fluid susceptibility for species s is $\chi_s = -\omega_s^2/(\omega^2 - k^2 v_s^2)$ which means we can ignore the ion susceptibility term on the left of the dispersion relation (6). Inserting the electron susceptibility $\chi_e \approx 1/k^2 \lambda_e^2$, the unmagnetized dielectric function (9), and the assumption $\omega = i\omega_i$ into the dispersion relation (6) we find

$$\frac{\omega_i}{\omega_e} = \left(\frac{3}{8} W_0 k_y^2 \lambda_e^2 - \frac{9}{4} k_y^4 \lambda_e^4 \right)^{1/2}, \quad (13)$$

whereupon the highest growth rate is

$$\omega_i/\omega_e = W_0/8, \quad (14)$$

which occurs at

$$k_y \lambda_e = (W_0/12)^{1/2}. \quad (15)$$

Now, how is this result modified when the magnetic field is included? Continuing to ignore the ions in the low frequency susceptibilities on the left of (6), there are two places where magnetic field effects enter. The first is in the high frequency dielectric function, where (12) replaces (9). One may think of the change as replacing $-3k^2 \lambda_e^2$ in (9) by $-3k^2 \lambda_e^2 + (\mu_{\pm}^2 - 1) \Omega_e^2 / \omega_e^2$ in (12). As both terms are negative, this effect is as if the wavenumber in (9) were increased; the result is merely a shift in the growth rate curve to smaller wavenumbers with no change in the maximum growth rate obtainable. This effect was first suggested to us by D. F. Smith and Tsytovich (1977).

The second place where the magnetic field effect enters is in the low frequency electron susceptibility. For the case under discussion with $\underline{k} \cdot \hat{B}_0 = 0$, the unmagnetized electron susceptibility, $(k \lambda_e)^{-2}$, is replaced by $\chi_e \approx \omega_e^2 / \Omega_e^2$, corresponding to polarization drift; and, neglecting for simplicity the high frequency magnetic effect of the previous paragraph, the dispersion relation (6) yields (without assuming ω purely imaginary)

$$\begin{aligned}
\frac{\omega^2}{\omega_e^2} &= \frac{9}{4} k^4 \lambda_e^4 - \frac{3}{8} \frac{W_0 k^4 \lambda_e^4 \omega_e^2}{\Omega_e^2} \\
&= \frac{9}{4} k^4 \lambda_e^4 \left(1 - \frac{W_0}{1} \frac{\omega_e^2}{\Omega_e^2} \right), \quad (16)
\end{aligned}$$

which does not predict instability at all for the parameters of the present paper. This crude calculation exhibits the reduction in the growth rate when the low frequency mode propagates with an angle of $(m_e/m_i)^{1/2}$ with the perpendicular to the magnetic field.

We emphasize that this great reduction in growth rate occurs only for the branch marked OTS in Figure 2. For the other branches marked PDI and SMI in Figure 2, the low frequency mode has an angle greater than $(m_e/m_i)^{1/2}$ to the perpendicular to the magnetic field, and propagates as if the medium were unmagnetized.

To make these remarks rigorous, we numerically solve the dispersion relation (6) with the parameters already mentioned ($\Omega_e/\omega_e = 0.1$). For the low frequency electron and ion susceptibilities we use the magnetized kinetic version which is given by (Bekefi 1966)

$$\begin{aligned}
\chi_s(\omega, \underline{k}) &= \frac{1}{k^2 \lambda_s^2} \left[1 + \zeta_s \exp(-a_s) \sum_{n=-\infty}^{\infty} I_n(a_s) \right. \\
&\quad \times \left. Z \left(\zeta_s - n \frac{\Omega_s}{2^{1/2} k_x v_s} \right) \right], \quad (17)
\end{aligned}$$

where $\zeta_s \equiv \omega/2^{1/2} k_x v_s$, $a_s \equiv k_y^2 \rho_s^2$, and the I_n are modified Bessel functions. For the high frequency dielectric functions we use the fluid versions (12). The solution of the instability dispersion relation (6) is shown in Figure 3. Comparing this figure to Figure 2, we notice several effects of the magnetic field. The most dramatic effect is the disappearance of the OTS branch, in agreement with the crude analytic calculation. The other dramatic effect is a squeezing of the contours in the \hat{y} -direction for both the PDI and SMI branches. We ascribe this effect almost totally to the magnetic term in the high frequency dielectric function (12).

It is important to note that despite the squeezing of the contours in the direction perpendicular to the magnetic field, the vertical extent of the region of fastest growth (the contours labelled 10) is only slightly affected by the magnetic field. This is true for both the SMI and the PDI branches; the maximum perpendicular extent of the "10" contour is reduced by only 10% of its unmagnetized value in each case.

Returning to the OTS branch, we have seen in Figure 2 that in the unmagnetized case it has as large a growth rate as any other branch, while when $\Omega_e/\omega_e = 0.1$ (Fig. 3) it has completely disappeared. In order to explore the nature of this transition, we show in Figure 4 curves of growth rate versus perpendicular wavenumber $k_y \lambda_e$ for various values of

Ω_e/ω_e , with $k_x = 0$. The horizontal axis of this figure should be identified with the dashed line labelled "A" in Figure 2. We see that even for the small value $\Omega_e/\omega_e = 0.005$, the instability has almost disappeared. The OTS branch is very sensitive to the presence of a weak magnetic field; the main reason for this is the resistance of the magnetic field to motion of electrons across field lines.

In this paper we have considered only longitudinal decay waves. There also exists a host of potential electromagnetic decay products. Although we have not performed a systematic numerical study of the electromagnetic decay possibilities, we have considered many specific examples within the context of the present parameters. In every case, we find growth rates far lower than the maximum growth rates of the SMI and PDI branches. Of course, in a particular region of wavenumber space, an electromagnetic instability can have the largest growth rate. For example, when the OTS instability is reduced to zero growth rate by the weak magnetic field, the region of wavenumber space which formerly contained the OTS can now support a parametric instability involving a magnetosonic wave. Whereas the low-frequency electron motion across field lines is inhibited by the magnetic field, a magnetosonic wave moves the field lines, thus allowing the electrons to move and enhancing the tendency toward instability. Our calculations indicate, however, that the resulting growth

rate is very much smaller than the growth rates of the PDI and SMI branches in the weakly magnetized case. Thus, we feel that there is no indication that electromagnetic effects would change the overall growth rate picture in the weakly magnetized case. The effort required to produce a comprehensive contour plot such as Figures 2 and 3 including all electromagnetic effects does not seem to be warranted.

This concludes our detailed calculations. All of the results of this section agree with the qualitative predictions of Nicholson et al. (1978).¹ In the next section we discuss the implications of these results for parametric instabilities and soliton collapse associated with Type III solar radio bursts.

¹In Section IV of this reference, the expression $k\rho_i = 800$ the sixth paragraph should be replaced by the expression $k\rho_i = 20$. Equation (13) should read

$$\omega^2 - k^2 c_s^2 - \frac{\Omega_i \Omega_e}{\left(1 - \frac{k_z}{k_x}\right)^2 \left(\frac{\Omega_e^2}{\omega^2} - 1\right)} = 0 .$$

V. SUMMARY AND DISCUSSION

In this section we summarize the preceding results and discuss the implications of these results for the theory of Type III solar radio bursts.

In the unmagnetized version, the parametric instabilities to which an intense monochromatic Langmuir wave is subject consist of three kinds, the OTS, PDI, and SMI. The maximum growth rates in each branch are comparable. One of these branches, the OTS, is very sensitive to the addition of a weak magnetic field. For the parameters of the present paper, this branch is virtually wiped out for a magnetic field such that $\Omega_e/\omega_e = 0.005$. The other two branches, the PDI and the SMI, are very insensitive to the addition of a weak magnetic field. This is true both for the maximum growth rate in each branch, and for the extent of each branch in the wavenumber direction perpendicular to the direction of the magnetic field.

We conclude that to the extent that the stream-excited Langmuir waves of a Type III burst are monochromatic, the linear parametric instabilities to which these waves are subject are not one dimensional in nature. The presence of a weak magnetic field does not change the overall growth rate picture. The detailed Type III Langmuir wave scenarios of earlier work (Bardwell and Goldman 1976,

Nicholson et al. 1978) need not be modified.

This strong conclusion must, of course, be tempered by repeating the observation that the Type III stream-excited Langmuir waves are not monochromatic, but have a spread of wavenumbers along the magnetic field and across the magnetic field. No satisfactory general theory of parametric instabilities due to a broadband pump wave presently exists even in the unmagnetized case, although some results have been obtained (Bardwell and Goldman 1976, Thomson and Karush 1974). However, numerical work (Nicholson et al. 1978) indicates that the broadband nature of the pump often does not substantially slow the nonlinear wave processes. In fact, the broadband pump can often speed the nonlinear processes, as in the case that the regions of constructive interference of Langmuir waves in real space undergo a direct collapse, thus bypassing the stage of parametric decay instability (Nicholson et al. 1978). The nonlinear evolution of a broadband pump in a weak magnetic field will be explored in detail in a future publication.

After the completion of this work (Weatherall et al. 1978), we became aware of related work by Freund and Papadopoulos (1979). They consider only the effect of the magnetic field on the high frequency waves, and ignore the effect of the magnetic field on the low frequency motions. Thus, they find the partial suppression of the OTS branch

due to the magnetic modification of the high frequency waves which we discuss in §IV; however, their work does not contain the low frequency magnetic effects which we find to be dominant in suppressing the OTS branch. Regarding the PDI branch, their work agrees with ours in finding it to be quite insensitive to a weak magnetic field.

Acknowledgements

This work was supported by the National Science Foundation, Atmospheric Research Section under ATM 76-14275 and by the Air Force Office of Scientific Research (M.V.G. and J.C.W.) under contract F49620-76-C-0005. We also thank the National Center for Atmospheric Research, supported by the National Science Foundation, for computer time used in this research.

REFERENCES

- Bardwell, S. 1976, Ph.D. thesis, University of Colorado at Boulder.
- Bardwell, S., and Goldman, M. V. 1976, Ap. J., 209, 912.
- Bekefi, G. 1966, Radiation Processes in Plasmas (New York: Wiley), p. 236.
- Dysthe, K. B., and Pécseli, H. L. 1978, Plasma Phys., 20, 971.
- Freund, H. P., and Papadopoulos, K. 1978, NRL Memorandum Report 4042.
- Fried, B. D., and Conti, S. D. 1961, The Plasma Dispersion Function (New York: Academic).
- Ginzburg, V. L. 1964, The Propagation of Electromagnetic Waves in Plasmas (Massachusetts: Addison-Wesley), p. 120.
- Goldman, M. V., and Nicholson, D. R. 1978, Phys. Rev. Letters, 41, 406.
- Goldstein, M. L., Papadopoulos, K., and Smith, R. A. 1980, Proc. Symp. Nonlinear Effects in Space Plasmas (Dordrecht: Reidel).
- Kaufman, A. N., and Stenflo, L. 1975, Phys. Scr. 11, 269.
- Kaw, P. K. 1976, in Advances in Plasma Physics, Vol. 6 (New York: Wiley).

- Krall, N. A., and Trivelpiece, A. W. 1973, Principles of Plasma Physics (New York: McGraw-Hill), p. 144.
- Montgomery, D. C. 1971, Theory of the Unmagnetized Plasma (New York: Gordon and Breach), p. 68.
- Nicholson, D. R., and Goldman, M. V. 1978, Phys. Fluids, 21, 1766.
- Nicholson, D. R., Goldman, M. V., Hoyng, P., and Weatherall, J. C. 1978, Ap. J., 223, 605.
- Nishikawa, K., Lui, C. S., Kaw, P. K., and Kruer, W. L. 1976, in Advances in Plasma Physics, Vol. 6 (New York: Wiley).
- Papadopoulos, K., Goldstein, M. L., and Smith, R. A. 1975, Ap. J., 190, 175.
- Porkolab, M., and Goldman, M. B. 1976, Phys. Fluids, 19, 872.
- Sanuki, H., and Schmidt, G. 1977, J. Phys. Soc. Japan, 42, 664.
- Smith, D. F., and Tsytovich, V. N. 1977, private communication.
- Smith, D. F., and Nicholson, D. R. 1980, in Proc. Symp. Nonlinear Effects in Space Plasmas (Dordrecht: Reidel).
- Smith, R. A., Goldstein, M. L., and Papadopoulos, K. 1976, Solar Phys., 46, 515.
- Thomson, J. J., and Karush, J. I. 1974, Phys. Fluids, 17, 1608.
- Weatherall, J., Goldman, M. V., and Nicholson, D. R. 1978, Bull. Am. Phys. Soc., 23, 787.

FIGURE CAPTIONS

Fig. 1—Relation among the four wavevectors involved in a parametric instability.

Fig. 2—Solution of the dispersion relation (6) in the unmagnetized case; the contours represent the imaginary part of the frequency (the growth rate) as a function of two-dimensional Langmuir wavenumber $\underline{k}^L \equiv \underline{k}_0 - \underline{k}$. This figure can be rotated about the k_x^L axis to obtain a fully three-dimensional picture. The contour labelled 1 represents a growth rate $\omega_i/\omega_e = 10^{-6}$, while the contour labelled 10 represents a growth rate $\omega_i/\omega_e = 10^{-5}$. The parameters are those of §III.

Fig. 3—Solution of the dispersion relation (6) in the weakly magnetized case. All parameters and contour labels are the same as in Figure 2, with $\Omega_e/\omega_e = 0.1$.

Fig. 4—Curves of growth rate versus wavenumber for the OTS branch of Figure 2, for different values of Ω_e/ω_e ; all other parameters are the same as in Figure 2. The horizontal axis of this figure should be thought of as the dashed line labelled "A" in Figure 2.

M. V. Goldman and J. C. Weatherall

Department of Astro-Geophysics

University of Colorado

Boulder, CO 80309

D. R. Nicholson

Department of Physics and Astronomy

University of Iowa

Iowa City, IO 52242

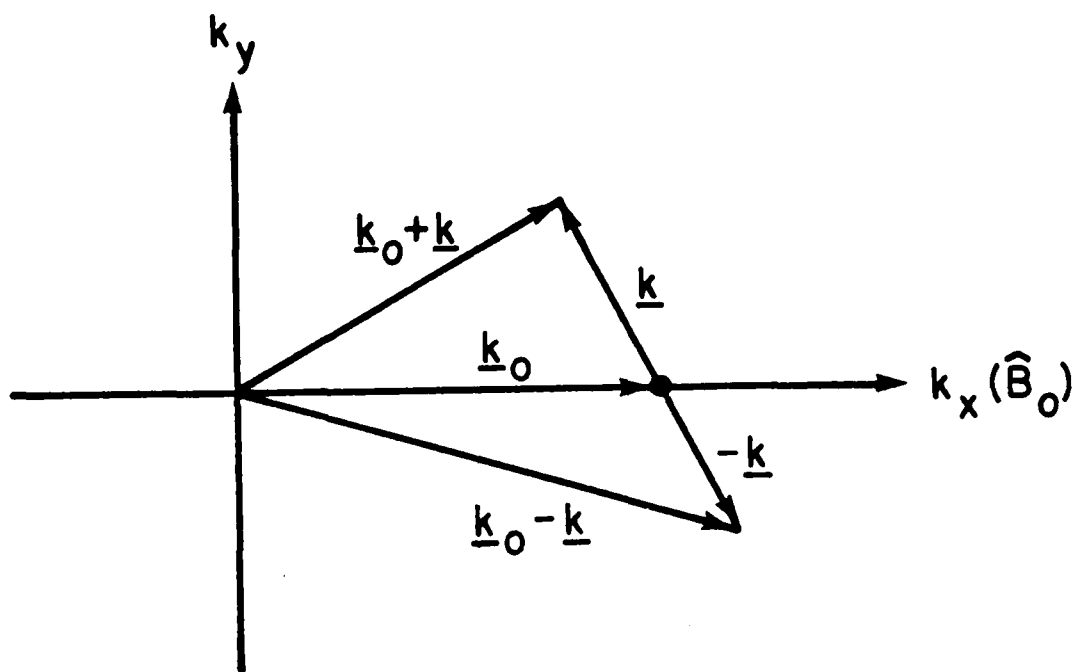


FIGURE 1

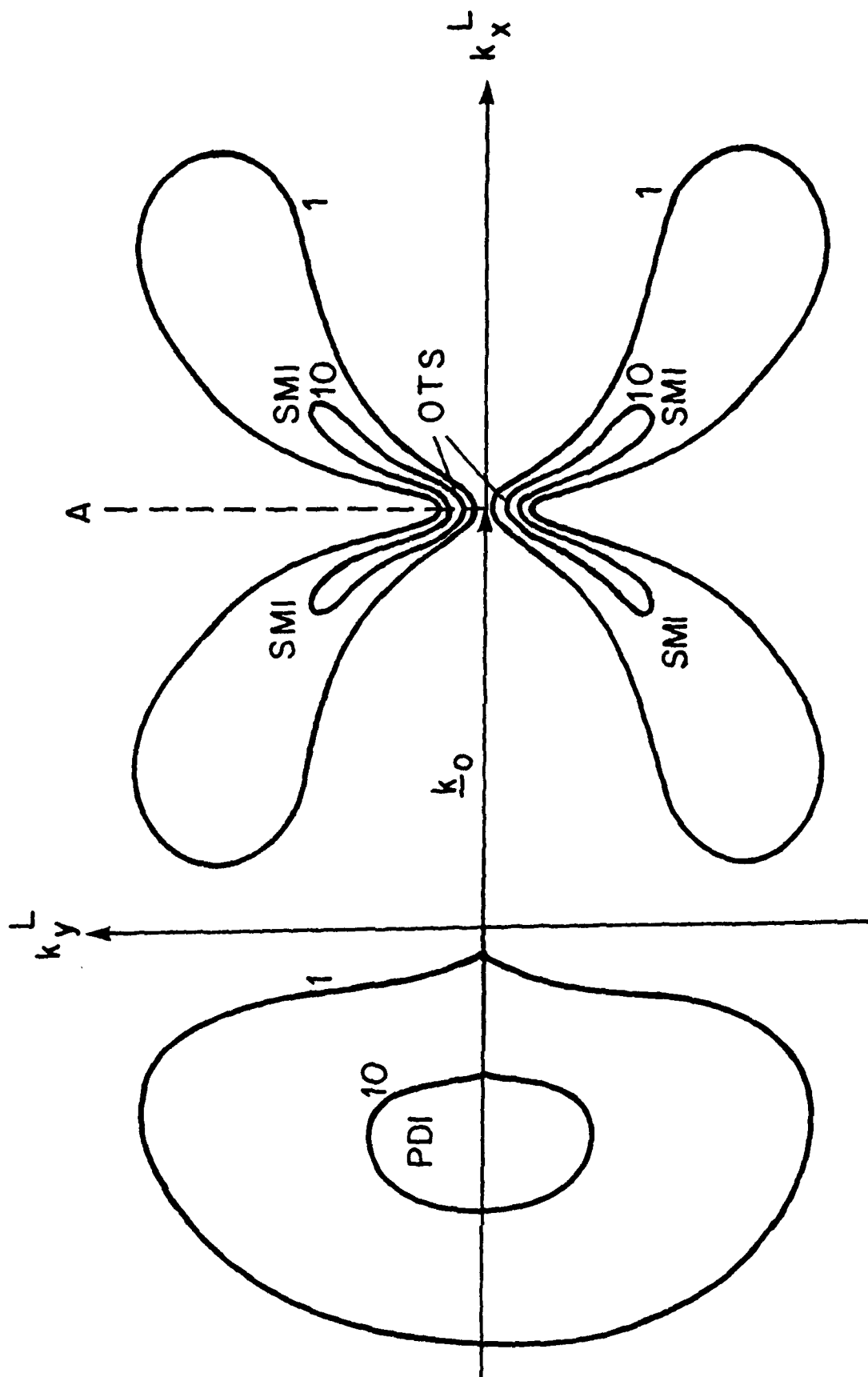


FIGURE 2

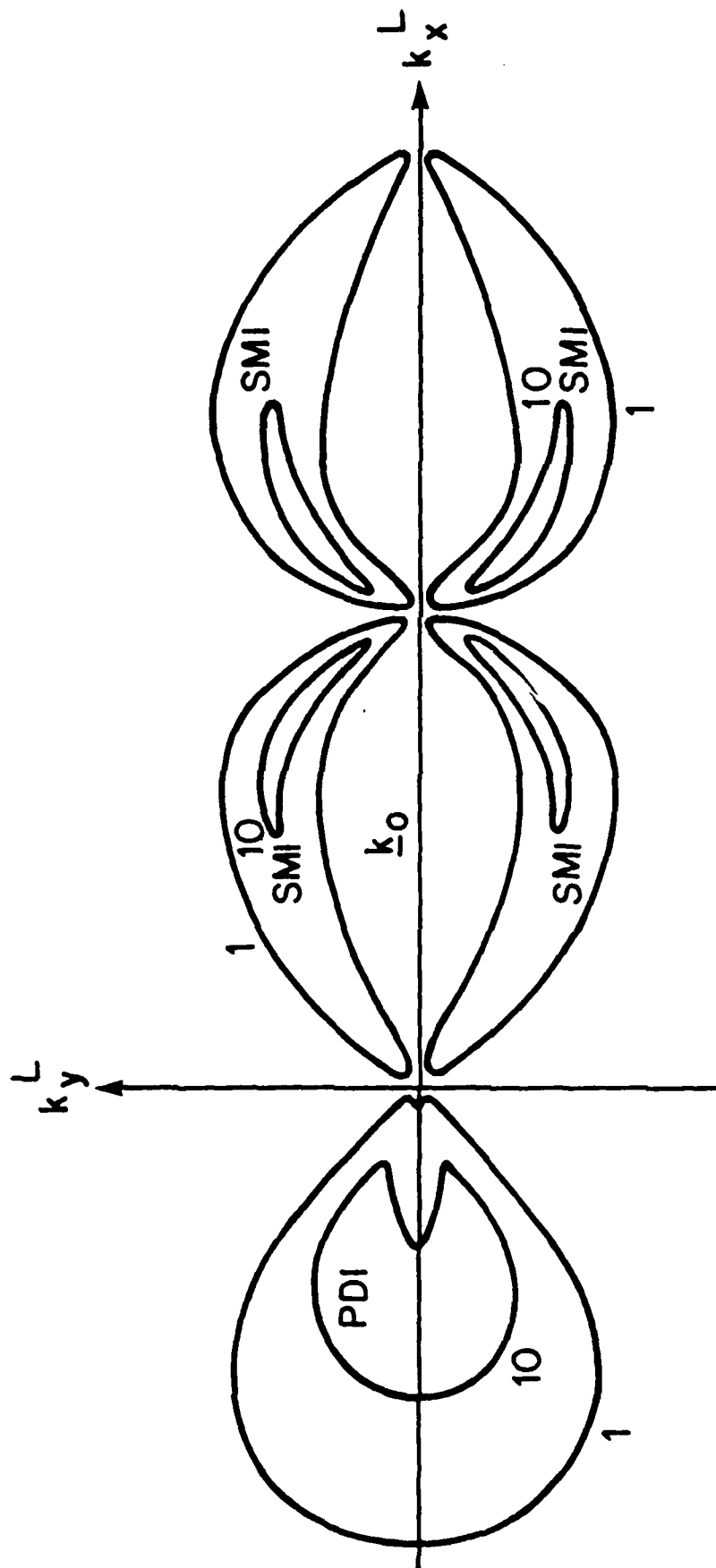


FIGURE 3

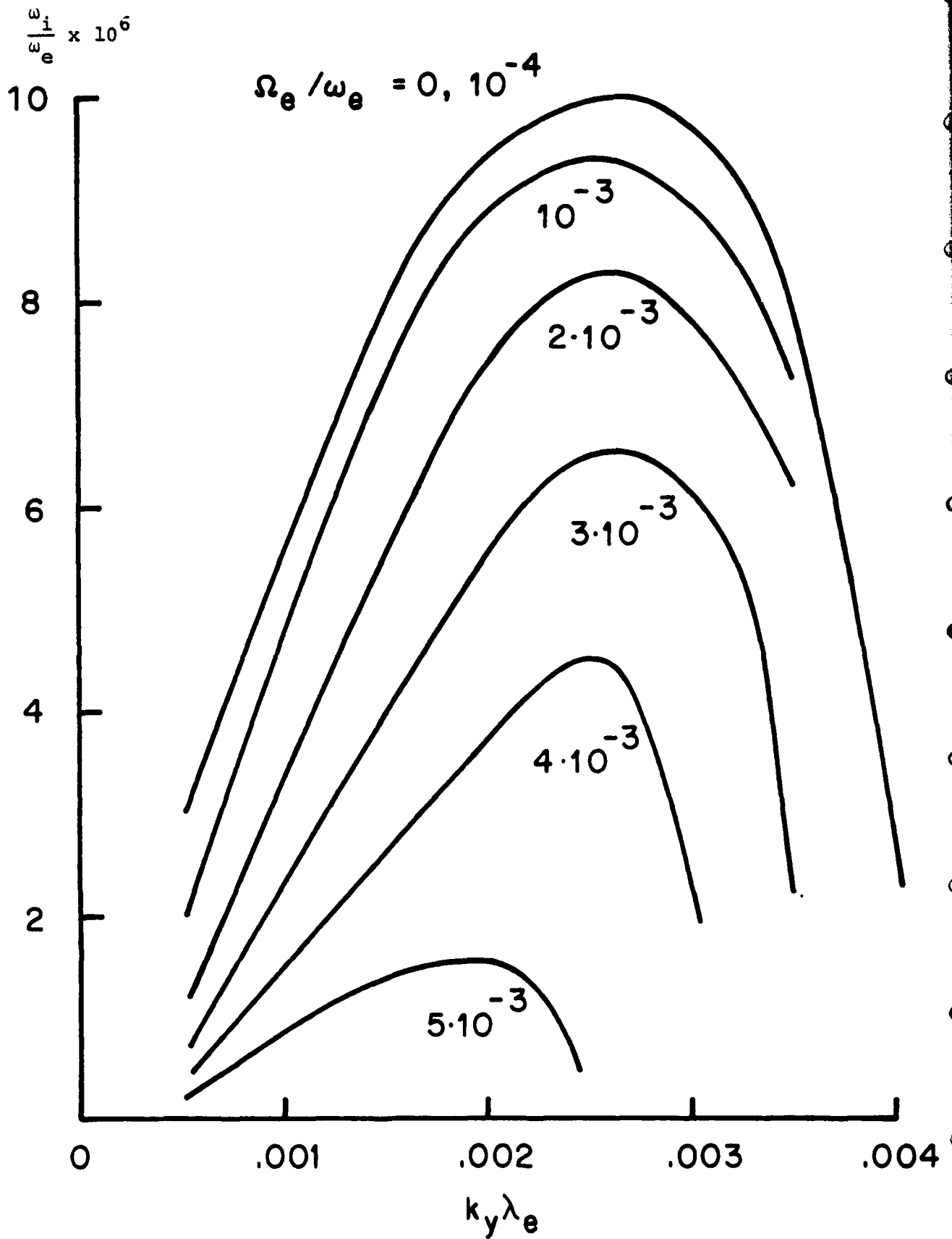


FIGURE 4

APPENDIX D

"A Statistical Theory of Langmuir Turbulence"

Journal de Physique

Colloq. #7, Tome 40, C7-601, July 1979

D. F. DuBois, H. A. Rose, and M. V. Goldman

CU 1036

November 1979

A STATISTICAL THEORY OF LANGMUIR TURBULENCE

by

D. F. DuBois and H. A. Rose
Theoretical Division
Los Alamos Scientific Laboratory
University of California
Los Alamos, New Mexico

and

M. V. Goldman
Department of Astrogeophysics
University of Colorado
Boulder, Colorado

ABSTRACT

A statistical theory of Langmuir turbulence is developed by applying a generalization of the ~~direction~~ interaction approximation (DIA) of Kraichnan to the Zakharov equations describing Langmuir turbulence.

A STATISTICAL THEORY OF LANGMUIR TURBULENCE

Recent advances in the theory of "strong" Langmuir turbulence¹ have concentrated on the evolution of modulational instabilities and their relation to soliton solutions (in 1-D) and Langmuir collapse² in higher dimensions. Most of the nonlinear theories in this area have emphasized initial value or similarity solutions for the coherent nonlinear structures of interest. In many situations we can conceive of the nonlinear excitations as developing from the thermal (particle) fluctuations in the plasma in the presence of external beams or A.C. fields which drive Langmuir instabilities. Numerical studies³ have shown the birth and decay of "collapsons", new collapsons being generated from the residual fluctuation debris of previously decayed collapsons. It is not unreasonable to try to construct a statistical turbulence theory to describe such situations. The present work represents a preliminary attempt in this direction.

Our method is a generalization to the Zakharov equations¹ of the direct-interaction approximation (DIA) of Kraichnan⁴ which was originally applied to the Navier-Stokes equations. We begin with the Zakharov equations in Fourier transform space, which can be written in the compact form:

$$L_{12}N_2 = \frac{1}{2}X_{123}^{(2)}N_2N_3 + \eta_1, \quad (1)$$

where $N_1 = N_{\alpha_1}(\underline{k}_1, t_1)$ is a three component vector with the discrete indices α_1 taking on the waves +, 0, -. Repeated indices such as 2 and 3 are understood to be summed on discrete indices α_2, α_3 and integrated over the continuous variables \underline{k}_2, t_2 , etc. The identification of the discrete indices is:

$$N_+(k_1, t_1) = \phi^+(k_1, t_1); N_0(k_1, t_1) = n(k_1, t_1);$$

$$N_-(k_1, t_1) = \phi^-(k_1, t_1), \quad (2)$$

where $\phi^+(k_1, t_1)$, $\phi^-(k_1, t_1)$ are the spatial Fourier transforms of the envelope function of the high frequency Langmuir potential and its complex conjugate $[\phi^+(k, t)^* = \phi^-(-k, t)]$ and $n(k, t)$ is the Fourier transform of the ion density deviation $[n(k, t) = n(-k, t)]$. The linear operator L_{12} is

$$\begin{bmatrix} \partial_{t_1} + \nu_e + ik_1^2 & 0 & 0 \\ 0 & \partial_{t_1}^2 + 2\nu_i \partial_{t_1} + k_1^2 & 0 \\ 0 & 0 & \partial_{t_1} + \nu_e - ik_1^2 \end{bmatrix} \cdot (2\pi)^3 \delta(k_1 - k_2) \delta(t_1 - t_2) \quad (3)$$

The only nonzero components of $X_{123}^{(2)}$ are

$$X_{+0-}^{(2)} = -X_{-0-}^{(2)} = -i(k_1 \cdot k_2) k_1^{-2} \delta_{123},$$

$$X_{++0}^{(2)} = -X_{--0}^{(2)} = -i(k_1 \cdot k_2) k_1^{-2} \delta_{123}; \quad (4)$$

$$X_{0+-}^{(2)} = X_{0-+}^{(2)} = -k_1^2 (k_2 \cdot k_3) \delta_{123}$$

$$\delta_{123} = (2\pi)^3 \delta^3(k_1 - k_2 - k_3) \delta(t_2 - t_3) \delta(t_1 - t_2).$$

Equation (1) is a general quadratically nonlinear form to which the DIA can be immediately applied,⁵ giving a set of equations coupling three important objects: the ensemble averaged (mean) fields $\langle N_1 \rangle$, the infinitesimal response function⁵ (given by a functional derivative) and the covariance:

$$R_{11}' = \delta \langle N_1 \rangle / \delta \langle \eta_1 \rangle; C_{11}' = \langle N_1 N_1' \rangle - \langle N_1 \rangle \langle N_1' \rangle \quad (5)$$

The equations connecting these are:

The equations connecting these are:

$$(L_{12} - \Sigma_{12})R_{21} = \delta_{11} \left[= \delta_{\alpha_1 \alpha_1} \delta^3(\underline{k}_1 - \underline{k}_1') \delta(t_1 - t_1') \right], \quad (6)$$

where,

$$\Sigma_{11} = X_{123}^{(2)} X_{231}^{(2)} R_{22} C_{33} + X_{123}^{(2)} \langle N_3 \rangle, \quad (7)$$

$$L_{12} \langle N_2 \rangle = \langle \eta_1 \rangle + \frac{1}{2} X_{123}^{(2)} (\langle N_2 \rangle \langle N_3 \rangle + C_{23}), \quad (8)$$

$$(L_{12} - \Sigma_{12})C_{21} = R_{12} S_{12}, \quad (9)$$

$$S_{11} = S_{11}^0 + \frac{1}{2} X_{123}^{(2)} X_{123}^{(2)} C_{22} C_{33}, \quad (10)$$

where S_{11}^0 is the correlation of the fluctuating part of the driving term η_1 which we can take, for example, to be white noise related to the damping decrements by a Nyquist theorem:

$$S_{11}^0 = \langle \delta \eta_1 \delta \eta_1 \rangle = \Gamma_{\alpha_1 \alpha_1} \delta^3(\underline{k}_1 - \underline{k}_1') \delta(t_1 - t_1'), \quad (11)$$

$$\Gamma_{+-} = \Gamma_{-+} = 4\pi T_e v_e k_1^{-2}; \quad \Gamma_{00} = 3k_1^2 (m_i/m_e) v_i;$$

$$\text{others zero.} \quad (12)$$

This set of nonlinear, non-Markoffian coupled equations is currently being studied by numerical analysis. The general initial value problem is difficult because of the long time histories which must be retained in an unstably evolving system. The DIA can be shown to have the general property that the mean constants of the motion of the Zakharov equations^{1,2} $\langle N \rangle$, $\langle P \rangle$ and $\langle H \rangle$ are independent of time. These conservation properties of the complete DIA give us some confidence that these equations contain at least some of the physics important for Langmuir collapse.²

We have investigated the steady state, spatially homogeneous solutions of these equations

for zero mean field. Here the $R(C)$ matrices have a diagonal (anti-diagonal) form. The explicit equations for the various components are:

$$[-i(\omega_1 - k_1^2) + \nu_e - \Sigma_{++}(k_1, \omega_1)] R_{++}(k_1, \omega_1) = 1 \quad (13a)$$

$$\begin{aligned} \Sigma_{++}(k\omega) &= (2\pi)^{-3} \int d^3 k_2 \int d\omega_2 \{ i(\underline{k}_1 \cdot \underline{k}_2)^2 k_1^{-2} k_2^2 \\ &\quad \cdot C_{+-}(\underline{k}_2, \omega_2) R_{00}(\underline{k}_3, \omega_3) + (\underline{k}_1 \cdot \underline{k}_2)^2 k_1^{-2} k_2^{-2} \\ &\quad \cdot R_{++}(\underline{k}_2, \omega_2) C_{00}(\underline{k}_3, \omega_3) \} ; \end{aligned} \quad (13b)$$

$$\begin{aligned} [-i(\omega_1 - k_1^2) + \nu_e - \Sigma_{++}(k_1, \omega_1)] C_{+-}(\underline{k}_1, \omega_1) \\ = R_{++}(\underline{k}_1, \omega_1) S_{+-}(\underline{k}_1, \omega_1) \end{aligned} \quad (14a)$$

$$\begin{aligned} S_{+-}(\underline{k}_1, \omega_1) &= S_{+-}^0(\underline{k}_1, \omega_1) + (2\pi)^{-4} \int d^3 k_1 \int d\omega_1 (\underline{k}_1 \cdot \underline{k}_3)^2 k_1^{-4} \\ &\quad \cdot C_{00}(\underline{k}_2, \omega_2) C_{+-}(\underline{k}_3, \omega_3) ; \end{aligned} \quad (14b)$$

$$[-\omega_1^2 + 2i\omega_1 \nu_i + k_1^2 - \Sigma_{00}(\underline{k}_1, \omega_1)] R_{00}(\underline{k}_1, \omega_1) = 1, \quad (15a)$$

$$\begin{aligned} \Sigma_{00}(\underline{k}_1, \omega_1) &= (2\pi)^{-4} \int d^3 k_2 \int d\omega_2 (-i)(\underline{k}_2 \cdot \underline{k}_3)^2 k_1^2 k_2^{-2} \\ &\quad \cdot [R_{++}(\underline{k}_2, \omega_2) C_{+-}(\underline{k}_3, \omega_3) - R_{--}(\underline{k}_2, \omega_2) C_{+-}(\underline{k}_3, \omega_3)] ; \end{aligned} \quad (15b)$$

$$\begin{aligned} [-\omega_1^2 + 2i\omega_1 \nu_i + k_1^2 - \Sigma_{00}(\underline{k}_1, \omega_1)] C_{00}(\underline{k}_1, \omega_1) \\ = R_{00}(\underline{k}_1, \omega_1) S_{00}(\underline{k}_1, \omega_1) , \end{aligned} \quad (16a)$$

$$\begin{aligned} S_{00}(\underline{k}_1, \omega_1) &= S_{00}^0(\underline{k}_1, \omega_1) + (2\pi)^{-4} \int d^3 k_1 \int d\omega_1 k_1^4 \\ &\quad \cdot (\underline{k}_2 \cdot \underline{k}_3)^2 C_{+-}(\underline{k}_2, \omega_2) C_{+-}(\underline{k}_3, \omega_3) ; \end{aligned} \quad (16b)$$

where throughout $\underline{k}_1 = \underline{k}_2 + \underline{k}_3$, $\omega_1 = \omega_2 + \omega_3$ and

$R_{--}(\underline{k}_1, \omega_1) = R_{++}(-\underline{k}_1, -\omega_1)^*$ and $C_{+-}(\underline{k}_1, \omega_1) = C_{+-}(-\underline{k}_1, -\omega_1)$.

What usually is described as weak turbulence theory is obtained from equations (14) and (16) by replacing the response functions R and everywhere by their zero order values $R_{++}^0 = [-i(\omega - k^2) + \nu_e]^{-1}$, $R_{00}^0 = [-\omega^2 + 2i\omega \nu_i + k^2]^{-1}$, $C_{+-}^0 = W(\underline{k}) k^{-2} (2\pi) \cdot \delta(\omega - k^2)$, etc., where $W(\underline{k})$ is the Langmuir energy

density. In this approximation, it is easily seen that the two terms in Σ_{++} and Σ_{00} describe induced decay processes of the form $L \rightarrow L+S$ which lead, for example, to the well-known cascade of wave energy toward lower k .

The DIA, on the other hand, treats the self-consistent renormalization of the response functions and this renormalization is necessary to preserve the mean constants of the motion. This renormalization has extremely important consequences: For example, if in (15b) we approximate the quantities R and C by their zero order values and then substitute the resulting Σ_{00} into (15a) we find that R_{00} has complex poles corresponding to the roots of the well-known modulational dispersion relation, i.e., the quantity in square brackets in (14) is just this dispersion relation generalized to the case of a broad Langmuir spectrum.⁶ Thus, in addition to the modified ion sound poles in R_{00} (modified by the decay branch of the dispersion relation) the modulational instability introduces new modulational poles in R_{00} . When this renormalization R_{00} is put into (13b), it appears that flow of Langmuir energy toward higher k becomes possible. Furthermore, C_{00} now has large components due to the modulational instability which produce a significant source term (14b) on the right-hand side of (14a). The renormalized Langmuir modes then have a finite turbulent damping in contrast to the marginally damped modes found in the usual theory of the cascade of energy toward small k .

A fully self-consistent solution of the DIA equations requires computer analysis. We will present results of 1-D numerical solutions of the DIA equations as well as a comparison of the results with direct computer solutions of the Zakharov equations. Questions concerning the spontaneous generation of a mean field at $k = 0$ to account for the Langmuir condensation and consequent modulational instability will also be addressed.

This research was performed under the auspices of U.S. DOE and AFOSR grant #F49620-76-C-0005.

References

1. L. I. Rudakov and V. N. Tsytovich, Phys. Reports 40, 1(1978); S. G. Thornhill and D. ter Haar, Phys. Reports 41, (1978).
2. M. V. Goldman and D. R. Nicholson, Phys. Rev. Letters 41, 406(1978).
3. D. R. Nicholson, M. V. Goldman, D. F. DuBois, and G. F. Reiter, "Numerical Study of Strong Langmuir Turbulence", Bull. Am. Phys. Soc. 23, 892 (1978).
4. R. H. Kraichnan, Phys. Rev. 113, 1181(1958).
5. D. F. DuBois and M. Espedal, Plasma Physics 20, 1209 (1978).
6. S. Bardwell and M. V. Goldman, Ap. J. 209, 912 (1976).
D. R. Nicholson and M. V. Goldman, Phys. Fluids 21, 1766(1978).

APPENDIX E

"Two Examples of the Decay Instability
in an Inhomogeneous Plasma"

Ph.D. Thesis
University of Colorado
Draft, 1979

Terence H. Rudolph

CU 1036
November 1979

TWO EXAMPLES OF THE DECAY INSTABILITY
IN AN INHOMOGENEOUS PLASMA

by

Terence Harvey Rudolph
A.B., Ripon College, Wisconsin, 1972

A thesis submitted to the Faculty of the Graduate
School of the University of Colorado in partial
fulfillment of the requirements for the degree of

Doctor of Philosophy

Department of Astro-Geophysics

1979

Rudolph, Terence Harvey (Ph.D., Astro-Geophysics)

Two Examples of the Decay Instability in an Inhomogeneous
Plasma

Thesis directed by Professor Martin V. Goldman

Saturation of the electron-ion decay instability can occur linearly in an inhomogeneous plasma due to the effects of Langmuir wave propagation. The Langmuir intensity spectrum resulting from this convective saturation is calculated from the WKB wave kinetic equation in two cases: 1) an ionospheric model including magnetic field and cyclotron harmonic damping, and 2) a dense plasma focus model. An application is made to the scattering experiment of Peacock, et al. The addition of a term corresponding to nonlinear Landau damping is also considered.

This abstract is approved as to form and content.
I recommend its publication.

Signed _____
Faculty member in charge of thesis

CHAPTER 1

GENERAL CONSIDERATIONS

Much work has been done in the past on the problem of parametric instabilities in an inhomogeneous plasma. (1-8) However, this work in large part is concerned with such matters as the calculation of inhomogeneous thresholds and the conditions for absolute and convective instabilities. ~~Much~~ Less attention has been paid to the calculation of actual wave intensities in the plasma, and the uses to which this information can be put. This present work calculates these intensities for the parametric decay instability in two different models and gives an example of an application.

The parametric decay instability has been studied in great detail elsewhere, (9-14) so only a brief discussion is necessary here. To physically understand the decay instability, consider a homogeneous, unmagnetized plasma. It is not necessary that the plasma be homogeneous and unmagnetized, but these conditions simplify the concept considerably. There ^{are} ~~will be~~ two electrostatic normal modes in the plasma, corresponding to Langmuir waves and ion acoustic waves. These waves ^{are} ~~will be~~ in thermal equilibrium

at a constant level of intensity. Now impose an electromagnetic "pump" wave on the plasma in such a manner that its frequency, ω_0 , and wave vector, \underline{k}_0 , satisfy,

$$\begin{aligned}\omega_0 &= \omega_L + \omega_{ia} \\ \underline{k}_0 &= \underline{k}_L + \underline{k}_{ia}\end{aligned}\tag{1-1}$$

where ^{the subscripts} L and ia refer to Langmuir and ion acoustic, respectively. Then the pump wave can beat against the thermal level of ion acoustic waves to produce a source for Langmuir waves, and against the thermal level of Langmuir waves to produce a source for ion acoustic waves. If the pump intensity is large enough, and the damping of the ion acoustic and Langmuir waves is not too large, energy can be continuously transferred from the pump to the normal modes of the plasma, resulting in an instability.

This process can also be seen mathematically in a simple fashion. The normal mode oscillations in the plasma in the absence of the pump will satisfy wave equations of the form,

$$\begin{aligned}\theta_L \phi_L(x,t) &= 0 \\ \theta_{ia} \phi_{ia}(x,t) &= 0,\end{aligned}\tag{1-2}$$

and the ϕ 's represent normal mode responses, where the θ 's are operators. ^{and the ϕ 's represent normal mode responses.} The Fourier transform in time and space of these equations gives the dispersion relation $\omega = \omega(\underline{k})$, and the solution of this the real frequency and damping rate. In the case of the Langmuir wave

one has $\omega = \omega_L + i\gamma_L$. Now, imposing the pump wave on the plasma produces source terms, transforming Equations (1-2) to,

$$\begin{aligned}\partial_L \phi_L(x,t) &= C_1 \phi_{ia}(x,t) \\ \partial_{ia} \phi_{ia}(x,t) &= C_2 \phi_L(x,t)\end{aligned}\tag{1-3}$$

Clearly $C_1 \phi_{ia}$ represents the beating of the pump, contained in C_1 and C_2 , against the acoustic wave level to produce the source for Langmuir waves. Now the two equations are coupled, because of the pump, and the procedure which led to $\omega = \omega_L + i\gamma_L$ for the Langmuir mode before ~~is~~ will be changed. Omitting the details which can be found in Reference 9, one will find that the Langmuir normal mode has shifted to $\omega' = \omega'_L + i\gamma'_L$. Normally $\omega'_L \approx \omega_L$ but it is possible, for appropriate parameters, to have $\gamma'_L + \gamma_L < 0$, meaning that γ_L has switched sign, so a natural damping has become growth. In essence, the new normal mode resulting from the presence of the pump is a naturally growing mode, rather than the naturally damped mode which it was in the absence of the pump.

Now consider what happens to the instability in an inhomogeneous plasma. A given Langmuir wave will no longer have a fixed k_L . As the wave propagates k_L will change, so the second of Equations (1-1), quantum mechanical momentum conservation, cannot be satisfied everywhere. Since the decay instability is active only in regions where this k

matching condition is approximately satisfied, propagation will take the Langmuir wave away from this active region, and hence saturate the instability linearly. This process is called convective saturation, and if it occurs quickly enough so that the Langmuir intensity at a given point in the plasma becomes constant with time, the instability is said to be convective. The decay instability can also be absolute. Although it is true that any given waves' intensity will saturate due to propagation out of the active region, if one observes a sequence of waves going past at a given point in the plasma, these waves can have increasingly large intensities. In this situation the Langmuir intensity at the observation point grows in time without bound linearly, and the instability is called absolute at that point. All calculations done in succeeding chapters are done in steady state, which implicitly assumes that a convective instability is present.

As mentioned earlier there are two models being addressed in this thesis. The first is a model of the ionosphere, dealt with in Chapters 2 and 3. Chapter 2 introduces the physical phenomena associated with ionospheric modification experiments and the concept of cyclotron harmonic damping.. Chapter 3 numerically integrates the WKB wave kinetic equation to find the Langmuir intensity spectra which the model predicts. Chapter 4 introduces the dense plasma focus scattering

experiment on which the second model is based. The fifth chapter deals with Langmuir wave propagation in the inhomogeneous, unmagnetized plasma. Chapter 6 and 7 integrate the wave kinetic equation for this model in one and two dimensions. Chapter 8 considers the problem of adding a nonlinear term to the inhomogeneous kinetic equation and derives conditions under which the convective terms can be ignored. The last chapter presents numerical results and the application to the focus scattering experiment. The appendices are concerned with the derivation of the WKB wave kinetic equation and the derivation and properties of Wilson's function.

CHAPTER 2

IONOSPHERIC MODIFICATION AND CYCLOTRON DAMPING

This section is meant to introduce the reader to the basic effects seen in ionospheric modification experiments. In these experiments a high intensity electromagnetic pump wave is reflected from electron density gradients in the ionosphere to produce local changes in such quantities as distribution functions, electron density, and electron temperature. For appropriate pump parameters, these changes are presumably brought about through the mechanism of the parametric decay instability. Energy travels from the pump wave through a spectrum of Langmuir waves and finally is deposited into the ionospheric particles via collisional and Landau damping. In addition, if the pump is operated so that at its reflection point its frequency is near the electron cyclotron frequency or a harmonic thereof, observations indicate an increase in the energy being deposited in the particles. This is consistent with the theoretical picture in which Langmuir waves with frequencies near the cyclotron

frequency or its harmonics will undergo cyclotron damping in addition to collisional and Landau damping. This section concludes with a brief discussion of cyclotron damping both physically and mathematically.

The following discussion is in large part taken from sections of a technical report written by the author late in 1976.

Intentional modification of the ionosphere using radio waves has been successfully accomplished since 1970. However, the theoretical beginnings of the subject go back much farther, to Baile^ey in 1938.²¹⁵ He predicted that the night sky could be visibly brightened by heating electrons in the ionosphere with a powerful radio transmitter. Later predictions raised the possibility of better long-range communication, since increased electron density in a modified region could enhance ionospheric reflections and result in a stronger signal at the receiver.²¹⁶ These predictions have been verified by recent experiments, and in addition many unexpected phenomena have been observed. Among these new phenomena were the presence of field aligned density fluctuations and wideband attenuation, to be described in some detail later.

The first phenomenon to be discovered

experimentally was that of artificial spread-F.^{#11,18} The term originates from the appearance of ionosonde records when the pump is on. The ionosonde is essentially a radio transmitter and receiver which transmits a range of frequencies into the ionosphere and measures the delay time until the reflected signal is received. This allows the measurement of electron density versus altitude, assuming that each frequency is reflected at a point where it is equal to the plasma frequency. Normally, an ideal ionosonde record is a sharp line, implying that the ionosphere has a smooth density variation. However, within seconds of the turn-on of a high intensity pump wave, this sharp line diffuses, indicating that density irregularities are building up in the ionosphere. When the pump is turned off, the diffuse area will again coalesce into a line, usually on the order of minutes, although sometimes longer. Spread-F is the most consistent of the phenomena to be discussed here, appearing whenever the pump is on, and also the most easily understood conceptually, since it only requires that density irregularities be present near the reflection altitude of the pump wave.

One of the least understood results from the modification experiments is wideband attenuation

(WBA).²¹ This is also seen on ionosonde records, although with not nearly the consistency of spread-F. To explain the phenomenon a short digression is necessary. The ionosonde record described previously is not really a simple single line, but rather a pair of lines, one corresponding to the ordinary mode of the ionosonde's radio wave and the other to the extraordinary mode. The two lines occur because the O-mode propagates to slightly higher altitude than the X-mode and therefore has a slightly longer delay time. WBA, when it occurs, is present if the pump is also operated in the O-mode. Then the ionosonde line which corresponds to the O-mode is cut off very near the pump frequency. No ionosonde frequencies higher than the pump frequency are reflected. The phenomenon tracks the pump very closely, meaning that WBA is present within seconds of the turn-on of the pump and disappears within seconds when the pump is turned off. The amount of the attenuation exceeds 10 db, and its cause is unknown. Explanations have been advanced, but none appears to be definitive. The extremely sporadic nature of WBA would appear to be one of the problems in developing a good theory.

A third and very important phenomenon associated with ionospheric modification is that of artificial

field aligned scattering (AFAS).^{#19-21} This is intimately connected with the density irregularities responsible for spread-F. Studies have been done to determine the configuration of the density irregularities with respect to the magnetic field. Essentially this is done by using a directional ionosonde.^{#17} For the Platteville, Colorado, pump site the ionosonde can be pointed slightly to the north of the zenith and then slightly to the south. It is found that for the same frequency the delay time for pulses sent to the south is longer. This indicates that the density irregularities are at a greater altitude toward the south than toward the north. Taking the magnetic field configuration into account, the differences in delay times observed are consistent with a modified region of the ionosphere that is aligned with the magnetic field.

Much of the experimental interest in these field aligned irregularities has been in determining their scattering properties. Pulsed radars are usually used for these studies, which show that scattering from the irregularities is much like specular reflection from the geomagnetic field lines. AFAS appears to be very aspect sensitive, with returning radar echoes dropping off sharply when the reflection conditions are not met.

The AFAS phenomenon is one in which large enhancements in scattering cross sections are seen when the pump is operating at approximately twice the cyclotron frequency in the heating region. A study by Fialer^{#19} shows an increase in cross section of about 10 dbsm from 55 dbsm to 65 dbsm for the highest probe frequency used, 75 MHz. This clearly indicates that there is some mechanism associated with the cyclotron harmonic which is enhancing energy transfer between the pump wave and the ionospheric plasma.

AFAS has already been used experimentally to facilitate long range radio communications.^{#22,23} Reproduction of transmitted material has been successfully achieved over distances too great for direct radio communication. The aspect sensitivity of AFAS is both a hindrance and a help to this communication. Its reflective property will result in less signal loss at the receiving station, but of course the same property severely limits the possible area of reception. However, for some applications this would not be considered a hindrance.

The last major effect of the heating experiments is the observed enhancement of the airglow above the heating installation.^{#24} Most of the interest is centered on the neutral oxygen airglow of the 6300 Å

and 5577 Å lines. A typical enhancement at 6300 Å would show the intensity going from about 50 Rayleighs with the pump off to about 90 Rayleighs with the pump on. The enhancement of 5577 Å radiation is much smaller, about 5 Rayleighs, due to the significantly greater amount of energy needed to excite the transition. This is a definite pumping effect, however, since the 5577 Å line can be seen to follow the modulation of the pump very closely, as the heating is turned on and off. The ratio of the intensities of the two lines can be used to determine the temperature assuming a Maxwellian distribution. This turns out to be of the order of 20,000 °K, which is unrealistic on the basis of the actual intensities observed, so clearly a non-Maxwellian electron distribution must be involved.

The region of deposition of pump energy and the region of enhanced airglow do not always coincide. Below about ²380 km, the regions are the same, but if the pumping region goes above this altitude, the airglow region stays at about 280 km. This necessitates a theory allowing for the transport of hot electrons from the pumping region to the airglow region where they give up their energy due to inelastic collisions with neutral atoms.

AD-A081 883

COLORADO UNIV AT BOULDER DEPT OF ASTRO-GEOPHYSICS

F/G 20/9

PLASMA WAVE TURBULENCE AND PARTICLE HEATING CAUSED BY ELECTRON --ETC(U)

NOV 79 M V GOLDMAN

F49620-76-C-0005

UNCLASSIFIED

CU-1036

AFOSR-TR-80-0167

NL

3 - 6

2 - 10/80

1 - 10/80

1 - 10/80

1 - 10/80

1 - 10/80

1 - 10/80

1 - 10/80

1 - 10/80

1 - 10/80

1 - 10/80

1 - 10/80

1 - 10/80

1 - 10/80

1 - 10/80

1 - 10/80

1 - 10/80

1 - 10/80

1 - 10/80

1 - 10/80

1 - 10/80

1 - 10/80

1 - 10/80

1 - 10/80

1 - 10/80

1 - 10/80

1 - 10/80

1 - 10/80

1 - 10/80

1 - 10/80

1 - 10/80

1 - 10/80

1 - 10/80

1 - 10/80

1 - 10/80

1 - 10/80

1 - 10/80

1 - 10/80

1 - 10/80

1 - 10/80

1 - 10/80

1 - 10/80

1 - 10/80

1 - 10/80

1 - 10/80

There is one instance of 6300 Å airglow observed when the pump operated at approximately twice the cyclotron frequency.^{R 24} This resulted in the intensity going from about 50 Rayleighs at turn-on to about 250 Rayleighs two minutes after turn-on. This is two and one-half times the "typical" enhancement when the pump is not near a cyclotron harmonic. The extra enhancement is more evidence for some phenomenon associated with the cyclotron frequency being an important mechanism for energy deposition.

Chapter 3 is concerned with calculating the spectrum of Langmuir waves in the ionosphere when the pump is near twice the electron cyclotron frequency. Although this work makes no application of the derived spectra, they can presumably be used for calculating energy transfer to the ionospheric particles and in making predictions for the observed quantities associated with the modification experiments. No application of the spectra was made here for two reasons. There are very few observations of ionospheric phenomena occurring when the pump was operated near $2\omega_{ce}$. No serious work has been done near the cyclotron frequency or any harmonic, and observations that have been reported have been mainly serendipitous. Secondly, the experimental work that

has been done probably does not fall within the region of validity of the calculations of Chapter 3. Since nonlinear effects have been excluded there, the limit on the ratio of pump intensity to threshold intensity for typical ionospheric parameters is about 13. The observations have taken place at intensities significantly larger than this, so nonlinear effects need to be considered and are probably dominant. Nevertheless, the spectra of Chapter 3 may be useful at lower pump intensities or in other magnetoactive, inhomogeneous plasmas.

The derivation of the mathematical form of cyclotron damping proceeds from the linear electron susceptibility in a magnetic field,

$$\chi_e(\omega, k) = \frac{k_{\perp}^2}{k^2} \left[1 + \frac{\omega}{\sqrt{2} k_{\parallel} v_e} \sum_{n=-\infty}^{\infty} e^{-a} I_n(a) Z\left(\frac{\omega - n \omega_{ce}}{\sqrt{2} k_{\parallel} v_e}\right) \right], \quad (2-1)$$

In this equation $a = k_{\perp}^2 v_e^2 / \omega_{ce}^2$, I_n is the modified Bessel function, and Z is the plasma dispersion function. k_{\perp} and k_{\parallel} refer to perpendicular and parallel to the magnetic field.

The damping is found by expanding the dispersion relation $1 + \chi_e(\omega, k) = 0$ about the real frequency ω_r . This procedure gives,

$$\gamma = - \frac{\text{Im } \chi_e}{\left. \frac{\partial \text{Re } \chi_e}{\partial \omega} \right|_{\omega=\omega_r}} \quad (2-2)$$

In the denominator of this expression it is sufficient to use the linear susceptibility in an unmagnetized plasma,

$$\chi_e^{\text{unmagnetized}} = 3 \frac{k^2}{k_D^2} - \frac{\omega^2}{\omega_p^2}$$

$$\left. \frac{\partial \text{Re } \chi_e^{\text{unmagnetized}}}{\partial \omega} \right|_{\omega=\omega_r} = - \frac{2\omega_r}{\omega_p^2} \quad (2-3)$$

Assuming the real frequency is near the plasma frequency, γ becomes,

$$\gamma = \frac{\omega_p^2}{2} \text{Im } \chi_e \quad (2-4)$$

It is unnecessary to deal with equation (2-1) in its exact form. Since $\text{Im } Z$ is largest for small arguments which occur when $\omega \approx n\omega_{ce}$, the Z function can be expanded for small arguments, ²⁵

$$\text{Im } Z \approx \sqrt{\pi} e^{-(\omega - n\omega_{ce})^2 / 2 k_H^2 v_e^2} \quad (2-5)$$

$$\gamma = \frac{k_p^2}{k^2} \sqrt{\frac{\pi}{2}} \frac{\omega_p^2}{k_H v_e} \sum_{n=-\infty}^{\infty} e^{-a} I_n(a) e^{-(\omega - n\omega_{ce})^2 / 2 k_H^2 v_e^2} \quad (2-6)$$

From this equation it is clear that as ω moves off resonance, that is, away from $n\omega_{ce}$, the cyclotron

damping drops sharply. In fact the width can be seen from the exponential term to be $\Delta\omega = \sqrt{2}k_{\perp}v_e$.

For the purposes of Chapter 3, where $\omega \approx 2\omega_{ce}$, only the $n = 2$ term in the sum of equation (2-6) contributes. The exponential factor removes all the other terms. Also, for typical ionospheric parameters, a is very small, so $e^{-a}I_n(a)$ can be expanded in the limit of small argument.²² Then, using $k_{\parallel} = k \cos \theta$, $k_{\perp} = k \sin \theta$, γ becomes,

$$\gamma_{cyc}|_{n=2} \approx \sqrt{\frac{\pi}{2}} \frac{k}{k_D} \omega_p \frac{\sin^4 \theta}{\cos \theta} e^{-(\omega - 2\omega_{ce})^2 / 2k^2 v_e^2 \cos^2 \theta} \quad (2-7)$$

Now, assuming that ω is very close to $2\omega_{ce}$ so that the exponential is essentially unity, and θ is small, so that $\sin \theta \approx \theta$ and $\cos \theta \approx 1$,

$$\gamma_{cyc}|_{n=2} \approx \sqrt{\frac{\pi}{2}} \frac{k}{k_D} \omega_p \theta^4. \quad (2-8)$$

To understand cyclotron damping physically, consider an electron and a Langmuir wave in a magnetized plasma. The electron will spiral around the magnetic field lines at a frequency of ω_{ce} . Allow the Langmuir wave to be slightly oblique to the magnetic field, so that a small perpendicular electric field component exists. This perpendicular component will

oscillate at the Langmuir frequency ω_L . Now consider what happens when the Langmuir frequency happens to be at some multiple of the cyclotron frequency. On each of its orbits, the electron will feel exactly the same electric field at exactly the same points. The field and the electron are in phase, so the electron can efficiently absorb energy from the field. If the Langmuir wave's frequency is slightly off-resonance this synchronous behavior is destroyed and the efficiency of energy transfer drops rapidly. This drop off is mathematically described by the exponential term in equation (2-7). The $\sin^4 \theta$ term in (2-7) basically determines how oblique the Langmuir wave is, and so fixes the size of the perpendicular electric field. Clearly a wave with larger E_L , and hence larger θ , can transfer energy more quickly to the electrons. This is stated mathematically by the θ^4 dependence in (2-8).

CHAPTER 3

THE KINETIC EQUATION INTEGRATED IN AN INHOMOGENEOUS PLASMA WITH MAGNETIC FIELD

To model the ionosphere near a frequency which is a harmonic of the electron cyclotron frequency, it is essential that the earth's magnetic field be included. In this chapter the wave kinetic equation is integrated in a semi-infinite inhomogeneous plasma with linear density profile in the presence of this magnetic field. The field appears in the kinetic equation in three places. The first is through the Langmuir ray paths, which are altered from the zero field case. This is simply a consequence of the appearance of the field in the dispersion relation for the Langmuir waves. Secondly, the growth rate for the Langmuir waves is slightly modified. This occurs because of the propagation characteristics of the ordinary wave transverse pump in the magnetoactive plasma. It is clear that in a stratified plasma without a magnetic field, a normally incident transverse pump wave will always have its electric field component oriented

perpendicular to the density gradient. Hence this is the direction of the most strongly pumped Langmuir waves. However, in a magnetoactive plasma the ordinary wave pump propagates so that at the reflection point, where the plasma frequency equals the pump frequency, the pump electric field is oriented along the magnetic field. The largest growth rate then occurs along the magnetic field rather than perpendicular to the density gradient. Finally, the field appears in the damping rate of the Langmuir waves. Since these waves will have frequencies which are near $2\omega_{ce}$, where ω_{ce} is the electron cyclotron frequency, cyclotron damping can be effective. ~~The presence of cyclotron damping can be effective.~~ The presence of cyclotron damping, discussed more fully in Chapter 2, is the reason that a realistic ^vlienar model can be constructed. Since this damping is proportional to Θ^4 , where Θ is the angle between the k of the Langmuir wave and the magnetic field, ^{it} is initially zero for the most strongly pumped waves. However, as these waves propagate, their wavevector rotates away from the field direction, increasing Θ and hence increasing the damping. This process eventually saturates the instability at linear [^]levels if the intensity of the pump field is not too high.

Listed below are the assumptions used in constructing the model:

a) linear density profile

$$\omega_p^2(x) = \omega_0^2 \left(1 - \frac{x}{L}\right), \quad \omega_p^2(x) = \frac{4\pi e^2}{m_e} n_e(x) \quad (3-1)$$

ω_0 = pump frequency, L = electron density scale length;

b) $T_e = T_i$;

c) $\gamma_{\text{damping}} = \gamma + \gamma_{\text{cyc}}$ (collisional and cyclotron damping included).

d) only two dimensions considered;

e) Airy function variation of E_0 (see Figure 3.1);

f) spontaneous and "beat" emission included.

Assumptions (d) and (e) require some further explanation. It is clear that this problem in its full~~y~~ generality is three dimensional. Referring to Figure ^{3.1}~~3.2~~, however, it is also clear that any wave which has a \underline{k} component outside of the x-y plane will have a larger cyclotron damping rate than the corresponding wave for which that \underline{k} component is zero. Therefore, one should expect to find the fastest growing waves in the x-y plane. This plane, determined by the density gradient and the magnetic field direction, is diagrammed in Figure ^{3.1}~~3.2~~. In what is to

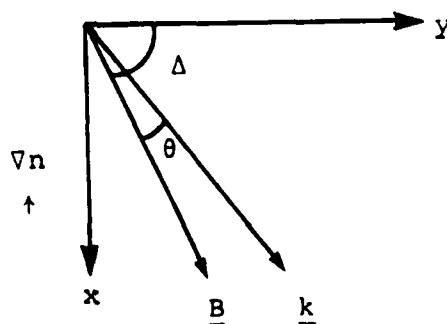
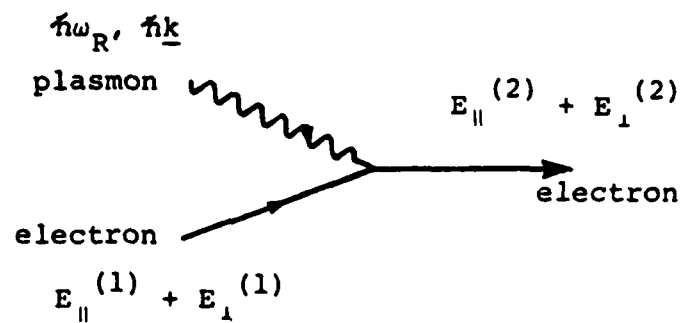


FIGURE 3.1 Schematic diagram of the plane determined by \underline{B} and ∇n .

follow, the z direction is ignored. As stated in (e) the pump electric field is assumed to have an Airy function variation in space. The field's intensity variation is graphed in Figure ^{3.2}~~3.1~~, on a typical ionospheric scale. The Airy function is the correct form for the electric field amplitude of a transverse wave impinging normally on plasma with a linear density profile.²⁷ It is incorporated into this model numerically.

Finally, the heart of the model, the kinetic equation, may be formally written down.

$$\left(\frac{\partial}{\partial t} + v_{gx} \frac{\partial}{\partial x} - \frac{\partial \omega_L}{\partial x} \frac{\partial}{\partial k_x} \right) I_{\underline{k}} + 2\gamma I_{\underline{k}} = 2S_{\underline{k}} \quad (3-2)$$

In this equation v_{gx} is the x component of the group velocity, ω_L is the Langmuir frequency, γ is the net growth rate, and S represents the sources. I , the field correlation function, may be written,

$$I(\underline{k}, \omega) = \lim_{VT \rightarrow \infty} \frac{1}{VT} \langle |E(\underline{k}, \omega)|^2 \rangle \quad (3-3)$$

where V , T refer to volume and time respectively, and the brackets denote an ensemble average. The quantity in the kinetic equation, $I_{\underline{k}}$, is obtained by integrating $I(\underline{k}, \omega)$ over the desired resonance, in this case the

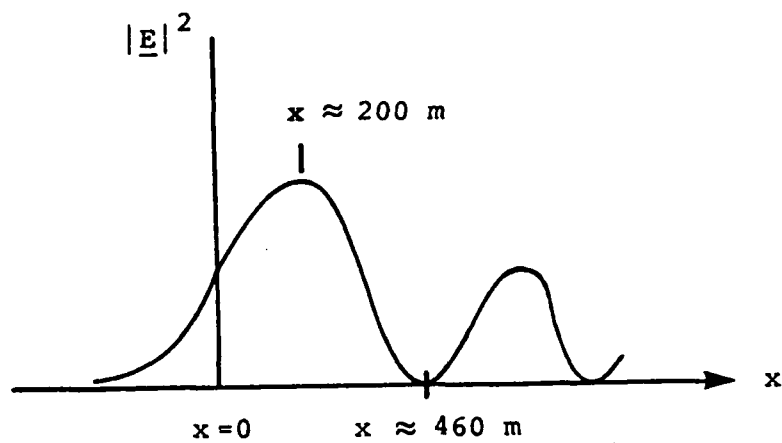


FIGURE 3.2 Pump intensity variation in the ionospheric plasma.

Langmuir resonance.

The first step in solving the kinetic equation is to derive the Langmuir wave ray paths. The ray path equation gives the altitude x as a function of Θ with ω_L and k_y as parameters. Since ω_L and k_y are conserved along a ray path, they serve to characterize a given wave. To derive $z(\Theta; \omega_L, k_y)$, the dispersion relation is necessary. This is found from the real part of the quasilongitudinal dielectric function,

$$1 - \frac{\omega_p^2}{\omega_L^2} + \omega_p^2 \left(\frac{1}{\omega_L^2} - \frac{1}{\omega_L^2 - \omega_{ce}^2} \right) \sin^2 \Theta - \frac{3k_y^2 v_e^2}{\omega_L^2} = 0 \quad (3-4)$$

The ray path equation is easily found by substituting (3-1) into (3-4) and assuming $\omega_L \approx 2\omega_{ce}$.

$$\frac{x}{L} = \left[1 - \frac{\omega_L^2}{\omega_0^2} + \frac{1}{3} \sin^2 \Theta + \frac{3k_y^2 v_e^2}{\omega_0^2} \right] \left(1 + \frac{1}{3} \sin^2 \Theta \right)^{-1}$$

Also note from Figure 3.2 that $k^2 = \frac{k_y^2}{\cos^2(\Delta - \Theta)}$, so,

$$\frac{x}{L} = \left[1 - \frac{\omega_L^2}{\omega_0^2} + \frac{1}{3} \sin^2 \Theta + \frac{3k_y^2 v_e^2}{\omega_0^2 \cos^2(\Delta - \Theta)} \right] \left(1 + \frac{1}{3} \sin^2 \Theta \right)^{-1} \quad (3-5)$$

Several examples of ray paths are plotted in Figure 3.3. The figure shows ray paths for a given ω_L with varying k_y .

The reflection points of the waves are points at

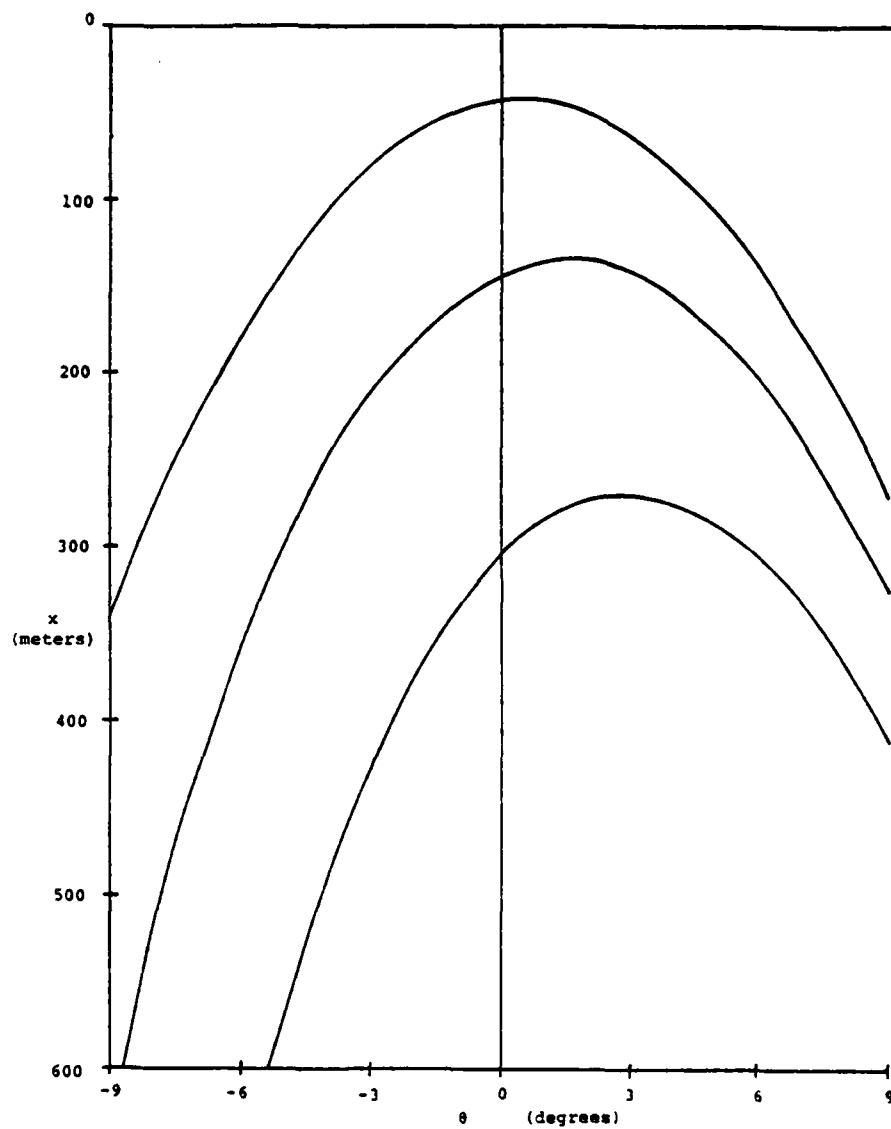


FIGURE 3.3 Langmuir ray paths in the ionospheric model (Equation 3-5).

which $dz/d\theta = 0$. Differentiating (3-5) and solving for θ_T in the approximation $\theta \ll 1$, so that $\Delta - \theta \approx \Delta$, $\sin \theta \approx \theta$, and $\cos \theta \approx 1$,

$$\theta_T \approx \frac{9 k_y^2 v_e^2 \sin \Delta}{\omega_0^2 \cos^3 \Delta} \quad (3-6)$$

Equation (3-5) gives no information about whether θ increases or decreases for a given wave. To determine this, use must be made of the Hamiltonian equation, $\dot{k}_x = - \frac{\partial \omega_L}{\partial x}$. For the adopted density profile, $\dot{k}_x > 0$, so k_x always increases. Referring to Figure 3.4 it is clear that if θ is originally small and positive, it will decrease to zero and then become negative. This means that the kinetic equation must be integrated from positive θ to negative θ .

It should be noted that only one of two possible cases is being considered here, the case with \underline{k} approximately parallel to \underline{B} . These are the waves with downward phase velocity. It is also possible to consider waves with upward phase velocity, or \underline{k} approximately antiparallel to \underline{B} . The propagation characteristics of these waves are illustrated in Figure 3.4. There are no significant differences between the two cases, so only one will be analyzed in detail.

The last step before actually integrating (3-2)

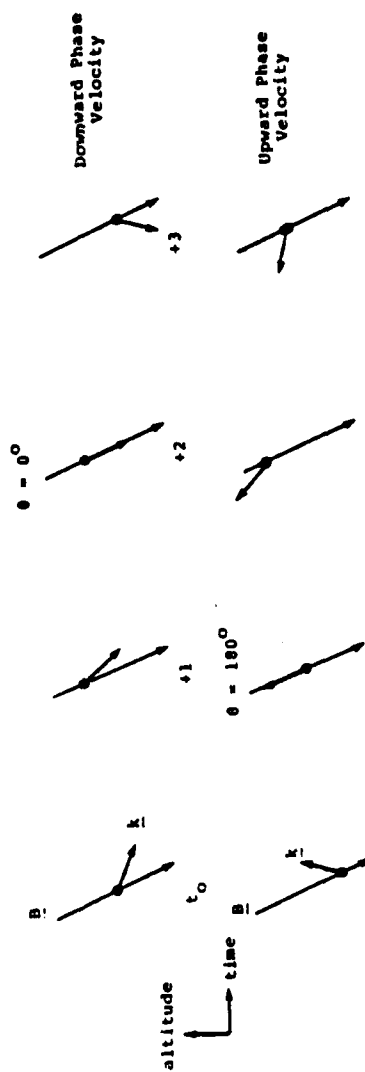


FIGURE 3.4 The spatial position and angle with respect to \underline{B} of the wavevector of a given Langmuir wave as it propagates. Time increases to the right.

is to make explicit the terms S_k and χ in the equation. The basis for much of what follows is drawn from Professor M. V. Goldman's Lausanne Notes, Reference 28 in the Bibliography.

The response of a plasma to given sources may be written as follows,

$$\begin{bmatrix} \epsilon(\chi) & \chi \\ \chi^* & \epsilon(\chi - \chi_0) \end{bmatrix} \begin{bmatrix} E(\chi) \\ E(\chi - \chi_0) \end{bmatrix} = \begin{bmatrix} s(\chi) \\ s(\chi - \chi_0) \end{bmatrix} \quad (3-7)$$

In this equation $\chi = (k, \omega)$, ϵ is the dielectric function of the plasma, χ is the susceptibility, s represents the spontaneous sources, and the subscript zero refers to a pump wave. Equation (3-7) takes into account only the downshifted, or Stokes, line, denoted by $\chi - \chi_0$, and ignores the upshifted anti-Stokes line. This procedure is valid only if $|\omega_A| \gg \gamma_g$, where ω_A is the ion acoustic frequency, and γ_g is the growth rate of the Langmuir mode.

Solving (3-7) for $E(\chi)$,

$$E(\chi) = \frac{s(\chi) - s(\chi - \chi_0) \chi / \epsilon(\chi - \chi_0)}{\epsilon(\chi) - |\chi|^2 / \epsilon(\chi - \chi_0)} \quad (3-8)$$

This is then related to $I(\chi)$ through equation (3-3).

A nonlinear dielectric function may now be defined.

$$\varepsilon^{NL} \equiv \varepsilon(k) - |\chi|^2 / \varepsilon(k - k_0) \quad (3-9)$$

Making a resonant approximation about a mode with frequency ω_r and growth rate γ gives,

$$\varepsilon^{NL} \approx \left. \frac{\partial \text{Re } \varepsilon^{NL}}{\partial \omega} \right|_{(\omega_r, \gamma)} (\omega - \omega_r + i\gamma) \quad (3-10)$$

Then, assuming $|\gamma| \ll \omega_r$, ω_r is the solution to $\text{Re } \varepsilon^{NL} = 0$, and,

$$\gamma = \left. \frac{\frac{\text{Im } \varepsilon^{NL}}{\partial \omega}}{\text{Re } \varepsilon^{NL}} \right|_{\omega = \omega_r}$$

These quantities must now be substituted into (3-8), and it in turn substituted into (3-3). Then, integrating over ω one finds,

$$I_k = \frac{(4\pi)^2}{\gamma \omega_r^2 \left(\frac{\partial \text{Re } \varepsilon^{NL}}{\partial \omega} \right) \big|_{\omega = \omega_r}} \left[S(k, \omega_r) + \frac{\omega_r^2}{(\omega_0 - \omega_r)^2} \frac{S(k - k_0, \omega_r - \omega_0)}{\varepsilon(k - k_0, \omega_r - \omega_0)} \right] \quad (3-11)$$

where,

$$S(k, \omega) \equiv \lim_{VT \rightarrow \infty} \frac{1}{VT} \frac{\omega^2}{(4\pi)^2} \langle |s(k, \omega)|^2 \rangle.$$

This can now be related to the general source term S_k in the kinetic equation through Kirchoff's law. In equilibrium,

$$2\gamma I_k = 2S_k. \quad (3-12)$$

The next step is to write $(\gamma/\omega)\text{Re } \epsilon^{NL}$, γ , ω_r , and S_k as function of the pump amplitude E_0 . By making resonant approximations for $\epsilon(\frac{\gamma}{\omega})$ and $\epsilon(\frac{\gamma}{\omega} - \frac{\gamma}{\omega_0})$, it is possible to find a general solution for the equation $\epsilon^{NL} = 0$. That solution is

$$\omega = \omega_r - i\gamma = \omega_L - i\gamma_D + i\frac{\Gamma^2}{\gamma_A} \frac{1}{1 + \delta/\gamma_A} + \frac{\Gamma^2}{\gamma_A} \frac{\delta/\gamma_A}{1 + \delta/\gamma_A}. \quad (3-13)$$

Here, $\Gamma^2 \equiv \frac{1}{4} |\chi|^2 \frac{k^2}{k_D^2} \omega_p \omega_A$, γ_D is the total Langmuir damping, and $\delta \equiv \omega_L + \omega_A - \omega_0$ is the frequency mismatch. γ_A is the ion acoustic damping, which is of the same order as ω_A for the equal temperature quasi-modes in this model. It is clear from (3-13) that the minimum threshold for growth, $\gamma = 0$, occurs when $\Gamma^2 = \gamma_D \gamma_A$ and $\delta = 0$.

It is now possible to put a more precise upper limit on pump intensity than was done previously. In connection with the neglect of the anti-Stokes line, it was mentioned that the condition $|\omega_A| \gg \gamma_g$ must be satisfied. Recognizing in (3-13) that $\gamma_g = \frac{\Gamma^2}{\gamma_A} \frac{1}{1 + \delta/\gamma_A}$,

$$\frac{\Gamma^2}{\gamma_A} \frac{1}{1 + \delta/\gamma_A} \leq \frac{\Gamma^2}{\gamma_A} \approx \frac{\Gamma^2}{\omega_A} \ll \omega_A. \quad (3-14)$$

Since Γ^2 contains E_0^2 through $|\chi|^2$, (3-14) is the condition on the allowable pump intensity. Using typical ionospheric parameters, the condition is found to be satisfied for ratios of pump intensity to threshold intensity of less than 13. Note also that when (3-14) is satisfied the last term (3-13) is much less than $\frac{1}{2}\omega_A$. Since this term represents the shift in the real frequency due to the presence of the pump, and $\omega_A \ll \omega_L$, (3-14) allows this frequency shift to be ignored. Hence ω_r can be identified as ω_L .

To find $\left. \frac{\partial \text{Re } \epsilon^{NL}}{\partial \omega} \right|_{\omega=\omega_L}$

it is necessary to write down explicitly the expression for ϵ^{NL} obtained when resonant approximations are used for $\epsilon(\frac{\chi}{k})$ and $\epsilon(\frac{\chi-k_0}{k-k_0})$. This is,

$$\epsilon^{NL} \approx \frac{2}{\omega_p} (\omega - \omega_L + i\gamma_L) + |\chi|^2 / 2 \frac{k_D^2}{k^2} \frac{1}{\omega_p} (\omega - \omega_0 + \omega_A + i\gamma_A)$$

$$\frac{\partial \text{Re } \epsilon^{NL}}{\partial \omega} = \frac{2}{\omega_p} + \frac{1}{2} |\chi|^2 \omega_A \frac{k^2}{k_D^2} \frac{\gamma_A^2 - (\omega - \omega_0 + \omega_A)^2}{[\gamma_A^2 + (\omega - \omega_0 + \omega_A)^2]^2}$$

$$\left. \frac{\partial \text{Re } \epsilon^{NL}}{\partial \omega} \right|_{\omega=\omega_L} \approx \frac{2}{\omega_p} \left[1 + \frac{\Gamma^2}{\gamma_A^2} \frac{1 - \delta^2/\gamma_A^2}{(1 + \delta^2/\gamma_A^2)^2} \right]$$

But $\frac{\Gamma^2}{\gamma_A^2} \ll 1$ from (3-14) and $\frac{1 - \delta^2/\gamma_A^2}{(1 + \delta^2/\gamma_A^2)^2} \leq 1$, so,

$$\left. \frac{\partial \operatorname{Re} \epsilon^{NL}}{\partial \omega} \right|_{\omega=\omega_L} \approx \frac{2}{\omega_p} \quad (3-15)$$

Substituting this into the source term,

$$2S_E = 8\pi^2 \left[S(\underline{k}, \omega_L) + \frac{\omega_L^2}{(\omega_L - \omega_0)^2} \frac{|\chi|^2 S(\underline{k}, \omega_L - \omega_0)}{|E(\underline{k}, \omega_L - \omega_0)|^2} \right] \quad (3-16)$$

$S(\underline{k}, \omega_L)$ includes Bremsstrahlung and cyclotron emission, and $S(\underline{k}, \omega_L - \omega_0)$ is low frequency Cerenkov emission which is upshifted by the pump into a source for Langmuir waves.¹² This is the reason for the label, "beat"

emission. $S(\underline{k}, \omega_L)$ is easily obtained through detailed balancing in equilibrium,

$$2Y_D I_E^{eq} = 8\pi^2 S(\underline{k}, \omega_L) \quad (3-17)$$

The equilibrium energy density is, (3-18)

$$\Theta = 2 \int \frac{d\omega}{2\pi} \lim_{\nu \rightarrow 0} \frac{1}{\nu T} \frac{1}{4\pi} \langle |E(\underline{k}, \omega)|^2 \rangle = \frac{1}{4\pi} I_E^{eq} \quad (3-18)$$

Combining (3-17) and (3-18),

$$S(\underline{k}, \omega_L) = \frac{1}{\pi} \Theta Y_D \quad (3-19)$$

$S(\underline{k}, \frac{\omega_L - \omega_0}{0})$ is most easily evaluated by noting that Y_g may be written,²⁸

$$Y_g = - \frac{|\chi|^2}{2/\omega_p} \operatorname{Im} \frac{1}{E(\underline{k}, \omega_L - \omega_0)} \quad (3-20)$$

From the fluctuation-dissipation theorem,

$$S(k, \omega_L - \omega_0) = \frac{1}{2\pi} \Theta(\omega_L - \omega_0) \text{Im } \epsilon(k, \omega_L - \omega_0) \quad (3-21)$$

Combining (3-20) and (3-21),

$$S(k, \omega_L - \omega_0) = \frac{\Theta}{\pi} \frac{\omega_L - \omega_0}{\omega_p} |\epsilon(k, \omega_L - \omega_0)|^2 \gamma_g / |\chi|^2 \quad (3-22)$$

Hence, the source term can finally be written,

$$2S_k = 8\pi \Theta \left(\gamma_0 + \frac{\omega_L}{\omega_0 - \omega_L} \gamma_g \right). \quad (3-23)$$

By substituting for $|\chi|^2$ in Γ^2 , an explicit expression for γ_g is found,

$$\gamma_g = (\hat{e}_0 \cdot \hat{k})^2 \frac{I_0(x)}{4nc \Theta} \omega_p \frac{1}{1 + \delta^2 / \omega_A^2} \quad (3-24)$$

Here n is the electron density, c is the speed of light, \hat{e}_0 is a unit vector in the direction of \underline{E}_0 , and $I_0(x)$ is the square of the Airy function. Note in (3-24) that n is assumed to be a constant. This can be done because its variation is very small over the region in which enhanced Langmuir waves exist. That is, cyclotron damping and Airy function variations tend

to restore equilibrium Langmuir levels at a small enough x that the density profile may be ignored in γ_g , and n may be evaluated at $x = 0$. This is also the justification for another approximation that has been made implicitly throughout this analysis: that $\omega_p = \omega_L$. As long as x always remains small compared to the density scale length L , this approximation will be accurate. In the actual calculations $x/L \lesssim 0.05$.

For completeness, γ_{cyc} from Chapter 2 is included here:

$$\gamma_{cyc} \big|_{n=2} = \sqrt{\frac{\pi}{2}} \frac{k}{k_D} \omega_p \theta^4 \quad (2-1)$$

Making all the relevant substitutions into the kinetic equation, (3-2),

$$\begin{aligned} \left(\frac{\partial}{\partial t} + v_{gx} \frac{\partial}{\partial x} - \frac{\partial \omega_L}{\partial x} \frac{\partial}{\partial k_x} \right) \frac{I_k}{4\pi\theta} + 2(\gamma_D - \gamma_g) \frac{I_k}{4\pi\theta} \\ = 2\gamma_D + 2 \frac{\omega_L}{\omega_0 - \omega_L} \gamma_g. \end{aligned} \quad (3-25)$$

In (3-18) it was shown that $I_{k_{eq}}^{eq} = 4\pi\theta$, so $I_k/4\pi\theta$ is clearly the enhancement of the Langmuir spectrum above equilibrium, which will be defined as f .

The operator on the left of (3-25) can now be simplified. First, all calculations will assume steady state, so $\partial/\partial t = 0$. The rest of the operator can be

transformed into a simple $d\downarrow/d\theta$ by making use of the invariance of ω_L along a ray path.

$$\frac{d\omega_L}{d\theta} = 0 = \frac{\partial \omega_L}{\partial x} \frac{dx}{d\theta} + \frac{\partial \omega_L}{\partial k_x} \frac{dk_x}{d\theta} = \frac{\partial \omega_L}{\partial x} \frac{dx}{d\theta} + v_{gx} \frac{dk_x}{d\theta} \quad (3-26)$$

Therefore,

$$v_{gx} = - \frac{\partial \omega_L}{\partial x} \frac{dx}{d\theta} \frac{d\theta}{dk_x}. \quad (3-27)$$

Then the operator on \downarrow becomes,

$$\begin{aligned} v_{gx} \frac{d}{dx} - \frac{\partial \omega_L}{\partial x} \frac{d}{dk_x} &= - \frac{\partial \omega_L}{\partial x} \left[\frac{d\theta}{dk_x} \frac{dx}{d\theta} \frac{d}{dx} + \frac{d}{dk_x} \right] \\ &= - \frac{\partial \omega_L}{\partial x} \frac{d\theta}{dk_x} \left[\frac{dx}{d\theta} \frac{d}{dx} + \frac{d}{d\theta} \right] \\ &= - \frac{\partial \omega_L}{\partial x} \frac{d\theta}{dk_x} \frac{d}{d\theta} \end{aligned} \quad (3-28)$$

Noticing from Figure 3.2 that $k_x = k_y \tan(\delta - \theta)$,

$$\frac{d\theta}{dk_x} = - \frac{1}{k_y} \cos^2(\delta - \theta). \quad (3-29)$$

Also, from (3-1),

$$\frac{d\omega_L}{dx} = -\frac{\omega_0}{2L}, \text{ for } x \ll L. \quad (3-30)$$

With these changes (3-25) becomes

$$\frac{dJ}{d\theta} - \frac{2Lk_y}{\omega_0 \cos^2(\theta - \theta_0)} \left[2(\gamma_D - \gamma_g)J - 2\gamma_D - 2\frac{\omega_L}{\omega_0 - \omega_L} \gamma_g \right] \quad (3-31)$$

The explicit integration of equation (3-31) offers two choices. First, since the equation is linear and first order, the formal solution is well known.

Writing (3-31) as

$$\frac{dJ(\theta)}{d\theta} + P(\theta)J(\theta) = Q(\theta)$$

the solution is, ~~is~~ ²⁹

$$J(\theta) = e^{-A(\theta)} \left[J(\theta_0) + \int_{\theta_0}^{\theta} Q(\theta') e^{A(\theta')} d\theta' \right] \quad (3-32)$$

$$\text{where } A(\theta) = \exp \left[\int_{\theta_0}^{\theta} P(\theta') d\theta' \right]$$

and $J(\theta_0)$ is the boundary condition. While this solution is fine in principle, it is virtually unusable in practice without further approximation because of the complicated integral over $Q(\theta')$. In fact, to perform the integrals over P and Q in (3-32)

it is necessary to make two approximations. The first is to assume a uniform pump intensity. This eliminates the Airy function as an obstacle to the integration. The second is to require Θ small enough so that $\cos(\Delta - \Theta) \approx \cos \Delta$ and $\sin \Theta \approx \Theta$. These allow the integral in $A(\Theta)$ to be done exactly and that over Q to be done approximately by a saddle point method. By this procedure one arrives at an approximate analytic solution. It is next necessary to ask how good the solution is. By comparison with the exact solution found later, the uniform pump approximation made above does not affect the solution significantly. The reason this is true is that the regions in which the approximation is bad are the same regions in which χ_{cyc} dominates χ_g . Therefore, the solution in these regions is dominated by the behavior of χ_{cyc} which is independent of the pump.

The approximation of small Θ does not fare as well. The major flaw is in replacing $\cos^2(\Delta - \Theta)$ by $\cos^2 \Delta$ near the boundary angle $\Theta = \Theta_0$. Since Θ_0 can be as large as ten to fifteen degrees, this results in a change in the $\cos^2 \Delta$ term of a factor of two. Unlike the case with the uniform pump approximation, this change is occurring in a term which is dominant in the equation. This can result in a difference of a factor

of two or three in intensity from the exact solution, depending on the ray path chosen.

This breakdown of the analytic approximation forces one to turn to numerical methods. Here there are again two choices. The first is to simply evaluate (3-32) numerically. This is rather time-consuming, however, because of the integral over Q . For every point used in the evaluation of this integral, it is necessary to numerically perform the integral in $A(\Theta)$.

By far the simpler method is to integrate (3-31) directly. This was done to get the exact solution mentioned earlier using a fourth order Runge-Kutta method. The integration was begun at a fixed x , the first zero of the Airy function, where the intensity was assumed to be in equilibrium. The method then stepped toward decreasing Θ until the intensity was well below its peak value achieved where the growth rate was equal to the damping rate at negative Θ . Parameters used in the integration which are ~~not~~^f dependent on the chosen ray path are listed below:

$$\Theta = k_B T_e = 0.09 \text{ eV}$$

$$v_e = 1.26 \times 10^7 \text{ cm/sec}$$

$$\omega_0 = 1.76 \times 10^7 \text{ sec}^{-1}$$

$$\omega_{ce} = 8.8 \times 10^6 \text{ sec}^{-1}$$

$$L = 3 \times 10^6 \text{ cm}$$

$$\nu/\omega_p = 10^{-5}$$

$m_i = 2.67 \times 10^{-23}$ gm (O_{16} assumed to be the main source of electrons at 250 km)

$$\Delta = 68^\circ$$

$$P = 4 \quad (P \equiv E_0^2/E_{\text{threshold}}^2).$$

Figure 3.5 shows a typical intensity spectrum along a ray path, characterized by $k_y = 0.0227 \text{ cm}^{-1}$ and $\omega_L = 1.7597 \times 10^7 \text{ sec}^{-1}$. It shows growth from positive to negative Θ until $\Theta \approx -5^\circ$ where the growth rate is equal to the damping rate. For $\Theta < -5^\circ$ the spectrum drops off sharply due to the strong Θ dependence of cyclotron damping. If cyclotron damping were not included in the model, the spectrum would grow to a much higher level and drop off much more slowly, probably necessitating the inclusion of nonlinear terms in the kinetic equation to get realistic results.

To apply these spectra to a physical problem, such as airglow calculation, which will not be done here, it is necessary to have the intensity spectrum at a given altitude rather than for a given ray path. It is reasonable to assume that the highest intensities will occur for altitudes above the first Airy zero, at $x \approx 460$ m. Then the procedure for calculating a constant altitude spectrum for a given frequency ω_L is simple. For fixed x and ω_L one chooses a Θ at which to evaluate

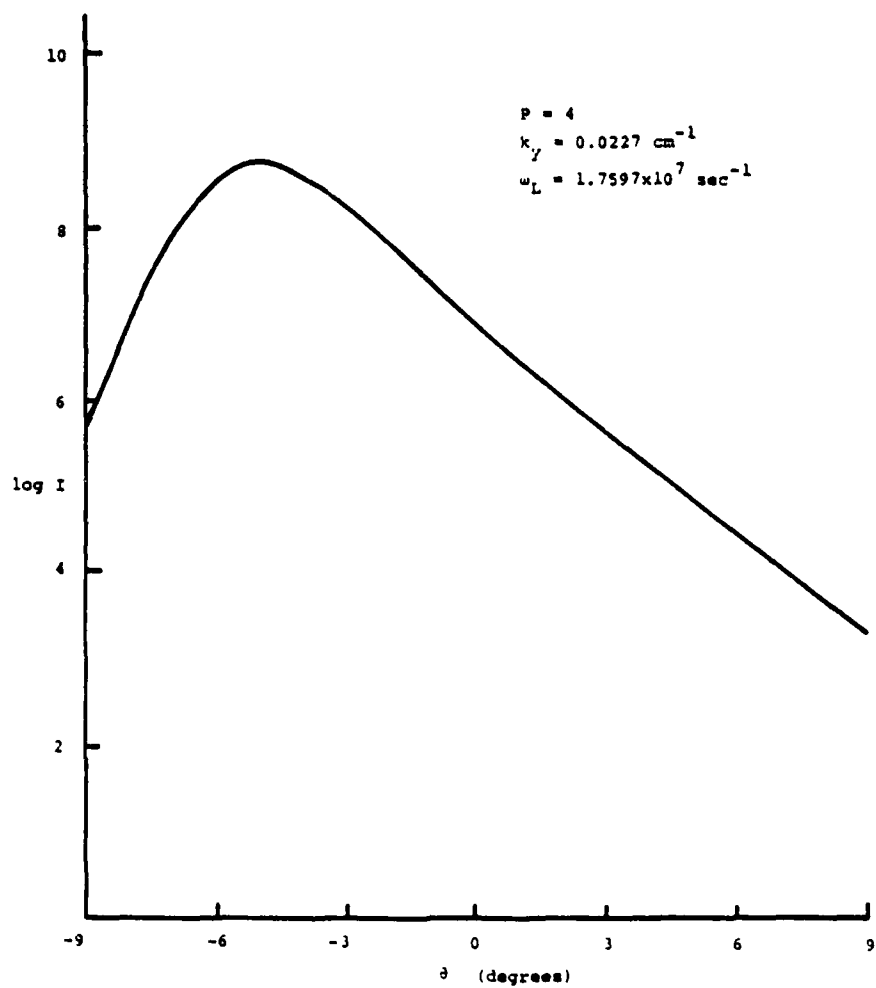


FIGURE 3.5 The intensity spectrum of a given Langmuir wave along its ray path in the ionosphere model.

the Langmuir intensity. Inverting (3-5) allows k_y to be found, so the relevant ray path has been determined. Then using ω_L and k_y (3-31) is integrated from Θ_0 to Θ to give the desired intensity. Equation (3-31) must be integrated once for each point in the constant altitude spectrum.

These constant altitude spectra are qualitatively very similar to the ray path spectrum in Figure 3.5. Figure 3.6 shows a typical spectrum with $\omega_L = 1.7597 \times 10^7$ sec⁻¹. This spectrum, being a synthesis of the intensities of many rays which have all grown by similar amounts, is somewhat flatter than the typical ray path spectrum. This is true in general for constant altitude spectra.

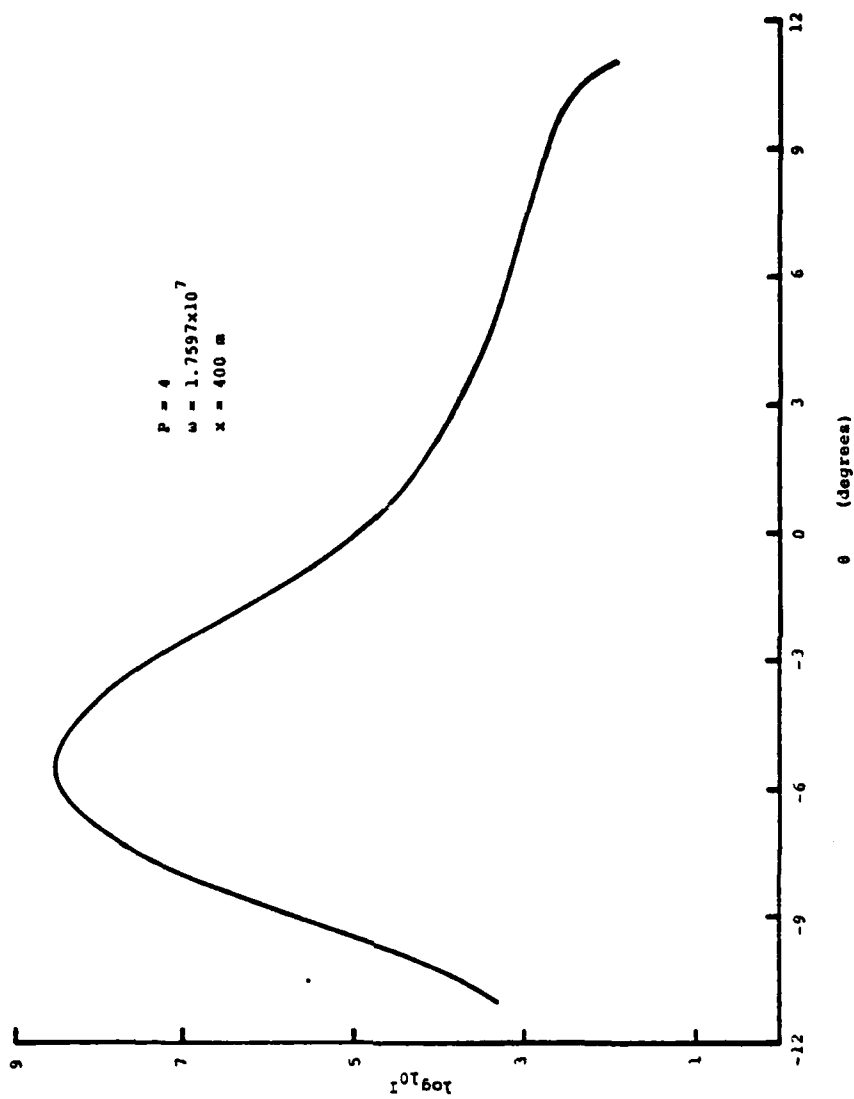


FIGURE 3.6 The intensity spectrum at a given altitude in the ionosphere model.

CHAPTER 4

THE DENSE PLASMA FOCUS SCATTERING EXPERIMENT

The motivation for the theoretical work to follow in Chapters 5-9 has been the scattering data obtained from the dense plasma focus machine operated by N. J. Peacock, et al.²³⁰⁻³² However, the use of convection to saturate the decay instability linearly should have much wider application. In fact, as will be seen in Chapter 9, the scattering experiment uses CO₂ pump intensities which can at best be called marginally in the range of validity of the two-dimensional linear calculations of Chapter 7. These pump intensities require the inclusion of both convective and nonlinear terms in the wave kinetic equation. Only a crude beginning has been made on this much more difficult problem, which is discussed in Chapter 8.

Even though the analytical work of Chapter 7 is not strictly applicable to the scattering experiment, it is useful to make the application anyway, to illustrate the procedures used to calculate scattering cross section from the Langmuir intensity spectra. When applying the theoretical calculations to an actual experiment, it is

necessary to also consider other possible sources of Langmuir turbulence. If the theory of Chapter 7 is to correctly predict measured cross sections, these other sources should be ~~negligible.~~
~~ignorable.~~

One possible source is resonant absorption of the pump wave.^{21,33-35} In this process an electromagnetic pump incident obliquely on an inhomogeneous plasma slab can drive Langmuir waves at the point in the plasma where the dielectric function is zero. The cylindrical geometry of the focus device assures that the CO₂ pump will be obliquely incident at some point, so resonantly driven waves could be important. However, it can be shown that this is not the case. Resonance absorption is most effective for an incident angle given by,²³⁵

$$(k_0 L)^{2/3} \sin^2 \phi \approx 0.7, \quad (4-1)$$

where k_0 is the free space wavenumber of the pump wave, and L is the plasma density scale length. For the parameters of the scattering experiment one finds $\phi \approx 4^\circ$. However, the scattering geometry is not right for Langmuir waves resulting from a pump incident at this angle, and hence these waves will not be measured. The geometry is correct for a pump wave incident at $\phi = 90^\circ$, but for this case resonance absorption will be insignificant, so ~~resonance absorption~~^{it} can be ruled out as an important factor in the experiment.

Harder to deal with is the question of the oscillating two stream instability (OTS).³⁶ This is a four-wave interaction between the pump, two counterstreaming Langmuir waves, and a nonresonant acoustic mode. In a homogeneous, equal temperature plasma OTS has comparable threshold and growth rate to the electron-ion decay instability. There is no reasonable way to neglect this instability. The best that can be done is to make the application to experimental data using only the decay instability, and if agreement is obtained, assume that OTS can be neglected. In the analysis of Chapter 9, any contribution by OTS is neglected.

The remainder of this chapter is devoted to a brief discussion of the dense plasma focus device and the scattering experiment. For more detailed information see References 37,38. The focus device is a cylindrical deuterium plasma through which an axial current is driven to "pinch" the plasma in the radial direction. This creates a high density at $r = 0$ which falls off approximately parabolically in the radial direction. The formation of the pinch is relatively well understood³⁹ and has been extensively diagnosed.³¹ The focus plasma is especially well suited for laser interactions studies, because of its high kinetic energy density. The ratio of the imposed laser energy density to the kinetic energy density of the focus is small, so the laser is unlikely to modify significantly such plasma properties at the temperature and density profiles.

A CO_2 laser is used as the pump, since its frequency is well-matched to the peak density at maximum compression of the pinch. Observations show that during the pinch phase of the experiment, when the peak plasma frequency exceeds the laser frequency, the laser energy is almost totally absorbed by the plasma. This is ~~consistent~~^{comcident} with the appearance of the decay and other instabilities for this situation.

The geometry for the scattering experiment is shown in Figure 4.1. A ruby laser is used as a probe to scatter from enhanced intensity levels of Langmuir waves. The CO_2 pump and the ruby laser beams are coaxial and arranged so that the Langmuir waves orthogonal to the density gradient and the axial current j will be most strongly pumped. After the ruby light is scattered an azimuthal mask selects those wave vectors which are parallel to the electric field of the CO_2 laser, and the scattering geometry, i.e., the location of the detector, determines the wavenumber of the probed Langmuir waves.

The results of the scattering experiment are as follows. During the pinch phase, when the plasma is still underdense, no enhanced scattering is observed. This is consistent with the theory of Chapter 7, since the decay instability has not yet appeared, and enhanced Langmuir intensity levels would not be expected. During the next phase, the plasma has peak plasma frequency larger than the CO_2 frequency, and enhanced scattering is observed, up to a

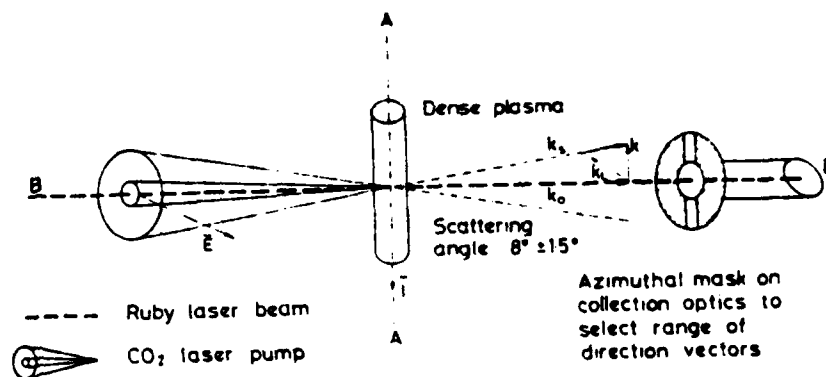


FIGURE 4.1 Schematic diagram of the dense plasma focus scattering experiment.

factor of thirty times the expected thermal level. This occurs for a density scale length of $L = 0.20 \pm 0.05$ cm^{and} is also qualitatively predicted by the theory of Chapter 7. The experimental points for this phase of the pinch are depicted in Figure 9.4. In the last phase of the pinch the plasma is still overdense, but the density scale length has decreased to about 0.025 cm. This is peak compression, and no enhanced scattering is observed. This is also consistent with Chapter 7, as a scale length as small as $L \approx 0.025$ cm will cause rapid convective saturation, so Langmuir levels do not build high enough for enhanced scattering to occur.

In conclusion, the results of the scattering experiment are qualitatively in agreement with theory. They are not expected to be in quantitative agreement, because the CO₂ intensity levels are in a nonlinear regime.

CHAPTER 5

LANGMUIR RAY PATHS IN THE INHOMOGENEOUS PLASMA

This chapter deals with the calculation of the Langmuir wave ray paths which are needed for the integration of the kinetic equation in Chapters 6 and 7. In these cases the magnetic field is unimportant and is, therefore ignored ~~here~~. The ray paths in the ionosphere case, for which the magnetic field plays a major role, are dealt with in Chapter 3. Also ignored here is the effect of WKB breakdown near the ray's turning point. WKB effects are considered in Chapter 9.

In Chapter 5 the form of the ray paths required is simple $\underline{x}(k)$. This is derived trivially by substituting the density profile into the Langmuir wave dispersion relation. It is also very easy to derive this same equation in parametric form, with time as the parameter. This form is of more use in the one dimensional calculation of Chapter 6.

The two equations needed here are the dispersion relation,

$$\omega_L^2 = \omega_p^2(x) + 3v_e^2 k^2 \quad (5-1)$$

and the density profile,

$$\omega_p^2(x) = \omega_0^2 \left(1 - \frac{x}{L}\right) \quad (5-2)$$

Where

$$\omega_p^2(x) = \frac{4\pi e^2}{m_e} n(x) \quad = \text{plasma frequency}$$

$$v_e = \sqrt{\frac{k_B T_e}{m_e}} \quad = \text{electron thermal velocity}$$

$$L \quad = \text{density scale length}$$

ω_0 = parameter corresponding here to the frequency of the pump wave.

The model here is a semi-infinite plane stratified plasma. The point $x = 0$ corresponds to the reflection point of the pump wave.

It is important to realize ~~here~~ that the ray paths are one-dimensional in the sense that $\underline{k} \neq \underline{k}(y, z)$ and $\dot{y} = \dot{z} = \text{constant}$. In the one-dimensional calculations of Chapter 6 it is permissible to deal only with \underline{k}_x and x . The two dimensions of Chapter 7 require the consideration of a nonvanishing k_y also, where y is the direction of the pump electric field. Along a ray path k_y is a constant as is any \underline{k} component perpendicular to

the density gradient. The Langmuir frequency ω_L , is also conserved along a ray path.

Substituting (5-2) into (5-1) trivially gives $x(k)$,

$$x(k) = L \left[\frac{1}{\omega_0^2} (3v_e^2 k^2 - \omega_L^2) + 1 \right]. \quad (5-3)$$

To find $x(t)$ and $k_x(t)$ it is necessary to calculate the group velocity, $v_g = \partial \omega_L / \partial k$, from (5-1),

$$v_g = \frac{3v_e^2}{\omega_L} k \quad (5-4)$$

Hence,

$$\begin{aligned} \frac{dx}{dt} &= \frac{3v_e^2}{\omega_L} k_x \\ \frac{dy}{dt} &= \frac{3v_e^2}{\omega_L} k_y \end{aligned} \quad (5-5)$$

The second of equations (5-5) is unimportant as it simply states that the wave moves uniformly in time in the y direction. Inverting (5-3) to find $k_x(x)$ and substituting into the first of (5-5) produces a differential equation for x:

$$k_x(x) = \left\{ \frac{1}{3v_e^2} \left[\omega_L^2 - \omega_0^2 \left(1 - \frac{x}{L} \right) \right] - k_{\perp}^2 \right\}^{1/2} \quad (5-6)$$

$$\frac{d}{dt} \left(\frac{x}{L} \right) = \frac{3v_e^2}{L\omega_L} \left\{ \frac{1}{3v_e^2} \left[\omega_L^2 - \omega_0^2 \left(1 - \frac{x}{L} \right) \right] - k_{\perp}^2 \right\}^{1/2} \quad (5-7)$$

$$k_{\perp}^2 \equiv k_y^2 + k_z^2.$$

Equation (5-7) can be integrated along with the boundary condition that $t = 0$ at the turning point of a given ray ($k_x = 0$) to give,

$$\frac{x}{L}(+) = \frac{3v_e^2}{4L^2} \frac{\omega_o^2}{\omega_L^2} t^2 + \frac{3v_e^2 k_{\perp}^2}{\omega_o^2} + 1 - \frac{\omega_L^2}{\omega_o^2} \quad (5-8)$$

Examples of these ray paths in x-y space are shown in Figure 5.1.

To find $k_x(t)$ substitute (5-8) into (5-6),

$$k_x(t) = \frac{\omega_o^2}{2L\omega_L} t \quad (5-9)$$

In this equation $t < 0$ refers to wavevectors with x component parallel to the density gradient and $t > 0$ to those with x component antiparallel.

By setting $t = 0$ in equation (5-8) x_T is found, where x_T represents the turning point of the Langmuir ray. This quantity is of interest because it is also the closest approach of the ray to the reflection point of the pump wave,

$$\frac{x_T}{L} = \frac{3v_e^2 k_{\perp}^2}{\omega_o^2} + 1 - \frac{\omega_L^2}{\omega_o^2} \quad (5-10)$$

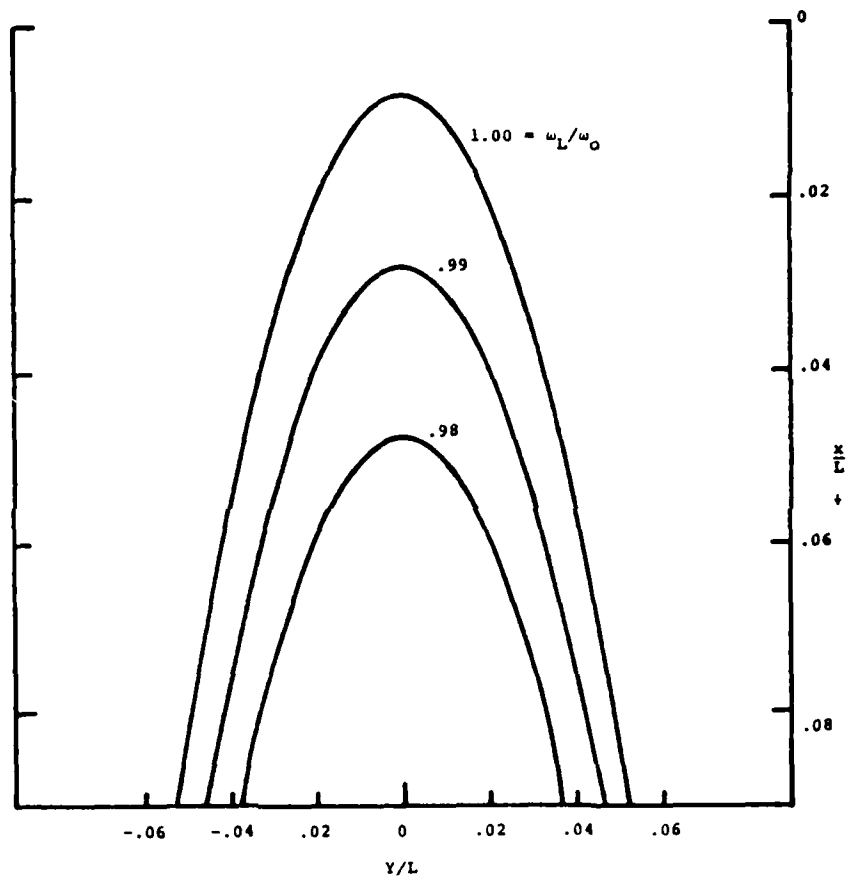


FIGURE 5.1 Langmuir ray paths assuming rectilinear geometry.

Since the form of the pump's intensity is really an Airy function rather than the uniform approximation used in Chapter 7, it is necessary that x_T not be too large. Langmuir waves which have values of ω_L/ω_0 which are too small will reflect before reaching the region where the Airy function is large. This is also true for waves with large k_\perp , but in this analysis k_\perp is fixed by scattering considerations (Chapter 4), and is therefore unimportant to this discussion. The first peak of the Airy function occurs at $x/L \approx (c/\omega_0 L)^{2/3}$, and Langmuir waves with x_T/L much larger than this will grow more slowly, because they sample regions of the Airy function where the pump is less intense. This is marginally the case for the k_\perp probed in the dense plasma focus scattering experiment discussed in Chapter 4.

Two other easily calculable quantities are t_e and k_{xe} , the time and x component of k at which the ray leaves the plasma. This occurs for $x/L = 1$,

$$t_e = 2L \frac{\omega_L}{\omega_0^2} \left(\frac{\omega_L^2}{3v_e^2} - k_\perp^2 \right)^{1/2}$$

$$k_{xe} = \left(\frac{\omega_L^2}{3v_e^2} - k_\perp^2 \right)^{1/2} \quad (5-11)$$

The slab geometry used in the above calculations is really an approximation to the actual cylindrical

geometry in the dense plasma focus device, ~~discussed in Chapter~~. It is also possible to derive the Langmuir ray paths in the cylindrical geometry, assuming a density which is linear in the radial direction,

$$\omega_p^2(r) = \omega_0^2 \left[1 - \frac{(r-r_0)}{L} \right] \quad (5-12)$$

Now r_0 becomes the point at which the plasma frequency is equal to the pump frequency. It cannot be called the reflection point of the pump wave except for rays which are normally incident on the plasma.

The equations of motion are still found from (5-4), and in cylindrical coordinates become,

$$\begin{aligned} \frac{dr}{dt} &= \frac{3v_e^2}{\omega_L} k_r \\ r \frac{d\phi}{dt} &= \frac{3v_e^2}{\omega_L} k_\phi \end{aligned} \quad (5-13)$$

Here k_ϕ is a conserved quantity along a ray path along with ω_L . The z direction is again unimportant as in the slab case, so only $r(\phi)$ will be derived.

Equations (5-13) can be combined to yield a differential equation for r in terms of ϕ ,

$$\frac{1}{r} \frac{dr}{d\phi} = k_r / k_\phi \quad (5-14)$$

From the dispersion relation,

$$k_r/k_\phi = \left\{ \frac{1}{3v_e^2 k_\phi^2} \left[\omega_L^2 - \omega_o^2 \left(1 + \frac{r_o}{L} - \frac{r}{L} \right) \right] - 1 \right\}^{1/2} \quad (5-15)$$

Eq (5-14) and (5-15) are easily solved along with the boundary condition that $\phi = \phi_o$ when $k_r = 0$ give,

$$\frac{r}{L} = A_o^2 \sec^2 \left[\frac{\omega_o A_o}{2\sqrt{3}v_e k_\phi} (\phi - \phi_o) \right]. \quad (5-16)$$

$$A_o \equiv \left(1 + \frac{r_o}{L} + \frac{3v_e^2 k_\phi^2}{\omega_o^2} - \frac{\omega_L^2}{\omega_o^2} \right)^{1/2}$$

It is clear simply from the boundary condition that for a given Langmuir wave minimum r occurs at the turning point where $k_r = 0$,

$$r_{T/L} = A_o^2 = 1 + \frac{r_o}{L} + \frac{3v_e^2 k_\phi^2}{\omega_o^2} - \frac{\omega_L^2}{\omega_o^2} \quad (5-17)$$

Figure 5.2 shows several Langmuir ray paths in the cylindrical geometry.

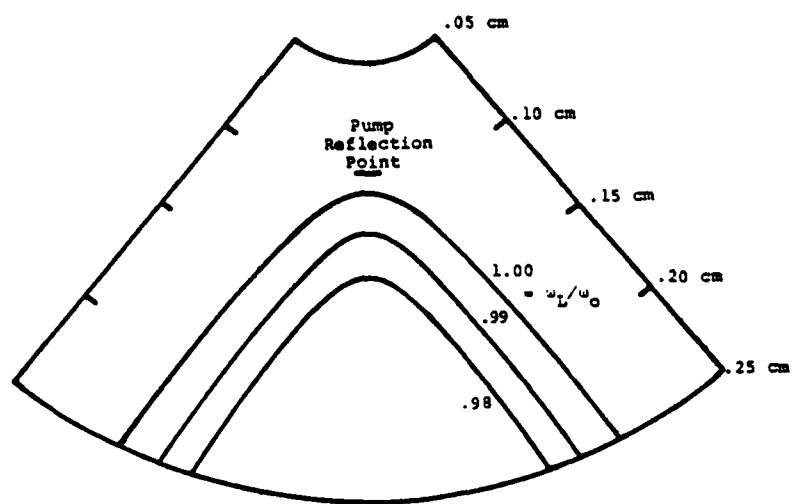


FIGURE 5.2 Langmuir ray paths assuming cylindrical symmetry.

CHAPTER 6

SOLUTION OF THE KINETIC EQUATION IN ONE DIMENSION

The integration of the kinetic equation in one dimension is the natural first step toward finding solutions both in higher dimensional and nonlinear cases. In the model considered here only wavevectors parallel or antiparallel to the density gradient are allowed. Clearly, the electric field vector of the pump wave must also be oriented along the density gradient. This allows only an electrostatic pump in any realistic model. The following additional assumptions are made in the model:

a) linear density gradient,

$$\omega_p^2(x) = \omega_0^2 \left(1 - \frac{x}{L}\right), \quad (6-1)$$

L - density scale length, ω_0 - pump frequency.

b) $T_e = T_i$,

c) uniform pump intensity (no variation with x),

d) only collisional damping considered,

e) spontaneous and "beat" emission allowed.

The only major approximation made here is (c), since

the real form of the pump intensity should be an Airy function, as is incorporated in the solution of the ionosphere case in Chapter 3. Assumption (c) is made to make the problem tractable analytically, and it is hoped that the uniform intensity represents in some sense an average to the Airy function. Assumption (d) is reasonable as long as the solution to be derived is not considered valid in regions where $k_x/k_{De} \gtrsim 1$ for which Landau damping becomes significant.

The kinetic equation for the model described above is formally identical to that solved in Chapter 3,

$$\left(\frac{\partial}{\partial t} + v_{gx} \frac{\partial}{\partial x} - \frac{\partial \omega_L}{\partial x} \frac{\partial}{\partial k_x} \right) I_k + 2\gamma I_k = 2S_k \quad (6-2)$$

Here, as in Chapter 3, I_k represents the field correlation function, γ the net damping, and S_k the sources. v_{gx} is the group velocity of the Langmuir waves in the x direction. In exactly the same fashion as in Chapter 3, S_k may be reduced to,

$$\frac{2S_k}{4\pi\Theta} = 2\gamma_D + 2 \frac{\omega_L}{\omega_0 - \omega_L} \gamma_g, \quad \Theta \equiv k_B T_e \quad (6-3)$$

γ_D represents the total damping rate and γ_g the parametric growth rate. The first term of equation (6-3) is Bremsstrahlung and the second "beat" emission.

The integration of equation (6-2) is to be done in steady state along the ray path of a Langmuir wave. Thus, ω_L is a constant and $\partial I_K / \partial t = 0$ in (6-2). It is convenient to use time as a parameter even though the solution is steady state. As used here t simply refers to a point on the ray path rather than an actual time. $x(t)$ and $k_x(t)$ are derived in Chapter 5 as equations (5-8) and (5-9). These transform (6-2) to,

$$\frac{dI}{dt} + 2(\gamma_D - \gamma_g)I = 2\gamma_D + 2\frac{\omega_L}{\omega_0 - \omega_L}\gamma_g, \quad I \equiv \frac{I_K}{4\pi\Theta} \quad (6-4)$$

I is now the intensity normalized to the equilibrium intensity. The damping and growth rates are,

$$\gamma_D = \nu_c, \quad (6-5)$$

only collisional damping, and

$$\gamma_g = P \nu_c f(\xi). \quad (6-6)$$

$P = E_0^2 / E_{\text{threshold}}^2$ is a measure of the pump intensity above the threshold intensity. $f(\xi)$ is an approximation to the mismatch function which saturates the instability as the Langmuir wave convects out of the growth region. Formally,

$$f(\xi) = \xi e^{-\xi^2/2}, \quad \xi \equiv \frac{\omega_0 - \omega_L}{|K|C_s} = \frac{\omega_0 - \omega_L}{2\alpha v_e |K|} \quad (6-7)$$

where $\alpha \equiv \sqrt{m_e/m_i}$. The complete mismatch function^{#40} and $f(\xi)$ are plotted against each other in Figure 6.1. In terms of t , ξ may be written,

$$\xi = \frac{\omega_0 - \omega_L}{2\alpha v_e} \frac{2L\omega_L}{\omega_0^2 |1|} = \frac{\beta}{|1|}, \quad \beta \equiv \frac{L\omega_L(\omega_0 - \omega_L)}{\alpha v_e \omega_0^2} \quad (6-8)$$

(-4) now becomes

$$\frac{dJ}{dt} + 2v_e \left(1 - 2P \frac{\beta}{|1|} e^{-\beta^2/2t^2} \right) J = 2v_e \left(1 + \frac{\omega_L}{\omega_0 - \omega_L} \right) \quad (6-9)$$

$$+ 2P \frac{\beta}{|1|} e^{-\beta^2/2t^2}$$

The validity of this equation is subject to the same constraints on P as were mentioned in connection with the magnetic field case in Chapter 3.

Formally, the solution (6-9) is,

$$J(t) = e^{A(t)} \left[J(t_0) + \int_{t_0}^t dt'' 2v_e \left(\frac{2P\omega_L}{\omega_0 - \omega_L} \frac{\beta}{|1|} e^{-\beta^2/2t''^2} + 1 \right) e^{-A(t'')} \right] \quad (6-10)$$

The integration is begun at some $t_0 < 0$ for which J is in equilibrium, ^{or} $J(t_0) = 1$,

$$A(t) \equiv \int_{t_0}^t dt' 2v_e \left(2P \frac{\beta}{|1|} e^{-\beta^2/2t'^2} - 1 \right) \quad (6-11)$$

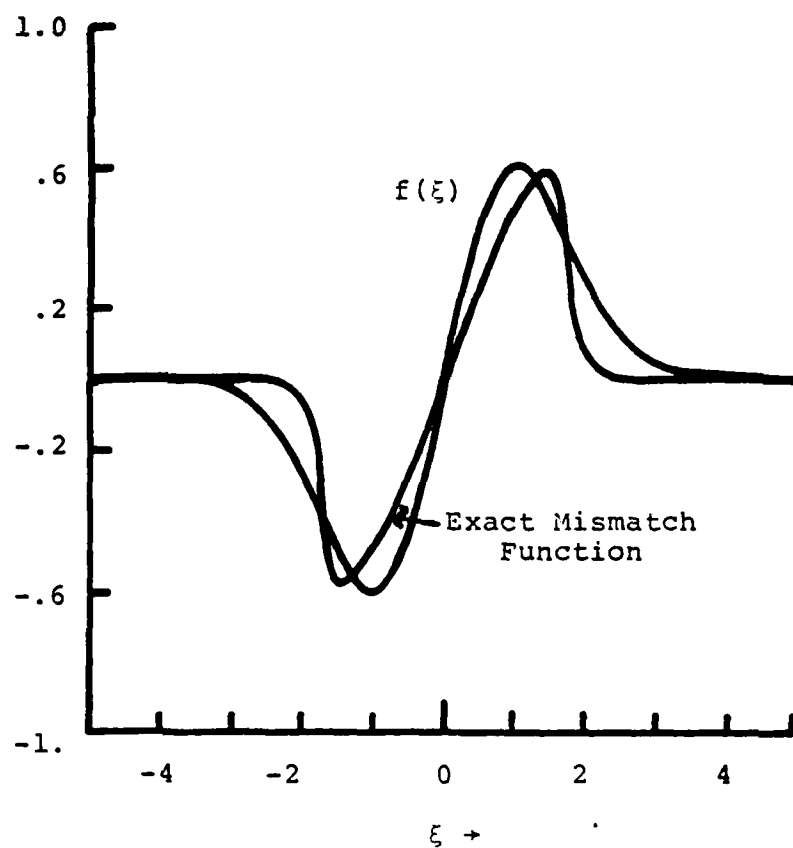


FIGURE 6.1 The exact mismatch function plotted against the approximation used in the text.

The rest of this chapter is devoted to the evaluation of the right side of Eq. (6-10).

Because of the presence of the absolute value of t in Equations (6-10) and (6-11), it is necessary to deal with the two cases $t < 0$ and $t > 0$. Let $A_-(t)$, $I_-(t)$ designate $A(t < 0)$ and $I(t < 0)$. In the same manner define $A_+(t)$ and $I_+(t)$ for $A(t > 0)$ and $I(t > 0)$.

The evaluation of (6-11) can be done exactly, so this equation will be dealt with first.

Case i) $t < 0$:

$$A_-(t) = -\frac{4}{\pi} v_c P \int_{t_0}^+ \frac{\beta}{t'} e^{-\beta^2/2t'^2} dt' - 2v_c \int_{t_0}^+ dt' \quad (6-12)$$

The first integral is solved with the substitution

$$u = e^{-\beta^2/2t'^2}$$

$$A_-(t) = 2v_c(t_0 - t) + 2\beta v_c \left[\text{li}(e^{-\beta^2/2t^2}) - \text{li}(e^{-\beta^2/2t_0^2}) \right] \quad (6-13)$$

where $\text{li}(x) \equiv \int_0^x \frac{du}{\ln u}$ is the tabulated logarithm integral function.

Case ii) $t > 0$:

$$A_+(t) = -\frac{4}{\pi} v_c P \int_{t_0}^0 \frac{\beta}{t'} e^{-\beta^2/2t'^2} dt' + \frac{4}{\pi} v_c P \int_0^+ \frac{\beta}{t'} e^{-\beta^2/2t'^2} dt' - 2v_c \int_{t_0}^+ dt' \quad (6-14)$$

The same substitution as in case (i) solves the

integrals,

$$A_+(t) = 2\nu_c(t_0 - t) - 2P\beta\nu_c \left[\text{li}(e^{-\beta^2/2t^2}) + \text{li}(e^{-\beta^2/2t_0^2}) \right] \quad (6-15)$$

Hence,

$$A_+(t) = A_-(t) - \frac{4}{2} P\beta\nu_c \text{li}(e^{-\beta^2/2t^2}) \quad (6-16)$$

The evaluation of (6-10) must also be done in the two cases $t < 0$ and $t > 0$. $t < 0$ is the simpler.

Case i) $t < 0$: Designate the integral in (6-10) by $B_-(t)$,

$$B_-(t) = -2\nu_c \int_{t_0}^T \left(\frac{2P\omega_c}{\omega_0 - \omega_c} \frac{\beta}{t'} e^{-\beta^2/2t'^2} + 1 \right) e^{-A_-(t')} dt' \quad (6-17)$$

Clearly B_- is too complicated to evaluate exactly, so saddle point methods will be used. The normal procedure would be to expand A_- in a Taylor series to second order in t' . $t' = t_m$ would then be found to maximize $e^{-A_-(t')}$. Then, assuming the other factor in the integral to be relatively uniform over the range where $e^{-A_-(t')}$ is significant, that factor would be evaluated at $t' = t_m$ and removed from the integral.

The remaining integral would then be that of a simple Gaussian.

This procedure is inconvenient in the present case, as the maximization of $e^{-A_-(t)}$ necessitates the solution of a transcendental equation. The alternative procedure used here is to assume that the first factor in the integrand is a strongly peaked function in t' and that $e^{-A_-(t)}$ is relatively uniform near that factor's maximum. To this end equation (6-17) is written,

$$B_-(t) = 2\nu_c \int_{t_0}^+ \exp \left[\ln \left(-\frac{2P\omega_c}{\omega_0 - \omega_c} \frac{\beta}{t'} e^{-\beta^2/2t'^2} + 1 \right) \right] e^{-A_-(t')} dt' \quad (6-18)$$

Now define $h(t')$,

$$h(t') \equiv \ln \left(-\frac{2P\omega_c}{\omega_0 - \omega_c} \frac{\beta}{t'} e^{-\beta^2/2t'^2} + 1 \right) \quad (6-19)$$

$h(t')$ is to be expanded to second order in a Taylor series about a point $t' = t_m$ for which $h'(t_m) = 0$. Differentiating (6-19) and setting $h'(t') = 0$ to find t_m leads to $t_m = \pm\beta$. Clearly in this case, $t < 0$, $+\beta$ must be thrown out to leave $t_m = -\beta$. $h(t')$ can be written,

$$h'(t') = \frac{1}{t'^3} (t'^2 - \beta^2) [e^{-h(t')} - 1]$$

The second derivative of $h(t')$ is also needed. When this is taken and evaluated at $t' = -\beta$,

$$h''(-\beta) = \frac{2}{\beta^2} [e^{-h(-\beta)} - 1]$$

$$h''(-\beta) = \frac{2}{\beta^2} \left[\left(\frac{P\omega_L}{\omega_0 - \omega_L} e^{-1/2} + 1 \right)^{-1} - 1 \right] \quad (b-20)$$

Clearly, $h''(-\beta) < 0$ so that $t' = -\beta$ gives a maximum for h as needed.

$B_-(t)$ is now,

$$B_-(t) \approx 2\nu_c \int_{t_0}^+ e^{-h(-\beta)} e^{\frac{1}{2}(t'+\beta)^2 h''(-\beta)} e^{-A_-(t')} dt' \quad (b-21)$$

Evaluating $A_-(t')$ at $t' = -\beta$ and removing it from the integral,

$$B_-(t) \approx 2\nu_c e^{h(-\beta)} e^{-A_-(-\beta)} \int_{t_0}^+ e^{\frac{1}{2}(t'+\beta)^2 h''(-\beta)} dt' \quad (b-22)$$

The normal procedure at this point for a saddle point integration is to assume that the remaining integration is over the entire Gaussian which comprises the integrand. It is somewhat more accurate to introduce error functions. When this is done (b-22) becomes,

$$B_-(t) \approx v_c e^{-A_-(-\beta) \sqrt{-\frac{2\pi}{k''(-\beta)}} \left(\frac{2P\omega_L}{\omega_0 - \omega_L} e^{-\frac{1}{2}k''(-\beta)} \right)} \\ \times \left\{ \operatorname{erf} \left[\sqrt{-\frac{1}{2}k''(-\beta)} (t + \beta) \right] - \operatorname{erf} \left[\sqrt{-\frac{1}{2}k''(-\beta)} x(t_0 + \beta) \right] \right\} \quad (6-23)$$

where $\operatorname{erf}(x) \equiv \frac{2}{\sqrt{\pi}} \int_0^x e^{-u^2} du$

Now $I_-(t)$ may be formally written,

$$I_-(t) \approx e^{A_-(t)} [1 + B_-(t)] \quad (6-24)$$

The evaluation of (6-10) for the case $t > 0$ is very similar to the preceding analysis. Only the highlights of this derivation are presented here.

Case ii) $t > 0$:

$$B_+(t) = 2v_c \int_{t_0}^0 \exp \left[\ln \left(-\frac{2P\omega_L}{\omega_0 - \omega_L} \frac{\beta}{t'} e^{-\beta^2/2t'^2} + 1 \right) \right] e^{-A_-(t')} dt' \\ + 2v_c \int_0^t \exp \left[\ln \left(\frac{2P\omega_L}{\omega_0 - \omega_L} \frac{\beta}{t'} e^{-\beta^2/2t'^2} + 1 \right) \right] e^{-A_+(t')} dt' \quad (6-25)$$

The first integral in (6-25) is identical to that done previously as (6-18) with $t = 0$. The second is done in an analogous manner by expanding the function $g(t')$ about its maximum at $t' = +\beta$, where,

$$g(t') \equiv \ln \left(\frac{2P\omega_L}{\omega_0 - \omega_L} \frac{\beta}{t'} e^{-\beta^2/2t'^2} + 1 \right) \quad (6-26)$$

A summary of the full solution concludes this

chapter.

Summary

i) $t < 0$: $I_-(t) \approx e^{A_-(t)} [1 + B_-(t)]$

$$B_-(t) = \nu_c e^{-A_-(-\beta)} \sqrt{-\frac{2\pi}{h''(-\beta)}} \left(\frac{2P\omega_L}{\omega_0 - \omega_L} e^{-\frac{1}{2}h_+} + 1 \right) \\ \times \left\{ \operatorname{erf} \left[\sqrt{-\frac{1}{2}h''(-\beta)} (t + \beta) \right] - \operatorname{erf} \left[\sqrt{-\frac{1}{2}h''(-\beta)} (t_0 + \beta) \right] \right\}$$

$$A_-(t) = 2\nu_c(t_0 - t) + 2P\beta\nu_c \left[\operatorname{li}(e^{-\beta^2/2t}) - \operatorname{li}(e^{-\beta^2/2t_0}) \right]$$

$$h''(-\beta) = \frac{2}{\beta^2} \left[\left(\frac{2P\omega_L}{\omega_0 - \omega_L} e^{-\frac{1}{2}h_+} + 1 \right)^{-1} - 1 \right]$$

ii) $t > 0$: $I_+(t) \approx e^{A_+(t)} [1 + B_+(t)]$

$$B_+(t) = B_-(0) + \nu_c \left(\frac{2P\omega_L}{\omega_0 - \omega_L} e^{-\frac{1}{2}h_+} + 1 \right) \sqrt{-\frac{2\pi}{g''(\beta)}} e^{-A_+(\beta)} \\ \times \left\{ \operatorname{erf} \left[\sqrt{-\frac{1}{2}g''(\beta)} (t - \beta) \right] - \operatorname{erf} \left[-\sqrt{-\frac{1}{2}g''(\beta)} \beta \right] \right\}$$

$$A_+(t) = 2\nu_c(t_0 - t) - 2P\beta\nu_c \left[\operatorname{li}(e^{-\beta^2/2t}) + \operatorname{li}(e^{-\beta^2/2t_0}) \right]$$

$$g''(\beta) = h''(-\beta)$$

CHAPTER 1

SOLUTION OF THE KINETIC EQUATION IN TWO DIMENSIONS

To model the dense plasma focus experiment in any realistic way, it is essential that two dimensions be considered. This chapter introduces a nonvanishing k_y to the solution of the kinetic equation. It also differs in several other respects from the one dimensional calculation of Chapter 6. First of all, the kinetic equation will be solved with k_x as the ray path parameter rather than t . This is simply a matter of choice, although k_x would seem to be the more natural variable in which to express the Langmuir intensities. Secondly, Landau damping is included here. Although it is not significant except for relatively large k_x , its presence presents no additional complication, so it has been added. Thirdly, saddle point methods are not used to evaluate the integral over the source term. Instead, an approximate form of the source term is used which allows the integral to be done exactly. Finally, the kinetic equation will be nondimensionalized for simplicity.

There are also several parallels to the one dimensional solution. The kinetic equation is again integrated along the Langmuir wave ray paths. In this context both ω_L and k_y are preserved along a ray path. The pump wave's intensity is again assumed to be uniform along the direction of the density gradient. This simplifies the solution of the equation, but caution must be used in applying the solution, as discussed in Chapter 5. The pump wave has its electric field polarized along \hat{y} and its \underline{k} vector is assumed to be zero once in the region of interest. Summarizing the main points of the model:

a) linear density gradient,

$$\omega_p^2(x) = \omega_0^2 \left(1 - \frac{x}{L}\right) \quad (7-1)$$

L - density scale length, ω_0 - pump frequency.

b) $T_e = T_i$,

c) uniform pump intensity,

d) pump polarized along \hat{y} ,

e) collisional and Landau damping included,

f) spontaneous and "beat" emission included, with "beat" emission assumed dominant.

The wave kinetic equation in steady state becomes, as in Chapter 6, but in vector form,

$$\left(\frac{v_g}{\partial x} - \frac{\partial \omega_L}{\partial x} \cdot \frac{\partial}{\partial k_x} \right) I_k + 2\gamma I_k = 2S_k \quad (7-2)$$

Because there are now two dimensions in the problem, more care must be exercised than before in dealing with the vector nature of the equation. In (7-2) the terms $v_{gy} \frac{\partial I_k}{\partial y}$ and $\frac{\partial \omega_L}{\partial y} \frac{\partial I_k}{\partial k_y}$ may be dropped. The first is set equal to zero, because no variation in I_k is expected in the y direction. The plasma is homogeneous in this direction, and therefore all points at a given x will be indistinguishable. The second term is zero because ω_L has no variation with y. Homogeneity in the y direction guarantees this also.

As in Chapter 6, it is again necessary to treat incoming and outgoing Langmuir waves separately. This is accomplished by splitting (7-2) into two equations for I_k^- and I_k^+ . I_k^- refers to incoming waves, or those with k_x parallel to the density gradient. I_k^+ refers to outgoing waves, which have k_x antiparallel to the density gradient. With these changes (7-2) becomes

$$\left(v_{gx} \frac{\partial}{\partial x} + \frac{\partial \omega_L}{\partial x} \frac{\partial}{\partial k_x} \right) I_k^\pm \pm 2\gamma I_k^\pm = \pm 2S_k \quad (7-3)$$

In this equation it is understood that only the magnitude of v_{gx} and $\partial \omega_L / \partial x$ are to be used, regardless

of sign. S_k is the same source term as found in Chapter 6, and now $\gamma = \gamma_D - \gamma_g$, the net damping, is $\gamma_{\text{Landau}} + \nu_c - \gamma_g$, where ν_c is collisional damping and γ_g the parametric growth rate. ν_{gx} is found from equation (5-4) to be $(3v_e^3/\omega_i)(k_x)$. $\partial\omega_L/\partial x$ is easily calculated from (7-1),

$$2\omega_L \frac{\partial\omega_L}{\partial x} = -\frac{\omega_o^2}{L}$$

$$\left| \frac{\partial\omega_L}{\partial x} \right| = \frac{\omega_o^2}{2L\omega_L}$$

As before,

$$2S_k = 4\pi\Theta \left[2\gamma_D + 2 \frac{\omega_o}{\omega_o - \omega_L} \gamma_g \right], \Theta \equiv k_B T_e \quad (7-4)$$

Substituting these quantities and normalizing I_k^\pm to the equilibrium intensity, $\mathcal{I}^\pm \equiv \frac{1}{4\pi\Theta} I_k^\pm$ (7-3) becomes

$$\left(\frac{3v_e^2}{\omega_L} k_x \frac{\partial}{\partial x} + \frac{\omega_o^2}{2L\omega_L} \frac{\partial}{\partial k_x} \right) \mathcal{I}^\pm \pm 2\gamma \mathcal{I}^\pm = \pm 2\gamma_D + 2 \frac{\omega_o}{\omega_o - \omega_L} \gamma_g \quad (7-5)$$

Nondimensionalization is carried out using the following substitutions:

$$\omega \equiv \frac{\omega_L}{\omega_o}, \quad \nu \equiv \frac{\nu_c}{\omega_o}, \quad \mu_x \equiv \frac{\nu_c}{\omega_o} k_x, \quad \mu_y \equiv \frac{\nu_c}{\omega_o} k_y$$

$$\bar{\mathcal{I}}^\pm \equiv \frac{\omega_o}{\nu_e} \mathcal{I}^\pm, \quad \chi \equiv \frac{x}{L}, \quad \mu^2 \equiv \mu_x^2 + \mu_y^2, \quad \beta \equiv \frac{\nu_c}{\omega_o L} \quad (7-6)$$

γ_g may again be written,

$$\gamma_g = 2P \nu f(\xi) \frac{n_y^2}{n^2} \quad (7-7)$$

where $f(\xi)$ is the mismatch function for equal temperatures, and $P = E_0^2 / E_{\text{threshold}}^2$ as in Chapter 6,

$$f(\xi) \approx \xi e^{-\xi/2}, \quad \xi \equiv \frac{\omega_0 - \omega_L}{|k| C_s}, \quad C_s - \text{sound speed.} \quad (7-8)$$

The factor $n_y^2 n^2$ arises from a factor $(\underline{k} \cdot \underline{E}_0)^2$ in the formal expression for γ_g , where \underline{E}_0 is the pump electric field. In nondimensional form,

$$\xi = \frac{\chi - 3n^2}{4\alpha n}, \quad \alpha \equiv \sqrt{m_e/m_i}. \quad (7-9)$$

Equation (7-9) makes use of the approximation

$3v_e^2 k^2 - \omega_0^2 \frac{\chi}{L} \ll \omega_0^2$. Also note that along a Langmuir ray path $\chi - 3n^2$ is invariant, since it is essentially $\omega_0 - \omega_L$. This quantity will be denoted by C ; $C \equiv \chi - 3n^2$.

Equation (7-5) is now, in compact form,

$$\beta \left(6n_x \frac{\partial}{\partial \chi} + \frac{\partial}{\partial n_x} \right) \bar{J}^{\pm} \pm 2\bar{\gamma} \bar{J}_e^{\pm} = \pm 2\bar{S} \quad (7-10)$$

where $\bar{\gamma}$ and \bar{S} , of course, denote the nondimensional forms of these quantities.

To integrate along a ray path it is only necessary to notice that since $C = \chi - 3n^2 = \chi - 3(n_x^2 + n_y^2)$ is a constant for a given path, the operator $6n_x (\partial/\partial n_x)|_{n_x} + (\partial/\partial n_x)|_{\chi}$ becomes $(\partial/\partial n_x)|_C$.

$$6n_x \frac{\partial}{\partial \chi} |_{n_x} = 6n_x \left(\frac{\partial n_x}{\partial \chi} |_{n_x} \frac{\partial}{\partial n_x} |_C + \frac{\partial C}{\partial \chi} |_{n_x} \frac{\partial}{\partial C} |_{n_x} \right) \quad (7-11)$$

$$= 6n_x \frac{\partial}{\partial C} |_{n_x}$$

$$\frac{\partial}{\partial n_x} |_{\chi} = \frac{\partial C}{\partial n_x} |_{\chi} \frac{\partial}{\partial C} |_{n_x} + \frac{\partial n_x}{\partial n_x} |_{\chi} \frac{\partial}{\partial n_x} |_C \quad (7-12)$$

$$= -6n_x \frac{\partial}{\partial C} |_{n_x} + \frac{\partial}{\partial n_x} |_C$$

Hence,

$$6n_x \frac{\partial}{\partial \chi} |_{n_x} + \frac{\partial}{\partial n_x} |_{\chi} = \frac{\partial}{\partial n_x} |_C \quad (7-13)$$

Equation (7-10) becomes,

$$\frac{\partial \bar{J}^{\pm}}{\partial n_x} |_C = \frac{1}{\beta} \left[\mp 2\bar{\gamma} \bar{J}^{\pm} \pm 2\bar{S} \right] \quad (7-14)$$

This pair of equations for \bar{J}^+ and \bar{J}^- can now be formally integrated. The \bar{J}^- equation will be dealt with first. It will be integrated from some initial n_x, n_x^i , for which $\bar{J}^-(n_x^i) = 1$ to n_x . Since \bar{J}^- has been normalized, this implies ^{the assumption} that the plasma is in

equilibrium at $n_x \stackrel{=}{\rightarrow} n_x^i$. Then,

$$\bar{I}^-(n_x) = e^{A^-(n_x)} \left[1 - \int_{n_x^i}^{n_x} \frac{2\bar{S}}{\beta} e^{-\frac{2}{\beta} \int_{n_x^i}^{n_x'} \bar{Y}(n_x'') dn_x''} dn_x' \right] \quad (7-15)$$

$$A^-(n_x) \equiv \frac{2}{\beta} \int_{n_x^i}^{n_x} \bar{Y}(n_x') dn_x' \quad (7-16)$$

The integral over \bar{S} is very complicated, but can be done exactly if the following approximation to \bar{S} is used:

$$\bar{S} = \bar{Y}_D + \frac{1}{1-\omega} \bar{Y}_g \approx \frac{1}{1-\omega} (\bar{Y}_g - \bar{Y}_D) = -\frac{1}{1-\omega} \bar{Y} \quad (7-17)$$

This assumes that the dominant contribution to the integral over \bar{S} in (7-15) comes from "beat" emission. The approximation will be good in regions where $\bar{Y}_g \gg \bar{Y}_D$, and very bad where $\bar{Y}_D > \bar{Y}_g$. Hence one would expect that the calculated intensities would be most accurate at their largest values and most inaccurate when near equilibrium. This is acceptable because the higher intensities are generally of more interest than the lower intensities, especially experimentally. Substituting the approximate \bar{S} in (7-15),

$$\bar{I}^-(n_x) = e^{A^-(n_x)} \left[1 + \int_{n_x^i}^{n_x} \frac{1}{\beta} \frac{2}{1-\omega} \bar{Y}(n_x') e^{-\frac{2}{\beta} \int_{n_x^i}^{n_x'} \bar{Y}(n_x'') dn_x''} dn_x' \right] \quad (7-17)$$

Now notice that the integrand in (7-17) has become a perfect differential,

$$\bar{J}^-(m_x) = e^{A^-(m_x)} \left[1 - \frac{1}{1-\omega} \int_{m_x'}^{m_x} \frac{d}{dm_x'} e^{-\frac{2}{\beta} \int_{m_x'}^{m_x''} \bar{Y}(m_x'') dm_x''} \right] \quad (7-18)$$

Performing the integral,

$$\bar{J}^-(m_x) = \left(1 + \frac{1}{1-\omega} \right) e^{A^-(m_x)} - \frac{1}{1-\omega} \quad (7-19)$$

In the bracketed term the 1 will be negligible compared to $1/(1-\omega)$. It is left in the bracket only to ensure that $\bar{J}^-(m_x^i) = 1$.

When integrating the equation for \bar{J}^+ the boundary condition needed is that $\bar{J}^+(m_x = 0) = \bar{J}^-(m_x = 0)$. Hence $\bar{J}^-(0)$ is recorded here for future reference:

$$\bar{J}^-(0) = \left(1 + \frac{1}{1-\omega} \right) e^{A^-(0)} - \frac{1}{1-\omega} \quad (7-20)$$

$$A^-(0) = \frac{2}{\beta} \int_{m_x'}^0 \bar{Y}(m_x') dm_x' \quad (7-21)$$

Formally, the integral for $\bar{J}^+(m_x)$ is written,

$$\bar{J}^+(m_x) = e^{-A^+(m_x)} \left[\bar{J}^-(0) - \int_0^{m_x} \frac{2}{\beta} \frac{1}{1-\omega} \bar{Y}(m_x') \right. \quad (7-22)$$

$$\left. e^{\frac{2}{\beta} \int_0^{m_x'} \bar{Y}(m_x'') dm_x''} dm_x' \right]$$

$$A^+(m_x) \equiv \frac{2}{\beta} \int_0^{m_x} \bar{Y}(m_x') dm_x' \quad (7-23)$$

Use has again been made of the approximation to \bar{S} discussed in connection with the solution for $\bar{J}^-(n_x)$. In exactly the same manner as (7-20) was obtained, the solution for $\bar{J}^+(n_x)$ can be found,

$$\bar{J}^+(n_x) = \left[\bar{J}^-(0) + \frac{1}{1-\omega} \right] e^{-A^+(n_x)} - \frac{1}{1-\omega} \quad (7-24)$$

This completes the formal solution. In practice, however, it is necessary to have explicit expressions for $A^+(n_x)$ and $A^-(n_x)$. The integrand \bar{Y} of A^\pm is,

$$\bar{Y}(n_x) = \sqrt{\frac{\pi}{q}} e^{-\frac{3}{2} \frac{1}{n^3}} e^{-\frac{1}{2} n^2} + \nu - \frac{2p\nu}{4\alpha} \frac{C n_y^2}{n^3} e^{-C^2/32 n^2} \quad (7-25)$$

The first term in this equation is, of course, the nondimensional form of the Landau damping. Notice that when integrating Y_{Landau} and Y_g over n_x the integrals are formally identical. This is the reason that the inclusion of Landau damping into the model was not a complication. The solution to these two integrals is dealt with in Appendix B in some detail. It is sufficient here to simply write down the resulting expressions for $A^\pm(n_x)$ in terms of Wilson's function, defined and analyzed in Appendix B.

$$\begin{aligned}
 A^-(n_x) = \frac{2}{\beta} \Big\{ & \nu n_x + \sqrt{\frac{\pi}{9}} e^{-3/2} \frac{n_x}{n n_y} e^{-1/2 n^2} \operatorname{Wi} \left[\frac{n_x^2}{n^2 n_y} \right] \\
 & - \frac{2PVC}{4\alpha} \frac{n_x}{n} e^{-c^2/32\alpha^2 n^2} \operatorname{Wi} \left[\frac{c^2}{16\alpha^2 n_y} \frac{n_x^2}{n^2} \right] \\
 & - \nu n_x^i - \sqrt{\frac{\pi}{9}} e^{-3/2} \frac{n_x^i}{n_y (n_x^2 + n_y^2)} e^{-1/2 (n_x^2 + n_y^2)} \operatorname{Wi} \left[\frac{1}{n_y} \frac{n_x^2}{n_x^2 + n_y^2} \right] \\
 & + \frac{2PVC}{4\alpha} \frac{n_x^i}{(n_x^2 + n_y^2)^{1/2}} e^{-c^2/32\alpha^2 (n_x^2 + n_y^2)} \operatorname{Wi} \left[\frac{c^2}{16\alpha^2 n_y} \frac{n_x^2}{n_x^2 + n_y^2} \right] \Big\} \quad (7-26)
 \end{aligned}$$

$$\begin{aligned}
 A^+(n_x) = \frac{2}{\beta} \Big\{ & \nu n_x + \sqrt{\frac{\pi}{9}} e^{-3/2} \frac{n_x}{n n_y} e^{-1/2 n^2} \operatorname{Wi} \left[\frac{n_x^2}{n^2 n_y} \right] \\
 & + \frac{2PVC}{4\alpha} \frac{n_x}{n} e^{-c^2/32\alpha^2 n^2} \operatorname{Wi} \left[\frac{c^2}{16\alpha^2 n_y} \frac{n_x^2}{n^2} \right] \Big\} \quad (7-27)
 \end{aligned}$$

$$A^-(0) = -A^+(n_x^i) \quad (7-28)$$

Summarizing the formal solution,

$$\bar{J}^-(n_x) = \left(1 + \frac{1}{1-\omega}\right) e^{+A^-(n_x)} - \frac{1}{1-\omega} \quad (7-19)$$

$$\bar{J}^+(n_x) = \left[\bar{J}^-(0) + \frac{1}{1-\omega}\right] e^{-A^+(n_x)} - \frac{1}{1-\omega} \quad (7-24)$$

$$\bar{J}^-(0) = \left(1 + \frac{1}{1-\omega}\right) e^{A^-(0)} - \frac{1}{1-\omega} \quad (7-20)$$

An example of the solution along a ray path is shown in Figure 9.1.

This chapter has dealt only with the solution to the wave kinetic equation along a ray path. It is of course possible to generate the Langmuir intensity in all of k_x - x space in a discrete way by simply varying the parameters C and η_y . It is necessary to do this to make any real application of the result to a physical situation.

CHAPTER 8

THE NONLINEAR EQUATION IN ONE DIMENSION

To completely model the data from the density plasma focus scattering experiment exhibited in Figure ^{9.4}~~4.1~~, a nonlinear theory is necessary. In that graph the point with largest CO_2 intensity clearly represents a saturation of the Landmuir spectrum which must be due to a nonlinear mechanism. Rough calculations of the pump intensity which would be expected to produce nonlinear saturation rather than convective saturation bear this out. Later in this chapter it will be shown that this point can be dealt with in a marginal sense with the use of a homogeneous, nonlinear saturation theory.

It is less clear from Figure ^{9.4}~~4.1~~, but will be shown in Chapter 9, that the three experimental points at intermediate pump intensity also require a nonlinear theory. These points are positioned at pump intensities where both convective and nonlinear terms are important in the kinetic equation. To deal with these points in detail would require a solution of the wave kinetic equation in two dimensions, including the appropriate nonlinear term.

CHAPTER 2

THE NONLINEAR EQUATION IN ONE DIMENSION

To completely model the dense plasma focus scattering experiment exhibited in Figure __, a nonlinear theory is necessary. In that graph the point with largest ω_p intensity clearly represents a saturation of the Langmuir spectrum which must be due to a nonlinear mechanism. Rough calculations of the pump intensity which would be expected to produce nonlinear saturation rather than convective saturation bear this out. Of course, to deal with this point in detail would require a solution of the wave kinetic equation in two dimensions, including the appropriate

nonlinear term. This section addresses the more modest task of formulating the problem in one dimension. Even so, the wave kinetic equation becomes a nonlinear integro-differential equation, the solution of which is decidedly nontrivial. However, it is possible, through the use of saddle point integration techniques, to reduce the equation to a partial differential equation. This reduction essentially introduces the

derivative approximation,^{B41-43} which masks any fine structure that may be present in the Langmuir spectrum. But the more important quantity for the present purpose, the total energy in the spectrum, is still expected to be accurate.

As will be shown later, the resulting set of two nonlinear coupled partial differential equations still presents great difficulties, largely because of uncertainty in the boundary conditions. The boundary conditions are well-posed for application to an analytic solution. However, in the absence of a suitable analytic solution, an inefficient iterative numerical approach to the solution is the best available method. It is very possible that this method can be improved, but any such improvement is beyond the scope of this work.

The dominant nonlinearity in the equal temperature plasma for pump powers which do not greatly exceed threshold is nonlinear Landau damping.^{B44-46} The saturation process is physically very simple. The pump wave produces a daughter wave at lower frequency via a three-wave decay. This daughter wave then may grow to sufficient intensity to act as a pump itself and produce another daughter wave at a still lower frequency. This cascade to lower frequencies will

occur until the dissipation from the normal damping of all the daughter waves matches the energy input of the original pump. Essentially then, nonlinear Landau damping saturates the instability by increasing the number of waves for which dissipation can occur. It is clear now why the intensity of the pump cannot be too large. No daughter wave can have frequency below the plasma frequency, so if the increased dissipation caused by a cascade from ω_0 to ω_p is insufficient to saturate the instability, other nonlinear saturation mechanisms must be considered.

Nonlinear Landau damping enters into the wave kinetic equation as an integral over the entire spectrum of Langmuir intensities. It is easy to see qualitatively why this occurs. At any point in the inhomogeneous plasma a spectrum of Langmuir wave intensities will exist. Any given wave, characterized by \underline{k} and $\omega_L(x, |\underline{k}|)$, will tend to be destabilized by all those waves with larger ω_L and stabilized by all those with smaller ω_L . Hence the net effect can be described by an integral over I_k , where the integrand also includes a weighting factor to pick out the most strongly coupled waves.

The one-dimensional steady state wave kinetic equation including the nonlinear Landau damping term is

written,

$$\left(\frac{\partial}{\partial x} \cdot \frac{\partial}{\partial \underline{k}} - \frac{\partial \omega_L}{\partial \underline{k}} \cdot \frac{\partial}{\partial \underline{k}} \right) I_{\underline{k}} = \left[\frac{1}{4} \omega_p \frac{E_0^2}{4\pi n_0} f(\underline{k}) - 2\nu_c \right. \\ \left. - \omega_0 \int I_{\underline{k}'} \bar{f}(\underline{k}, \underline{k}') d\underline{k}' \right] I_{\underline{k}} \quad (8-1)$$

In this equation $f(\underline{k})$ represents the coupling to the constant amplitude pump wave, and $\bar{f}(\underline{k}, \underline{k}')$ the coupling between waves in the Langmuir spectrum. \bar{f} is then the weighting factor spoken of earlier,

$$f(\underline{k}) = \xi e^{-\xi^2/2}, \quad \xi \equiv \frac{\omega_0 - \omega_L}{2\alpha \nu_c |\underline{k}|}, \quad \alpha \equiv \sqrt{\frac{m_e}{m_i}} \\ \bar{f}(\underline{k}, \underline{k}') = \bar{\xi} e^{-\bar{\xi}^2/2}, \quad \bar{\xi} \equiv \frac{\omega_L - \omega_{L'}}{2\alpha \nu_c |\underline{k} - \underline{k}'|} \quad (8-2)$$

Two points should be noted about equation (8-1). First, vector notation has been retained in the operator on the left side. This does not indicate the presence of more than one dimension, but only the fact that \underline{k} can be oriented either parallel or antiparallel to the density gradient. Secondly, the source term in (8-1) has been dropped. This was done simply as a matter of convenience to make the problem mathematically simpler. The justification for dropping this term is that when dealing with nonlinear steady state Langmuir intensity levels, one would expect the contribution of the source term to be negligible.

Notice also that the only linear damping mechanism retained in (8-1) is collisional damping. This is the only real dissipation in the problem, since nonlinear Landau damping only moves energy around in \underline{k} space, rather than dissipating it directly.

The factors \underline{v}_g and $\partial \omega_L / \partial \underline{x}$ are easily found from the Langmuir wave dispersion relation, $\omega_L^2 = \omega_p^2(x) + 3v_e^2 k^2$, and the expression for the density profile, $\omega_p^2(x) = \omega_0^2(1-x/L)$. Here, L is again the density scale length and ω_0 the pump wave frequency,

$$\underline{v}_g = \frac{\partial \omega_L}{\partial \underline{k}} = \frac{3v_e^2}{\omega_L} \underline{k}$$

$$\frac{\partial \omega_L}{\partial \underline{x}} = - \frac{\omega_0^2}{2\omega_L L} \hat{x} \quad (8-3)$$

Equation (8-1) now becomes,

$$\left(\frac{3v_e^2}{\omega_L} \underline{k} \cdot \frac{\partial}{\partial \underline{x}} + \frac{\omega_0^2}{2\omega_L L} \hat{x} \cdot \frac{\partial}{\partial \underline{k}} \right) I_k = \left[4P\nu_c f(\underline{k}) - 2\nu_c - \omega_0 \int I_{k'} \bar{f}(\underline{k}, \underline{k}') d\underline{k}' \right] I_k \quad (8-4)$$

$$\text{where } P \equiv \frac{E_0^2}{E_{\text{threshold}}^2} = \frac{\omega_p E_0^2}{64\pi \nu_c n \Theta}.$$

As in past chapters, it is convenient to split I_k into two functions, I_k^+ and I_k^- . I_k^- again deals with waves which have \underline{k} parallel to the density gradient and

I_k^+ those with oppositely directed \underline{k} 's. Of course, it is clear that $I_k^+ = I_{-k}^-$, where the subscript k 's now refer to absolute values.

The splitting of I_k into two functions allows the elimination of the vector notation in (8-4) at the expense of going to two coupled equations,

$$\begin{aligned} \left(-\frac{3v_e^2}{\omega_L} k \frac{1}{\partial x} - \frac{\omega_0^2}{2\omega_L} \frac{1}{\partial k} \right) I_k^- &= \left[4Pv_e f(k) - 2v_e \right. \\ &\quad \left. - \omega_0 \int_0^\infty I_{k'}^- \bar{f}(k, k') dk' - \omega_0 \int_0^\infty I_{k'}^+ \bar{f}(k, k') dk' \right] I_k^- \quad (8-5) \\ \left(\frac{3v_e^2}{\omega_L} k \frac{1}{\partial x} + \frac{\omega_0^2}{2\omega_L} \frac{1}{\partial k} \right) I_k^+ &= \left[4Pv_e f(k) - 2v_e \right. \\ &\quad \left. - \omega_0 \int_0^\infty I_{k'}^- \bar{f}(k, k') dk' - \omega_0 \int_0^\infty I_{k'}^+ \bar{f}(k, k') dk' \right] I_k^+ \end{aligned}$$

In (8-5) all k 's are now assumed to be positive. The upper limit in the integrations over $I_{k'}^\pm$ can be allowed to go to infinity rather than some finite value, because the integrand becomes negligible for $k > k_0$, where $k_0(x)$ is defined by the equation $\omega_0^2 = \omega_p^2(x) + 3v_e^2 k_0^2(x)$.

Because of the form of $\bar{f}(k, k')$ nonlinear interactions between I_k^+ and I_k^- can be ignored. The same is true for I_k^- . This can be done because \bar{f} is exponentially small unless \underline{k} and \underline{k}' are antiparallel, which will be seen more clearly later ~~when \bar{f} is explicitly~~ when \bar{f} is explicitly written out. Dropping

the costreaming terms, (8-5) becomes,

$$\left(\frac{3v_e}{\omega_L} k \frac{\partial}{\partial x} + \frac{\omega_0^2}{2\omega_L} \frac{\partial}{\partial k} \right) I_k^\pm = \pm \left[4Pv_e f - 2v_e \right. \\ \left. - \omega_0 \int_0^\infty I_{k'}^\pm f dk' \right] I_k^\pm \quad (8-6)$$

It is now possible to express ξ and $\bar{\xi}$, defined in (8-2), in a more explicit form. It is clear that in the expression for ξ , $|\underline{k}| = k$. Because only counterstreaming nonlinear interactions are of interest, in $\bar{\xi}$, $|\underline{k}-\underline{k}'| = k+k'$. Then, using the Langmuir wave dispersion relation for ω_L , ω_L' ,

$$\xi = \frac{\omega_0 - \omega_L}{2\omega_L v_e k} = \frac{\omega_0 - [\omega_0^2(1 - x/L) + 3v_e^2 k^2]^{1/2}}{2\omega_L v_e k} \approx \frac{\omega_0}{4\omega_L v_e k} \left(\frac{x}{L} - \frac{3v_e^2 k^2}{\omega_0^2} \right) \\ \bar{\xi} = \frac{\omega_L - \omega_L'}{2\omega_L v_e (k+k')} \approx \frac{3}{4} \frac{v_e}{\omega_0} \frac{(k^2 - k'^2)}{k+k'} = \frac{3v_e}{4\omega_0} (k - k') \quad (8-7)$$

Both of these equations assume $|3v_e^2 k^2 - (x/L)\omega_0^2| \ll \omega_0^2$.

From the expression for $\bar{\xi}$ it can now be seen why the costreaming interactions were ignored. In that case $|\underline{k}-\underline{k}'| = k-k'$, so $\bar{\xi} = (3v_e/4\omega_0)(k+k')$. Since \bar{f} maximizes where $\bar{\xi} = 1$, a strong costreaming interaction would need $k+k' = 4\omega_0/3v_e$ or $k/k_D + k'/k_D = 4\omega_0/3$, where $k_D = \omega_0/v_e$ is the Debye wavenumber. Hence the costreaming interaction can be effective only for very

small wavenumbers, since $k, k' > 0$. For the counterstreaming interaction, the same argument gives strong coupling for waves which satisfy $k/k_D - k'/k_D = 4\pi/3$. This equation specifies only a difference between wavenumbers rather than an upper limit on their magnitude. So the counterstreaming interaction can be effective throughout the entire k range of the Langmuir spectrum, and is therefore far more important than the costreaming interaction.

At this point it is convenient to non-dimensionalize the equations as was done in Chapter 7. As before, define,

$$\omega \equiv \frac{\omega_L}{\omega_0}, \quad \nu \equiv \frac{v_c}{\omega_0}, \quad \eta \equiv \frac{v_c}{\omega_0} k \quad (8-8)$$

$$\bar{I}^\pm = I^\pm \frac{\omega_0}{v_c}, \quad \chi = \frac{x}{L}$$

Equations (8-6) and (8-7) become,

$$\left(\frac{\partial}{\partial \chi} + \frac{1}{6\eta} \frac{\partial}{\partial \eta}\right) \bar{I}^\pm = \pm \frac{\omega}{3\beta\eta} \left[4P_\nu f(\eta) - 2\nu - \int_0^\infty \bar{I}^\mp f(\eta') d\eta' \right] \bar{I}^\pm \quad (8-9)$$

$$\bar{\zeta} = \frac{3}{4\alpha} (\eta - \eta')$$

$$\zeta = \frac{1}{4\alpha\eta} (\chi - 3\eta^2), \quad (8-10)$$

where $\beta \equiv v_e/\omega_0 L$ and the Langmuir wave dispersion relation has become $\omega^2 = 1 - \chi + 3\eta^2$.

Equations (8-9) are a set of coupled nonlinear

integro-differential equations for which the solution, or even a method of solution, is not readily apparent. It is possible to transform the integral terms by means of saddle point techniques. This method is essentially the same as the derivative approximation employed in References 41-43.

To transform the integrals it is necessary to assume that \bar{I}^{\pm} is slowly varying with η over the region where the exponential factor in \bar{f} is significant. As discussed in Reference 42, this assumption is only marginally valid in the case of a homogeneous plasma, but does give the correct energy values. Designating the integrals to be transformed by NT for nonlinear term,

$$NT = \frac{3}{4\alpha} \int_0^{\infty} \bar{I}^{\pm}(\eta') (\eta - \eta') e^{-9(\eta - \eta')^2/16\alpha^2} d\eta' \quad (9-11)$$

Recognize first that the coupling factor can be written as a derivative with respect to η , which can then be removed from the integral.

$$\begin{aligned} NT &= \frac{3}{4\alpha} \int_0^{\infty} \bar{I}^{\pm}(\eta') \left(-\frac{8\alpha^2}{9}\right) \frac{1}{\alpha} e^{-9(\eta - \eta')^2/16\alpha^2} d\eta' \\ &= -\frac{2\alpha}{3} \frac{1}{\alpha} \int_0^{\infty} \bar{I}^{\pm}(\eta') e^{-9(\eta - \eta')^2/16\alpha^2} d\eta' \quad (8-12) \end{aligned}$$

Now notice that the exponential in the integrand has a

sharp peak at $\eta' = \eta$. Evaluating \bar{I}^\pm at that point and removing it from the integral,

$$NT = -\frac{2\alpha}{3} \frac{1}{\delta\eta} \bar{I}^\pm(\eta) \int_0^\infty e^{-9(\eta-\eta')^2/16\alpha^2} d\eta'. \quad (8-13)$$

What remains is not quite a simple Gaussian integral, since it still depends on η . Letting $u = -(\eta-\eta')$,

$$NT = -\frac{2\alpha}{3} \frac{1}{\delta\eta} \bar{I}^\pm(\eta) \int_{-\eta}^\infty e^{-9u^2/16\alpha^2} du.$$

By extending the lower limit of this integral to $-\infty$ the maximum possible error made is a factor of two. Then the integral is a simple Gaussian integration. Hence,

$$NT = -\frac{4\alpha^2}{9} \sqrt{\pi} \frac{1}{\delta\eta} \bar{I}^\pm(\eta). \quad (8-14)$$

With this substitution, the coupled equations (8-9) become,

$$\left(\frac{1}{\delta\eta} + \frac{1}{6\eta} \frac{1}{\delta\eta}\right) \bar{I}^\pm = \pm \frac{\omega}{3\beta\eta} \left[4P_V f(\eta) - 2v + \frac{4\alpha^2\sqrt{\pi}}{9} \frac{1}{\delta\eta} \bar{I}^\pm \right] \bar{I}^\pm \quad (8-15)$$

The transformation from an integral to a partial derivative in the nonlinear term is a considerable simplification. Whereas previously the equations were nonlocal, depending on integrals over all η , they have

now become local, with only derivatives at a point entering.

One more step can be made by investigating the form of the equations along a ray path. Making use of the fact that ω is constant long a ray path, the dispersion relation $\omega^2 = \text{constant} = 1 - \chi + 3\eta^2$ gives,

$$\frac{\partial}{\partial \chi} \Big|_{\eta} + \frac{1}{6\eta} \frac{\partial}{\partial \eta} \Big|_{\chi} = \frac{1}{3\eta} \frac{\partial}{\partial \eta} \Big|_{\omega}. \quad (8-16)$$

Equations (8-15) become,

$$\frac{\partial \bar{I}^{\pm}}{\partial \eta} \Big|_{\omega} = \pm \frac{\omega}{\beta} \left[4\rho_{\nu} f(\eta) - 2\nu + \frac{4\sqrt{\pi}}{9} \frac{\partial \bar{I}^{\mp}}{\partial \eta} \Big|_{\chi} \right] \bar{I}^{\pm}. \quad (8-17)$$

Care must be taken to recognize that the two derivatives with respect to η are different. On the left the derivative is taken along a ray path with ω constant, and on the right it is taken at a given density with χ constant.

It is convenient at this time to point out the difficulties that remain in finding solutions to equations (8-15). Since they are still coupled nonlinear partial differential equations an analytical solution, though desirable, seems rather unlikely. Any numerical integration scheme will run into immediate problems in dealing with boundary conditions. The true

boundary condition is that \bar{I}^- is in equilibrium at large η where damping overwhelms growth. An artificial boundary condition is created by the split into two equations for \bar{I}^+ and \bar{I}^- . This condition is that $\bar{I}^+(\chi, \eta=0) = \bar{I}^-(\chi, \eta=0)$. The condition on \bar{I}^- is difficult to apply because of the absence of a source term in this model. Normally with a source term present an integration can be started at large η well away from any growth and the source term will hold up \bar{I}^- to equilibrium levels. If this were tried with the present model \bar{I}^- would damp to nearly zero before the growth region was reached. This is clearly nonphysical. So any numerical integration must be started near where the growth rate equals the damping rate in order to keep \bar{I}^- near the equilibrium level.

The boundary condition on \bar{I}^+ is nearly impossible to apply numerically in any efficient manner. Because of the coupled nature of the equations, it would be much more convenient to have a boundary condition on \bar{I}^+ of the same nature as that on \bar{I}^- . That is, one would like to know $\bar{I}^-(\chi_0, \eta) = I_{\text{equilibrium}}$ and $\bar{I}^+(\chi_0, \eta) = I_{\text{equilibrium}} + \Delta(\chi_0, \eta)$. The Δ is necessary because \bar{I}^+ will only approach equilibrium asymptotically as η increases, and the difference from equilibrium is very important in the integration. At present the best

method to numerically integrate equations (8-15) is to guess the function Δ , do the integration and test to see if the condition $\bar{I}^+(\eta=0) = \bar{I}^-(\eta=0)$ is satisfied. Since in general this condition will not be satisfied, Δ will need to be adjusted and the integration redone. Clearly this iterative method is very inefficient and a better method may be possible.

It may be argued that for large pump intensities, nonlinear saturation occurs rapidly, and therefore the convective derivatives on the left of equations (8-15) can be ignored. The rest of this section is devoted to calculating the pump intensities for which this is true.

Assuming $\bar{I}^+ = \bar{I}^-$, which is reasonable under strongly nonlinear conditions, equations (8-15) can be written as one equation:

$$\beta \left(6\eta \frac{\partial}{\partial x} + \frac{\partial}{\partial \eta} \right) \bar{I} = \omega \left[4P_v f(\eta) - 2\nu + B \frac{\partial \bar{I}}{\partial \eta} \right] \bar{I}. \quad (8-18)$$

The magnitude of B , which is simply the coefficient of the nonlinear terms in (8-15), is unimportant in this calculation as long as the nonlinearity is assumed to be fully active. That is, the details of B are unnecessary, except that it is larger than some P -dependent lower limit.

If it is now assumed that the solution is such that the convective terms in (8-18) may be ignored, what remains is essentially the nonlinear equation in a homogeneous plasma,

$$4Pvf(\eta) - 2v + B \frac{\partial \bar{I}}{\partial \eta} = 0 \quad (8-19)$$

Assuming B is independent of η , as is true in equations (8-15), the solution of (8-19) may be written,

$$\bar{I} = \frac{2v}{B} \int_{\eta_c}^{\eta} [2Pf(\eta) - 1] d\eta', \quad (8-20)$$

where η_c is the point at which $f(\eta) = 0$, so $\bar{I}(\eta_c) \approx 0$.

For this homogeneous solution to be valid, it is necessary that the convective terms be small enough to not significantly alter the balance of the terms on the right of equation (8-18). Since (8-20) shows large gradients in η , it is likely that $\beta (\partial \bar{I} / \partial \eta)$ is the dominant convective term. The magnitude of this term is found from equation (8-19),

$$\left| \beta \frac{\partial \bar{I}}{\partial \eta} \right| = \frac{2\beta v}{B} [2Pf(\eta) - 1]. \quad (8-21)$$

The homogeneous solution will not be significantly changed, therefore, if the following condition is

satisfied:

$$2\nu\omega [2Pf(\xi) - 1] \bar{I} \gg \frac{2B\nu}{B} [2Pf(\xi) - 1]$$

$$\bar{I} \gg \frac{B}{B\omega} \quad (8-22)$$

Choosing the maximum value of the homogeneous solution, \bar{I}_{peak} , for \bar{I} , (8-22) becomes,

$$\bar{I}_{peak} \gg \frac{B}{B\omega} \quad (8-23)$$

Equation (8-23) represents a "best possible case" for the homogeneous solution. All other \bar{I} 's will be smaller than \bar{I}_{peak} , and will be harder pressed to satisfy (8-22). By using \bar{I}_{peak} , however, the calculation finds the lowest P which might possibly satisfy the original condition.

Clearly \bar{I}_{peak} will be realized where $d\bar{I}/d\eta = 0$, or where $2Pf(\xi) - 1 = 0$. Therefore,

$$\bar{I}_{peak} = \frac{2\nu}{B} \int_{\eta_1}^{\eta_c} [2Pf(\xi) - 1] d\eta' \quad (8-24)$$

$$\bar{I}_{peak} = \frac{4\nu P}{B} \int_{\eta_1}^{\eta_c} f(\xi) d\eta' + \frac{2\nu}{B} (\eta_1 - \eta_c)$$

where η_1 is the point at which $2Pf(\xi) - 1 = 0$.

For sufficiently large P the range $\eta_1 \leq \eta \leq \eta_c$ contains all the significant values of f , so the

integral over η' can be approximated by,

$$\frac{4\nu P}{B} \int_{\eta_1}^{\eta_c} f(\xi) d\eta' \approx \frac{4\nu P}{B} \int_0^{\eta_c} f(\xi) d\eta' \approx \frac{4\nu P}{B} \frac{2\alpha}{3} \quad (8-25)$$

Substituting this into (8-24),

$$\bar{I}_{peak} \approx \frac{2\nu}{B} \left[\frac{4\alpha P}{3} + \eta_1 - \eta_c \right]. \quad (8-26)$$

$\eta_1 - \eta_c$ can be approximated by investigating $f(\xi)$ more closely. From (8-10),

$$f(\xi) = \xi e^{-\xi^2/2}, \quad \xi \equiv \frac{\chi - 3\eta^2}{4\alpha\eta}.$$

η_c occurs where $f(\xi) = 0$, or $\xi = 0$. Therefore,

$$\eta_c = \frac{1}{3} \sqrt{3\chi}. \quad (8-27)$$

For any other ξ ,

$$\eta = \frac{1}{3} (-2\alpha\xi + \sqrt{4\alpha^2\xi + 3\chi}) \approx \frac{1}{3} (-2\alpha\xi + \sqrt{3\chi}). \quad (8-28)$$

Hence,

$$\eta_1 - \eta_c \approx \frac{1}{3} (-2\alpha\xi_1 + \sqrt{3\chi}) - \frac{1}{3} \sqrt{3\chi} = -\frac{2}{3} \alpha \xi_1. \quad (8-29)$$

Now ξ_1 is determined by $\xi_1 \exp(-\xi_1^2/2) = 1/2P$ or

$\zeta_1 = (2 \ln 2 P \zeta_1)^{1/2}$. A single iteration of this implicit equation gives acceptable accuracy for typical P's, so ζ_1 may be written,

$$\zeta_1 \approx \sqrt{2 \ln 6 P}, \quad (8-30)$$

where $\zeta_1 = 3$ has been arbitrarily substituted under the ~~this~~ square root as a first approximation. Full iterations using typical P's show this to be a reasonable choice. Substituting (8-30) into (8-29) and then into (8-26) gives,

$$\bar{I}_{peak} \approx \frac{2V}{B} \left[\frac{4\alpha P}{3} - \frac{2}{3} \alpha \sqrt{2 \ln 6 P} \right] = \frac{8\alpha V P}{3B} \left[1 - \frac{1}{2P} \sqrt{2 \ln 6 P} \right], \quad (8-31)$$

For large P the bracketed factor is essentially unity, so,

$$\bar{I}_{peak} \approx \frac{8\alpha V P}{3B}. \quad (8-32)$$

Then the condition for validity of the homogeneous solution, inequality (8-23), becomes

$$\frac{8\alpha V P}{3B} \gg \frac{B}{B\omega}$$

$$P \gg \frac{3B}{8\alpha V \omega} = \frac{3V e \omega_0}{8\alpha V_c \omega_L L} \quad (8-33)$$

Substituting numbers appropriate to the dense plasma focus device, (8-33) requires $P \gg 13$. Since this represents a best possible case for the homogeneous solution, it is probable that this solution cannot be applied to the ^{highest intensity} ~~nonlinear~~ point in the scattering experiment mentioned earlier. However, in a medium such as the ionosphere model of Chapter 3, for which (8-33) gives $P \gg 1.5$, the homogeneous solution should be applicable in many cases.

CHAPTER 9

NUMERICAL RESULTS AND APPLICATION

All numerical examples in this section make use of parameters appropriate to the dense plasma focus experiment described in Chapter 4. These parameters are listed below:

$$\alpha = \sqrt{m_e/n_i} = 0.0165 \text{ (deuterium plasma)}$$

$$T_e \text{ (electron temperature)} = 300 \text{ eV}$$

$$k_y \text{ (wavenumber selected by scattering geometry)} \\ = 1.26 \times 10^4 \text{ cm}^{-1}$$

$$k_D \text{ (Debye wavenumber)} = 2.44 \times 10^5 \text{ cm}^{-1}$$

$$L \text{ (density scale length)} = 0.15\text{--}0.25 \text{ cm}$$

$$\omega_0 \text{ (pump frequency)} = 1.77 \times 10^{14} \text{ sec}^{-1}$$

$$n_0 \text{ (reflection density)} = 4.8 \times 10^{18} \text{ cm}^{-3}$$

$$\nu_c \text{ (collision frequency)} = 2.19 \times 10^{10} \text{ sec}^{-1}$$

$$I_{vac} \text{ (vacuum CO}_2 \text{ intensity)} = 5 \times 10^9\text{--}2.1 \times 10^{10} \text{ W cm}^{-2}.$$

These numbers correspond to the parameters measured during the pinch phase of the focus device, at a time when the decay instability should be active. This is also the time at which enhanced scattering is observed.

Equations (7-19), (7-20), and (7-24) represent the solution of the wave kinetic equation for the intensity

spectrum along a ray path. Two examples of this spectrum are given in Figure 9.1 for differing scale lengths. The Langmuir waves represented there move from negative k_x to positive k_x . They are started in equilibrium at the point k_x^i where the damping rate is twice the growth rate. The ray grows until it reaches a maximum at positive k_x where the damping rate is equal to the growth rate. From this point the intensity drops slowly due to collisional damping until $k_x/k_D \approx 0.2$ where linear ~~Langmuir~~^{Landau} damping becomes significant. This drops the intensity quickly back to the equilibrium level.

The ray path intensity spectrum is the elementary unit from which all subsequent linear results in this chapter are derived. For example, Figures 9.2a and 9.2b are contour maps of the Langmuir intensity ~~I~~^I as a function of k_x and x . These maps are simply a synthesis of many ray path spectra. This is possible because the choice of a point (k_x, x) uniquely determines the Langmuir frequency ω_L for given k_y . Hence, only one Langmuir wave can pass through the point (k_x, x) ~~as~~^{and} its intensity, calculated along a ray path, determines the intensity there.

To apply the theory of Chapter 7 to the dense plasma focus experiment some assumptions must be made. The theory uses a rectangular slab geometry and a linear density gradient. Neither of these conditions is realized exactly in the focus device. However, if one assumes that the

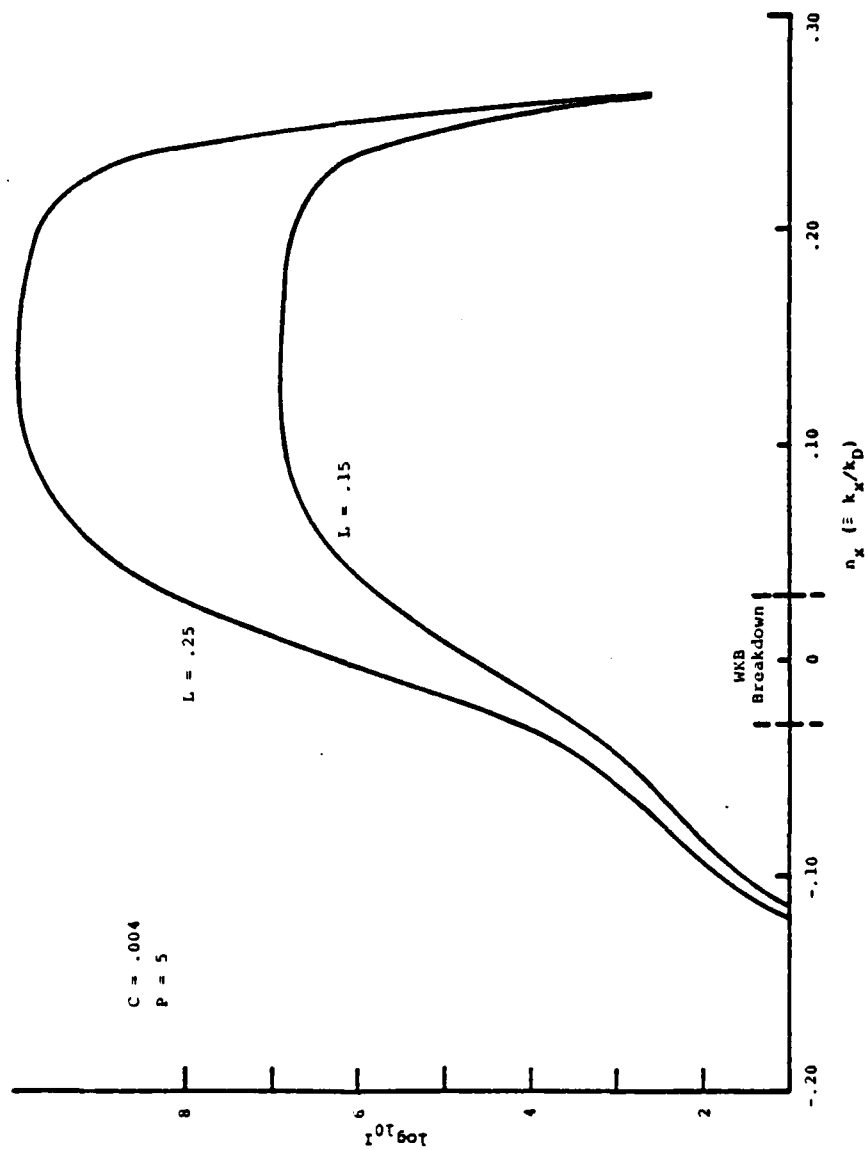


FIGURE 9.1 The intensity spectrum of a given Langmuir wave along its ray path in the dense plasma focus model of Chapter 7; for two different scale lengths.

angular width of the region of Langmuir waves being measured is small, the slab geometry will be a good approximation to the actual cylindrical geometry. Note that the important quantity is the width of the measured region, which is not necessarily the same as the total region of enhanced Langmuir waves. The measured region is in general smaller, because the scattering experiment is designed to exclude some waves.

A linear density gradient will be a good approximation to the actual gradient if the width in the radial direction is small compared to the actual scale length. Simply stated, this just means that any smooth density profile, such as parabolic or exponential, can be locally approximated by a straight line.

Another of the difficulties in applying the theory is that the pump intensity in the focus plasma is not the uniform intensity used in the theory. In fact it is not clear exactly what the pump intensity spatial variation is in the cylindrical geometry. The assumption is made here that the intensity will vary as the square of the Airy function (Figure 3.2), which would be appropriate for a slab geometry. What is needed next is to choose a uniform intensity level in some fashion so that the intensities calculated are as close as possible to the intensities which would be found from using the Airy function pump. There is no obvious way to do this. The procedure adopted here is

the following. Geometric optics determines the maximum intensity in the plasma at the peak of the Airy lobe nearest the reflection point of the pump wave. A crude average over the Airy oscillations will give an average intensity of half of ~~the~~^{this} maximum intensity. This leaves only the variation in the Airy envelope to account for. ~~This~~^{The} envelope varies as $x^{-1/2}$, and a strict spatial average over the growth region of the Langmuir waves would result in another reduction of one-third. However, in order to roughly account for the fact that the Langmuir wave spends more time near its turning point where the Airy envelope is larger, this has been arbitrarily changed to a reduction of one-fourth. The net result is that the uniform intensity chosen is three-eighths of the maximum intensity predicted by geometric optics. In terms of the focus parameters,

$$P = 8 \times 10^{-10} I_{vac} \text{ (W cm}^{-2}\text{)} , \quad (9-1)$$

where P is the ratio of pump intensity in the plasma to the local threshold intensity.

It is convenient at this point to discuss one last difficulty in applying the theory of Chapter 7 to the scattering observations. Three ranges in P exist. The first, $1 < P < P_1$, includes intensities which are linearly saturated by convection. This is the range for which the calculations of Chapter 7 apply. The second range,

$P_1 < P < P_2$, includes intensities for which both convective and nonlinear effects are important. There is no well-defined theory for this range. For $P > P_2$, the calculation at the end of Chapter 8 applies, and only the nonlinearity need be considered. The difficulty in applying the convective theory is that the experimental point with lowest CO_2 intensity has $P \approx P_1$, so it can only marginally be described by that theory. At the other end of the experimental scale, the point with highest CO_2 intensity has $P \approx P_2$, so the one-dimensional homogeneous nonlinear theory only marginally applies. The three intermediate points are roughly in the center of the undescribed region and can probably best be described by an interpolation between the other two regions.

The calculation of the scattering cross section from the known intensities uses the following equation:

$$\frac{\sigma}{r_e^2} = \frac{k_V^2}{k_D^2} n_0 V_s \delta\Omega_s \quad (9-2)$$

In this equation previously undefined quantities are the electron radius, r_e ; the scattering volume V_s ; and the solid angle subtended by the scattering optics, $\delta\Omega_s$.

Numerically $r_e^2 = 7.94 \times 10^{-26} \text{ cm}^2$ and $\delta\Omega_s = 6.83 \times 10^{-3} \text{ sr}$.

The scattering volume can be further broken down into $l A_s$, where $l = 0.075 \text{ cm}$ is the axial length of the scattering volume, determined by the CO_2 spot size, and A_s is the

in the plane perpendicular to the focus axis.
 scattering area ~~shown in Figure~~. ~~From that figure it~~
~~can be seen that~~ A_s can be further written as,

$$A_s = 2\delta\theta_s r_0 \delta r. \quad (9-3)$$

$\delta\theta_s = 5^\circ$ is the range of scattering angles accepted by the experiment, $r_0 = 0.023$ cm the radial distance at which the scattering area is located, and δr the radial width of the scattering area. δr will be determined later from the Langmuir intensities.

Substituting all of these quantities into Equation (9-2) gives,

$$\frac{\sigma}{r_e^2} = 5.16 \times 10^{10} \delta x (\text{cm}) \mathcal{I}. \quad (9-4)$$

In this expression δr has been replaced by δx as a reminder that slab geometry is being assumed.

There remain two ^{questions} ~~equations~~ to be answered. What ~~\mathcal{I}~~ should be chosen and how is δx determined? The choice of ~~\mathcal{I}~~ in (9-4) is clear. Since the scattering experiment is designed to measure Langmuir waves having $\underline{k} = k_y$, $\mathcal{I}(\underline{k} = k_y) = \mathcal{I}(k_x = 0)$ should be substituted in (9-4). A glance at Figures 9.2a and 9.2b will show, however, that $\mathcal{I}(k_x = 0)$ is not a uniquely determined value. \mathcal{I} is also a function of the spatial coordinate x . Figure 9.3 is a plot of $\log_{10} \mathcal{I}$ versus x at $k_x = 0$. It is just a cut through the contour

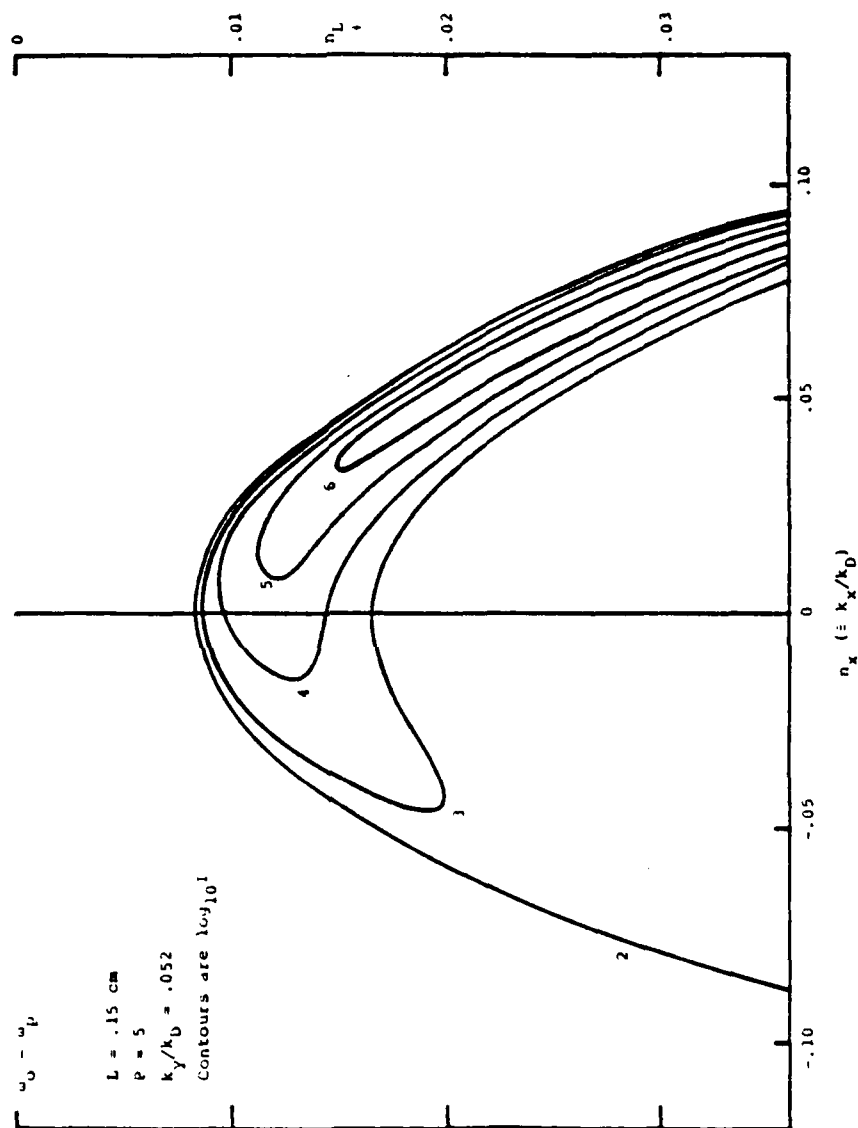


FIGURE 9.2a Contour maps for two different scale lengths of $I(k_x, x)$ for the model of Chapter 7. Contour labels are $\log_{10} I$.

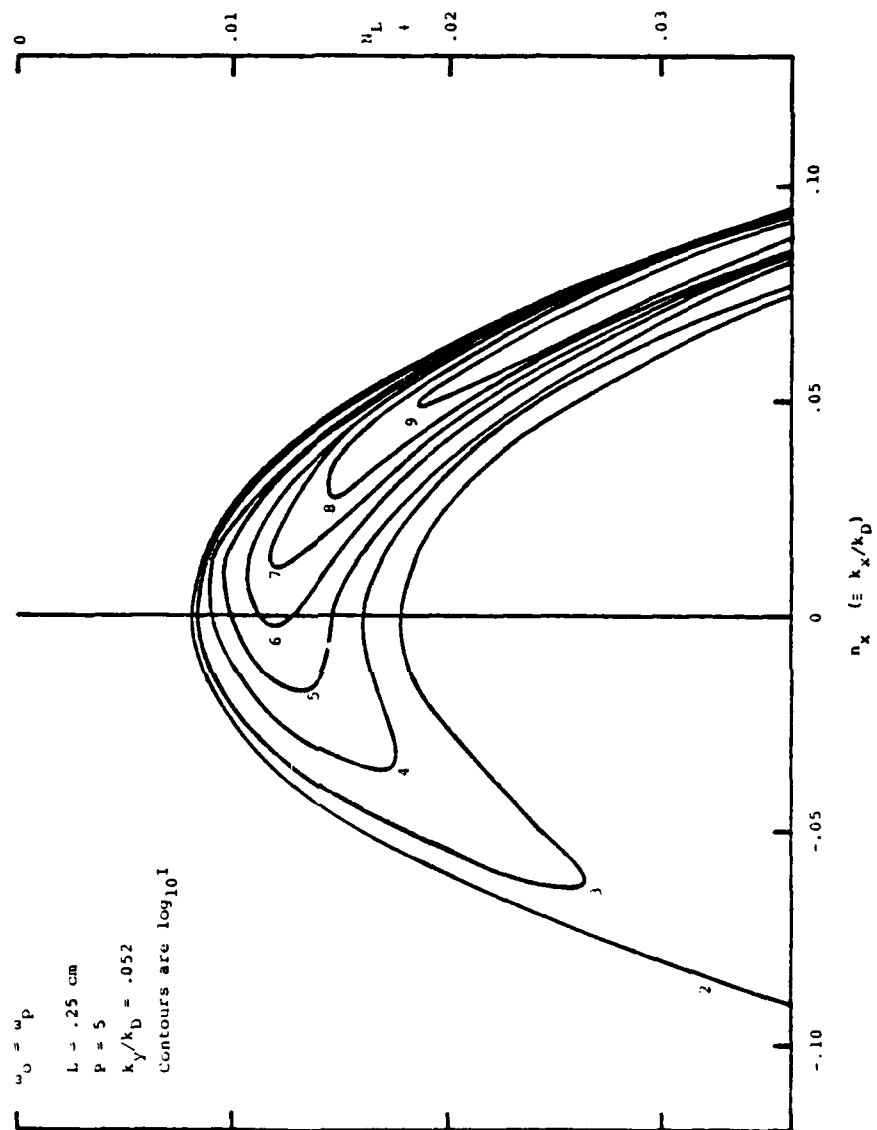


FIGURE 9.2b

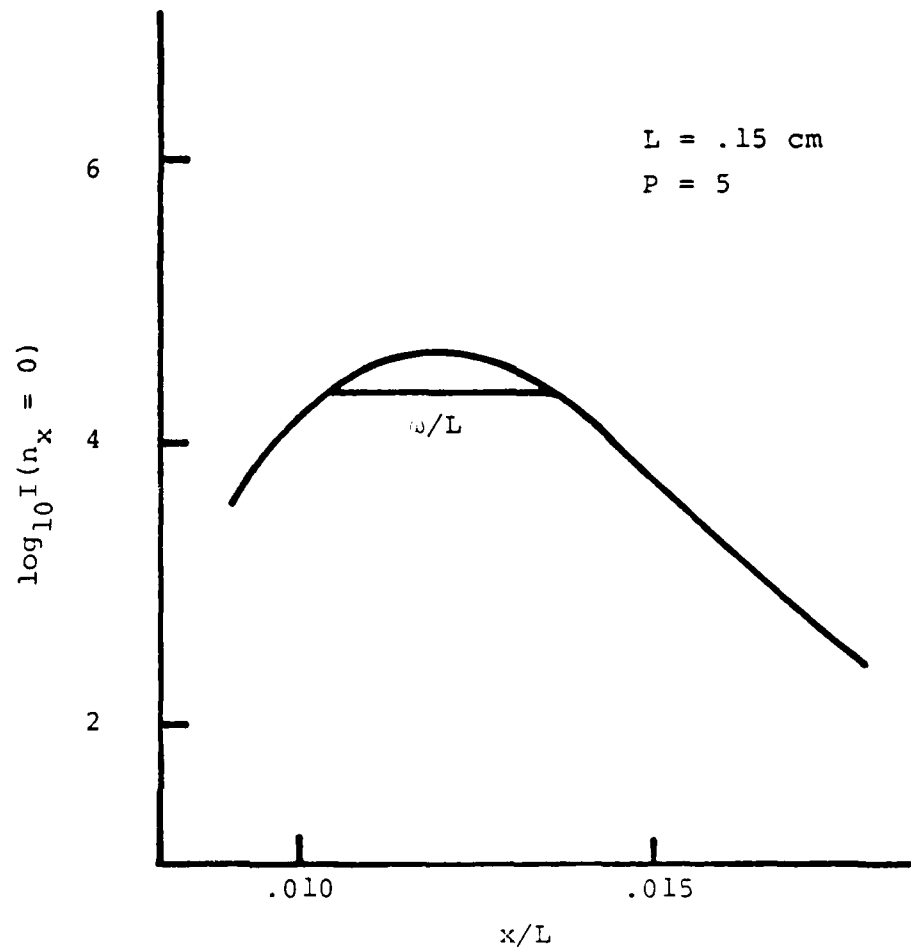


FIGURE 9.3 Plot of $\log_{10} I(k_o = 0, x)$. This is simply a cut along the $k_x = 0$ axis of the contour map of Figure 9.2

AD-A081 883

COLORADO UNIV AT BOULDER DEPT OF ASTRO-GEOPHYSICS

F/8 20/9

PLASMA WAVE TURBULENCE AND PARTICLE HEATING CAUSED BY ELECTRON --ETC(U)

NOV 79 M V GOLDMAN

F49620-76-C-0005

UNCLASSIFIED

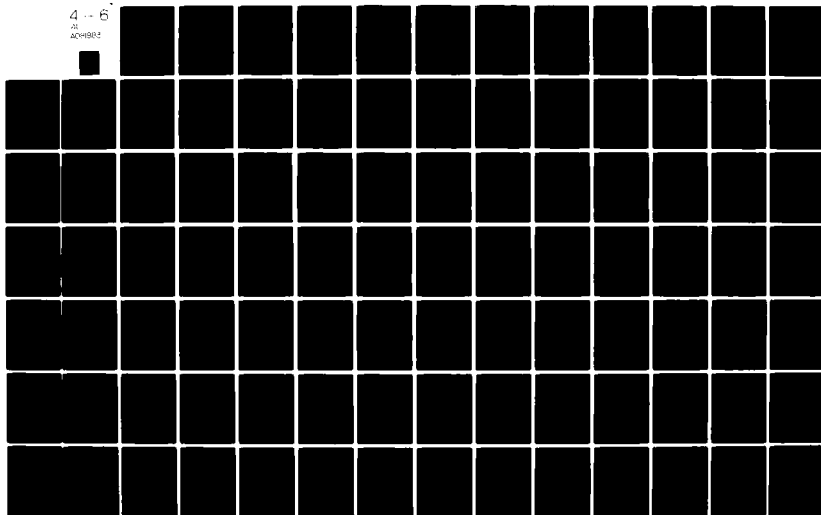
CU-1036

AFOSR-TR-80-0167

NL

4 -- 6

AD-A081 883



map of Figure 9.2a along the axis $k_x = 0$. Clearly the most reasonable choice for I in Equation (9-4) is the maximum I in Figure 9.3. It is also reasonable to define the x coordinate of this maximum as the center of the scattering area of Equation (9-3). The radial width of the scattering area is also determined by Figure 9.3. It is defined as the distance between the points which are at one-half the maximum intensity. Analyzing graphs like Figure 9.3 for various pump powers and density scale lengths and applying Equation (9-4) generates Table 9.1.

Clearly, not all of the P values listed in Table 9.1 can be considered linear. In fact, as will be seen shortly, nonlinear terms become significant for Langmuir intensity levels of the order 10^5 - 10^6 . In Figure 9.4 the results of the linear theory are plotted against the experimental points. There the linear theory is extended beyond the range $P \lesssim 4$ where it should be valid. Agreement with the experiment at $P \approx 10$ for $L = 0.15$ cm should be considered fortuitous, since Table 9.1 shows clearly nonlinear Langmuir levels for this P value.

The demonstration at the end of Chapter 8 shows that for $P \gg 13$, inhomogeneity becomes unimportant and only nonlinear effects need be considered. Hence the one-dimensional, homogeneous, nonlinear solution of Goldman and DuBois^R may be used to calculate I . In essence, this means that at each x , the plasma is assumed to be

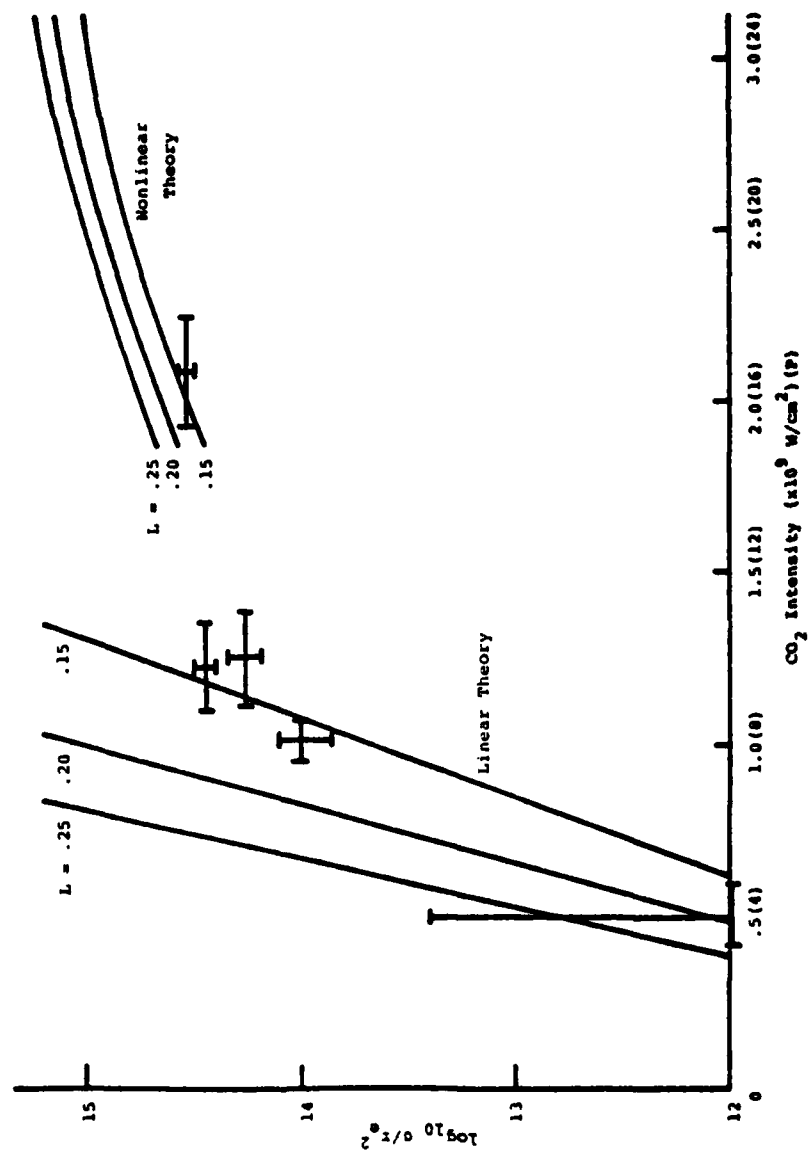


FIGURE 9.4 Linear and nonlinear theoretical curves plotted against the experimental points of Peacock et al.

TABLE 9.1

P	$I_{\max}(k_x=0)$	$\delta x/L$	σ/r_e^2
<u>L = .15 cm</u>			
5	4.59×10^4	.0030	1.07×10^{12}
10	3.55×10^7	.0020	5.50×10^{14}
15	2.95×10^{10}	.0017	3.88×10^{17}
20	2.51×10^{13}	.0016	3.11×10^{20}
25	2.43×10^{16}	.0014	2.63×10^{23}
<u>L = .20 cm</u>			
5	2.62×10^5	.0025	6.76×10^{12}
8	5.01×10^7	.0020	1.03×10^{15}
11	1.07×10^{10}	.0017	1.88×10^{17}
15	1.46×10^{13}	.0015	2.26×10^{20}
20	1.27×10^{17}	.0013	1.70×10^{24}
<u>L = .25 cm</u>			
2	2.95×10^3	.0036	1.37×10^{11}
4	1.78×10^5	.0026	5.97×10^{12}
5	1.49×10^6	.0023	4.42×10^{13}
6	1.29×10^7	.0021	3.49×10^{14}
8	1.10×10^9	.0017	2.41×10^{16}

homogeneous with density given by Equation (7-1). Then the Goldman-DuBois theory is used to calculate $I(k_y)$ at that x . The scattering experiment determines the k_y^{scatt} to be chosen from this spectrum. Then finding $I(k_y^{\text{scatt}})$ for various x generates a graph analogous to Figure 9.3 for the nonlinear solution. From this graph I_{max} and δx can be found exactly as in the linear case.

The one-dimensional, homogeneous, nonlinear solution may be written,^{#41}

$$I(n_y; \chi) = \frac{1}{24\pi n_y^2 d} \int_{n_y}^{n_y^c} [Pf(n_y; \chi) - 1 - \frac{1}{v} \chi_{\text{Landau}}] dn_y. \quad (9-5)$$

Here, as in Chapter 8, $v = v_{\text{col}}/\omega_0$, $n_y = k_y v_e/\omega_0$, $\chi = x/L$, $\chi_{\text{Landau}} = \sqrt{\pi}/8 e^{-3/2} (1/n_y^3) e^{-1/2 n_y^2}$, and $d = (\alpha^2/432\pi^2)(k_D^3/n_0)(\omega_p/v_{\text{coll}})$, where $\alpha^2 = m_e/m_i$. The quantity n_y^c is the point at which $f = 0$ and clearly is also dependent on χ . The coupling function f is written

$$f(\xi) = \xi e^{-\xi^2/2}, \quad \xi \equiv \frac{\chi - 3n_y^2}{2\alpha n_y}. \quad (9-6)$$

From this equation it is easily seen that,

$$n_y^c = \sqrt{\frac{1}{3}\chi}. \quad (9-7)$$

Inserting the dense plasma focus parameters and integrating, Equation (9-5) becomes,

$$I(.052; \chi) = 6.55 \times 10^6 \left[P \int_{.052}^{\sqrt{\pi_3}} f(\xi) d\eta_y - (\sqrt{\pi_3} - .052) - 1.13 \times 10^3 e^{-3/2\chi} \right] \quad (9-8)$$

In this equation η_y^{scatt} 0.052 has been substituted.

Equation (9-8) is graphed in Figure 9.5 for $P = 15$. This figure is analogous to Figure 9.3 in the linear case. Note first the maximum nonlinear intensity of about 10^6 . Obviously this sets an upper limit on the validity of the linear model. Any calculated linear level nearing or exceeding this value cannot be believed. Secondly, notice that in this nonlinear case $\int x/L$ is much larger than in the linear case. In the linear the drop in intensity toward larger x is caused by the increasing mismatch between the pump and the Langmuir wave. That is, the frequency matching condition $\omega_0 = \omega_L + \omega_{ia}$ becomes increasingly difficult to satisfy as x increases. This mismatch factor causes the intensity to decrease quickly with x . In the nonlinear case one finds that the character of the nonlinearity makes this mismatch effect unimportant. Instead the decrease in intensity with increasing x is caused by the increase in the integrated damping rate, as can be seen from Equation (9-8). This effect is much slower than that which is active in the linear case, resulting in large $\int x$.

The right side of Figure 9.4 shows the results of the nonlinear calculation plotted against the one experimental

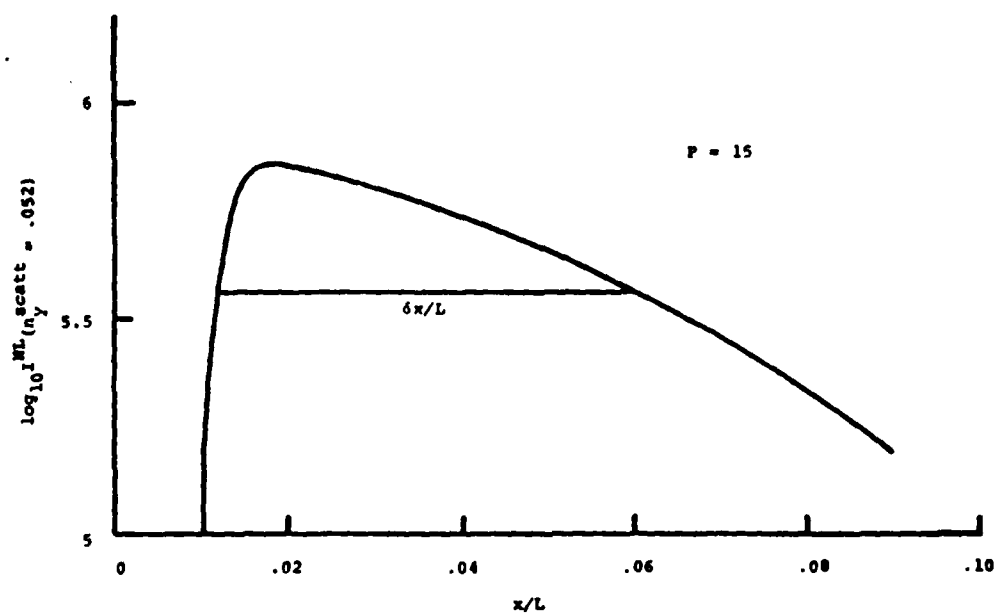


FIGURE 9.5 Plot of $\log_{10} I$ ($k_x = 0, x$) for the homogeneous one-dimensional nonlinear model considered in Chapter 8.

point which might marginally be in this nonlinear range. Although this point has $P \approx 17$, which is not much larger than 13, it seems to be reasonably well-described, at least for the smaller scale length of 0.15 cm.

From the preceding discussion it should be clear that this particular scattering experiment is rather ill-suited as a test of either the linear or nonlinear theory. What is needed to describe the experiment is really an inhomogeneous, nonlinear theory in two dimensions. Some of the difficulties this presents in one dimension are discussed in Chapter 8. To thoroughly test either of the theories developed here, data points at lower and higher P are needed.

To conclude this section, consider the problem of WKB breakdown. Since the wave kinetic equation is a WKB equation, its solutions need not be valid near the reflection point of a Langmuir wave, where $k_x \approx 0$. This becomes important when one recalls that the intensities used for the theoretical curves in Figure 9.4 were characterized by $k_x = 0$, exactly in the center of the region of WKB breakdown. This region is shown in Figure 9.1 along with the intensity spectrum along a ray path. Clearly, there can be no rigorous justification for assuming WKB intensities are ^{correct} ~~valid~~ in a region where WKB is not valid. However, one would expect physically a smooth joining between the two regions in which WKB is valid. One would hope, then, that

since the solutions to the kinetic equation calculated earlier in this chapter provide that smooth joining, the WKB intensities are "close" to the real intensities. In addition, the breakdown region does not contain a major portion of the Langmuir wave's growth. For example, in Figure 9.1 the spectrum labeled $L = 0.25$ cm has less than two percent of the total growth in this region. The other spectrum has less than eight percent. Hence, most of the growth of the Langmuir waves occurs in regions where WKB is valid.

To calculate where WKB is valid, one begins with the well-known condition,

$$\frac{1}{k_x} \frac{\partial k_x}{\partial x} \ll k_x, \quad (9-9)$$

and the Langmuir wave dispersion relation,

$$\omega_L^2 = \omega_0^2 \left(1 - \frac{x}{L}\right) + 3v_e^2 (k_x^2 + k_y^2). \quad (9-10)$$

Solving for k_x^2 ,

$$k_x^2 = \frac{1}{3v_e^2} \left[\omega_L^2 - \omega_0^2 \left(1 - \frac{x}{L}\right) \right] - k_y^2. \quad (9-11)$$

Now, $\partial k_x / \partial x$ is easily found to be

$$\frac{\partial k_x}{\partial x} = \frac{\omega_0^2}{6v_e^2 L} \frac{1}{k_x}. \quad (9-12)$$

Hence, the condition for WKB validity is,

$$k_x \gg \left(\frac{\omega_0^2}{6v_e L} \right)^{1/3}, \quad (9-13)$$

or in the dimensionless notation of Chapter 7,

$$\mathcal{M}_x \gg \left(\frac{\beta}{6} \right)^{1/3}, \quad (9-14)$$

where $\mathcal{M}_x \equiv (\omega_0/v_e)k_x$, and $\beta \equiv v_e \omega_0 L$. For the dense plasma focus parameters,

$$\mathcal{M}_x \gg .015. \quad (9-15)$$

This can also be expressed as a condition on $\chi (\equiv x/L)$,

$$\chi \gg \chi_T + 3 \left(\frac{\beta}{6} \right)^{1/3}, \quad (9-16)$$

where χ_T is the reflection point of the Langmuir wave and is defined as $\chi_T \equiv 1 - \omega^2/\omega_0^2$, $\omega \equiv \omega_L/\omega_0$.

APPENDIX A

DERIVATION OF THE WAVE KINETIC EQUATION

The following derivation of the WKB wave kinetic equation is taken in substantially unaltered form from the lectures notes of Prof. M. V. Goldman.

The starting point is the wave equation for the fluctuating part of the electric field which comes directly from Maxwell's equations,

$$c^2 \nabla \times (\nabla \times \underline{\underline{E}}) + \frac{\partial^2}{\partial t^2} \underline{\underline{E}} = -4\pi \frac{\partial}{\partial t} (\tilde{\underline{\underline{j}}}_e + \tilde{\underline{\underline{j}}}_i) \quad (\text{A-1})$$

For longitudinal waves this can be integrated once in time to give,

$$\frac{\partial}{\partial t} \underline{\underline{E}}(x_1) + 4\pi \int dx_3 \nabla(x_1, x_3) \underline{\underline{E}}(x_3) = -4\pi \tilde{j}_0(x_1) \quad (\text{A-2})$$

Here \tilde{j}_0 represents spontaneous emission and the polarization current has been absorbed into ∇ . Also the notation $x_i = (\underline{r}_i, t_i)$ has been introduced. Note that Equation (A-2) is simply Faraday's law for longitudinal fields. Multiplying Equation (A-2) by $\underline{\underline{E}}(x_2)$ and ensemble averaging,

$$\frac{\partial}{\partial t_1} I(x_1, x_2) + 4\pi \int dx_3 \sigma(x_1, x_3) I(x_3, x_2) = 4\pi W_0(x_1, x_2), \quad (A-3)$$

where

$$I(x_1, x_2) \equiv \langle E(x_1) E(x_2) \rangle, \quad W_0(x_1, x_2) \equiv - \langle \tilde{j}_0(x_1) E(x_2) \rangle,$$

and the brackets denote the ensemble average. Next, add Equation (A-3) to itself with variables x_1 and x_2 interchanged to obtain,

$$\left(\frac{\partial}{\partial t_1} + \frac{\partial}{\partial t_2} \right) \frac{1}{4\pi} I(x_1, x_2) = \left[- \int dx_3 \sigma(x_1, x_3) I(x_3, x_2) + W_0(x_1, x_2) \right] + [x_1 \leftrightarrow x_2], \quad (A-4)$$

where $[x_1 \leftrightarrow x_2]$ indicates the preceding term with arguments x_1 and x_2 interchanged.

Introduce now sum (or "centroid") and difference (or "relative") coordinates, defined by,

$$x = x_1 - x_2 \quad (r = r_1 - r_2, \quad t = t_1 - t_2) \quad (A-5a)$$

$$X = \frac{x_1 + x_2}{2} \quad (R = \frac{r_1 + r_2}{2}, \quad T = \frac{t_1 + t_2}{2}). \quad (A-5b)$$

These coordinates allow a natural definition of multiple time and space scales. In these new coordinates, Equation (A-4) becomes,

$$\frac{\partial}{\partial T} \frac{I(x, X)}{4\pi} = \left[- \int dx_3 \sigma(x, -x_3, \frac{x_1+x_3}{2}) I(x_1-x_3, \frac{x_1+x_3}{2}) + W_0(x, X) \right] + [x_1 \leftrightarrow x_2] . \quad (A-6)$$

In a homogeneous, stationary plasma, the correlation functions do not depend at all on the centroid coordinates, but in an inhomogeneous plasma they do. This can be dealt with by assuming that the variation with the centroid coordinates of all the functions is slow compared to the variation with the relative coordinates of all the functions. Then a WKB approximation can be made in the slow, centroid spatial coordinate, and a multiple time scale approximation as well. First note that the centroid coordinates of the correlation functions in the integral may be expressed as,

$$\frac{x_1+x_3}{2} = X + \frac{x_2-x_3}{2} \quad (A-7a)$$

$$\frac{x_2+x_3}{2} = X - \frac{x_1-x_3}{2} . \quad (A-7b)$$

Now an expansion of the integrand in Equation (A-6) can be made, and the integral becomes,

$$\int dx_3 \left[\sigma(x, -x_3, X) + \left(\frac{x_2-x_3}{2} \right) \frac{\partial}{\partial X} \sigma(x, -x_3, X) \right] \times \left[I(x_1-x_3, X) - \left(\frac{x_1-x_3}{2} \right) \frac{\partial}{\partial X} I(x_1-x_3, X) \right] . \quad (A-8)$$

Only terms up to first order in space-time derivatives are to be retained in this expansion. Equation (A-6) has now

become local in its dependence on the centroid coordinates,

X.

Fourier transforming (A-6) in the difference variables x , and integrating by parts to replace the factors $(x_3 - x_2)/2$ and $(x_1 - x_3)/2$ in (A-8) by derivatives with respect to $K \equiv (\underline{k}, \omega)$, the transform of (A-8) becomes,

$$\begin{aligned} & \int dx_3 dx_2 e^{-iKx} \left\{ \frac{dK'}{(2\pi)^4} \frac{dK''}{(2\pi)^4} e^{iK'(x_1 - x_2) + iK''(x_1 - x_3)} \right. \\ & \quad \times \left\{ \sigma(K') I(K'') - \frac{1}{2i} \frac{\partial \sigma(K')}{\partial X} \frac{\partial I(K'')}{\partial K''} + \frac{1}{2i} \frac{\partial \sigma(K'')}{\partial K'} \frac{\partial I(K')}{\partial X} \right\} \\ & \quad \left. = \sigma(K) I(K) - \frac{1}{2i} \left[\frac{\partial \sigma(K)}{\partial X} \frac{\partial I(K)}{\partial K} - \frac{\partial \sigma(K)}{\partial K} \frac{\partial I(K)}{\partial X} \right] \right\} \quad (A-9) \end{aligned}$$

The common X dependence of σ and I has here been suppressed.

The transform of the interchange term $[x_1 \leftrightarrow x_2]$ in Equation (A-6) is identical to the right side of (A-9), but with $-K$ replacing K . From reality conditions it follows that $\sigma(-K) = \sigma(K)^*$ and $I(-K) = I(K)^*$. In addition, from the symmetry of $I(x_1, x_2)$ under interchange, it follows that $I(K, X)$ is real. Thus, the Fourier transform of (A-6) becomes,

$$\begin{aligned} \frac{\partial}{\partial T} \frac{I(K)}{4\pi} &= -2 \operatorname{Re} \sigma(K) I(K) + \left(\frac{\partial \operatorname{Im} \sigma(K)}{\partial X} \right) \frac{\partial I(K)}{\partial K} \\ &\quad - \left(\frac{\partial \operatorname{Im} \sigma(K)}{\partial X} \right) \frac{\partial I(K)}{\partial X} + 2 \operatorname{Re} W_0(K). \quad (A-10) \end{aligned}$$

Introducing the longitudinal dielectric function,

$$\epsilon_L(\underline{k}, \omega) = 1 + \frac{4\pi i}{\omega} \tau(\underline{k}, \omega), \quad (\text{A-11})$$

then Equation (A-10) becomes, returning to conventional notation,

$$\begin{aligned} \frac{\partial I}{\partial T} = & -2\omega \text{Im} \epsilon I + \frac{\partial}{\partial T} [\omega (\text{Re} \epsilon - 1)] \frac{\partial I}{\partial \omega} - \frac{\partial}{\partial \omega} [\omega (\text{Re} \epsilon - 1)] \frac{\partial I}{\partial T} \\ & - \left(\frac{\partial \omega \text{Re} \epsilon}{\partial k} \right) \cdot \frac{\partial I}{\partial k} + \left(\frac{\partial \omega \text{Re} \epsilon}{\partial R} \right) \cdot \frac{\partial I}{\partial R} + 8\pi \text{Re} W_0, \end{aligned} \quad (\text{A-12})$$

where $I = I(\underline{k}, \omega, \underline{R}, T)$, $\epsilon = \epsilon_L(\underline{k}, \omega, \underline{R}, T)$, and $W_0 = W_0(\underline{k}, \omega, \underline{R}, T)$.

After some manipulation of the partial derivatives, (A-12) can be rewritten as,

$$\begin{aligned} \frac{\partial}{\partial T} \left[I \frac{\partial}{\partial \omega} (\omega \text{Re} \epsilon) \right] - \frac{\partial}{\partial \omega} \left[I \frac{\partial}{\partial T} (\omega \text{Re} \epsilon) \right] - \frac{\partial}{\partial k} \left[I \frac{\partial}{\partial k} (\omega \text{Re} \epsilon) \right] \\ + \frac{\partial}{\partial R} \left[I \frac{\partial}{\partial R} (\omega \text{Re} \epsilon) \right] + 2I\omega \text{Im} \epsilon = 8\pi \text{Re} W_0. \end{aligned} \quad (\text{A-13})$$

Effects of order $(kL)^{-1}$ and $(\omega T)^{-1}$ have been included in (A-13), where L and T are typical scale lengths and time intervals associated with the centroid variation of I and τ , and k and ω are a typical inverse length and time associated with the relative coordinates. Dissipation ($\propto \text{Im} \epsilon$) and spontaneous emission ($\propto \text{Re} W_0$) are also included, and are often of the same order as $(kL)^{-1}$, $(\omega T)^{-1}$. (In fact, $\text{Im} \epsilon$ sets the scales of L, T in a homogeneous plasma boundary value ^{or} initial value problem.)

In order to proceed with the reduction of (A-13) to an

energy balance equation for normal modes, it is necessary to return to Equation (A-14) and work to "zero-order" in the small parameters. To zero-order in $(kL)^{-1}$, $(\omega T)^{-1}$, γ/ω , and ω_0 , Equation (A-4) becomes,

$$\frac{\partial}{\partial t} I(x, X) + 4\pi \int dx_3 \sigma(x_1 - x_3, X) I(x_1 - x_3) = 0. \quad (A-14)$$

Now interchange x_1 and x_2 , and subtract the equation from itself [rather than adding as in the previous development of (A-4)]. The result can be written,

$$\begin{aligned} 2 \frac{\partial}{\partial t} I(x, X) + 4\pi \int dx_3 \sigma(x_1 - x_3, X) I(x_1 - x_3) \\ - 4\pi \int dx_3 \sigma(x_2 - x_3, X) I(x_2 - x_3) = 0 \end{aligned} \quad (A-15)$$

Fourier transforming this in $x = (\underline{r}, t)$,

$$-2i\omega \operatorname{Re} \epsilon(k, \omega, E, T) I(k, \omega, E, T) = 0 \quad (A-16)$$

The solution to (A-16) can be expressed as,

$$I(k, \omega) = \delta[\operatorname{Re} \epsilon(k, \omega)] I_1 \quad (A-17)$$

The delta function is appropriate, since I must be zero unless $\operatorname{Re} \epsilon = 0$, and since the ω or k integrals of I must be non-zero. The dependence on centroid coordinates has been suppressed in (A-17). I_1 in (A-17) cannot be determined

from (A-16), because it is a homogeneous equation. However, I_1 can be determined from the first order energy balance equation (A-13). Note in (A-17) that $\text{Re } (\underline{k}, \underline{\omega}, \underline{R}, T) = 0$ at one or more real frequencies of the form $\omega = \omega_R(\underline{k}, \underline{R}, T)$. In the present case only stationary plasmas are being considered, so,

$$\omega_R = \omega_R(\underline{k}, \underline{R}). \quad (\text{A-18})$$

Now rewrite (A-17), in the vicinity of $\omega = \omega_R$, as,

$$I(\underline{k}, \omega) = \pi \delta(\omega - \omega_R) I(\omega_R), \quad (\text{A-19})$$

where

$$I(\omega_R) \equiv I_1 / \pi (\partial \text{Re} \xi / \partial \omega)_{\omega = \omega_R}.$$

This notation is consistent with the definition of the spectral mode function in the homogeneous case. Therefore, $I(\omega_R, \underline{R}, T)$ can be interpreted as the spectral mode function for mode ω_R . [More generally, (A-19) should include both positive and negative frequencies and a sum over all branches of normal mode solutions, ω_R , to $\text{Re} \xi = 0$.]

Inserting (A-19) into (A-13) and taking the integral over ω yields,

$$\begin{aligned}
& \frac{\partial}{\partial T} \left(I(\omega_R) \left[\frac{\partial}{\partial \omega} (\omega \operatorname{Re} \varepsilon) \right]_{\omega_R} \right) - \frac{d}{dR} \cdot \left(I(\omega_R) \left[\frac{\partial}{\partial K} (\omega \operatorname{Re} \varepsilon) \right]_{\omega_R} \right) \\
& + \frac{d}{dK} \cdot \left(I(\omega_R) \left[\frac{\partial}{\partial R} (\omega \operatorname{Re} \varepsilon) \right]_{\omega_R} \right) + 2\omega_R \operatorname{Im} \varepsilon(\omega_R) I(\omega_R) \\
& = 8\pi \operatorname{Re} W_0(\omega_R),
\end{aligned} \tag{A-20}$$

where

$$W_0(\omega_R) \equiv \int_{\omega_R} \frac{d\omega}{\pi} \operatorname{Re} W_0(K, \omega),$$

and the total derivatives d/dR , and d/dK are,

$$\begin{aligned}
\frac{d}{dR} & \equiv \frac{\partial}{\partial R} + \frac{\partial \omega_R}{\partial R} \frac{\partial}{\partial \omega_R} \\
\frac{d}{dK} & \equiv \frac{\partial}{\partial K} + \frac{\partial \omega_R}{\partial K} \frac{\partial}{\partial \omega_R}.
\end{aligned}$$

It is also reasonable to define the energy density and the damping rate as in the homogeneous case,

$$\begin{aligned}
U(\omega_R, R, T) & \equiv \left[\frac{\partial}{\partial \omega} (\omega \operatorname{Re} \varepsilon) \right]_{\omega_R} \frac{I(\omega_R)}{8\pi} \\
& = \omega_R \frac{\partial}{\partial \omega} \operatorname{Re} \varepsilon \Big|_{\omega_R} \frac{I(\omega_R)}{8\pi},
\end{aligned} \tag{A-21}$$

$$Y(K, R) \equiv \frac{\operatorname{Im} \varepsilon(\omega_R)}{(\partial \operatorname{Re} \varepsilon / \partial \omega)_{\omega_R}}. \tag{A-22}$$

Then (A-20) takes the form,

$$\begin{aligned}
& \frac{\partial}{\partial T} U(\omega_R) + \frac{d}{dR} \cdot [v_g U(\omega_R)] + \frac{d}{dK} \cdot [a U(\omega_R)] \\
& + 2Y U(\omega_R) = \operatorname{Re} W_0(\omega_R).
\end{aligned} \tag{A-23}$$

The first term is the time rate of change of the energy density associated with $\omega_R(\underline{k}, \underline{R})$. The damping and spontaneous emission terms are as in the Kirchoff's law for the inhomogeneous steady state case. The second and third terms on the left describe the flow of energy in \underline{R} - \underline{k} phase space. The group velocity \underline{v}_g and the vector \underline{a} are defined by,

$$\underline{v}_g(\underline{k}, \underline{R}) \equiv - \left[\frac{\partial}{\partial \underline{k}} \text{Re} \epsilon \right]_{\omega_R} / \left[\frac{\partial}{\partial \omega} \text{Re} \epsilon \right]_{\omega_R} = \frac{\partial \omega_R}{\partial \underline{k}}, \quad (\text{A-24a})$$

$$\underline{a}(\underline{k}, \underline{R}) \equiv \left[\frac{\partial}{\partial \underline{R}} \text{Re} \epsilon \right]_{\omega_R} / \left[\frac{\partial}{\partial \omega} \text{Re} \epsilon \right]_{\omega_R} = - \frac{\partial \omega_R}{\partial \underline{R}}, \quad (\text{A-24b})$$

The second equality in (A-24a) follows from taking the total derivative $d/d\underline{k}$ of $\text{Re} \epsilon[\omega_R(\underline{k}, \underline{R}), \underline{k}, \underline{R}] = 0$, and the second equality in (A-24b) follows from the derivative $d/d\underline{R}$. It is important to note that Equations (A-23) and (A-24a,b) involve independent Eulerian coordinates, \underline{k} and \underline{R} . Using Equations (A-24a,b), because of this independence, the order of differentiation may be changed, and the following identity proven:

$$\frac{d}{d\underline{R}} \cdot \underline{v}_g + \frac{d}{d\underline{k}} \cdot \underline{a} = 0.$$

This enables (A-23) to be rewritten as,

$$\begin{aligned} & \left(\frac{\partial}{\partial t} + \frac{\partial \omega_R}{\partial \underline{k}} \cdot \frac{d}{d\underline{R}} - \frac{\partial \omega_R}{\partial \underline{R}} \cdot \frac{d}{d\underline{k}} \right) U(\omega_R) + 2\gamma U(\omega_R) \\ & = \text{Re } W_0(\omega_R). \end{aligned} \quad (\text{A-24})$$

The energy density, $U(\omega_R)$, should be thought of as defined in a six-dimensional \underline{R} - \underline{k} phase space. Along an arbitrary path in this space, ω_R is not constant (although $\text{Re}[\omega_R(\underline{k}, \underline{R}), \underline{k}, \underline{R}]$ is constant and equal to zero). However, along the "characteristic" or "ray" paths in this space, ω_R is constant. The same idea is employed in integrations of the collisionless Boltzmann equation, where the particle energy is conserved along a characteristic. One defines the ray paths by introducing the Lagrangian coordinates $\underline{R}(T)$, $\underline{k}(T)$, which obey the equations,

$$\frac{\partial \underline{R}}{\partial T} = \frac{\partial \omega_R}{\partial \underline{k}} \quad (\text{A-26a})$$

$$\frac{\partial \underline{k}}{\partial T} = - \frac{\partial \omega_R}{\partial \underline{R}}, \quad (\text{A-26b})$$

Using Equations (A-26a,b) and the assumption of a stationary plasma, it immediately follows that $\omega_R[\underline{R}(T), \underline{k}(T)] = \text{constant}$, since,

$$\frac{d}{dT} \omega_R = \frac{\partial \omega_R}{\partial T} + \frac{\partial \underline{R}}{\partial T} \cdot \frac{\partial \omega_R}{\partial \underline{R}} + \frac{\partial \underline{k}}{\partial T} \cdot \frac{\partial \omega_R}{\partial \underline{k}} = 0. \quad (\text{A-27})$$

Along a given ray path, associated with a particular ω_R , (A-25) reduces to,

$$\frac{d}{dT} U + 2\gamma U = \text{Re } W_0. \quad (\text{A-28})$$

The ray path equations (A-26a,b) are Hamilton's equations, when $\hbar\omega_R$ is interpreted as a Hamiltonian, and $\hbar\mathbf{k}$ as a "momentum." The quantum mechanical boson occupation number, N , for the normal mode ω_R , is related to the energy density $U(\omega_R)$ along a ray path by,

$$U(\omega_R) = N\hbar\omega_R. \quad (\text{A-29})$$

In the absence of damping and spontaneous emission, N is conserved along a ray path. Damping and spontaneous emission provide a sink and source for N , as (A-28) shows. Hamilton equations such as (A-26a,b) are commonly invoked in quantum mechanical and semi-classical discussions of wave-particle duality; it can be seen here that they apply to all the weakly damped modes in plasmas and other dispersive media which are slowly varying.

Appendix B

~~MATHEMATICAL APPENDIX~~

THE INTEGRAL OF γ_g AND γ_{LANDAU}

The integral required in the derivation of equation (7-26) from equation (7-24) is of the form,

$$\text{Int.} = \int \frac{1}{(a^2+x^2)^{3/2}} e^{-A/(a^2+x^2)} dx \quad (\text{B-1})$$

This is true both for the Landau damping contribution and the parametric growth contribution. However, in the growth rate the effect of pump swelling near the reflection point in the inhomogeneous plasma has been ignored. The pump is assumed to be spatially uniform.

To perform the integral, consider the substitution,

$$w = \frac{x^2}{a^2+x^2}, \quad dw = \frac{2a^2x}{(a^2+x^2)^2} dx \quad (\text{B-2})$$

Also, then

$$x^2 = \frac{a^2 w}{1-w}, \quad a^2+x^2 = \frac{a^2}{1-w} \quad (\text{B-3})$$

$$\begin{aligned}
\text{Int.} &= \int \left(\frac{1-w}{a^2} \right)^{3/2} e^{-A(1-w)/a^2} \frac{(a^2+x^2)^2}{2a^2x} dw \\
&= \int \left(\frac{1-w}{a^2} \right)^{3/2} e^{-A(1-w)/a^2} \frac{a^4}{(1-w)^2} \frac{1}{2a^2} \sqrt{\frac{1-w}{a^2w}} dw \\
&= \frac{1}{2a^2} e^{-A/a^2} \int w^{-1/2} e^{Aw/a^2} dw \quad (B-4)
\end{aligned}$$

The remaining integral can now be done by parts.

$$\text{Int.} = \frac{1}{2a^2} e^{-A/a^2} \left[2w^{1/2} e^{Aw/a^2} - 2 \frac{A}{a^2} \int w^{1/2} e^{Aw/a^2} dw \right]$$

The remaining integral can ^{again} ~~now~~ be done by parts and in this way an infinite series is generated. The final result is,

$$\text{Int.} = \frac{1}{a^2} w^{1/2} e^{-A(1-w)/a^2} \sum_{m=0}^{\infty} \frac{1}{(2m+1)!!} \left(-\frac{2A}{a^2} w \right)^m \quad (B-5)$$

Returning to the x ^{variable} ~~variation~~,

$$\text{Int.} = \frac{x}{a^2 \sqrt{a^2+x^2}} e^{-A/(a^2+x^2)} \sum_{m=0}^{\infty} \frac{1}{(2m+1)!!} \left(-\frac{2A}{a^2} \frac{x^2}{a^2+x^2} \right)^m \quad (B-6)$$

Some further investigation can be done into the nature of the series appearing in equation (B-6), which will be designated Wilson's function, or $W_i(y)$.

$$W_i(y) = \sum_{m=0}^{\infty} \frac{(-1)^m y^m}{(2m+1)!!}, \quad y \geq 0. \quad (B-7)$$

An alternate form is,

$$\omega_i(y) = \sum_{m=0}^{\infty} \frac{(-1)^m m!}{(2m+1)!} (2y)^m \quad (\text{B-8})$$

Several properties of $\omega_i(y)$ are listed below:

1) $\omega_i(y)$ is absolutely convergent and continuous for finite y ;

2) $\omega_i(y)$ is uniformly convergent on any closed interval;

$$3) \sum_{m=0}^{\infty} \frac{y^m}{(2m+1)!!} < e^y, \quad y > 0$$

4) $\omega_i(y) > 0$ for all finite y ;

$$5) \sum_{m=0}^{\infty} \frac{(-1)^m y^m}{(2m+1)!!} \approx \frac{1}{y} \left(1 + \frac{1}{y}\right), \quad y \gg 1.$$

Property (1) can be shown with the ratio test for infinite series. The Weierstrass M-test^{47,48} proves uniform convergence. Term by term comparison of the sum in property (3) with the Maclaurin series for e^y proves (3). To prove property (4), the differential equation which $\omega_i(y)$ satisfies must be derived. First multiply $\omega_i(y)$ by $y^{1/2}$.

$$y^{1/2} \omega_i(y) = \sum_{m=0}^{\infty} \frac{(-1)^m y^{m+1/2}}{(2m+1)!!}$$

The derivative of both sides of this equation must now

be taken. The derivative on the right hand side can be taken term by term, because the differentiated series is uniformly convergent. Hence,

$$\begin{aligned}
 [y^{1/2} \omega_i(y)]' &= \sum_{m=0}^{\infty} \frac{(-1)^m (m + \frac{1}{2}) y^{m - \frac{1}{2}}}{(2m+1)!!} \\
 2 \left[\frac{1}{2} y^{-1/2} \omega_i(y) + y^{1/2} \omega_i'(y) \right] &= y^{-1/2} + \sum_{m=1}^{\infty} \frac{(-1)^m y^{m - \frac{1}{2}}}{(2m-1)!!} \\
 2 y^{1/2} \omega_i'(y) + y^{-1/2} \omega_i(y) &= y^{-1/2} - \sum_{m=0}^{\infty} \frac{(-1)^m y^{m + \frac{1}{2}}}{(2m+1)!!} = y^{-\frac{1}{2}} - y^{\frac{1}{2}} \omega_i(y)
 \end{aligned}$$

Collecting terms gives the differential equation,

$$2y \omega_i'(y) + (1+y) \omega_i(y) = 1 \quad (\text{B-9})$$

It is now easy to show that $\omega_i'(y)$ is greater than zero for $y \geq 0$. Letting $y = 0$, (B-9) gives $\omega_i'(0) = 1$.
~~For~~ For $y > 0$,

$$\omega_i'(y) = \frac{1}{2y} [1 - (1+y) \omega_i(y)] \quad (\text{B-10})$$

Assume now that $\omega_i'(y) = 0$ for some $y = y_0$. Then, at that point,

$$\omega_i'(y_0) = \frac{1}{2y_0} > 0 \quad (\text{B-11})$$

Therefore, the slope at any finite y_0 for which $\omega'_i(y_0) = 0$ is positive and $\omega'_i(y)$ can never pass through zero.

Property (5) concerns the asymptotic nature of $\omega'_i(y)$. The analysis leading to the spectra calculated in Chapter 9 requires the evaluation of $\omega'_i(y)$ for large y ($y \approx 100$). The alternating character of the series form (B-7) makes this evaluation difficult. For the computer and compiler used in this thesis round-off errors began affecting the accuracy of $\omega'_i(y)$ near $y = 50$. This made the development of an asymptotic expression necessary. To derive this, consider the series $\sum_{m=1}^{\infty} \frac{a_m}{y^m}$ in conjunction with (B-9). Substituting,

$$-2 \sum_{m=1}^{\infty} \frac{m a_m}{y^m} + \sum_{m=1}^{\infty} \frac{a_m}{y^{m-1}} = 1$$

Equating coefficients of equal powers of y gives,

$$a_1 = 1, \quad a_2 = 1, \quad a_3 = 3,$$

$$a_4 = 15, \quad a_5 = 105, \quad \dots$$

$$a_m = (2m-3)!! \quad , \quad m = 2, 3, \dots$$

Hence, the sum becomes:

$$S = \frac{1}{y} + \sum_{m=1}^{\infty} \frac{(2m-1)!!}{y^{m+1}} \quad (B-12)$$

\bar{R} S is used here rather than $\omega_{\frac{1}{2}}^i(y)$ because the series clearly does not converge. However, it is useful for computational purposes if only a few terms are used. In particular, for $y = 50$, accuracy of within 1 part in 10^6 is obtained by summing the first four terms. For the purposes of the calculation in Chapter 9, it is sufficient to sum only the first two terms. Hence,

$$\omega_i(y) \approx \frac{1}{y} + \frac{1}{y^2} = \frac{1}{y} \left(1 + \frac{1}{y} \right), \quad y \gg 1 \quad (B-13)$$

$\omega_{\frac{1}{2}}^i(y)$ is listed below for $0 \leq y \leq 200$.

TABLE B.1

y	$\omega_i(y)$	y	$\omega_i(y)$
0.00	1.000	15.00	.0726
.10	.967	20.00	.0530
.20	.936	25.00	.0418
.30	.906	30.00	.0346
.40	.877	35.00	.0295
.50	.849	40.00	.0257
.60	.822	45.00	.0228
.70	.796	50.00	.0204
.80	.772	60.00	.0169
.90	.748	70.00	.0145
1.00	.725	80.00	.0127
1.50	.623	90.00	.0112
2.00	.538	100.00	.0101
2.50	.468	110.00	.00917
3.00	.410	120.00	.00840
3.50	.361	130.00	.00775
4.00	.320	140.00	.00719
4.50	.286	150.00	.00671
5.00	.256	160.00	.00629
6.00	.210	170.00	.00592
7.00	.176	180.00	.00559
8.00	.151	190.00	.00529
9.00	.131	200.00	.00503
10.00	.116		

REFERENCES

1. F. W. Perkins and J. Flick, Phys. Fluids 14, 2012 (1971).
2. M. N. Rosenbluth, Phys. Rev. Lett. 29, 565 (1972).
3. D. Pesme, G. Laval, and R. Pellat, Phys. Rev. Lett. 31, 203 (1973).
4. M. N. Rosenbluth, R. B. White, and C. S. Liu, Phys. Rev. Lett. 31, 1190 (1973).
5. C. Moroli, J. Plasma Phys. 10, 165 (1973).
6. D. F. DuBois, D. W. Forslund, and E. Williams, Phys. Rev. Lett. 33, 1013 (1974).
7. D. Arnush, B. D. Fried, and C. F. Kennel, J. Geophys. Res. 79, 1885 (1974).
8. D. F. DuBois, M. V. Goldman, and D. McKinnis, Phys. Fluids 16, 2257 (1973).
9. K. Nishikawa, J. Phys. Soc. Japan 24, 916 (1968).
10. D. F. DuBois and M. V. Goldman, Phys. Rev. Lett. 14, 544 (1965).
11. M. V. Goldman, Annals of Phys. (N.Y.) 38, 95 (1966).
12. D. F. DuBois and M. V. Goldman, Phys. Rev. 164, 207 (1967).
13. K. Nishikawa and C. S. Liu, Adv. Plasma Phys. 6, 3 (1976).
14. E. A. Jackson, Phys. Rev. 153, 235 (1967).
15. V. A. Bailey, Phil. Mag. 26, 425 (1938).
16. V. A. Bailey, J. Atmos. Terr. Phys. 14, 299 (1959).
17. E. M. Allen, G. D. Thome, and P. G. Rao, Radio Sci. 9, 905 (1974).
18. W. F. Utlaut and E. J. Violette, Radio Sci. 9, 895 (1974).

19. P. A. Fialer, Radio Sci. 9, 923 (1974).
20. J. Minkoff, P. Kugelman, and I. Weissman, Radio Sci. 9, 941 (1974).
21. G. D. Thome and D. W. Blood, Radio Sci. 9, 917 (1974).
22. G. H. Barry, Radio Sci. 9, 1025 (1974).
23. A. D. Stathacopoulos and G. H. Barry, Radio Sci. 9, 1021 (1974).
24. J. C. Haslett and L. R. Megill, Radio Sci. 9, 1005 (1974).
25. B. D. Fried and S. D. Conte, The Plasma Dispersion Function (Academic Press, New York, 1961).
26. A. Abramowitz and I. A. Stegun, Handbook of Mathematical Functions (Dover, New York, 1972).
27. V. L. Ginzburg, The Propagation of Electromagnetic Waves in Plasmas (Pergamon, Oxford, 1970).
28. M. V. Goldman, University of Colorado, Astro-Geophysics Report #1010 (1974).
29. T. M. Apostol, Calculus (Blaisdell, Waltham, Mass., 1967).
30. N. J. Peacock, Proceedings of the Third International Conference on Plasma Physics and Controlled Nuclear Fusion Research, Novosibirsk, U.S.S.R. 2, 51 (1968).
31. N. J. Peacock, Air Force Weapons Laboratory Report AFWL-TR-73-147, Kirtland AFB, New Mexico (1973).
32. N. J. Peacock, M. G. Hobby, and P. D. Morgan, Proceedings of the Fourth International Conference on Plasma Physics and Controlled Nuclear Fusion Research 1, 537 (1971).
33. N. G. Denkov, Soviet Physics, JETP 4, 544 (1957).
34. D. A. Tidman, Phys. Rev. 117, 366 (1960).
35. J. P. Friedberg, R. W. Mitchell, R. L. Morse, and L. I. Rudzinski, Phys. Rev. Lett. 28, 795 (1972).
36. K. Nishikawa, J. Phys. Soc. Japan 24, 1152 (1968).

37. N. J. Peacock, M. J. Forrest, P. D. Morgan, M. V. Goldman, T. Rudolph, and A. A. Offenberger, *Journal de Physique* 38, C6-43 (1977).
38. N. J. Peacock, M. J. Forrest, M. V. Goldman, T. Rudolph, P. D. Morgan, K. Kuriki, and A. A. Offenberger, *Proceedings of the Sixth International Conference on Plasma Physics and Controlled Nuclear Fusion Research*, 1976.
39. D. E. Potter, *Phys. Fluids* 14, 1911 (1971).
40. W. L. Kruer and E. J. Valeo, *Phys. Fluids* 16, 675 (1973).
41. D. F. DuBois and M. V. Goldman, *Phys. Rev. Lett.* 28, 218 (1972).
42. M. V. Goldman and D. F. DuBois, *Air Force Weapons Laboratory Report AFWL-TR-72-101*, Kirtland AFB, New Mexico (1972).
43. D. F. DuBois and M. V. Goldman, *Phys. Fluids* 15, 919 (1972).
44. R. Z. Sagdeev and A. A. Galeev, *Nonlinear Plasma Theory* (Benjamin, New York, 1969).
45. E. J. Valco, *Phys. Rev. Lett.* 28, 340 (1972).
46. W. L. Kruer, *Advances in Plasma Physics* 6, 237 (1976).
47. R. G. Bartle, *The Elements of Real Analysis* (Wiley and Sons, New York, 1964).
48. D. V. Widder, *Advanced Calculus* (Prentice-Hall, Inc., Englewood Cliffs, N.J., 1961).

EFFECTS OF IMPURITY RADIATION
ON REVERSED-FIELD PINCH EVOLUTION

by

Edward James Caramana

S.B., Massachusetts Institute of Technology, 1971

M.S., University of Colorado, 1975

A thesis submitted to the faculty of the Graduate
School of the University of Colorado in partial
fulfillment of the requirements for the degree of

Doctor of Philosophy

Department of Physics and Astrophysics

1979

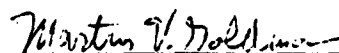
This Thesis for the Doctor of Philosophy Degree by

Edward James Caramana

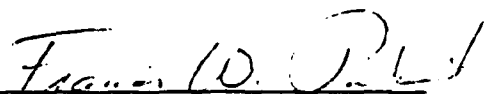
has been approved for the

Department of
Physics and Astrophysics

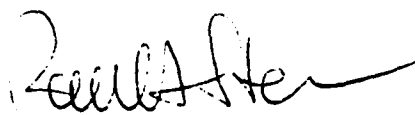
by



Martin V. Goldman



Francis W. Perkins



Raul A. Stern

Date 25 October 1979

Caramana, Edward James (Ph.D., Physics)

Effects of Impurity Radiation on Reversed-Field Pinch
Evolution

Thesis directed by Professor Martin V. Goldman

We study the effects of impurity radiation on the evolution of a reversed-field pinch plasma by means of a one-dimensional MHD simulation code that includes both plasma transport and impurity effects, and follows the plasma through a series of equilibrium states. The equations are split into two sets, one that contains plasma transport and another that contains atomic physics effects. Two codes were developed and linked together to solve the full problem.

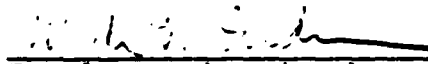
Results are presented for the ZT-S, ZT-40, and RFX experiments with a fixed set of parameters, typical or envisioned, and various concentrations of impurities. Radiation barriers are encountered, and limits are found on the acceptable level of low Z impurities that may be present in these devices. It is shown that the temperatures currently observed in the ZT-S experiment are radiation limited. Next, a criterion for radiation barrier burn-through is derived in terms of appropriate nondimensional parameters and calibrated by comparison to the numerical simulations for the case of oxygen.

In addition, the subject of thermal instability in the reversed-field pinch is explored. Namely, a current carrying plasma can become thermally unstable due to

current diffusion into regions of low resistivity, which through ohmic heating, leads to a lower resistivity feeding an instability. This instability is studied for the case of a reversed-field pinch in a nearly force-free equilibrium, after the formation phase, as the plasma attempts to ohmically heat to a significant beta. Two cases, stationary electron temperature (where impurity radiation balances ohmic heating), and nonstationary electron temperature are considered. It is found that fine-scale current perturbations remaining from the formation phase can be greatly enhanced by the presence of impurity cooling. The theory of these phenomena is developed analytically and compared to numerical simulation.

This abstract is approved as to form and content. I recommend its publication.

Signed


Faculty member in charge of thesis

ACKNOWLEDGMENTS

I wish to thank my thesis advisor Dr. Francis Perkins for his aid and guidance over the past three years, without which this work would not have been possible. I wish to thank Dr. Martin Goldman for introducing me to the reversed-field pinch concept, for starting my work in this field, and for his support of my efforts since this time. I want to express my gratitude to both Rip and Marty for making it possible for me to spend two years as a visiting graduate student in the Department of Astrophysical Sciences at Princeton University, which was a most rewarding and productive experience. For the two summers that I spent with the reversed-field pinch group at the Los Alamos Scientific Laboratory I wish to thank Dr. Don Baker and the members of CTR Division for their hospitality and stimulating discussions.

I dedicate this thesis to my family: to my wife Christina for her patience and support throughout the course of this work, to my daughter Cynthia for her vivaciousness and the joy she has brought during the past year, to my mother Louise Caramana for the influence she has had upon my life, and to the memory of my father James Caramana who always encouraged my study of science and would have been very proud to have seen me complete this degree.

TABLE OF CONTENTS

CHAPTER	PAGE
1. INTRODUCTION	1
2. EQUATIONS	4
2.1 Transport Model Equations	4
2.2 Radiation Model Equations	8
2.2.1 Atomic Physics	9
2.3 Poloidal Flux Coordinate System	11
2.4 Transport Model Equations in Lagrangian Form	12
2.4.1 Boundary Conditions	16
2.5 Radiation Model Equations in Lagrangian Form	17
2.6 Summary of the Physics Model	18
3. RESULTS FOR POINT CASES	20
3.1 Results for ZT-S	23
3.2.1 Results for ZT-40	28
3.2.2 Oxygen Plus Aluminum	32
3.3 Results for RFX	35
3.4 Stability of Point Cases	37
4. SCALING OF RFP DEVICES	41
5. THERMAL INSTABILITY IN THE RFP	49
5.1 Physical Considerations	49
5.2 Derivation of the Thermal Instability .	54
5.3 Nonstationary Electron Temperature . .	61

	PAGE
5.3.1 Numerical Simulation	64
5.3.2 Saturation of the Instability .	70
5.3.3 Anomalous Transport	73
6. CONCLUSION	75
REFERENCES	79
APPENDIX: The Numerical Solution of the Multi-Fluid, Quasi-Equilibrium MHD Equations in One Dimension	81

LIST OF FIGURES

FIGURE		PAGE
1.	Initial profiles for ZT-S, ZT-40, and RFX . .	21
2.	ZT-S magnetic field profiles.	24
3.	ZT-5 results with oxygen as an impurity distributed as a constant fraction of the hydrogen density	25
4.	ZT-S results with oxygen as an impurity distributed uniformly in space	29
5.	ZT-40 results with oxygen as an impurity . .	30
6.	ZT-40 results with both oxygen and aluminum as impurities	34
7.	RFX results with oxygen as an impurity . . .	36
8.	The pitch and electron temperature in ZT-40 as a function of radius and time in the absence of impurities	38
9.	The pitch and electron temperature in RFX as a function of radius and time in the absence of impurities	39
10.	The ZT-S, ZT-40, and RFX results are given in terms of nondimensional variables	43
11.	An oxygen radiation barrier burn-through criterion is shown	47
12.	The cooling rate of oxygen as a function of temperature	52

13. The parallel current and the electron temperature are given as a function of radius for the stationary zeroth order electron temperature case 60
14. The parallel current and the electron temperature are given as a function of radius for the non-stationary zeroth order electron temperature case with a 2.5 cm wavelength perturbation in the current and a uniform plasma density of $1 \times 10^{14} \text{ cm}^{-3}$. . . 66
15. The parallel current and the electron temperature are given as a function of radius for the non-stationary zeroth order electron temperature case with a 4 cm wavelength perturbation in the current and a uniform plasma density of $1 \times 10^{14} \text{ cm}^{-3}$. . . 67
16. The parallel current and the electron temperature are given as a function of radius for the non-stationary zeroth order electron temperature case with a 2.5 cm wavelength perturbation in the current and a uniform plasma density of $4 \times 10^{14} \text{ cm}^{-3}$ 69
17. The parallel current, electron temperature, and ion temperature are shown as a function of radius at four different times 72

CHAPTER 1

INTRODUCTION

The reversed-field pinch (RFP) is a promising approach to controlled fusion that has received considerable attention in recent years. It is an axisymmetric toroidal device that has demonstrated theoretically and experimentally MHD stable plasma confinement at the relatively high beta of 30-40%.^(1,2) It has roughly equal poloidal and toroidal magnetic fields which provide the shear that permits MHD stable operations at current densities substantially above the Kruskal-Shafranov limit. Hence, in comparison to the tokamak the RFP has a large toroidal current and the potential to reach fusion temperatures with ohmic heating alone. Therefore the RFP is attractive as a possible fusion reactor.

Unfortunately, recent RFP experiments such as ZT-S⁽³⁾ HBTX-1,⁽⁴⁾ and ETA-BETA⁽⁵⁾ have not been able to fully realize this potential. These experiments are relatively small (~7cm minor radius), use field programming to set up the reversed toroidal field and operate at relatively high densities ($1 \times 10^{15} \text{ cm}^{-3}$). Their main difficulty is a very low electron temperature (30 ev in ZT-S), seemingly due to energy loss caused by radiation from low Z plasma impurities, principally oxygen.

The high particle density in these experiments offsets the advantage of high current density by lowering the Ohmic heating rate per particle and by increasing the radiation loss rate, which for a fixed impurity concentration is proportional

to the square of the electron density. In addition, measurements of oxygen impurities in ZT-S show a concentration of .3% - 1% relative to deuterium ($2 \times 10^{15} \text{ cm}^{-3}$).⁽⁶⁾ This is a higher density of oxygen than is observed in tokamaks and in conjunction with the high electron density may explain why RFP experiments encounter a low temperature radiation barrier and tokamaks do not.

At the low temperatures currently observed in these devices, the transport of particles and magnetic fields in the post-implosion phase, where magnetic forces and pressure gradients are in magnetohydrostatic equilibrium, can be explained by classical coefficients. The discharge terminates because the initially stable magnetic field profiles diffuse to unstable ones on the classical diffusion time.⁽⁷⁾ Whether the transport remains classical at temperatures of a few hundred electron volts is unknown. Hence, it is imperative that future RFP experiments, such as ZT-40 and RFX, overcome low temperature radiation barriers so that the potential of this concept can be fully explored, and anomalous transport processes, if any, identified.

It is the purpose of this paper to study theoretically some of the effects of impurities in the RFP with numerical and analytical methods. We have developed a computer code based on the equations of MHD, which includes both transport and radiation effects in the post-implosion phase, to simulate existing RFP experiments and to predict results for

future ones. This code enables us to normalize analytical treatments of radiation barrier burn-through and thermal instability.

Section 2 presents the physics model used in the numerical computations; section 3 presents results for typical operating parameters of ZT-S, ZT-40, and RFX with various concentrations of impurities. Section 4 develops a general criterion, in terms of nondimensional parameters, for whether a RFP will burn through a radiation barrier. This criterion is normalized by comparison with numerical results for the case of oxygen. Section 5 discusses the subject of thermal instabilities in the RFP. We find an instability due to the coupling of current diffusion and Ohmic heating. This instability was first derived by Kadomtsev, who calls it the "Superheating Instability."⁽⁸⁾ He assumed a uniform magnetic field, small current and a stationary zeroth order temperature that is the same for electrons and ions. We remove these restrictions and develop the theory of this instability in the post-implosion phase of the RFP, in cylindrical geometry, for both stationary and evolving zeroth order electron and ion temperatures.

The importance of impurities in creating fine-scale current density and temperature gradients in RFP's is demonstrated.

CHAPTER 2

EQUATIONS

Our basic approach to investigating the combined effects of impurity radiation and classical resistive diffusion on the evolution of plasma and magnetic field profiles in the RFP is to split the problem into two parts. The resistive diffusion is governed by the two fluid MHD equations given by Braginskii.⁽⁹⁾ Our computations of impurity radiation rests on a multifluid MHD model which provides heat sink terms in the electron temperature equation but is otherwise ideal. Electrons, deuterium ions, and each charge state of an impurity species are modelled as separate fluids. These two sets of equations taken together define our complete physical model.

Both sets of equations are transformed to a Lagrangian coordinate system based on a normalized poloidal flux coordinate. The dependent variables are changed to quantities that remain invariant during adiabatic motion of the plasma. This representation of the equations is useful for both numerical and analytical work.

2.1. Transport Model Equations

Starting with the full two fluid MHD equations in Ref (9), we assume that the plasma evolves in time through a series of equilibrium states. This is equivalent to ordering the resistivity, velocity, and the time derivative of any quantity as a small number ϵ and then neglecting terms of order ϵ^2 . Thus the inertia and all terms arising from the plasma

viscosity are neglected. This yields a set of equations valid on the resistive diffusion time scale and is equivalent to ordering the velocity small in comparison to the Alfvén speed. Cylindrical geometry and symmetry is assumed so that all quantities vary only in the radial direction. With these approximations the equations become:

$$\frac{\partial n}{\partial t} + \vec{v} \cdot (\vec{v}n) = 0 \quad , \quad (1)$$

$$\frac{\partial B_\theta}{\partial t} + \frac{\partial}{\partial r} (V_r B_\theta - \frac{cR_z}{en}) = 0 \quad , \quad (2)$$

$$\frac{\partial B_z}{\partial t} + \frac{1}{r} \frac{\partial}{\partial r} r (V_r B_z + \frac{cR_\theta}{en}) = 0 \quad , \quad (3)$$

$$\frac{3}{2} \frac{\partial}{\partial t} nT_e + \frac{3}{2} \vec{v} \cdot \vec{v} nT_e + nT_e \vec{v} \cdot \vec{v} = -\vec{v} \cdot \vec{q}_e + \frac{\vec{R} \cdot \vec{j}}{en} - Q_i \quad , \quad (4)$$

$$\frac{3}{2} \frac{\partial}{\partial t} nT_i + \frac{3}{2} \vec{v} \cdot \vec{v} nT_i + nT_i \vec{v} \cdot \vec{v} = -\vec{v} \cdot \vec{q}_i + Q_i \quad , \quad (5)$$

$$\frac{\partial p}{\partial r} = \frac{-1}{4\pi} [B_z \frac{\partial}{\partial r} B_z + \frac{B_\theta}{r} \frac{\partial}{\partial r} r B_\theta] \quad , \quad (6)$$

where $p = n(T_e + T_i)$, $\vec{R} = \vec{R}_u + \vec{R}_T$ is the total force between electrons and ions due to friction \vec{R}_u and temperature gradient \vec{R}_T , \vec{q}_e and \vec{q}_i are the electron and ion heat fluxes respectively, Q_i is the electron-ion equilibration term, and \vec{j} is the current.

$$\vec{R}_U = en\eta_n \vec{j}_n + en\eta_i \vec{j}_i$$

$$\vec{R}_T = \beta_A^{UT} \vec{v}_T \times \frac{\vec{B}}{|B|}$$

$$\vec{q}_e = -\chi_1^e \frac{\partial T_e}{\partial r} \hat{r} + \beta_A^{UT} \frac{cT_e}{en|B|} \frac{\partial B}{\partial r} \hat{r}$$

$$\vec{q}_i = -\chi_1^i \frac{\partial T_i}{\partial r} \hat{r}$$

$$Q_i = \frac{3m_e n}{M \tau_e} (T_e - T_i)$$

$$\vec{j} = \frac{c}{4\pi} \vec{v} \times \vec{B}$$

For the resistivity η , the thermal conductivity χ , and the thermoelectric coefficient β_A^{UT} , the classical values in the strong field limit are assumed,

$$\eta_n = \frac{.513 m_e}{e^2 n \tau_e} ,$$

$$\eta_i = \frac{m_e}{e^2 n \tau_e} ,$$

$$\chi_1^e = \frac{4.66 n^2 T_e c^2}{B^2} \eta_i ,$$

$$\chi_1^i = \frac{2nT_i}{M \omega_{ci} \tau_i}$$

$$\beta_A^{UT} = \frac{3}{2} \frac{en^2 c}{B} \eta_i ,$$

where $\omega_{ci} = eB/MC$. The electron and ion collision times, τ_e and τ_i , are,

$$\tau_e = \frac{3m_e^{1/2} T_e^{3/2}}{4(2\pi)^{1/2} \lambda e^4 n}$$

$$\tau_i = \frac{3m_i^{1/2} T_i^{3/2}}{4(2\pi)^{1/2} \lambda e^4 z^2 n}$$

and λ is the Coulomb logarithm.

In our model we assume that the plasma extends to the vacuum chamber wall at radius a , and that there may be a conducting wall at a larger radius b . The region between these two radii is a magnetic flux reservoir.

The boundary conditions at the plasma edge on Eqs.

(1) - (6) are the electric fields E_z and E_θ calculated from values given at the conducting wall and specified "pedestal" values for n , T_e , and T_i . The electric field is not only the natural quantity to use as a boundary condition when magnetic flux is a variable, but also the quantity controlled by external circuits. Magnetic flux variables occur in the Lagrangian representation of these equations.

The origin is an artificial boundary due to the use of cylindrical coordinates. Here we require there be no flux of any quantity.

2.2. Radiation Model Equations

An ideal MHD model, which includes all radiation effects and treats every charge state of a given impurity species as a separate fluid, is now presented. There is adiabatic expansion and contraction of the plasma but no transport. The equations describing this model are given for one impurity species of charge Z . The extension to more than one impurity species is obvious.

$$n_e = n_i + \sum_{j=1}^{Z+1} (j-1)n_j, \quad (7)$$

$$\frac{\partial n_i}{\partial t} + \vec{v} \cdot \vec{\nabla} n_i = 0, \quad (8)$$

$$\frac{\partial n_j}{\partial t} + \vec{v} \cdot \vec{\nabla} n_j = n_e [n_{j-1} \beta_{j-1} - n_j (\beta_j + \alpha_j) + n_{j+1} \alpha_{j+1}], \quad (9)$$

$$\frac{\partial \vec{B}}{\partial t} - \vec{v} \times (\vec{v} \times \vec{B}) = 0, \quad (10)$$

$$\frac{3}{2} \frac{\partial n_e T_e}{\partial t} + \frac{3}{2} \vec{v} \cdot \vec{\nabla} n_e T_e + n_e T_e \vec{v} \cdot \vec{\nabla} = n_e \sum_j n_j A_j, \quad (11)$$

$$\frac{3}{2} \frac{\partial n_i T_i}{\partial t} + \frac{3}{2} \vec{v} \cdot \vec{\nabla} n_i T_i + n_i T_i \vec{v} \cdot \vec{\nabla} = 0, \quad (12)$$

$$\vec{v}_p = \frac{1}{c} \times \vec{B} \quad (p = n_e T_e + n_i T_i + T_i \sum_j n_j), \quad (13)$$

where,

α_j = coefficient for recombination from state
j to j-1 ($\alpha_1 = 0$),

β_j = coefficient for ionization from state j - 1 to
j ($\beta_{Z+1} = 0$).

A_j is the energy loss rate per electron per impurity ion of charge j+1 due to excitation and recombination radiation and bremsstrahlung. It does not currently include the energy loss from electrons due to the ionization potential of the impurity. This energy is generally small compared to the energy lost by radiation during the ionization process, but it will be included in future work. All ion species have been assumed to have the same temperature. ⁽¹⁰⁾

The boundary condition imposed on this set of equations is that the electric field, and thus the radial velocity, vanish at the vacuum chamber wall. Consequently, there is no flux of any quantity at $r = a$.

2.2.1. Atomic Physics

For the range of operating densities ($n < 2 \times 10^{15} \text{ cm}^{-3}$) and time scales ($t > 10 \text{ ns}$) relevant to RFP experiments, the time-dependent coronal atomic physics model is valid. ^(11,12,13) In this model, ionization and excitation occur by the collision of an electron with an atom or ion in its ground state; recombination is to the ground state by means of radiative and dielectric recombination; de-excitation is due to spontaneous emission and occurs on a time scale short compared

to all other processes. This model ignores collisional recombination, collisional de-excitation, photo-ionization, and photo-excitation.

It is assumed that all radiation is lost from the plasma. This is true even if the plasma is not optically thin (though RFP's are generally optically thin), provided that the collisional de-excitation time is sufficiently long. (13)

The ionization and recombination coefficients and radiation loss rates are obtained, for an arbitrary element, from an atomic physics code developed by Dr. Russell Hulse. This code utilizes generalized formulae given in Ref. (14). For each ionic species of the element under consideration, it calculates energy levels, oscillator strengths, and transition energies. The generalized formulae for the rates of electron collisional ionization, radiative recombination, and dielectronic recombination are evaluated for each species using these oscillator strengths and energies together with the given plasma density and electron temperature. Similarly, radiation rates are computed for each ionic species, including excitation of $\Delta n = 0$ and $\Delta n \neq 0$ line transitions, radiation associated with the recombination processes, and bremsstrahlung.

2.3. Poloidal Flux Coordinate System

The two sets of equations (1) - (6) and (7) - (13) must be solved numerically, but are not in a convenient form for numerical solution because the velocity in these equations is determined indirectly by the magnetohydrostatic equilibrium constraint. By transforming to a Lagrangian coordinate system and by changing the dependent variables to adiabatic invariant quantities, this velocity can be eliminated and the equations so obtained can be directly advanced in time.

Our Lagrangian coordinate system is defined by:

$$X(r,t) = \int_0^r \chi(r',t) dr', \quad \frac{\partial \chi}{\partial t} + \frac{\partial}{\partial r} V\chi = 0 \quad (14a,b)$$

$$\frac{\partial}{\partial t_L} = \frac{\partial}{\partial t} + V \frac{\partial}{\partial r}, \quad \frac{\partial r}{\partial t_L} = V \quad (14,c,d)$$

where $\frac{\partial}{\partial t_L}$ is the Lagrangian time derivative and

$$\chi = \frac{B_\theta}{\phi_{PT}}, \quad \phi_{PT}(t) = \int_0^a B_\theta(r,t) dr,$$

$$V = V_r - \frac{cR_z}{enB_\theta} + \frac{F(t)}{E_\theta} + \frac{X}{B_\theta} \frac{\partial \phi_{PT}}{\partial t},$$

$$F(t) = \frac{cR_z}{en} (r = 0, t),$$

$$\frac{\partial \phi_{PT}}{\partial t} = cE_z(r = a, t) - F.$$

$X(r,t)$ is the Lagrangian coordinate defined as the poloidal flux at a given radius divided by the total poloidal flux ϕ_{PT} in the system at any given time. V is the velocity followed in the Lagrangian frame. It contains a term F/B_θ that is a consequence of poloidal flux destruction at the origin, and another term $\frac{X}{B_\theta} \frac{\partial \phi_{PT}}{\partial t}$, that is due to normalizing B_θ by ϕ_{PT} in the definition of X . Physically, this latter term relabels the dependent variables so that the domain of the independent variable X remains $0 \leq X \leq 1$.

For this transformation to be valid, $V(r = 0, t)$ must equal zero. This requires that n , T_e , and j_z be parabolic near the origin, a result that follows from the diffusive nature of the equations.

2.4. Transport Model Equations in Lagrangian Form

Equations (1) - (6) are transformed in nondimensional form to the Lagrangian coordinate system defined by Eqs. (14). Let us define a reference poloidal flux ϕ_0 , temperature T_0 , and length a (vacuum wall radius) and construct a reference resistivity η_0 , time τ_0 , and density n_0 from the relations

$$\eta_0 = \frac{4(2\pi)^{1/2}}{3} \frac{m_e^{1/2} e^2}{T_0^{3/2}} \lambda(T_0), \quad \tau_0 = \frac{\pi a^2}{c^2 \eta_0},$$

$$s_0 = \frac{8\pi n_0 T_0 a^2}{\phi_0^2} = 1.$$

Then the nondimensional time τ and resistivity $\tilde{\eta}$ are $\tau = \frac{t}{\tau_0}$ and $\tilde{\eta} = \frac{\eta}{\eta_0}$.

We choose $Y(X,t) = r^2/a^2$ as the radial coordinate. Then from Eqs. (14) $Y' \equiv \frac{\partial Y}{\partial X} = \frac{2r\dot{\phi}_0}{a^2 B_e}$ (where $\phi = \phi_{PT}/\phi_0$) is the nondimensional volume per normalized poloidal flux. This is used to construct new dependent variables. In place of the Eulerian variables B_z, n, T_e , and T_i we define:

$$P = \frac{aB_z}{2\phi_0} Y', \quad (15a)$$

$$N = \frac{n_e}{2n_0} Y', \quad (15b)$$

$$\theta_e = \frac{T_e}{T_0} Y'^{2/3}, \quad (15c)$$

$$\theta_i = \frac{T_i}{T_0} Y'^{2/3}, \quad (15d)$$

P is the toroidal flux per normalized poloidal flux or the pitch of a field line, an important quantity in considering the MHD stability of the RFP. ⁽¹⁵⁾ N is the number density per normalized poloidal flux; θ_e and θ_i are a measure of the electron and ion entropy per particle respectively. Using these variables, one can recast equations (1) - (6) into a pitch equation

$$\frac{\partial P}{\partial \tau} = \frac{\partial}{\partial X} \left[\left(\frac{X\dot{\phi}}{\phi} + \frac{f}{\phi} - \frac{\tilde{n}_n}{Y'} \right) P + \frac{\tilde{n}_n Y}{Y'^2} \frac{\partial P}{\partial X} \right], \quad (16)$$

and a density equation

$$\frac{\partial N}{\partial \tau} = \frac{\partial}{\partial Y} UN, \quad (17)$$

where

$$U = \frac{X\phi}{\phi} + \frac{f}{\phi} + \frac{\tilde{n}_n y^2 p}{y'^2 (p^2 + y\phi^2)} \frac{\partial}{\partial X} \left(\frac{p}{y'} \right) +$$

$$\frac{\tilde{n}_1 y}{4(p^2 + y\phi^2)} \left[\frac{\partial}{\partial X} \frac{N(\theta_e + \theta_i)}{y'^{5/3}} - \frac{3N}{2y'} \frac{\partial}{\partial X} \left(\frac{\theta_e}{y'^{2/3}} \right) \right].$$

The electron temperature equation becomes

$$\frac{\partial \theta_e}{\partial \tau} = \frac{\partial}{\partial X} U \theta_e - \frac{1}{3} \theta_e \frac{\partial U}{\partial X} + \frac{y'^{2/3}}{6N} \frac{\partial}{\partial X} \left\{ \frac{\tilde{n}_1 y \phi_e}{y' (p^2 + y\phi^2)} \right.$$

$$\times \left[4.66N^2 \frac{\partial}{\partial X} \frac{\theta_e}{y'^{2/3}} - \frac{3}{2} y' N \frac{\partial}{\partial X} \frac{N(\theta_e + \theta_i)}{y'^{5/3}} \right] \Bigg\} \quad (18)$$

$$- \Lambda \tilde{n}_1 \frac{N(\theta_e - \theta_i)}{2y'} + \frac{8\phi^2 \tilde{n}_n y'^{5/3}}{(p^2 + y\phi^2)N} \left(\frac{y'}{y'} \right)^4 \left[\frac{\partial}{\partial X} \left(\frac{p}{y'} \right) \right]^2$$

$$+ \frac{\tilde{n}_1 y y'^{5/3}}{6N(p^2 + y\phi^2)} \left[\frac{\partial}{\partial X} \frac{N(\theta_e + \theta_i)}{y'^{5/3}} \right]^2$$

$$- \frac{\tilde{n}_1 y y'^{2/3}}{4(p^2 + y\phi^2)} \left[\frac{\partial}{\partial X} \frac{\theta_e}{y'^{2/3}} \right] \left[\frac{\partial}{\partial X} \frac{N(\theta_e + \theta_i)}{y'^{5/3}} \right],$$

the ion temperature equation is

$$\frac{\partial \theta_i}{\partial \tau} = \frac{\partial}{\partial X} U \theta_i - \frac{1}{3} \theta_i \frac{\partial U}{\partial X} + \frac{\Lambda \tilde{n}_1 N(\theta_e - \theta_i)}{2y'} \quad (19)$$

$$+ \frac{1}{3} \left(\frac{M}{m} \right)^{1/2} \frac{y'^{2/3}}{N} \left[\frac{\partial}{\partial X} \left(\frac{y' N^2}{\theta_i^{1/2} y'^{2/3} (p^2 + y\phi^2)} \right) \frac{\partial}{\partial X} \frac{\theta_i}{y'^{2/3}} \right],$$

and the magnetohydrostatic equilibrium equation takes the form

$$\frac{\partial^2 y}{\partial X^2} = y' \left[\frac{\frac{\partial}{\partial X} (P^2 + 2y\phi^2) + \frac{1}{2} y'^{1/3} \frac{\partial}{\partial X} N(\theta_e + \theta_i)}{2(P^2 + y\phi^2) + 5/6 y'^{1/3} N(\theta_e + \theta_i)} \right]. \quad (20)$$

The net rate of change of the normalized poloidal flux $\dot{\phi}$ is determined by $\dot{\phi} = \epsilon_z - f$, where ϵ_z and f are the nondimensional z electric fields at the plasma edge and at the origin respectively,

$$f = (\phi \tilde{n}_n / y') \quad x = 0$$

In the electron-ion equilibration term,

$$\Lambda = \phi_0^2 e^2 / T_0 M c^2$$

is the square of the plasma radius divided by the reference ion gyroradius.

Unlike Eqs. (1) - (6), Eqs. (16) - (20) can be directly advanced in time. First P, N, θ_e, θ_i and ϕ are advanced; then equation (20) can be solved for the new equilibrium $y(X, t)$. In addition, equations (16) - (20) display the physics more clearly than did their Eulerian counterparts. For instance, the pitch P depends only on the parallel electric field $n_n j_n$, and the current \vec{j} has been resolved into its parallel ($j_n = \partial/\partial r B_z / r B_\theta = \partial/\partial x P/y$) and perpendicular ($j_\perp = \frac{\partial p}{\partial r} \sim \frac{\partial}{\partial x} N(\theta_e + \theta_i)$) components rather than along the θ and z directions, which have no physical significance.

2.4.1. Boundary Conditions

The boundary condition on Eqs. (16) - (19) at $x = 0$ is that the flux of P, N, θ_e and θ_i vanish, which is automatically satisfied by the definition of f .

The pedestal values of density and temperature, specified at the wall for Eqs. (1) - (6), become for Eqs. (16) - (20),

$$\left(\frac{N}{Y}\right)_{x=1} = \text{const.}, \quad (21a)$$

$$\left(\frac{\theta_e}{Y^{2/3}}\right)_{x=1} = \text{const.}, \quad (21b)$$

$$\left(\frac{\theta_i}{Y^{2/3}}\right)_{x=1} = \text{const.} \quad (21c)$$

The z electric field is specified at the plasma edge $\epsilon_z(x=1)$, and along with f determines $\dot{\phi}$, which enters as a convective term in Eqs. (16-19). The boundary condition on the pitch equation (16) at $x=1$ is the poloidal electric field ϵ_θ . Given the poloidal electric field at the conducting wall V_θ , ϵ_θ at the plasma edge can be expressed solely in terms of plasma quantities. This yields a time dependent boundary condition for the pitch equation at $x=1$

$$V_\theta + \left(\frac{b^2}{a^2} - 1\right) \frac{\partial P}{\partial \tau} = - \epsilon_z P - \frac{\tilde{n}_e y^2}{Y^{2/3}} \frac{\partial}{\partial X} \left(\frac{P}{Y}\right). \quad (22)$$

The boundary condition on the magnetohydrostatic equilibrium equation (20) at $x=0$ and at $x=1$ is

$$Y(x=0) = 0 \quad , \quad Y(x=1) = 1 \quad . \quad (23a,b)$$

2.5. Radiation Model Equations in Lagrangian Form

In the Lagrangian coordinate system defined by Eq. (14) the radiation model equations (7)-(13) become in nondimensional form,

$$N_e = N_i + \sum_{j=1}^{Z+1} (j-1)N_j \quad (24)$$

$$\frac{\partial N_i}{\partial \tau} = 0 \quad (25)$$

$$\frac{\partial N_j}{\partial \tau} = \frac{N_e}{Y'} [N_{j-1} \tilde{s}_{j-1} - N_j (\tilde{s}_j + \tilde{\alpha}_j) + N_{j+1} \tilde{\alpha}_j] \quad (26)$$

$$\frac{\partial P}{\partial \tau} = 0 \quad (27)$$

$$\frac{\partial S_e}{\partial \tau} = \frac{N_e}{Y', 1/3} \sum_j N_j \tilde{A}_j \quad (28)$$

$$\frac{\partial S_I}{\partial \tau} = 0 \quad (29)$$

$$\frac{\partial^2 Y}{\partial X^2} = Y' \left[\frac{\frac{\partial}{\partial X} (P + 2Y\phi^2)}{2(P^2 + Y\phi^2)} + \frac{\frac{1}{2} Y', 1/3 \frac{\partial}{\partial X} (S_e + S_I)}{\frac{5}{6} Y', 1/3 (S_e + S_I)} \right] \quad (30)$$

where $N_j = \frac{2n_j}{n_0} Y'$, and $S_e = N_e \theta_e$, $S_I = N_i \theta_i + \theta_i \sum_j N_j$ are a measure of the electron and ion entropies respectively. α_j , β_j , and \bar{A}_j are the nondimensional form of α_j , s_j , and A_j defined previously.

Note that in the Lagrangian representation all of the radiation model equations have become ordinary differential equations. A convective velocity, common to all the plasma particle species and the magnetic fields, caused by radiation energy loss, has been explicitly eliminated!

2.6. Summary of the Physics Model

The multi-fluid MHD equations, where each charge state of an impurity is treated as a separate fluid and the plasma evolves through a series of equilibria, has been split into two independent and self-consistent sets. This decomposition was motivated by noticing that the velocity, determined by all dissipative processes, separates into two components, one which arises from plasma resistivity and another from atomic processes. The original set of equations is approximated by numerically solving the two simpler sets in succession.

In the transport model equations the impurity ions have been neglected; therefore, the number of ions is not the same in the two models. In successively solving these two sets of equations the electron and ion entropy and the electron density are kept constant to insure that the same

equilibrium is passed between the two models. When the transport model equations are advanced in time, the impurity density is held fixed in physical space. Impurity diffusion can be important and will be treated in future work.

Standard numerical techniques are used to solve both sets of equations, the details of which will be presented elsewhere. (16)

CHAPTER 3

RESULTS FOR POINT CASES

Results of the numerical solution of our physics model for various concentrations of impurities are presented for ZT-S, ZT-40, and RFX with a fixed set of parameters, typical or envisioned, for each experiment. The effect of oxygen, and also aluminum for ZT-40, on the electron and ion temperatures and the magnetic energy is studied.

The parameters chosen to simulate these experiments are given in Table 1. In Figure 1 the normalized pitch $P = \frac{rB_z}{aB_\theta}$ and the parallel current density $j_{||}$ versus r/a are shown at the initial time. The pitch is the same for all three cases. The parallel current density, given by the dashed line for ZT-S and ZT-40 and by the dash-dot line for RFX, has a 60% peak off axis corresponding to a current sheath in the early post-implosion phase. The hydrogen density is specified by a parabolic distribution which decreases from a maximum on axis to a value at the vacuum chamber wall of 5% of the on axis density (see Table 1). The initial electron and ion temperature is assumed to be uniform at 10 eV for all cases; the electric fields at the conducting wall are set to zero; the pedestal values of density and temperature at the vacuum chamber wall are given by their initial value or the value at the point next to the wall, whichever is less.

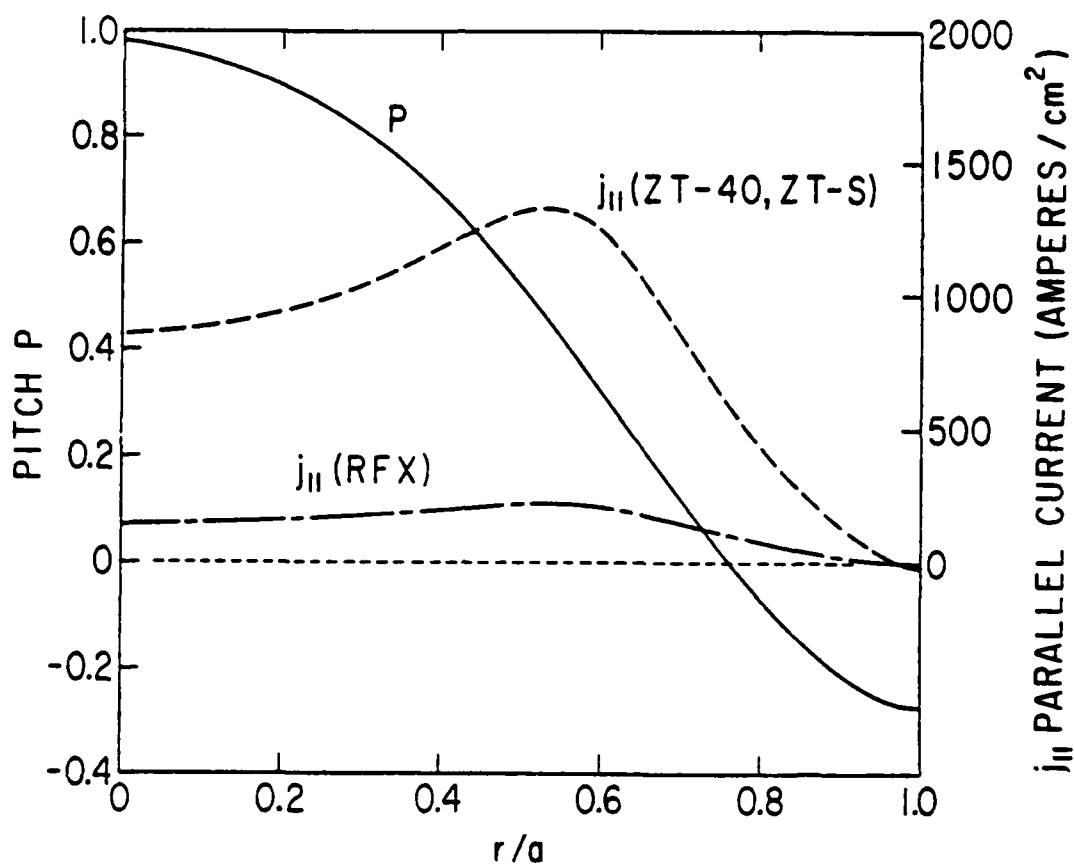


Figure 1

The initial pitch ($P = rB_z/aB_\theta$) and current profiles used in the simulations of ZT-S, ZT-40, and RFX are plotted as a function of r/a , the radius divided by the wall radius.

TABLE 1

	ZT - S	ZT - 40	RFX
Vacuum Wall Radius	7.7 cm	20 cm	60 cm
Conducting Wall Radius	7.9 cm	22 cm	63 cm
I_z Current	70 KA	500 KA	700 KA
Toroidal Field On Axis	4000 G.	10,500 G.	5100 G.
Density On Axis	$1 \times 10^{15} \text{ cm}^{-3}$	$5 \times 10^{14} \text{ cm}^{-3}$	$5 \times 10^{13} \text{ cm}^{-3}$
Initial Temperature	10 ev	10 ev	10 ev
Initial Beta	5.1 %	.38 %	.16 %

3.1. Results for ZT-S

In Fig. 2 is shown the B_z and B_θ fields for the ZT-S simulation at the initial time and at 35 μ s (the lifetime of a typical ZT-S discharge) for 0% and .4% oxygen.

For the impurity free case the total Z current ($-B_\theta(a)$) in the plasma at 35 μ s is greater (by about 5%) than the initial, even though the energy contained in the poloidal field has decreased. This is because the diamagnetic current created by ohmic heating has a substantial component along the Z direction in the central and outer regions of the plasma. The numerical simulations show this to be a characteristic feature of diffuse RFP profiles.

The degradation of the magnetic field profiles from enhanced ohmic heating due to low electron temperatures caused by radiation from oxygen impurities can also be seen in Fig. 2. At 35 μ s one third more magnetic energy has gone into ohmic heating in the .4% oxygen case than in the zero impurity case.

In Fig. 3(a), (b), and (c) results of ZT-S simulations are given for 0%, .2% and .4% oxygen impurity, distributed as a constant fraction of the hydrogen density ($1 \times 10^{15} \text{ cm}^{-3}$ on axis). In Fig. 3(a) the average electron temperature \bar{T}_e , defined as

$$\bar{T}_e = \frac{1}{n_L} \int_0^a 2\pi n T_e r dr$$

(where $n_L = \int_0^a 2\pi n r dr$ is the line density), is plotted as a function of time for these three cases. On the right-hand-

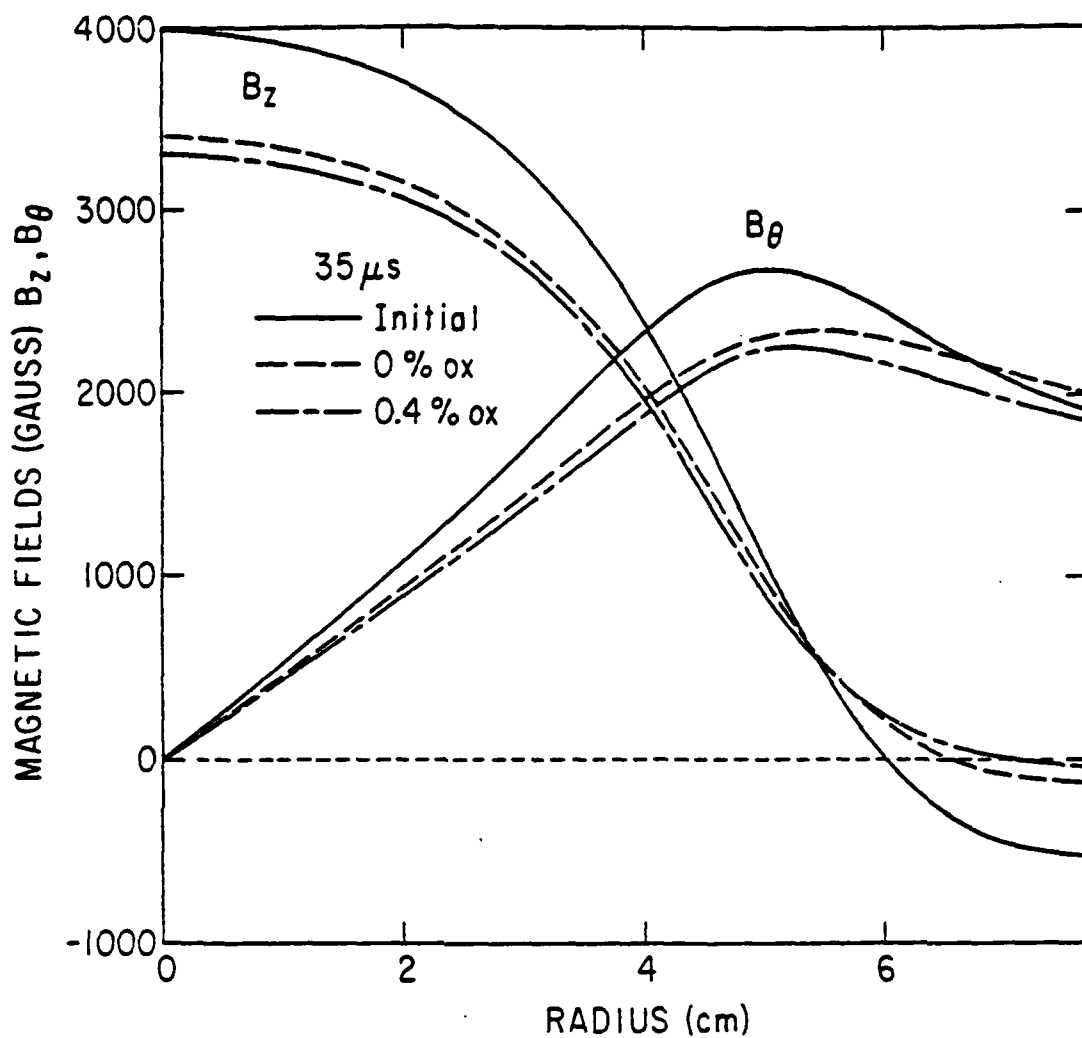


Figure 2

ZT-S magnetic field profiles. Solid curves: B_z and B_θ at the initial time; dashed curves: B_z and B_θ at 35 μ s with no impurity present; chain dash curves: B_z and B_θ at 35 μ s with an oxygen impurity concentration of .4% of the deuterium density ($1 \times 10^{15} \text{ cm}^{-3}$ on axis).

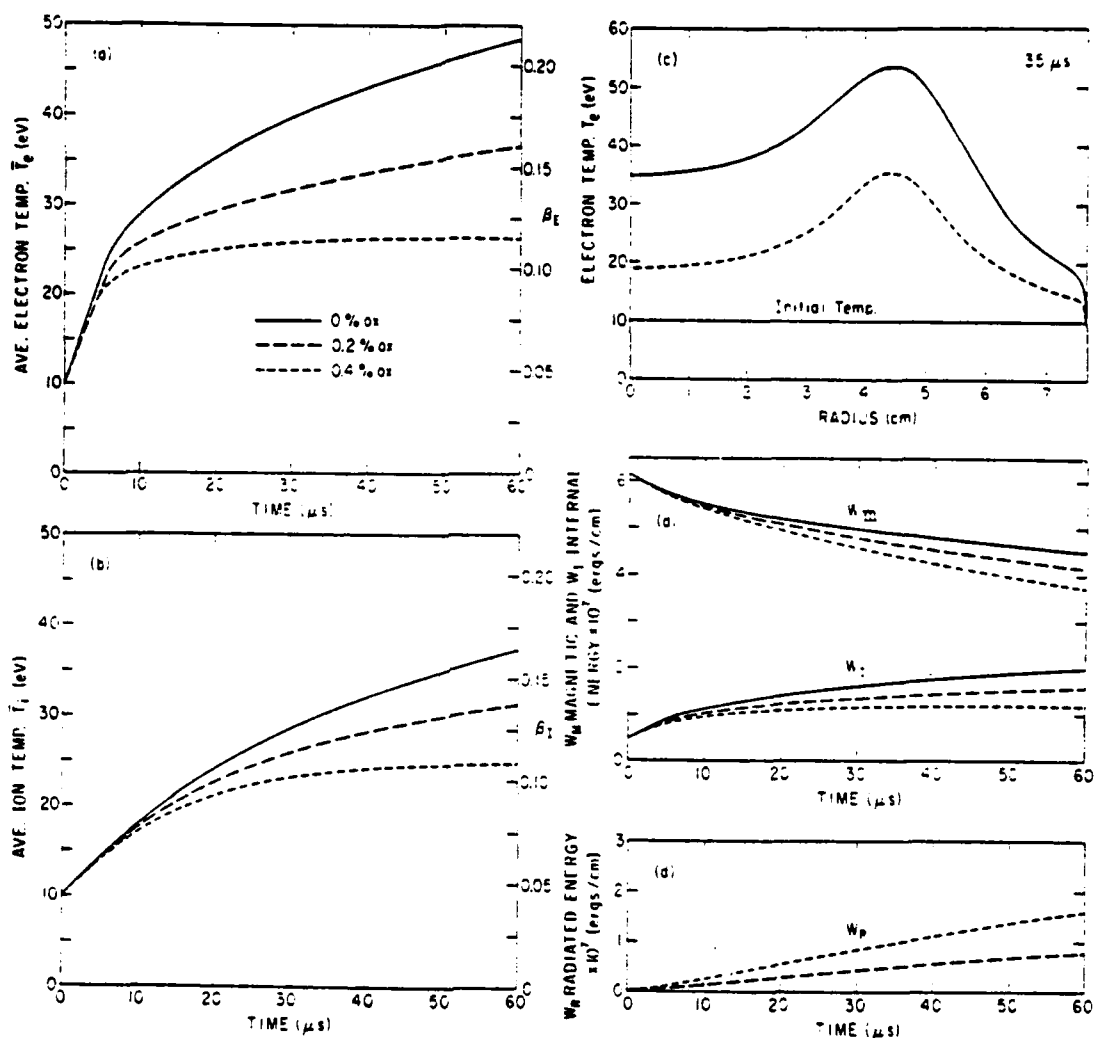


FIGURE 3

(a) The average electron temperature \bar{T}_e and β_e in ZT-S as a function of time with oxygen impurity concentrations of 0%, .2%, and .4% that of deuterium ($1 \times 10^{15} \text{ cm}^{-3}$ on axis). (b) The average ion temperature \bar{T}_i and β_i as a function of time. (c) The electron temperature as a function of radius at 35 μs for 0% and .4% oxygen impurity. The electron temperature at the initial time is a uniform 10 eV. (d) The magnetic energy W_m and internal energy W_i , and the total energy radiated W_R as a function of time for 0%, .2%, and .4% oxygen impurity.

side of Fig. 3(a) is labeled the nondimensional quantity β_E , defined as

$$\beta_E \equiv \frac{1}{W_p(0)} \int_0^a 2\pi n T_e r dr$$

where $W_p(0) = \int_0^a \frac{B_\theta^2}{4} (r,0) r dr$ is the poloidal magnetic energy at the initial time. β_E is a measure of the electron poloidal beta (also a nondimensional temperature) referenced to the initial poloidal magnetic energy. This energy is roughly the amount of magnetic energy available to ohmic heat the plasma. Analogous quantities \bar{T}_i and β_i , defined with respect to the ion temperature T_i , are given as a function of time in Fig. 3(b). In Fig. 3(d) the internal energy $W_I = \int_0^a 3\pi n (T_e + T_i) r dr$, the magnetic energy $W_M = \int_0^a (B_z^2 + B_\theta^2)/4r dr$, and the energy radiated until the current time $W_R = \int_0^t \int_0^a 2\pi n \sum_{j=1}^{z+1} n_j A_j r dr$ are plotted as a function of time for all three cases.

From Fig. 3(a) one sees that for the impurity free case T_e rises steadily in time but at a decreasing rate due to the $T_e^{-3/2}$ dependence of the resistivity. For .2% oxygen impurity \bar{T}_e also increases steadily but at a rate that is substantially less than the zero impurity case after the first 5-10 μ s. The 4% oxygen impurity case shows a radiation limited electron temperature for ZT-S. Here the average electron temperature rises rapidly from 10 eV to 24 eV in the first 10 μ s and then remains flat for the next 50 μ s. What we see is that after the first few microseconds the plasma encounters the oxygen radiation barrier which is sharply peaked at about 25 eV (See Fig. 12).

In Fig. 3(c) the electron temperature as a function of radius is shown at 35 μ s for the zero impurity and for the .4% oxygen impurity case. It is seen that the electron temperature remains between 20 eV and 30 eV nearly everywhere for the latter case. There is a temperature peak off axis due to the combined effect of the off axis current peak and the falling density.

Fig. 3(d) shows for the .4% oxygen case that although the internal plasma energy is constant after 10 μ s, the magnetic energy continues to decrease rapidly, appearing as radiation energy loss (the flux of energy at the plasma edge is small). At 35 μ s nearly 60% of the magnetic energy that has been converted into plasma energy has been lost to radiation. For the .2% oxygen case this number is reduced to 35%.

From Fig. 3(b) one sees that the average ion temperature is more nearly equilibrated with the average electron temperature for a higher concentration of impurity since the resistivity and thus the electron-ion equilibration rate is increased. The density profile for all cases remains relatively unchanged from its initial value, although the electron density increases somewhat due to impurity ionization.

All of this demonstrates that for a .4% oxygen concentration at $1 \times 10^{15} \text{ cm}^{-3}$ density the temperatures in the ZT-S experiment are very radiation limited. Since this amount of impurity is at the low range of the measured amount of oxygen in this device⁽⁶⁾ (.3%- 1% oxygen at $2 \times 10^{15} \text{ cm}^{-3}$ density), it is seen that ZT-S has not been able to operate in a regime where impurity radiation is not the principal physics effect.

The major uncertainty in the results leading to the above conclusion is the manner in which the oxygen impurity is spatially distributed. For instance, if all of the oxygen were concentrated very near the edge, the effect on the plasma could be slight. However, this is not expected since it is well known that for classical transport the impurity ions always diffuse preferentially toward the hydrogen maximum. (17)

To see what happens for a different spatial distribution of impurity, we show in Fig. 4 the average electron temperature as a function of time for oxygen distributed uniformly in space at a concentration of 0%, .2%, and .4% that of the line density. Fig. 4 shows the same qualitative behavior for \bar{T}_e as did Fig. 3(a). At 35 μ s there has been 30% less energy radiated by the .4% uniform oxygen density case. This is not significant enough to modify our above conclusion.

3.2.1. Results for ZT-40

ZT-40 simulations were performed for the operating parameters listed in Table 1 for both oxygen and aluminum as an impurity since this device has an aluminum oxide ceramic vacuum vessel. In Fig. 5 results are shown for 0%, .4%, .8%, and 1.6% oxygen impurity distributed as a constant fraction of the hydrogen density ($5 \times 10^{14} \text{ cm}^{-3}$ on axis). The first three cases are run to 1.5 ms and the last to 150 μ s.

In Figs. 5(a) and 5(b) the average electron and ion temperatures \bar{T}_e and \bar{T}_i are given as a function of time for these four cases. For the 1.6% oxygen case \bar{T}_e undergoes a

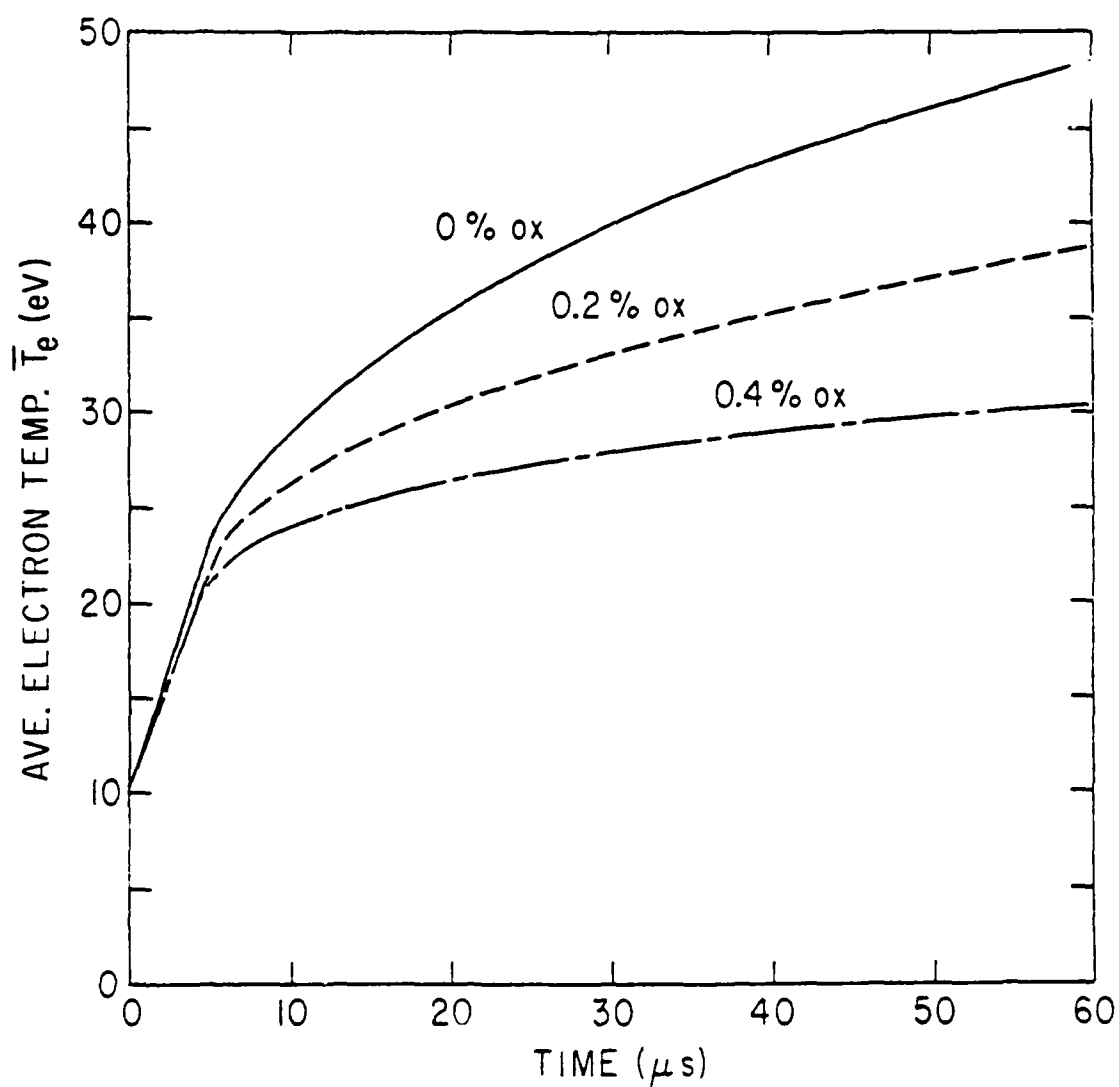


Figure 4

The average electron temperature \bar{T}_e in ZT-S as a function of time for oxygen concentrations of 0%, .2%, and .4% of the line density distributed uniformly in space.

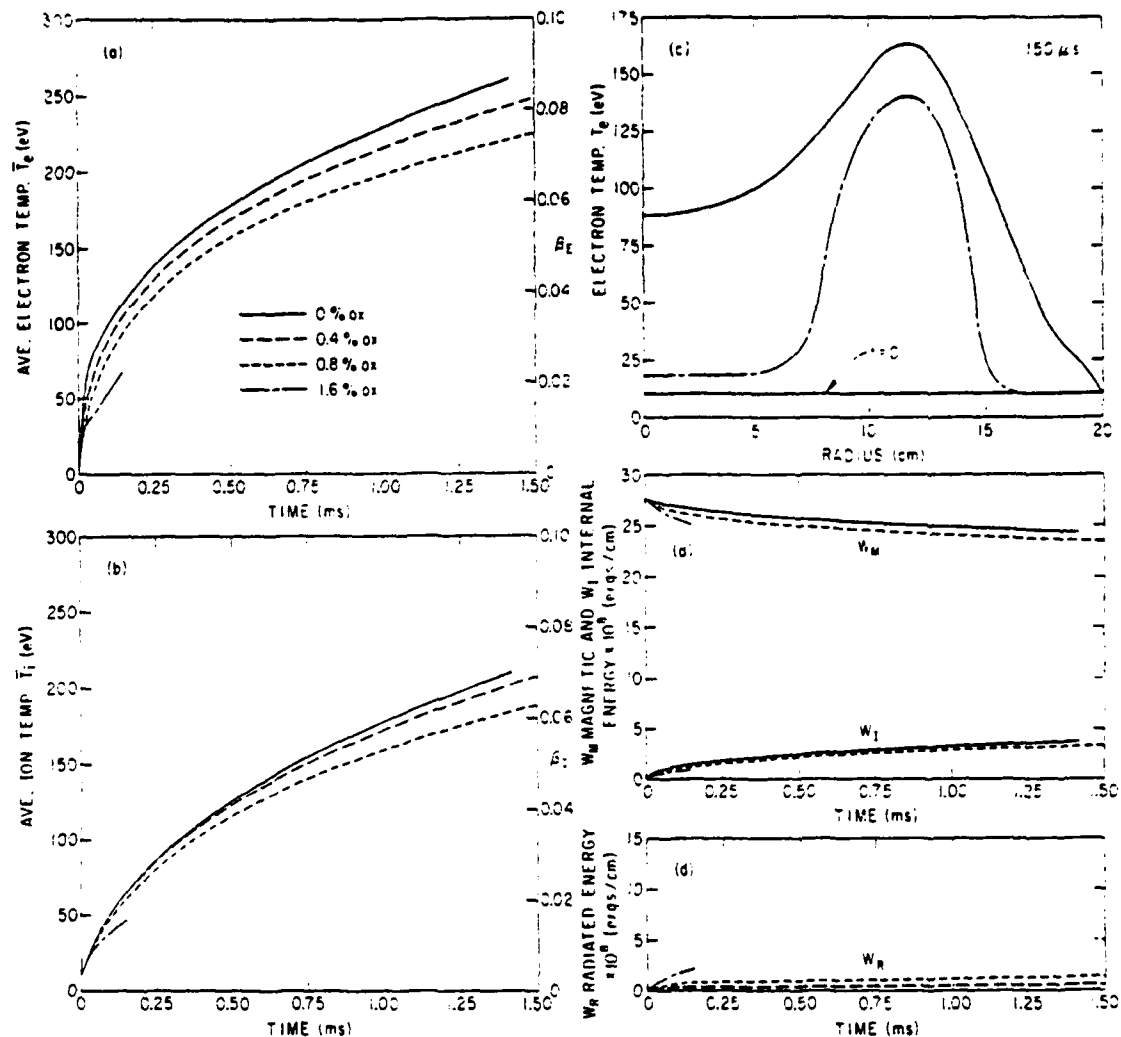


FIGURE 5

(a) Average electron temperature \bar{T}_e and β_e in ZT-40 as a function of time with oxygen impurity concentrations of 0%, .4%, .8%, and 1.6% that of deuterium ($5 \times 10^{14} \text{ cm}^{-3}$ on axis). (b) The average ion temperature \bar{T}_i and β_i as a function of time for the above mentioned impurity concentrations. (c) The electron temperature as a function of radius at 150 μ s for 0% and 1.6% oxygen impurity. The electron temperature at the initial time is a uniform 10eV. (d) The magnetic energy W_M and internal energy W_I , and the total energy radiated W_R as a function of time for 0%, .8%, and 1.6% oxygen impurity.

sharp change in slope at about 30 eV. The temperature in the inner 7 cm of the discharge becomes radiation limited, but a middle region of the discharge where the current density is maximum does burn through the radiation barrier. Only this middle region contributes to the increase in \bar{T}_e . Thus one sees in Fig.5(a) a distinct difference between a case where a significant portion of the plasma is radiation limited and one where the radiation barrier is overcome at all spatial points.

Because of the low value of β (less than 2.5%) the electron thermal conductivity is not effective in transporting energy from the hot middle region to the cold inner region. In fact, the principal classical transport process is magnetic field diffusion (see section 5).

The current in the radiation limited region diffuses into the hot, lower resistivity middle region of the discharge, further exacerbating the situation in the cold region. This leads to very large electron temperature gradients as is illustrated in Fig.5(c), where the electron temperature is plotted as a function of radius at 150 μ s for the zero impurity and 1.6% oxygen impurity case. This is markedly different from ZT-S (see Fig.3(c)) where the electron temperature profile was radiatively depressed by approximately the same amount throughout the middle and inner regions, so that the size of the temperature gradient was not substantially different from the impurity free case. This qualitative

difference between these radiation-limited cases (note that these two cases follow the expected density squared dependence of the radiation loss rate for a fixed impurity concentration) is due to the large difference in beta for these devices ($\beta \sim 2\%$ for ZT-40; $\beta \sim 25\%$ for ZT-S). This follows from the fact that $\beta \sim n/a^2$ for a fixed current density.

In Fig.5(d) the internal, magnetic, and radiated energy is given as a function of time. Unlike in ZT-S, the radiated energy is only a small fraction of the magnetic energy. This is again a consequence of the low value of beta in ZT-40. Thus ZT-40 should be able to radiate a substantial portion of its ohmic heating power for a long time, slowly surmounting a radiation barrier, without depleting a large amount of its magnetic energy reservoir.

3.2.2. Oxygen Plus Aluminum

The radiation cooling curve for aluminum⁽¹⁴⁾ is much the same as that for oxygen (Fig. 12) except that the peak is shifted to about 100 eV and broadened. Thus it is to be expected that a given amount of aluminum will present a much more difficult radiation barrier to burn through than the same amount of oxygen since the ohmic heating power at the peak has decreased by a factor of 8.

To study the effect of aluminum as well as oxygen on ZT-40, the .4% oxygen case shown in Fig. 5 was repeated with .2% and .4% aluminum added to it. These results are shown in Figure 6.

In Figs. 6(a) and 6(b) \bar{T}_e and \bar{T}_i are given as a function of time for four cases: zero impurity, .4% O, .4% O plus .2% Al, and .4% O plus .4% Al. We see that radiation from aluminum is severe after \bar{T}_e rises above 75 eV and completely dominates the energy loss from oxygen. The .2% Al case burns through the aluminum radiation barrier everywhere. In the inner portion of the plasma this burn through is slow, as it takes nearly a millisecond for the temperature in the central region to rise above 100 eV. For the .4% Al case the temperature in the inner 6 cm of the plasma is radiation limited at a temperature of about 60 eV while temperatures in the middle portion of the plasma continue to rise. The current in this inner region diffuses away. Thus we see on a longer timescale the same qualitative phenomena as occurred for the oxygen radiation barrier.

Figure 6(c) shows that the energy radiated by aluminum can be a significant fraction (greater than 10%) of the magnetic energy. At one millisecond, for the .4% Al case, 10% of the initial magnetic energy has been lost to radiation (80% of this due to aluminum), which is greater than the internal energy contained in the plasma at this time.

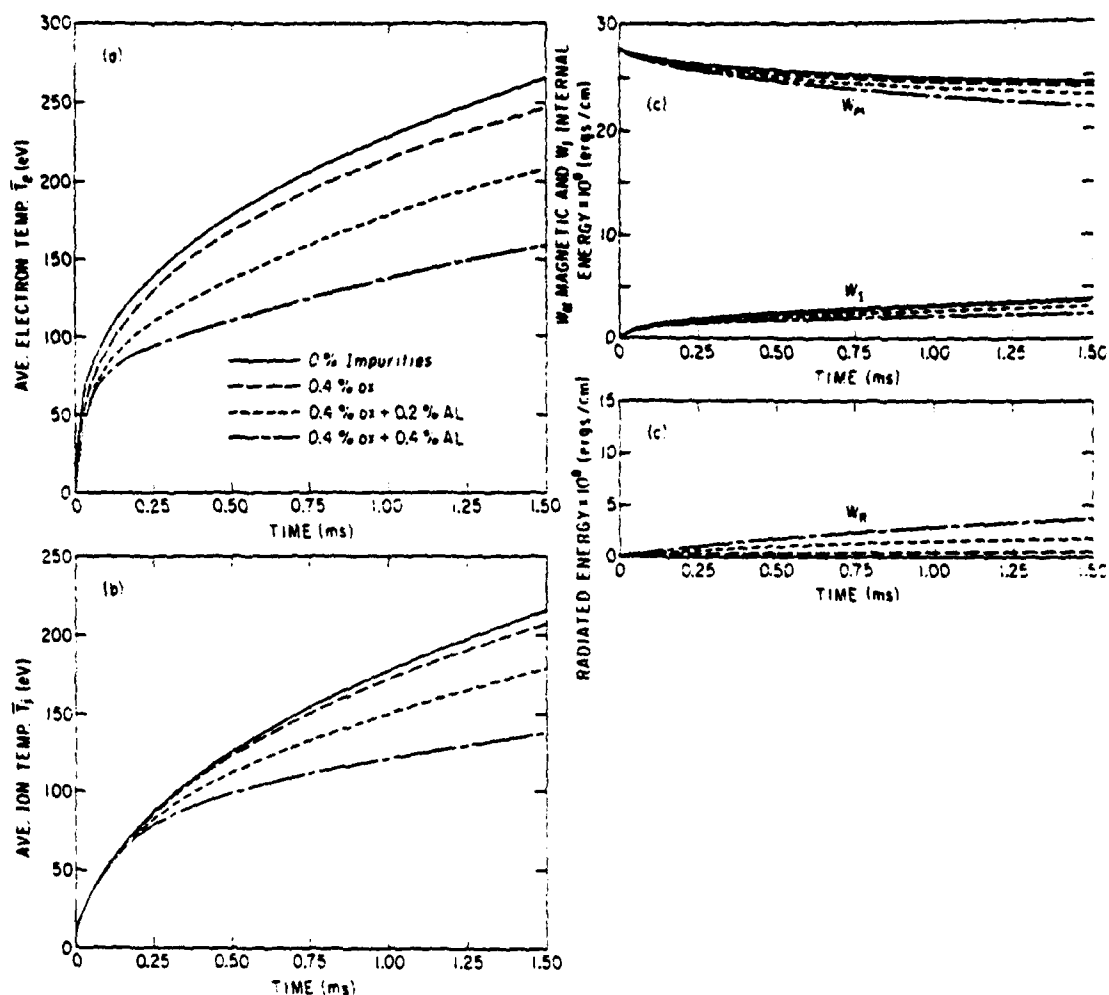


FIGURE 6

(a) The average electron temperature \bar{T}_e in ZT-40 as a function of time with impurity concentrations of 0% O_x, .4% O_x, .4% O_x + .2% AL, and .4% O_x + .4% AL that of deuterium ($4 \times 10^{14} \text{ cm}^{-3}$ on axis). (b) The average ion temperature \bar{T}_i as a function of time for the above mentioned impurity concentrations. (c) The magnetic energy W_m and internal energy W_i , and the total energy radiated W_R as a function of time for the above mentioned impurity concentrations.

3.3. Results for RFX

RFX has a much lower current density than ZT-40 and therefore less ohmic heating power. However it also has a radius three times as large and is expected to operate at a low density ($5 \times 10^{13} \text{ cm}^{-3}$ on axis) and on a long time-scale.⁽¹⁸⁾ From Fig. 1 we see that for the parameters chosen here it has a beta of about half that of ZT-40 for the same temperature and one order of magnitude lower density. Because of this lower density the fractional concentration of impurities is greater.

In Figs. 7(a) and 7(b) \bar{T}_e and \bar{T}_i are given as a function of time for 0%, 2%, and 4% oxygen impurity distributed as a constant fraction of the hydrogen density. The impurity free and 2% oxygen cases are run to 5 ms and the 4% oxygen case to 1 ms. In the 2% oxygen case at 1 ms 45% of the ohmic heating power has gone into radiation. At 5 ms the amount of ohmic heating power lost is 33%. The temperatures for the 4% oxygen case are radiation limited in the inner 20 cm of the discharge. \bar{T}_e shows the same characteristic behavior as the radiation limited case of ZT-40 in Fig. 5(a). At 1 ms 75% of the ohmic heating power has been dissipated as radiation. However, this is still only 6% of the initial magnetic energy.

In absolute terms RFX becomes radiation limited for a much lower amount of oxygen than does ZT-40. We therefore conclude that for this experiment to be successful a plasma that is cleaner than ZT-40 by more than a factor of four must be maintained.

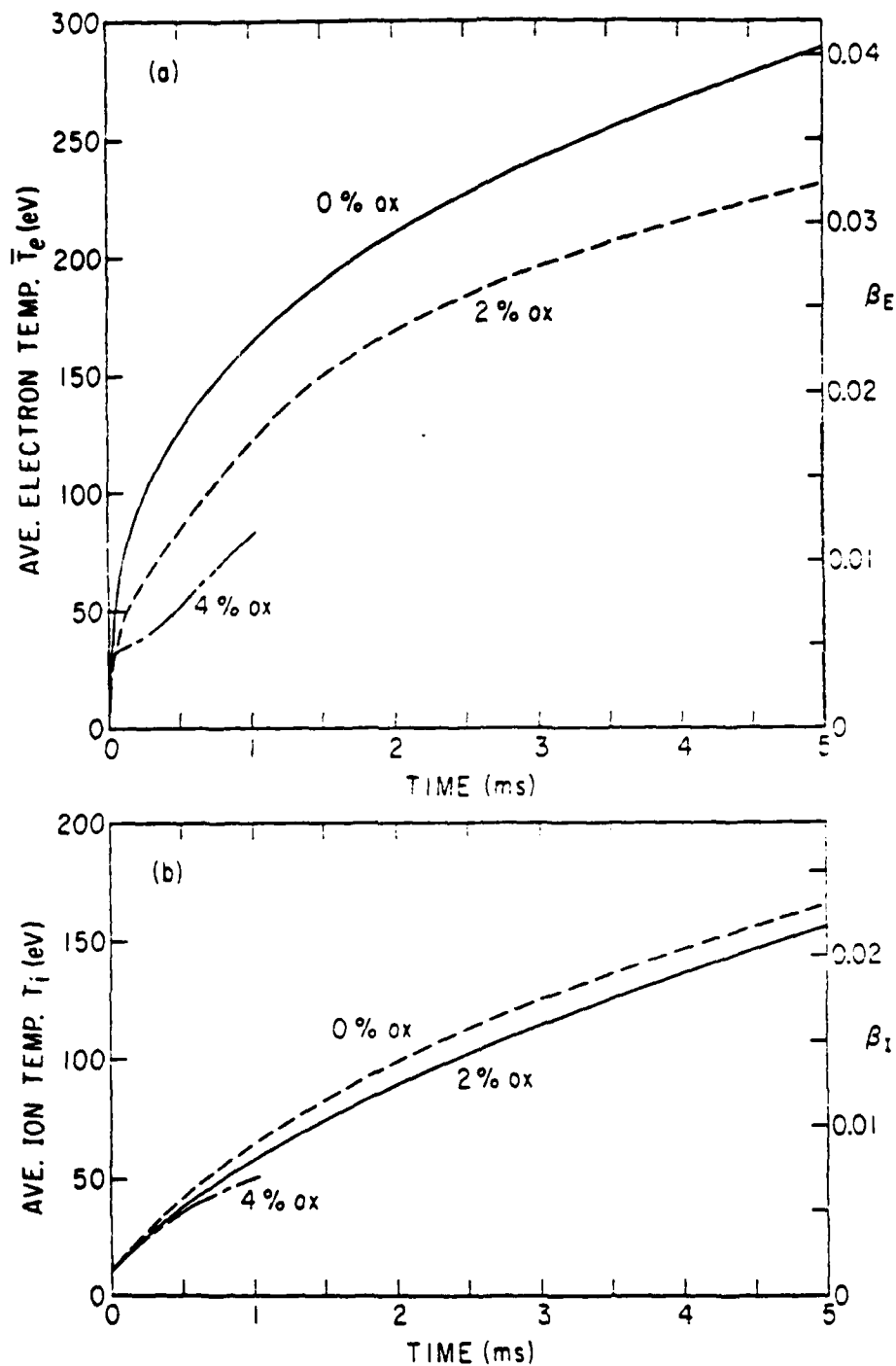


FIGURE 7

(a) The average electron temperature \bar{T}_e and β_E in RFX as a function of time with oxygen impurity concentrations of 0%, 2%, and 4% that of deuterium ($5 \times 10^{13} \text{ cm}^{-3}$ on axis). (b) The average ion temperature \bar{T}_i and β_i as a function of time for the above mentioned impurity concentrations.

With respect to the limits on impurities found for RFX and ZT-40 assuming classical transport, one point must be kept in mind. For a low beta plasma there is enough magnetic energy available to burn through low Z radiation barriers with higher impurity limits than those given here if an anomalous mechanism is present to convert the magnetic energy to plasma energy fast enough. Since the depletion of the magnetic field is small, this can be done without necessarily causing the plasma to go MHD unstable.

3.4. Stability of Point Cases

The first requirement for stability of the point cases is that the reversed toroidal field not disappear. The reversed field disappears at 62 μ s, 46 μ s, and 38 μ s for the 0%, .2%, and .4% oxygen impurity ZT-6 simulations shown in Fig. 3, otherwise, it remains for all other cases.

It is always seen that the Suydam criterion is violated in the outer regions of the plasma. This can have important consequences for two reasons: first, it can cause enhanced transport in the vicinity of the B_z reversal point leading to a more rapid annihilation of the reversed field; second, it has been shown that violation of the Suydam criterion implies the existence of a nonlocalized rapidly growing $m = 1$ kink mode.⁽¹⁹⁾ To illustrate the extent to which our profiles are Suydam unstable, we present in Figs. 8(a), (b), and Figs. 9(a), (b) three dimensional graphs

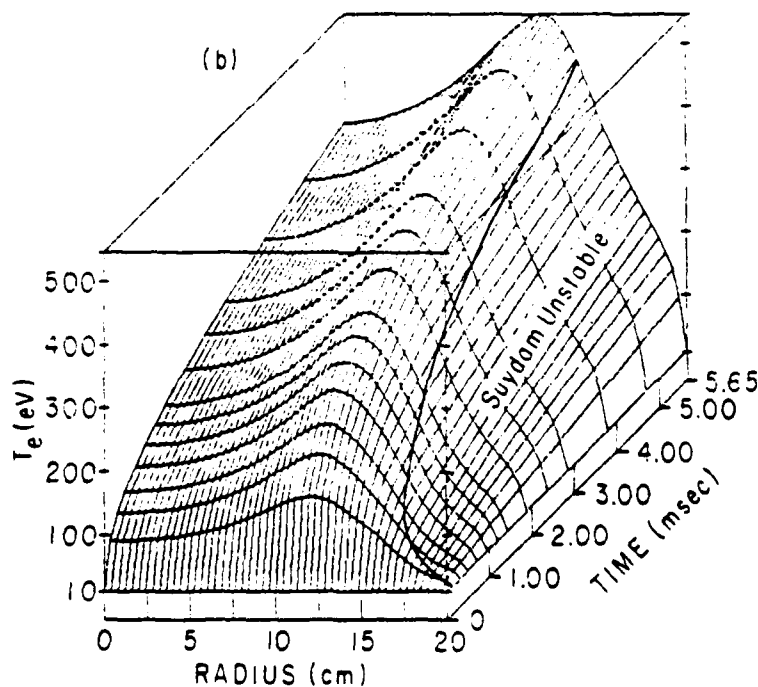
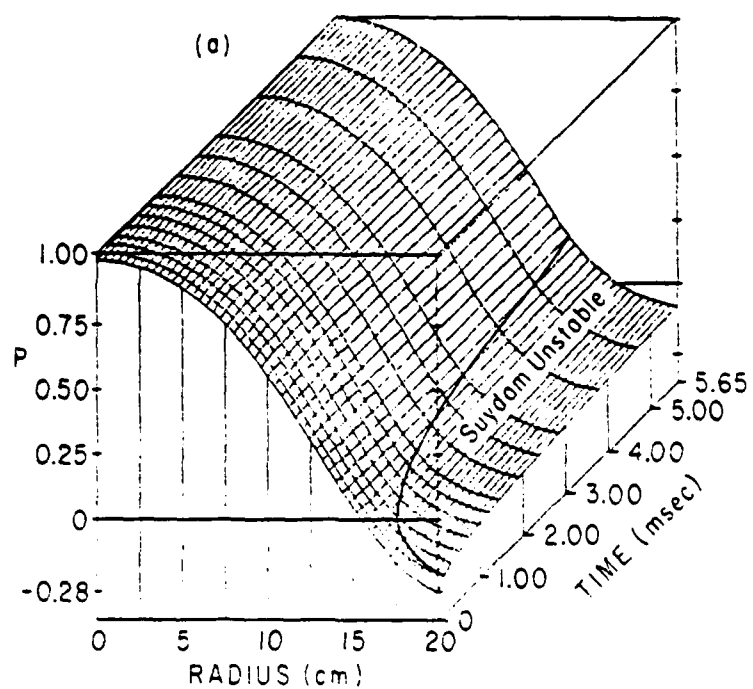


Figure 8

(a) The nondimensional pitch $P = rB_z/aB_0$ as a function of radius and time for ZT-40 with no impurities. The Suydam unstable region intersects the pitch reversal point at about 1 ms. (b) The electron temperature as a function of radius and time.

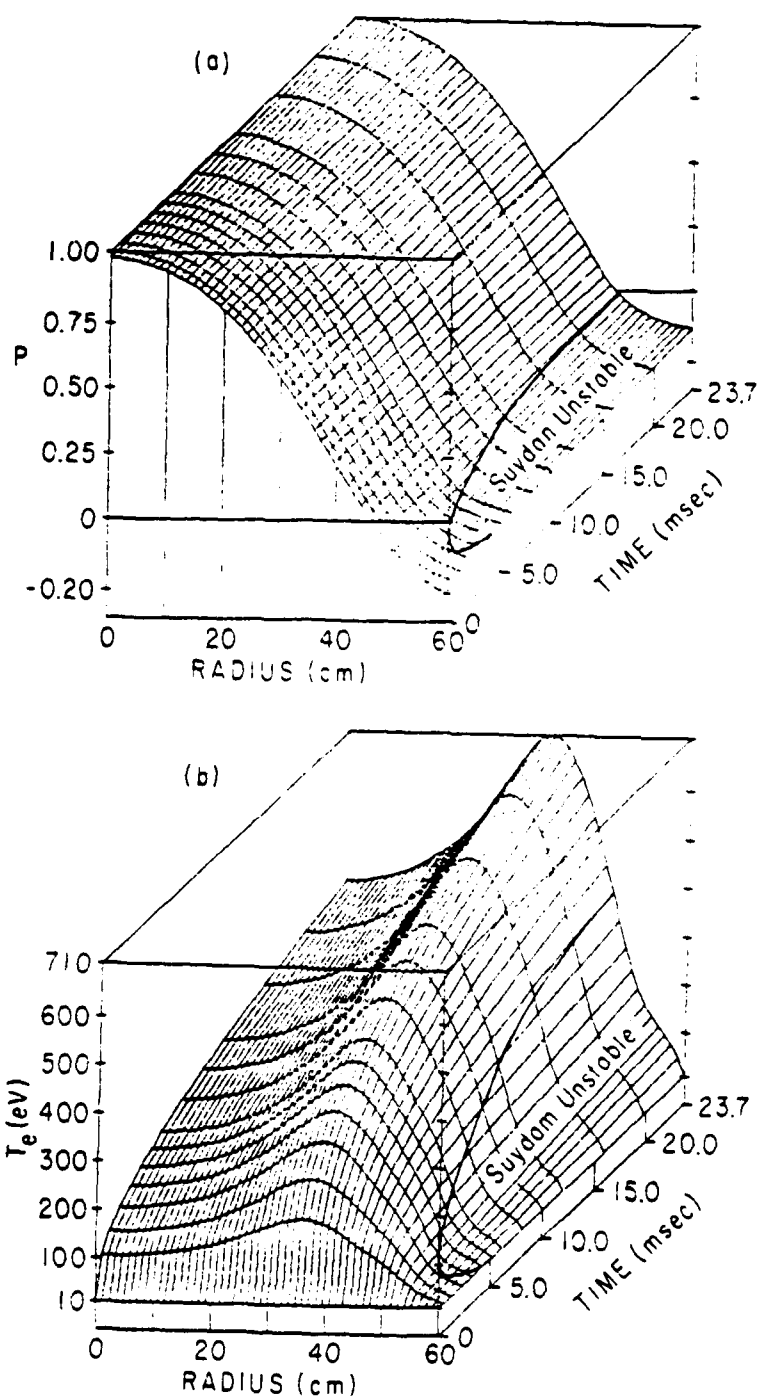


FIGURE 9

(a) The nondimensional pitch $P = rB_z / aB_\theta$ as a function of radius and time for RFX with no impurities. The Suydam unstable region does not intersect the pitch reversal point. (b) The electron temperature as a function of radius and time.

of the pitch and electron temperature as a function of radius and time for ZT-40 and RFX respectively, for the impurity free case. In each of these graphs the Suydam unstable region is sketched. From Fig. 8 we see that the ZT-40 simulation becomes Suydam unstable after 100 μ s and that this unstable region rapidly grows to cover the outer quarter of the discharge. From Fig. 9 the RFX simulation becomes unstable after the first 2ms in the outer 10 cm of the plasma. The field reversal point is not included in the Suydam unstable region until after 1ms for ZT-40 and 20ms for RFX. The violation of the Suydam criterion is less severe for RFX because the broader current profile gives rise to a smaller temperature gradient near the plasma edge than in ZT-40 (c.f. Figs. 8(b) and 9(b)).

Impurities are seen to steepen temperature gradients and in particular to create very hollow temperature profiles where \vec{v}_n and \vec{v}_T are in opposite directions. This, as is well known, may give rise to the universal instability. In addition, it will be shown in section 5 that impurities may aid the growth of fine-scale gradients in the current and temperature.

CHAPTER 4

SCALING OF RFP DEVICES

A general criterion is now developed in terms of nondimensional parameters for whether a RFP can overcome a specified radiation barrier given only general design parameters. This criterion is then calibrated by comparison with the point cases for ZT-S, ZT-40, and RFX discussed in section 3.

To make a consistent and uniform comparison of the three devices the results of our point cases must be expressed in terms of nondimensional parameters. This can be done by defining a nondimensional representation of the temperature as

$$\beta_T \equiv \beta_E + \beta_I \quad (32a)$$

(where β_E and β_I are the electron and ion poloidal beta defined in section 3 and specified by a second axis parallel to \bar{T}_e and \bar{T}_i on the RHS in Figs. 3(a,b), 5(a,b), and 7(a,b)), and a nondimensional time τ by the decay of the poloidal magnetic energy W_p ,

$$W_p(t) = W_p(0)e^{-2\tau} \quad (32b)$$

The results of Figs. 3(a,b), 5(a,b), and 7(a,b) for ZT-S, ZT-40, and RFX are shown in Figs. 10(a), 10(b), and 10(c), respectively, in terms of β_T versus τ . From Fig. 10 we see that in the impurity free case $\beta_T(\tau)$ is a straight line that has nearly the same slope for all three devices (note that β_T and τ have different scales in Figs. 10(a,b,c)) and that the effect of impurity radiation is to change the slope of this line toward the horizontal. For example, in Fig. 10(b) for ZT-40 the .4% and .8% oxygen cases show a decrease in the slope of $\beta_T(\tau)$, compared to the impurity free case, at small values of τ where the radiation barrier is being surmounted. At large τ where the radiation barrier has been overcome and energy loss from radiation is small, $\beta(\tau)$ is a straight line with almost the same slope for all three cases. For these values of τ the effect on the magnetic field of overcoming the oxygen radiation barrier can be seen by the amount that τ has increased over the impurity free case. The radiation limited case (1.6%O) is quite distinct from the rest. Here $\beta_T(\tau)$ has a small slope that does not increase with τ as do the two cases which burn through the radiation barrier. Notice that a value of τ has been reached by this case that is as large as that attained by the 0%, .4%, and .8% O simulations, even though it has been run only a tenth as far in physical time. Results similar to those noted above are seen in Fig. 10(c) for RFX. Fig 10(a) once again shows the severe radiation problems encountered by ZT-S. Thus it is seen that this nondimensional

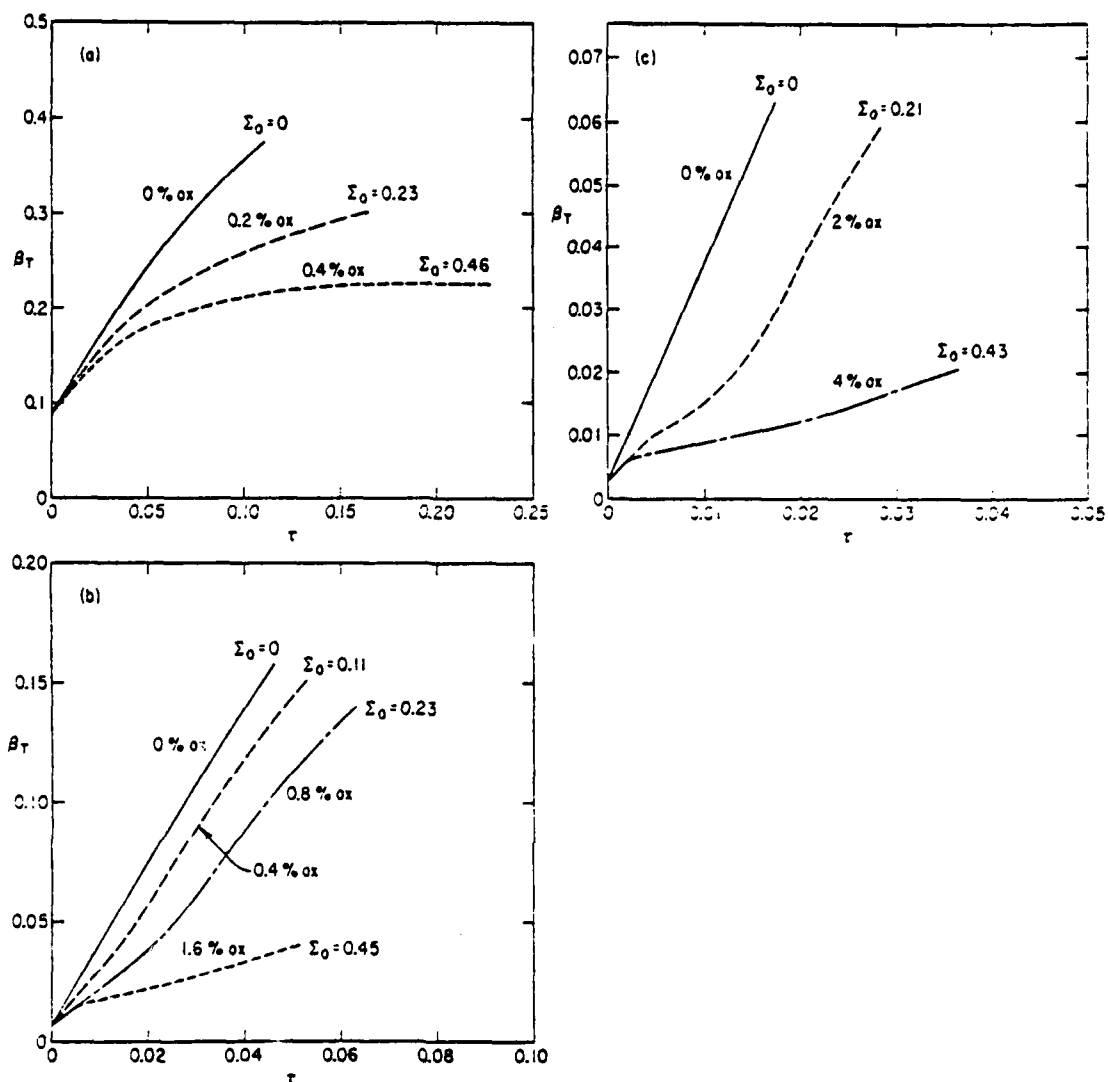


FIGURE 10

(a) The nondimensional temperature $\beta_T = \beta_E + \beta_I$ is given as a function of the nondimensional time τ (see Eqs. (32a,b)) for the ZT-S cases (0%, .2%, and .4% oxygen) shown previously in Fig. 3. The curves are labeled by Σ_0 , the ratio of the impurity radiation rate to the ohmic heating rate at the 25 eV peak of the oxygen cooling curve (see Eq. (35b)). (b) β_T versus τ is given for the ZT-40 cases (0%, .4%, .8%, and 1.6% oxygen) shown in Fig. 5. (c) β_T versus τ is given for the RFX cases (0%, 2%, and 4% oxygen) shown in Fig. 7.

representation of our point cases provides a good correlative description of these results.

Next, a radiation barrier burn through criterion is derived. Consider the zero-dimensional temperature equation

$$\frac{3}{2} n \frac{\partial T}{\partial t} = n j^2 - n n_I C(T), \quad (33)$$

where $C(T)$ is the energy loss rate per electron per impurity ion, and n_I is the impurity density. By means of the resistive diffusion time $\tau_0 = \pi a^2 / c^2 n$, a nondimensional time $\tau = t / \tau_0$ can be defined and Eq. (33) becomes

$$d\tau = \frac{dT}{\epsilon [1 - \bar{\Sigma}(T)]}, \quad (33a)$$

where $\epsilon = \pi a^2 j^2 / c^2 n$ is the magnetic energy per particle ($\epsilon = \epsilon_0 e^{-2\tau}$ and $\epsilon_0 = \pi a^2 j^2 / c^2 n|_{t=0}$) and $\bar{\Sigma} = n n_I C(T) / n j^2$ is the ratio of the radiation rate to the ohmic heating rate. $\bar{\Sigma}(T)$ is assumed to have a sharply peaked Lorentzian shape (see Fig. 12) given by

$$\bar{\Sigma}(T) = \frac{\bar{\Sigma}_0}{1 + \frac{(T - T_0)^2}{(\Delta T)^2}},$$

where $\bar{\Sigma}_0$ is the peak of $\bar{\Sigma}(T)$ at temperature T_0 and ΔT is the half width of the peak at half maximum. With this, Eq. (33a) can be integrated to some temperature $T > T_0$, with the result

$$\frac{1 - e^{-2\tau}}{2} = \frac{T - T_1}{\epsilon_0} + \frac{\pi \Delta T}{\epsilon(T_0)} \frac{\bar{\Sigma}_0}{(1 - \bar{\Sigma}_0)^{3/2}} \quad (34)$$

where T_1 is the initial temperature. Notice that as \sum_0 approaches unity τ becomes infinite. For a RFP to attain a temperature T above the radiation barrier τ must be small, otherwise significant decay of the magnetic fields will have occurred. This implies that both \sum_0 and $(T-T_1)/\epsilon_0$ (a measure of beta) must be small.

Assuming $\epsilon(T_0) = \epsilon_0$, we can rewrite Eq. (34) in a form more suited to comparison with the point cases

$$\frac{1-e^{-2\tau}}{2} = a_1 \epsilon_D \left(1 + a_2 \frac{\sum_0}{(1-\sum_0)^{1/2}} \right). \quad (34a)$$

To compare this with the numerical simulations we take ϵ_D to be

$$\epsilon_D = \epsilon_T(\tau) - \epsilon_T(0) \quad (35a)$$

$$\sum_0 = \langle n \rangle \langle n_I \rangle C(T) / \langle j \rangle^2 \Big|_{T_0} \quad (35b)$$

is computed for oxygen ($C(T) = 9 \times 10^{-19} \text{ erg cm}^3/\text{sec}$)¹⁴, where $T_0 = 25\text{eV}$, using the zero dimensional quantities $\langle n \rangle$, $\langle n_I \rangle$, and $\langle j \rangle$ defined from the one dimensional profiles by a density weighted average, i.e.,

$$\langle A \rangle = \frac{\int_0^a 2\pi n A r dr}{\int_0^a 2\pi n r dr},$$

since it is quantities measured relative to the plasma density rather than physical space that are of interest. $\bar{\Gamma}_0$ is given in Figs. (10a,b,c). It is seen that $\bar{\Gamma}_0 = .45$ corresponds to the radiation limited cases of ZT-S, ZT-40, and RFX. a_1 and a_2 are parameters determined by fitting Eq. (34a) to the results of the numerical simulations as given in Figs. (10a,b,c). a_1 is determined from the impurity free cases to be .318. a_2 is found, by fitting Eq. (34a) to the radiation limited cases, to have value of about 2π (if a_2 were determined by fitting Eq. (34a) to other cases it would be found to have a value smaller than 2π , and would give a less restrictive limit on the parameters necessary for a RFP to burn through the oxygen radiation barrier).

Using these values of a_1 and a_2 , we plot in Fig. 11 curves of β_D versus $\bar{\Gamma}_0$ for constant τ (notice the sharp dependence of β_D on $\bar{\Gamma}_0$). In this figure squares, circles, and triangles are drawn that represent ZT-S, ZT-40, and RFX respectively at values of β_D and $\bar{\Gamma}_0$ that correspond to the point cases at a temperature of 40ev, which is above the 25ev peak of the oxygen radiation barrier. This figure is then divided into four regions: region 1, where ($\bar{\Gamma}_0 > .45$) the oxygen impurity content is too great for the plasma to overcome the radiation barrier; region 2, where the energy lost to radiation is substantial and the τ at which burn-through occurs may be large, corresponding to a significant degradation of the magnetic fields; region 3, where the

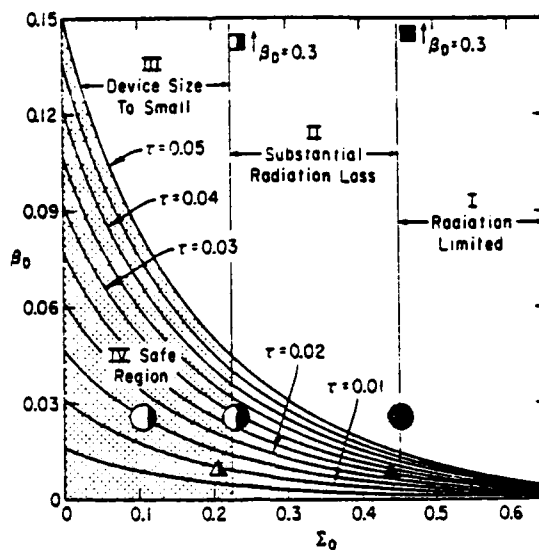


FIGURE 11

$\beta_D = \beta_T(\tau) - \beta_T(0)$ (Eq. (35a)) is drawn as a function of Σ_0 (Eq. 35b)) for constant values of τ (see Eq. (34a)). The ZT-S, ZT-40, and RFX cases shown in Figs. 10(a), (b), and (c) are represented by squares, circles and triangles respectively, drawn for a β_D corresponding to $T_e = 40$ eV. Full, half, and quarter shaded symbols represent respectively the maximum, half and quarter maximum oxygen impurity cases of Figure 10. Four regions of parameter space are delineated: region I, where the plasma temperatures are radiation limited; region II where there is substantial radiation loss; region III, where the device size is too small for burn through at low beta; region IV, which is safe for burning through the oxygen radiation barrier. The $\tau = .05$ curve corresponds to a 10% degradation in the magnetic energy available for ohmic heating.

device size is too small, i.e., the beta corresponding to 40ev already implies a large value of τ ; and region 4, where the radiation barrier can be safely overcome. We see that for ZT-S the device size is too small regardless of the impurity concentration. ZT-40 and RFX are at a low enough beta at 40ev that they can potentially lie in the safe region if the oxygen impurity density is low enough.

Figure 11 may be used to predict the rough behavior of any proposed RFP confronted with the oxygen radiation barrier simply by constructing β_D and \bar{L}_O using the design parameters.

CHAPTER 5

THERMAL INSTABILITY IN THE RFP

As pointed out previously, ^(8,20) an ohmically heated plasma can be thermally unstable. Under proper conditions, the current will diffuse into a region of low resistivity, increase the ohmic heating in that region, further lower the resistivity, and thereby feed an instability. Here this phenomena is studied in the context of the RFP.

We consider a low beta plasma model governed by the Lagrangian MHD equations. We construct an equilibrium on the ohmic heating time scale and develop the theory of this instability for a stationary zeroth order electron temperature. The case of nonstationary temperature is then considered, and the theoretical predictions are compared to results of numerical simulations, wherein the full set of equations is solved.

5.1. Physical Considerations

To determine the important physical effects at low beta, we construct order of magnitude estimates of the terms in Eqs. (1)-(6) by scaling all gradients to the system size and by setting all coefficients constant. The following simple relations are obtained among the particle diffusion rate γ_{PD} , the magnetic field diffusion rate γ_{MD} , the ohmic heating rate γ_{OH} , the electron thermal conduction rate γ_{ETC} , the ion thermal conduction rate γ_{ITC} , and the electron-ion equilibration rate γ_{EI} :

$$\gamma_{PD} = \beta^2 \gamma_{OH} \quad , \quad \gamma_{MD} = \beta \gamma_{OH} \quad (36a,b)$$

$$\gamma_{EI} = \Lambda \beta^2 \gamma_{OH} \quad , \quad \gamma_{ETC} = \beta^2 \gamma_{OH} \quad (36c,d)$$

$$\gamma_{ITC} = \beta^2 \left(\frac{M}{m}\right)^{1/2} \gamma_{OH} \quad , \quad (36e)$$

where β is the plasma beta, $\frac{M}{m}$ is the ion to electron mass ratio, and Λ is the square of the plasma radius divided by the ion gyroradius. It is seen that for low beta the ohmic heating rate dominates all other plasma processes.

In the electron temperature equation (18) a radiation loss term is included that has the functional form $C N_e N_I \theta_e^\alpha / Y$, $\frac{2\alpha+1}{3}$, where C and α are constants and N_I is the impurity density. Then a low beta steady-state of Eqs. (16)-(20) on the ohmic heating time scale is given by

$$\frac{\partial P}{\partial \tau} = \frac{\partial N}{\partial \tau} = 0 \quad , \quad (37a,b)$$

$$\frac{8\phi^2 \tilde{n}_n Y^{5/3}}{N(P^2 + Y\phi^2)} \left(\frac{Y}{Y}\right)^4 \left[\frac{\partial}{\partial X} \frac{P}{Y}\right]^2 = \frac{C N_e N_I \theta_e^\alpha}{Y \frac{2\alpha+1}{3}} \quad (38)$$

$$\frac{\partial^2 Y}{\partial X^2} = Y \left[\frac{\frac{\partial}{\partial X} (P^2 + 2Y\phi^2)}{2(P^2 + Y\phi^2)} \right] \quad (39)$$

where the electron-ion equilibration term, and therefore the ion temperature equation, has been neglected

$$(\Lambda\beta^2 = \frac{e^2 \phi_o^2 \beta^2}{T_o Mc^2} = \beta \frac{8\pi n_o a^2 e^2}{Mc^2} \text{ and can be large or small}$$

depending on β , n_o , and a). The case where this term is included ($\Lambda\beta^2$ of order unity) is considered later.

The character of this low beta equilibrium is now investigated by examining the form of a typical radiation cooling curve such as the one shown in Fig. 12 for oxygen, where the radiation power versus electron temperature is plotted logarithmically. It follows from Eq. (37a) ($\frac{\partial P}{\partial T} = \frac{\partial}{\partial X} n_e j_e = 0$) that $n_e j_e = \text{const.}$ Therefore, either both the electron temperature and current density are spatially uniform or $j_e \sim n_e^{-1}$. In Fig. 12 the ohmic heating rate is plotted as a function of electron temperature for both cases. The uniform temperature and current density case ($n_e j_e^2 \sim T_e^{-3/2}$) is shown as the solid line intersecting points A and B of the cooling curve, which represent equilibria described by Eqs. (37) - (39). For this case, point A is stable and point B is unstable with respect to small perturbations in temperature (an equilibrium is stable if the slope of the cooling curve is greater than that of the heating curve). However, if $j_e \sim n_e^{-1}$ the ohmic heating rate ($n_e j_e^2 \sim T_e^{3/2}$) is represented by the dashed curve intersecting point A. In this case perturbations in temperature about point A are unstable.

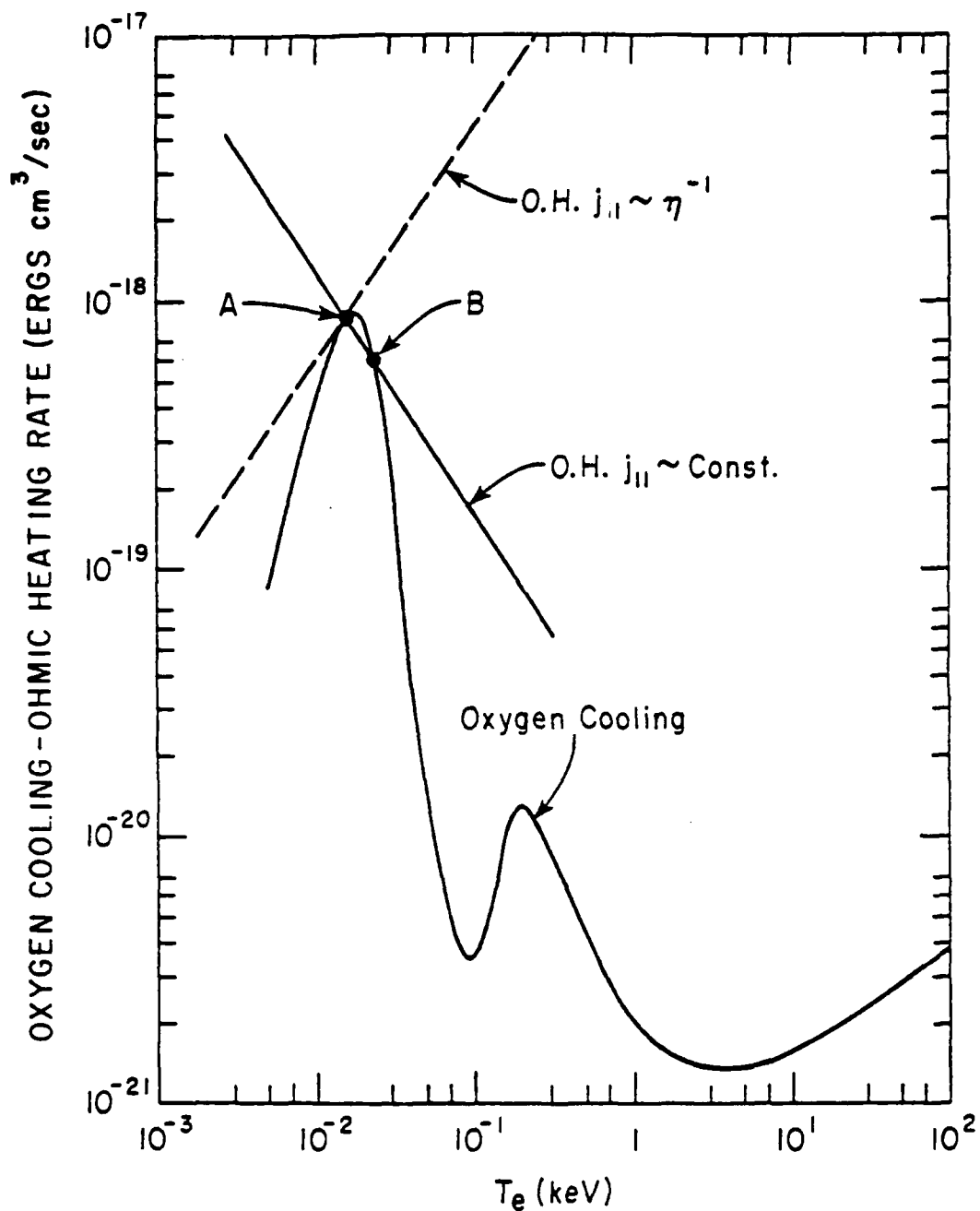


FIGURE 12

The radiation cooling rate due to oxygen (energy per electron, per oxygen ion, per second) is given as a function of temperature. Also drawn are the ohmic heating rate for a constant current density (solid line), which intersects this curve at points A and B, and the ohmic heating rate for $j_{||} \sim \eta^{-1}$ (dashed line), which intersects the cooling curve at point A.

Consequently, if a low beta plasma reaches a radiation barrier, as illustrated by the solid line intersecting point A, it can burn through this barrier at isolated spatial points by following the $j_{\parallel} \sim n^{-1}$ ohmic heating curve. The plasma switches from the $j_{\parallel} = \text{const.}$ to $j_{\parallel} \sim n^{-1}$ heating curve via current diffusion into regions of lower resistivity, and thus splits up into high and low temperature regions. This may occur with little change in the plasma density since the rate of particle diffusion is a factor of 6 less than the rate of current diffusion (c.f. Eq. (36)).

5.2. Derivation of the Thermal Instability

The theory of the thermal instability previously discussed in physical terms is now developed through means of a linear stability analysis.

We begin by considering Eqs. (16)-(20) and assume the existence of a stationary equilibrium described by Eqs. (37)-(39). A small perturbation in the parallel current $\epsilon P'_1$ ($j_{\parallel} \sim \frac{\partial}{\partial X}(\frac{P}{Y}) \sim P'$), where the smallness is in ϵ , and in the electron temperature $\epsilon \theta_1$ is assumed that has a scale length $\bar{\lambda}$ small compared to one. Therefore,

$$P' = P'_0 + \epsilon P'_1(X, \tau), \quad (40a)$$

$$\theta_e = \theta_0 + \epsilon \theta_1(X, \tau), \quad (40b)$$

where the zeroth order quantities $(\frac{P_0}{Y_0})'$ and θ_0 are assumed uniform in space and stationary in time.

The perturbation in the current P'_1 causes, through Eq. (39), perturbations in Y , Y' , and Y'' . These perturbations are now estimated and it is shown that:

$$Y'' = Y''_0 + \epsilon Y''_1, \quad (41a)$$

$$Y' = Y'_0 + \epsilon \bar{\lambda} Y'_1, \quad (41b)$$

$$Y = Y_0 + \epsilon \bar{\lambda}^2 Y_1. \quad (41c)$$

First from Eq. (40a)

$$P = P_0 + \epsilon \bar{X} P_1, \quad (42)$$

since P_1' is a monotone function only over a scale \bar{X} . Eq. (41a) follows directly from using Eqs. (40a) and (42) in Eq. (39). To show Eq. (41b) we write Eq. (39) as,

$$Y'(X) = (P^2 + Y\phi^2) \exp - \int_0^X \frac{PP'}{P^2 + Y\phi^2} dx. \quad (43)$$

Then with Eq. (40a), (42) and because $\int_0^X \epsilon P_1' P_0 dx \sim O(\bar{X}\epsilon)$, Eq. (41b) follows. Similarly, Eq. (41c) can be shown by integrating Eq. (43) and proceeding as before. Since $N=nY'$, and because n is stationary for low beta (see Eq. (36)),

$$N = N_0 + \epsilon \bar{X} N_1. \quad (44)$$

The assumption that the perturbed current is due mainly to P_1' can now be verified. Using Eqs. (40) and (41) we have

$$j_{\parallel} \sim \left(\frac{P}{Y}\right)' \sim \left(\frac{P_0}{Y_0}\right)' + \epsilon \left(\frac{P_1}{Y_0}\right)' - \epsilon \bar{X} \left(\frac{P_0}{Y_0} Y_1\right)',$$

which shows that the perturbed current $\delta j_{\parallel} \sim \epsilon \left(\frac{P_1}{Y_0}\right)'$.

Next the density and time are scaled by nondimensional factors \bar{N} and $\bar{\tau}$ respectively. Since a reference density n_0 was defined by setting the reference beta equal to one in deriving Eqs. (16)-(20), the low beta assumption implies $\bar{N} = \beta$. The size of $\bar{\tau}$ and \bar{X} is now related to \bar{N} and equations are derived that describe the time evolution of θ_1 and $\left(\frac{P_1}{Y_0}\right)'$.

Including the radiation loss term in Eq. (18) and scaling it by $\bar{\tau}$ and \bar{N} , the order of the terms is found to be

$$1 = \bar{\tau}, \bar{N}\bar{\tau}: \bar{\tau}, \bar{N}\bar{\tau}: \bar{N}\bar{\tau}: \bar{N}\bar{\tau}\Lambda: \frac{\bar{\tau}}{\bar{N}}: \bar{\tau}\bar{N}: \bar{\tau}\bar{N}: \bar{\tau}\bar{N}: C\bar{\tau}\bar{N}^2.$$

By setting $\bar{\tau} = N = \delta$, the equilibrium equation (38) is retrieved. Ohmic heating can be balanced against radiation loss since C is an arbitrary parameter. All other terms are small of order δ or δ^2 ($\Lambda\delta^2$ is still assumed small). Thus, the nondimensional time scale of the equilibrium is of order δ .

Taking the derivative with respect to X of the pitch equation (16) we have,

$$\frac{\partial}{\partial \tau} \epsilon P'_1 = \frac{\partial^2}{\partial X^2} \left[\left(\frac{x\phi}{\phi} + \frac{f}{Y'} \right) P + \frac{\bar{n}_n Y}{Y'^2} P' \right]. \quad (45)$$

Since $\left(\frac{P_0}{Y_0} \right)'' = 0$, the leading term on the RHS of Eq. (45) is of order ϵ . Scaling the independent variables to $\bar{\tau}$ and \bar{X} , the terms are of relative order,

$$1 = \frac{\bar{\tau}}{\bar{X}} : \frac{\bar{\tau}}{\bar{X}^2}.$$

This equation can be balanced by setting $\bar{X} = \bar{\tau}^{1/2} = \delta^{1/2}$, giving the scale length of the perturbation. Using Eqs. (40), (41), (42) and the relation

$$\bar{n} = \bar{n}_0 \left(1 - 3/2 \frac{\epsilon}{\epsilon_0} \right) \quad (46)$$

in Eq. (45), dropping terms of order $\delta^{1/2}$, and keeping only terms linear in ϵ , we obtain the result

AD-A081 883

COLORADO UNIV AT BOULDER DEPT OF ASTRO-GEOPHYSICS

F/G 20/9

PLASMA WAVE TURBULENCE AND PARTICLE HEATING CAUSED BY ELECTRON --ETC(U)

NOV 79 M V GOLDMAN

F49620-76-C-0005

CU-1036

AFOSR-TR-80-0167

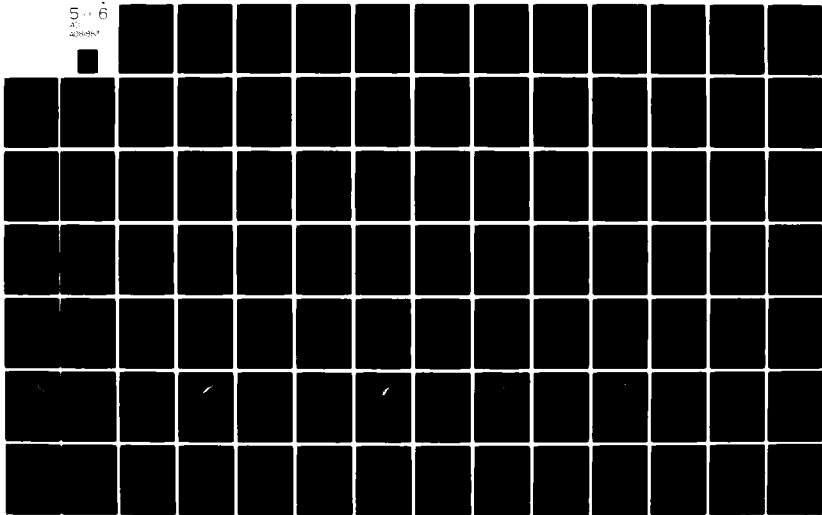
NL

UNCLASSIFIED

5 6

AT

AD-A081 883



$$\frac{\partial}{\partial \tau} \left(\frac{P_1}{Y_0} \right)' = \frac{\partial^2}{\partial X^2} \left[C_1 \tilde{n}_0 \left(\frac{P_1}{Y_0} \right)' - \frac{3}{2} C_1 \left(\frac{P_0}{Y_0} \right)' \frac{\theta_1}{\theta_0} \right], \quad (47)$$

where $C_1 = Y_0^2 / Y_0'^2$.

An equation is now derived for θ_1 . With the scale length $\bar{X} \sim \beta^{1/2}$ for perturbed quantities, terms in Eq. (18) that were of order $\bar{\tau} \sim \beta$, $\bar{N} \bar{\tau} \sim \beta^2$ in the unperturbed quantities become of order $\frac{\bar{\tau}}{\bar{X}} \sim \beta^{1/2}$ and $\frac{\bar{N} \bar{\tau}}{\bar{X}^2} \sim \beta$ in an equation for θ_1 and can still be dropped. With this in mind and using Eqs. (38), (40), (41), (42), (44), and (46) in Eq. (18), and keeping terms linear in ϵ we find that

$$\begin{aligned} \frac{\partial \theta_1}{\partial \tau} = & 2C_2 \tilde{n}_0 \left(\frac{P_0}{Y_0} \right)' \left(\frac{P_1}{Y_0} \right)' - (3/2) C_2 \frac{\tilde{n}_0}{\theta_0} \left(\frac{P_0}{Y_0} \right)'^2 + \\ & + C_3 \alpha \theta_0^{\alpha-1} \theta_1, \end{aligned} \quad (48)$$

where Eq. (38) can be written as $C_2 \tilde{n}_0 \left(\frac{P_0}{Y_0} \right)'^2 = C_3 \theta_0^\alpha$, defining C_2 and C_3 .

Assuming $\left(\frac{P_1}{Y_0} \right)' \sim \theta_1' \sim e^{ikx + \omega t}$ and using Eq. (38), the growth rate ω is found from Eqs. (47) and (48) to be

$$\omega = \frac{-(a_1 + a_2) \pm \sqrt{(a_1 + a_2)^2 - 4(a_1 a_2 - b_1 b_2)}}{2} \quad (49)$$

where, $a_1 = C_1 k^2 \tilde{n}_0$, $a_2 = \frac{C_2 \tilde{n}_0 \left(\frac{P_0}{Y_0} \right)'}{\theta_0} (\alpha + 3/2)$, $b_1 = -\frac{3}{2} \frac{C_1 k^2 \tilde{n}_0}{\theta_0} \left(\frac{P_0}{Y_0} \right)'$, $b_2 = -2C_2 \tilde{n}_0 \left(\frac{P_0}{Y_0} \right)'$.

There are two possibilities to be considered:

$a_2 < 0$ and $a_2 > 0$. The case $a_2 < 0$, or $\alpha < \frac{3}{2}$, corresponds to the unstable equilibrium shown in Fig. 12 as point B. This is the zero-dimensional case; the growth rate is the ohmic heating rate.

For the case $a_2 > 0$ there is an instability if $b_1 b_2 > a_1 a_2$, which becomes $\alpha < 3/2$. This is the equilibrium shown in Fig. 12 as point A, where an instability can develop due to current diffusion into regions of low resistivity. By examining Eqs. (47) and (48), it is seen that b_1 and b_2 represent the driving terms for this process. The growth rate ω is found to be a monotone increasing function of k , vanishing at $k = 0$ and reaching a limiting value for large k of

$$\omega = a_2 = \gamma_{OH} (3/2 - \alpha). \quad (50)$$

Notice that Eq. (50) does not apply for $k \gg \beta^{-1}$, since stabilizing terms, such as thermal conductivity, from Eq. (18) must then be included in Eq. (48).

Results of numerical simulations that verify the predicted $\alpha < 3/2$ thermal instability condition are presented. Typical ZT-40 parameters were chosen with initially uniform electron and ion temperatures (100 eV) and density ($2 \times 10^{13} \text{ cm}^{-3}$). The initial conditions contain a 10% perturbation of several wavelengths in an otherwise uniform parallel current. An ad-hoc electron energy loss term of the form $C(X) (T_e/T_o)^\alpha$ is

included in the computer code, where $T_0 = 100$ eV and $C(X)$ is the ohmic heating rate of the unperturbed current at 100 eV, and allows us to simulate the stationary zeroth order electron temperature case.

Figures 13(a) and 13(b) present graphs of the parallel current and the electron temperature as a function of radius at the initial time and at 50 μ s for different values of α . There is good agreement with the instability condition $\alpha < 3/2$. For the unstable case ($\alpha = 0$) the initial current perturbation decays during the time in which a temperature perturbation is being created, but then both grow. In a stable case ($\alpha = 2$) the current perturbation creates a temperature perturbation, but then both decay. For the unstable $\alpha = 1$ case the current perturbation at 50 μ s is only slightly larger than its initial value, therefore, only the temperature perturbation is shown.

Let us now consider the role of electron-ion temperature equilibration in this thermal instability. Assume that the only loss term in the electron temperature equation (18) is the electron-ion equilibration term (now $\Lambda\beta^2$ is considered to be of order unity), that the zeroth order electron temperature θ_0 is still constant (an artificial assumption), and that no perturbations in the ion temperature may arise, i.e., γ_{ITC} is infinite. Then, proceeding as before we find that the growth rate ω in the limit of large k is

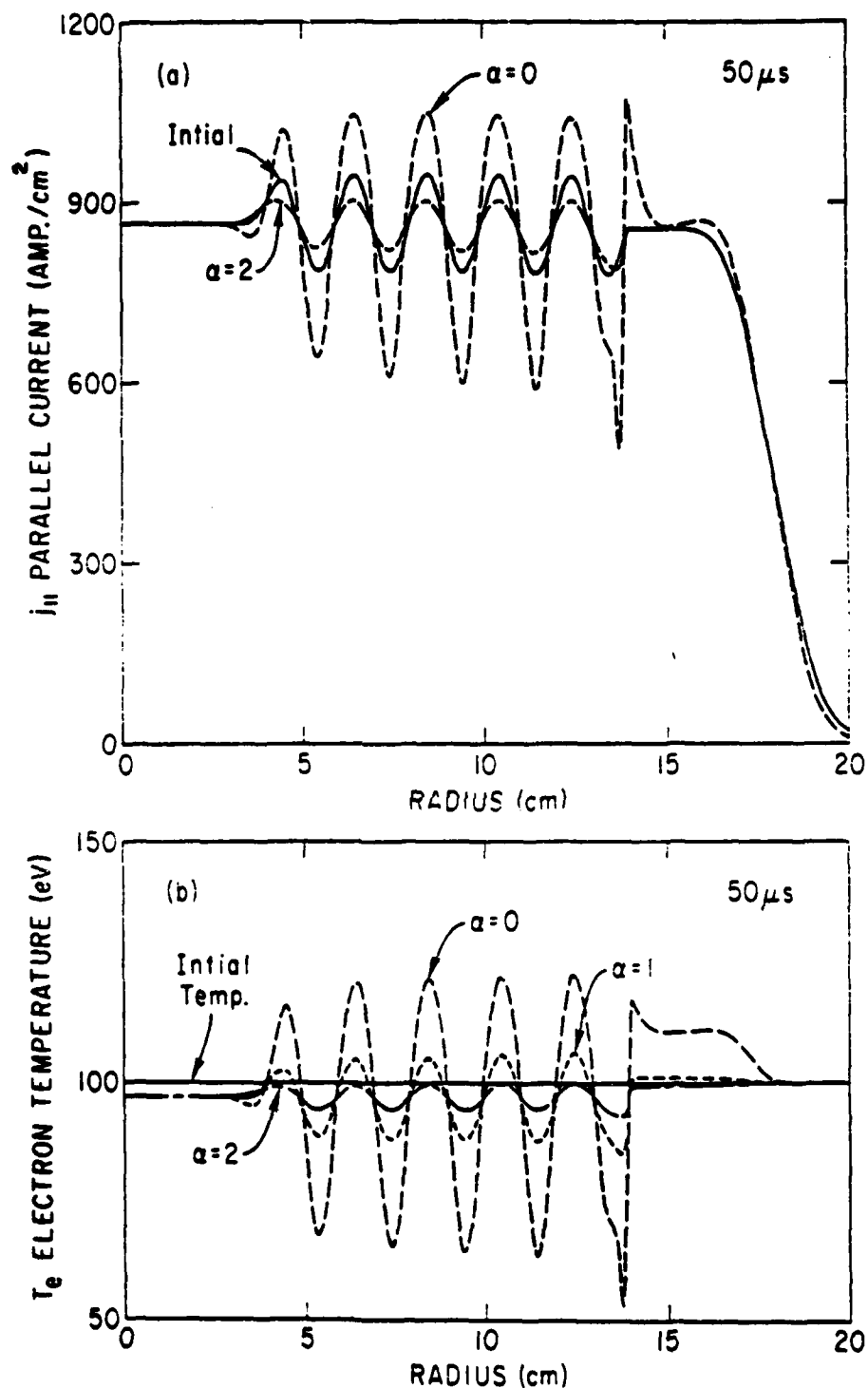


FIGURE 13

(a) The parallel current is shown at the initial time with a 10%, 2 cm wavelength perturbation from 4 cm to 16 cm, and at $50 \mu s$ for $\alpha = 0$ and $\alpha = 2$. (b) The electron temperature is shown at the initial time (a uniform 100 eV) and at $50 \mu s$ for $\alpha = 0, 1$, and 2.

$$\omega = \gamma_{OH} \left(3 - \frac{\theta_o}{\theta_o - \theta_{io}} \right), \quad (51)$$

and the instability threshold becomes $\theta_{io} < 2/3 \theta_o$ (note that for $\theta_{io} = 0$ this reduces to Eq. (50) with $\alpha = -1/2$).

For the case where both the electron-ion equilibration term and an arbitrary loss term proportional to θ_e^α is present, the growth rate in the limit of large k is

$$\omega = \gamma_{OH} (3/2 - \alpha) + \gamma_{EI} \left[(3/2 + \alpha) \frac{\theta_o - \theta_{io}}{\theta_o} - 1 \right]. \quad (52)$$

5.3. Nonstationary Electron Temperature

When a low beta plasma burns through a radiation barrier there is no stationary θ_o since the electron temperature increases rapidly everywhere. What happens to our thermal instability when this is the case is now considered.

Suppose that initially there are some small, short scale length perturbations in the current that remain from the setting up phase, and that the radiation loss rate is a small fraction of the ohmic heating power. Then the current distribution will give rise to an electron temperature profile that can be written as

$$\theta_e = \theta_o(\tau) + \epsilon \theta_1(X, \tau), \quad (53)$$

where both the zeroth order temperature and the perturbation are increasing in time.

Including the electron-ion equilibration term, this case is described by Eqs. (47) and (48) for $(\frac{P_1}{Y_0})'$ and θ_1 , along with an equation for $\theta_0(\tau)$,

$$\frac{\partial \theta_0}{\partial \tau} = C_2 \bar{n}_0 \left(\frac{P_0}{Y_0}\right)^2 - C_3 \theta_0^\alpha - C_4 \bar{n}_0 (\theta_0 - \theta_{i0}), \quad (54)$$

where $C_4 = \frac{\Lambda N_0}{Y_0}$. By Fourier analyzing Eq. (47) in space, we can write the solution for P_1' as

$$P_1' = \frac{3}{2} \frac{P_0'}{\theta_0} \theta_1 + \text{const.} \exp \frac{-\bar{n}_0 Y_0 k^2 \tau}{Y_0'^2}. \quad (55)$$

Taking the short wavelength limit one obtains the steady-state solution,

$$P_1' = \frac{3}{2} P_0' \frac{\theta_1}{\theta_0} \quad (56)$$

This shows that the current perturbation P_1' is driven by the relative temperature perturbation $\frac{\theta_1}{\theta_0}$, and not θ_1 alone. If θ_1 and θ_0 are growing at the same rate, P_1' is stationary and the instability does not exist (if Eq. (56) is used in Eq. (48) along with Eq. (38) the result for ω in short wavelength, stationary θ_0 case, Eq. (50), is obtained). Therefore, the role of the radiation loss term is to decrease the growth rate of θ_0 , thereby increasing the growth of the relative perturbation θ_1/θ_0 , and through Eq. (56) P_1' .

By combining Eqs. (48) and (54), an equation for the relative temperature perturbation $\xi \equiv \theta_1/\theta_0$ can be obtained

$$\begin{aligned} \frac{\partial \xi}{\partial \tau} = & \frac{C_2 \bar{n}_0 \left(\frac{P_0}{Y_0}\right)^{1/2}}{2\theta_0} \xi + C_3 (1-\alpha) \theta_0^{\alpha-1} \xi + \\ & + C_4 \bar{n}_0 \left(\frac{3}{2} - \frac{5}{2} \frac{\theta_{10}}{\theta_0}\right) \xi \end{aligned} \quad (57)$$

which gives a growth rate

$$\begin{aligned} \omega_\xi = & \frac{C_2 \bar{n}_0 \left(\frac{P_0}{Y_0}\right)^{1/2}}{2\theta_0} + C_3 (1-\alpha) \theta_0^{\alpha-1} + \\ & + C_4 \bar{n}_0 \left(\frac{3}{2} - \frac{5}{2} \frac{\theta_{10}}{\theta_0}\right). \end{aligned} \quad (58)$$

The actual growth of ξ is then given by

$$\xi(\tau) = \xi(0) e^{\int_0^\tau \omega_\xi d\tau}. \quad (59)$$

Whereas in the θ_0 stationary case the instability condition was $\alpha < 3/2$, ω_ξ will nearly always be positive, independent of α , since the radiation loss rate is much less than the ohmic heating rate. In fact, it is positive when there is no energy loss from the electron temperature equation ($C_3=C_4=0$). Using Eqs. (54) and (58) in Eq. (59) ξ can be calculated for this case, with the result

$$\xi(\tau) = \xi(0) (1 + 5/2 \gamma_{OH} \tau)^{1/5}, \quad (60)$$

where γ_{OH} is the ohmic heating rate at the initial temperature. This shows that the growth of ξ , which was exponential for stationary θ_0 , has been greatly reduced, but is not zero.

Although Eq. (60) indicates that current perturbations in a low beta RFP, remaining from the formation phase, have a natural tendency to grow in the absence of any electron energy loss, it does not estimate that growth rate realistically because the electron-ion equilibration term was omitted. As seen from Eq. (58), this term is destabilizing if the electron and ion temperatures are not closely equilibrated (for this term to be net stabilizing $\theta_{i0}/\theta_0 > \frac{3}{5}$). The effect of this term and that of various impurity concentrations on the growth of initial current perturbations in the RFP are studied numerically.

5.3.1. Numerical Simulation

This section presents results of numerical studies of the effect of impurities on the growth of fine-scale current and temperature gradients in the RFP. Plasma parameters typical of ZT-40 are chosen (see table 1) with a uniform plasma density. There is an initial 10% perturbation in the parallel current from a radius of 4 cm to 17 cm. The unperturbed current is uniform until 17 cm after which it drops sharply to zero by 18.5 cm.

In Figs. 14(a) and 14(b) the parallel current and electron temperature is plotted as a function of radius at the initial time and at 100 μ s for three cases: impurity free, 2% oxygen, and 4% oxygen, where there is a uniform plasma density of 10^{14} cm $^{-3}$. The initial current perturbations have a 2.5 cm wavelength. For the impurity free case the current perturbations have grown by 25% at 100 μ s. This is due to the effect of the electron-ion equilibration term, since these perturbations are nearly stationary when the same case is run with this term omitted. For the 2% oxygen case the current perturbations have grown by 120%, and for the 4% oxygen case by a huge 350%. From Fig. 14(b) we see that although the zeroth order temperature (seen from the inner 4 cm) has climbed well above the peak of the oxygen radiation barrier for all cases, the temperature depressions corresponding to the 4% oxygen case are actually hung up on this barrier. This has been brought about by current diffusion out of these regions. The temperature actually rises above the peak of the oxygen radiation barrier but then collapses as the current diffuses away. This figure shows that the role of the impurity radiation is to decrease the growth of the zeroth order temperature and thereby increase the growth of the relative temperature perturbation driving the perturbed current, a point made previously from Eq. (56).

From the expression for ω in the stationary θ_0 case, Eq. (49), it was noted that the growth rate of this instability decreases as the wavelength increases. Figs. 15(a) and 15(b)

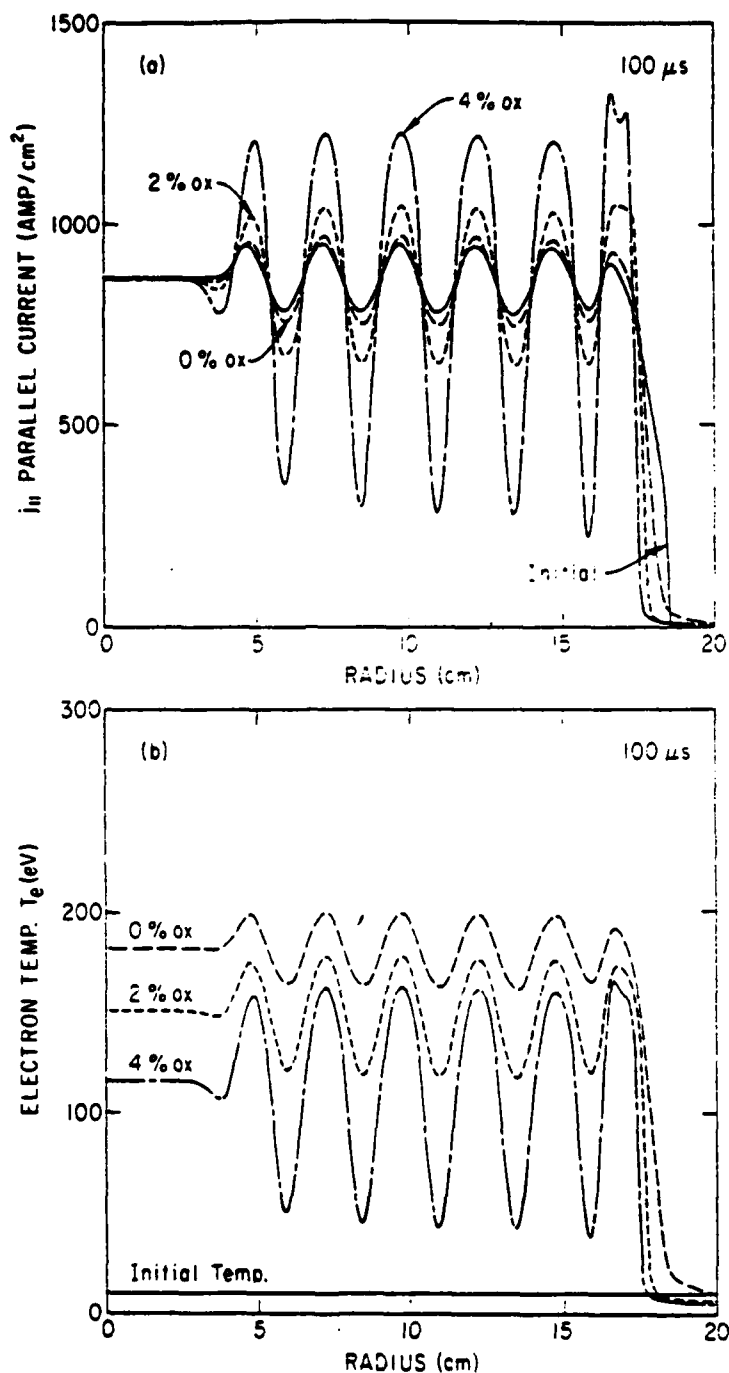


FIGURE 14

(a) Parallel current is shown at the initial time, with a 10%, 2.5 cm wavelength perturbation from 4 cm to 17 cm, and at 100 μs for ZT-40 parameters with oxygen impurity concentrations of 0%, 2%, and 4% of the deuterium density ($1 \times 10^{14} \text{ cm}^{-3}$). (b) The electron temperature is shown at the initial time and at 100 μs for the above mentioned impurity concentrations.

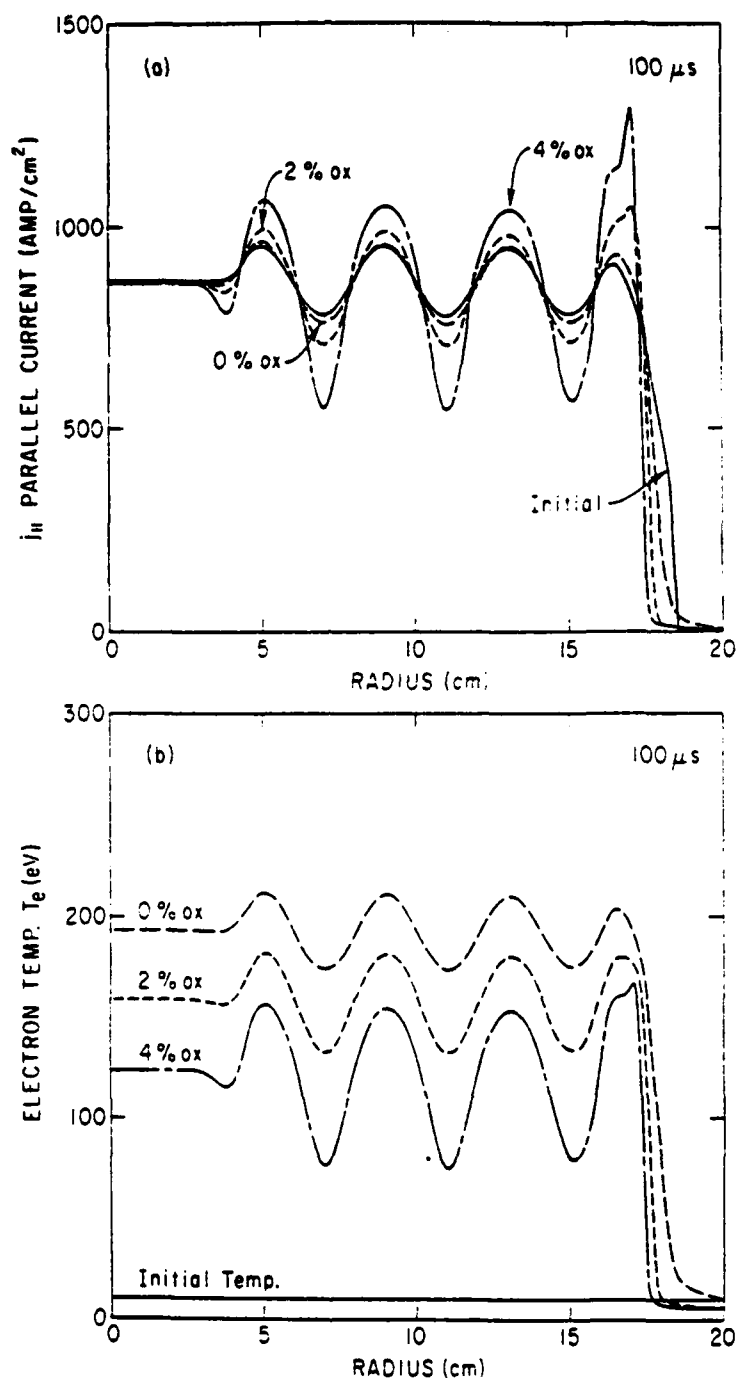


FIGURE 15

(a) The parallel current is shown at the initial time, with a 10%, 4 cm wavelength perturbation from 4 cm to 17 cm, and at 100 μs for ZT-40 parameters with oxygen impurity concentrations of 0%, 2%, and 4% of the deuterium density ($1 \times 10^{14} \text{ cm}^{-3}$). (b) The electron temperature is shown at the initial time and at 100 μs for the above mentioned impurity concentrations.

show results at 100 μ s for cases identical to those in figure 14 except that the wavelength of the initial current perturbation has been increased to 4 cm. We see that the growth of the initial current perturbation has been greatly reduced from that in the 2.5 cm wavelength case. For the 2% oxygen simulation the current perturbation has grown by 55% in 100 μ s and for 4% oxygen the temperature depressions are not caught on the oxygen radiation barrier.

Note that there is a sharp peak in the current just near the wall in Fig. 15(a). This is due to current in the cold outermost region diffusing inward. The current channel tries to constrict but cannot do so.

Since the ohmic heating rate is inversely proportional to the plasma density but the radiation loss rate is directly proportional to the density squared for a fixed impurity concentration, it is interesting to compare simulations at different densities. A series of simulations were performed for initial conditions identical to those cases shown in figure (14) except for a density of $4 \times 10^{15} \text{ cm}^{-3}$ with oxygen impurity concentrations of 0%, .25% and .5%. The results of these simulations are shown in Figs. 16(a,b). Although no simple scaling between different density cases can be given in general (due to the temperature dependence of η), the magnitude of the current and temperature perturbations in the .5% O and .25% O simulations of figure (16) and the 4% O and 2% O simulations of figure (14) are very similar except that

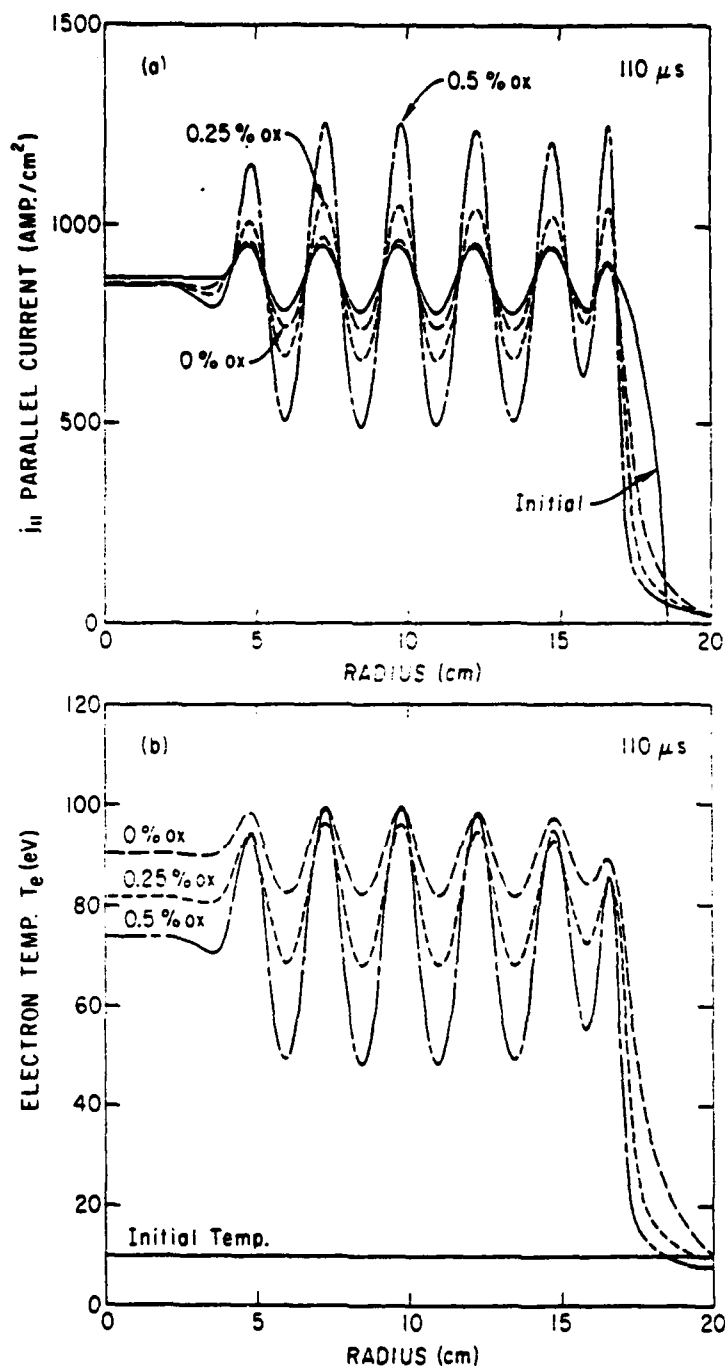


FIGURE 16

(a) The parallel current is shown at the initial time, with a 10%, 2.5 cm wavelength perturbation from 4 cm to 17 cm, and at 100 μ s for ZT-40 parameters with oxygen impurity concentrations of 0%, .25%, and .5% of the deuterium density (4×10^{14} cm⁻³).

(b) The electron temperature is shown at the initial time and at 100 μ s for the above mentioned impurity concentrations.

the .5 0 case does not have temperature wells that are caught on the radiation barrier (note the difference in the zeroth order temperatures between Figs. 14(b) and 16(b)). Thus we see that by increasing the plasma density by a factor of four and decreasing the impurity density by a factor of two we have achieved very similar results.

It is often seen in the numerical simulations that the wells in the initial current perturbation grow faster than the peaks. This is due to the dependence of the radiation loss term on position. That is, the perturbation in ξ is caused not only by the current perturbation, with the radiation loss as a uniform background slowing the growth of θ_0 , but also by the spatial variation of the radiation loss term (the assumption that θ_1/θ_0 is small can break down so that the growth rate ω_ξ must be expressed in terms of θ_e instead of θ_0). An extreme case of this is where there is an isolated point at which the radiation barrier is not overcome (c.f. Fig. 14(b)). The current will diffuse out of this region creating a deep well but not a comparable peak.

5.3.2. Saturation of the Instability

If beta becomes large enough the temperature perturbations will be smoothed by the electron thermal conductivity and by the ion thermal conductivity once the electron and ion temperatures are sufficiently equilibrated, and the instability will be quenched. In Figs. 17(a,b,c) the parallel

current and electron and ion temperatures are plotted, respectively, as a function of radius at the initial time and at three later times for the .25% oxygen impurity case of Fig. (16). The instability reaches a peak at about 100 μ s and then begins to decay as beta increases. We see that at 310 μ s the growth of the current perturbation has decreased to about half of its maximum value and that by 910 μ s it is substantially less than its initial value. The decay of the current perturbation and the relative temperature perturbation begins at a beta of about 4% and corresponds to the point where the ratio of the zeroth order ion to electron temperature becomes greater than $3/5$, the threshold at which the electron-ion equilibration term becomes stabilizing (c.f., Eq. (58)). Thus it is the ion thermal conductivity which is the damping mechanism. Notice from Eq. 17(c) that perturbations in the ion temperature do not develop.

Because beta must increase to a value such that the electron and ion temperatures become closely equilibrated before these perturbations begin to damp, it is expected that some anomalous process will actually provide the damping mechanism.

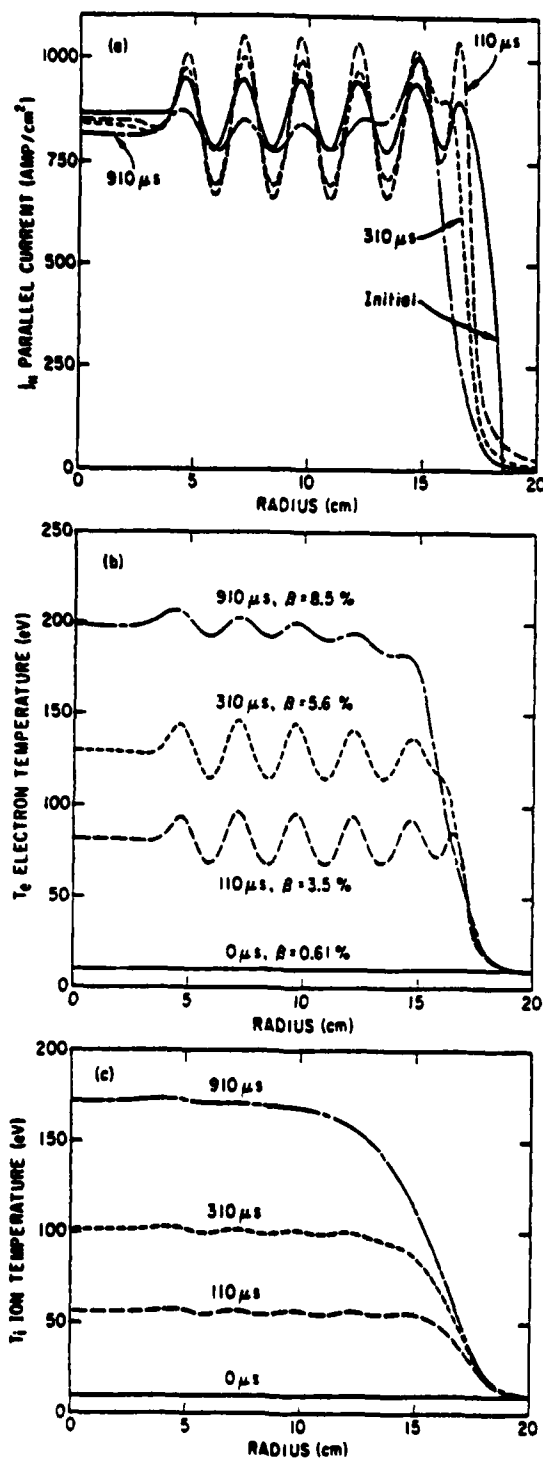


FIGURE 17

The parallel current, electron temperature, and ion temperature are given in parts (a), (b), and (c) respectively, for the .25% oxygen impurity case of Fig. 16, at the initial time and at 110 μs , 310 μs , and 910 μs .

5.3.3 Anomalous Transport

It is not known what transport coefficients actually apply in the post-implosion phase of a RFP. The coefficients may be anomalous due to many mechanisms, including unstable drift waves driven by fine-scale current and temperature gradients that are created by the thermal instability just discussed.

How anomalous transport effects our thermal instability picture, based on classical transport, depends on how χ_{le}/n_e scales from the classical to the anomalous case. If χ_{le}/n_e is enhanced sufficiently, then the electron thermal conductivity can smooth perturbations in the electron temperature. If χ_{le}/n_e remains unchanged, as in the case where χ_{le} and n_e are both modified by an effective collision frequency (for example, the ion acoustic instability), then only the time scale changes and the character of the thermal instability is the same as in the classical case.

It is interesting to note that in the tokamak the experimentally observed electron thermal conductivity is approximately one hundred times its classical value. When simulations were performed with an initial 10%, 2.5 cm wavelength current perturbation, a modest level of oxygen impurity, and the electron thermal conductivity enhanced by this amount, the current perturbation simply decayed. Since the electron thermal conductivity must be enhanced by such a large factor to stabilize this perturbation, one would expect that for a classical electron thermal conductivity very fine-scale (wavelengths greater than

1 mm) current perturbations will be unstable.

The anomalous, hundred times classical electron thermal conductivity observed in tokamaks is unexplained theoretically. It is possible that this phenomena could be the consequence of a microinstability that is the result of the need to stabilize these short wavelength current perturbations. However, since a microinstability that could be responsible for this effect is not known, this hypothesis can only be meant as mere speculation.

CHAPTER 6

CONCLUSION

The effect of energy loss due to impurity radiation on the evolution of RFP plasma and magnetic field profiles in the post-implosion phase has been studied by numerical simulation for the ZT-S, ZT-40, and RFX experiments using oxygen (and also aluminum in ZT-40) as a typical impurity. Assuming classical transport and typical operating parameters, limits are found on the levels of these impurities above which the electron temperature becomes radiation limited. The ability of a reversed-field pinch to burn through a radiation barrier is shown to depend on the electron and impurity densities, current density, and device size.

It is found that the ZT-S experiment has a radiation limited temperature in agreement with the experimental observations and the measured oxygen impurity level. Because of its small size and high density, the value of beta in ZT-S is large at the temperature where the oxygen radiation barrier is a maximum ($\beta \sim 17\%$ at 30 eV with a $1 \times 10^{15} \text{ cm}^{-3}$ density). Therefore, there is only a small magnetic energy reservoir available to heat the plasma above this value or to be lost to radiation without causing a large degradation of the magnetic fields and consequent loss of stability. Both ZT-40 and RFX have the advantage that for projected operating parameters the peak of the oxygen radiation barrier occurs at a low value of beta. However, RFX has a much lower current density than ZT-40 and we find, for similar plasma and magnetic field profiles and

for the projected operating parameters, that the density of oxygen necessary to produce a radiation limited temperature in RFX is approximately four times less than in ZT-40.

The results show that if a low beta plasma burns through the radiation barrier in some region the classical electron thermal conductivity will not be large enough to aid burn-through in the rest of the plasma and steep temperature gradients will be formed leading presumably to anomalous transport. It is seen that the Suydam criterion is violated in the outer regions of the plasma for ZT-40 and RFX even if there is no steepening of temperature gradients due to impurity effects. Thus, classical transport cannot be expected in this region.

The one-dimensional results were suitably reduced to zero-dimensional ones and used to calibrate an analytical formula that describes the ability of a plasma to burn through the oxygen radiation barrier given only the design parameters: size, total current, electron density, and impurity density. This criterion is useful in roughly estimating how a proposed RFP will perform when confronted with the oxygen radiation barrier.

The role of impurities in producing a thermal instability in the RFP that is due to the coupling of current diffusion and ohmic heating was studied for the case where there is a nearly force free, low beta equilibrium, after the formation phase, as the plasma attempts to ohmic heat to a significant beta. Two cases, stationary and nonstationary

electron temperature, were considered.

For the stationary electron temperature case it was shown that in a radiation limited plasma the current (and, therefore, the temperature, but not the density) can break up into filaments. It was found that the growth rate of this phenomena is a monotone increasing function of k , which vanishes for $k = 0$ and for large k is proportional to the ohmic heating rate. The condition that must be satisfied for this instability to occur was derived, and verified through numerical simulation. This indicates how a radiation limited RFP plasma may destroy itself.

The nonstationary electron temperature case, which is of more general interest, yields important new results. It is found that the thermal instability previously considered is still operable even in the case where there is no energy loss from radiating impurities. Thus, fine-scale current perturbations remaining from the formation phase, have a natural tendency to grow, although the growth rate is much reduced from the ohmic heating rate. It was shown analytically and verified numerically that the role of a uniform background energy loss is to decrease the growth of the uniform, zeroth order electron temperature θ_0 , while not affecting the growth of the perturbed, short wavelength electron temperature θ_1 . The growth of the current perturbations depends upon the relative temperature perturbation θ_1/θ_0 , which explains the role of impurity radiation in aiding the growth of the current perturbations. Numerical simulations show that only modest

impurity levels are necessary to produce large current and temperature gradients in relatively short periods of time.

The classical damping mechanism is the ion thermal conductivity, which makes the electron-ion equilibration term net stabilizing after the electron and ion temperatures have equilibrated sufficiently. This requires a modest value of beta. Therefore, it is expected that the effect of a low level of plasma impurities in conjunction with fine-scale perturbations in the initial current distribution will be to create large current and temperature gradients, via thermal instability, that will be saturated by a nonclassical mechanism, which preferentially increases the electron thermal conductivity.

REFERENCES

1. Baker, D. A., et al., Plasma Physics and Controlled Nuclear Fusion Research 1974 (Proc. 5th Int. Conf. Tokyo, 1974), 3, IAEA, Vienna (1975), 35.
2. Boden, H. A. B., Third Topical Conference on Pulsed High Beta Plasmas, Culham 1975, paper Bl.1, p. 39, Pergamon Press.
3. Baker, D. A., et al., Los Alamos Scientific Laboratory Report, LA-6173-MS (1975).
4. Butt, E. P., et al., Plasma Physics and Controlled Nuclear Fusion Research 1974 (Proc. 5th Int. Conf. Tokyo, 1974), 3, IAEA, Vienna (1975), 417.
5. Buffa, A., et al., Plasma Physics and Controlled Nuclear Fusion Research 1974 (Proc. 5th Int. Conf. Tokyo, 1979), 3, IAEA, Vienna (1975), 431.
6. Baker, D. A., et al., Plasma Physics and Controlled Nuclear Fusion Research 1978 (Proc. 7th Int. Conf. Austria, 1978), 2, IAEA, Vienna (1979), 3.
7. Baker, D. A., et al., Plasma Physics and Controlled Nuclear Fusion Research 1976 (Proc. 6th Int. Conf. Berchtesgaden, 1976), 1, IAEA, Vienna (1977), 419.
8. Kadomtsev, B. B., Reviews of Plasma Physics, edited by M. A. Leontovich (Consultants Bureau, New York, 1966), Vol. 2, p. 153.
9. Braginskii, S. I., Reviews of Plasma Physics, edited by M. A. Leontovich (Consultants Bureau, New York, 1965), Vol. 1, p. 205.
10. Duchs, D. F., Post, D. E., and Rutherford, P. H., Nucl. Fusion 17 (1977), 565.
11. McWhirter, R. W. P., Plasma Diagnostic Techniques, edited by R. H. Huddleston and S. L. Leonard (Academic Press 1975), p. 201.
12. Kolb, A. C., and McWhirter, R. W. P., Phys. Fluids 7 (1974), 519.
13. Duchs, D., Engelhardt, W., Koppendorfer, W., Nucl. Fusion 14 (1974), 73.

14. Post, D. E., et al., Atomic Data and Nuclear Data Tables 20, No. 5 (1977), 397.
15. Robinson, D. C., Plasma Physics 13 (1971), 439.
16. Caramana, E. J., and Perkins, F. W., submitted for publication, see Appendix of this thesis.
17. Dnestrovskij, Y. N., Inovenkov, I. N., and Kostomarov, D. P., Nucl. Fusion 16 (1976), 513.
18. Cristiansen, J. P., and Roberts, K. V., Nucl. Fusion 18 (1978), 181.
19. Goedbloed, J. P., Sakanaka, P. H., Phys. Fluids 17 (1974), 908.
20. Furth, H. P., Rosenbluth, M. N., Rutherford, P. H., and Stodiek, W., Phys. Fluids 13 (1970), 3020.

APPENDIX

THE NUMERICAL SOLUTION OF THE MULTI-FLUID,
QUASI-EQUILIBRIUM MHD EQUATIONS IN ONE DIMENSION

THE NUMERICAL SOLUTION OF THE MULTI-FLUID,
QUASI-EQUILIBRIUM MHD EQUATIONS IN ONE DIMENSION

ABSTRACT

We present a method for solving the MHD equations with impurity ion species, in the cylindrical approximation for the case where the plasma evolves through a series of equilibrium states. The MHD equations are split into two independent and self-consistent sets: one that contains all transport processes and another that contains all atomic physics processes. These two sets of equations are solved in succession to obtain the solution of the original problem. Each set of equations is in itself a coupled initial value and boundary value problem. To solve these two systems of equations a Lagrangian coordinate system is developed based on a normalized poloidal flux coordinate. In conjunction with a change in dependent variables to quantities that are invariant under adiabatic motion of the plasma, this allows each set of equations to be directly advanced in time with standard numerical techniques. An example of the numerical solution is given for the ZT-40 reversed-field pinch experiment.

1.0 Introduction

We present a method of solving the equations of magnetohydrodynamics in one dimension for an arbitrary number of ion species, including atomic physics effects, for the case where a magnetohydrostatic equilibrium is maintained in time. This system of equations describes the slow time evolution of a high-beta plasma such as in the reversed-field pinch (RFP), spheromak, or high-beta tokamak, with the restriction that the assumption of cylindrical symmetry be a sufficiently valid approximation. This assumption is reasonable for plasmas where the magnetic flux surfaces have an approximately circular shape as in the reversed-field pinch and spheromak, but may not always be a good approximation for the high-beta tokamak.

Section 2 presents the equations that describe the complete physics model. In Section 3 these equations are split into two simpler but self-consistent sets, one which describes plasma transport due to finite resistivity (i.e., particle collisions) and another which describes processes that are a consequence of atomic physics. Taken together, these two sets of equations contain the same physics as the original set. Section 4 develops a Lagrangian coordinate system based on a normalized poloidal flux variable, and in Section 5 the two sets of equations given in Section 3 are transformed into this coordinate representation. Section 6 describes the numerical methods used to solve these equations, and Section 7 gives results of their numerical solution for the 2T-40 reversed-

field pinch experiment.

2.0 Complete Physics Model

We start with the MHD equations as given by Braginskii¹ and neglect inertia, plasma viscosity, and assume a cylindrical geometry and symmetry so that all dependent variables are a function only of the radial coordinate r . The plasma is taken to consist of electrons, deuterium ions, and an impurity species of charge Z (the extension to the case where there is more than one impurity species will be obvious). Our equations then become; the continuity equations for electrons, deuterium ions, and Z impurity fluids

$$\frac{\partial n_e}{\partial t} + \vec{v} \cdot \vec{v}_{er} n_e = A_e , \quad (1)$$

$$\frac{\partial n_i}{\partial t} + \vec{v} \cdot \vec{v}_{ir} n_i = A_i , \quad (2)$$

$$\frac{\partial n_j}{\partial t} + \vec{v} \cdot \vec{v}_{jr} n_j = n_e [n_{j-1} \beta_{j-1} - n_j (\beta_j + \alpha_j) + n_{j+1} \alpha_{j+1}] , \quad (3)$$

where $j = 1 \dots Z$ and all velocities are in the radial direction; the magnetic field equations

$$\frac{\partial \vec{B}}{\partial t} - \vec{\nabla} \times (\vec{V}_{er} \times \vec{B}) = \vec{\nabla} \times \frac{c \vec{R}_e}{en_e} ; \quad (4)$$

the internal energy equations

$$\frac{3}{2} \frac{\partial}{\partial t} n_e T_e + \frac{3}{2} \vec{\nabla} \cdot n_e T_e \vec{V}_{er} + n_e T_e \vec{\nabla} \cdot \vec{V}_{er} = W_e , \quad (5)$$

$$\frac{3}{2} \frac{\partial}{\partial t} n_i T_i + \frac{3}{2} \vec{\nabla} \cdot n_i T_i \vec{V}_{ir} + n_i T_i \vec{\nabla} \cdot \vec{V}_{ir} = W_i , \quad (6)$$

$$\frac{3}{2} \frac{\partial}{\partial t} n_j T_j + \frac{3}{2} \vec{\nabla} \cdot n_j T_j \vec{V}_{jr} + n_j T_j \vec{\nabla} \cdot \vec{V}_{jr} = W_j , \quad (7)$$

and the magnetohydrostatic equilibrium equation

$$\vec{\nabla} p = \frac{j}{c} \times \vec{B} \quad (p = n_e T_e + (n_i + \sum_j n_j) T_i) . \quad (8)$$

A_e and A_i are electron and deuterium ion source terms that are a consequence of ionization of impurities and neutral gas (an explicit description of neutrals is not given here, however, see Ref. (3)). β_j and α_j are ionization and recombination coefficients respectively. \vec{R}_e is the total force between electrons and all ion species due to both friction and thermoelectric effects. W_e , W_i , and W_j are energy source and

sink terms that are due to such processes as ohmic heating, electron-ion energy equilibration, thermal conduction, and energy loss due to impurity radiation and charge exchange.

Note that all terms on the RHS of Eqs. (1)-(7) are due to non-ideal MHD effects. Also, all ion species have been assumed to have the same temperature², thus Eqs. (6) and (7) are not independent.

The velocities in Eqs. (1)-(7) can be expressed in terms of one another by

$$\vec{v}_{kr} = \frac{c}{ez_k n_k B_z} \vec{R}_k \times \vec{B} + \frac{c \vec{E} \times \vec{B}}{B^2} , \quad (9)$$

which is the momentum equation for the kth species (where $\vec{R}_k = \sum_l \vec{R}_{kl}$, and \vec{R}_{kl} is the force between species k and l, has the property $\vec{R}_{kl} = -\vec{R}_{lk}$, and can be expressed in terms of plasma quantities). Therefore, if one of these velocities is determined the rest can be found.

The velocities are a consequence of all dissipative processes, regardless of origin, and the driving electric fields at the plasma edge in conjunction with the boundary conditions on plasma density and temperature. This is easily seen by constructing an explicit equation for any one of the \vec{v} 's. To do this we take the time derivative of Eq. (8) and then use Eqs. (4)-(7) to eliminate these time derivatives. This yields

$$\frac{3}{2} \sum_k \vec{v} (\vec{v} \cdot n_k T_k \vec{v}) + \frac{3}{2} \sum_k \vec{v} (n_k T_k \vec{v} \cdot \vec{v})$$

$$- \frac{\vec{B}}{4\pi} \times \vec{v} \times \vec{v} \times (\vec{v} \times \vec{B}) + (\vec{v} \times \vec{B}) \times [\vec{v} \times (\vec{v} \times \vec{B})] = S, \quad (10)$$

where Eq. (9) has been used to eliminate all \vec{v}_k 's in favor of the selected \vec{v} (the sum over k in Eq. 10 includes all plasma components). Equation (10) is a complicated second order ordinary differential equation that is linear in \vec{v} and contains all of the source terms in Eqs. (1) - (7) (the RHS) as the inhomogeneous driving term S . At the wall radius a , the velocity \vec{v} must obey Eq. (9), where E is given by the external circuit, and at the origin $\vec{v} = 0$. Thus, the velocities in Eqs. (1)-(7) are not determined as an initial value problem as are the other dependent variables. One velocity is determined by the magnetohydrostatic equilibrium equation (8) and the others by Eq. (9). That is, Eqs. (1)-(8) form a coupled initial value and boundary value problem where the velocity is constrained to be such that the plasma evolves through a series of equilibrium states. Although Eqs. (1)-(8) are highly nonlinear, a linear equation determines \vec{v} so that the effect of different dissipative mechanisms (e.g., resistive transport and radiation energy loss) can simply be superposed. That is, the highly nonlinear nature of Eqs. (1)-(8) is reflected in Eq. (10) only through the time dependence of the coefficients

and the driving term S . We can thus split \vec{V} into two separate components: \vec{V}_T , which arises from all terms that are due to resistive transport, and \vec{V}_R , which arises from all terms that are a consequence of atomic physics processes. To obtain the total \vec{V} the two results are simply added. Thus, instead of advancing the full set of equations in time (by some means that is as yet unspecified) retaining in them the total velocity \vec{V} , we perform a time step by first advancing the equations with only \vec{V}_T and then with only \vec{V}_R . Since the coefficients and the inhomogeneous term in Eq. (10) change with time, the time step must be small enough that this change is not appreciable if we are to expect that this two-step process will closely approximate the solution of the original set of equations.

Operationally, advancing Eqs. (1)-(8) keeping only \vec{V}_T means that all terms that are due to atomic physics processes are dropped, and advancing them keeping only \vec{V}_R means that all terms that are a consequence of resistive transport are dropped. Our original set of equations is thus split into two independent and self-consistent sets, one that contains all resistive transport processes and one that contains all atomic physics processes.

It is interesting to note that Eqs. (1)-(8) possess an energy integral⁴ of the form

$$\frac{\partial}{\partial t} \int_0^a \left(\frac{3}{2} p + \frac{B^2}{8\pi} \right) 2\pi r dr = F_T + E_R \quad , \quad (11)$$

where F_T is the total energy flux at the plasma edge due to resistive transport and external electric fields, and E_R is the total energy loss due to atomic physics processes. Thus our two simpler sets of equations will separately conserve energy, and therefore the total energy associated with Eqs. (1)-(8) cannot diverge as a result of this approximation.

What we have done is to start with a very complicated set of equations and show that they can be split into two simpler sets that can be solved in succession. This is a splitting method with noncommuting operations. It can be expected that the solution obtained in this manner will converge to the solution of the original equations because of the linear properties of Eq. (10) for \vec{V} , and the fact that this method keeps the total energy associated with the original system of equations bounded.

In the next section we present the transport model equations associated with the velocity \vec{V}_T , and the radiation model equations associated with the velocity \vec{V}_R .

3.0 Transport Model Equations

To obtain the transport model equations from Eqs. (1)-(8) we drop all terms which arise due to atomic physics effects. In addition, some other properties of these equations, which allow them to be written in a more simplified form, are noted.

First, the quasi-neutrality condition is contained in our physics model. This can be seen by considering Eq. (9) in conjunction with Ampere's law. From the assumption of cylindrical symmetry and Ampere's law we have

$$j_r = (\hat{\nabla} \times \hat{B})_r = \sum_k z_k e n_k v_{rk} = 0 .$$

Using Eq. (9), it follows that

$$n_e = \sum_j z_j n_j + n_i . \quad (12)$$

The quasi-neutrality condition can be used to replace any one equation of continuity; which one must be decided on physical grounds.

Because the ion-electron momentum transfer time is long compared to the momentum transfer time between different ion species (due to the mass difference), the friction force on a particular ion impurity species will be almost solely due the other ion species. From the form of \hat{R}_{im} ,¹

$$\hat{R}_{im} = \frac{M_i n_i}{\tau_{im}} (\hat{V}_{Dm} - \hat{V}_{Di}) , \quad (13)$$

where

$$\hat{V}_{Dm} = \frac{-c}{Z_m n_m e B z} \hat{\nabla} P_m \times \hat{B}$$

is the diamagnetic drift velocity of the m th ion species and τ_{lm} is the momentum transfer time between species l and m , it can be shown that there is an ambipolar diffusion of ions such that impurities diffuse inward toward the deuterium ion density maximum. This maximum subsequently flattens as deuterium diffuses outward in such a manner that quasi-neutrality is satisfied (note that a steady state, $\hat{R}_{lm} = 0$, is reached only when $n_l = \text{const. } n_m^{Z_l/Z_m}$ for all species l and m). This physical process motivates us to use the quasi-neutrality condition to determine the deuterium ion density n_i . If this condition were used to determine the electron density we would in effect be adding together oppositely directed ion fluxes, leading to an inaccurate result.

A convenient form of the ion temperature equation is now constructed from Eqs. (6) and (7), which as noted previously are not independent. Since there are fluxes of different ion species in opposite directions, one would like to have an ion temperature equation which follows the electron velocity V_{er} . Then the electron density and electron and ion temperatures will be interdependent, but without ion diffusion effects. Such an equation can be constructed by multiplying Eq. (7) by Z_j and adding Eqs. (6) and (7), using Eq. (9) and remembering that $\hat{R}_{lm} = -\hat{R}_{ml}$. This results in an equation for $n_e T_i$, which follows the electron velocity. Using the electron continuity equation, equations can then be found for the

electron and ion temperatures.

With the above results, the transport model equations become:

$$\frac{\partial n_e}{\partial t} + \vec{v} \cdot \vec{v}_{er} n_e = 0, \quad (14)$$

$$n_i = n_e - \sum_j z_j n_j, \quad (15)$$

$$\frac{\partial n_j}{\partial t} + \vec{v} \cdot \vec{v}_{jr} n_j = 0, \quad (16)$$

$$\frac{\partial \vec{B}}{\partial t} - \vec{v} \times (\vec{v}_{er} \times \vec{B}) = \vec{v} \times \frac{c \vec{R}_e}{en}, \quad (17)$$

$$\frac{\partial T_e}{\partial t} + \vec{v}_{er} \cdot \vec{v} T_e + \frac{2}{3} T_e \vec{v} \cdot \vec{v}_{er} = \frac{2}{3} \frac{W_{eT}}{n_e}, \quad (18)$$

$$\frac{\partial T_i}{\partial t} + \vec{v}_{er} \cdot \vec{v} T_i + \frac{2}{3} T_i \vec{v} \cdot \vec{v}_{er} = \frac{2}{3} \frac{W_{iT}}{n_e}, \quad (19)$$

$$\vec{v}_p = \frac{j}{c} \times \vec{B}, \quad (20)$$

where $W_{iT} = W_{iT} + \sum_j z_j W_{jT}$ and the subscript T denotes

quantities that contain only resistive transport processes.

The boundary conditions on Eqs. (14)-(20) are that at the origin \vec{v}_{kr} vanish (there may be no flux of any quantity at $r = 0$), and that at the plasma edge values of the density and temperature of plasma species be specified, and also, the electric fields E_z and E_θ . E_z and E_θ are the natural boundary conditions to use when toroidal and poloidal flux replace B_z and B_θ as variables. This is what occurs in the poloidal flux coordinate representation of these equations.

3.1 Radiation Model Equations

To obtain the radiation model equations from Eqs. (1)-(8), we drop all terms that are due to resistive transport.

In this case quasi-neutrality is merely an expression of charge conservation. It is convenient to use this condition to determine the electron density since electrons are added and subtracted from the plasma by atomic physics processes that affect the ions.

An equation for the total ion energy is formed by simply adding Eqs. (6) and (7).

The radiation model equations now become:

$$n_e = n_i + \sum_j Z_j n_j \quad . \quad (21)$$

$$\frac{\partial n_i}{\partial t} + \vec{v} \cdot \vec{v}_r n_i = A_i , \quad (22)$$

$$\frac{\partial n_j}{\partial t} + \vec{v} \cdot \vec{v}_r n_j = n_e [n_{j-1} \beta_{j-1} - n_j (\beta_j + \alpha_j) + n_{j+1} \alpha_j] , \quad (23)$$

$$\frac{\partial \vec{B}}{\partial t} - \vec{v} \times (\vec{v}_r \times \vec{B}) = 0 , \quad (24)$$

$$\frac{\partial}{\partial t} n_e T_e + \vec{v} \cdot n_e T_e + \frac{2}{3} n_e T_e \vec{v} \cdot \vec{v}_r = \frac{2}{3} W_{eR} , \quad (25)$$

$$\frac{\partial}{\partial t} n_I T_i + \vec{v} \cdot n_I T_i \vec{v}_r + \frac{2}{3} n_I T_i \vec{v} \cdot \vec{v}_r = \frac{2}{3} W_{IR} , \quad (26)$$

$$\vec{v}_p = \frac{\vec{j}}{c} \times \vec{B} , \quad (27)$$

where $n_I = n_i + \sum_j n_j$, $W_{IR} = W_{iR} + \sum_j W_{jR}$ and subscript R denotes quantities that contain only atomic physics processes.

Notice that because there is no transport all plasma components have the same radial velocity. This velocity is due to adiabatic expansion and contraction of the plasma.

The boundary conditions on Eqs. (21)-(27) are that \vec{v}_r vanish at the origin and that the electric fields at the plasma edge are zero, which implies (c.f., Eq. (9)) that \vec{v}_r vanish

also at the plasma edge.

An important advantage of this splitting method, aside from the fact that it produces two sets of equations less complicated than the original set, is that it allows the use of variables and physical conditions in a manner that is suited to the physics contained in each set. For example, it was seen that it is appropriate to use the quasi-neutrality condition to determine the deuterium ion density when considering the diffusion of impurity ion species, and the electron density when considering atomic physics processes. Also, it is necessary to use temperature rather than internal energy as a dependent variable in the transport model equations (otherwise difficulty arises in finite differencing the thermal conduction terms), but convenient to use internal energy as a variable in the radiation model equations because this avoids the appearance of electron source terms due to ionization and recombination that would occur in an equation for the temperature.

4.0 Solution of the Initial-Boundary Value Problem

The full system of equations was simplified by splitting it into two independent, self-consistent sets. We now concern ourselves with the solution of these two systems of equations.

As noted in section 2, the principle difficulty in numerically solving the transport model equations (14)-(20) or the radiation model equations (21)-(27) is that the velocity which occurs in these equations is determined implicitly by the equilibrium constraint. One can picture the evolution of the plasma through successive equilibria as a series of two step processes whereby the Eulerian plasma variables B_z , B_θ , etc., are perturbed due to dissipation and are no longer in equilibrium, but then relax adiabatically to a new equilibrium state. A numerical scheme for the solution of these equations can be based directly on this physical picture⁵, however, a more powerful approach is to analytically restructure the equations before attempting a numerical solution. This latter method is what is developed here.

We construct a Lagrangian coordinate system based on the magnetic flux and transform the equations into this representation, changing the dependent variables to quantities that remain invariant under adiabatic motion of the plasma. In this manner the adiabatic relaxation of the plasma is automatically accounted for, and the velocity that is determined by the equilibrium constraint equation can be explicitly eliminated. This yields a system of equations that can be directly advanced in time.

4.1 Poloidal Flux Coordinate System

The poloidal flux is chosen as the variable on which to base our Lagrangian coordinate system. This is because it is a single valued function of the radius in both the reversed-field pinch and spheromak, whereas the toroidal flux is not. However, there are two difficulties associated with the use of the poloidal flux as an independent variable:

1. Poloidal flux is destroyed at the origin due to plasma resistivity.

2. Poloidal flux may be added to the system by an externally driven electric field. It is now shown how these two difficulties can be overcome, and a fixed domain of integration obtained, based on this variable.

In general, the transformation in one dimension to a Lagrangian coordinate x based on the variable χ is defined by

$$x = \int_0^r \chi dr \quad , \quad \frac{\partial \chi}{\partial t} + \frac{\partial}{\partial r} V \chi = 0 \quad , \quad (28a,b)$$

where r is the variable that denotes physical space and V is the velocity followed in the frame of reference of the Lagrangian coordinate. In the Lagrangian coordinate system Eq. (28b) becomes an identity. However, in order for the variable x to have a domain that is constant in time

$$V(r=0) = 0 \text{ and } V(r=a) = 0 \quad , \quad (29a,b)$$

where a is the maximum value of the coordinate r .

Consider the poloidal component of the magnetic field equation in the transport model, Eq. (17)

$$\frac{\partial B_\theta}{\partial t} + \frac{\partial}{\partial r} \left(V_{er} B_\theta - \frac{cR_z}{en} \right) = 0 \quad . \quad (30)$$

In order to construct a Lagrangian coordinate system based on the poloidal flux, Eq. (30) must be cast in the form of Eq. (28b). By noticing that an arbitrary function of time $F(t)$ may be inserted under the spatial derivative in Eq. (30), this equation can be written as

$$\frac{\partial B_\theta}{\partial t} + \frac{\partial}{\partial r} \left(V_{er} - \frac{cR_z}{enB_\theta} + \frac{F(t)}{B_\theta} \right) B_\theta = 0 \quad . \quad (31)$$

We choose

$$F(t) = \frac{cR_z}{en}(r=0) \quad , \quad (32)$$

then since $\frac{cR_z}{en} \sim (\vec{n} \cdot \vec{j})$ (where n is the resistivity and \vec{j} is the current) is parabolic in r near the origin and B_θ is linear in r , the total velocity vanishes at the origin,

$$V(r=0) = \left[V_{er} - \frac{cR_z}{enB_\theta} + \frac{F(t)}{B_\theta} \right]_{r=0} = 0 \quad .$$

Thus using the freedom allowed by the constant of integration in Eq. (30), we can construct a Lagrangian coordinate system based on the poloidal flux defined as $x = \int_0^r B_\theta(r', t) dr'$, which satisfies Eq. 29(a) but not Eq. 29(b). So although the problem of poloidal flux destruction at the origin has been solved, the domain of the independent variable x varies with time.

A poloidal flux variable with a fixed domain can be constructed by setting $x = \frac{B_\theta}{\phi_{PT}(t)}$ ($\phi_{PT}(t) = \int_0^a B_\theta dr$) in Eq. (28a). Now x is the poloidal flux divided by the total amount of poloidal flux in the system at the current time, and always has the domain $0 < x < 1$. By substituting $B_\theta = x\phi_{PT}(t)$ into Eq. (31) and after some straight-forward algebra, there results

$$\frac{\partial x}{\partial t} + \frac{\partial}{\partial r} \left(V_{er} - \frac{CR_z}{enB_\theta} + \frac{F(t)}{B_\theta} + \frac{x}{B_\theta} \frac{\partial \phi_{PT}}{\partial t} \right) x = 0, \quad (33)$$

where

$$\frac{\partial \phi_{PT}}{\partial t} = cE_z(r=a) - F \quad (34)$$

is rate of change of the total poloidal flux in the system.

The velocity $V = V_{er} - \frac{CR_z}{enB_\theta} + \frac{F(t)}{B_\theta} + \frac{x}{B_\theta} \frac{\partial \phi_{PT}}{\partial t}$ still vanishes at the origin, but also vanishes at the wall radius, where

$$V(x=1) = V_{er} - \frac{cR_z}{enB_\theta} + \frac{cE_z}{B_\theta} = 0$$

merely states that the z component of the nonideal MHD Ohm's law is satisfied.

In summary, a Lagrangian coordinate system based on a normalized poloidal flux variable, which has a fixed domain, has been constructed. This coordinate system is defined by Eqs. (28a,b) where

$$x = \frac{B_\theta}{\phi_{PT}}, \quad V = V_{er} - \frac{cR_z}{en} + \frac{F(t)}{B_\theta} + \frac{x}{E_\theta} \frac{\partial \phi_{PT}}{\partial t} \quad (35a,b)$$

and

$$\phi_{PT}(t) = \int_0^a B_\theta(r,t) dr, \quad F(t) = \frac{cR_z}{en}(r=0,t),$$

$$\frac{\partial \phi_{PT}}{\partial t} = cE_z(r=a,t) - F.$$

It provides a suitable basis for restructuring the transport model and radiation model equations.

4.2 Transport Model Equations in Lagrangian Form

A. Equations

Our computer code currently contains only electrons and one ion species in the transport model. Therefore the terms in Eqs. (14)-(20) due to multiple ion species are dropped and only the two fluid transport model is presented in Lagrangian form. However, the diffusion of impurities can be important and will be included in future work.

In transforming the transport model equations into the normalized poloidal flux coordinate system, we can explicitly eliminate the velocity V followed by the Lagrangian frame of reference by making a change in the dependent variables. This involves interchanging Lagrangian space and time derivatives in the transformed equations.

Using Eqs. (28) and (35), which define the transformation to the Lagrangian coordinate system, and keeping in mind that

$$\frac{\partial}{\partial t_L} = \frac{\partial}{\partial t} + V \frac{\partial r}{\partial r}, \quad \frac{\partial r}{\partial t_L} = V,$$

where $\frac{\partial}{\partial t_L}$ is the Lagrangian time derivative, the two fluid transport model equations become, a pitch equation

$$\frac{\partial P}{\partial t} = \frac{\partial}{\partial x} \left[\left(\frac{x}{\phi_{PT}} \frac{\partial \phi_{PT}}{\partial t} + \frac{F}{\phi_{PT}} \right) P - \left(\frac{y'}{2} \right)^2 \frac{c R_e}{\phi_{PT} e N} \cdot \vec{B} \right], \quad (36)$$

and a density equation

$$\frac{\partial N}{\partial t} = \frac{\partial}{\partial x} UN, \quad (37)$$

where

$$U = \left(\frac{x}{\phi_{PT}} \frac{\partial \phi_{PT}}{\partial t} + \frac{F}{\phi_{PT}} - \frac{y' c R_{ez}}{2 \phi_{PT} e N} \right).$$

The electron temperature equation becomes

$$\frac{\partial \theta_e}{\partial t} = \frac{\partial}{\partial x} U \theta_e - \frac{1}{3} \theta_e \frac{\partial U}{\partial x} + \frac{2}{3} \left(\frac{y'}{2} \right)^{5/3} \frac{W_{eT}}{N}, \quad (38)$$

the ion temperature equation is

$$\frac{\partial \theta_i}{\partial t} = \frac{\partial}{\partial x} U \theta_i - \frac{1}{3} \theta_i \frac{\partial U}{\partial x} + \frac{2}{3} \left(\frac{y'}{2} \right)^{5/3} \frac{W_{iT}}{N}, \quad (39)$$

and the magnetohydrostatic equilibrium equation takes the form

$$\frac{\partial^2 y}{\partial x^2} = y' \left[\frac{\frac{\partial}{\partial x} (P^2 + 2y\phi_{PT}^2) + \pi^{2^{8/3}} y'^{1/3} \frac{\partial}{\partial x} (N(\theta_e + \theta_i))}{2(P^2 + y\phi_{PT}^2) + \frac{5\pi}{3} 2^{8/3} (N(\theta_e + \theta_i))} \right], \quad (40)$$

where the subscript L has been dropped on the time derivatives.

The Lagrangian dependent variables in terms of the Eulerian dependent variables are

$$y = r^2, \quad y' \equiv \frac{\partial y}{\partial x} = \frac{2r}{B_\theta} \phi_{PT}, \quad (41a,b)$$

$$P = B_z \frac{y'}{2}, \quad (42a)$$

$$N = n \frac{y'}{2}, \quad (42b)$$

$$\theta_e = T_e \left(\frac{y'}{2} \right)^{2/3}, \quad (42c)$$

$$\theta_i = T_i \left(\frac{y'}{2} \right)^{2/3}. \quad (42d)$$

The Lagrangian dependent variables have physical interpretations. y' is the volume per normalized poloidal flux. P is the toroidal flux per normalized poloidal flux or the pitch of a field line, an important quantity in considering the MHD stability of the RFP.⁶ N is the mass in a normalized poloidal flux element. θ_e and θ_i are a measure of the electron and ion entropy per particle respectively. Notice that if there is no dissipation P , N , θ_e and θ_i are all constant. Therefore, these variables are invariant when there is adiabatic motion of the plasma.

The major advantage of Eqs. (36)-(40) is that it is possible to directly advance them in time. That is, the time dependent equations for P , N , θ_e , θ_i , and ϕ_{PT} can be advanced (with y and y' held constant), and then inserting these quantities into Eq. (40) the new equilibrium configuration can be found. Another important property of Eqs. (36)-(40) is that the current is naturally expressed in terms of a parallel component $j_{\parallel} \sim \frac{\partial}{\partial r} \frac{B_z}{r B_{\theta}} \sim \frac{\partial}{\partial x} \left(\frac{P}{Y} \right)$ and a perpendicular component $j_{\perp} \sim \frac{\partial}{\partial r} n(T_e + T_i) \sim \frac{\partial}{\partial x} N(\theta_e + \theta_i)$, instead of θ and z components as in the Eulerian representation. For instance, in the pitch equation (36) $\vec{R} \cdot \vec{B} \sim n_{\parallel} j_{\parallel} \sim n_{\parallel} \frac{\partial}{\partial x} \frac{P}{Y}$, which means that this equation also decouples in its highest derivatives from the other equations (note that the evolution of the pitch is governed only by the parallel resistivity, a point that is made apparent in this representation). It is coupled to them only through its coefficients.

In equations (36)-(39) we see that the two terms $\frac{F}{\phi_{PT}}$ and $\frac{x}{\phi_{PT}} \frac{\partial \phi_{PT}}{\partial t}$, that were a consequence of poloidal flux destruction at the wall and constructing a poloidal flux variable with a fixed domain, appear as convective velocities with respect to the Lagrangian coordinate x . The size of $\frac{F}{\phi_{PT}}$ depends on the plasma resistivity at the origin and will therefore be of the same order as other resistive terms in the equations. However, $\frac{x}{\phi_{PT}} \frac{\partial \phi_{PT}}{\partial t}$ can be arbitrarily large, since this term contains the external driving electric field. To study the effect of this term, suppose that it is so large that

all other terms in Eqs. (36)-(39) can be dropped. This corresponds physically to forming a plasma through a series of equilibrium states, adding magnetic flux at the wall but allowing no diffusion. Then Eqs. (36)-(39) decouple from the equilibrium constraint Eq. (40), and can be solved explicitly. For example, the pitch equation becomes

$$\frac{\partial P}{\partial t} = \frac{\partial}{\partial x} CxP \quad , \quad (43)$$

where $C = \frac{1}{\phi_{PT}} \frac{\partial \phi_{PT}}{\partial t}$. If we substitute $v = xP$ in Eq. (43), then it is seen that $xe^{Ct} = \text{const.}$ are the characteristics of this equation. Thus Eq. (43) has the solution

$$P = \frac{1}{x} f(xe^{Ct}) \quad ,$$

where f is an arbitrary function of xe^{Ct} .

The role of the term $x/\phi_{PT} \partial \phi_{PT}/\partial t$ can now be analyzed in terms of the characteristics. For example, in the $x - t$ plane $x = 0$ is a characteristic, therefore, the value of P given initially at the origin determines the solution along this line and no boundary condition can be specified at this point. For $C > 0$ (corresponding to magnetic flux being added to the system), values of P initially given at points where $x > 1$ will be propagated along the characteristics until a time when they occur at $x = 1$. They then appear as the boundary condition $P(x=1, t)$ on Eq. (43) (remember that the physical

extent of the plasma is $0 < x < 1$). Notice that no two characteristics will ever intersect each other in the finite $x - t$ plane.

What we have seen is that the term $\frac{x}{\phi_{PT}} \frac{\partial \phi_{PT}}{\partial t}$ causes no pathological behavior to occur in our system of equations, and that in the case of a dissipationless, adiabatic plasma formation actually makes possible a significant simplification, since the evolution equations can then be analytically solved independent of the equilibrium constraint.

B. Boundary conditions

The boundary condition on Eqs. (36)-(38) at $x = 0$ is that the flux of P, N, θ_e , and θ_i vanish. This is automatically satisfied by the definition of $F(t)$.

Pedestal values of density and temperature are specified at the plasma edge $x = 1$. In the Lagrangian representation they become

$$\left(\frac{N}{Y}\right)_{x=1} = \text{const.} , \quad (44a)$$

$$\left(\frac{\theta_e}{Y^{2/3}}\right)_{x=1} = \text{const.} , \quad (44b)$$

$$\left(\frac{\theta_i}{Y^{2/3}}\right)_{x=1} = \text{const.} . \quad (44c)$$

The z electric field is also specified at the plasma edge $E_z(x = 1)$, and along with F determines $\partial\phi_{PT}/\partial t$. Note that this factor appears in Eqs. (36)-(39) not just at the boundary, but at all points, because it occurs in the term that analytically remeshes the coordinate grid so that $0 < x < 1$. The boundary condition on the pitch equation (36) is the poloidal electric field $E_\theta(x=1)$, since this determines the rate at which toroidal flux enters the system.

We allow for a conducting wall at a radius b outside of the vacuum chamber wall at a radius a . The region $a < r < b$ is a magnetic flux reservoir and is coupled to the plasma. By considering the expression for the rate of change of the total amount of toroidal flux inside the conducting wall and using Eq. (36), $E_\theta(x=1)$ can be expressed solely in terms of the poloidal electric field at the conducting wall V_θ and plasma quantities at the vacuum chamber wall. This yields a time dependent boundary condition for the pitch equation at $x = 1$.

$$cV_\theta + 2\pi(b^2 - a^2) \frac{\partial}{\partial t} \left(\frac{P}{Y^2} \right) = - \frac{2\pi}{\phi_{PT}} E_z P - 2c^2 \frac{n_p Y^2}{Y'^2} \frac{\partial}{\partial x} \left(\frac{P}{Y} \right) . \quad (45)$$

The boundary conditions on the magnetohydrostatic equilibrium equation (40) at $x = 0$ and $x = 1$ are

$$y(x = 0) = 0 , \quad y(x = 1) = a^2 . \quad (46a,b)$$

4.3 Radiation Model Equations in Lagrangian Form

In the normalized poloidal flux coordinate system the radiation model equations (21)-(27) become

$$N_e = N_i + \sum_{j=1}^{Z+1} (j-1)N_j, \quad (47)$$

$$\frac{\partial N_i}{\partial t} = \frac{y'}{2} A_i, \quad (48)$$

$$\frac{\partial N_j}{\partial t} = \frac{2N_e}{y'} [N_{j-1} \beta_{j-1} - N_j (\beta_j + \alpha_j) + N_{j+1} \alpha_{j+1}] , \quad (49)$$

$$\frac{\partial P}{\partial t} = 0, \quad (50)$$

$$\frac{\partial S_e}{\partial t} = \frac{2}{3} \left(\frac{y'}{2}\right)^{5/3} W_{eR}, \quad (51)$$

$$\frac{\partial S_I}{\partial t} = \frac{2}{3} \left(\frac{y'}{2}\right)^{5/3} W_{IR}, \quad (52)$$

$$\frac{\partial^2 y}{\partial x^2} = y' \left[\frac{\frac{\partial}{\partial x} (P^2 + 2y \phi_P^2) + \pi^{2/3} y^{-1/3} \frac{\partial}{\partial x} (S_e + S_I)}{2(P^2 + y \phi_P^2) + \frac{5\pi}{3} 2^{8/3} (S_e + S_I)} \right], \quad (53)$$

where $N_j = n_j y'/2$, and $S_e = N_e \theta_e$, $S_I = N_i \theta_i + \theta_i \sum_j N_j$ are a measure of the electron and ion entropies respectively.

Notice that in the Lagrangian representation all of the radiation model equations have become ordinary differential equations (remember that there is no applied electric field at the plasma edge, c.f., 3.1). A convective velocity common to all of the plasma particle species and the magnetic fields, caused by radiation energy loss, has been explicitly eliminated.

The only boundary conditions are Eqs. 46(a,b) applied to the equilibrium constraint equation.

5.0 Numerical Solution of the Equations

A. Transport Model Equations

The transport model equations (36)-(40) are essentially a coupled set of diffusion equations. They are appropriately written in nondimensional form and advanced in time by a predictor-corrector scheme with variable time centering⁷. The numerical grid consists of points equally spaced in x , located at mesh cell centers, with a point on the boundary at $x = 1$ as shown below.

$$\begin{array}{ccccccc} & | & x & | & x & | & \dots & | & x & | \\ x=0 & & & & & & & & & x=1 \end{array}$$

Since the pitch equation (36) is coupled to the other equations only through its coefficients, it is finite differenced, along with its boundary condition Eq. (45), in conservation law form⁸ and is advanced in time separately from

the other equations. The equations for N , θ_e , and θ_i are coupled in their second spatial derivatives and form a 3×3 block tri-diagonal set that are advanced together in time by the standard algorithm⁹.

After the equations for P , N , θ_e , and ϕ_{PT} have been advanced in time the equilibrium Eq. (39) is solved for the new equilibrium configuration specified by y and y' . This is a two point boundary value problem, and a simple shooting method is used to obtain the solution¹⁰. The values of P , N , θ_e , and θ_i are extended across the full domain of x by means of a cubic spline interpolation¹⁰. Values of P , N , θ_e , and θ_i are defined at $x = 0$ by linear extrapolation, since these quantities as well as x all have a parabolic dependence on radius near the origin. Given initial values of y and y' at $x = 0$, Eq. (40) is advanced across the mesh by the common fourth-order Runge Kutta method¹¹.

B. Radiation Model Equations

The numerical solution of the radiation model equations (47)-(53) (neutral gas is presently ignored in this model so $A_i = W_{IR} = 0$) is essentially trivial except for the atomic physics rate equations (49). These are a set of stiff ordinary differential equations and can therefore be troublesome to solve.

Since we alternate between transport and radiation model equations, multi-step methods are inappropriate and we must seek a different method. We would like the numerical

scheme used to solve these equations to be unconditionally stable and to conserve particle number. The well known backwards Euler method has both of these properties.¹² This method is defined by

$$u^{n+1} - u^n = f(u)^{n+1} \Delta t, \quad (54)$$

where u is a vector and $f(u)$ is a linear function of u . The difficulty with this method is that it is only first-order accurate in time. However, it yields a tri-diagonal system of difference equations, which can be solved very efficiently. Therefore this method can be used to solve the rate equations if a proper criterion can be found to adjust the time step so that sufficient accuracy can be obtained. This time step may be substantially shorter than the time step used for the radiation model equations as a whole.

The time step used in solving the radiation model equations is determined by either, the time step from the transport phase or, the change in S_e due to radiation energy loss. The radiation loss is due mostly to line radiation, which is caused by inelastic collisions of electrons with ions that leave the ions in an excited state. The electrons that are principally responsible for this are those that lie in the central region of the Maxwellian velocity distribution, whereas those electrons that cause ionization lie on the high velocity tail of the Maxwellian distribution. Therefore, the time for

S_e to change by an amount that is large enough that the equilibrium configuration must be updated may be longer than the time for the ion species populations to change appreciably.

To see how to set the time step to obtain proper accuracy in solving the rate equations by the backwards Euler method, consider Eq. (48) written in the form

$$\frac{\partial N_j}{\partial t} + \frac{2N_e}{Y^*} [s_j + \alpha_j] N_j = S_j, \quad (55)$$

where

$$S_j = \frac{2N_e}{Y^*} [s_{j-1}N_{j-1} + \alpha_{j+1}N_{j+1}] \quad (56)$$

is the source function for species N_j . Since the plasma as a whole is either ionizing or recombining, one S_j will be the largest and will govern the size of the others. A time step on which the rate equations can be solved accurately is determined by requiring that this S_j change by only a small fraction. Therefore, we limit Δt so that

$$\frac{\Delta t}{S} \frac{dS}{dt} < \epsilon, \quad (57)$$

where $S = \text{Sup } S_j$ is the largest S_j and ϵ is some small number. An approximate expression can be found for $\frac{dS_j}{dt}$ from Eqs. (55) and (56) by ignoring the time dependence of all quantities

except the impurity densities. This yields

$$\begin{aligned} \frac{dS_j}{dt} = \frac{2N_e}{Y} & \left[\beta_{j-1} (S_{j-1} - \frac{2N_e}{Y} (\beta_{j-1} + \alpha_{j-1}) N_{j-1}) \right. \\ & \left. + \alpha_{j+1} (S_{j+1} - \frac{2N_e}{Y} (\beta_{j+1} + \alpha_{j+1}) N_{j+1}) \right] . \end{aligned} \quad (58)$$

Consequently, for each time step of the radiation model equations (i.e., for each time the equilibrium equation (53) is solved), the atomic physics rate equations may be solved some arbitrary number of times, determined by Eq. (57), in each mesh cell. The accuracy of this method has been verified by successively slashing the time step by decreasing ϵ . It is found that for $\epsilon < .01$ very good accuracy (better than .1%) is attained.

C. The Successive Solution of the Transport and Radiation Model Equations

A complete time step of size Δt is performed in the following manner. First, the transport model equations are advanced in time by $\Delta t/2$. For this to be successful the predictor-corrector scheme must converge to within a set tolerance in a few iterations and all dependent variables must vary by less than a predetermined amount, normally 10%. Next, the radiation model equations are advanced in time by an amount Δt . This must be done in no more than two separate

steps. The dependent variables must not change by more than a predetermined amount per step, again usually 10%. If this is not successful the total time step Δt for the code is reduced and the process starts over again beginning with a transport step. Finally, after the radiation model equations have been advanced by Δt , the transport model equations are advanced by another $\Delta t/2$, completing the time step. A full time step is then composed of two time steps, (unless the energy loss to radiation is so small that the radiation model equations can be advanced by Δt in one step), one where the transport model equations are solved first and the radiation model equations second and one where this process is reversed. In this way errors which arise because the two sets of equations do not exactly commute tend to be minimized.¹³

In the transport model equations the impurity ions have been neglected; therefore, the number of ions is not the same in the two models. In successively solving these two sets of equations the electron and ion entropy and the electron density are kept constant to insure that the same equilibrium is passed between the two models. When the transport model equations are advanced in time, the impurity density is held fixed in physical space. This is accomplished by remeshing the impurity density in x after each transport step. The new impurity density is constructed by weighting the densities that existed in the overlapping mesh cells before the transport step by their respective areas. In this manner the total number of

impurities is exactly preserved.

The accuracy of the solution is monitored by checking equation (11) for global energy balance, which is separately satisfied by both sets of equations. The code is found to conserve the sum of the internal plasma energy and the magnetic field energy, taking into account energy sources and sinks due to radiation, thermal conduction, and the flux of both plasma internal energy and magnetic energy at the wall, by better than .1%.

6.0 Results for the ZT-40 Reversed-Field Pinch Experiment

The reversed-field pinch is a promising approach to controlled fusion that has received considerable attention in recent years. It is an axisymmetric toroidal device that has poloidal and toroidal magnetic fields roughly equal in magnitude. A large amount of magnetic shear, created by reversing the direction of the toroidal field in the outer region of the plasma, permits MHD stable operation at the relatively high beta of 30-40%. A principal difficulty with RFP experiments has been low electron temperatures caused by energy loss from radiating impurities, principally oxygen. Here we present a simulation of the ZT-40¹⁴ reversed-field pinch as an example of the kind of results that the computer code is capable of producing.

The major operating parameters for the ZT-40 experiment are:

Vacuum wall radius = 20 cm

Conducting wall radius = 22 cm

Total toroidal current = 500 kA

Density on axis = $5 \times 10^{14} \text{ cm}^{-3}$.

We begin the calculation with a diffuse current profile that is somewhat peaked off axis. The initial density profile is parabolic and peaked on axis; the electron and ion temperatures are set at a uniform 10 eV. The impurity studied is oxygen, with a density of 0.4% that of the local deuterium density.

The pedestal values of density and temperature at the vacuum chamber wall are given by their initial value or the value at the point next to the wall, whichever is less. The electric fields at the conducting wall are set to zero.

We are therefore simulating the post-implosion phase of this device assuming that diffuse profiles already exist, and allow the plasma to evolve from this initial state in isolation from any external driving circuit. In the transport model we assume classical transport coefficients in the strong field limit as given by Braginskii.¹ In the radiation model we assume that the coronal approximation is valid¹⁵ and that all radiation energy is lost from the plasma.¹⁶ The actual atomic physics data used in the radiation model equations is furnished by an atomic physics code developed by Dr. Russell Hulse. This code utilizes generalized formulae¹⁷ to calculate ionization

and recombination coefficients and radiation loss rates for an arbitrary element.

In Figs. 1(a,b,c) plots of B_z , B_θ , and $P = \frac{rB_z}{aB_\theta}$ are given as a function of radius and time. We see that during the 2 ms that the code was run these quantities show little change. The largest change is in the B_z field at the vacuum chamber wall, which, although it has decayed from -1300 g to -500 g, is still reversed.

The reason for the small change in the magnetic field profiles is that the beta is low ($\beta \sim .4\%$ initially and 12% at 2 ms). For classical transport the ohmic heating is the dominate process at low beta. The magnetic field diffusion and the particle diffusion are smaller than this process by the factors β and β^2 respectively. In Figs. 2(a,b,c), where j_z , j_θ , and I_z are given as a function of radius and time we see the same stationary behavior. However, notice that the total z current actually increases by a small amount with time. This is because the diamagnetic current created by ohmic heating has a significant component in the z direction.

In Figs. 3(a,b,c,d) the density n , the electron and ion temperatures T_e and T_i , and the pressure p are given as a function of radius and time. We see that although the density is again approximately stationary, the electron and ion temperatures and the pressure are peaked off axis and show steep gradients that correspond to the distribution of the parallel current. Due to the large ion thermal conductivity

the ion temperature profile is much smoother than the electron temperature profile.

In Figs. 4(a,b) are shown the total oxygen density (the sum over all states) and the average charge of oxygen as a function of radius and time. The total oxygen density, as expected (diffusion of impurities has been omitted in the transport model), is nearly stationary. From Fig. 4(b) it is seen that oxygen reaches the helium like state in a very short period of time across nearly the entire plasma radius. Then the last two electrons are slowly ionized in 2 ms, but only where the parallel current density is a maximum. Therefore, we see that for this concentration of oxygen the plasma has easily burned through the oxygen radiation barrier, which has a peak at about 25 eV. At 2 ms the average electron temperature is 280 eV and the average ion temperature is 240 eV. At this time only 15% of the magnetic field energy that has gone into ohmic heating has been lost to radiation.

In Fig. 5 is shown the Suydam criterion as a function of radius and time. It is seen that after a short period of time this criterion is violated in the outer quarter of the plasma. Thus one expects anomalous transport in this region.

Global energy balance was checked for this simulation and found to be satisfied to better than .01%. The computer code took approximately 150 time steps and 1-1/2 hours of CPU time on the PDP-10 computer to run to 2 ms.

7.0 Conclusion

We have shown that the MHD equations, for the case where there are many ion fluids due to the presence of an impurity, and where the plasma and magnetic field configuration evolves through a series of equilibrium states, may be simplified by splitting these equations into two self-consistent and independent sets: one that contains all transport processes and one that contains all atomic physics processes. It was then shown that the coupled initial value and boundary value problem, that results from the equilibrium equation appearing as a constraint on the plasma and magnetic field evolution equations, can be cast into a form more amenable to numerical solution than is the usual Eulerian representation. This involved transforming both the transport model and radiation model equations into a Lagrangian coordinate system based on a normalized poloidal flux variable that has a fixed domain, and changing the dependent variables to quantities that remain invariant during adiabatic motion of the plasma. This resulted in a system of equations that could then be directly advanced in time by elementary numerical methods.

It was shown that the atomic physics rate equations could be solved efficiently and accurately by the backwards Euler method, once a suitable criterion was derived for setting the time step associated with this absolutely stable but only first order accurate method.

The present computer code contains only electrons and ions in the transport model equations, although the manner in which impurity fluids are to be added is discussed in Section 3.0. The full multi-fluid transport model, where impurity diffusion is treated, will be developed in future work.

References

1. Braginskii, S. I., Reviews of Plasma Physics, edited by M. A. Leontovich (Consultants Bureau, New York, 1965) Vol. 1, p. 205.
2. Duchs, D. F., Post, D. E., Rutherford, P. H., Nucl Fusion 17 (1977) 565.
3. Hughes, M. H., Post, D. E., J. Computational Phys. 28 (1978) 43.
4. Landau, L. D., Lifshitz, E. M., "Electrodynamics of Continuous Media," Addison Wesley (1960), p. 215.
5. Roberts, K. V., Christiansen, J. P., Long, J. W., Computer Phys. Commun. 10 (1975) 264.
6. Robinson, D. C., Plasma Physics 13 (1971) 439.
7. Douglas, J., Jones, F. B., J. Soc. Indust. Appl. Math. 11 (1963) 195.
8. Potter, D., "Computational Physics," John Wiley and Sons, Inc. (1973).
9. Killeen, J., Nucl. Fusion 16 (1976) 841.
10. Carnahan, B., Luther, H. A., Wilkes, J. O., "Applied Numerical Methods," John Wiley and Sons, Inc. (1969).
11. Hildebrand, F. B., "Advanced Calculus for Applications", Prentice-Hall (1962).
12. Gear, C., "Numerical Initial Value Problems in Ordinary Differential Equations," Prentice-Hall (1972).

13. Gary, J., "The Numerical Solution of Partial Differential Equations," Univ. of Colo. (1975), unpublished.
14. Baker, D. A., Machalek, M. D., Los Alamos Scientific Laboratory report, LA-6625-P (1977).
15. McWhirter, R. W. P., Plasma Diagnostic Techniques, edited by R. H. Huddlestone and S. L. Leonard, Academic Press 1965, p. 201.
16. Duchs, D., Engelhardt, W., Köppendorfer, W., Nucl. Fusion 14 (1974) 73.
17. Post, D. E., et al., Atomic Data and Nuclear Data Tables 10, No. 5 (1977) 397.

Figure Captions

Fig. 1(a,b,c). The toroidal magnetic field B_z (gauss), the poloidal magnetic field B_θ (gauss), and the pitch $P = \frac{rB_z}{aB_\theta}$ are shown as a function of radius and time.

Fig. 2(a,b,c). The parallel current density j_\parallel (amp./cm²), the toroidal current density j_z (amp./cm²), and the total toroidal current I_z (amp) are shown as a function of radius and time.

Fig. 3(a,b,c,d). The density n (cm⁻³), the electron temperature T_e (eV), the ion temperature T_i (eV), and the pressure p (dynes/cm²) are shown as a function of radius and time.

Fig. 4(a,b). The oxygen density n_{Ox} (cm⁻³) and average charge $\langle Z \rangle$ are given as a function of radius and time.

Fig. 5. The Suydam criterion is plotted in arbitrary units as a function of radius and time.

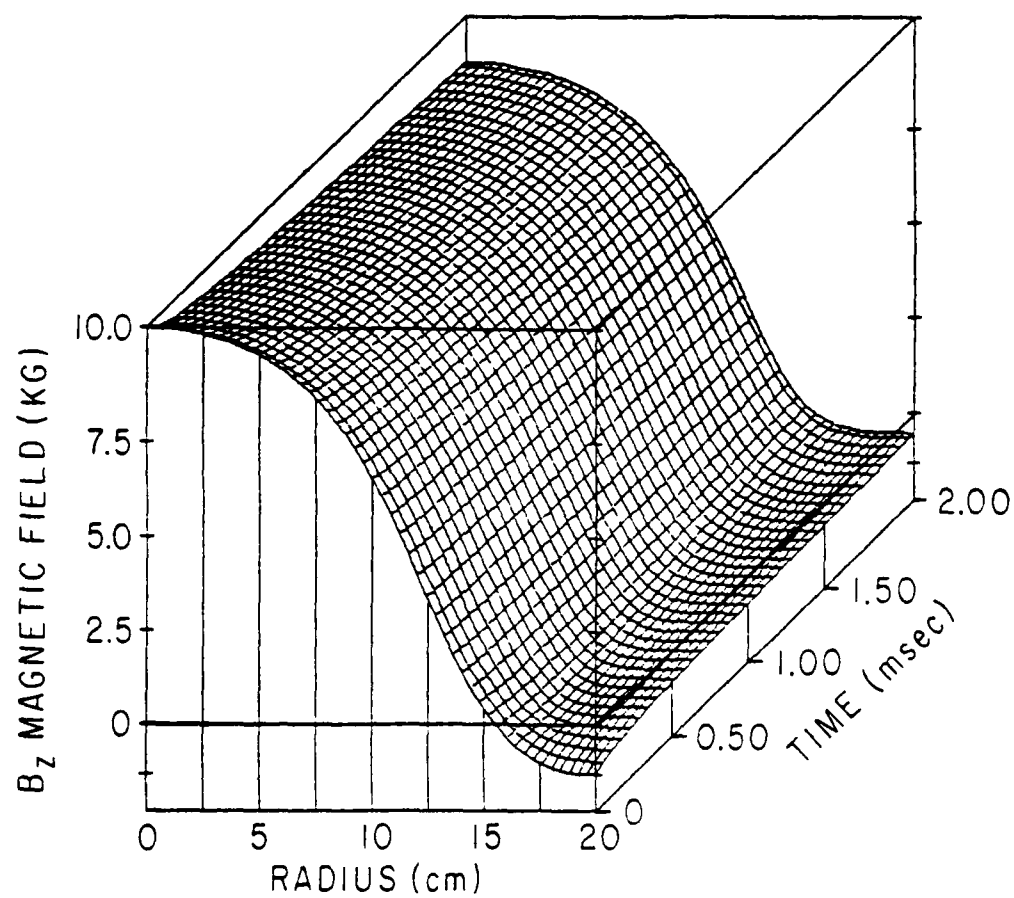


Figure 1 (a)

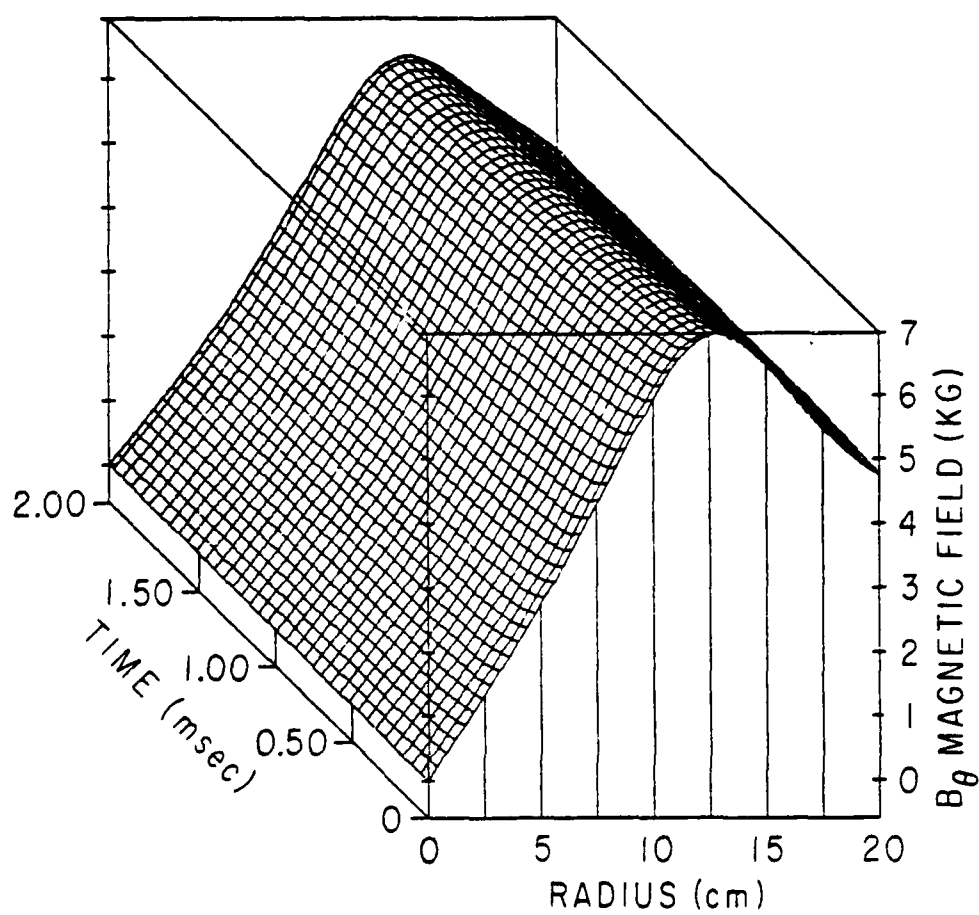


Figure 1 (b)

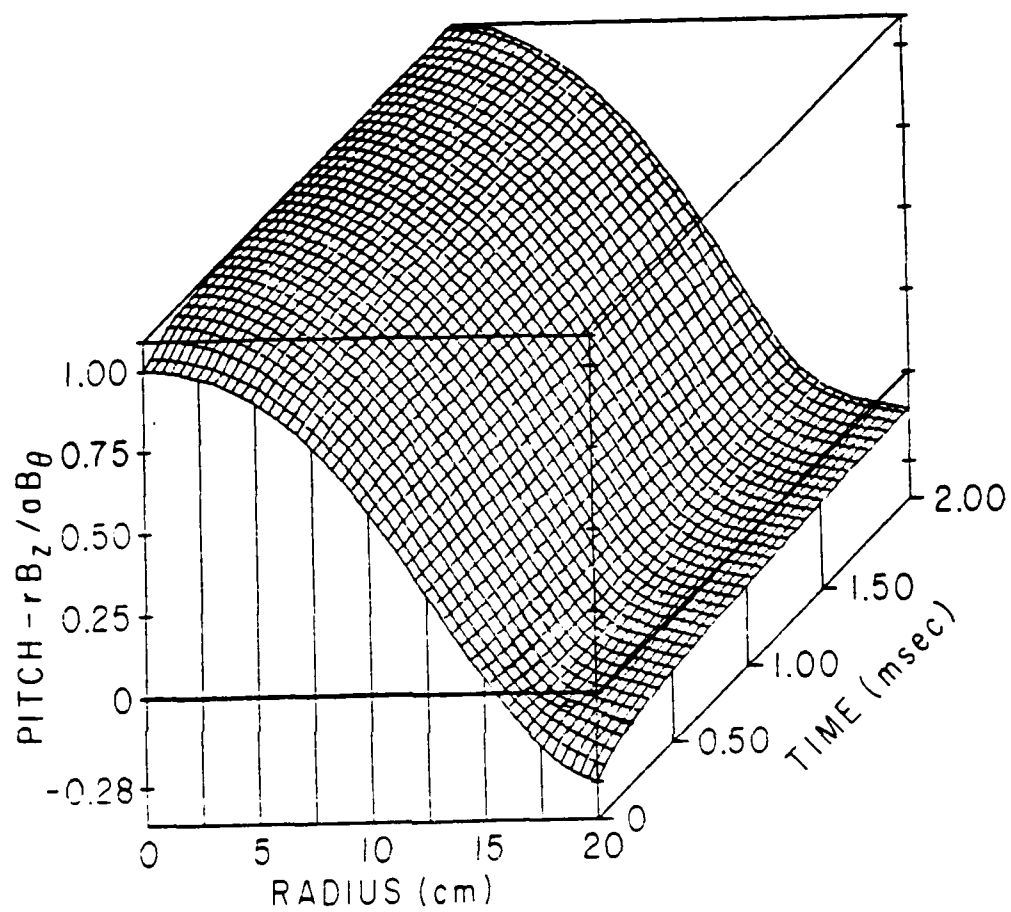


Figure 1 (c)

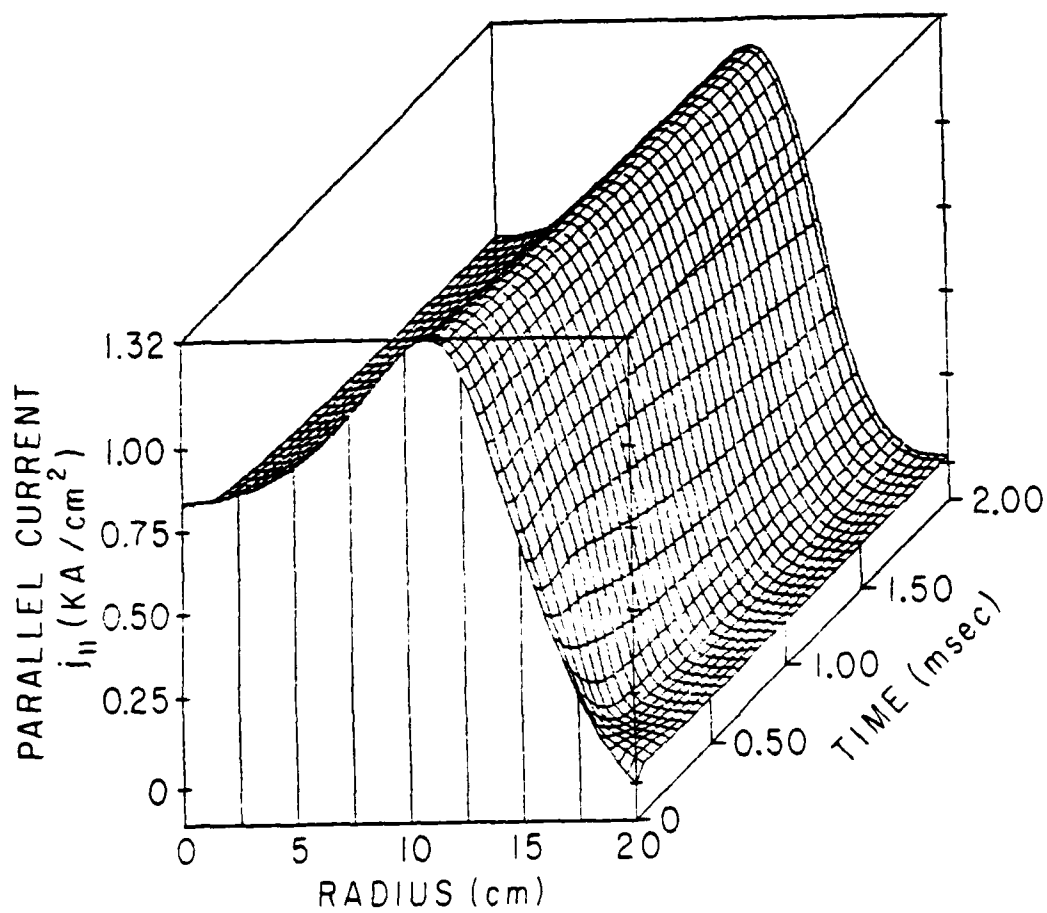


Figure 2 (a)

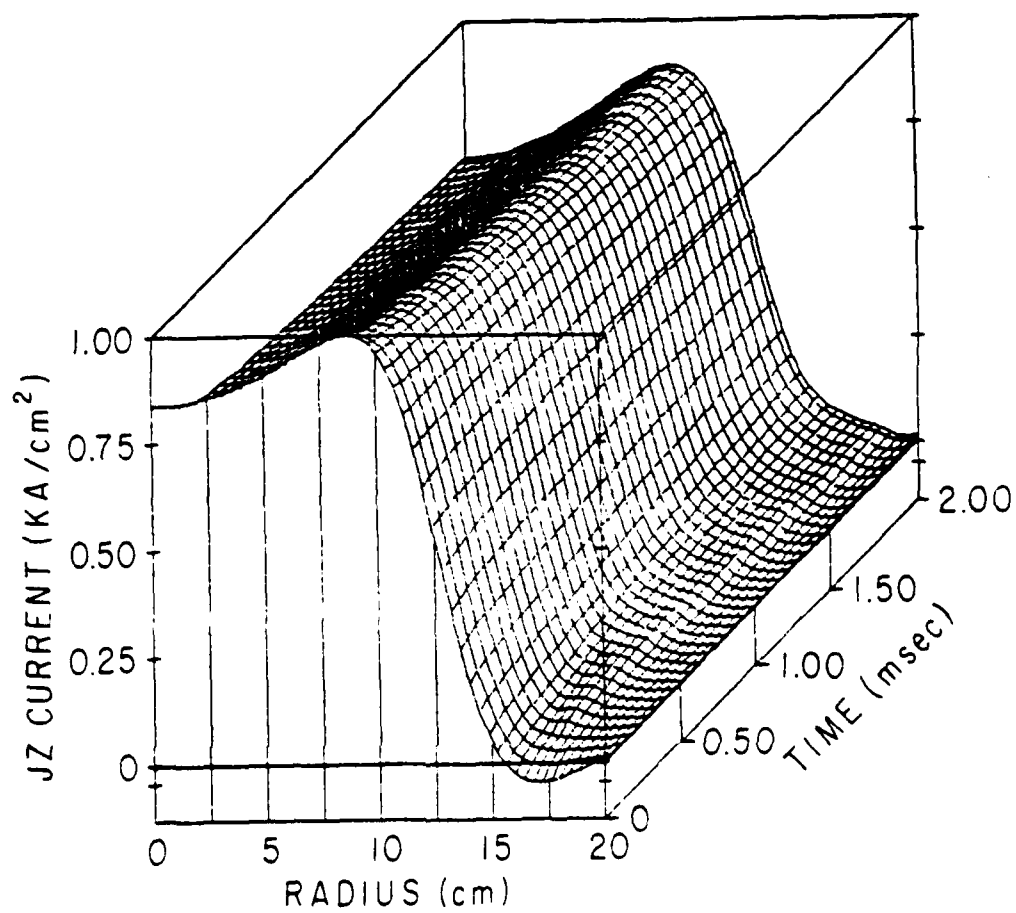


Figure 2 (b)

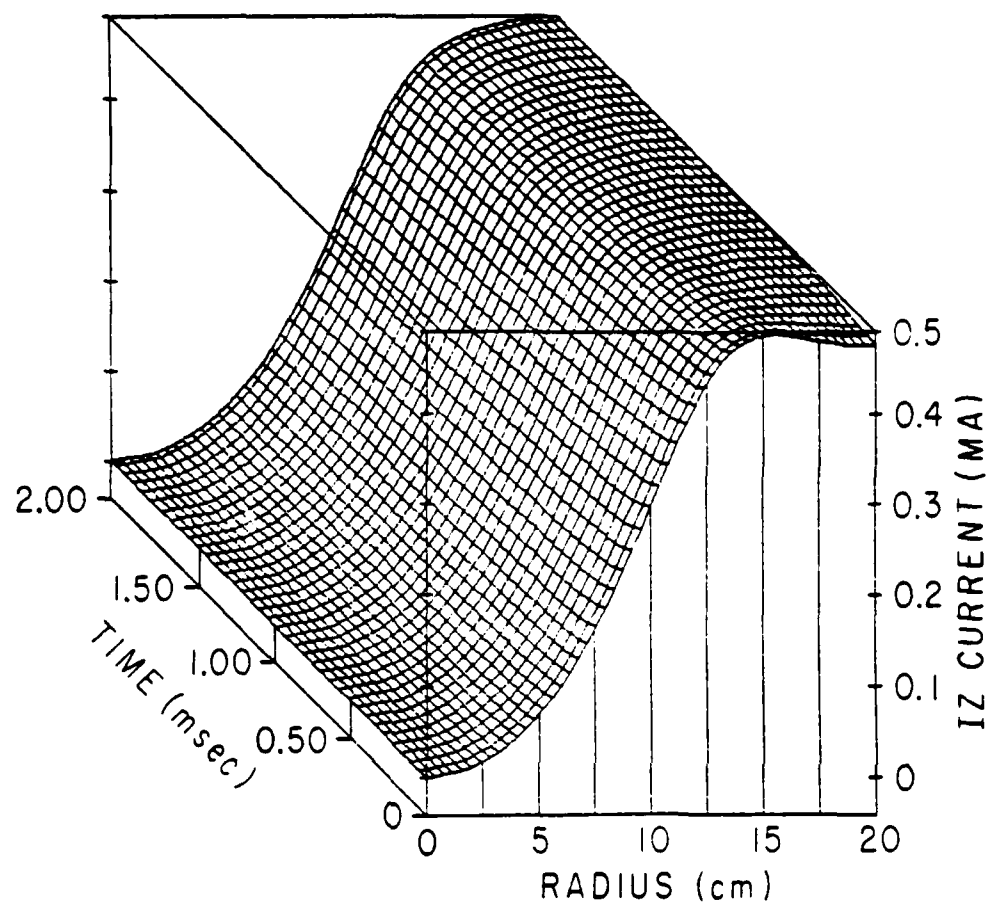


Figure 2 (c)

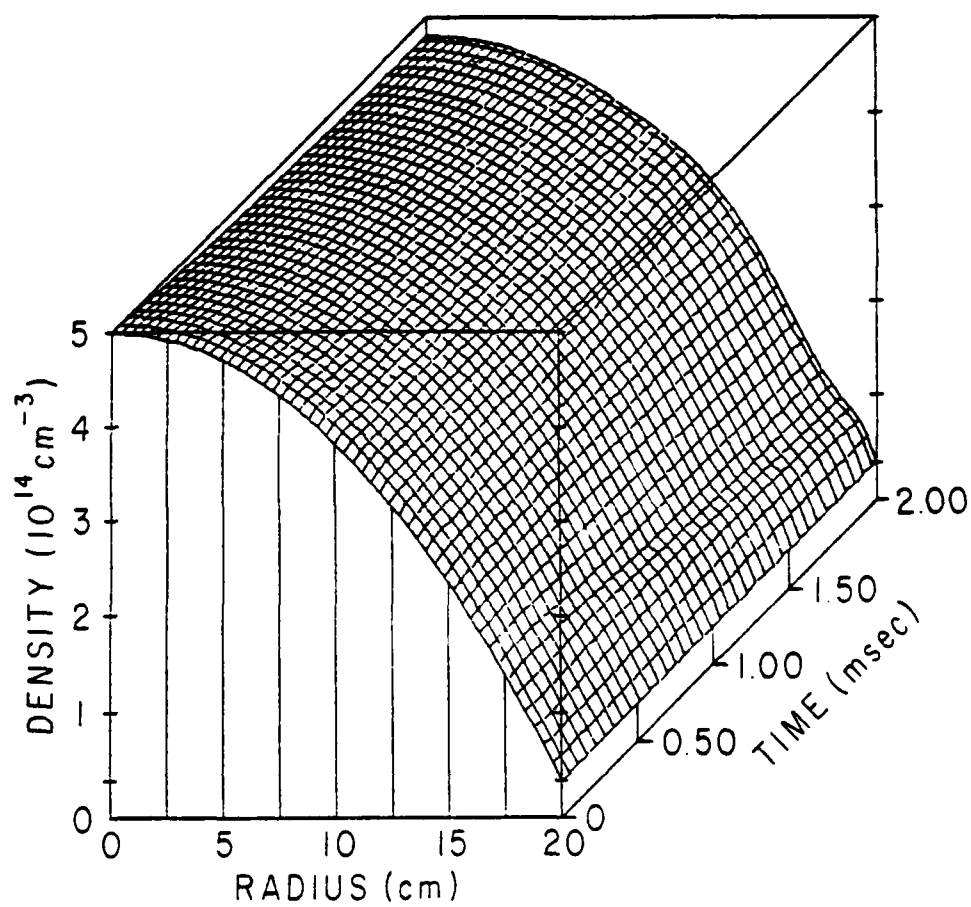


Figure 3 (a)

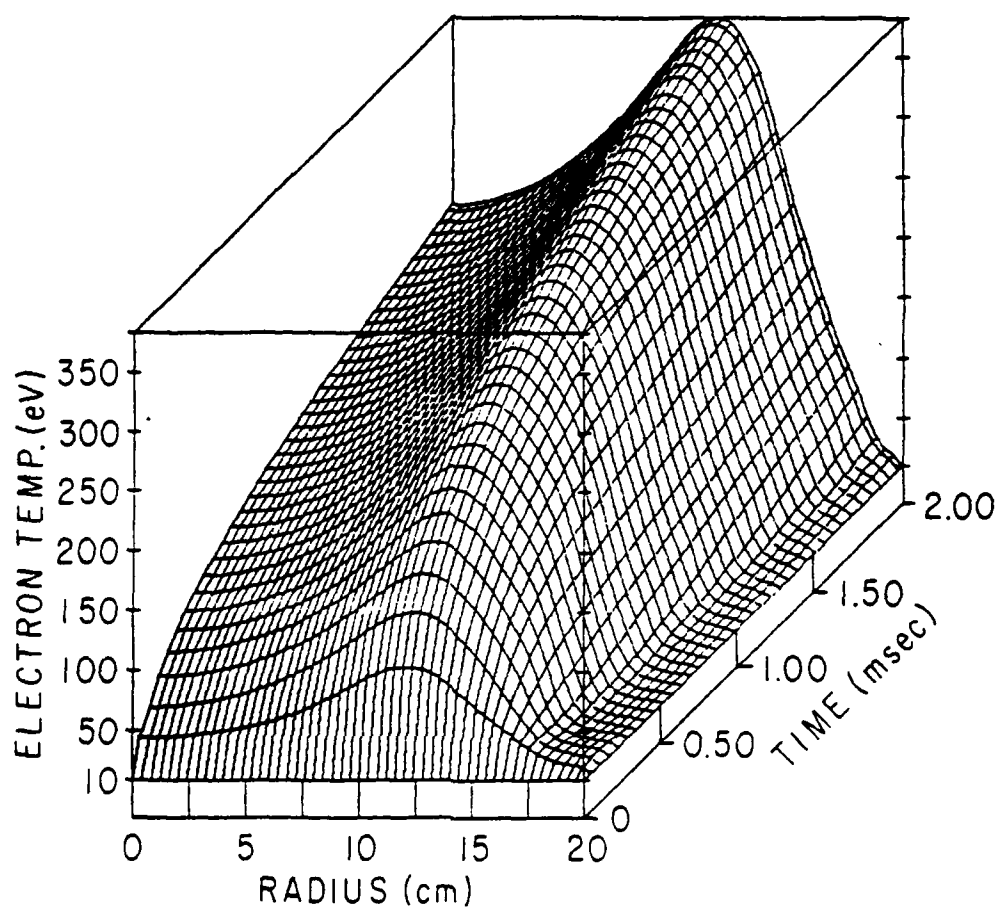


Figure 3 (b)

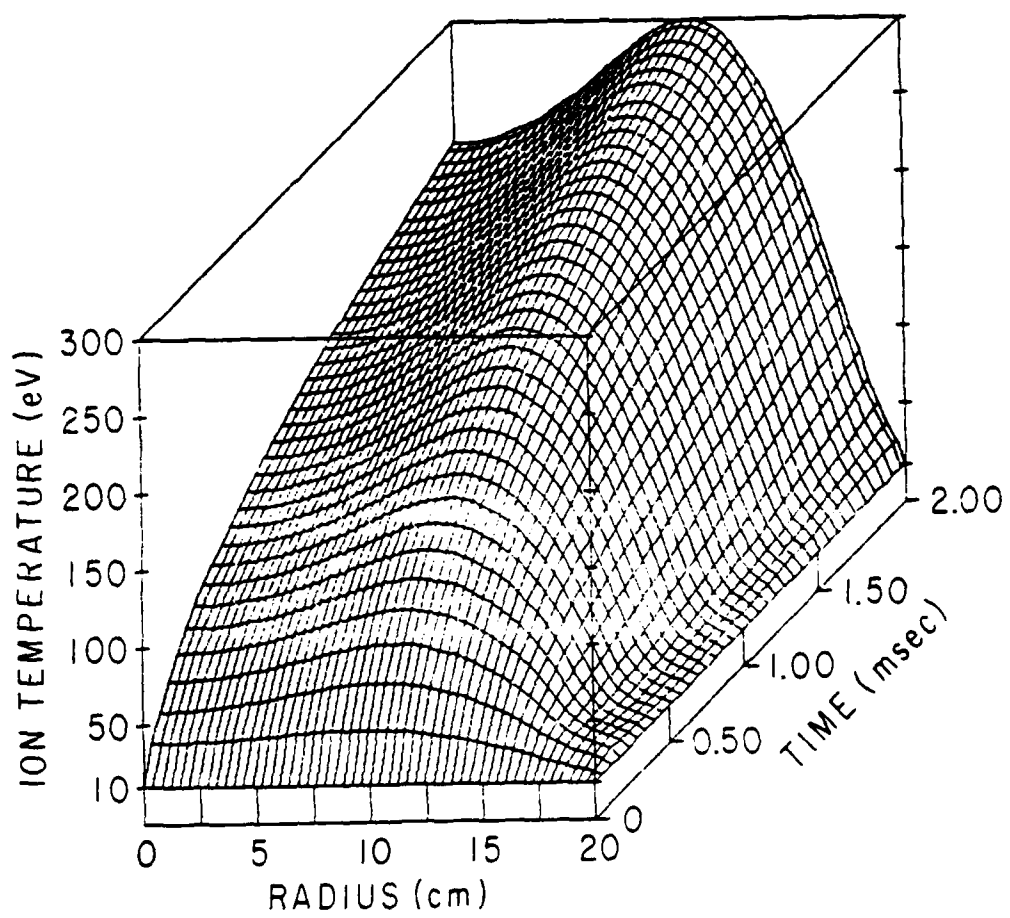


Figure 3 (c)

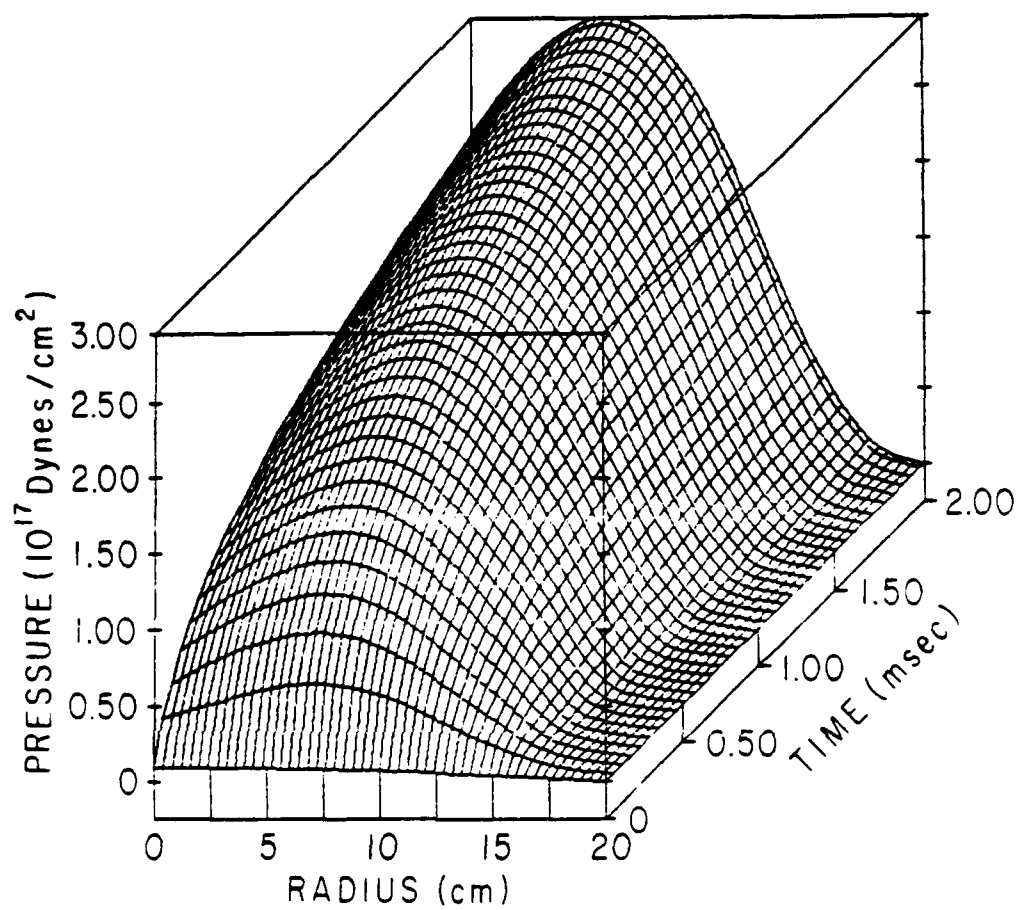


Figure 3 (d)

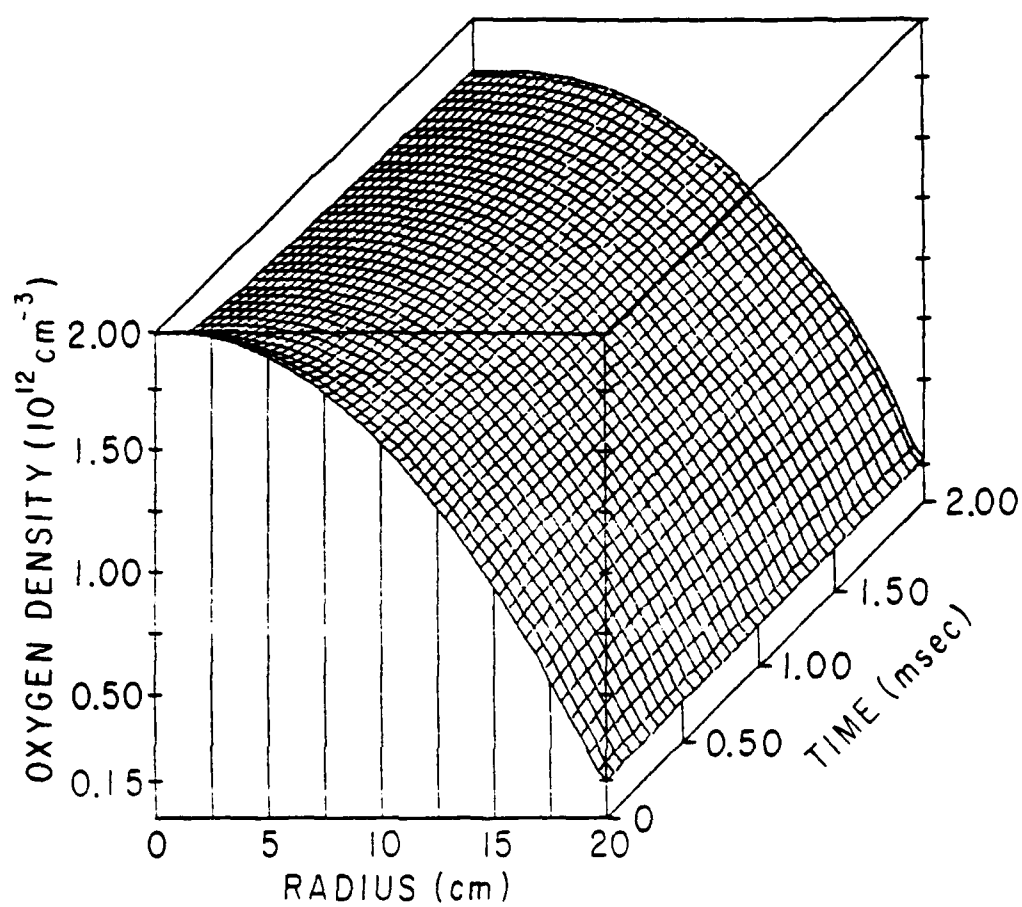


Figure 4 (a)

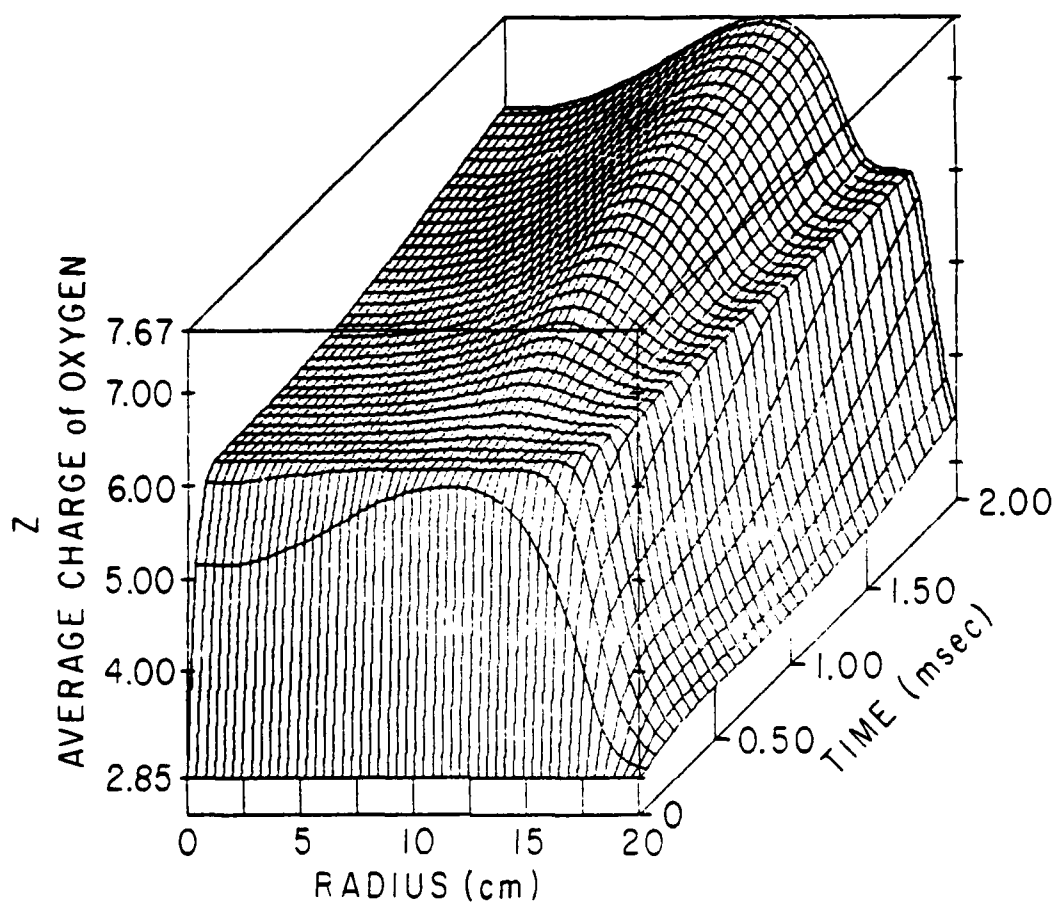


Figure 4 (b)

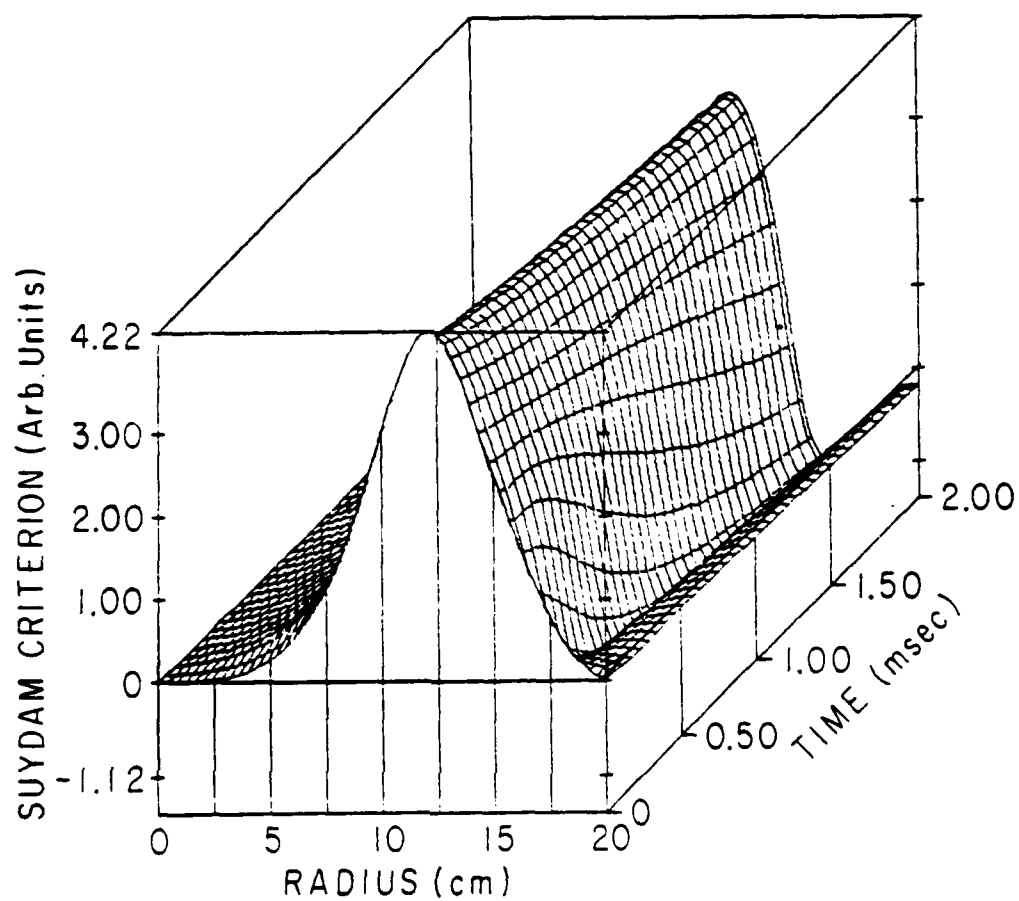


Figure 5

APPENDIX G

"Comparison of Raman Induced Kerr Effect (RIKE)
with Incoherent Scatter (INSC) in a Plasma"

Memorandum to R. Hellwarth and N. Peacock

October 1978

Martin V. Goldman

CU 1036

November 1979

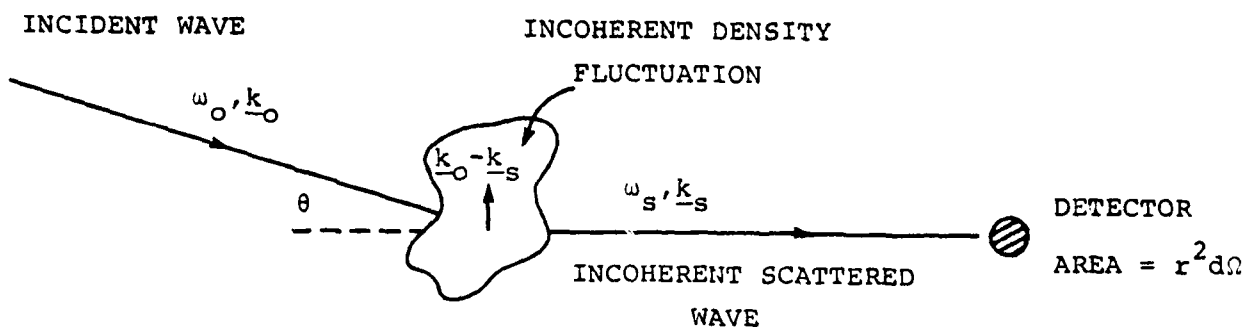
MEMORANDUM

TO: R. Hellwarth and N. Peacock

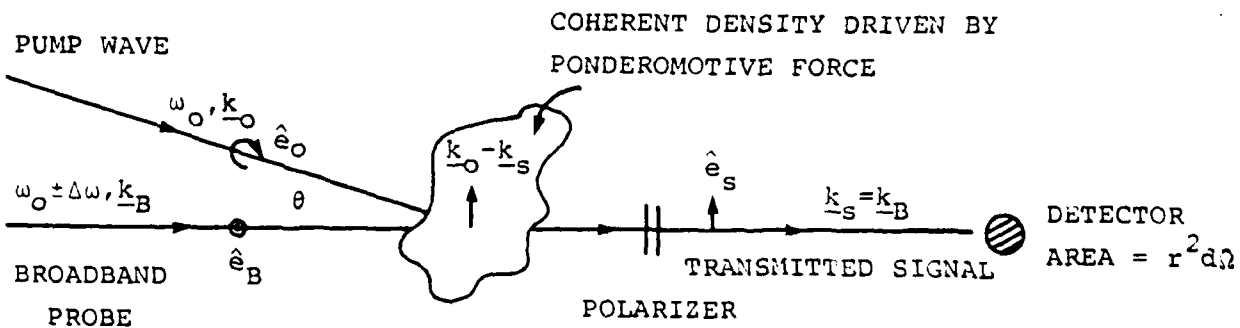
October 26, 1978

FROM: M. Goldman

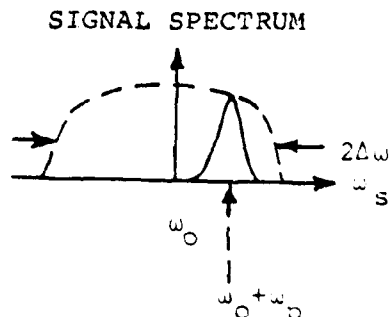
SUBJ: Comparison of Raman Induced Kerr Effect (RIKE)
with Incoherent Scatter (INSC) in a Plasma



INCOHERENT SCATTER



RAMAN-INDUCED KERR



The purpose of this memo is to present a classical theory of the Raman-induced Kerr effect (RIKE) based on the notion of ponderomotive force, and to exhibit its potential advantages over incoherent scattering as an optical diagnostic of collective excitations in a high density plasma.

In the figure, the laser configuration for RIKE is compared with incoherent scatter. In RIKE, a broadband probe laser is incident on a plasma between crossed polarizers. A photon detector on the other side receives no signal until a second, circularly polarized "pump" laser is turned on. The detector then receives the plasma wave spectrum imprinted within the bandwidth of the probe laser. The detected radiation is produced by a third-order current which has the polarization of the pump, the wave vector of the probe, and is inversely proportional to the square dielectric function of the plasma. In effect, density fluctuations are driven by the ponderomotive beat force due to the two incident lasers, so this is a coherent effect.

I. In both cases, the power received at the detector is

$$P = \frac{cr^2\Delta\Omega}{4\pi} |\underline{E}_s(\underline{r}, t)|^2, \quad (1)$$

where \underline{E}_s is the signal field at the observation point \underline{r} (measured from the plasma), and $cr^2\Delta\Omega$ is the area subtended at the detector. \underline{E}_s is related in the usual way to the Fourier transform of the plasma current $\underline{j}(\underline{k}_s, \omega_s)$ which generates \underline{E}_s :

$$\underline{E}_s(\underline{r}, \omega_s) = \frac{i\omega_s}{c^2} \hat{r} \times \hat{r} \times \underline{j}_s(\underline{k}_s, \omega_s) \frac{e^{ikr}}{r}. \quad (2)$$

In both cases, the current is proportional to the high-frequency velocity of electrons induced by an externally incident field \underline{E}_0 , times a lower frequency density, n_L (characteristic of the collective mode being probed). When Fourier transformed, the relationship is

$$i\omega_s j_s(\underline{k}_s, \omega_s) = \frac{e^2}{m} \frac{\underline{E}_0}{2} \left[n_L(\omega_s - \omega_0; \underline{k}_s - \underline{k}_0) + n_L(\omega_s + \omega_0; \underline{k}_s + \underline{k}_0) \right] . \quad (3)$$

for $\omega_s > 0$, the second term is negligible, and for $\omega_s < 0$, the first term is negligible, since the plasma has no high frequency response at $|\omega_s| + \omega_0$. If we time-average (or ensemble average) (1), we get

$$\begin{aligned} \langle P \rangle &= \frac{c r^2 \Delta \Omega}{4\pi} \frac{1}{T} \int_0^T |\underline{E}_s(\underline{r}, t)|^2 dt \\ &= \frac{r^2 \Delta \Omega c}{4\pi} 2 \sum_{\omega_s > 0} \frac{1}{T^2} \underline{E}_s(\underline{r}, \omega_s) \cdot \underline{E}_s(\underline{r}, -\omega_s) . \end{aligned} \quad (4)$$

Hence, combining Eqs. (2)-(4), into Eq. (1) gives the usual result

$$\langle P \rangle = I_0 \sigma_T \Delta \Omega \frac{1}{T} \sum_{\omega_s > 0} \frac{|n_L^e(\omega_s - \omega_0; \underline{k}_s - \underline{k}_0)|^2}{T} , \quad (5)$$

where $I_0 = c |\underline{E}_0|^2 / 8\pi$ is the time-average incident intensity, and $\sigma_T = r_0^2 [1 - (\hat{r} \cdot \hat{e}_0)^2]$ is the usual Thompson scattering cross section.

II.

The only difference between RIKE and INSC is in the physics of n_L . In INSC it is an incoherent density fluctuation driven by spontaneous emission sources, and in RIKE it is a coherent density response, driven by ponderomotive force.

We first consider INSC in an equilibrium non-magnetic plasma. The electron charge density response consists of the polarization density (proportional to longitudinal field fluctuations, \mathcal{E}_L), and electron spontaneous emission, n_{SP}^e ,

$$-en_L^e = -\frac{ik}{4\pi} \chi_L^e \mathcal{E}_L - en_{SP}^e, \quad (6)$$

where χ_L^e is the usual electron susceptibility. When Eq. (6) and its ion counterpart are inserted into Poisson's equation, we obtain

$$\epsilon_L \mathcal{E}_L = \frac{4\pi}{k} i(en_{SP}^e - en_{SP}^i), \quad (7)$$

where $\epsilon_L = 1 + \chi_e + \chi_i$ is the longitudinal dielectric function.

Combining (6) and (7),

$$n_L^e(\omega, k) = \left(1 - \frac{\chi_L^e}{\epsilon_L}\right) n_{SP}^e + \frac{\chi_L^e}{\epsilon_L} n_{SP}^i. \quad (8)$$

Whenever $\omega \gg kv_i$, the ions can be ignored. (This is the case, for example, near the Langmuir wave resonance). Then,

$$\lim_{\omega \gg kv_i} n_L^e(\omega, k) \approx \left(1 - \frac{\chi_L^e}{\epsilon_L}\right) n_{SP}^e. \quad (9)$$

The density correlation function which enters into (5) is then

$$S(\underline{k}, \omega) \equiv \frac{\langle |n_L^e(\omega, \underline{k})|^2 \rangle}{n_0 VT} = \frac{\langle |n_{SP}^e|^2 \rangle}{n_0 VT} \times \left| 1 - \frac{\chi_L^e}{\epsilon_L} \right|^2 \quad (10)$$

where V is the scattering volume, and n_0 the mean electron density. By using the fluctuation-dissipation theorem, we find an expression for the SPONTANEOUS EMISSION correlation function contribution on the right side.

$$\frac{\langle |n_{SP}^e(\underline{k}, \omega)|^2 \rangle}{n_0 VT} = \frac{2k^2}{k_D^2 \omega} \text{Im } \epsilon_L(\underline{k}, \omega) \quad (11)$$

In the vicinity of the Langmuir resonance, this becomes

$$\frac{\langle |n_{SP}^e(\underline{k}, \omega)|^2 \rangle}{n_0 VT} = \frac{4k^2}{k_D^2 \omega_p^2} \gamma_L \quad (12)$$

where γ_L is the Langmuir damping rate (collisional or Landau). Now we compare with RIKE. Here, the electron density response is due to the ponderomotive force associated with the total externally impressed electric field. This force, F_p , is

$$F_p = \frac{-ike^2 |\mathcal{E}_{ext}|^2}{4m\omega_0^2} \quad (13)$$

The total external field is the real part of $\mathcal{E}_{ext}(t)e^{-i\omega_0 t}$, where the envelope field \mathcal{E}_{ext} is given by

$$\mathcal{E}_{ext}(t) = \mathcal{E}_0 e^{i\mathbf{k}_0 \cdot \mathbf{r}} + \mathcal{E}_B(t) e^{i\mathbf{k}_B \cdot \mathbf{r}} \quad (14)$$

The field \mathcal{E}_0 is that of the circularly polarized (narrow band) pump, and $\mathcal{E}_B(t)$ is the linearly polarized broadband probe field.

The part of the ponderomotive force relevant to RIKE is due only to the beat term in $|\mathcal{E}_{\text{ext}}|^2$, which is $\mathcal{E}_{\text{B}}(t) \cdot \mathcal{E}_{\text{O}}^* e^{i(\underline{k}_{\text{B}} - \underline{k}_{\text{O}}) \cdot \underline{r}}$. The electrons respond linearly to the electric plus ponderomotive force $(-e\mathcal{E}_{\text{L}} + F_{\text{p}})$. Thus,

$$-en_{\text{L}}^e = -\frac{ik}{4\pi} \chi_{\text{L}}^e (\mathcal{E}_{\text{L}} - F_{\text{p}}/e) . \quad (15a)$$

When this is inserted in Poisson's equation, we obtain

$$\epsilon_{\text{L}} \mathcal{E}_{\text{L}} = \chi_{\text{L}}^e F_{\text{p}}/e . \quad (15b)$$

Combining these two yields,

$$n_{\text{L}}^e(\omega, \underline{k}) = \left(1 - \frac{\chi_{\text{L}}^e}{\epsilon}\right) \left(\frac{-ik\chi_{\text{L}}^e F_{\text{p}}}{4\pi e^2}\right) . \quad (16)$$

By comparing equation (16) with equation (9), we see that the coherent quantity which plays the same formal role as n_{SP}^e , (as a source term, which drives a dynamically screened polarization density response), is the effective external source,

$$n_{\text{ext}}^e(t) = \frac{-ik\chi_{\text{L}}^e F_{\text{p}}(t)}{4\pi e^2} . \quad (17)$$

In particular, in terms of n_{ext}^e , the counterpart of Eq. (10) becomes

$$\frac{|n_{\text{L}}^e(\omega, \underline{k})|^2}{n_{\text{O}} VT} = \frac{|n_{\text{ext}}^e(\omega)|^2}{n_{\text{O}} VT} \times \left|1 - \frac{\chi_{\text{L}}^e}{\epsilon}\right|^2 . \quad (18)$$

Hence, to compare RIKE with INSC, we need to compare the source term $|n_{\text{ext}}^e(\omega)|^2/n_{\text{O}} VT$ with the correlation of SPONTANEOUS EMISSION

density fluctuations given in Eq. (12). Combining (17), (13), and (14),

$$\frac{|n_{\text{ext}}^e(\underline{k}, \omega)|^2}{n_o VT} = \frac{v^2 |\chi_L^e|^2 k^4}{n_o V 16 (4\pi)^2 m^2 \omega_o^4} \frac{|\mathcal{E}_B(\omega)|^2 |\mathcal{E}_o|^2 |\hat{e}_B \cdot \hat{e}_o^*|^2}{T} \quad (19)$$

where $\underline{k} = \underline{k}_B - \underline{k}_o$. For the broadband probe field, we assume,

$$\frac{|\mathcal{E}_B(\omega)|^2}{T} = \frac{\Delta\omega}{\omega^2 + (\Delta\omega)^2} \overline{|\mathcal{E}_B(t)|^2}, \quad (20)$$

(where the bar indicates a time average with $T \sim (\Delta\omega)^{-1}$). When ω is near the plasma frequency, ω_p , and assuming the bandwidth $\Delta\omega$ is much greater than ω_p , this is proportional to $1/\Delta\omega$. Since $|\chi_L^e| \approx 1$ near the plasma frequency, when we combine (20) and (19), the result becomes,

$$\frac{|n_{\text{ext}}^e(\underline{k}, \omega)|^2}{n_o VT} = \frac{v n_o}{16 \Delta\omega} \frac{k^4}{k_D^4} \Lambda_B^2 \Lambda_o^2 |\hat{e}_B \cdot \hat{e}_o^*|^2, \quad (21)$$

where $\Lambda_{B,o} = v_{B,o}/v_e$, $v_{B,o}$ is the oscillating velocity of an electron in the probe or pump field:

$$v_{B,o} \equiv \frac{e |\mathcal{E}_{B,o}|}{m \omega_o}, \quad (22)$$

and v_e is the electron thermal velocity. Λ_B is the parameter which measures nonlinear effects, and should be small if RIKE is to be a non-perturbing measurement. We can also express $\Lambda^2 = (2\omega_p^2/\omega^2) (I/mnc)$, where I is the average intensity of the radiation beam in question. The ratio of the RIKE to INSC

signal intensities at a particular frequency is therefore just the ratio of Eq. (21) to Eq. (12), or

$$R = \frac{P_{\text{RIKE}}}{P_{\text{INSC}}} = \frac{n_0 V}{64} \frac{\omega_p}{\Delta\omega} \frac{\omega_p}{\gamma_L} \frac{k^2}{k_D^2} \Lambda_B^2 \Lambda_O^2 \frac{|\hat{e}_B \cdot \hat{e}_O^*|^2}{4} \quad (23)$$

(The extra factor of 1/4 comes from the second polarizer in RIKE.) The term $n_0 V$ is the number of electrons in the volume of plasma occupied by the crossed beams. This appears because RIKE is a coherent effect, whereas INSC is not. It can be very large in high density plasmas where n_0 is on the order of 10^{19} cm^{-3} . The other large factor is ω_p/γ_L , which is the effective Q of the Langmuir mode. This enters because $\langle |n_{\text{SP}}^e|^2 \rangle$ is proportional to γ (by the Nyquist theorem), whereas $\langle |n_{\text{ext}}^e|^2 \rangle$ is independent of γ . The other factors are all small, but rough estimates indicate that R can be at least 10^6 . Suppose the pump and probe lasers have an output of 5 J in 15 nsec at frequencies close to 10 times the plasma frequency of a plasma with $\theta = 1 \text{ keV}$, $n = 10^{19}$. If the lasers are focused down to a spot size of $3 \times 10^{-2} \text{ cm}$, then the intensity at the spot will be $I = 3 \times 10^{11} \text{ W cm}^{-2}$, and $\Lambda^2 \approx 10^{-4}$ for the probe or pump laser. The number of electrons participating in RIKE will be $n_0 \times (3 \times 10^{-2})^3 = 3 \times 10^{14}$. If we arrange for $k/k_D = 1/10$, the damping will be collisional, and $\gamma_c/\omega_p = 2 \times 10^{-5}$. Inserting these numbers into Eq. (23) gives $R \approx 10^6$.

These estimates only give a relative comparison with incoherent scatter. To obtain the magnitude of the transmitted

RIKE power, we must insert Eq. (18) into (5). When the scattering is from a Langmuir wave, the coefficient $|1 - (\chi_L^e / \epsilon_L)|^2$ in Eq. (18) can be approximated as,

$$|\epsilon|^{-2} \approx \frac{\omega_p^2}{4} \frac{1}{|\omega - \omega_L(k)|^2 + \gamma^2}, \quad (24)$$

where $\omega_L^2 = \omega_p^2 + 3v_e^2 k^2$. We do not carry out the details here, although it is straightforward to do so.

In practice, it is probably preferable to replace the broadband probe by a probe offset in frequency by ω_L , and having a narrower bandwidth, $\Delta\bar{\omega}$ in the range $\gamma \ll \Delta\bar{\omega} \ll \omega_p$. Under these conditions the Lorentzian in Eq. (20) should be replaced by $\Delta\bar{\omega} / [(\omega - [\omega_{PR} - \omega_0])^2 + (\Delta\bar{\omega})^2]$, where ω_{PR} is the central frequency of the probe, and $\Delta\bar{\omega}$ its width. Near the Langmuir resonance this becomes $(\Delta\bar{\omega})^{-1}$, so Eq. (23) is again valid, with $\Delta\omega \rightarrow \Delta\bar{\omega}$. However, now $\omega_p / \Delta\bar{\omega}$ is larger than unity, so R is enhanced even further.

III. Effects of a Magnetic Field in the Plasma

It is formally trivial to generalize these results to an anisotropic plasma such as a magnetized plasma. In this case, the density response is given not by Eq. (15a), but rather by

$$-en_L^e = \frac{-ik}{4\pi} \cdot \underline{\chi}^e \cdot [\underline{\mathcal{E}} - \hat{k}F_p/e], \quad (25)$$

where $\underline{\chi}^e$ is the linear electron susceptibility tensor which is well known, and can be obtained from either hot or cold linear magnetoplasma equations. (See, for example, T. Stix, "Theory of Plasma Waves," Chapter 9, 1962). The field $\underline{\mathcal{E}}$ is not, in general, longitudinal, so we must use the full set of Maxwell equations instead of Poisson's equation to obtain the generalization of Eq. (15a). This brings in currents, and we may use, in place of Eq. (25),

$$\underline{j}^e = \frac{-i\omega}{4\pi} \underline{\chi}^e \cdot |\underline{\mathcal{E}} - \hat{k} F_p/e| . \quad (26)$$

Eq. (25) is identical to the longitudinal component of Eq. (25) when we use the continuity equation, $\rho^e = \underline{k} \cdot \underline{j}^e / \omega$. (Equivalently, we could use the conductivity tensor $\underline{\sigma}^e$, where $\underline{\chi}^e \equiv 4\pi i \underline{\sigma}^e / \omega$.) With Eq. (26) inserted in Maxwell's equation, the generalization of Eq. (15b) is:

$$\begin{aligned} \underline{M} \cdot \underline{\mathcal{E}} &= \left(\underline{\chi}^e \cdot \hat{k} \frac{F_p}{e} \right) \\ &= \underline{\chi}^e \hat{k} F_p / e , \end{aligned} \quad (27)$$

where \underline{M} is given by

$$\underline{M} = \underline{\epsilon} + \frac{c^2}{\omega^2} (\underline{k} \underline{k} - k^2 \underline{1}) , \quad (28)$$

and

$$\underline{\epsilon} \equiv 1 + \underline{\chi}^e + \underline{\chi}^i . \quad (29)$$

All of the electrostatic and electromagnetic collective modes of the plasma can be found from the zeros of $\det \underline{M}$. If we deal with real frequencies and include dissipation, then $\det \underline{M}$ gets small near a collective mode but is not zero. Hence, we can insert (27) to obtain

$$\underline{E} = \underline{M}^{-1} \cdot \underline{X}^e \cdot \hat{k} F_p / e . \quad (30)$$

Inserting this into (25) gives

$$-en_L^e = \frac{-ik \cdot \underline{X}^e}{4\pi e} \cdot [\underline{M}^{-1} \cdot \underline{X}^e \cdot \hat{k} - \hat{k}] F_p . \quad (31)$$

Near a resonance, the second term is small, and the electron density response is proportional to the diagonal component of \underline{M}^{-1} associated with the direction $\hat{k} \cdot \underline{X}^e$. When \underline{k} is oblique to the anisotropy direction (e.g., \hat{B}_0) the density n_L^e will get large near the minima of $\det M$, which will occur at the electromagnetic and electrostatic normal modes of the plasma. Hence, RIKE may offer a method for probing electromagnetic collective modes of a plasma. In order to evaluate the RIKE signals associated with a particular collective excitation in a magnetoplasma we need to carry out the detailed algebraic analysis of \underline{M} and \underline{M}^{-1} in the vicinity of the frequency and wave vector of that excitation. This program is currently underway.

APPENDIX H

"Plasmon-Plasmon Interactions"

Physical Review Letters

40, 257-260 (1978)

Donald F. DuBois and Martin V. Goldman

CU 1036

November 1979

Plasmon-Plasmon Interactions

D. F. DuBois

Theoretical Division, Los Alamos Scientific Laboratory, Los Alamos, New Mexico 87545

and

M. V. Goldman

Department of AstroGeophysics, University of Colorado, Boulder, Colorado 80302

(Received 19 September 1977)

It is shown that cancellations in a consistent calculation strongly reduce the attractive interaction of plasmons in an electron gas and eliminate the possibility of a bound state of two plasmons in a metal. In degenerate semiconductors with a large static dielectric constant, a residual binding of two plasmons may remain.

Recently Ruvalds and co-workers^{1,2} (RRCG) claimed that residual plasmon-plasmon interactions in a degenerate electron gas could lead, under certain circumstances, to a bound state of two plasmons. Earlier the present authors³ had examined this problem using the diagrammatic Green's function formulation of the many-electron problem and found that to zero order in the plasmon-plasmon momentum transfer (\vec{q}), the plasmon-plasmon interaction in an electron gas was zero! Ruvalds and co-workers examined our unpublished notes and concluded¹ that our calculations agreed to within a numerical factor. This conclusion is not correct because it was based only on part of our calculation.

We found that the plasmon-plasmon interaction has contributions from two distinct classes of irreducible scattering graphs as shown in Fig. 1. The box graphs represented by Fig. 1(a) and its five topologically distinct transformations lead to a coupling parameter (in the notation of RRCG) of

$$g_{44} = -\frac{3}{8} \frac{\omega_p^2}{nE_F} [1 + O(q^2/k_F^2)] \quad (1)$$

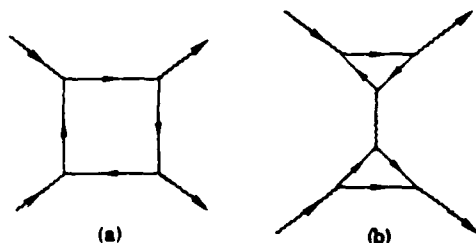


FIG. 1. (a) One of six topologically distinct box graphs, whose sum leads to the plasmon-plasmon interaction coupling in Eq. (1). (b) One of eight topologically distinct graphs, whose sum leads to the plasmon-plasmon coupling in Eq. (2).

which is exactly the result found by RRCG. Here $\vec{q} = \vec{k} - \vec{k}'$ is the momentum transfer between plasmons and k_F is the Thomas-Fermi screening momentum. [Note that $|\vec{q}| < 2k_F$ and $k < k_F \approx 3k_F$ is the condition for weakly damped plasmons in the RPA (random-phase approximation).] On the basis of this result RRCG claimed that our calculation agreed with theirs.³

However, we went on to consider the eight distinct graphs represented by Fig. 1(b) which led to the contribution

$$g_{4b} = \frac{3}{8} \frac{\omega_p^2}{nE_F} [1 + O(q^2/k_F^2)], \quad (2)$$

which exactly *cancels* the contribution of the diagrams of Fig. 1(a) to terms of order q^2/k_F^2 !

Ruvalds and co-workers used the Bohm-Pines collective-coordinate transformation of the many-body Hamiltonian which is still exact. It appears then that RRCG neglected some contributions in this Hamiltonian which are equivalent to the graphs of Fig. 1(b).

In the remainder of this Letter we will point out the ubiquitous nature of this type of cancellation in collective phenomena in quantum and classical plasmas and will give some results for a two-component plasma for which the cancellation is not complete. Further we will argue that in a degenerate semiconductor the cancellation may not be complete because of lattice effects. These effects may leave a residual attractive interaction between plasmons and the remote possibility of a bound state or resonance.

The cancellation noted above is a well-known one in plasma theory. In Fig. 2 we draw representative diagrams (in each case there are additional topological variations of these) for the processes of Compton scattering of plasmons from electrons [2(a)],⁴ optical absorption into a plasmon and electron-hole pair [2(b)],⁵ and light scat-

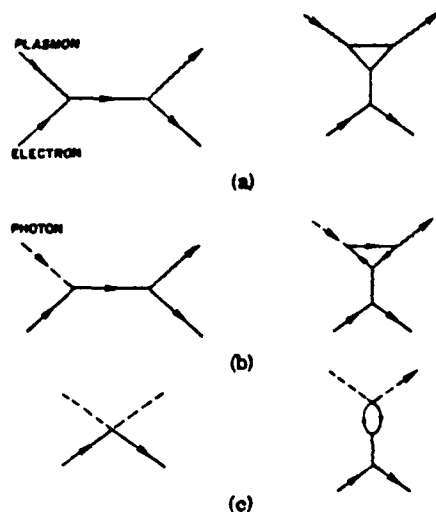


FIG. 2. Representative graphs for (a) Compton scattering of plasmons from electrons; (b) optical absorption of a photon into an electron-hole pair plus a plasmon; and (c) light scattering from electrons. In each case, cancellation occurs between the contributions from the two types of graphs.

tering from electrons² [2(c)]. In the case of plasmon-plasmon scattering we note the close relationship of this process with Compton scattering in the sense of a generalized optical theorem. In each case the transition amplitude involved is proportional to

$$1 - \chi_e(q, \Delta\omega)/\epsilon(q, \Delta\omega), \quad (3)$$

where $\chi_e(q, \omega)$ is the RPA electron susceptibility function (i.e., the electron-hole propagator) where q and $\Delta\omega$ are the momentum and energy transfer on scattering. The factor unity comes from the (noncollective) graphs on the left-hand side in each set and the $-\chi_e/\epsilon$ arises from the second or class of diagrams on the right-hand side, which in each case represent scattering from the screening cloud surrounding each electron. Note that for an electron gas $\epsilon = 1 + \chi_e$ and $1 - \chi_e/\epsilon = (1 + \chi_e)^{-1} = \chi_e^{-1} \approx q^2/k_F^2$ in the limit of static screening ($qV_F \gg \Delta\omega$). Thus the combined effect is of order q^2/k_F^2 rather than unity. For a two-component system or a material characterized by a background dielectric constant ϵ_0 , we can write $\epsilon = \epsilon_0 + \chi_e$ and $1 - \chi_e/\epsilon = \epsilon_0/(\epsilon_0 + \chi_e)^{-1}$. If ϵ_0 is comparable to or larger than q^2/k_F^2 , a much larger residual interaction can occur. For example, in an electron-ion plasma $\epsilon_0 \approx 1 + k_{Di}^2/k^2$ when $\Delta\omega$

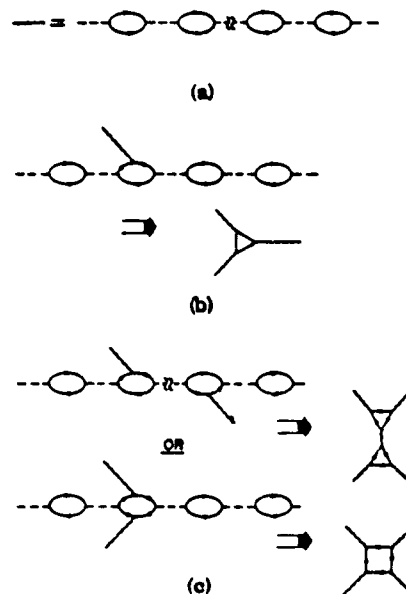


FIG. 3. (a) The plasmon propagator as the sum of bubble or polarization graphs. (b) The three-plasmon interaction obtained by the insertion of an additional plasmon-particle vertex in the graphs of (a). (c) The two types of four-plasmon interaction graphs by a second plasmon-particle insertion in the graphs of (b).

$\ll kV_i$ [$V_i = (T_i/M_i)^{1/2}$] and we have $1 - \chi_e/\epsilon \approx k_{Di}^2/k_F^2 - T_e/T_i \gg 1$ resulting in a much larger residual interaction when $q \ll k_F$.

A similar, but not identical, cancellation occurs in the calculation of plasmon damping into two electron-hole pairs as shown by DuBois and Kivelson.³

In Fig. 3 we demonstrate graphically how the various contributions to plasmon-plasmon coupling arise. In Fig. 3(a) the plasmon propagator in the RPA is represented as the well-known summation of bubble diagrams. Three-plasmon coupling is represented by inserting a simple plasmon-particle vertex into the electron-hole lines in all possible ways. This produces the "triangle" coupling shown in Fig. 3(b). Note that formally this insertion of a plasmon-particle vertex can be accomplished by taking the functional derivative of the one-plasmon propagator with respect to an external potential $V_{ex}(x_1, t_1) = V_{ex}(1)$ which acts on the electrons. The functional derivative acting on each electron or hole propagator G produces

$$\left. \frac{\delta G(1, 2)}{\delta V_{ex}(3)} \right|_{V_{ex}=0} = - \int d5 \int d6 G(1, 5) \frac{\delta G^{-1}(5, 6)}{\delta V_{ex}(3)} G(6, 2) \Big|_{V_{ex}=0} = -G(1-3)G(3-2)$$

thus turning $G(1-2)$ into $-G(1-3)G(3-2)$ which transforms the simple bubble graphs into triangles. Four-plasmon coupling is obtained by a second functional derivative which is equivalent to another plasmon insertion. We can have insertions in two separate bubbles [Fig. 3(c)] or two insertions in one bubble [Fig. 3(d)]. Summing to all orders then leads to the two types of plasmon-plasmon interaction graphs in Fig. 1.

We have carried out an analysis of the two-plasmon thermal Green's function

$$D_2(k_1, t_1; k_2, t_2; k_3, t_3; k_4, t_4) = \langle T \rho(k_1, t_1) \rho(k_2, t_2) \rho(k_3, t_3) \rho(k_4, t_4) \rangle, \quad (4)$$

where $\langle O \rangle = \text{Tr}(e^{-\beta(H - \mu N)} O) / \text{Tr}(e^{-\beta(H - \mu N)})$ and $\rho(k, t)$ is the density operator. The technical details are similar but not identical to those discussed in Rajagopal, Grest, and Ruvalds.² The approximation solves the Bethe-Salpeter equation for D_2 by summing ladders of the fundamental interaction diagrams in Fig. 1. The momentum-frequency space Green's function can be decomposed into relative momentum-energy variables $k = (\vec{k}, \omega)$ and center-of-mass variables $K = (\vec{K}, \Omega)$,

$$D_2(\frac{1}{2}K + k, \frac{1}{2}K - k; \frac{1}{2}K' + k', \frac{1}{2}K' - k') = \hat{D}_2(k, k'; K) \delta^4(K - K'). \quad (5)$$

The reduced Green's function is related to a generally non-Hermitian operator and can be decomposed into a complete set of biorthogonal amplitudes X_n and φ_n

$$\hat{D}_2(k, k'; K) = \sum_n \frac{\varphi_n^*(\vec{k}, \vec{K}) \psi_n(\vec{k}', \vec{K})}{\Omega - E_n}. \quad (6)$$

The following "Schrödinger" equation for $\psi_n(k')$ results from carrying out this procedure:

$$[E_n - \omega_+ - \omega_- + i(\gamma_+ + \gamma_-)] \psi_n(\vec{k}, \vec{K}) = [1 + g(\omega_+) + g(\omega_-)] \int \frac{d^3k'}{(2\pi)^3} V_{\text{eff}}(\vec{k}, \vec{k}'; \vec{K}) \psi_n(\vec{k}', \vec{K}), \quad (7)$$

where

$$\omega_{\pm} = \omega_{\text{pl}}(\frac{1}{2}\vec{K} \pm \vec{k}) \quad (8)$$

are the two plasmon energies and γ_+ and γ_- are the corresponding damping decrements. The statistical factors are

$$g(\omega) = (e^{\beta\omega} - 1)^{-1} \quad (9)$$

with $\beta = (k_B T)^{-1}$, and $V_{\text{eff}}(\vec{k}, \vec{k}'; \vec{K})$ is the effective (nonlocal) plasmon-plasmon interaction

$$V_{\text{eff}}(\vec{k}, \vec{k}'; \vec{K}) = -\frac{\hbar \omega_p^2}{2nm\langle v^2 \rangle} \frac{(\vec{k} \cdot \vec{k}')^2}{k^2 k'^2} \frac{q^2}{k_s^2} \chi_s(\vec{q}, \Delta\omega) \left[1 - \frac{\chi_s(\vec{q}, \Delta\omega)}{\epsilon(q, \Delta\omega)} \right] \quad (10)$$

[with $\vec{q} = (\vec{k} - \vec{k}')$ and $\Delta\omega = \omega_{\text{pl}}(\frac{1}{2}\vec{K} + \vec{k}) - \omega_{\text{pl}}(\frac{1}{2}\vec{K} + \vec{k}')$, which is proportional to $1 - \chi_s/\epsilon$ as advertised.

The result of RRCG is obtained by neglecting the term χ_s/ϵ and using the static approximation for $\chi_s = k_s^2/q^2$ [valid when $\Delta\omega \sim (qk/k_F)V_F \ll kV_F$]. The cancellation of the terms in square brackets reduces V_{eff} from their value by a factor q^2/k_s^2 which is always less than unity for undamped plasmons. (Note $q_{\text{max}} \sim 2k$, $k^2 < k_s^2 \approx \frac{1}{3}k_s^2$.) The solution of (7) with the q -dependent interaction is much more difficult and we have not carried out a detailed solution. We estimate, using variational methods, that the binding energy for an s state is now reduced by a factor of about $\frac{1}{3}$. This would push the bound-state threshold estimated by RRCG up to an unrealistic value of $r_s \approx 14$. Here we have included the factor of 3 resulting from angular averaging as discussed in Ref. 4.

For doped semiconductors ϵ_0 is the lattice di-

electric constant arising from virtual interband transitions and is a constant if $\hbar\Delta\omega \ll E_g$, the least band-gap energy. In this case ϵ_0 may be of order 10 or more and may significantly enhance the binding. The condition $\hbar\Delta\omega = \hbar[\omega_{\text{pl}}(k) - \omega_{\text{pl}}(k')] \ll E_g$, where $\omega_{\text{pl}}(k) \approx \omega_p + \frac{3}{10}V_F^2 k^2/\omega_p$ for degenerate electrons, leads to the restriction

$$\frac{3}{10} \frac{q^2}{k_F^2} \ll \left(\frac{E_g}{E_F} \right)^2 \left(\frac{\hbar\omega_p}{E_g} \right). \quad (11)$$

If the right-hand side of this inequality can be chosen to be of order unity or greater, the above estimates for the binding potential are valid. In this case there is an effective attractive q -dependent potential (using $\chi_s = k_s^2/q^2$)

$$V_{\text{eff}} \propto -\frac{(\vec{k} \cdot \vec{k}')^2}{k^2 k'^2} \frac{\epsilon_0}{\epsilon_0 + k_s^2/q^2}$$

AD-A081 883

COLORADO UNIV AT BOULDER DEPT OF ASTRO-GEOPHYSICS

F/6 20/9

PLASMA WAVE TURBULENCE AND PARTICLE HEATING CAUSED BY ELECTRON --ETC(U)

NOV 79 M V GOLDMAN

F49620-76-C-0005

UNCLASSIFIED

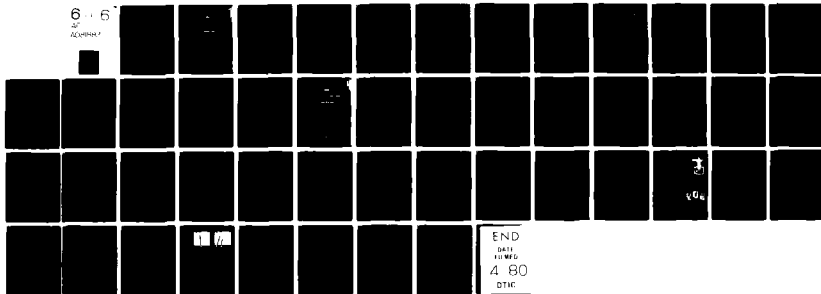
CU-1036

AFOSR-TR-80-0167

NL

6 6

REPRODUCTION



which leads to a coupling parameter comparable to (1) provided $q^2/\hbar^2 < 1/\epsilon_0$. Again, the detailed analysis of this case remains to be carried out. In a degenerate semiconductor with a large value of ϵ_0 (> 10) it appears that the attractive interaction might be strong enough to permit a plasmon bound state or resonance. In this case the resonance could not be observed in electron scattering but might be observable from light scattering experiments or in optical absorption.

The plasmon interaction with the screening clouds surrounding the electrons again is seen to lead to important cancellations. We conclude that, at least for $r_s < 1$, plasmons are nearly independent excitations of an electron gas with a weak attractive interaction. The challenge which remains is to extend these calculations beyond lowest-order terms in r_s , to encompass the regime of physical densities.

This research was supported in part by Hughes Research Laboratories, Malibu, California, the U. S. Air Force Office of Scientific Research, and the U. S. Energy Research and Development

Administration.

¹J. Ruvalds, A. K. Rajagopal, J. Carballo, and G. S. Grest, *Phys. Rev. Lett.* **36**, 274 (1976).

²A. K. Rajagopal, G. S. Grest, and J. Ruvalds, *Phys. Rev. B* **14**, 67 (1976).

³D. F. DuBois and M. V. Goldman, Hughes Research Laboratories, Quarterly Report, September 1963 (unpublished).

⁴RRCG correctly pointed out a numerical error in our unpublished notes which when corrected leads to the numerical result of (1). However, they did not account for the canceling contribution (2). In addition, we believe that the numerical factor 3 in (1) and (2) is in error. The angular factor $(\vec{k} \cdot \vec{k}')^2/\hbar^2 k'^2 = \cos^2 \theta_{kk'}$, which appears in both theories was set equal to 1 by RRCG. However, when we solve our Eq. (7) in the approximation with $1 - \chi_0/\epsilon$ in (10) set equal to 1, we find a factor of $\frac{1}{2}$ resulting from the angular average of $\cos^2 \theta_{kk'}$ in the lowest bound state, which is an s state.

⁵D. F. DuBois and M. G. Kibelson, *Phys. Rev.* **186**, 409 (1969).

⁶D. F. DuBois and V. Gillinsky, *Phys. Rev.* **133**, A1308, A1317 (1964).

NONLINEAR LANGMUIR WAVES DURING TYPE III SOLAR RADIO BURSTS

DWIGHT R. NICHOLSON, MARTIN V. GOLDMAN, PETER HOYNG, AND JAMES C. WEATHERALL

Department of Astro-Geophysics, University of Colorado

Received 1977 May 16; accepted 1978 January 31

ABSTRACT

Type III solar radio bursts are thought to be associated with intense levels of electron beam excited Langmuir waves. We numerically study the nonlinear evolution of these waves, in time and in two spatial dimensions, due to their coupling to other waves. For parameters appropriate to one-half the Earth-Sun distance, we find nonlinear effects to be important, as in previous one-dimensional work. However, a new and important phenomenon, two-dimensional soliton collapse, is found to occur. This collapse, induced directly by the wave packet nature of the beam excited waves, produces two-dimensional wave spectra extending over a much broader range of wavenumbers than has been predicted by inhomogeneous quasi-linear theory. Our results compare favorably with certain aspects of recent observations. We neglect the background magnetic field; while substantially justified for the present parameters, this neglect may require reexamination at locations closer to the Sun.

Subject headings: plasmas — Sun: radio radiation

1. INTRODUCTION AND REVIEW OF PREVIOUS WORK

Type III solar radio bursts are thought to be caused by a stream of electrons, emitted at the Sun's surface, which propagate to the Earth's orbit and beyond (for detailed reviews of Type III phenomena, see the 1974 June/July issue of *Space Science Reviews* and the 1976 February issue of *Solar Physics*). As the stream propagates, Langmuir waves are emitted due to the well-known linear process of Landau growth, also known as weak beam-plasma instability. The Langmuir waves interact with low-frequency density perturbations to produce electromagnetic radiation with frequency near the local electron plasma frequency; this radiation is observed at the Earth and is called fundamental radiation. The Langmuir waves can also interact with each other to produce electromagnetic radiation with frequency near twice the local electron plasma frequency; this radiation is also observed near the Earth and is called harmonic radiation.

The Langmuir waves associated with Type III bursts utilize the free energy available in the stream and can produce quasi-linear diffusion of the stream electrons in velocity space. The Langmuir waves also undergo nonlinear wave-wave interactions which can saturate their growth. The purpose of this paper is to present a two-dimensional treatment of these waves, including the relevant wave-wave nonlinearities, while ignoring plasma inhomogeneity, wave-particle interactions, and effects of the background magnetic field. First, let us briefly discuss previous work on quasi-linear and nonlinear wave effects.

The quasi-linear diffusion of stream electrons by Langmuir waves was first considered in the Type III context by Sturrock (1964), whose model of an infinitely extended homogeneous plasma lead to the

disheartening conclusion that the stream would diffuse in velocity space in a very short time, so short that no well-defined stream could propagate from the Sun to the Earth. Fortunately, this conclusion has been reversed by more recent analyses (Baldwin 1964; Zaitsev, Mityakov, and Rapoport 1972; Zaitsev *et al.* 1974; Magelssen 1976; Magelssen and Smith 1977; Takakura and Shibahashi 1976) which take into account the inhomogeneous nature of the stream (the inhomogeneous nature of the plasma is less important). The idea of inhomogeneous quasi-linear theory (one-dimensional) is as follows: At time $t = 0$, an energetic group of electrons is created near the Sun's surface in a short time Δt . At a given position x_0 between the Sun and the Earth, there are no stream particles until time $t_1 \sim x_0/v_1$, where v_1 is the speed of the fastest electrons in the group (Fig. 1). At time $t_1 \gg \Delta t$ and position x_0 , Langmuir waves grow due to linear Landau growth, with growth rate proportional to the slope of the electron distribution function $f(v)$, in the region indicated in Figure 1. At a later time t_2 , at the same position x_0 , the fast electrons of speed v_1 have passed by and disappeared, and the stream is represented by particles of slower speed $v_2 \sim x_0/t_2$, as shown in Figure 1. Now the slope of $f(v)$ is negative in the region of velocity space with $v > v_2$, and Langmuir waves with phase speeds in this region are damped. Thus, waves emitted at time t_1 can be damped at time t_2 . In this way, by continuous emission and reabsorption of waves, the stream can propagate from the Sun to the Earth with little energy loss, retaining the form of a distinct beam, in agreement with observations.

The inhomogeneous quasi-linear theory of the preceding paragraph could be the final story were it not for the fact that the Langmuir wave levels predicted by that theory are also subject to nonlinear

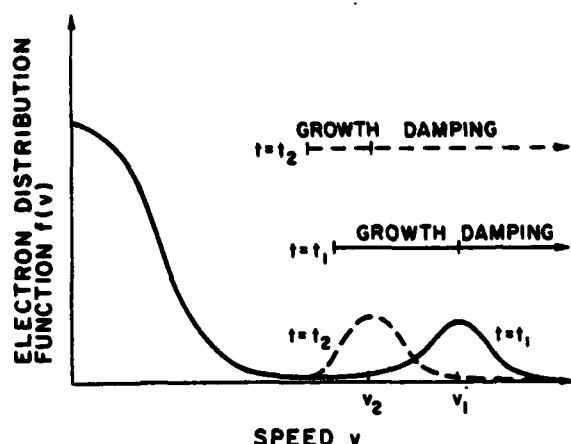


FIG. 1.—Predictions of inhomogeneous quasi-linear theory for the electron distribution function $f(v)$. This picture is valid at a particular position x_0 between the Sun and the Earth. Growth and damping refer to Langmuir waves with phase speeds in the indicated regions.

wave-wave interactions. In the context of homogeneous beam-plasma interaction (Sturrock 1964), Kaplan and Tsytovich (1968) consider induced scattering of Langmuir waves off the polarization clouds surrounding individual ions. With the assumption of a monoenergetic beam and isotropic waves, they find the scattering to proceed fast enough to stabilize the quasi-linear diffusion, even in the absence of the inhomogeneous quasi-linear effects of the preceding paragraph. This conclusion is challenged by the work of Zheleznyakov and Zaitsev (1970), and by Smith and Fung (1971), who relax the assumption of monoenergetic beam and isotropic waves. By allowing repeated scatterings of waves in one dimension, they show that the net scattering of waves out of resonance with the beam is too slow to prevent quasi-linear relaxation. This result is supported by the work of Heyvaerts and de Genouillac (1974), who numerically treat instability plus induced scattering off the polarization clouds of ions; even without allowing for repeated scatterings, they conclude that the scattering is too slow to prevent quasi-linear relaxation in a homogeneous system.

It has long been known that in addition to induced scattering off the polarization clouds of ions, which may be thought of as a three-wave process (ion-acoustic quasi-mode decay instability), Langmuir waves are also subject to a four-wave process known as the oscillating two-stream instability, OTSI (Silin 1965; Nishikawa 1968). The OTSI was first considered in the context of Type III bursts by Papadopoulos, Goldstein, and Smith (1974), and by Papadopoulos (1975). With a one-dimensional homogeneous model, taking the beam-excited Langmuir waves to have infinite wavelength, they find that the OTSI produces Langmuir waves with wavenumbers so large that they do not resonate with the beam; this suppresses homogeneous quasi-linear relaxation. This work is

extended by that of Smith, Goldstein, and Papadopoulos (1976), who again use a one-dimensional homogeneous model. In a set of coupled equations they include Langmuir wave growth due to beam-plasma interaction and the OTSI, but not the decay instability. Their conclusion is that waves are rapidly removed from phase velocity regions which resonate with the beam, so rapidly that the beam is stabilized against homogeneous quasi-linear relaxation. Although the calculations of Smith, Goldstein, and Papadopoulos (1976) are completely one dimensional, their paper does contain the speculation that in more than one dimension the process of Langmuir soliton collapse may be important.

The importance of two-dimensional effects and finite pump wavelength on the OTSI and related instabilities was first demonstrated for Type III burst parameters near one solar radius by Bardwell and Goldman (1976), and by Bardwell (1976) for distances up to 1 AU. They show that if the beam-excited Langmuir waves can be considered monochromatic, and for a broad range of relevant Type III parameters, the OTSI and related instabilities result in Langmuir waves which remain in resonance with the stream. Thus, these instabilities may not prevent quasi-linear diffusion.

It is the purpose of the present paper to unify and extend the previous work on the nonlinear evolution of Langmuir waves associated with Type III bursts, while ignoring for the present the inhomogeneous quasi-linear effects. We accomplish this purpose by numerically solving a set of equations, known as the nonlinear Schrödinger equation, which completely describes the nonlinear evolution of Langmuir waves in time and in two spatial dimensions. The treatment includes the processes of decay instability, OTSI, stimulated modulational instability (Bardwell and Goldman 1976), and the completely nonlinear phenomenon of Langmuir soliton collapse. The relation of our work to previous nonlinear treatments is indicated in Table 1. We find that nonlinear wave effects, including soliton collapse in two dimensions, are important for Type III parameters at $\frac{1}{2}$ AU. The result of these effects is a much broader spectrum of Langmuir waves in wavenumber space than would be predicted by inhomogeneous quasi-linear theory (Magneissen 1976; Magneissen and Smith 1977), while the total wave energies predicted by both theories are comparable.

II. NONLINEAR SCHRÖDINGER EQUATION

The important nonlinear wave effects which Langmuir waves can experience are contained in a set of equations known as the nonlinear Schrödinger equation, first studied by Zakharov (1972; see Nicholson and Goldman 1976 and Goldman and Nicholson 1977 for an extensive list of references). The derivation of this set of equations proceeds from the two-species plasma fluid equations, with five assumptions: (i) the high-frequency and low-frequency time scales are well separated; (ii) low-frequency motions are quasi-neutral; (iii) high-frequency electrostatic

TABLE 1
EFFECTS INCLUDED IN PRESENT WORK COMPARED TO EFFECTS INCLUDED IN PREVIOUS WORK

Investigators	2-D	Decay	Mod	Repeated Wave-Wave Interaction
Kaplan and Tsytovich 1968.....	...	✓	...	✓
Zheleznyakov and Zaitsev 1970.....	...	✓	...	✓
Smith and Fung 1971.....	...	✓	...	✓
Heyvaerts and de Genouillac 1974.....	✓	✓
Papadopoulos, Goldstein, and Smith 1974.....	✓	...
Smith, Goldstein, and Papadopoulos 1976.....	✓	✓
Bardwell and Goldman 1976.....	✓	✓	✓	...
Present work.....	✓	✓	✓	✓

NOTE.—“Mod” refers to four-wave interactions such as the OTSI and the stimulated modulational instability.

energy density is much less than electron kinetic energy density; (iv) low-frequency ion speeds are much less than high-frequency electron speeds multiplied by the square root of the electron-to-ion mass ratio; (v) only electrostatic wave polarization is permitted. The equations thus obtained are

$$\left(i\partial_t + \frac{i\nu_e}{2} + \frac{3T_e}{2\omega_e m_e} \nabla^2\right) \hat{\nabla} \cdot \tilde{\mathbf{E}}(\tilde{\mathbf{x}}, \tilde{t}) = \frac{2\pi e^2}{m_e \omega_e} \hat{\nabla} \cdot (\tilde{n} \tilde{\mathbf{E}}) \quad (1)$$

$$(\partial_{\tilde{t}}^2 + \tilde{\nu}_i \partial_{\tilde{t}} - c_s^2 \tilde{\nabla}^2) \tilde{n}(\tilde{\mathbf{x}}, \tilde{t}) = \frac{1}{4\pi m_i} \tilde{\nabla}^2 |\tilde{\mathbf{E}}|^2, \quad (2)$$

where $\tilde{\mathbf{E}}(\tilde{\mathbf{x}}, \tilde{t})$ is the low-frequency envelope of the total high-frequency electric field $E^{\text{TOT}}(\tilde{\mathbf{x}}, \tilde{t}) = \tilde{\mathbf{E}}(\tilde{\mathbf{x}}, \tilde{t}) \exp(-i\omega_e \tilde{t})$ plus the complex conjugate; $\tilde{n}(\tilde{\mathbf{x}}, \tilde{t})$ is the variation of the ion density from its average value n_0 ; ω_e is the background electron plasma frequency, $\omega_e = (4\pi n_0 e^2 / m_e)^{1/2}$; $m_e(m_i)$ is the electron (ion) mass; e is the magnitude of the electronic charge; $\nu_e(\nu_i)$ is the high (low) frequency phenomenological damping rate; the sound speed $c_s = [(\gamma_i T_i + \gamma_e T_e) / m_i]^{1/2}$, where $\gamma_e(\gamma_i)$ is the electron (ion) specific heat ratio characteristic of low-frequency oscillations; $T_e(T_i)$ is the electron (ion) temperature; and $\tilde{\mathbf{x}} = (\tilde{x}, \tilde{y})$ and \tilde{t} represent dimensional space and time, while $\tilde{\nabla}$ is the dimensional gradient operator. Throughout this paper, a tilde indicates a dimensional variable. It is convenient to introduce the dimensionless variables

$$\begin{aligned} t &= (2\eta/3)(m_e/m_i)(\omega_e \tilde{t}), \\ (x, y) &= \frac{2}{3} \left(\frac{\eta m_e}{m_i} \right)^{1/2} \frac{(\tilde{x}, \tilde{y})}{\lambda_e}, \\ n &= (3m_i/4\eta m_e)(\tilde{n}/n_0), \\ E &= \frac{1}{\eta} \left(\frac{m_i}{m_e} \right)^{1/2} \left(\frac{3E^2}{16\pi n_0 T_e} \right)^{1/2}, \\ \nu_{e,i} &= (3/2\eta)(m_i/m_e)(\nu_{e,i}/\omega_e), \end{aligned} \quad (3)$$

where the electron Debye length $\lambda_e = (T_e/m_e \omega_e^2)^{1/2}$ and the dimensionless ratio $\eta = (\gamma_e T_e + \gamma_i T_i)/T_e$. With the definitions (3), equations (1) and (2) become

$$[i\partial_t + i(\nu_e/2) + \nabla^2] \nabla \cdot \mathbf{E}(x, t) = \nabla \cdot (n\mathbf{E}), \quad (4)$$

$$(\partial_t^2 + \nu_i \partial_t - \nabla^2) n(x, t) = \nabla^2 |\mathbf{E}|^2. \quad (5)$$

The physics contained in these equations can be understood as follows: Without the nonlinear terms on the right-hand sides of (4) and (5), they yield the linear Langmuir wave dispersion relation and the dispersion relation for heavily damped (assuming $T_e \sim T_i$) linear ion acoustic quasi-modes. The nonlinearity on the right-hand side of (4) represents the change in the local electron plasma frequency due to the nonlinear density perturbation n . The nonlinearity on the right-hand side of (5) represents the effect of the ponderomotive force (Landau and Lifshitz 1960; Schmidt 1966), which repels all charged particles from regions of intense high-frequency field; it acts most strongly on the electrons and is communicated to the ions by the requirement of quasi-neutrality. Equation (4) is seen to correspond to the quantum mechanical Schrödinger equation, with the damping term ignored and the right-hand side acting as a nonlinear “potential energy.”

Several distinct physical processes are described by (4) and (5). A given large-amplitude monochromatic Langmuir wave can produce a second Langmuir wave and an associated ion response; this three-wave interaction is called induced scattering off the polarization clouds of ions or equivalently the parametric decay instability, and has been discussed in detail by Bardwell and Goldman (1976). Likewise, a given large-amplitude monochromatic Langmuir wave can produce two other Langmuir waves and an associated ion response; this four-wave interaction can either be an OTSI or a stimulated modulational instability, both of which have also been discussed in detail by Bardwell and Goldman (1976). Finally, the completely nonlinear phenomenon of Langmuir soliton collapse is contained in (4) and (5), as discussed by Zakharov

(1972) and many others (Litvak, Fraiman, and Yunkovskii 1974; Nishikawa, Lee, and Liu 1975; Zakharov, Mastryukov, and Synakh 1974, 1975; Degtyarev and Zakharov 1974, 1975; Degtyarev, Zakharov, and Rudakov 1975, 1976; Galeev *et al.* 1975; Budneva, Zakharov, and Synakh 1975; Pereira, Sudan, and Denavit 1977; Polyudov and Sigov 1976). Consider a region of space which contains a slightly higher level of Langmuir waves than surrounding regions: the ponderomotive force will push plasma out of this region; the resulting lower density will tend to refract more Langmuir waves into this region, thus enhancing the originally high level of waves in this region. In one dimension, this collapse can be stopped by the effects of dispersion, and the final balanced state is called a soliton. In two or three dimensions, the collapse cannot be stopped by dispersion; it proceeds faster than exponentially until the spatial localization produces wavenumbers large enough that strong electron Landau damping sets in, or alternatively until the wave intensities become so large that the validity of equations (4) and (5) breaks down.

We solve equations (4) and (5) numerically in time and in two spatial dimensions, using a technique known as the split-step Fourier method. Our method is almost identical to that used by Pereira, Sudan, and Denavit (1977; see also Hardin and Tappert 1973, and Schamel and Elsässer 1976, for a list of references). The idea is to use complementary grids in real space and in wavenumber space, as shown in Figure 2 for

the case where each grid consists of 32 points in each dimension. Mathematically, both grids are infinitely periodic in both dimensions; only one periodicity length is shown in Figure 2. Each time step consists of two parts. In the first part, the linear terms in (4) and (5) are integrated exactly in wavenumber space. In the second part, the nonlinear terms in (4) and (5) are evaluated in real space, then Fourier transformed to wavenumber space, and the Fourier components of E and n are advanced in time using an implicit Runge-Kutta method (the midpoint rule). In the wavenumber grid in Figure 2, the Fourier components of E and n lying outside the smaller rectangle are set to zero; this is done to avoid problems of aliasing, as discussed by Pereira, Sudan, and Denavit (1977) and by Schamel and Elsässer (1976).

III. EXAMPLES

In this section we perform numerical calculations appropriate to Type III burst parameters at a spatial location roughly half the distance from the Sun to the Earth ($\frac{1}{2}$ AU). This position is chosen for convenient comparison with the inhomogeneous quasi-linear calculations of Magelssen and Smith (1977) and Magelssen (1976), and with the experimental observations of Gurnett and Anderson (1976 and 1977).

We perform a series of four calculations. First, as initial condition we take a large-amplitude monochromatic Langmuir wave with amplitude and wavenumber appropriate to $\frac{1}{2}$ AU as determined by

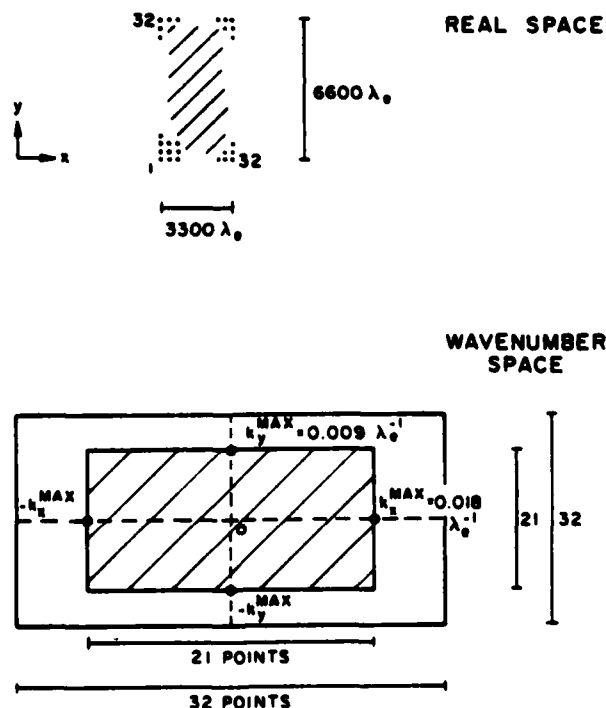


FIG. 2.—Numerical grids in real space and in wavenumber space, for the case where each consists of 32×32 points. Wavenumber components lying outside the smaller rectangle in wavenumber space are set to zero, to avoid problems of aliasing. The physical size of the grids is shown in terms of the electron Debye length.

Magelssen (1976) and by Magelssen and Smith (1977). Second, as initial condition we take a set of waves, having a spread in wavenumbers both perpendicular and parallel to the stream direction, as determined by Magelssen (1976) and by Magelssen and Smith (1977), with the same total energy as in the first case. Third, the monochromatic wave of the first calculation is allowed to grow exponentially from noise, with a growth rate characteristic of the weak beam instability. Fourth, the broad-band set of waves of the second calculation is allowed to grow from noise with the same growth rate as in the third calculation.

As parameters appropriate to a Type III burst near $\frac{1}{2}$ AU, we choose the following: background density $n_0 \approx 50 \text{ cm}^{-3}$, electron plasma frequency $\omega_p \approx 4.0 \times 10^6 \text{ s}^{-1}$, electron temperature $T_e \approx 2 \times 10^6 \text{ K} = 20 \text{ eV}$, $\eta = (\gamma_e T_e + \gamma_i T_i)/T_e \approx 2$, and $m_e/m_i = 1836$. Since the ion temperature is of the same order as the electron temperature, ion motions are heavily damped, so we choose low-frequency damping rates in Fourier space equal to twice the ion acoustic frequency (Bardwell and Goldman 1976): $\nu_i(k) = 2kc_i$. Assuming a Maxwellian plasma, both collisional and Landau damping are negligible for the Langmuir waves considered here, so the high-frequency damping rate is ignored: $\nu_e = 0$. Let us consider each of the four calculations in detail.

a) Case A: Monochromatic Pump Wave

During the numerical evolution of a model Type III burst at $\frac{1}{2}$ AU, Magelssen (1976) and Magelssen and Smith (1977) obtained a quasi-steady state characterized by an energy density $W = |E|^2/4\pi n_0 T_e = 10^{-4}$ centered about a central wavenumber $\bar{k}_0 \lambda_e = 0.011$ with a total spread of parallel wavenumbers $\Delta k \lambda_e = 0.004$. (Note that W and E here are one-half as large as in Bardwell and Goldman 1976.) In our first approximation (case A), we take an initial condition consisting of a single large-amplitude Langmuir wave, having a wavenumber $\bar{k}_0 \lambda_e = 0.011$ and an amplitude such that $W(t=0) = 10^{-4}$. All other Langmuir modes are given initial values roughly characteristic of thermal noise, while initial density perturbations are zero.

In the absence of thermal noise in the other modes our initial condition has the form $E(x, t=0) = E_0 \exp(ik_0 x)$, $n(x, t=0) = 0$, where we have chosen the pump wavenumber in the x direction. Inserting this initial condition into the nonlinear Schrödinger equation (4) and (5), we see that $E(x, t) = E_0 \times \exp(ik_0 x - ik_0^2 t)$, $n(x, t) = 0$ for all time; this is a large-amplitude traveling Langmuir wave which obeys the linear Langmuir dispersion relation in dimensionless units. Now consider the presence of the initially small amplitudes in the other Langmuir modes. In certain regions of wave-vector space, these modes will grow exponentially due to various instabilities, as studied by Bardwell and Goldman (1976) near 1 solar radius, and by Bardwell (1976) at distances from the Sun up to 1 AU. As the modes grow, various nonlinear effects can become important: if the mode amplitudes

attain values which are substantial fractions of the pump amplitude, the pump amplitude must decrease in order to conserve energy; the growing modes can themselves act as pumps for other growing modes; the concept of a set of interacting linear modes may itself completely break down with the appearance of totally nonlinear structures such as collapsing solitons. This nonlinear evolution must be studied numerically.

The dispersion relation for parametric instabilities can be obtained from (4) and (5) by inserting an electric field of the form

$$\begin{aligned} E(x, t) = & E_0 \exp(-i\omega_0 t + ik_0 \cdot x) \\ & + E_1 \exp[-i(\omega_0 + \omega)t + i(k_0 + k) \cdot x] \\ & + E_2 \exp[-i(\omega_0 - \omega^*)t + i(k_0 - k) \cdot x], \end{aligned}$$

where (ω_0, k_0) satisfy the Langmuir dispersion relation, and a density variation of the form $n(x, t) = n' \exp(-i\omega t + ik \cdot x)$ plus complex conjugate, where the pump amplitude $|E_0|$ is considered very large compared to $|E_1|$, $|E_2|$, and n' . We obtain the dispersion relation

$$\begin{aligned} -\omega^2 - 2ik\omega + k^2 \\ = -k^2 |E_0|^2 \left(\frac{\mu_+^2}{\omega - k^2 - 2k_0 \cdot k} - \frac{\mu_-^2}{\omega + k^2 - 2k_0 \cdot k} \right), \end{aligned} \quad (6)$$

where $\mu_{\pm}^2 = (\hat{k}_0 \cdot k \pm k_0)^2$, ω and k are frequency and wavenumber of a low-frequency ion response, and \hat{k} is a unit vector in the k direction. The solution of the dispersion relation is sensitive to the three dimensionless parameters (m_e/m_i) , $(\bar{k}_0 \lambda_e)^2$, and W . In this example we have $W \approx (\bar{k}_0 \lambda_e)^2 < m_e/m_i$.

For a three-wave interaction, which we call the parametric decay instability and which is the fluid limit of the process of induced scattering off the polarization clouds of ions, the frequency matched Langmuir wave frequency is $\omega_L = \omega_0 - \omega^*$, and the Langmuir wavenumber is $k_L = k_0 - k$. In the present example this instability has a maximum growth rate

$$\gamma/\omega_0 \approx 3^{3/2} W/16\eta = 1.62 \times 10^{-3} \quad (7)$$

which occurs at the low-frequency mode wavenumber

$$\bar{k}_L \lambda_e \approx 2\bar{k}_0 \lambda_e - (4\eta m_e/27m_i)^{1/2} = 0.009, \quad (8)$$

corresponding to a Langmuir wavenumber $\bar{k}_L = 0.002$. (This instability is often thought of as a backscatter instability with $\bar{k}_L \approx -\bar{k}_0$ when the second term in (8) is negligible; in the present case, $\bar{k}_0 \lambda_e = 0.011$ is so small that the second term in (8) is not negligible and the Langmuir decay wavenumber is shifted to a value $\bar{k}_L \lambda_e = +0.002$.)

The four-wave interaction called OTSI (Bardwell and Goldman 1976) involves a low-frequency mode wavenumber perpendicular to the pump wavenumber, $k \cdot k_0 = 0$. We then find from the dispersion relation

(6) a purely growing instability with maximum growth rate, obtained approximately from a quartic equation,

$$\frac{\gamma}{\omega_s} \approx \frac{W}{2\eta} \left[1 - \frac{W}{3\eta(k_0\lambda_e)^3} - \left(\frac{3m_e W}{m_i \eta^2} \right)^{1/2} \right] \\ = 1.23 \times 10^{-8}, \quad (9)$$

where the second and third terms are assumed small compared to the first term; this growth rate occurs at a low-frequency wavenumber

$$k\lambda_e \approx (W/3\eta)^{1/2} = 0.0041. \quad (10)$$

The two Langmuir decay waves involved in OTSI have frequencies $\omega_0 + \omega$, $\omega_0 - \omega$, and wavenumbers $k_0 \pm k$. Thus, since $k \perp k_0$ and $|k| < |k_0|$, the Langmuir waves are near k_0 but form a cone around it. In our two-dimensional approximation the cone projects into two wave vectors, displaced above and below k_0 .

We shall not consider in detail the other four-wave instability, called the stimulated modulational instability; this instability involves Langmuir wavenumbers near those for the OTSI and usually has a slightly smaller growth rate than the OTSI (Bardwell and Goldman 1976). We conclude from (7) and (9) that, for the parameters of this example, the decay and the OTSI have comparable growth rates.

We proceed to follow numerically the nonlinear evolution of these waves; the results are displayed in Figures 3a-3e. The Langmuir growth rate at a relatively early time, $\omega_e t = 3.4 \times 10^6$, is seen (Fig. 3a) to have local maxima corresponding to the decay instability and the OTSI. The numerical value of the decay growth rate is within a few percent of that predicted by (7), while the wavenumber of maximum growth for this branch is on the k_x axis at a small positive value as predicted below (8). The maximum growth rate of the OTSI branch is almost exactly that predicted by (9), at a wavenumber with exactly the k_x component predicted below (10) and about two-thirds the k_y component. Given the approximate nature of the analytic results (7)-(10), and the limited resolution of our 32×32 numerical grid, this level of agreement is very satisfactory.

At a later time $\omega_e t = 8.3 \times 10^6$, the electric fields corresponding to maximum decay and OTSI growth rates in wave-vector space have reached substantial amplitudes; in real space (Fig. 3b) the magnitude of the electric field has evolved from its initially constant value to a mottled form, which is partly due to a linear superposition of modes, and partly due to the nonlinear reinforcement of regions of intense electric field. At the time $\omega_e t = 1.0 \times 10^7$, the intense field regions of Figure 3b have become a set of collapsing solitons (Fig. 3c), with corresponding broadening in wave-vector space (Fig. 3d) and density depletions (Fig. 3e). At this time, the solitons are only a few numerical grid spacings in size, so we must end the calculation. Presumably, a numerical calculation with a more detailed grid would show that the solitons continue their collapse to a size of a few Debye

lengths, at which time strong Landau damping would deplete most of the electrostatic energy and a group of fast electrons would be formed. It is noteworthy that the solitons in Figure 3c are elongated in the y -direction, in accordance with accepted two-dimensional soliton behavior. According to the terminology of Zakharov (1972), a soliton is subsonic when $W_{\text{soliton}} < m_e/m_i$ at its center, while it is supersonic if $W_{\text{soliton}} > m_e/m_i$; in Figure 3c, we have $W_{\text{soliton}} = 7.5m_e/m_i$ in the most intense soliton (lower left corner) so that we are somewhat into the supersonic regime.

The collapse observed in this example is facilitated by small Langmuir wave group speeds. The initial pump wavenumber is $k_0\lambda_e < (m_e/m_i)^{1/2}$; this results in a group speed of the initial wave $\bar{v}_g = 3(k_0\lambda_e)v_e \approx 0.03v_e \approx c_s$, where v_e is the electron thermal speed. Thus, after the OTSI and decay branches have grown somewhat, the electric field in real space consists of wave packets having group speeds less than $\sim c_s$; these wave packets can begin an immediate evolution into collapsing solitons with group speeds less than $\sim c_s$. (The simple physical picture of a collapsing soliton is valid only for soliton speeds less than c_s .) For cases not considered explicitly here, such as a Type III burst near the Sun's surface (Bardwell and Goldman 1976), the wavenumbers in the pump are larger than at $\frac{1}{2}$ AU, the initial group speeds are much larger than the sound speed, and one might expect a more complicated wave evolution before collapse could occur (Nicholson and Goldman 1978).

We have shown that in a time $\omega_e t \sim 10^6$ the initially monochromatic wave evolves nonlinearly to a state of collapsing solitons. This time scale is much shorter than the time scale $\omega_e t \sim 10^8$ for which Langmuir waves are found to remain at high levels at a given spatial location, in both inhomogeneous quasi-linear calculations (Magelssen 1976; Magelssen and Smith 1977) and in observations (Gurnett and Anderson 1976 and 1977) at $\frac{1}{2}$ AU. Rather than make a detailed comparison of the numerical results of this section with observations, let us proceed to consider the effect of the finite bandwidth of the initial pump wave; indeed, we find this effect to have important consequences.

b) Case B: Broad-Band Pump Wave

While the calculation of the previous subsection uses a monochromatic pump as initial condition, in practice we know that the stream-excited Langmuir waves will occupy a region of wavenumber space with finite extent both parallel to the stream direction and perpendicular to it. The width of the spectrum parallel to the stream direction can be taken from the inhomogeneous, one-dimensional quasi-linear calculations (Magelssen 1976; Magelssen and Smith 1977); as indicated in Figure 4, this width is $\Delta k_x = \frac{1}{2}k_0$. The width in the perpendicular dimension can be crudely estimated from the two-dimensional homogeneous quasi-linear calculations (Magelssen 1976; Appert, Tran, and Vaclavik 1976); for the present case, we choose a width in perpendicular k -space $\Delta k_y = \Delta k_x$.

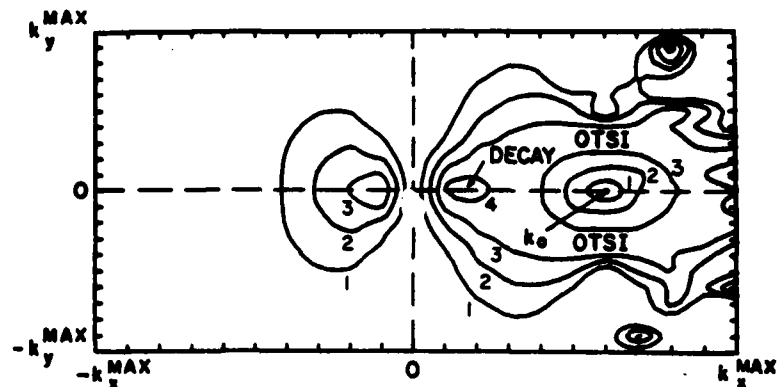


FIG. 3a.—Langmuir growth rate versus Langmuir wavenumber for case A at the early time $\omega_p \bar{t} = 3.4 \times 10^6$. The growth rate exhibits local maxima in the regions marked DECAY and OTSI. The local maximum at negative k_x can be considered part of the DECAY branch; other local maxima are transient phenomena. The large dot at the pump wavenumber indicates a local minimum where the growth rate is zero. Note that the contours give a deceptive feeling for the resolution of the numerical grid; the actual grid spacing is indicated by hatch marks around the border. Numbers on the contours indicate relative growth rate, with contour 1 indicating $\gamma/\omega_p = 3.6 \times 10^{-6}$ and contour 4 indicating $\gamma/\omega_p = 1.5 \times 10^{-6}$.

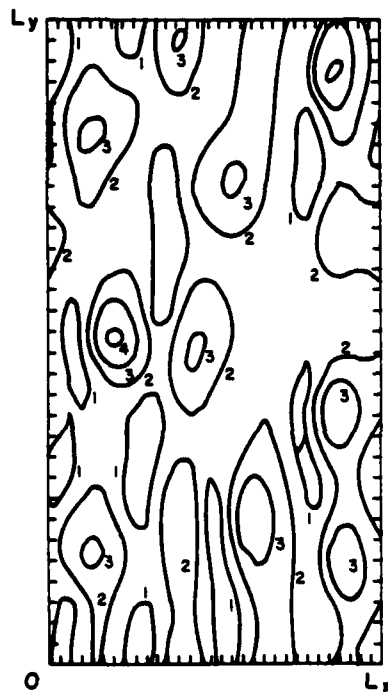


FIG. 3b.—Langmuir electric field amplitude in real space at $\omega_p \bar{t} = 8.3 \times 10^6$. Note mottled appearance with the beginnings of soliton formation. Contours indicate relative absolute value of electric field, with contour 1 indicating $W = 2.9 \times 10^{-5}$ and contour 4 indicating $W = 4.6 \times 10^{-4}$.

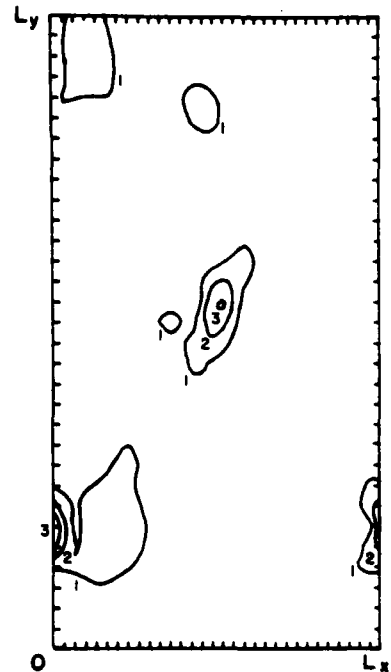


FIG. 3c.—Langmuir electric field amplitude in real space at $\omega_p \bar{t} = 1.0 \times 10^6$. Solitons are collapsing rapidly. Contours indicate relative absolute value of electric field, with contour 1 indicating $W = 2.6 \times 10^{-4}$ and contour 3 indicating $W = 2.3 \times 10^{-5}$.

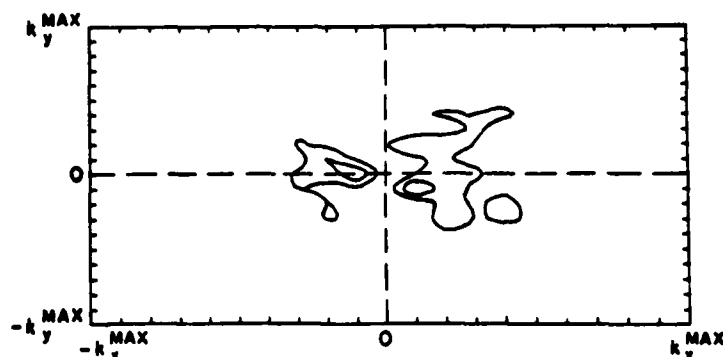


FIG. 3d.—Langmuir wave amplitude in wavenumber space at $\omega_p f = 1.0 \times 10^6$. Much broadening has occurred.

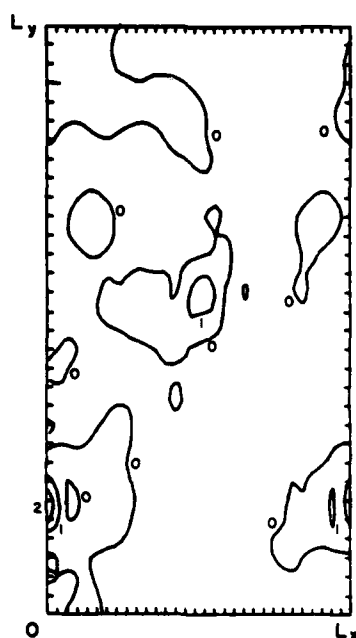


FIG. 3e.—Density perturbation in real space at $\omega_p f = 1.0 \times 10^6$. Note depressions corresponding to collapsing solitons of Fig. 3c. Contours indicate relative density variation, with contour level 0 corresponding to $\delta/n_0 = 0$, contour level 1 corresponding to $\delta/n_0 = -4.3 \times 10^{-4}$, and contour level 2 corresponding to $\delta/n_0 = -8.6 \times 10^{-4}$.

Our initial condition (Fig. 4) is then a set of 15 Langmuir waves; the net average spatial energy density is $W = 10^{-4}$ as in the previous case for a monochromatic pump. Each of the 15 modes has an initial phase $\exp(i\theta)$, where θ is a random number, $0 \leq \theta < 2\pi$.

The broad-band nature of this initial condition introduces two effects not present in the monochromatic case. First, this initial condition would not maintain itself for all time in the absence of thermal fluctuations, as would the monochromatic initial condition; rather, each of the initial k -space modes can couple to every other mode to produce disturbances at

each sum and difference wavenumber. This behavior is generally not thought to be associated with the random phase approximation for an ensemble of initial pump wave packets, but should occur in any particular realization of the ensemble; one important consequence is that soliton collapse begins immediately. The broad-band nature of the pump in k -space will appear in x -space as a set of wave packets; these wave packets have a very small group speed, $V_g = 3(k_0 \lambda_e) v_e \approx 0.03 v_e \approx c_s$, where v_e is the electron thermal speed. A wave packet with a group speed V_g of order the sound speed c_s will very effectively exert a ponderomotive force as described earlier, and soliton collapse may proceed spontaneously. For Type III parameters closer to the Sun, the beam-excited waves have larger wavenumbers, $k_0 \lambda_e > (m_e/m_i)^{1/2}$, and thus group speeds greater than c_s . There, we would expect a somewhat more complicated evolution in wavenumber space before soliton collapse can begin (Nicholson and Goldman 1977).

Second, the broad-band pump will tend to reduce the growth rates of parametrically unstable noise. In a given situation, this effect acts in the opposite

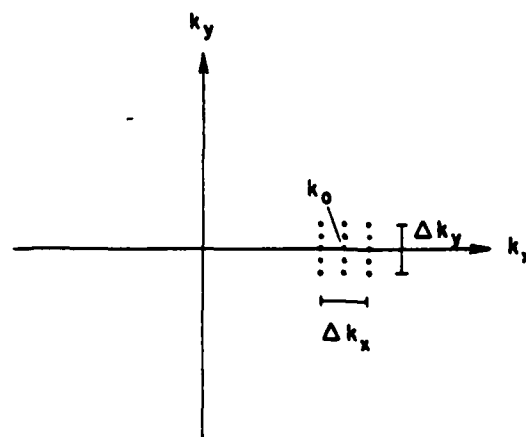


FIG. 4.—Broad-band pump initial condition for the calculations of cases B and D. All of the 15 modes have equal initial amplitude, and random initial phase.

direction to the effect discussed in the preceding paragraph, tending to slow the nonlinear evolution of initially small waves (Thomson and Karush 1974).

With the broad-band initial condition, we follow the time evolution numerically (Figs. 5a-5e). The initial condition in k -space (Fig. 4) results in a wave packet structure in real space (Fig. 5a). A short time later, at $\omega_e t = 5.2 \times 10^4$, the most intense initial wave packet has propagated to the right (recall the periodicity) and has nonlinearly intensified (Fig. 5b), with a concomitant density depression (not shown) and spreading in k -space (Fig. 5c). The soliton collapse continues at $\omega_e t = 8.6 \times 10^4$ (Figs. 5d, 5e). We end the calculation at this time, since electric field energy approaches our boundaries in k -space; presumably, a numerical calculation with a finer x -space grid, covering larger area in k -space, would show collapse until a size of a few Debye lengths is attained, at which time strong Landau damping would remove electric field energy from the system and result in a component of fast electrons. At the center of the most intense soliton in Figure 5e, we have $W_{\text{soliton}} = 2.8(m_e/m_i)$, which is slightly supersonic.

We conclude that soliton collapse removes electrostatic energy from this system in a time $\omega_e t < 10^5$ which is even faster than for a monochromatic pump and, consequently, is much shorter than the time $\omega_e t \sim 10^6$ that intense wave levels are maintained in the inhomogeneous quasi-linear calculations (Magelsen 1976; Magelsen and Smith 1977). Therefore, nonlinear wave effects must be an important factor in the temporal evolution of Type III Langmuir waves near $\frac{1}{2}$ AU. A complete treatment of Langmuir waves in Type III bursts would need to include these nonlinear wave effects in addition to the inhomogeneous quasi-linear effects which we do not treat in this paper. We shall discuss this point further in § IV.

We have repeated this calculation with a computer code utilizing a grid of 64×64 points in both x -space and k -space. The k -space grid covers the same region of k -space as in the 32×32 case, while the x -space grid covers a region 4 times larger. The initial condition then has a k -space extent as shown in Figure 4 for the 32×32 case, but uses 45 modes instead of 15, each with an initially random phase. The results of this calculation are very similar to those for the 32×32 case. This agreement gives confidence that none of the results of this paper are overly sensitive to the number of grid points.

Let us proceed in the next two subsections to consider the effect of a pump wave growing exponentially due to the weak beam-plasma instability, for both the monochromatic pump model and the broad-band pump model.

c) Case C: Growing Monochromatic Pump Wave

The calculations of the two preceding subsections used initial values of Langmuir wave energy densities and wavenumbers characteristic of inhomogeneous quasi-linear calculations, although no beam-unstable

Langmuir wave evolution was permitted. Here we perform a different calculation, in which a monochromatic pump wave is allowed to grow exponentially from noise with a linear growth rate characteristic of the weak beam-plasma instability. A typical linear growth rate $\tilde{\gamma}_L$ can be crudely inferred from the inhomogeneous quasi-linear calculations; we use $\tilde{\gamma}_L/\omega_e = 10^{-6}$. We expect this growth to proceed until the pump becomes large enough to drive parametric instabilities having growth rates larger than the pump's linear growth rate. Using (9) to predict the parametric growth rate, we obtain $W > 4 \times 10^{-6}$ as an estimate for the maximum pump energy; after it reaches this amplitude, it will rapidly drive parametric instabilities and be depleted. We note that the pump's linear growth is included in a very natural fashion in (4) by allowing the damping rate ν_e to have an appropriate negative value, for the k component of E corresponding to the pump mode.

The numerical results are as follows (Figs. 6a, 6b): The pump grows linearly until it reaches a substantial amplitude $W \approx 10^{-4}$; parametric instabilities are now growing rapidly. At time $\omega_e t = 7.4 \times 10^6$ we have reached a nonlinear state with a broad spread of electric field wavenumbers and soliton structure in electric field and in density. The total electrostatic energy W_{TOT} versus time (Fig. 6a) is seen to reach a maximum when $\omega_e t = 8 \times 10^6$, and then decreases to a value of $W_{\text{TOT}} \approx 10^{-4}$. The decrease in energy after $\omega_e t = 8 \times 10^6$ is due to a numerical effect allowing energy to disappear when the wave intensities of the modes indicated in Figure 2 are set to zero. Thus, the calculation is not quantitatively accurate after $\omega_e t = 8 \times 10^6$. However, we expect that the same calculation with Landau damping and a much larger k -space grid would yield similar qualitative results after $\omega_e t = 8 \times 10^6$. The pump electrostatic energy W_p is seen (Fig. 6b) to reach a value $W_p \approx 2 \times 10^{-4}$ at $\omega_e t = 8 \times 10^6$ and then to deplete to less than $W_p \approx 10^{-5}$.

The saturation of the total energy W_{TOT} can be thought of as follows: The only mechanism for energy input into the system is through the linear growth of the pump energy W_p , so the total energy W_{TOT} can increase:

$$\frac{dW_{\text{TOT}}}{dt} \sim 2\tilde{\gamma}_L W_p \sim \frac{dW_p}{dt}. \quad (11)$$

When parametric instabilities have acted to deplete W_p to very tiny values, the right-hand side of (11) becomes very small, and W_{TOT} stops growing. In a more complete calculation including Landau damping, W_{TOT} will then decrease, in qualitative agreement with the numerical behavior shown in Figure 6a.

Rather than discuss these results in detail, let us proceed to an even more realistic calculation, namely, that of a broad-band pump wave with linear growth rate.

d) Case D: Linearly Growing Broad-Band Pump

We expect Type III Langmuir waves to grow linearly from a low level and to have a finite bandwidth. Here

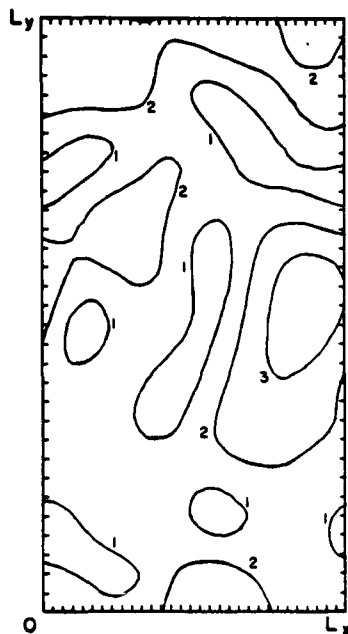


FIG. 5a.—Initial electric field amplitude in real space for case B. Note the presence of localized wave packets. Contours indicate relative absolute value of electric field, with contour 1 indicating $W = 2.9 \times 10^{-3}$ and contour 3 indicating $W = 2.6 \times 10^{-4}$.

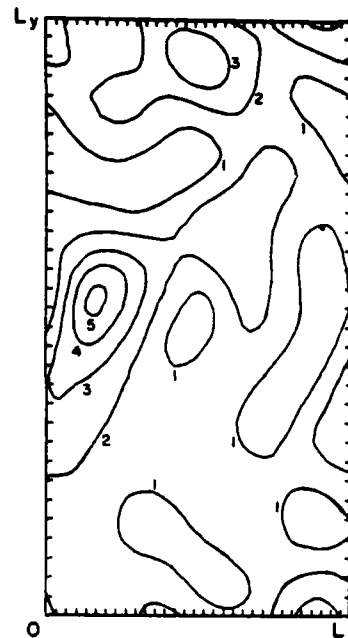


FIG. 5b.—Electric field in real space at $\omega_0 t = 5.2 \times 10^4$, for case B. The localized wave packets are more intense than in Fig. 5a, with contour definitions the same in each figure.

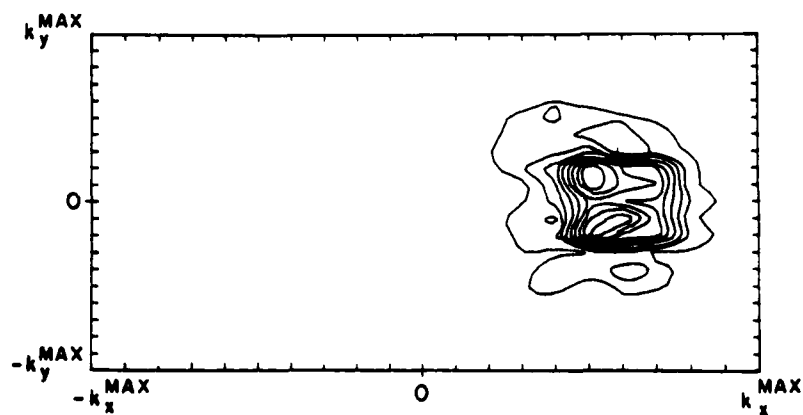


FIG. 5c.—Electric field amplitudes in wavenumber space at $\omega_0 t = 5.2 \times 10^4$, for case B

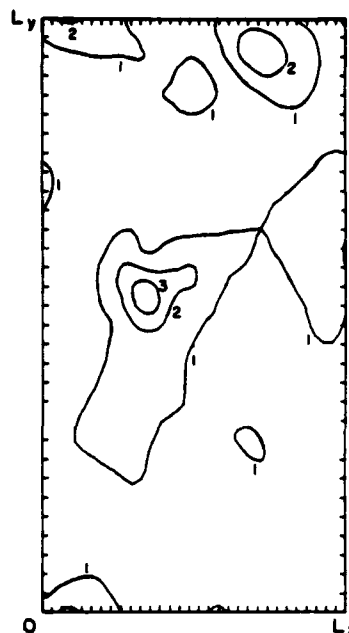


FIG. 5d

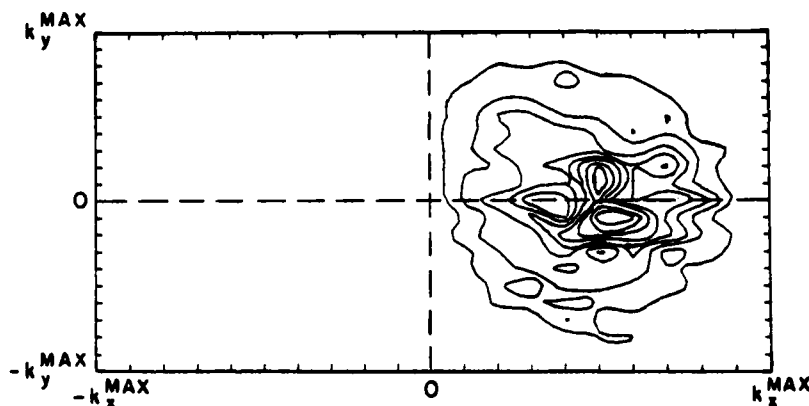


FIG. 5e

FIG. 5d.—Electric field amplitude in real space at $\omega_e t = 8.6 \times 10^4$, for case B. Contours indicate relative absolute value of electric field, with contour 1 indicating $W = 1.2 \times 10^{-4}$ and contour 3 indicating $W = 1.0 \times 10^{-3}$, for case B.

FIG. 5e.—Electric field amplitude in wavenumber space at $\omega_e t = 8.6 \times 10^4$, for case B.

we treat this situation numerically. A group of waves, the same group as in the large-amplitude broad-band case, case B, is allowed to grow exponentially from an initially low level with the same linear growth rate $\gamma/\omega_e = 10^{-6}$ as in case C for the growing monochromatic pump wave. The initial phases are random. At a relatively early time, the group of waves in k -space has a wave packet structure in x -space which is entirely due to linear superposition. At a later time $\omega_e t = 4.9 \times 10^6$, the wave packets have begun a nonlinear collapse, resulting in a wider spectrum in k -space and at least one collapsing soliton in x -space. The total electrostatic energy W_{TOT} (Fig. 7) reaches a maximum

of about $W_{TOT} = 10^{-4}$. After the time $\omega_e t = 5.0 \times 10^6$ when the electrostatic energy saturates, the calculation becomes somewhat inaccurate for the same reasons discussed in case C; nevertheless, we expect that a more accurate calculation would show the same general behavior and approximately the same saturation amplitude. Each of the original pump modes is greatly depleted at late time, even though each retains its linear growth term for all time.

We regard the present calculation as perhaps the most realistic of the four cases. We note that the saturated electrostatic energy $W_{TOT} \approx 10^{-4}$ is about the same value found in the inhomogeneous quasi-

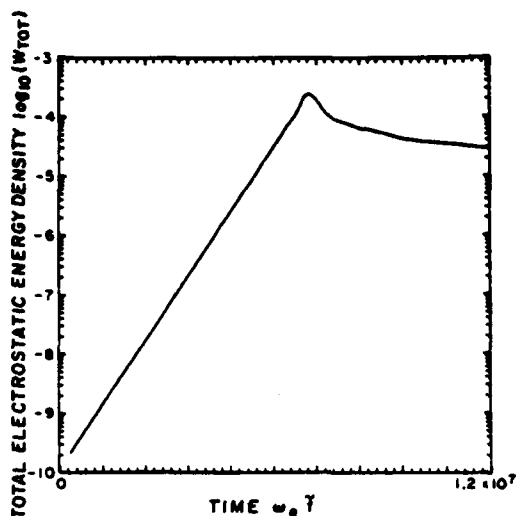


FIG. 6a.—Total high-frequency electrostatic energy versus time for case C. The results are not quantitatively accurate after $\omega_p t = 8 \times 10^6$.

linear calculations (Magelssen 1976; Magelssen and Smith 1977). However, the spread in k -space is much larger for the present calculation than in the inhomogeneous quasi-linear calculations. The importance of this spread in k -space is emphasized by the result of case B, where an initial condition consisting of the same total energy as found here, but with the narrow k -space extent characteristic of the inhomogeneous quasi-linear calculation, is found to be immediately unstable to soliton collapse. We conclude that nonlinear wave effects are indeed important for a complete description of Type III Langmuir waves near $\frac{1}{2}$ AU. This is not to discount the importance of inhomogeneous quasi-linear effects; a complete treat-

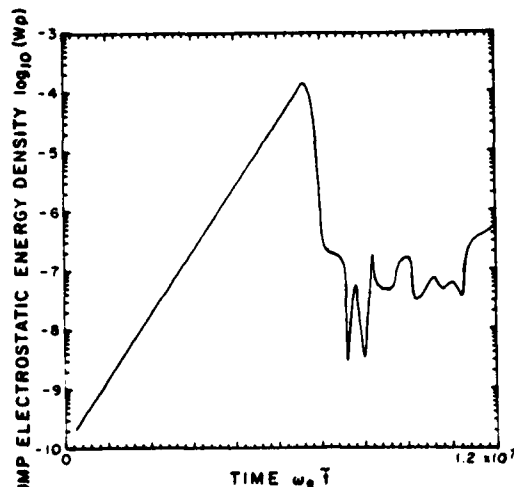


FIG. 6b.—Pump electrostatic energy versus time for case C. The results are not quantitatively accurate after $\omega_p t = 8 \times 10^6$.

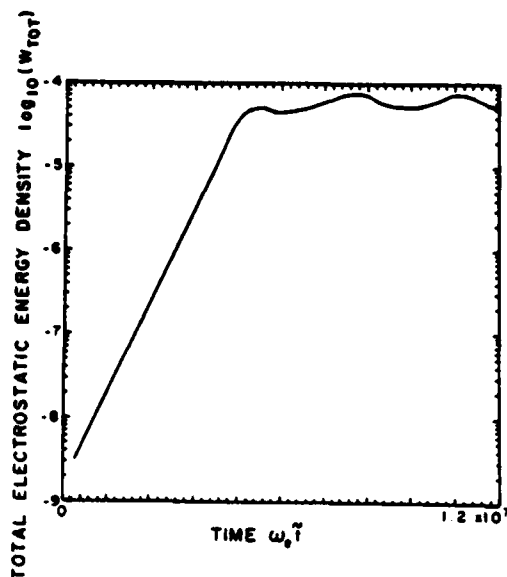


FIG. 7.—Total electrostatic energy versus time for case D. The results are not quantitatively accurate after the first maximum, at $\omega_p t = 5 \times 10^6$.

ment would include, in at least two spatial dimensions, both the nonlinear wave effects considered here and the inhomogeneous quasi-linear effects considered elsewhere.

IV. MAGNETIC FIELD EFFECTS

This work has neglected the effects of the background magnetic field, as did previous two-dimensional work (Heyvaerts and de Genouillac 1974; Bardwell and Goldman 1976). Here we justify this neglect by showing that known (fluid) magnetic field effects are of only marginal importance and would not be expected to qualitatively affect the results of § III.

The magnetic field near 1 AU can be estimated to be of the order of $B = 2 \times 10^{-4}$ gauss, and for purposes of this discussion has a direction along the Type III stream direction. This results in an ordering of frequencies $\Omega_i \ll \Omega_e \ll \omega_i \ll \omega_e$ with $\Omega_e = 0.01 \omega_e$, where $\Omega_{e,i} = |eB/m_{e,i}c|$ is the (electron, ion) gyrofrequency and c is the speed of light. The ratio of magnetic field energy density to background thermal electron energy density is substantial, $B^2/8\pi nT_e \sim 1$.

We separately consider magnetic effects on the two cases A and B (monochromatic and broad-band), and we separately consider the high-frequency and the low-frequency motions. In case A, the effects of the magnetic field on high-frequency Langmuir waves appear as an additional term in the dispersion relation, which in dimensional terms becomes

$$\omega^2 = \omega_e^2 \left[1 + 3k^2 \lambda_e^2 + \left(\frac{\Omega_e}{\omega_e} \right)^2 \sin^2 \theta \right], \quad (12)$$

where θ is the angle between the Langmuir wave vector and the background magnetic field.

For wavenumbers of order the pump wavenumber $k_0\lambda_e \sim 0.01$, the magnetic term is only one-third the dispersive term even for waves traveling perpendicular to the magnetic field; for more typical waves at $\theta < 45^\circ$, the ratio is less than 1/6. The magnetic field term can be included in the dispersion relation (6), where it appears in the two denominators on the right. Consider now the two branches OTSI and decay (see Fig. 5a). For the OTSI we formerly obtained the growth rate (9). In the limit when the two small terms in the middle of (9) can be ignored, we find for the present case (with the magnetic field included) exactly the same growth rate (9). However, the low-frequency wavenumber of maximum growth rate is shifted toward smaller values; in the present case, this shift is 13% of its unmagnetized value. Thus, the OTSI branch is affected only slightly by the magnetic modifications of the high-frequency waves. For the decay branch, the maximum growth rate occurs on the k_x axis, where $\theta = 0$, so that it will be unaffected by the magnetic field. For wavenumbers in the decay branch with a k_y component, the magnetic term can be comparable to the dispersive term and thus would have the effect of somewhat distorting the contours of constant growth, while leaving the maximum growth rate (where $k_y = 0$) unaffected. We conclude that both the decay and the OTSI branches (and by implication the stimulated modulational instability branch) are substantially unaffected (in this example) by the magnetic modifications on the high-frequency waves.

Consider now the magnetic effects on the low-frequency electrostatic waves. For the decay branch (see Fig. 3a), we need low-frequency waves with $k \sim k_0$, and predominantly in the k_0 direction. For the present parameters, this yields $k\rho_e \sim 1$ and $k\rho_i \sim 2000$ (ρ_e and ρ_i are typical electron and ion gyroradii), while the frequencies of interest are in the range $\Omega_i < |\omega| \ll \Omega_e$, where we use the growth rate (7) to estimate $|\omega|$. Thus, the ions can be taken to be unmagnetized, while the electrons are magnetized across the magnetic field. However, since k is along k_0 for the decay branch, and there is no inhibition of electron motion parallel to k_0 , we expect only very minor magnetic field effects on this branch.

For the OTSI branch, we are interested in waves with low-frequency wavenumbers predominantly across the magnetic field, with wavenumbers as given by (10) yielding $k\rho_e = 0.4$ and $k\rho_i = 800$; estimating $|\omega|$ from (9), we have again $\Omega_i < |\omega| \ll \Omega_e$. Thus, the ions are unmagnetized while the electrons are magnetized. While a value $k\rho_e = 0.4$ demands a kinetic treatment of the waves involved, we can make some progress with a fluid approach. Since we are trying to generalize the ion acoustic quasi-mode represented by the left-hand side of (2), we look for quasi-neutral electrostatic waves. Using the electron and ion continuity equations, the unmagnetized ion force equation, and the magnetized electron force equation, we find that the magnetized analog to the left-hand

side of (2) can be represented by the dispersion relation

$$\omega^2 - k^2 c_s^2 - \frac{\Omega_e \Omega_i}{(1 - k_x^2/k_y^2)(\Omega_e^2/\omega^2 - 1)} = 0. \quad (13)$$

(For heuristic purposes, we ignore here the strong ion Landau damping.) For the wavenumber of maximum OTSI growth, we have $k_x = 0$ and the dispersion relation is $\omega^2 = k^2 c_s^2 + \Omega_e \Omega_i$, corresponding to the usual cold plasma lower hybrid resonance together with a thermal effect. At this wavenumber (eq. [10]), the magnetic term is about 5 times the dispersive term, showing that when (13) is substituted into the left-hand side of the dispersion relation (6), the magnetic term will indeed contribute and may change the growth rate obtained from this dispersion relation. If we now perform the mental exercise of holding $|k|$ fixed while letting k_x increase, we see that at a small value of $(k_x/k_y) \sim (m_e/m_i)^{1/2}$, the denominator in (13) can vanish, causing ω^2 to be very much changed over the unmagnetized case. However, in the presence of instability, ω in (13) will be complex, and this effect will be smeared out. For larger values of (k_x/k_y) , one term in the denominator of (13) dominates, and we have

$$\omega^2 - k^2 c_s^2 - \omega^2 \left(\frac{k_y^2 m_e}{k_x^2 m_i} \right) = 0, \quad (14)$$

from which we see that the magnetic term is negligible for $k_x/k_y > (m_e/m_i)^{1/2}$. We conclude that the magnetic field has an important effect on the low-frequency waves, only for waves traveling almost perpendicular to the magnetic field. The net effect should again be a shifting of the growth rate contours in Figure 3a, with some reduction in the maximum growth rate obtained for low-frequency wavenumbers directly across the magnetic field, and practically no change for most of the region labeled OTSI in Figure 3a, together with its neighboring stimulated modulational instability region.

Combining our conclusions on high-frequency and low-frequency effects, we have shown that while there may be a distortion of the growth rate contours shown in Figure 3a, the overall linear growth rate picture is not substantially changed by the inclusion of magnetic field effects for the parameters appropriate to Type III bursts at $\frac{1}{2}$ AU.

Given that the linear growth proceeds substantially as found in § III, we may ask how the magnetic field will affect the completely nonlinear phenomenon of soliton collapse. Referring to Figures 2 and 3b, we see that solitons are initially formed with size $\sim 1000\lambda_e \sim 10\rho_e$. We may arbitrarily say that soliton collapse has obtained a good start when the density perturbation has reached $\tilde{n}/n_0 \sim m_e/m_i$ (this is also the criterion for the onset of "supersonic" collapse). To dig a density hole of this magnitude in the stated region of size $\sim 10\rho_e$ requires (in two dimensions) that a typical electron move a distance $10\rho_e(\tilde{n}/n_0) \sim 0.01\rho_e$. Each electron must therefore move only a small fraction of a gyroradius in order that soliton

collapse be vigorously in progress, and thus the magnetic field should have only a small inhibitive effect on soliton collapse. At almost all spatial points of the initial wave packet, the ponderomotive force has a component along the magnetic field as well as a component across the magnetic field. The component along the magnetic field can easily move electrons away from the soliton, thus allowing the soliton collapse to proceed rapidly. Since the time scale for collapse is the fastest time scale in the overall wave evolution, any small changes in the time scale due to the magnetic field will not affect the overall scenario. These comments also apply to Case B of § III, where we found direct soliton collapse due to the wave packet structure of the initial conditions.

In conclusion, we have shown that the simplest electrostatic corrections (due to the magnetic field) to our electrostatic wave equations produce only marginal effects on the wave interactions considered in § III, and they are not expected to qualitatively change the results of that section. This conclusion agrees with those of Kuznetsov (1974) and Zakharov (1975), who included electromagnetic effects in the same parameter regime. These electromagnetic effects, as well as effects involving low-frequency kinetic Alfvén waves, electromagnetic whistler waves, etc., should eventually be considered in the present context. Such a complete catalog of all possible effects consistent with Maxwell's equations would be very interesting and should properly be done with a kinetic approach for the particles, but is far beyond the scope of the present paper. At present, there is no evidence that such effects would qualitatively affect the results of this paper.

V. DISCUSSION AND CONCLUSION

We conclude that nonlinear effects including soliton collapse are important in the evolution of Type III Langmuir waves; these effects (even in the absence of inhomogeneous quasi-linear effects) can explain the experimentally observed saturation of wave intensities at low levels.

Gurnett and Anderson (1976 and 1977) have observed intense levels of plasma waves at $\frac{1}{2}$ AU in conjunction with Type III solar radio bursts. Their most intense burst consisted of a series of spikes, the largest of which had a plasma wave energy level $W \sim 10^{-8}$, existing in a large spatial volume which can be inferred (Smith 1977) to be of size $\sim 10^3 \lambda_e$. Thus, this spike should be thought of as a large spatial region of Langmuir waves which may be stable to nonlinear effects. This observed wave energy level is less than one order of magnitude lower than found by us in our most realistic model, case D. Given the specialization of our model, these two values may be considered to show a certain amount of agreement.

Earlier measurements (Gurnett and Frank 1975) near 1 AU found an almost complete absence of plasma waves during Type III bursts, with levels $W < 10^{-8}$ even while the Type III electrons themselves were present. Our model does not help to resolve

this mystery; since the solar wind parameters vary by at most one order of magnitude from $\frac{1}{2}$ AU to 1 AU, we would expect our numerical model to yield results somewhat similar to those of the present paper for parameters characteristic of 1 AU.

The results of our model provide a nice explanation for the observed (Gurnett and Anderson 1976, 1977) values of second harmonic electromagnetic emission during Type III bursts. This emission, at frequency $\tilde{\omega} \approx 2\omega_e$, satisfies (Smith 1977) the dispersion relation for an electromagnetic wave in a plasma $\tilde{\omega}^2 = \omega_e^2 + (k^{\text{EM}})^2 c^2$, where k^{EM} is the wavenumber of the electromagnetic wave. For the parameters of this paper we find $k^{\text{EM}} \lambda_e = 0.011$. We further require the equality $k^{\text{EM}} = k_1 + k_2$, where k_1 and k_2 are Langmuir wave vectors, and we require $k_1 \times k_2 \neq 0$ and $k_1 \cdot k_2 \neq 0$. The wavenumber distribution in case D is ideal for satisfying these requirements: we have much wave energy at wavenumbers $0 < |k| < |k^{\text{EM}}| = |k_0|$, and the spread in wavenumbers in both dimensions is substantial. A detailed, approximate calculation of the second harmonic generation from a plasma wave distribution similar to ours has been performed by Smith (1977), whose distribution of waves results from an inhomogeneous quasi-linear calculation plus an assumed broadening in k -space due to induced scattering. He finds that the levels of second harmonic emission observed by Gurnett and Anderson (1976 and 1977) are easily explainable, and in fact are overestimated. This approximate result can also be taken to apply to our own distribution of waves in case D, where the broad distribution of waves in k -space is an immediate consequence of the completely nonlinear wave treatment.

The present treatment has ignored the possible effects of small magnetic fields, background density fluctuations, and damping of Langmuir waves due to non-Maxwellian background electron distribution functions.

We have shown that nonlinear effects including soliton collapse are an important factor in the behavior of Type III Langmuir waves. We have not included inhomogeneous quasi-linear effects. The one-dimensional inhomogeneous quasi-linear calculations, in the absence of nonlinear effects, lead to wave intensities comparable to those found here in cases C and D, but with a much narrower k -space extent; hence they are unstable to nonlinear effects as shown here in cases A and B. A completely realistic calculation must include both nonlinear effects and inhomogeneous quasi-linear effects, in at least two dimensions for both electrons and waves.

This work has greatly benefited from the advice of D. F. Smith on the physics of solar bursts, and of F. Tappert on numerical methods. We thank R. Aamodt, D. DuBois, G. Dulk, A. Kaufman, R. Lin, G. Magelssen, D. Melrose, K. Papadopoulos, N. Pereira, A. Riddle, S. Smerd, R. Smith, and G. Tarnstrom for useful discussions. Part of this work was performed while two of us (M. G. and D. N.) were the guests of

the Aspen Institute for Physics and Astrophysics; their hospitality is appreciated. Part of this work was done while one of us (P. H.) was on leave at the High Altitude Observatory of the National Center for Atmospheric Research. Acknowledgment is made to the National Center for Atmospheric Research, which is sponsored by the National Science Foundation, for

computer time used in this research. This work was supported by the Atmospheric Research Section, National Science Foundation, ATM 76-14275. The work of one of us (M. G.) was also supported by the Air Force Office of Scientific Research contract F49620-76-C-0005. We appreciate the helpful comments of an anonymous referee.

REFERENCES

- Appert, K., Tran, T. M., and Voslavik, J. 1976, *Phys. Rev. Letters*, **37**, 502.
- Baldwin, D. E. 1964, *Phys. Letters*, **12**, 202.
- Bardwell, S. 1976, Ph.D. thesis, University of Colorado.
- Bardwell, S., and Goldman, M. V. 1976, *Ap. J.*, **209**, 912.
- Budneva, O. B., Zakharov, V. E., and Synakh, V. S. 1975, *Fiz. Plazmy*, **1**, 606 (English transl. in *Soviet J. Plasma Phys.*, **1**, 335).
- Destyarev, L. M., and Zakharov, V. E. 1974, *Zh. Exp. Teoret. Fiz. Pis'ma*, **20**, 365 (English transl. in *JETP Letters*, **20**, 164).
- 1975, *Zh. Exp. Teoret. Fiz. Pis'ma*, **21**, 9 (English transl. in *JETP Letters*, **21**, 4).
- Destyarev, L. M., Zakharov, V. E., and Rudakov, L. I. 1975, *Zh. Exp. Teoret. Fiz.*, **68**, 115 (English transl. in *Soviet Phys.—JETP*, **41**, 57).
- 1976, *Fiz. Plazmy*, **2**, 438 (English transl. in *Soviet J. Plasma Phys.*, **2**, 240).
- Galeev, A. A., Sagdeev, R. Z., Sigov, Yu. S., Shapiro, V. D., and Shevchenko, V. I. 1975, *Fiz. Plazmy*, **1**, 10 (English transl. in *Soviet J. Plasma Phys.*, **1**, 5).
- Goldman, M. V., and Nicholson, D. R. 1977, *Phys. Fluids*, **20**, 756.
- Gurnett, D. A., and Anderson, R. R. 1976, *Science*, **194**, 1159.
- 1977, *J. Geophys. Res.*, **82**, 632.
- Gurnett, D. A., and Frank, L. A. 1975, *Solar Phys.*, **45**, 477.
- Hardin, R. H., and Tappert, F. D. 1973, *SIAM Rev.*, **15**, 423.
- Heyvaerts, J., and de Genouillac, G. Verdier. 1974, *Astr. Ap.*, **190**, 175.
- Kaplan, S. A., and Tsytovich, V. N. 1968, *Soviet Astr.—AJ*, **11**, 956.
- Kuznetsov, E. A. 1974, *Zh. Exp. Teoret. Fiz.* **66**, 2037 (English transl. in *Soviet Phys.—JETP*, **39**, 1003).
- Landau, L. D., and Lifshitz, E. M. 1960, in *Course of Theoretical Physics* (Massachusetts: Addison-Wesley), Vol. 1, pp. 93-95, "Mechanics."
- Litvak, A. G., Fraiman, G. M., and Yunakovskii, A. D. 1974, *Zh. Exp. Teoret. Fiz. Pis'ma*, **19**, 23 (English transl. in *JETP Letters*, **19**, 13).
- Magelsen, G. 1976, Ph.D. thesis, University of Colorado.
- Magelsen, G., and Smith, D. F. 1977, submitted to *Solar Phys.*
- Nicholson, D. R., and Goldman, M. V. 1976, *Phys. Fluids*, **19**, 1621.
- 1978, submitted to *Phys. Fluids*.
- Nishikawa, K. 1968, *J. Phys. Soc. Japan*, **24**, 916, 1152.
- Nishikawa, K., Lee, Y. C., and Liu, C. S. 1975, *Comm. Plasma Phys.*, **2**, 63.
- Papadopoulos, K. 1975, *Phys. Fluids*, **18**, 1769.
- Papadopoulos, K., Goldstein, M. L., and Smith, R. A. 1974, *Ap. J.*, **190**, 175.
- Pereira, N. R., Sudan, R. N., and Denavit, J. 1977, *Phys. Fluids*, **20**, 936.
- Polyudov, A. N., and Sigov, Yu. S. 1976, Soviet Inst. of Applied Math. preprint No. 123.
- Schamel, H., and Elsäßer, K. 1976, *J. Comp. Phys.*, **22**, 501.
- Schmidt, G. 1966, *Physics of High Temperature Plasmas* (New York: Academic), pp. 47-50.
- Silin, V. P. 1965, *Zh. Exp. Teoret. Fiz.*, **48**, 1679 (English transl. in *Soviet Phys.—JETP*, **21**, 1127).
- Smith, D. F. 1977, *Ap. J. (Letters)*, **216**, L53.
- Smith, D. F., and Fung, P. C. W. 1971, *J. Plasma Phys.*, **5**, 1.
- Smith, R. A., Goldstein, M. L., and Papadopoulos, K. 1976, *Solar Phys.*, **46**, 515.
- Sturrock, P. A. 1964, in *AAS-NASA Symposium on the Physics of Solar Flares*, ed. W. N. Hess (NASA SP-50), p. 357.
- Takakura, T., and Shibahashi, H. 1976, *Solar Phys.*, **46**, 323.
- Thomson, J. J., and Karush, J. I. 1974, *Phys. Fluids*, **17**, 1608.
- Zaitsev, V. V., Kunilov, M. V., Mityakov, N. A., and Rapoport, V. O. 1974, *Soviet Astr.*, **18**, 147.
- Zaitsev, V. V., Mityakov, N. A., and Rapoport, V. O. 1972, *Solar Phys.*, **24**, 444.
- Zakharov, V. E. 1972, *Zh. Exp. Teoret. Fiz.*, **62**, 1745 (English transl. in *Soviet Phys.—JETP*, **35**, 908).
- 1975, *Zh. Exp. Teoret. Fiz. Pis'ma*, **21**, 479 (English transl. in *JETP Letters*, **21**, 221).
- Zakharov, V. E., Mastryukov, A. F., and Synakh, V. S. 1974, *Zh. Exp. Teoret. Fiz. Pis'ma*, **20**, 7 (English transl. in *JETP Letters*, **20**, 3).
- 1975, *Fiz. Plazmy*, **1**, 614 (English transl. in *Soviet J. Plasma Phys.*, **1**, 339).
- Zheleznyakov, V. V., and Zaitsev, V. V. 1970, *Soviet Astr.—AJ*, **14**, 47.

MARTIN V. GOLDMAN, DWIGHT R. NICHOLSON, and JAMES C. WEATHERALL: Department of Astro-Geophysics, University of Colorado, Boulder, CO 80309

PETER HOYNG: Space Research Laboratory of the Astronomical Institute, Utrecht, The Netherlands

Virial Theory of Direct Langmuir Collapse

Martin V. Goldman and Dwight R. Nicholson

Department of Astro-Geophysics, University of Colorado, Boulder, Colorado 80309

(Received 18 April 1978)

A general virial theorem is proved without any assumption of special symmetries and used to calculate the threshold and time for direct collapse of a two-dimensional Langmuir wave packet. The analysis is shown to apply to "bump-on-tail" instabilities, when the "bump" is broad, low, and at high velocity. The example of the type-III solar radio-burst problem is treated both numerically and analytically.

A large-amplitude wave packet of Langmuir waves in a homogeneous nonmagnetic plasma is capable of a wide variety of distinct nonlinear evolutions, depending on its mean energy, wave

vector, and spread in wave numbers.

Often, the wave packet drives secondary Langmuir wave instabilities such as induced scattering off ions and modulational instabilities.¹⁻³

These secondary instabilities are driven by the ponderomotive force $-\nabla(\bar{\delta}_0 \cdot \bar{\delta}_1 + \bar{\delta}_0 \cdot \bar{\delta}_1^*)$, where $\bar{\delta}_0$ is the envelope field of the primary packet, and $\bar{\delta}_1$ that of the small (noise) perturbation. The perturbation $\bar{\delta}_1$ grows as $e^{\gamma_1 t}$, where^{3,4} $\gamma_1/\omega_p \propto W = \langle \bar{\delta}_0^2 \rangle / 4\pi n\theta$. After many e foldings, a new field configuration $\bar{\delta}$ results, and in regions of space where the ponderomotive force $-\nabla|\bar{\delta}|^2$ is large, a process of Langmuir collapse may occur in which the localization region shrinks to dimensions of several Debye lengths. We shall refer to this scenario as indirect collapse. Indirect collapse is always preceded by the exponentiation of background noise. There are numerous examples in the plasma physics literature of indirect collapse after modulational instability⁵⁻⁷ and after backscattering from ions.^{8,9}

A distinct competing process is direct collapse.⁷ This cannot be described as a linear instability. The time, τ_c , for direct collapse is often much faster than γ_1^{-1} , and is proportional to \sqrt{W} , rather than W [see Eq. (10b)]. Direct collapse is driven by the ponderomotive force, $-\nabla|\bar{\delta}_0|^2$, associated with the primary wave packet, rather than with the noise-interference terms.

Direct collapse is often confused with the linear modulational instability, first predicted by Vedenov and Rudakov.¹ One reason for this confusion seems to be that both thresholds are proportional to the square of the Fourier-space spectral width, Δk , of the primary field $\bar{\delta}_0$. However, the processes are generally distinguishable by their different time scales. Direct collapse is usually faster, except when W is orders of magnitude above threshold. The situation is familiar from nonlinear optics. Here, self-focusing, or "nonlinear lensing," of a coherent laser beam is an example of direct collapse.¹⁰ A competing modulational instability may cause the beam to break up into filaments,^{10,11} which then proceed to self-focus separately (indirect collapse). When W is only a few times threshold this "filamentation" instability does not operate, and only self-focusing of the primary beam occurs.¹⁰ In this Letter we are concerned with the Langmuir wave analog of this direct process.

After proving a general virial theorem which makes no assumption of special symmetry (as in the spherically-symmetric virial theorem of Zakharov⁷), but does assume a certain ordering of wave-packet parameters, we calculate analytically the threshold and time for direct collapse. We show that direct collapse can occur for bump-on-tail instabilities, when the bump is fairly

broad, low, and at high velocity. An important example is furnished in connection with type-III solar radio bursts.¹²

Consider the cubic nonlinear Schrödinger equation for the envelope, $\bar{\delta}$, of a Langmuir wave $\bar{E} = \text{Re}[\bar{\delta} \exp(-i\omega_p t)]$:

$$i\partial_t \bar{\delta} + \frac{1}{2} \nabla \cdot \bar{\delta} + |\bar{\delta}|^2 \bar{\delta} = 0. \quad (1)$$

This equation assumes adiabatic ions⁷ and ignores a $c^2 \nabla \times \nabla \times \bar{\delta}$ term¹³ associated with coupling to nonelectrostatic field polarizations [see Eqs. (11) and (12)]. Time is measured in units of inverse plasma frequency, ω_p^{-1} , and length in units of $\sqrt{3}$ times the Debye length, $\sqrt{3}k_D^{-1}$, and $|\bar{\delta}|^2$ has the units of $32\pi n(\theta_e + \theta_i)$, where θ_e and θ_i are the electron and ion temperatures.

From the gauge and translational invariance of the Lagrangian density^{14,15} associated with Eq. (1), a number of continuity equations and associated conservation laws follow. For our purposes, the important ones are

$$\partial_t |\bar{\delta}|^2 + \nabla \cdot \bar{s} = 0, \quad (2a)$$

$$\partial_t \bar{p} + \nabla \cdot \bar{T} = 0. \quad (2b)$$

Here, \bar{s} is the current density, and \bar{p} is the momentum density of the field. For Eq. (1), they are both equal:

$$\bar{s} = \bar{p} = \frac{1}{2i} [\bar{\delta}^* \nabla \bar{\delta} - \bar{\delta} \nabla \bar{\delta}^*]. \quad (3)$$

The stress tensor \bar{T} is given by¹⁶

$$T_{ij} = \text{Re}[(\nabla \cdot \bar{\delta}) \nabla_j \bar{\delta}_i + \bar{\delta}_i \nabla_j \bar{\delta}^* - \frac{1}{2} \delta_{ij} (|\bar{\delta}|^4 + \nabla \cdot (\text{Re} \bar{\delta}^* \nabla \bar{\delta}))]. \quad (4)$$

For localized fields, Eqs. (2a) and (2b) may be integrated to give the two conserved quantities $N = \int d^3r |\bar{\delta}|^2$ and $\bar{S} = \int d^3r \bar{s}$. In addition, the field energy, \mathcal{H} , is conserved:

$$\mathcal{H} = \frac{1}{2} \int d^3r (|\nabla \cdot \bar{\delta}|^2 + |\bar{\delta}|^4). \quad (5)$$

In order to discuss particlelike behavior of a wave packet, it is useful to introduce the spatial average of any function $f(\mathbf{r})$, using $|\bar{\delta}|^2/N$ as a probability weighting factor: $\langle f \rangle = \int d^3r f(\bar{\mathbf{r}}) |\bar{\delta}|^2/N$. Thus, we define for a wave packet its centroid coordinate $\langle \bar{\mathbf{r}} \rangle$, its rms spatial width $\langle \delta r^2 \rangle^{1/2}$ [where $\delta r^2 = |\bar{\mathbf{r}} - \langle \bar{\mathbf{r}} \rangle|^2$], and its mean intensity $\langle |\bar{\delta}|^2 \rangle$. From (2a) we then obtain the Ehrenfest theorem, $\partial_t \langle \bar{\mathbf{r}} \rangle = \bar{S}/N = \text{const}$. From Eqs. (2a) and (2b) and the fact that $\bar{s} = \bar{p}$, it is trivial to prove the following virial theorem:

$$\partial_t^2 \langle \delta r^2 \rangle = +2 \left[\frac{1}{N} \int d^3r \text{Tr} \bar{T} - \left(\frac{\bar{S}}{N} \right)^2 \right]. \quad (6)$$

Using Eqs. (4) and (5) and integrating twice in time, this yields

$$\langle \delta r^2 \rangle = At^2 + Bt + C + (2-D) \int_0^t dt' \int_0^{t'} dt'' \langle |\delta|^2 \rangle. \quad (7)$$

Here, D is the number of spatial dimensions, B and C are integration constants, and A is the following invariant:

$$A = 2C/N - \bar{S}^2/N^2. \quad (8)$$

Since $\langle \delta r^2 \rangle$ and $\langle |\delta|^2 \rangle$ are positive definite, it follows that collapse of $\langle \delta r^2 \rangle$ to zero occurs in a finite time whenever $A < 0$ and $D \geq 2$. The field $\vec{\delta}$ must then become singular,¹⁷ since N is conserved. Physically, however, the collapse will stop when $\langle \delta r^2 \rangle^{1/2}$ is a few Debye lengths, because of Landau damping,¹⁸ which has been omitted from Eq. (1).

Let us now apply the virial theorem to study the stability of an initial wave packet in two dimensions. We assume that initially

$$\vec{\delta}(\vec{r}, t=0) = -\varphi_0 \nabla \exp[\vec{k}_0 \cdot \vec{r} - \frac{1}{2} r^2 (\Delta k)^2], \quad (9)$$

where φ_0 is a constant amplitude, related to the mean intensity by $\langle |\delta|^2 \rangle_0 = \frac{1}{2} k_0^2 \varphi_0^2$. Assuming $\Delta k \ll k_0$, for this wave packet we find $B=0$, $C = \langle \delta r^2 \rangle_0 = (\Delta k)^{-2}$, and $A = 4[(\Delta k)^2 - \langle |\delta|^2 \rangle_0]$. The threshold and time for direct collapse are therefore given (in physical units) by

$$\frac{(\langle |\delta|^2 \rangle_{th})}{2\pi n(\nu_e + \nu_i)} = \frac{48(\Delta k)^2}{k_D^2}, \quad (10a)$$

$$\frac{1}{\omega_p t_c} = \frac{1}{2} \frac{\Delta k}{k_D} \left[\frac{(\langle |\delta|^2 \rangle_0 - \langle |\delta|^2 \rangle_{th})}{2\pi n(\nu_e + \nu_i)} \right]^{1/2}. \quad (10b)$$

Note that the threshold and collapse time are independent of k_0^2 . An approximate calculation in three dimensions shows that these values are not greatly changed.¹⁶

In order to justify the adiabatic ion approximation which underlies Eq. (1), we must verify that the inertial term in the ion hydrodynamic equation is much smaller than the pressure term. Since the ion density in this approximation is proportional to $|\delta|^2$, and the inertial term to $\partial_t^2 |\delta|^2 = \nabla \nabla \cdot \vec{T}$, the comparison is easily made for the assumed initial wave packet. We find¹⁶

$$\frac{9}{2} \frac{k_0^2}{k_D^2} \frac{(\langle |\delta|^2 \rangle_0)}{32\pi n(\nu_e + \nu_i)} \ll \frac{m}{M}, \quad (11)$$

which is the adiabatic ion approximation.

In order to justify the electrostatic approximation, it is necessary¹⁹ to have $m/c^2 |\nabla \times \nabla \times \vec{\delta}| \ll 30 |\nabla \nabla \cdot \vec{\delta}|$. This is automatically satisfied

at time $t=0$, since we begin with the pure electrostatic field given by Eq. (9). However, even with a pure electrostatic field, $|\vec{\delta}|^2 \vec{\delta}$ will have a transverse component, which acts as a source for $\nabla \times \nabla \times \vec{\delta}$. An approximate condition for the validity of the electrostatic approximation is

$$\Delta k \ll k_0, \quad (12)$$

which is the electrostatic approximation. In the late stages of collapse, both the adiabatic and electrostatic approximations usually break down.

One condition for the adiabatic ion approximation (11) is that $k_0/k_D < (m/M)^{1/2}$. For a beam instability, k_0 is roughly determined to be v_e/v_i , the ratio of electron thermal to beam speed. Hence, the adiabatic ion condition can only be satisfied for very high-velocity beams, moving through relatively cold plasmas. A good example is provided by the electron beams in the solar corona, which are associated with type-III solar radio bursts.^{12,19} Here v_e can be as large as $c/2$, and k_0/k_D can be on the order of 10^{-2} . The half-width, Δk , is controlled by the beam width, Δv_e ($=v_e/3$), and can be of order $k_0 \Delta v_e / 6v_e$. Using this, the threshold value of $W = \langle |\delta|^2 \rangle / 4\pi n\theta$ for direct collapse is found from Eq. (10a) to be 10^{-5} assuming $\Delta k = k_0/18$. Values of W this high have been measured at about 0.5 a.u. by spacecraft²⁰ during type-III bursts. All of the inequalities of (11) and (12) can be satisfied initially for these parameters, and one could expect all but the final stages of the time history of direct collapse to be properly described by our virial theory, provided one can ignore the continuous input of energy into the beam modes by the beam, and provided secondary instabilities driven by the beam mode are slower than collapse. We have studied such effects²¹ by numerical solutions¹² of a more general set of equations than (1).

In the numerical work,¹² dynamic ions are introduced through the use of a hydrodynamic equation for the ion density. Heavy linear damping of the ion-acoustic (quasi-) modes is included. In addition, in the equation for the envelope field, $\vec{\delta}$, constant (quasilinear theory) growth rate for the beam modes is retained. In this work the real and envelope fields are related by $E = 2 \text{Re}[\vec{\delta} \times \exp(-i\omega t)]$, leading to a definition of W which is one-quarter that of the present Letter.

These equations were solved numerically, starting with initial white noise. The beam modes were observed to grow slowly, until they rose about a factor of 3 above the threshold for direct collapse, to a value $W = |\delta|^2 / 4\pi n\theta = 4 \times 10^{-4}$. At

this point a very rapid direct collapse sets in. The beam modes have no time to grow during this collapse, and, in fact, these waves are quickly depleted, as energy flows to regions of k space out of phase with the beam. Effectively, the plasma decouples from the beam; further growth of the beam modes becomes irrelevant, and the system evolves like an initial-value problem. In fact, a numerical solution with no beam, but with an initial random wave packet having $W = 4 \times 10^{-4}$ and $\Delta k = k_0/6$, gives the identical subsequent evolution, which is illustrated in Fig. 1. The time for collapse obtained numerically is about $9 \times 10^4 \omega_p^{-1}$, compared with the prediction of Eq. (10b), which is $7 \times 10^4 \omega_p^{-1}$.

The quasilinear growth rate of the beam modes, $\gamma_B = (n_b/3n_e)(v_b/\Delta v_b)^2 \omega_p$, can be ignored during collapse if $\gamma_B t_c \ll 1$. Quasilinear beam-plateau formation cannot occur if the resonant modes never acquire an energy density comparable to that of the beam, or, equivalently, if $W \ll 4(n_b/n_e)(v_b/v_e)^2$. The energy density, W , in these two inequalities is effectively set by the collapse threshold to be several times $48(\Delta k)^2$, where Δk is determined by the beam width, Δv_b . We thus arrive at the following necessary ordering of beam parameters for the virial theory of direct collapse: $9(\Delta v_b/v_e)^2(v_e/v_b)^4 \ll n_b/n_e \ll \frac{3}{2}(\Delta v_b/v_e)^4 \times (v_e/v_b)^2$. For the type-III burst problem, $n_b/n_e \approx 10^{-6}$, and these inequalities are well satisfied.

It is also necessary that the collapse time, t_c , be short compared to the time for several e foldings of the secondary-wave instabilities driven by the beam modes, if the collapse is to be direct, rather than indirect. Typical of the competing secondary instabilities are induced (forward) scattering off ions and the forward-cone modulational instability.^{3,12} The main parameter which determines whether collapse is faster than secondary instability is Δk , the width of the beam-mode wave packet. The collapse time t_c decreases with Δk , while the secondary instabilities take longer to develop as Δk increases. This is because the growth rate is reduced by so-called broadband pump effects.^{9,22} Let γ_e' be the (reduced) growth rate for one of these instabilities. The two conditions for direct collapse are therefore that the threshold (10a) be exceeded, and that $\gamma_e' t_c / \ln A \ll 1$, where A is the noise amplification factor. Both are well satisfied for the parameters of the type-III burst problem.

We wish to acknowledge important conversations with G. Reiter, W. Manheimer, D. F. DuBois, R. Perkins, C. Bardos, U. Firsch,

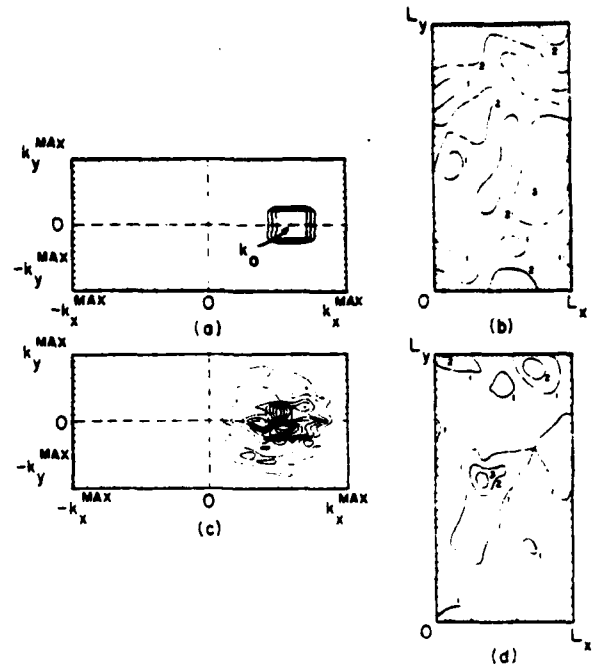


FIG. 1. Evolution of a set of waves, as found numerically by solving a set of equations with ion hydrodynamics included, but reducing to (1) in the present parameter regime (see Ref. 9). The initial spatially averaged electric field energy density is $W = \langle |\delta|^2 \rangle / 4\pi n_0 = 4 \times 10^{-4}$. The central wave number is $k_0 \lambda_e = 0.011$, while the full width in either wave-number direction of the initial spectrum is $k_0/3$. Numerically, the initial wave-number distribution consists of nine modes, each with a random phase. (a) Initial electric field amplitude in wave-number space. (b) Initial electric field amplitude in real space. Contours indicate relative absolute value of electric field, with contour 1 indicating $W = 1.2 \times 10^{-4}$ and contour 3 indicating $W = 10^{-3}$. (c) Electric field amplitude in wave-number space at time $9 \times 10^4 \omega_p^{-1}$. (d) Electric field amplitude in real space at time $9 \times 10^4 \omega_p^{-1}$. Contours indicate relative absolute value of electric field, with contour 1 indicating $W = 4.8 \times 10^{-4}$ and contour 3 indicating $W = 4 \times 10^{-3}$.

F. Tappert, and A. Wong. One of us (M.V.G.) wishes to thank the Guggenheim Foundation for a fellowship during most of this research, and Culham Laboratories, Imperial College, and the University of California at Los Angeles for their kind hospitality. We also wish to thank the Aspen Center for Physics for portions of this research performed there. This work was supported in part by the Atmospheric Research Section, National Science Foundation, Grant No. ATM 76-14275. The work of one of us (M.V.G.) was also supported by the U. S. Air Force Office

of Science Research, Grant No. F49620-76-C-0005. We thank the National Center for Atmospheric Research, supported by the National Science Foundation, for computer time used in this study.

¹A. A. Vedenov and L. I. Rudakov, Dokl. Akad. Nauk SSSR 159, 767 (1964) [Sov. Phys. Dokl. 9, 1073 (1965)].

²K. Nishikawa, J. Phys. Soc. Jpn. 24, 916, 1152 (1968).

³S. Bardwell and M. V. Goldman, Astrophys. J. 204, 912 (1976).

⁴This growth rate assumes adiabatic ions.

⁵G. J. Morales, Y. C. Lee, and R. B. White, Phys. Rev. Lett. 32, 457 (1974).

⁶R. N. Sudan, in *Proceedings of the Sixth European Conference on Controlled Fusion and Plasma Physics, Moscow* (Joint Institute for Nuclear Research, Moscow, U. S. S. R., 1973), Vol. 2, p. 185.

⁷V. E. Zakharov, Zh. Eksp. Teor. Fiz. 62, 1745 (1972) [Sov. Phys. JETP 35, 908 (1972)].

⁸A. Y. Wong and B. H. Quon, Phys. Rev. Lett. 34, 1499 (1975).

⁹D. R. Nicholson and M. V. Goldman, Phys. Fluids (to be published).

¹⁰B. R. Suydam, IEEE J. Quantum Electron. 11, 225 (1975).

¹¹A. J. Campillo, S. L. Shapiro, and B. R. Suydam, Appl. Phys. Lett. 23, 628 (1973).

¹²D. R. Nicholson, M. V. Goldman, P. Hoyng, and J. Weatherall, Astrophys. J. (to be published).

¹³E. A. Kuznetsov, Zh. Eksp. Teor. Fiz. 66, 2037 (1974) [Sov. Phys. JETP 39, 1003 (1974)].

¹⁴J. Gibbons, S. G. Thornhill, M. J. Wardrop, and D. ter Haar, J. Plasma Phys. 17, 153 (1977).

¹⁵I. M. Gelfand and S. V. Fomin, *Calculus of Variations* (Prentice-Hall, New Jersey, 1963).

¹⁶M. V. Goldman, to be published.

¹⁷R. T. Glassey, J. Math. Phys. (N.Y.) 18, 1794 (1977); S. N. Vlasov, V. A. Reprishchev, and V. I. Talanov, Sov. Radiophys. 14, 1063 (1971). These papers were brought to our attention after the completion of this work.

¹⁸N. R. Pereira, R. N. Sudan, and J. Denavit, Phys. Fluids 20, 936 (1977).

¹⁹K. Papadopoulos, M. Goldstein, and R. Smith, Astrophys. J. 190, 175 (1974).

²⁰D. A. Gurnett and R. R. Anderson, J. Geophys. Res. 82, 632 (1977).

²¹We have also studied the effects of the solar-coronal magnetic field for the case of type-III solar radio bursts.

²²J. J. Thomson and J. I. Karush, Phys. Fluids 17, 1608 (1974).

Cascade and collapse of Langmuir waves in two dimensions

Dwight R. Nicholson and Martin V. Goldman

Department of Astro-Geophysics, University of Colorado, Boulder, Colorado 80309
(Received 28 November 1977)

The temporal evolution of intense Langmuir waves in an unmagnetized plasma of two spatial dimensions is studied numerically. When the inequality $W > (k\lambda_e)^2$ is satisfied, the evolution quickly leads to a state of collapsing solitons. Here, W is the ratio of electric field energy density to the particle kinetic energy density, k is a typical Langmuir wavenumber, and λ_e is the electron Debye length.

I. INTRODUCTION

Intense Langmuir waves are frequently encountered in plasma physics, notably in cases where an external energy source such as an electron beam, laser, or coherent radio wave impinges on a plasma. In 1972, Zakharov¹ introduced a model set of fluid equations, the coupled nonlinear Schrödinger equation, to describe these intense waves. This equation includes the physics of linear Langmuir waves and ion acoustic waves, as well as the effect of the ponderomotive force, which acts most strongly on electrons, conveying its effects to ions via the requirement of quasi-neutrality. Under suitable conditions, the equation includes the phenomena of linear parametric instabilities such as the parametric decay instability, oscillating two-stream instability, stimulated modulational instability, and a fluid analogue to the weak turbulence process of induced scattering by ions. Further, the equation describes the completely nonlinear phenomenon of soliton collapse, which in two and three dimensions can proceed catastrophically when damping is ignored, mathematically resulting in a singularity and physically proceeding to an intensity so large that the validity of the equation ceases.

The two- and three-dimensional soliton collapse has been extensively studied, analytically and numerically, in situations where it is isolated from other physical processes.²⁻¹³ There has been less work involving the evolution of an initially more or less uniform system toward a state of collapsing solitons. Pereira *et al.*,¹⁴ have numerically studied the case where an external uniform (dipole) driver acts on an initially uniform plasma; parametric instabilities, initiated by noise, grow until they saturate via a Landau damped soliton collapse. In a many-particle computer simulation, Polyudov and Sigov¹⁵ studied similar phenomena; their simulation can be presumed to have much the same physical content as Zakharov's model equations. Nicholson *et al.*¹⁶ numerically study the temporal evolution of an initially intense Langmuir wave, there being no external source of energy. Working in the regime $k\lambda_e < (m_e/m_i)^{1/2}$ [where k is the Langmuir wavenumber, λ_e is the electron Debye length, and $m_e(m_i)$ is the electron (ion) mass], they find an evolution toward soliton collapse under various circumstances, and they apply their results to a particular case of electron beam plasma interaction, the type III solar radio burst.

In the present paper, we numerically study the evolu-

tion of initially intense Langmuir waves, in time and in two spatial dimensions, in the regime $k\lambda_e > (m_e/m_i)^{1/2}$; this regime is complementary to that of Nicholson *et al.*¹⁶ We find that collapse occurs very quickly when the inequality $W > (k\lambda_e)^2$ is satisfied, where W is the ratio of initial electric field energy density to background particle kinetic energy density. In applying this inequality, we find that it is not necessary to distinguish between the central wavenumber k_0 and the spread of wavenumbers Δk about the central wavenumber. The reason for this is that in most cases, the initial wave evolution is a parametric decay instability leading to wave growth at Langmuir wavenumbers near $-k_0$. Thus, the effective spread in wavenumbers quickly becomes of the same order as the initial wavenumber. This behavior, in the regime $k\lambda_e > (m_e/m_i)^{1/2}$, is in direct contrast to the behavior in the complementary regime $k\lambda_e < (m_e/m_i)^{1/2}$ considered in our earlier numerical work¹⁶ and in our analytic work.¹⁷ There, the inequality $W > (\Delta k\lambda_e)^2$ must always be applied to the spread of wavenumbers about the central wavenumber. We shall discuss the reasons for this difference in Sec. IV.

We note that the criterion $W > (k\lambda_e)^2$ is also the criterion used in earlier work^{1,16,19} as a necessary condition for the modulational instability of a set of Langmuir waves having a spread of wavenumbers k about the origin of wavenumber space [see Ref. 1, Eq. (2.11), valid in the present regime $k\lambda_e > (m_e/m_i)^{1/2}$]. Up until now, the connection between this linear modulational instability and soliton collapse has been speculative. In this paper, we demonstrate that soliton collapse indeed occurs when this inequality $W > (k\lambda_e)^2$ is satisfied. The numerical results indicate that it may be somewhat naive to think in terms of linearized modulational instabilities; rather, we find direct collapse of localized packets of waves moving at speeds less than the sound speed. This point will be discussed further in Sec. IV. When the inequality is not satisfied, we recover the multiple scattering toward smaller wavenumbers predicted by weak turbulence theory.²⁰

In Sec. II we discuss our numerical studies which lead to the conclusions of the preceding paragraph; these studies are performed with a model low frequency damping characteristic of an equal temperature plasma. The section concludes with a discussion of the possible modification of these results when the electron temperature T_e is much greater than the ion temperature T_i .

Section III discusses the effect on the results of Sec. II of a finite wavenumber spread for the initial Langmuir wave. Conclusions are given in Sec. IV.

II. NUMERICAL STUDIES WITH MONOCHROMATIC INITIAL CONDITION

The derivation of Zakharov's model equations proceeds from the plasma fluid equations, with five assumptions: high and low frequency time scales are well separated, low frequency motions are quasi-neutral, high frequency wave energy is much less than particle kinetic energy, low frequency ion speeds are much less than high frequency electron speeds multiplied by $(m_e/m_i)^{1/2}$, and all wave motions are curl free. We then have

$$\left(i\partial_t + \frac{3T_e}{2\omega_e m_e} \nabla^2\right) \tilde{\psi} \cdot \tilde{\mathbf{E}}(\tilde{\mathbf{x}}, \tilde{t}) = \frac{2\pi e^2}{m_e \omega_e} \nabla \cdot (\tilde{n} \tilde{\mathbf{E}}),$$

$$\tilde{\nabla} \times \tilde{\mathbf{E}} = 0 \quad (1)$$

$$(\partial_t^2 + \tilde{\nu}_i \partial_t - c_s^2 \nabla^2) \tilde{n}(\tilde{\mathbf{x}}, \tilde{t}) = \frac{1}{4\pi m_i} \nabla^2 |\tilde{\mathbf{E}}|^2, \quad (2)$$

where $\tilde{\mathbf{E}}(\tilde{\mathbf{x}}, \tilde{t})$ is the low frequency envelope of the total high frequency electric field $\tilde{\mathbf{E}}(\tilde{\mathbf{x}}, \tilde{t}) \exp(-i\omega_e \tilde{t})$ plus complex conjugate; $\tilde{n}(\tilde{\mathbf{x}}, \tilde{t})$ is the variation of the ion density from its average value n_0 ; ω_e is the background electron plasma frequency, $\omega_e = (4\pi n_0 e^2 / m_e)^{1/2}$; e is the magnitude of the electronic charge; $\tilde{\nu}_i$ is the low frequency phenomenological damping rate; the sound speed $c_s = [(\gamma_i T_i + \gamma_e T_e) / m_i]^{1/2}$, where γ_i (γ_e) is the electron (ion) specific heat ratio characteristic of low frequency oscillations; T_e (T_i) is the electron (ion) temperature; and $\tilde{\mathbf{x}} = (\tilde{x}, \tilde{y})$ and \tilde{t} represent dimensional space and time, while ∇ is the dimensional gradient operator. A tilde always indicates a dimensional variable. We introduce the dimensionless variables

$$t = \left(\frac{2\eta}{3}\right) \left(\frac{m_e}{m_i}\right) (\omega_e \tilde{t}), \quad (x, y) = \frac{2}{3} \left(\frac{\eta m_e}{m_i}\right)^{1/2} \frac{(\tilde{x}, \tilde{y})}{\lambda_e},$$

$$n = \left(\frac{3m_i}{4\pi m_e}\right) \left(\frac{\tilde{n}}{n_0}\right), \quad \mathbf{E} = \frac{1}{\eta} \left(\frac{m_i}{m_e}\right)^{1/2} \left(\frac{3}{16\pi n_0 T_e}\right)^{1/2} \tilde{\mathbf{E}},$$

$$\nu_i = (3/2\eta) (m_i/m_e) (\tilde{\nu}_i/\omega_e), \quad (3)$$

where the electron Debye length is $\lambda_e = (T_e/m_e \omega_e^2)^{1/2}$ and the dimensionless ratio $\eta = (\gamma_e T_e + \gamma_i T_i)/T_e$. Equations (1) and (2) become

$$(i\partial_t + \nabla^2) \nabla \cdot \mathbf{E}(\mathbf{x}, t) = \nabla \cdot (n \mathbf{E}), \quad \nabla \times \mathbf{E} = 0, \quad (4)$$

$$(\partial_t^2 + \nu_i \partial_t - \nabla^2) n(\mathbf{x}, t) = \nabla^2 |\mathbf{E}|^2. \quad (5)$$

We also allow the electric field to have a component $\mathbf{E}_{\perp 0}$ of infinite wavelength,^{14,16} satisfying $i\partial_t \mathbf{E}_{\perp 0} = (n \mathbf{E})_{\perp 0}$; this component is required by the magnetic field-free Ampere's law. Physical processes contained in these equations include three wave interactions such as the parametric decay instability, four-wave interactions such as the oscillating two-stream instability, and completely nonlinear processes such as soliton collapse.

In this paper we are interested in the solution of (4) and (5) when the initial condition is one large Langmuir wave; we study both the monochromatic and the broad-

band cases. Equations (4) and (5) are solved numerically; as described earlier,¹⁶ the technique is almost identical to that used by Pereira *et al.*¹⁴ All operations are performed in wavenumber space, with physical space being used only to evaluate the nonlinear terms in (4) and (5). We use either a 32 by 32 point grid, or a 64 by 64 point grid, in both real space and wavenumber space.

As representative parameters, we choose $\tilde{k}_0 \lambda_e = 0.1$, where \tilde{k}_0 is the wavenumber of the initially intense Langmuir wave, and $m_i/m_e = 1836$; we thus have $\tilde{k}_0 \lambda_e > (m_e/m_i)^{1/2}$, which is opposite to that used in earlier work.¹⁶ As a model of a plasma with equal electron and ion temperatures, we choose $\eta = 2$, and use a rather large low frequency damping rate equal to the acoustic frequency: $\tilde{\nu}_i(\tilde{\mathbf{k}}) = 2\tilde{k} c_s$, or $\nu_i(\mathbf{k}) = 2k$; the validity of this model expression has been discussed by Bardwell and Goldman.²¹ Now, the initially intense Langmuir wave is itself capable of acting as a pump for parametric instabilities which grow from noise; this noise is part of the numerical initial condition. We do not attempt to numerically include spontaneous emission. The dispersion relation from which one obtains the parametric growth rates is easily obtained from (4) and (5), and is given by¹⁶

$$-\omega^2 - 2ik\omega + k^2 = -k^2 |E_0|^2 \left(\frac{\mu_z^2}{\omega - k^2 - 2k_0 \cdot \mathbf{k}} - \frac{\mu_z^2}{\omega + k^2 - 2k_0 \cdot \mathbf{k}} \right), \quad (6)$$

where $\mu_z^2 = (\tilde{k}_0 \cdot \tilde{\mathbf{k}}_*)^2$, ω and \mathbf{k} are the frequency and wavenumber of the low frequency response, \tilde{k} is a unit vector in the \mathbf{k} direction, E_0 is the amplitude of the initial Langmuir wave, and $\kappa_* = \mathbf{k} \pm \mathbf{k}_0$.

As discussed earlier²¹ in detail, the dispersion relation (6) yields three main regions of instability: the decay branch, with Langmuir wavenumbers $k^L \sim -k_0$; the oscillating two-stream instability branch, with Langmuir wavenumbers $k^L \sim k_0$, but shifted up and down in the direction perpendicular to k_0 ; and the stimulated modulational instability branch, with wavenumbers and growth rates comparable²¹ to those for the oscillating two-stream instability.

We proceed to study three cases, with $W \equiv |\tilde{\mathbf{E}}_0|^2 / 4\pi n_0 T_e = 10^{-1}$, 10^{-2} , and 3×10^{-3} .

Case A: $W = 10^{-1}$. In this case we have $W \gg (\tilde{k}_0 \lambda_e)^2 = 10^{-2}$. The numerical results, obtained with a numerical grid having 32 by 32 points in real space and in wavenumber space, are displayed in Figs. 1-3. Figure 1 shows the location of the initial Langmuir wavenumber along with contours of constant growth rate at the relatively early time $\omega_e \tilde{t} = 1420$. The decay branch is seen to have the highest growth rates; the very highest numerical growth rate is $\tilde{\gamma}/\omega_e = 4.8 \times 10^{-3}$, in excellent agreement with the prediction of Eq. (6). This highest growth rate occurs at the Langmuir wavenumber $\tilde{k}^L \lambda_e = -0.08$. At a later time $\omega_e \tilde{t} = 3180$, Fig. 2 shows that a substantial fraction of the wave energy has appeared in the backscatter direction; the linear superposition of the modes of Fig. 2 results in the collection of intense regions and depleted regions of $|\mathbf{E}(\mathbf{x})|$ shown in Fig. 3 at the same time $\omega_e \tilde{t} = 3180$. The regions of

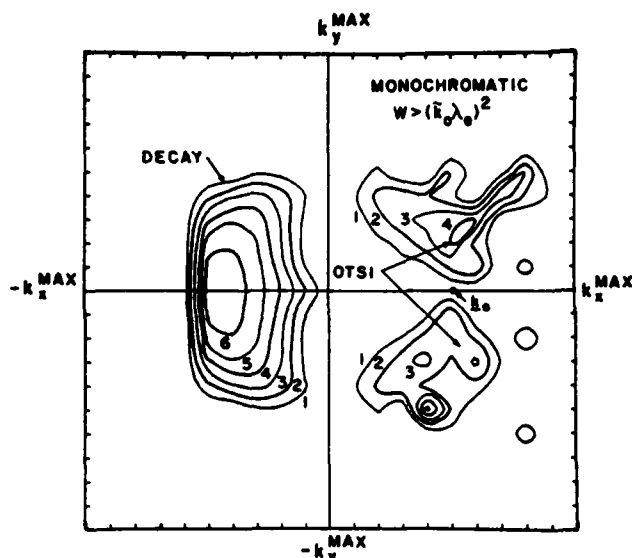


FIG. 1. Initial growth rates in wavenumber space for case A, Sec. II, at the relatively early time $\omega_e t = 1420$. Throughout this paper, the maximum wavenumber amplitude in either direction is $0.2 \lambda_e^{-1}$. The decay branch is indicated by "DECAY," and the oscillating two-stream branch by "OTSI." The contour labels indicate relative magnitudes, with contour 1 corresponding to a growth rate $\tilde{\gamma}/\omega_e = 7.3 \times 10^{-4}$.

constructive interference in Fig. 3 begin to collapse of their own accord, soon violating our initial assumption $W \ll 1$. The ultimate evolution of these very intense regions of trapped Langmuir energy with $W \sim 1$ is a topic of current investigation, and is by no means completely understood. The value of W in this example is so large that we should regard this calculation as simply illustrative; even at the initial time the conditions for the validity of the basic equations are only margin-

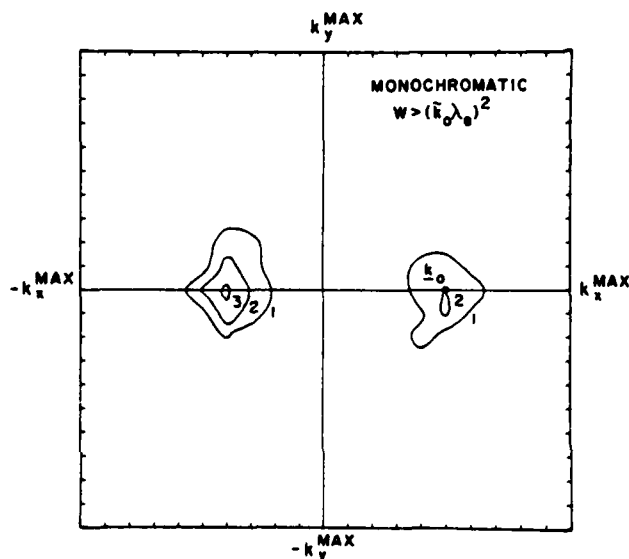


FIG. 2. Wave intensity in wavenumber space for case A, Sec. II, at time $\omega_e t = 3180$. The contour levels indicate relative magnitudes.

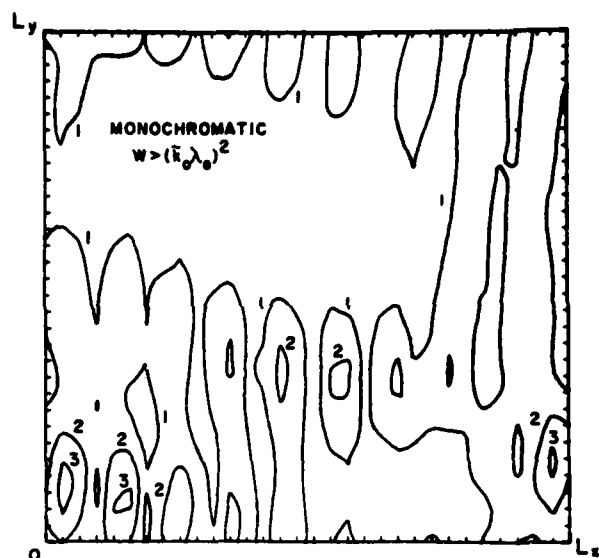


FIG. 3. Absolute value of electric field in real space for case A, Sec. II, at time $\omega_e t = 3180$. $\tilde{L}_x/\lambda_e = \tilde{L}_y/\lambda_e = 300$. The contour levels indicate relative magnitudes of electric field, with contour 1 corresponding to $W = 0.073$. Contour 3 thus corresponds to $W \approx 0.7$, such that our initial assumption $W \ll 1$ is beginning to break down.

ally satisfied. In any case, the further evolution of this example is certainly not described either by the ideas of weak turbulence theory²⁰ nor by Zakharov's model equations.

Case B: $W = 10^{-2}$. In this regime, the dispersion relation (6) predicts a maximum decay instability growth rate

$$\frac{\tilde{\gamma}}{\omega_e} = \left(\frac{3^{3/2}}{16\eta} \right) W \approx 1.6 \times 10^{-3} \quad (7)$$

at the Langmuir wavenumber \tilde{k}^L given by

$$\tilde{k}^L \lambda_e = -\tilde{k}_0 \lambda_e + \frac{2}{3} \left(\frac{\eta m_e}{3m_i} \right)^{1/2} \approx -0.09. \quad (8)$$

Equations (7) and (8) are valid in the intensity regime $W \ll 4\eta^2 (\tilde{k}_0 \lambda_e) (m_e/\eta m_i)^{1/2}$. The oscillating two-stream growth rate in this regime can be estimated from (6) to be

$$\frac{\tilde{\gamma}}{\omega_e} = \frac{1}{\eta} \left(\frac{8m_e W}{3m_i} \right)^{1/2} \approx 1.9 \times 10^{-3}, \quad (9)$$

which occurs at wavenumbers with $\tilde{k}_x = \tilde{k}_0$, and components perpendicular to \tilde{k}_0 given roughly by $\tilde{k}_y \lambda_e = \pm (W/3\eta)^{1/2} = \pm 0.041$. Thus, the latter has a faster growth rate in this case than the decay instability. The numerical results, obtained with a 64 by 64 point grid, are displayed in Figs. 4, 5, and 6. Numerically, we find that the decay instability immediately begins to grow with roughly its predicted growth rate (7), at very nearly the predicted wavenumber (8). However, the oscillating two-stream does not immediately obtain its predicted growth rate, but seems to experience a period of indecision before obtaining its predicted growth rate. We attribute this behavior to the fact that this

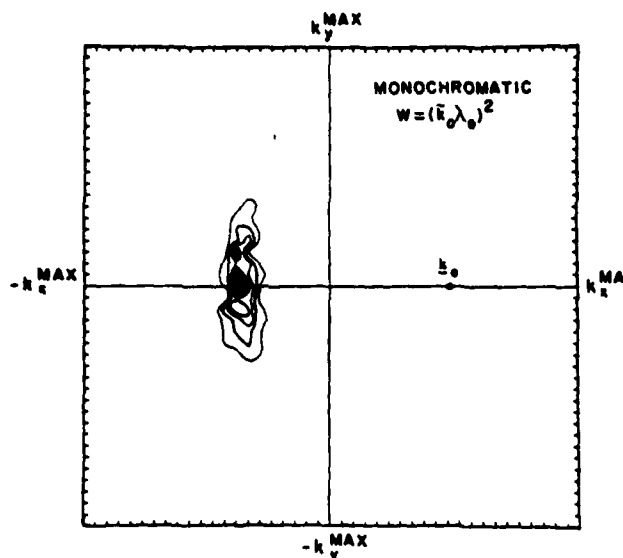


FIG. 4. Electric field intensity in wavenumber space for case B, Sec. II, at time $\omega_p t = 1.5 \times 10^4$.

instability is a four-wave process, requiring a definite phase relation between the initial monochromatic wave, the low frequency response, and two separate Langmuir waves. A certain period of time is required to set up this delicate phase relationship. The result of this period of indecision is that the decay branch obtains a head start, and actually obtains substantial amplitudes slightly earlier. Of course, this result does depend on the initial noise levels, which to be physically realistic we have chosen reasonably large. Further, the oscillating two-stream branch occurs at wavenumbers so close to the initial wavenumber that the product waves are themselves drivers of the decay branch. When the initial wave begins to deplete due to the growth

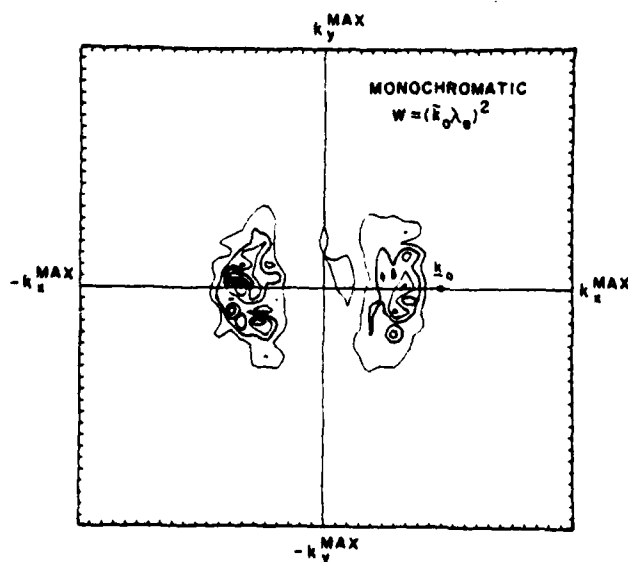


FIG. 5. Electric field intensity in wavenumber space, for case B, Sec. II, at time $\omega_p t = 1.8 \times 10^4$.

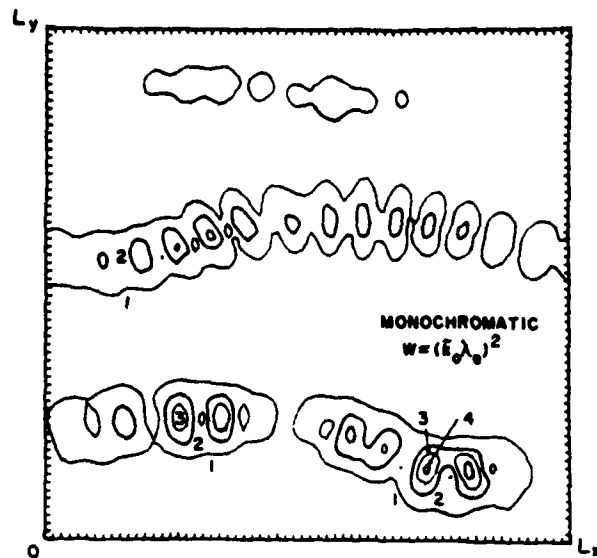


FIG. 6. Absolute value of electric field in real space, for case B, Sec. II, at time $\omega_p t = 1.8 \times 10^4$. $L_x/\lambda_0 = L_y/\lambda_0 \approx 600$. The contour levels indicate relative values of electric field magnitude, with contour 1 corresponding to $W = 0.012$, and contour 4 corresponding to $W = 0.19$.

of both branches, the oscillating two-stream growth stops and the product waves themselves deplete, giving up their energy to the decay waves. We therefore find at time $\omega_p t = 1.5 \times 10^4$ that all the initial energy has gone to the decay branch, as shown in Fig. 4. The decay branch, as in the previous section, now acts as a pump for its own decay branch in the forward directions (along k_0), resulting at time $\omega_p t = 1.8 \times 10^4$ in the wavenumber space picture shown in Fig. 5. The corresponding picture in real space, Fig. 6, indicates several regions of intense wave energy which are the initial stages of collapsing solitons. The electric field intensity in the most intense regions corresponds to $W \approx 0.19$, and these regions have a size of a few $\Delta \tilde{x}$, where $\Delta \tilde{x} = 9.8 \lambda_0$ is our numerical grid spacing. Thus, we expect rapid soliton collapse, with strong Landau damping after this time.

We have repeated this calculation with a numerical grid of only 32 by 32 points in real space and in wavenumber space, covering the same region in wavenumber space but only one-fourth the area in real space. The quantitative and qualitative behavior is substantially the same as the 64 by 64 case, resulting in soliton collapse at approximately the same time. This agreement gives confidence that our results are not overly sensitive to the resolution in wavenumber space; we expect that these results are an accurate representation of the physically interesting limit of an infinite number of modes in wavenumber space.

We conclude that the borderline case, $W = (\vec{k}_0 \lambda_0)^2$, results in a rapid evolution toward a state of collapsing solitons, in agreement with the speculations of Zakharov.¹

Case C: $W = 3 \times 10^{-3}$. In this case we are below pre-

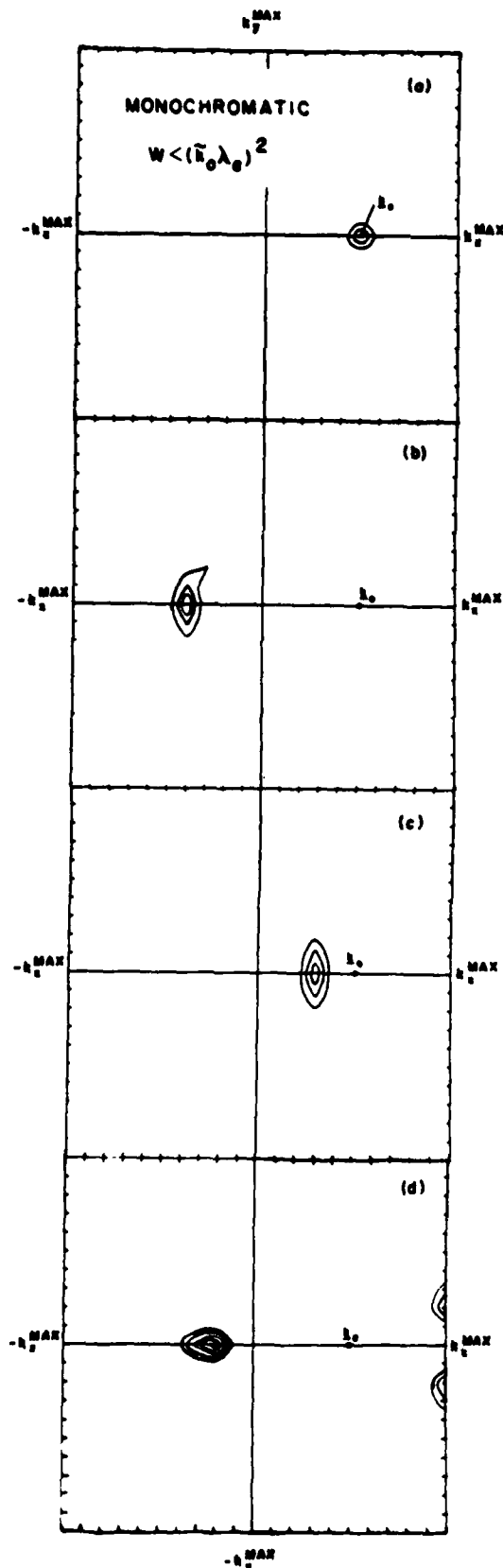


FIG. 7. Electric field intensity in wavenumber space, for case C, Sec. II. The time is (a) $\omega_p t = 2.2 \times 10^4$; (b) $\omega_p t = 4.4 \times 10^4$; (c) $\omega_p t = 5.5 \times 10^4$; (d) $\omega_p t = 1.0 \times 10^5$.

viously suggested thresholds for rapid collapse, and we might expect an evolution more reminiscent of the ideas of weak turbulence; namely, repeated scatters in wavenumber space, with each scatter yielding a set of waves in the opposite direction and with wavenumbers having slightly smaller magnitudes. For this case we use a numerical model of 32 by 32 points. The initial evolution contains a decay branch with numerical growth rate $\tilde{\gamma}/\omega_e \approx 4.6 \times 10^{-4}$, in excellent agreement with the value 4.9×10^{-4} predicted by (7). The predicted oscillating two-stream growth rate is comparable to the decay growth rate in this case, but as in the previous case, we find that this branch suffers a period of hesitation, allowing the decay branch to gain a head start. Thus, the initial wave at $\tilde{k}_0 \lambda_e = 0.10 \hat{x}$ [Fig. 7(a) at the relatively early time $\omega_p t = 2.2 \times 10^4$] decays to $\tilde{k}^L \lambda_e = -0.08 \hat{x}$ [Fig. 7(b) at $\omega_p t = 4.4 \times 10^4$], which in turn decays to $\tilde{k}^L \lambda_e = 0.06 \hat{x}$ [Fig. 7(c) at $\omega_p t = 5.5 \times 10^4$], decaying finally to $\tilde{k}^L \lambda_e = -0.04 \hat{x}$ [Fig. 7(d) at $\omega_p t = 1.0 \times 10^5$]. Thus, we observe three distinct scatters, as predicted by weak turbulence theory,²⁰ with no evidence of soliton collapse. The contours on the far right of Fig. 7(d) are presumably a spurious numerical effect, inducing us to end this run at this time. We might speculate that the further evolution of this example could soon lead to a soliton collapse, since the typical wavenumber k^L at time $\omega_p t = 1.0 \times 10^5$ once again satisfies the relation $W > (\tilde{k}^L \lambda_e)^2$. However, it is also possible that a more physically realistic calculation, with many more modes in wavenumber space, would show a greater amount of spreading in wavenumber space than found in Figs. 7(b), 7(c), and 7(d). Thus, it is conceivable that further evolution in wavenumber space stops, leaving a set of essentially linear Langmuir waves with a relatively uniform distribution in wavenumber space from zero to a value k^L such that $W \approx (\tilde{k}^L \lambda_e)^2$. The resolution of this question awaits future, more detailed, work. However, we have observed the latter scenario in a separate calculation for the initial condition $W = 10^{-5}$, $\tilde{k}_0 \lambda_e = 10^{-2}$.

We note that each scatter in this example produced a wavenumber change somewhat greater than that predicted by the backscatter relation (8); this effect is partially due to our limited resolution in wavenumber space.

We conclude that this example confirms the collapse threshold $W = (\tilde{k} \lambda_e)^2$; since we have $W < (\tilde{k}_0 \lambda_e)^2$, we find no rapid soliton collapse but rather a cascade in wavenumber space as predicted by weak turbulence theory.²⁰

Finally, one might inquire into the possible modification of these results for cases A, B, and C when $T_e \gg T_i$, in which case one can ignore the low frequency damping term. From the dispersion relation (6), dropping the middle term on the left side, it is easily shown that the parametric growth rates for cases A ($W = 10^{-1}$) and B ($W = 10^{-2}$) are very close to their equal temperature values, so we expect the same rapid evolution toward a state of collapsing solitons. For case C ($W = 3 \times 10^{-3}$) one finds a decay growth rate several times larger than its equal temperature value. However, upon repeating the numerical calculation of case C

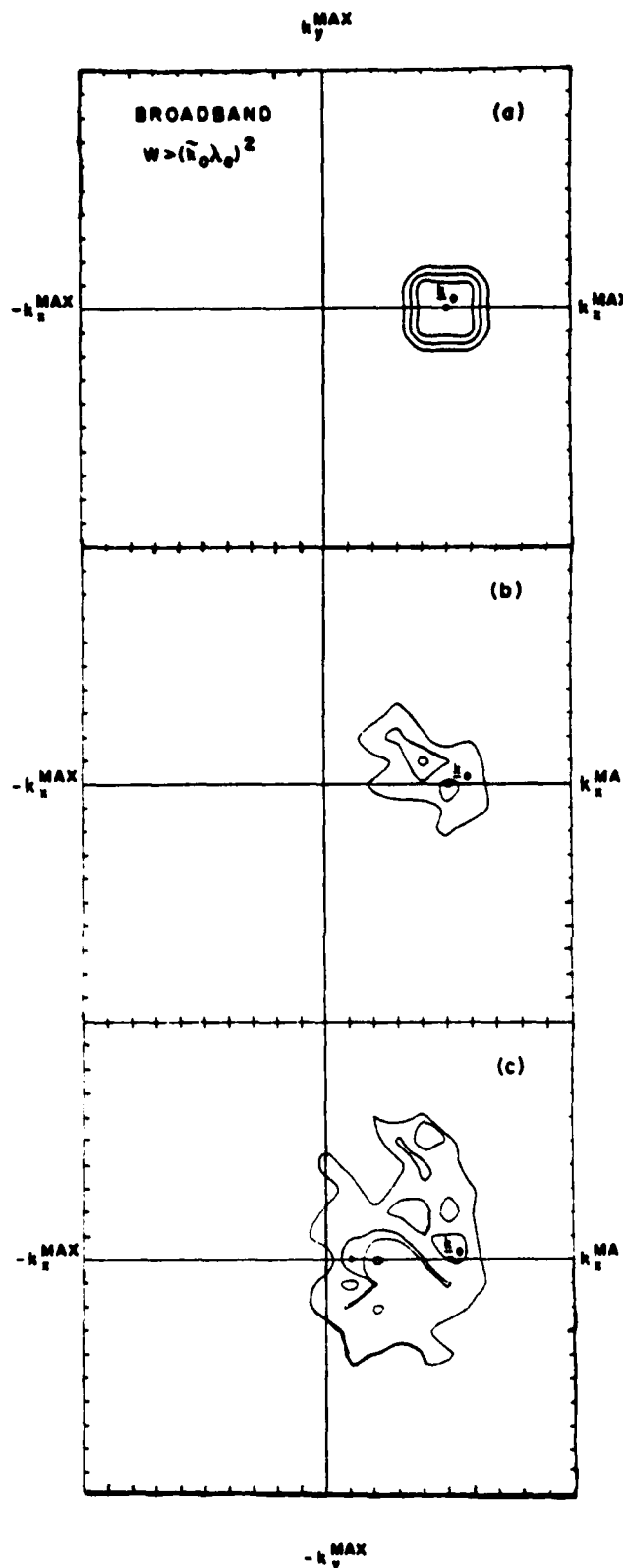


FIG. 8. Electric field intensity in wavenumber space, for case A, Sec. III. Contour definitions change from figure to figure, so the contour diagrams should be viewed qualitatively. The time is (a) $\omega_p t = 220$; (b) $\omega_p t = 1100$; (c) $\omega_p t = 1760$.

without the low frequency damping, we find the same qualitative result as in case C; namely, repeated back-scatters in wavenumber space with each stage having slightly smaller wavenumber magnitudes, and with no tendency toward a rapid soliton collapse. We conclude that the results of this section are substantially the same for $T_e \gg T_i$ and $T_e = T_i$. There are, of course, differences in detail, such as the radiation of ion sound waves in the $T_e \gg T_i$ case,^{22,23} which we do not discuss here.

III. BROADBAND INITIAL CONDITION

The calculations of the previous section used, as an initial condition, an intense monochromatic Langmuir wave with small noise levels in other modes. In a physically realistic problem, such as the interaction of an electron beam with a plasma, one would expect a set of Langmuir waves to be produced, having a spread of wavenumbers both along the central wavenumber, and perpendicular to the direction of the central wavenumber. In this section, therefore, we proceed to consider the temporal behavior of an initial condition consisting of a set of intense Langmuir waves having a finite wavenumber spread, with small noise levels in all other modes.

Numerically, we place equal amounts of initial energy in each of nine modes; the central mode is the same as that used in Sec. II, at $k_0 \lambda_e = 0.1 \hat{x}$, the nine modes having values $k_x \lambda_e = 0.08, 0.10, 0.12$, and $k_y \lambda_e = -0.02, 0.0, +0.02$. Each of the nine modes is given a random phase, and all other modes have random noise levels.

Case A: $W = 10^{-1}$. At the very early time $\omega_p t = 220$, the nine modes of equal intensity appear as a plateau in wavenumber space as shown in Fig. 8(a). The initial modes undergo a strongly nonlinear interaction among themselves, leading to a spreading in wavenumber space and a migration of wave energy toward smaller wavenumbers as shown in Fig. 8(b) at time $\omega_p t = 1100$ and Fig. 8(c) at time $\omega_p t = 1760$. At the last time, the electric field in real space has evolved into a set of collapsing solitons, as shown in Fig. 9. The maximum wave intensity in Fig. 9 corresponds to $W = 0.7$, the same as in the corresponding case with monochromatic initial condition, Fig. 3. However, in this broadband case, this intensity is reached in a time only one-half as long as in the monochromatic case. We interpret this fact as being due to the wave packet nature of the initial conditions. The linear superposition of the initial nine modes results in regions of initially enhanced wave energy due to constructive interference in real space. These regions can intensify themselves and begin a soliton collapse immediately, rather than first going through a period of parametric instability; thus, a state of collapsing solitons is reached faster in the broadband case than in the monochromatic case.

We note that this behavior would not be changed greatly by the use of more initial modes in wavenumber space, provided that the overall width in wavenumber space of the initial conditions is held constant. The real space statistical properties of a set of N modes

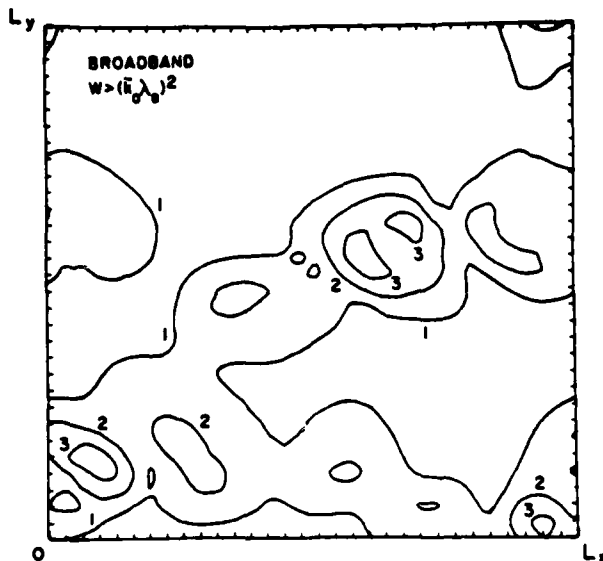


FIG. 9. Absolute value of electric field in real space, for case A, Sec. III, at time $\omega_i t = 1760$, the same time as in Fig. 8(c). The contour levels indicate relative values of electric field magnitude, with contour 1 corresponding to $W = 0.073$, and contour 3 corresponding to $W \approx 0.7$.

(in each dimension of wavenumber space) with random initial phases are equivalent to the statistical properties of an infinite set of modes, to within terms of order $(1/N)$. For our purposes we treat $N=3$ as a large number.

In one dimension, we know that solitons involving density depressions propagate stably at speeds less than the sound speed, whereas solitons whose speeds are greater than the sound speed involve density humps and are unstable to one-dimensional perturbations. We therefore would not expect to obtain, from arbitrary initial conditions, solitons with speeds greater than the sound speed in one dimension. Physically, we expect this statement to hold in two and three dimensions as well. Now in the present case the linear group velocity of the initial regions of constructive interference is faster than the ion sound speed, thus inhibiting immediate soliton collapse. However, in this case the nonlinear term in Eq. (4), of order $W = 10^{-1}$, is much larger than the linear dispersive term of order $(\tilde{k}_0 \lambda_e)^2 = 10^{-3}$, thus invalidating the concept of a linear group velocity and facilitating an immediate soliton collapse, at a "center of mass" speed well below the sound speed.

In the present broadband case, with $\Delta k_x = \Delta k_y \approx k_0/3$, we find immediate collapse, whereas in the monochromatic case, with $\Delta k_x = \Delta k_y = 0$, we found (Sec. II, case A, $W = 10^{-1}$) a backscatter to occur before soliton collapse. Thus, for a given wave level W , such that collapse is possible, the initial bandwidths determine whether soliton collapse, favored by large bandwidth, or parametric backscatter, favored by small bandwidth, is the fastest initial process.

As in case A of the previous section, the value of W is so large in this calculation that we should consider

it to be for illustration only; the conditions for validity of the basic equations are only marginally satisfied even at the initial time.

Case B: $W = 10^{-2}$. The initial conditions are distributed as in case A. In contrast to case A, here we do not find an immediate soliton collapse, but rather a parametric decay producing a backscatter wave as shown in Fig. 10(a) at time $\omega_i t = 9.9 \times 10^3$. Further mode coupling leads to a migration in wavenumber space towards smaller wavenumbers, as seen in Fig. 10(b) at time $\omega_i t = 1.3 \times 10^4$ and Fig. 10(c) at time $\omega_i t = 1.8 \times 10^4$ at which time we have at least one collapsing soliton as shown in Fig. 11. The maximum value of electric field intensity in Fig. 11 corresponds to $W = 0.10$, indicating that the soliton collapse in this case is only slightly less developed than in the corresponding monochromatic case at the same time, where Fig. 6 shows a maximum $W = 0.19$. Our interpretation of this case is that with $W = (\tilde{k}_0 \lambda_e)^2 = 0.01$, the nonlinear effects are not strong enough to force an immediate soliton collapse due to wave packet initial conditions, but rather the waves must first undergo a scatter in wavenumber space as in the case of a monochromatic initial condition. The parametric growth rates are somewhat reduced due to the broadband pump, causing the evolution to lag slightly behind the corresponding case with monochromatic initial condition, case B of Sec. II.

Case C: $W = 3 \times 10^{-3}$. The initial conditions are distributed as in the previous cases A and B. At early times, we find a parametric decay instability, at a wave vector opposite in direction and slightly smaller in magnitude compared with k_0 . The parametric decay growth rate at early time is not steady, but tends to fluctuate with an average value about half that observed in the corresponding monochromatic example, case C in Sec. II. This reduction in growth rate is due to the broadband nature of the pump, as discussed more fully later. The parametric decay instability results in the backscatter waves shown in Fig. 12(a) at time $\omega_i t = 4.4 \times 10^4$. A cascade toward lower wavenumbers now occurs, as in Fig. 12(b) at time $\omega_i t = 5.5 \times 10^4$ and Fig. 12(c) at time 9.3×10^4 . At this time there is also substantial wave energy in the zero wavenumber modes, both $E_{x,1=0}$ and $E_{y,1=0}$, not indicated in Fig. 12(c). At the last time, we have $W > (\tilde{k}_0 \lambda_e)^2$, where \tilde{k} is a typical wavenumber having large intensity. The nonlinearity in Eqs. (4) and (5) takes advantage of this inequality to produce the collapsing soliton shown in Fig. 13 at time $\omega_i t = 9.3 \times 10^4$, the same time as in Fig. 12(c).

This example, to the best of our knowledge, is the first known demonstration of a scenario which has been the subject of speculation for many years; namely, that an initial spectrum of waves with $W < (\tilde{k}_0 \lambda_e)^2$, \tilde{k} being a typical wavenumber, will undergo a cascade to very small wavenumbers, at which point no further cascade is possible. There will then occur a modulational instability, eventually leading to soliton collapse which removes wave energy to large wavenumbers where it can be Landau damped.

We note that most of the wave energy at time $\omega_i t$

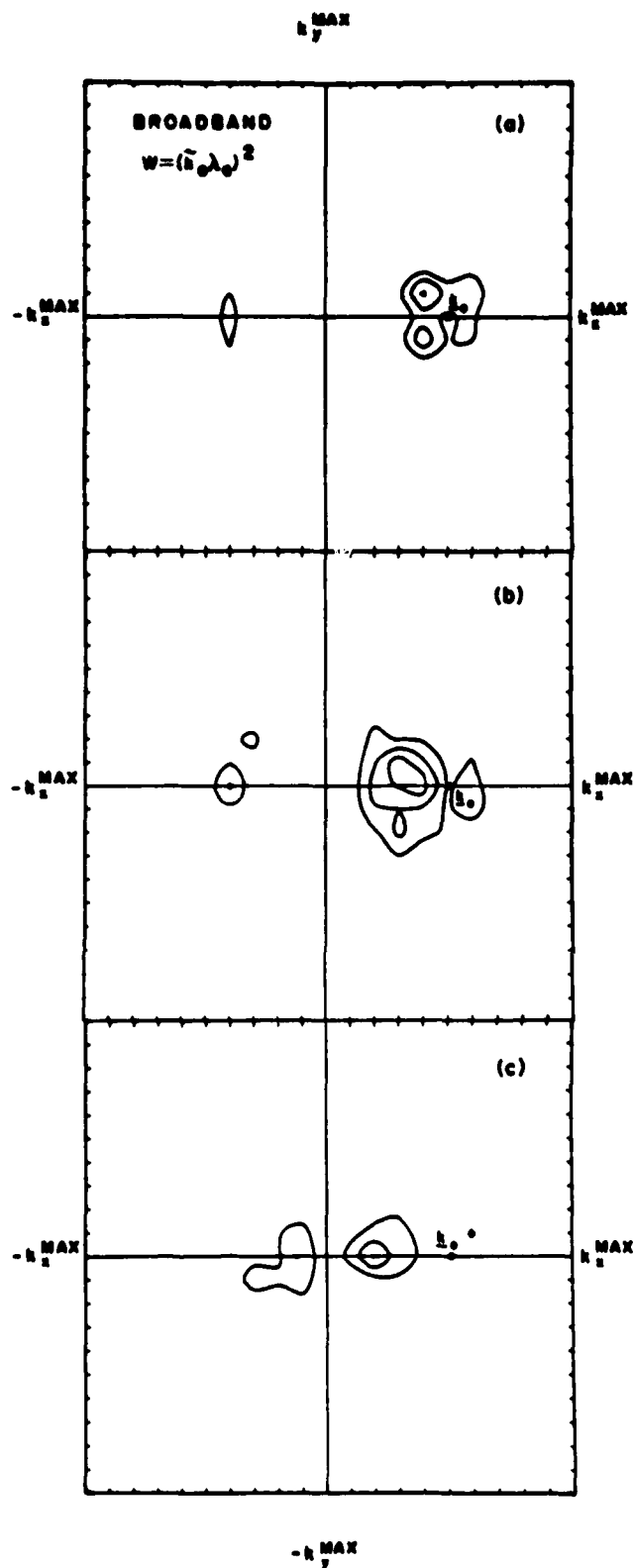


FIG. 10. Electric field intensity in wavenumber space, for case B, Sec. III. Contour definitions change from figure to figure, so the contour diagrams should be viewed qualitatively. The time is (a) $\omega_p t = 9.9 \times 10^3$; (b) $\omega_p t = 1.3 \times 10^4$; (c) $\omega_p t = 1.8 \times 10^4$.

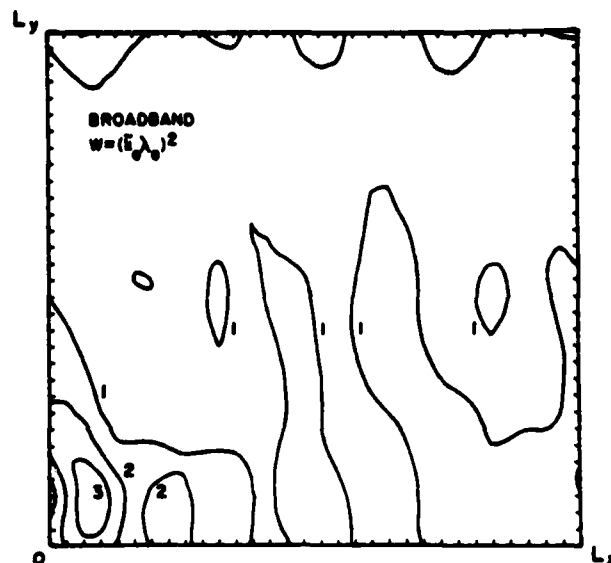


FIG. 11. Absolute value of electric field in real space, for case B, Sec. III, at time $\omega_p t = 1.8 \times 10^4$, the same time as Fig. 10(c). The contour levels indicate relative values of electric field amplitude, with contour 1 corresponding to $W = 0.012$, and contour 3 corresponding to $W = 0.10$.

$= 9.3 \times 10^4$ is concentrated in three numerical modes in wavenumber space, the $k = 0$ mode and the two modes immediately to the right and to the left of it [see Fig. 12(c)]. Thus, a calculation using more modes in wavenumber space could conceivably yield significantly different quantitative and perhaps even qualitative results.

In this case C, it is possible to analytically treat the growth of the decay branch at early times. For a pump with constant amplitude in a certain volume V of wavenumber space, with each component having the same amplitude but random phase, the dispersion relation (6) is replaced by

$$-\omega^2 - 2i\omega k + k^2 = \frac{-k^2 |E_0|^2}{V} \int_V d^2 k' \left(\frac{\mu^2(k')}{\omega - 2k' \cdot k - k^2} - \frac{\mu^2(k')}{\omega - 2k' \cdot k + k^2} \right), \quad (10)$$

where $\mu^2 = (\hat{k} \cdot \hat{k}')^2$, $\kappa = k \pm k'$. Equation (10) is valid only when $W_0 \ll (\hat{k} \cdot \hat{k}_0)^2$ for all k' in V ; then, each component of the pump approximately obeys the linear dispersion relation. Taking V to be a square centered about k_0 , as in Fig. 8(a), we neglect the first term on the right side of (10) to treat the decay instability. We then find that the spread of initial wavenumbers in the k_x direction enters only through the factor $\mu^2(k')$ in the numerator, yielding a small reduction in growth rate which is only about 3% in this case. The spread in k_y enters only through the denominator, where we find a substantial growth rate reduction whenever the spread in k_y wavenumbers produces a spread in initial wave frequencies which is greater than the decay growth rate in the monochromatic case. This result is in agreement with the well-known behavior²⁴ of parametric in-

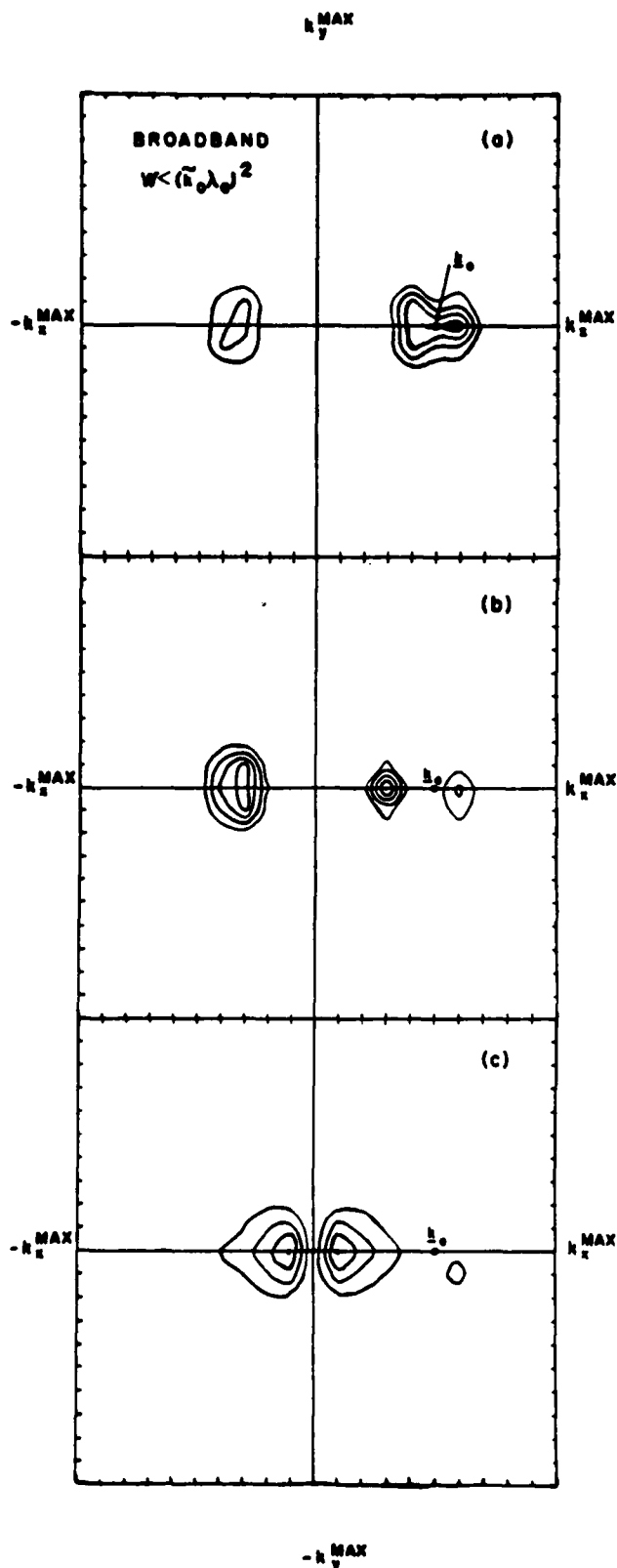


FIG. 12. Electric field intensity in wavenumber space, for case C, Sec. III. Contour spacing is the same in each figure. The time is (a) $\omega_p t = 4.4 \times 10^4$; (b) $\omega_p t = 5.5 \times 10^4$; (c) $\omega_p t = 9.3 \times 10^4$.

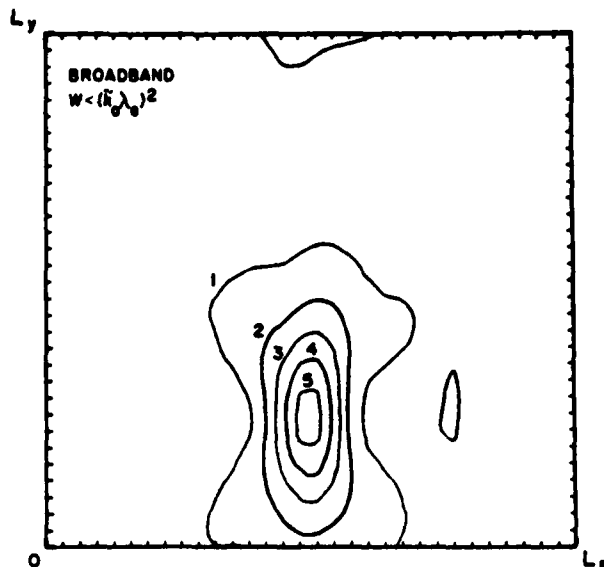


FIG. 13. Absolute value of electric field in real space, for case C, Sec. III, at time $\omega_p t = 9.3 \times 10^4$, the same time as Fig. 12(c). The contour levels indicate relative values of electric field amplitude, with contour 1 corresponding to $W = 0.0029$, and contour 5 indicating $W = 0.073$.

stabilities in the presence of an initial wave of finite bandwidth.

In the present case C, the spread of initial wave frequencies is greater than 10 times the monochromatic growth rate, and Eq. (10) would predict a great reduction in growth rate, almost to zero. This prediction is somewhat at variance with the actual numerical result, where we find a reduction in growth rate of only about a factor of two over the monochromatic case. The most likely explanation for this discrepancy is that, in the present case, the use of only three discrete values of k_x is not a good approximation to an infinite number of wavenumbers covering the same region of k_x space. This dependence on the number of modes is in contrast to case A of the present section, where $W_0 \gg (\tilde{k}_0 \lambda_0)^2$, implying that the linear pump frequency spread is no longer important. There, the important effect is the wave packet nature in real space, which induces soliton collapse, and which is only slightly different for three modes than for an infinite number of modes.

In conclusion, this section shows that when $W_0 \gg (\tilde{k}_0 \lambda_0)^2$, the most important effect of a broadband initial wave is the wave packet nature in real space, which induces soliton collapse. When $W_0 < (\tilde{k}_0 \lambda_0)^2$, the parametric growth rates are reduced by the broadband nature of the initial wave. When nine pump modes are used, there is still a substantial parametric growth rate, resulting in a weak turbulence cascade. In the one example studied here, the cascade results at a late time in the inequality $W \gg (\tilde{k}_0 \lambda_0)^2$ being once again satisfied, and a soliton collapse is produced.

IV. CONCLUSIONS

We have shown numerically that intense Langmuir waves satisfying the inequality $W \gg (\bar{k}\lambda_e)^2$ proceed rapidly to a state of collapsing solitons. When the opposite inequality is satisfied, there is no rapid soliton collapse, but rather a cascade in wavenumber space as predicted by weak turbulence theory.²⁸ Note that our work has neglected linear high frequency dissipation; the cascade and collapse scenarios presented here will be modified if their time scales are not faster than that of linear dissipation.

It is interesting to compare the results of this paper, in the regime $\bar{k}_0\lambda_e \gg (m_e/m_i)^{1/2}$, to earlier work¹⁶ in the regime $\bar{k}_0\lambda_e < (m_e/m_i)^{1/2}$. When $W \gg (\bar{k}_0\lambda_e)^2$, there seems to be no difference between these regimes; in either regime the nonlinear effect swamps the linear group velocity, producing immediate soliton collapse in the broadband case, and soliton collapse after one backscatter in the monochromatic case.

In the borderline case, $W \approx (\bar{k}\lambda_e)^2$, there is an important difference between the two wavenumber regimes. When $\bar{k}_0\lambda_e < (m_e/m_i)^{1/2}$, the group speed of the initial waves is less than the ion acoustic speed. Thus, any wave packet nature in real space can resonate strongly with ion motions, producing immediate soliton collapse in the broadband case and soliton collapse after one scatter in the monochromatic case. In this case, the inequality $W > (\Delta\bar{k}\lambda_e)^2$ must always be applied to the spread in wavenumbers about the central wavenumber.^{16,17} By contrast, when $\bar{k}_0\lambda_e \gg (m_e/m_i)^{1/2}$, the Langmuir group speed is much greater than the acoustic speed, and a monochromatic wave must undergo two backscatters in order to set up a standing wave pattern in real space which can then collapse (Sec. III, case B, Figs. 5 and 6); a broadband wave must undergo one backscatter in order to set up a collapsible standing wave pattern in real space (Sec. III, case B, Figs. 10 and 11).

In the case $W < (\bar{k}_0\lambda_e)^2$, there is at least one important difference between the two wavenumber regimes. When $\bar{k}_0\lambda_e \gg (m_e/m_i)^{1/2}$, it is possible for wave energy to cascade to smaller wavenumbers via repeated backscatters, resulting in the inequality $W \lesssim (\bar{k}\lambda_e)^2$ being satisfied at a later time and therefore possibly in a soliton collapse, as found in Sec. III, Case C, Figs. 12 and 13. When $\bar{k}_0\lambda_e < (m_e/m_i)^{1/2}$, this scenario is not possible; the decay branch is suppressed, and four-wave instabilities become more important; these tend to put energy into larger wavenumbers, thus reinforcing the inequality $W < (\bar{k}\lambda_e)^2$, and forever inhibiting soliton collapse.

We have recently developed an analytic theory¹⁷ which applies to the regime $\bar{k}_0\lambda_e < (m_e/m_i)^{1/2}$, i.e., to the regime of our earlier numerical work.¹⁶ We find that the initial wavenumber \bar{k}_0 is not important, but rather the initial spread in wavenumbers $\Delta\bar{k}$. When $W > (\Delta\bar{k}\lambda_e)^2$, but $\Delta\bar{k}\lambda_e$ greater than some threshold, we find a direct collapse induced by the wave packet nature of the initial conditions. When $W > (\Delta\bar{k}\lambda_e)^2$, but $\Delta\bar{k}\lambda_e$ is too small, the direct collapse rate is slower than the parametric

instability growth rate, and parametric instability grows fastest. When $W < (\Delta\bar{k}\lambda_e)^2$, there is no collapse. These analytic results¹⁷ are in very good agreement with our earlier numerical results.¹⁶

The work discussed here is of relevance to a very important physical situation: the passage of an electron beam of speed v , through a plasma with thermal speed v_e . Such a beam produces Langmuir waves with frequency $\omega = \omega_e$, and wavenumber k_e , such that the phase speed is $\omega_e/k_e = v$, or $k_e\lambda_e = v_e/v$. Linear and quasi-linear plasma theories then often predict wave intensities large enough for the soliton collapse ideas of this paper to apply, for reasonable laboratory²⁹ and astrophysical¹⁶ parameters.

ACKNOWLEDGMENTS

This paper has benefitted greatly from the advice and numerical expertise of P. Hoyng and F. Tappert. We thank R. Aamodt, D. DuBois, N. Pereira, G. Reiter, T. Rudolph, D. F. Smith, R. Sudan, and J. Weatherall for useful discussions.

This work was supported by the Atmospheric Research Section, National Science Foundation, ATM76-14275. The work of one of us (M. V. G.) was also supported by AFOSR contract No. F49620-76-C-0005. We thank the National Center for Atmospheric Research, supported by the National Science Foundation, for computer time used in this study. Part of this work was performed while the authors were the guests of the Aspen Institute for Physics and Astrophysics; their hospitality is appreciated.

¹V. E. Zakharov, Zh. Eksp. Teor. Fiz. 62, 1745 (1972) [Sov. Phys.-JETP 35, 908 (1972)].

²A. G. Litvak, G. M. Fraiman, and A. D. Yunkovskii, Zh. Eksp. Teor. Fiz. Pis'ma Red. 19, 23 (1974) [JETP Lett. 19, 13 (1974)].

³E. A. Kuznetsov, Zh. Eksp. Teor. Fiz. 66, 2037 (1974) [Sov. Phys.-JETP 39, 1003 (1974)].

⁴K. Nishikawa, Y. C. Lee, and C. S. Liu, Comments Plasma Phys. 2, 63 (1974).

⁵V. E. Zakharov, A. F. Mastryukov, and V. S. Synakh, Zh. Eksp. Teor. Fiz. Pis'ma Red. 20, 7 (1974) [JETP Lett. 20, 3 (1974)].

⁶L. M. Degtyarev and V. E. Zakharov, Zh. Eksp. Teor. Fiz. Pis'ma Red. 20, 365 (1974) [JETP Lett. 20, 184 (1974)].

⁷L. M. Degtyarev, V. E. Zakharov, and L. I. Rudakov, Zh. Eksp. Teor. Fiz. 68, 155 (1975) [Sov. Phys.-JETP 41, 57 (1975)].

⁸L. M. Degtyarev and V. E. Zakharov, Zh. Eksp. Teor. Fiz. Pis'ma Red. 21, 9 (1974) [JETP Lett. 21, 4 (1975)].

⁹A. A. Galeev, R. Z. Sagdeev, Yu. S. Sigov, V. D. Shapiro, and V. I. Shevchenko, Fiz. Plazmy 1, 10 (1975) [Sov. J. Plasma Phys. 1, 5 (1975)].

¹⁰V. E. Zakharov, A. F. Mastryukov, and V. S. Synakh, Fiz. Plazmy 1, 614 (1975) [Sov. J. Plasma Phys. 1, 339 (1975)].

¹¹V. E. Zakharov, Zh. Eksp. Teor. Fiz. Pis'ma Red. 21, 479 (1975) [JETP Lett. 21, 221 (1975)].

¹²O. B. Budneva, V. E. Zakharov, and V. S. Synakh, Fiz.

- Plazmy 1, 606 (1975) [Sov. J. Plasma Phys. 1, 335 (1975)].
- ¹³L. M. Degtyarev, V. E. Zakharov, and L. I. Rudakov, Fiz. Plazmy 2, 438 (1976) [Sov. J. Plasma Phys. 2, 240 (1975)].
- ¹⁴N. R. Pereira, R. N. Sudan, and J. Denavit, Phys. Fluids 20, 936 (1977).
- ¹⁵A. N. Polyudov and Yu. S. Sigov, Soviet Institute of Applied Mathematics Report No. 123 (1976).
- ¹⁶D. R. Nicholson, M. V. Goldman, P. Hoyng, and J. C. Weatherall, Astrophys. J. 213, 606 (1978).
- ¹⁷M. V. Goldman and D. R. Nicholson, Phys. Rev. Lett. 41, 406 (1978).
- ¹⁸A. A. Vedenov and L. I. Rudakov, Dokl. Akad. Nauk SSSR 159, 767 (1964) [Sov. Phys.-Dokl. 9, 1073 (1965)].
- ¹⁹A. A. Vedenov, A. V. Gordeev, and L. I. Rudakov, Plasma Phys. 9, 719 (1967).
- ²⁰V. N. Tsytovich, *Nonlinear Effects in Plasma* (Plenum, New York, 1970).
- ²¹S. Bardwell and M. V. Goldman, Astrophys. J. 309, 912 (1976).
- ²²A. N. Lebedev and V. N. Tsytovich, Phys. Scr. 11, 266 (1975).
- ²³K. Nishikawa, H. Hojo, K. Mima, and H. Ikezi, Phys. Rev. Lett. 33, 148 (1974).
- ²⁴J. J. Thomson and J. I. Karush, Phys. Fluids 17, 1608 (1974).
- ²⁵A. Y. Wong (private communication).

ABSORPTION OF CO₂ LASER LIGHT BY A DENSE, HIGH TEMPERATURE PLASMA

N. J. PEACOCK, M. J. FORREST, P. D. MORGAN (*),
M. V. GOLDMAN (**), T. RUDOLPH (**), A. A. OFFENBERGER (***)

Culham Laboratory, Abingdon, Oxon. OX14 3DB, U. K.
(Euratom/UKAEA Fusion Association)

Résumé. — L'interaction entre le faisceau pulsé d'un laser au CO₂ et le plasma produit par un dispositif *plasma focus* est examinée des points de vue théorique et expérimental. Le faisceau du laser CO₂, qui est dirigé perpendiculairement à l'axe, suivant le gradient de densité, ne perturbe que faiblement le plasma car la densité de rayonnement de 30 J cm⁻³ (compte tenu du facteur d'amplification de Airy) est néanmoins plus faible que l'énergie thermique du plasma (≤ 1 kJ cm⁻³). Au contraire, le rayon du laser est fortement affecté par le plasma.

Durant la phase de compression en *pinch* quand la fréquence du plasma $\omega_{pe} > \omega_{co_2}$, l'absorption du faisceau est beaucoup plus importante que celle prévue en utilisant la résistivité classique.

Les fluctuations de densité à la fréquence de Langmuir sont mesurées directement par diffusion frontale à l'aide du faisceau sonde d'un laser à rubis. Etant donné que les nombres d'ondes correspondent à $(K\lambda_D) \sim 0,1$ les ondes de Langmuir devraient apparaître dans le spectre diffusé comme des raies électroniques, décalées de 427 Å par rapport à la longueur d'onde du laser à rubis. A faible intensité de pompage du laser au CO₂, l'intensité des ondes électroniques est proche du niveau thermique. Si on augmente l'intensité de pompage au-delà d'un seuil de 3×10^9 W/cm², on observe une forte augmentation du rayonnement diffusé, qui peut dépasser d'un facteur 30 le niveau thermique.

L'étude WKB de l'instabilité de dégénérescence électron-ion est en assez bon accord avec les mesures. Cette étude tient compte de la croissance linéaire des ondes à température électronique et ionique égales, et des phénomènes de convection dans un plasma inhomogène.

Abstract. — The interaction between a pulsed, CO₂ laser beam and the plasma produced in a plasma focus device is investigated theoretically and experimentally. The CO₂ laser radiation, directed orthogonal to the pinch axis and along the density gradient only weakly perturbs the focus since the radiation density of 30 J cm⁻³ (allowing for the Airy enhancement factor near the critical layer), is still less than the plasma thermal energy $\gtrsim 1$ kJ cm⁻³. On the contrary, the CO₂ laser beam is grossly affected by the plasma and absorption during the compressed pinch phase when the plasma frequency $\omega_{pe} \gtrsim \omega_{co_2}$ is much more complete than can be predicted by classical resistivity.

Density fluctuations at the Langmuir frequency are measured directly by forward scattering from a probe, ruby laser beam. Since the wave numbers correspond to $(K\lambda_D) \sim 0.1$ the Langmuir waves should appear as electron 'lines' in the scattered spectrum shifted by 427 Å from the ruby laser wavelength. At low CO₂ laser pump intensity the electron wave intensity is close to the thermal level. As the pump is increased beyond a threshold of $\sim 3 \times 10^9$ W/cm² (in vacuo) enhanced scattering is observed, reaching a factor of 30 above thermal.

A WKB treatment of the electron-ion decay instability which takes into account the linear growth of waves at equal electron and ion temperatures and their convection in an inhomogeneous plasma is reasonably consistent with the observations.

1. Introduction. — The aim of this paper is to report on the absorption and redistribution of energy in a CO₂ laser beam by a pre-formed and pre-heated plasma, in circumstances where anomalous heating processes might be expected. The plasma is the dense pinch formed in a plasma focus device [1].

In contrast to the many experimental studies which have been reported in the literature on laser beam interactions with solid [2, 3] or gaseous [4] targets, the use of a preformed plasma which is not substantially altered by the pump beam has a number of advantages. In the plasma focus the kinetic energy density is considerably higher than the threshold, radiation intensity required for the most readily-excited instabilities. Among these, there are, for example, the parametric decay instability [5, 6, 7], the oscillating two-stream instability [8] and the

(*) Now at Ecole Polytechnique Fédérale de Lausanne, Switzerland.

(**) University of Colorado, Boulder, U. S. A.

(***) University of Alberta, Edmonton, Canada.

stimulated Brillouin instability, all of which can be excited with pump intensities between 10^{10} and 10^{12} W/cm $^{-2}$.

During the pinch compression phase of the plasma focus the electron plasma frequency is matched to the frequency of infra-red light at least over a limited spatial region and for a limited time duration. A CO $_2$ laser operating at 10 microns wavelength might be expected to act therefore as a pump for Langmuir waves in the plasma.

The focus device has been relatively well diagnosed by a number of groups [9, 10, 11], and using a variety of measurement techniques; but this advantage is to be offset against its somewhat irreproducible characteristics and inherent density fluctuations which, for certain wave-vectors, can be considerably above the thermal level due to current-driven instabilities [12].

In this study we observe absorption of the pump beam and enhancement of the Langmuir wave intensity when a CO $_2$ laser irradiates the partially-compressed pinch. The enhancement is described in terms of non-linear processes induced by the pump beam.

2. Plasma characteristics with no external pump beam. — The evolution of the highly-compressed plasma in a Mather type, open-ended, coaxial gun focus is shown schematically in figure 1. The dimensions of the inner and outer electrodes are 5 cm and 10 cm respectively. The stored energy in the capacitor bank is 40 kJ at 30 kV and the ambient filling pressure of deuterium is between 2.5 and 3.0 torr.

Time-resolved interferograms of the converging, cusped, conical plasma front are shown in figure 2 and the density distributions, suitably Abel-inverted, are shown as a function of time in figure 3. It is to be noted that the density has a peak value of the order of 3×10^{19} cm $^{-3}$ and it remains higher than

$$n_{ee} = 9.94 \times 10^{18} \text{ cm}^{-3},$$

the critical density, for reflection of the CO $_2$ laser light, for several tens of nanoseconds. During the late stage of the compression of the plasma onto the axis of symmetry of the coaxial electrodes, the scale length for the density gradient,

$$L = \left[\frac{1}{n_e} \frac{\partial n_e}{\partial r} \right]^{-1},$$

changes rapidly in time, figure 4. Typically L will vary from 0.3 to 0.03 cm in the 40 nanoseconds up to peak compression.

The particle energy distribution and the background level of turbulence in the plasma has been measured in some detail [11, 13] using the scattered light from ruby laser probes. Most of the analyses have been based on the intensity and frequency spread of the *ion feature* in the scattered light spec-

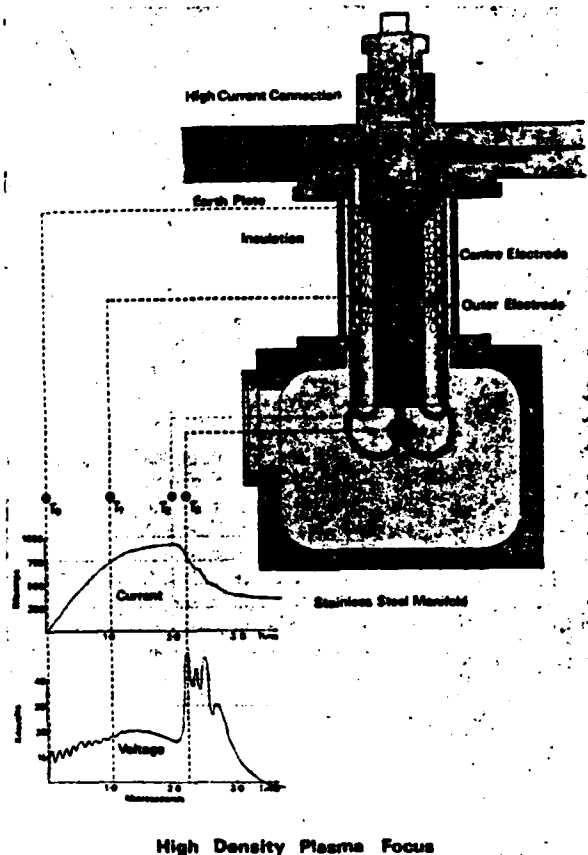


FIG. 1. — Schematic diagram of the spatial variation in the location of the plasma boundary and the associated electric waveforms in the plasma focus device.



FIG. 2. — One nanosecond exposure time sequence of three interferograms at -30, 0 and +30 nanoseconds where time 0 refers to moment when the compression front first reaches the axis of symmetry on Plasma Focus.

trum. Samples [13] of the spectral broadening, $\Delta\omega = 1.6 Kv_i$, where v_i is the ion thermal velocity and K the differential scattering wavenumber, are shown for values of the scattering parameter, $(K\lambda_D)^{-1}$, between 1 and 2, in figure 5. The experimental points have been fitted to thermal distributions of the electrons and ions following Evans (1970) [14].

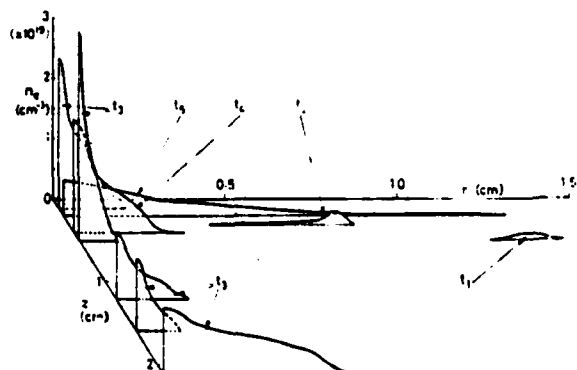


FIG. 3. — Temporal variation of density distribution in the plasma focus, after Abel inversion $t_1, t_2 \dots t_3$ denotes a time sequence lasting 150 ns, with t_3 corresponding to peak compression.

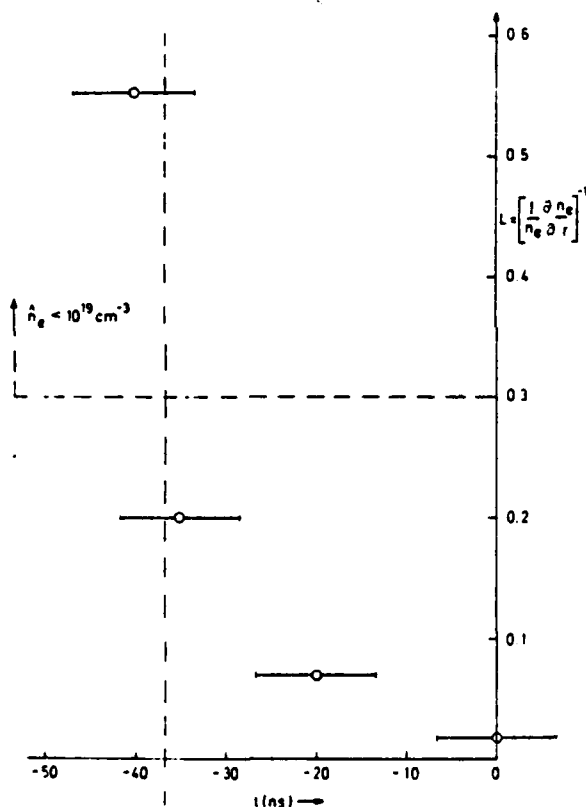


FIG. 4. — Temporal variation of the radial density scale length,

$$L(\text{cm}) = \left[\frac{1}{n_e} \frac{\partial n_e}{\partial r} \right]^{-1},$$

in the plasma focus, derived from interferometry. For $n_e < 10^{19} \text{ cm}^{-3}$

the scale length is measured at the peak of the density profile while for $n_e > 10^{19}$, the scale length is appropriate to the pump beam, cut-off density, $n_{oe} = 9.94 \times 10^{18} \text{ cm}^{-3}$.

The maximum ion and electron temperatures occur at peak compression and are of the same order, i. e. $\hat{T}_e \approx \hat{T}_i \approx 2 \text{ keV}$. An adiabatic scaling, $T_e r^{2(\gamma-1)} = \text{constant}$, is appropriate to the fluid model constructed by Potter (1971) [15], and has

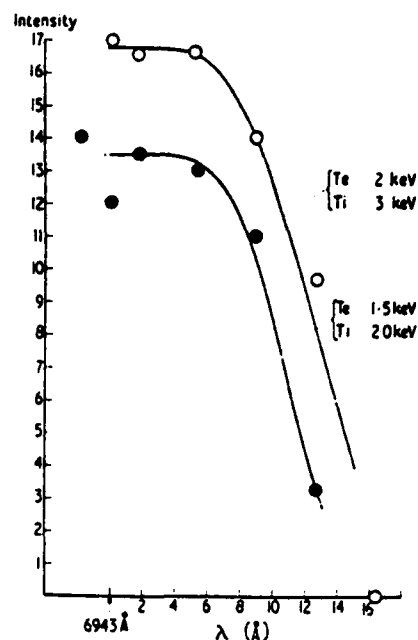


FIG. 5. — Electron and ion temperatures at peak compression derived from the collective, $K\lambda_D = 0.56$, ion feature of the scattered visible light spectrum. Forrest and Peacock (1974).

been used to calculate the variation in the peak temperature during the compression, figure 6.

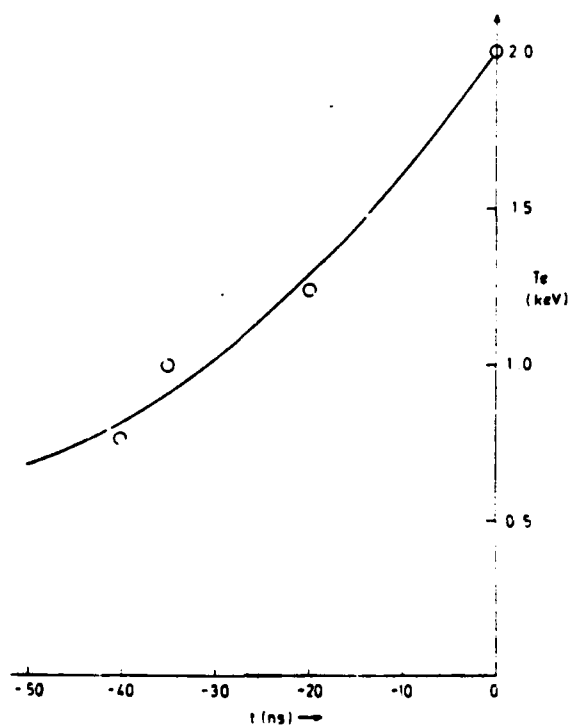


FIG. 6. — Variation in peak temperature during the pinch phase of the plasma focus, assuming 2-dimensional adiabatic compression.

The scattered light intensity in the ion feature is measured on an absolute basis and is given by

$$I_s = I_0 \cdot V_s \cdot \frac{d\Omega_s}{2\pi} \cdot \sigma_T \cdot n_e \int_0^{2k_{v1}} S(\omega, k) d\omega \quad (1)$$

where I_0 is input ruby laser intensity and V_s and $d\Omega_s$ are the scattering volume and solid angle respectively, subtended by the detector. σ_T is the Thomson scattering cross-section. For $\alpha = (K\lambda_D)^{-1} \sim 1$, the factor

$$[n_e S(K)] = \frac{n_e}{(1 + \alpha^2)},$$

for a thermal plasma. In these experiments [13] we find $[n_e S(K)] \approx 2 n_e$, indicating a nearly thermal plasma for scattering vectors, \bar{K}_\perp orthogonal to the current flow, \bar{j} . In complementary studies [11], Bernard and co-authors have found a somewhat similar level of background wave activity with, again, $[n_e S(K)] \approx n_e$ for $\bar{K}_\perp \cdot \bar{K}_\parallel$. However for scattering vectors, \bar{K}_\parallel , parallel to \bar{j} , there is considerable enhancement above the thermal level, as shown in figure 7, especially at around 3 torr ambient pressure, which is our present operating conditions.

3. Irradiation of the Focus Plasma by a CO₂ Laser Beam. — A double discharge TEA, CO₂ laser delivering 10 joules in an initial, gain switched pulse of 40 ns duration has been used to irradiate plasma orthogonal to the pinch axis of symmetry. The experimental arrangement is shown in figure 8. After

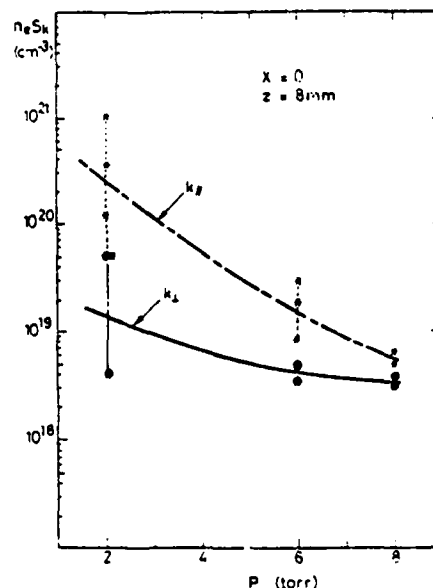


FIG. 7. — Absolute level of the collective ion feature, K_D/K_\perp and $K_D/K_\parallel \gg 1$, in the spectrum of scattered ruby laser light from the plasma focus. The level is expressed in terms of the product of electron density and the dynamic form factor for the scattered light spectrum, $S(K)$. p (torr) is the ambient filling density, x and z are the radial and axial positions, in cylindrical coordinates, of the plasma responsible for scattering the laser light. \bar{K}_\parallel and \bar{K}_\perp refer to differential scattering vectors parallel and orthogonal respectively to the current flow; Bernard *et al.* (1974).

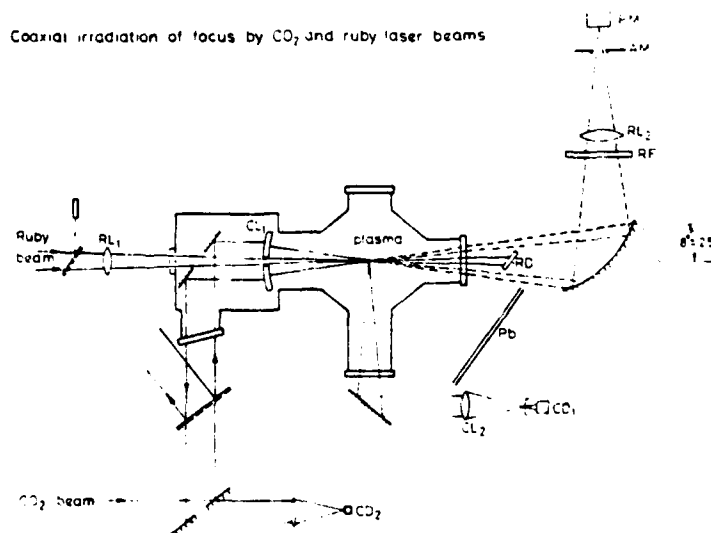


FIG. 8. — Optical layout (Plan-view) of the CO₂ laser interaction experiment with the dense plasma focus. The ruby laser probe beam and associated visible light scattering optics are coaxial with the CO₂ beam. Input of CO₂ laser beam, 10 → 20 J/50 ns, enters focus chamber (from below) via KCl beam splitter and Ge window. It is then focused via a F/5.5 germanium lens (CL₁) onto the plasma axis. Refracted CO₂ laser light is detected at 45°, 90° and 135° to incident beam and focused via a KCl lens (CL₂) onto appropriate detectors; CD₁ is a sensitive Au-doped Ge or Pb:Sn:Te photodetector shielded from the discharge with lead (Pb). CD₂ is a photon drag detector. Input of the ruby laser beam, 5 J/18 ns, enters chamber from left and is focused onto the axis of the plasma via a glass lens (RL₁). The ruby light dump (RD) completely attenuates the primary probe beam but scattered ruby laser light is detected (PM) through a narrow band filter, $6.500 \pm 25 \text{ \AA}$ (RF), lens (RL₂) and azimuthal mask (AM).

losses in the optics the average CO₂ laser intensity, focussed in vacuo through an F/5.5 germanium lens on a 0.75 mm spot at the focus axis, is

$$2 \times 10^{10} \text{ W/cm}^{-2}.$$

Mode beating during the irradiation pulse will result in peak values of twice this intensity. Polarizers made from KCl plates inside the oscillator cavity ensure that 95 % of the output CO₂ laser energy is plane polarised [16]. The CO₂ laser beam is arranged to pump electron waves orthogonal to the density gradient with either p-type polarisation in which the electric vector, E , is orthogonal to \hat{j} , or alternatively s-type polarisation with E parallel to \hat{j} . The incident intensity, transmission, refraction and back-scatter of the CO₂ beam are measured by photon drag detectors, or Au-doped Ge, and Pb; Sn; Te detectors, the last two being liquid N₂-cooled, ensuring a wide range of detectivities for the infra-red radiation. A summary of the parameters of the irradiation conditions is shown in table I.

The effect of the plasma on the pump beam is taken into account in table I. In particular, the intensity, swollen by the Airy peaks near the critical surface, is given by

$$\Phi_{pi} \approx \Phi_0 (\text{vacuum}) / \eta_{min}, \quad (2)$$

where η_{min} is the minimum value of the refractive index compatible with geometric optics,

$$\eta_{min}^{-1} = 3.8(L\omega_0/c)^{1/3}.$$

This swelling factor allows the pump intensity to exceed the threshold for the instabilities listed in the table. The energy density in the beam is seen to be small compared to the plasma kinetic energy.

Before discussing the results of the CO₂ laser beam/plasma interaction it is instructive to consider theoretically the absorption and refraction in an inhomogeneous plasma in which classical resistivity is the only absorption mechanism. For a plane wave incident on a cylindrical plasma the reflectivity [17] is given by

$$R = \exp(-2p \cos^2 \theta) \quad (3)$$

where θ is the angle of the incident light to the radius normal and

$$p = \frac{16}{15} K_r L,$$

where L is the density scale length and K_r , the resistive absorption coefficient,

$$K_r = \omega_{pe}^2 / c \omega_{CO_2} \tau (\omega_{CO_2}^2 - \omega_{pe}^2)^{1/2} \quad (4)$$

where τ is the electron-ion collision time [18]. In our plasma conditions, the paraxial rays, only, will penetrate to the critical reflection surface and will therefore suffer the greatest absorption with

$$R_{parax} = \exp \left(-2 \int_0^{L \text{ at turning point}} K(v) dl \right) \\ \sim 0.64 \text{ for } \begin{cases} L = 0.20 \text{ cm} \\ \hat{T}_e = 900 \text{ eV} \\ \hat{n}_e = 0.99 n_{ec} \end{cases}$$

Thus the back reflected light should be substantial when the plasma density exceeds the critical value for reflection i. e. when $n_{ec} \gtrsim 9.94 \times 10^{18} \text{ cm}^{-3}$. Other light rays will be refracted with little loss in light intensity as is illustrated for the plasma at peak compression in figure 9.

Following the logic that, on theoretical considerations only a relatively small fraction will be absorbed from the pump beam in the high temperature plasma, it is instructive to neglect absorption completely as in the model calculations shown in figure 10. In this figure the pump beam $I_0 e^{-(r/r_0)^2}$ is incident from the right on a high temperature plasma, with a parabolic density distribution, whose peak density and radius correspond to those measured interferometrically during the pinch phase of the plasma. It is evident, figure 10, that in the under-dense plasma, the pump beam is transmitted without much deviation; but that as the electron density reaches, or exceeds, n_{ec} then there is a rapid angular variation in the refracted light. For $n_e \gg n_{ec}$, the light is mainly refracted back towards the incoming beam.

TABLE I

 Summary of parameters of CO₂ beam interaction with plasma focus

Focused pump-beam intensity	Cut-off density	Ratio of oscillatory to electron thermal velocities	Energy density in CO ₂ beam	Plasma Parameters		
				\hat{n}_e	\hat{T}_e	$L = \left(\frac{1}{n_e} \frac{dn_e}{dr} \right)^{-1}$
Φ_0 (in vacuo)	n_{ec}	$V \sim V_{th} $	$E^2/8\pi$ (in vacuo)	cm ⁻³	eV	cm
$< 4 \times 10^{10} \text{ W/cm}^{-2}$	$9.94 \times 10^{18} \text{ cm}^{-3}$	~ 0.02	0.7 J/cm^{-3}	9.94×10^{18}	2,500	0.3 0.03
Φ_{pi} (in plasma)	Threshold intensity for non-thermal processes e. g. osc. 2-stream; electron-ion decay		$E^2/8\pi$ (in plasma)	Internal kinetic energy $n_e k T_e$		
$\Phi_{pi} \approx (10 \rightarrow 40) \times \Phi_0$	$\Phi_{thresh} \sim 10^{11} \text{ W/cm}^{-2}$		$\sim 30 \text{ J/cm}^{-3}$	$0.2 \rightarrow 1.5 \text{ kJ/cm}^{-3}$		

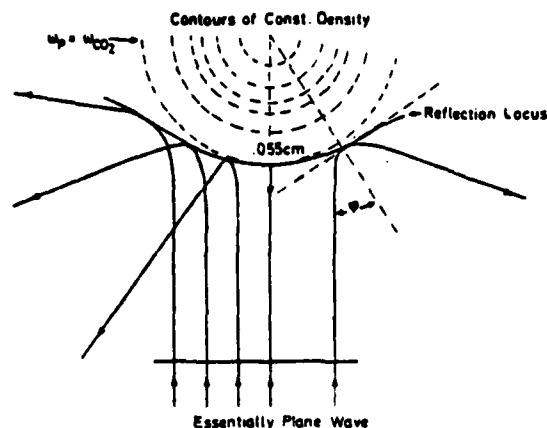


FIG. 9. — Schematic of refracted rays from CO₂ laser pump beam at the time of peak compression during the dense pinch phase of the plasma focus. CO₂ ray paths :

$$\omega_{co_2}^2 = \omega_p^2(r) + c^2(k^2 + K_{inc}^2 \sin^2 \varphi)$$

Reflection Points : ($K_r = 0$)

$$\omega_p(r) = \omega_{co_2} \cdot \varphi.$$

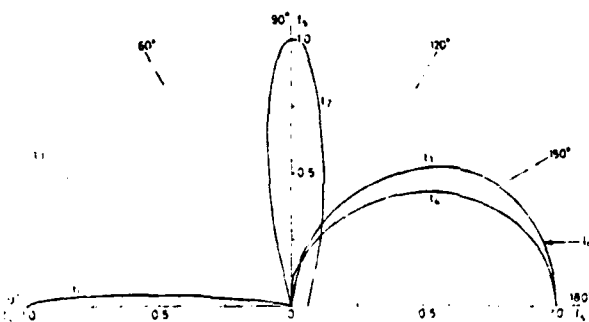


FIG. 10. — Theoretical model for the refracted light, intensity I_a , from a CO₂ laser pump beam during the dense pinch of the plasma focus. I_a is normalised to the peak of the angular intensity distribution at different times, t_1 through t_4 , during the compression. The CO₂ laser operates in the TEM (0, 0) mode with a focal spot diameter, d , of 750 μ m. The density distributions corresponding to n_e and r (plasma) are parabolic.

\hat{n}_e	r	d
$t_1 : 4.0 \times 10^{18} \text{ cm}^{-3}$	0.5 cm	0.075 cm
$t_2 : 1.03 \times 10^{19} \text{ cm}^{-3}$	0.2 cm	0.075 cm
$t_3 : 1.75 \times 10^{19} \text{ cm}^{-3}$	0.15 cm	0.075 cm
$t_4 : 3.5 \times 10^{19} \text{ cm}^{-3}$	0.1 cm	0.075 cm

In practice, the interaction of the CO₂ beam is quite different from what has been anticipated (above) on the basis of a cylindrical plasma with a smooth density gradient and classical resistivity. The results of the irradiation experiments are as follows :

(i) Transmission of the paraxial rays is interrupted for a period of about 80 nanoseconds centred around peak compression. This cut-off in transmission, figure 11, corresponds approximately to the duration for which the plasma is over dense i. e.

$$n_e > n_{ec} = 9.94 \times 10^{18} \text{ cm}^{-3}.$$

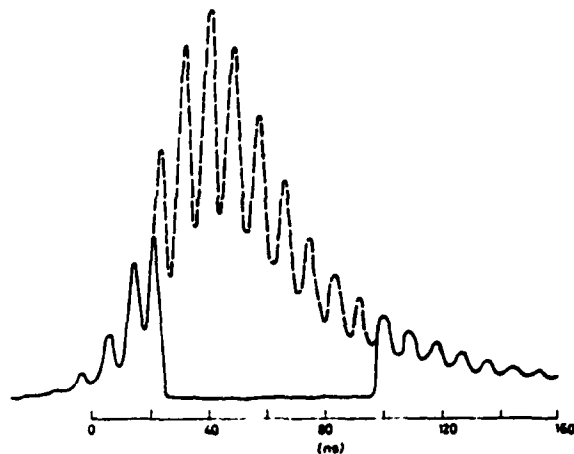


FIG. 11. — Oscillogram of transmitted CO₂ beam intensity during gainswitched pulse ; ----- corresponds to absence of absorbing medium ; ——— corresponds to transmission during dense pinch phase of the plasma focus. Note cut-off in transmission due to plasma when $n_e > n_{ec}$.

Less than one per cent of the incident light Φ_0 is backscattered.

(ii) The refracted intensity, Φ_{ref} , of the pump beam is extremely low being of the same order as the scattered intensity from the underdense outer layers of the plasma i. e.

$$\Phi_{ref} \sim \Phi_0 \sigma_T d\Omega \int_0^{r_{co}} n_e(r) dr.$$

This result appears to be independent of the value of Φ_0 up to the maximum intensity used. It is also independent of the plane of polarisation of the incident pump beam ; both s- or p-type polarisation have been used. The poloidal distribution of Φ_{ref} does not change sharply in time as predicted.

(iii) No gross changes in the operation of the focus, such as the dI/dt characteristic or the neutron yield (in D₂) has been detected when the plasma is irradiated by the CO₂ beam. This is not unexpected since the high thermal conductivity of the electrons will ensure that any fractional change in the heat content due to laser energy absorption is quickly redistributed.

(iv) However, two clear indications of non-linear processes have been observed and those are correlated with absorption of the CO₂ beam by the plasma. Firstly, we observe an increase by about a factor of two in the intensity of the hard x-rays ($E > 70$ keV), presumably due to accelerated electrons striking the central anode. The second feature, which is the subject of most of the remainder of this paper, is an enhancement of the collectively scattered light from a visible (ruby) laser probe.

4. Discussion of CO₂ Laser Beam Absorption. — In addition to resistive absorption, direct resonance coupling between the EM wave and the electron

plasma waves can lead to enhanced absorption at oblique incidence [19]. Maximum resonance absorption can occur for small angles given by

$$\theta_{res} = \sin^{-1} (0.8(K_{CO_2} L)^{-1/3}). \quad (5)$$

Typical scale lengths in this experiment are ~ 0.2 cm so that θ_{res} is close to the experimental angle of incidence set by the F/5.5 focussing lens, figure 8. Appreciable resonance absorption can occur even in under-dense plasma where it is associated with multiple reflections between stratified layers [20]. We anticipate therefore that the refracted 10.6 μ m energy, while finite, will be considerably less than the value, equation (3), calculated from resistive absorption alone.

Resonance absorption is ineffective for the paraxial rays and it is this part of the beam energy which will reach the critical density layer and give rise to non-linear heating. Enhanced absorption of the pump radiation has been predicted in the presence of the decay instability [21] and in view of the consistency of the ruby scattering observations, section 5, with this non-linear process, it may well explain the absence of backscatter in our experiments.

In solid target irradiation experiments corrugation of the critical density surface by the ponderomotive force of the pump beam has been treated theoretically [22, 23]. These authors find that enhanced resonance absorption can result if radiation is trapped in the ripples induced by the laser light pressure. High energy electrons can be generated by a number of mechanisms [24], including acceleration by the electric fields, associated with local plasma oscillations which are created by resonance absorption.

However, in the present experiments the radiation pressure is generally much lower than considered by these authors unless self focussing or *hot spots* occur in the irradiated plasma. Also we observe almost complete loss of the outer regions of the beam which should be refracted well away from the critical surface.

Non-linear, self focusing of the pump beam has been treated by Kaw *et al.*, (1973) [25]. In a slab plasma with $v_{\perp}/v_{th} \sim 0.02$, the plasma length required for self-focusing [26] is several cms, which is longer than our characteristic plasma dimensions. In our conditions, with nearly parabolic density distribution, filamentation of the pump beam is therefore unlikely.

The possibility of a highly-resistive and therefore absorbing region with $n_e \ll n_{ec}$ at larger radii and lower density than the compressed pinch has been raised by recent probe experiments in the plasma focus [27]. The abrupt onset of loss in beam transmission which we observe when $n_e \approx n_{ec}$ tends to discount this explanation.

In summary we can say that the interruption of the transmitted pump beam and the observation of enhanced visible light scattering from electron waves is to be expected in these experiments. On the other hand the extremely low level for the refracted pump

beam intensity lacks a convincing explanation and more experimental work, with fine-scale, angular resolution of the reflected and scattered light is required, as in the studies of Donaldson *et al.* (1976) [28].

5. Light Scattering from Induced Langmuir waves. — Among several instabilities which can arise at relatively low threshold irradiance as a result of strong coupling between the incident light and plasma waves perhaps the most important, apart from optical resonance [19], are the parametric, electron-ion (convective) decay instability (EID) and the oscillating two-stream (absolute) instability (OTS). Either of these mechanisms being operative, Langmuir waves will be driven in the direction of the E field polarisation vector of the pump beam. Stimulated Brillouin scattering with a slightly higher threshold is also a possibility especially since this instability can take place in the under-dense plasma region. Absence of a measurable backscatter of the incident beam due to ion-acoustic fluctuations tends to make us discount this instability in the present experiments. Figure 12 illustrates the geometry chosen to detect ruby laser

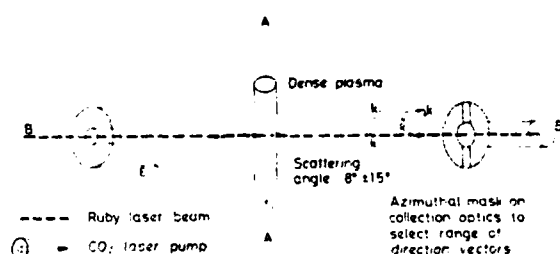


FIG. 12. — Schematic diagram of CO₂ pump beam and ruby laser probe beam relative to axis of symmetry, AA, of the focus device. Scattered ruby light is collected in the forward direction at 8° to the incident beam. The azimuthal mask can be rotated to select \vec{K}_L vectors which are parallel to the polarisation vector \vec{E} of the CO₂ laser.

light scattered preferentially from the induced electron waves. We discriminate against waves due to optical resonance coupling by probing only those waves \vec{K}_L which are orthogonal to $\vec{\nabla} n_e$. Likewise, \vec{K}_L is orthogonal to \vec{j} and to current-driven ion acoustic waves.

Experimentally scattering from the electron waves will show up as a rather narrow spectral feature, shifted from the ruby frequency ω_0 by an amount given by

$$\omega_L = \omega_{CO_2} - \omega_i. \quad (6)$$

Inserting the dispersion relation for the Langmuir waves, ω_L , the ion acoustic waves, ω_i , we have

$$\begin{aligned} \omega_{pe} [1 + 3(K_L/K_D)^2]^{1/2} &= \\ &= \omega_{CO_2} - 1.8 \left(\frac{m_e}{m_i} \right)^{1/2} \cdot \left(\frac{K_L}{K_D} \right) \cdot \omega_{pe} \end{aligned} \quad (7)$$

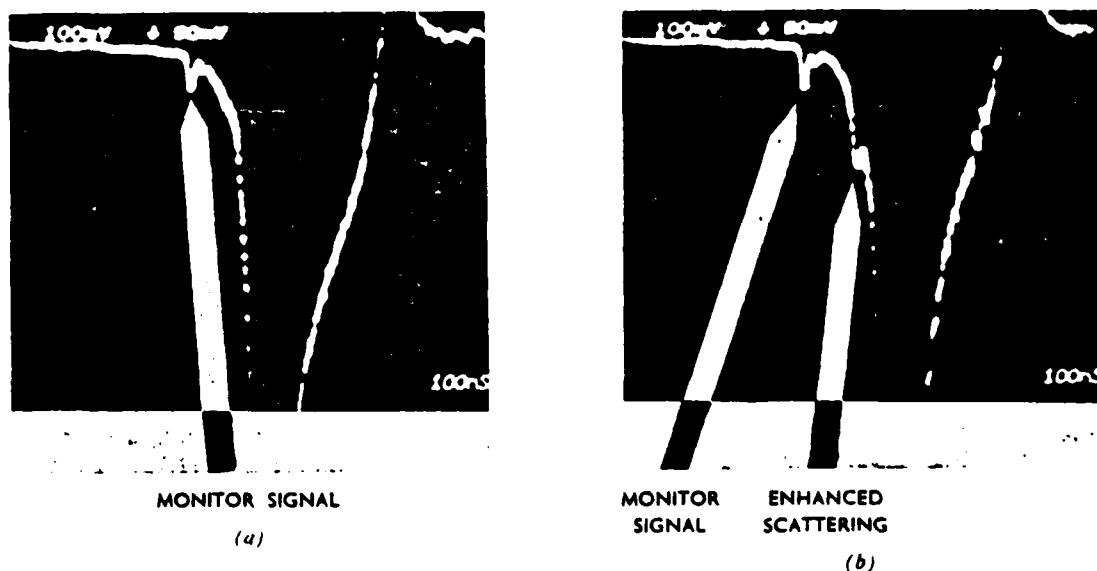


FIG. 13. — Light signal accepted by photomultiplier in the ruby laser scattering optics (Fig. 8). A photodiode provides a prompt, monitor signal of the ruby laser pulse, 35 nanoseconds before peak compression of the pinch. Scattered light signal and background light from the plasma are delayed 110 ns relative to prompt pulse. (a) No CO₂ laser irradiation; (b) CO₂ laser focused on pinch.

where ω_p is the local plasma frequency and the ratio of the inverse Debye length, $K_D = 1/\lambda_D$, to the Langmuir wave number, $K_L = 2\pi/\lambda_L$, i. e. (K_D/K_L) , can be identified with the scattering parameter α . In our experiment with a mean scattering angle, $\theta = 8^\circ$ and $\alpha \approx 10$ then the differential scattering vector

$$|\vec{K}| = |\vec{K}_0 - \vec{K}_s| = \frac{K_D}{\alpha} = 1.26 \times 10^4 \text{ cm}^{-1}. \quad (8)$$

The frequency shift imposed on the scattered ruby light due to scattering from the electron waves, is from equation (7),

$$\omega_L \approx \omega_{CO_2} = 1.78 \times 10^{14} \text{ s}^{-1} \quad (9)$$

corresponding to a wavelength shift of,

$$\Delta\lambda = \pm 427.4 \text{ \AA}.$$

A narrow band filter, accepts scattered light in the region $6500 (\pm 25) \text{ \AA}$, is inserted in the scattering optics, figure 8, to suppress spuriously scattered laser light and background light from the discharge.

Under conditions of no pump irradiation no signal above the noise level was measured indicating that the background intensity of Langmuir waves in the unpumped plasma is not more than a factor of two or so above the thermal level.

Similar conclusions have been reported for the intensity of the ion waves by Forrest and Peacock (1974) [13]. When irradiated by the pump beam, however, the intensity of the ruby light scattered from electron waves is observed, figure 13, and can reach a factor of 30 above the thermal level

as the pump intensity is increased beyond a threshold of about $3 \times 10^9 \text{ W/cm}^2$, in vacuo.

Figure 14 shows the effect of the CO₂ laser pump intensity on the intensity of the scattered probe light at a time corresponding to 30 ± 10 nanoseconds before peak compression. The density scale length at this time is $L \sim 0.2 \pm 0.05 \text{ cm}$ and the density, $n_e \sim 10^{19} \text{ cm}^{-3}$, is sufficiently high for frequency matching of the pump and the electrostatic plasma waves according to equation (7). No scattered signal is observed above the thermal level at times earlier

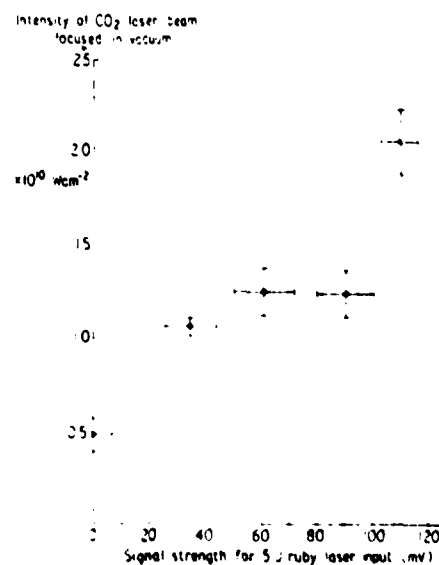


FIG. 14. — Intensity of light scattered from ruby laser by electron waves, as a function of CO₂ laser pump intensity.

in the pinch compression when $n_e \ll n_{ec}$, even with maximum pump power. Again, no enhanced scattering is observed at peak compression when, although $n_e \lesssim n_{ec}$, the density scale length, L , has decreased to 0.03 cm.

A summary of the time-dependence of the scattered light signal is shown schematically in figure 15 up to the time $t = 0$ ns when maximum compression occurs.

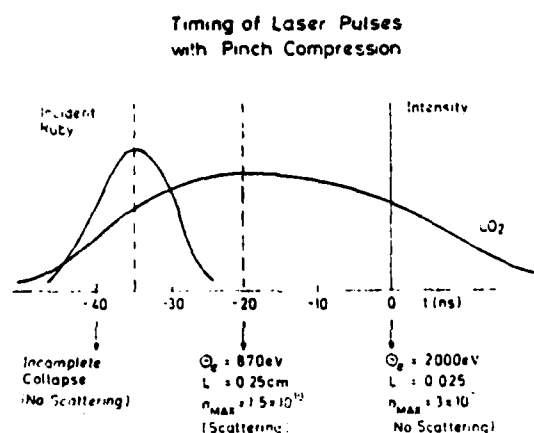


FIG. 15. — Summary of plasma parameters and relative durations of CO₂ and ruby laser pulses during the compression phase of the plasma focus.

6. Intensity of the Induced Langmuir waves. —

Consideration of the processes giving rise to enhanced intensity in the electrostatic waves indicated that «OTS» and «EID» instabilities require about the same threshold intensity. This is set by the requirement that wave growth exceeds losses due to damping and convection out of the interaction region. In its simplest form the threshold intensity is reached when

$$(v_e/v_{th})^2 > \gamma/\omega_{pe}, \quad (10)$$

where γ is the electron wave damping rate. Using the analysis of Perkins and Flick (1971) [29] for an inhomogeneous plasma, where $T_e \gg T_i$, the threshold for EID is

$$(v_e/v_{th})^2 \gtrsim (1 + 3T_i/T_e) \frac{8}{K_L L} \left(\frac{\gamma_i}{\omega_i} \right)^{1/2} + 3.2 \left(\frac{\gamma_i}{\omega_i} \right) \left(\frac{v_e}{\omega_{pe}} \right) \quad (11)$$

v_e is the effective electron-ion collision frequency and γ_i the ion damping frequency. In our experiment $(v_e/v_{th}) < 0.1$ and terms of the order $(K_L L)^{-1}$ tend to restrict the wave growth, rather than collisional processes. The threshold pump intensity when the swelling of the pump wave, equation (4), is taken into account is $\Phi_{th}(\text{vacuo}) \sim 3 \times 10^9 \text{ W/cm}^2$; close to the observed value, figure 14. It is worth noting that when $L < 0.05 \text{ cm}$ which occurs close to

peak compression, figure 4, then $\Phi_{th}(\text{vacuo})$ exceeds the available pump power. More recently, Goldman and Rudolph in [30], have calculated the linear growth of electron waves driven by the EID instability and their convection in an inhomogeneous $T_e = T_i$ plasma, using WKB theory and including swelling of the pump intensity. Their derivation of the threshold intensity agrees with equation (11) and their derivation of the *absolute* intensity allows a direct comparison with the observed scattering cross-sections. Firstly, however, we require to calculate the plasma volume responsible for the scattered light signal. Each radial layer, within which the frequency match, equation (6), is satisfied, will contribute to the intensity of the electron feature.

The total spread in frequency of the electron feature is made up of a shift from the pump frequency equal to $\pm \omega_i$, the ion acoustic frequency, and a broadening $\delta\omega_m$ due to an allowed mismatch

$$\delta\omega_m = PK_L v_e (m_e/m_i)^{1/2} / \sqrt{2} \quad (12)$$

where P is the pump intensity above threshold. There is in addition, a spread in frequency due to the finite range of wave vectors accepted by the scattering optics. Typically, the ion acoustic frequency, ω_i , produces a wavelength shift of $0.5 \rightarrow 1.0$ angstrom and the total broadening $(\delta\omega_m + \delta\omega_{optics})$ amounts to a few angstroms. The incremental plasma radius contributing to the electron feature is therefore

$$(\omega_i + \delta\omega_m + \delta\omega_{optics}) \left| \frac{\partial\omega_{pe}}{\partial r} \right|^{-1}. \quad (13)$$

This radial increment is defined in figure 16 by the inner boundary r_{co} at which $\omega_L = \omega_{CO_2}$ and an outer boundary r_t , where the frequency match condition, equation (6), can just be satisfied. A typical value for $r_{co} - r_t$ is 100 microns which is considerably smaller than the radial increment viewed by the 50 Å band-pass filter. An enhancement of 30 above the thermal level is observed, averaged over the 50 Å volume; it would appear therefore that much higher wave intensities is to be expected locally, within $r_t - r_{co}$.

A plot of the radial variation of the plasma frequency and of the scattering parameter $\alpha = K_D/K$, emphasises the constraints in real space and time over which the conditions for enhanced scattering from either EID or OTS driven electron waves can be satisfied. As shown in figure 17 the density is only sufficiently high for a frequency match between the pump EM beam and electron plasma oscillations within the 40 nsecs prior to peak compression.

Typically within this period $\omega_{pe} = \omega_{CO_2}$ at a plasma radius $r_{co} \sim 0.02 \text{ cm}$ where the scattering parameter $\alpha \gtrsim 15$. This high value of α ensures that Landau damping of the electron waves is negligible compared to resistive damping. (The ion waves are heavily Landau damped since $T_e \approx T_i$.) On the other hand

the Langmuir intensity is $\frac{1}{2}$ of its value, $I(t_f)$ at its turning point.

In figure 18b we illustrate the curved scattering volume by an equivalent slab with the orthogonal Langmuir wave number $K_y = K_L = K_D/\alpha$. In this figure x_0 is the reflection point.

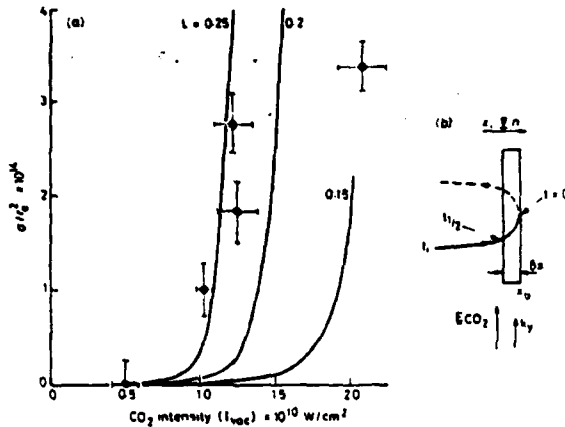


FIG. 18. — (a) Plasma scattering cross section as a function of focussed CO₂ laser intensity. Experimental points are compared with predictions of WKB theory with the parameter density scale length, L , assuming values of 0.25, 0.2 and 0.15 cm and with a constant value of $T_e = 300$ eV. (b) Langmuir ray paths.

Integration along the ray path from an initial time t_i , at which the net growth rate is zero and $I(t_i)$ is unity, to a final time t_f at which the Langmuir wave is reflected, gives

$$I(t_f) = \left[\frac{\alpha(m_i/m_e)^{1/2}}{1.7} \right] \exp \left[\frac{5}{256} \cdot L K_y \cdot \frac{\bar{E}^2}{n K T_e} \right]. \quad (18)$$

The exponent contains the local CO₂ laser electric field strength, \bar{E}^2 , modified from the vacuum intensity by absorption and by the geometric optics swelling factor. The dominant term in the wave amplitude is

the spontaneous beat emission which leads to fluctuation levels which are several orders of magnitude above thermal and which are confined to a very limited region in space with $\delta r \approx 5 \times 10^{-4}$ cm i. e. $\ll r_i - r_{co}$.

The integrated scattering cross section is given approximately by

$$\sigma = (r_e/\alpha)^2 \cdot n_e \cdot V_s \cdot \delta\Omega_s \cdot I(K). \quad (19)$$

Here r_e is the electron radius and $\delta\Omega_s$ is the solid angle subtended by the scattering optics.

$$I(K) = \lim_{V \rightarrow 0} \langle |\delta E(K)|^2 \rangle / 4 \pi n k T_e V$$

is the spectral intensity of the longitudinal field fluctuations normalised to unity in equilibrium.

Evaluation of all the quantities in equation (19) leads to the plots for σ/r_e^2 shown in figure 18a with the scale length L as a parameter. T_e is assumed to be 300 eV and the frequency matched density 9.8×10^{18} cm⁻³. The observed scale length $L = 0.25$ cm gives about the best fit with the theory at least up to the intensity where one might expect the linear saturation theory to break down.

In summary, the calculated threshold for the parametric electron ion — decay instability and its dependence on scale length is consistent with the experiment; and the inhomogeneous linear saturation theory appears to give a fairly satisfactory fit to the data at CO₂ laser intensities around 10^{10} W/cm² and below. A definite identification of the electron-ion decay instability may be resolved with further measurements, particularly of the *off set* frequency difference between the Langmuir waves and the driving CO₂ laser frequency.

Finally, it is interesting to note that broadly similar experimental results have been reported in quite independent plasma focus experiments [31] by Tanimoto and co-authors (1976), using somewhat higher CO₂ laser irradiation intensities. These authors conclude that the parametric instability is the most likely cause of induced Langmuir waves.

References

- [1] PEACOCK, N. J. *et al.*, 3rd IAEA Conf. on Plasma Physics and Controlled Nuclear Fusion Research, Novosibirsk, Proceedings 2, 51-65 (Published IAEA Vienna) (1969).
- [2] SIGEL, R., EIDMANN, K., PANT, H. C., SACHSENMAIER, P., *Phys. Rev. Lett.* 36 (1976) 1369.
- [3] YAMANAKA, C., Proceedings of Seminar on Laser Interaction with Matter, 32-50. Institute of Laser Engineering, Osaka University (1977).
- [4] OFFENBERGER, A. A., CERVENAN, M. R., YAM, A. M., PASTERNAK, A. W., *J. Appl. Phys.* 47 (1976) 1451-1458.
- [5] DUBOIS, D. F. and GOLDMAN, M. V., *Phys. Rev. Lett.* 14 (1965) 544-546.
- [6] DUBOIS, D. F. and GOLDMAN, M. V., *Phys. Rev.* 164 (1967) 207-222.
- [7] GOLDMAN, M. V., *Ann. Phys.* 38 (1966) 117-169.
- [8] NISHIKAWA, K., *J. Phys. Soc. Japan* 24 (1968) 1152-1158.
- [9] MORGAN, P. D. and PEACOCK, N. J., Proceedings of 2nd Topical Conference on Pulsed High Beta Plasmas, Garching (1972) 179-182 (Max Planck Inst. für Plasma-physik, IPP 1/127).
- [10] MORGAN, P. D., « Optical Refractivity Studies of Plasma Focus », Ph. D Thesis, University of London (1974).
- [10] PEACOCK, N. J., HOBBS, M. G. and MORGAN, P. D., Proceedings of 4th Int. Conf. on Plasma Physics and Controlled Nuclear Fusion Research (Published IAEA Vienna) Vol. 1, 1971 537-552.
- [11] BERNARD, A. *et al.*, 5th IAEA Conf. on Plasma Physics and Controlled Nuclear Fusion Research, Tokyo, Proceedings (Published IAEA Vienna) 3 (1975) 83-98.
- [12] BERNARD, A. *et al.*, *Phys. Fluids* 18 (1975) 180-194.

- [13] FORREST, M. J. and PEACOCK, N. J., *Plasma Phys.* 16 (1974) 489-498.
- [14] EVANS, D. E., *Plasma Phys.* 12 (1970) 573.
- [15] POTTER, D. E., *Phys. Fluids* 14 (1971) 1911-1924.
- [16] KURIKI, K. and PEACOCK, N. J., «Plane-polarised CO₂ laser beam from an unstable confocal resonator», Culham Report CLM-P446 (1976).
- [17] SHEARER, J. W., *Phys. Fluids* 14 (1971) 183-185.
- [18] DAWSON, J., KAW, P. and GREEN, B., *Phys. Fluids* 12 (1969) 875-882.
- [19] FREIDBERG, J. P., MITCHELL, R. W., MORSE, R. L. and RUDSINSKI, L. I., *Phys. Rev. Lett.* 28 (1972) 795-799.
- [20] MUELLER, M. M., *Phys. Rev. Lett.* 30 (1973) 582-585.
- [21] DUBOIS, D. F., GOLDMAN, M. V. and MCKINNIS, D., *Phys. Fluids* 16 (1973) 2257-2269.
- [22] FORSLUND, D. W., KINDEL, J. M., LEE, K., LINDMAN, E. L., *Phys. Rev. Lett.* 36 (1976) 35-38.
- [23] KINDEL, J. M., LEE, K., LINDMAN, E. L., *Phys. Rev. Lett.* 34 (1975) 134.
- [24] BEZZERIDES, B., DUBOIS, D. F., FORSLUND, D. W., KINDEL, J. M., LEE, K. and LINDMAN, E. L., 6th IAEA Conf. on Plasma Physics and Controlled Nuclear Fusion Research, Berchtesgaden. Proceedings series. Supplement Vol. 1, 123-129 (Published IAEA Vienna) 1977.
- [25] KAW, P., SCHMIDT, G. and WILCOX, T., *Phys. Fluids* 16 (1973) 1522-1525.
- [26] HAAS, R. A., BOYLE, M. J., MANES, K. R., SWAIN, J. E., *J. Appl. Phys.* 47 (1976) 1318-1321.
- [27] BERNARD, A. et al., 6th IAEA Conf. on Plasma Physics and Controlled Nuclear Fusion Research, Berchtesgaden. Proceedings series. Supplement Vol. 3, 471-482 (Published IAEA Vienna) 1977.
- [28] DONALDSON, T. P., HUBBARD, M., SPALDING, I. J., *Phys. Rev. Lett.* 37 (1976) 1348-1351.
- [29] PERKINS, F. W. and FLICK, J., *Phys. Fluids* 14 (1971) 2012-2018.
- [30] FORREST, M. J. et al., *Phys. Rev. Lett.* 37 (1976) 1681-1684.
- [31] TANIMOTO, M., KOYAMA, K., MATSUMOTO, Y. and SUGIURA, M., 6th IAEA Conf. on Plasma Physics and Controlled Nuclear Fusion Research, Berchtesgaden. Proceedings series. Supplement Vol. 2 605-612 (Published IAEA Vienna) (1977).